

7-309

Middle Atmosphere Program

HANDBOOK FOR MAP VOLUME 22

Edited by
James M. Russell, III

(NASA-TN-89273) MIDDLE ATMOSPHERE
COMPOSITION REVEALED BY SATELLITE
OBSERVATIONS (NASA) 309 P

CSCL 04A

N87-13874

Unclas
G3/46 43611

ICSU

International Council of Scientific Unions

SCOSTEP

Scientific Committee on Solar-Terrestrial Physics

J. G. Roederer, President
W. I. Axford, Vice President
C. H. Liu, Scientific Secretary

MAP ORGANIZATION

MIDDLE ATMOSPHERE PROGRAM STEERING COMMITTEE

S. A. Bowhill, SCOSTEP, Chairman
K. Labitzke, COSPAR, Vice Chairman
C. H. Liu, SCOSTEP, Secretary

H. S. Ahluwalia, IUPAP
R. D. Bojkov, WMO
A. D. Danilov, COSPAR
J. C. Gille, COSPAR
I. Hirota, IUGG/IAMAP
A. H. Manson, SCOSTEP

L. R. Megill, IUGG/IAGA
T. Nagata, SCAR
R. G. Roper, IAMAP
P. C. Simon, IAU
J. Taubenheim, IUGG/IAGA
T. E. VanZandt, URSI

R. A. Vincent, URSI

MAP STANDING COMMITTEES

Data-Management -- G. Hartmann and I. Hirota, Co-Chairmen
Dynamics Calendar -- T. E. VanZandt, Chairman
Publications -- C. F. Sechrist, Jr., Chairman

MAP STUDY GROUPS

MSG-5 Ions and Aerosols, F. Arnold and M. P. McCormick, Co-Chairmen
MSG-8 Atmospheric Chemistry, G. Witt, Chairman
MSG-9 Measurement of Middle Atmosphere Parameters by Long Duration
Balloon Flights, J. E. Blamont, Chairman

APPROVED MAP PROJECTS

	Coordinator		Coordinator
AMA:	T. Hirasawa	MAC-Epsilon:	E. V. Thrane
ATMAP:	J. M. Forbes	MAC-SINE:	E. V. Thrane
CAMP:	G. Witt	MAE:	R. A. Goldberg
CLIMAT:	J. M. Russell	MASH:	A. O'Neill
DYNAMICS:	K. Labitzke	MSTRAC:	P. K. Rastogi
GLOBMET:	R. G. Roper	NIEO:	S. Kato
GLOBUS:	J. P. Pommereau	OZMAP:	D. F. Heath
GOSSA:	M. P. McCormick	SSIM:	P. C. Simon
GRATMAP:	D. C. Fritts	WINE:	U. von Zahn

MAP REGIONAL CONSULTATIVE GROUP

Europe M. L. Chanin, Chairman

M I D D L E
A T M O S P H E R E
P R O G R A M

HANDBOOK FOR MAP

Volume 22

Edited by

James M. Russell, III

September 1986

Published for the ICSU Scientific Committee on Solar-Terrestrial Physics (SCOSTEP) with financial assistance from the National Aeronautics and Space Administration under the 1986 Middle Atmosphere Program Management contract and Unesco Subvention 1986-1987.

Copies available from SCOSTEP Secretariat, University of Illinois, 1406 W. Green Street, Urbana, Illinois 61801

Table of Contents

Introduction	1
Experiment Descriptions.	4
LIMS.	4
SAMS.	8
SAM II.	11
SAGE.	13
SBUV.	15
SME	17
Satellite Data Description	18
Temperature	18
Ozone (O_3).	19
Nitrogen Dioxide (NO_2).	22
Methane (CH_4), Nitrous Oxide (N_2O), and Water Vapor (H_2O) . . .	25
Nitric Acid (HNO_3).	28
Carbon Monoxide (CO).	30
Aerosols.	30
Summary.	32
Acknowledgments.	32
References	32

Figures

Temperature

LIMS monthly zonal mean temperature cross section	39
SAMS monthly zonal mean temperature cross section	53

Ozone

LIMS and SBUV monthly zonal mean and SAGE 2-day zonal mean ozone profile comparisons.	77
Comparison of zonal mean LIMS ozone with SME and the Kureger- Minzer annual mean ozone climatology	78
LIMS monthly zonal mean ozone cross section	79
SBUV monthly zonal mean ozone cross sections.	107
SAGE monthly zonal mean ozone cross section	163
SME monthly zonal mean ozone cross sections	173

Nitrogen

LIMS monthly zonal mean cross sections.	197
SAGE monthly zonal mean cross sections.	218

Methane, Nitrous Oxide, and Water vapor

SAMS monthly zonal mean CH_4 cross sections.	237
SAMS monthly zonal mean N_2O cross sections.	249
LIMS monthly zonal mean H_2O cross sections and polar stereographic plots.	261

Nitric Oxide

LIMS monthly zonal mean HNO_3 cross sections and stereographic projections.	275
Derived OH compared with in situ observations	289

Carbon Monoxide

SAMS carbon monoxide volume mixing ratio profiles	290
---	-----

Aerosols

SAGE monthly zonal mean aerosol extinction ratio.	291
SAGE seasonal zonal mean aerosol cross sections	298
SAM II measurements in the Northern Hemisphere.	301
SMA II measurements in the Southern Hemisphere.	302

Middle Atmosphere Composition Revealed by Satellite Observations

by

James M. Russell III¹, Susan Solomon², M. P. McCormick¹,
A. J. Miller³, J. J. Barnett⁴, R. L. Jones⁶, and D. W. Rusch⁵Introduction

A significant step forward has occurred in middle atmosphere studies with the launches of the Nimbus 7, Atmospheric Explorer II (AEM-II), Solar Mesospheric Explorer (SME), and Earth Radiation Budget (ERBS) satellites. These flights, coupled with earlier Nimbus missions, now provide a good data base for scientific investigation of photochemistry, dynamics, and radiation processes and for study of coupling among these processes and between solar variations and the atmosphere. The earlier flight of the Backscatter Ultraviolet (BUV) instrument on Nimbus 4 and the flight of the Solar Backscatter Ultraviolet (SBUV) experiment on Nimbus 7 has provided data for study of long-term ozone trends and their relation to solar flux. In addition, for the first time, a comprehensive near-global data base on the odd nitrogen (NO_x) chemistry is available from the Nimbus 7 Limb Infrared Monitor of the Stratosphere (LIMS) experiment, the Stratospheric and Mesospheric Sounder (SAMS), the Solar Mesosphere Explorer (SME), and the AEM II Stratospheric Aerosol and Gas Experiment (SAGE) which collectively provided data on vertical profiles of temperature, O_3 , NO_2 , N_2O , HNO_3 , H_2O , CH_4 , CO , and aerosols. In addition, the SAGE II experiment on the ERBS is now collecting data on ozone, NO_2 , H_2O , and aerosols. These data will be available in the future after the validation period is over. No global data exist at present on the odd chlorine (Cl_x) and odd hydrogen (HO_x) chemistry although important information has been obtained on the HO_x source molecules CH_4 and H_2O by SAMS and LIMS, respectively. The odd chlorine chemistry is one focus of the Upper Atmosphere Research Satellite (UARS) to be launched near the end of this decade. UARS will also provide the first opportunity for simultaneous global observation of two chemical families (NO_x and Cl_x).

Much of the data collected has been reduced and archived, and a number of scientific studies have been conducted. Data from Nimbus 7 that have been archived at the National Space Sciences Data Center (NSSDC) includes 1 year of

✓¹NASA Langley Research Center, Hampton, Virginia

²NOAA, Environmental Research Laboratory, Boulder, Colorado

³NOAA, National Weather Service, Washington, D.C.

⁴Oxford University, Oxford, England

⁵U. of Colorado, Laboratory for Atmospheric and Space Physics, Boulder, Colorado

⁶British Meteorological Office, Bracknell, England. Work performed while at Oxford University.

SBUV results, 2 years of SAMS temperature, N_2O , and CH_4 results, all 7 months of LIMS data (temperature, O_3 , NO_2 , HNO_3 , and H_2O), and 4 years of aerosol data from the Stratospheric Aerosol Measurement II (SAM II). All 3 years of aerosol, O_3 , and NO_2 data from the SAGE experiment launched in February 1979 have been archived as have 1 year of data (1982) from SME launched October 6, 1981. The SME data includes solar flux in the 1100 Å region and vertical profiles of O_3 , NO_2 , and temperature. Daily averaged O_3 is available from SME in 5° latitude bins for the pressure range 0.002 mb to ~ 30 mb in the first 3 months and ~ 0.002 mb to 1 mb in the remainder of the year. NO_2 data are available in the 2 mb to 30 mb range for the first 3 months only. After that time, eruption of the El Chichon Volcano caused an atmospheric aerosol loading that swamped or severely contaminated the signal. Beginning April 1982, SME provided data on the spatial extent and variability of the volcanic cloud. Data reduction is continuing for later years of the mission. For the first time, the data base exists to address many of the key middle atmosphere questions outlined in Table 1. A summary of investigations and findings from all these missions is included in the following paragraphs.

Several general features of the upper atmosphere have emerged from the data analyses conducted thus far. It is clear from LIMS, SAGE, and SME data that NO_2 exhibits rapid latitudinal variations in winter and shows hemispheric asymmetry with generally higher vertical column amount in the summer hemisphere. It also appears that southern summer values are greater than mixing ratios in the northern summer presumably because of differences in the circulation patterns. LIMS HNO_3 data show that this gas is highly variable

TABLE 1 - KEY MIDDLE ATMOSPHERE QUESTIONS

- WHAT ARE THE GLOBAL DISTRIBUTIONS OF KEY CONSTITUENTS?
 - WHAT ARE THE DAILY AND SEASONAL CHANGES IN THESE CONSTITUENTS?
 - HOW DRY IS THE STRATOSPHERE? IS THERE A HYGROPAUSE?
 - IS METHANE OXIDATION AN IMPORTANT STRATOSPHERIC H_2O SOURCE?
 - HOW ARE WATER VAPOR AND OTHER CONSTITUENTS TRANSPORTED INTO AND OUT OF THE UPPER ATMOSPHERE?
 - WHAT IS THE REASON FOR THE STEEP NO_2 DECREASE WITH INCREASING LATITUDE IN WINTER?
 - IS THE THERMOSPHERE/MESOSPHERE A NO_x SOURCE OR SINK FOR THE STRATOSPHERE?
 - WHAT ARE THE GLOBAL BUDGETS OF NO_x AND H_2O ?
 - IS THERE A POLAR NIGHT NO_x STORAGE MECHANISM, AND IF SO, WHAT IS IT?
-

with both latitude and season. The mixing ratio is smallest in the Tropics and largest in the winter hemisphere at high latitudes. The data also show that O_3 , NO_2 , and HNO_3 levels are strongly affected during a major stratospheric warming event. The results demonstrate for example, that O_3 tends to propagate downward in altitude during a high latitude warming situation, NO_2 latitudinal gradients are greatly reduced, and the HNO_3 high latitude longitudinal gradients are diminished. LIMS has also provided the first detailed view of the global water distribution. There is a persistently low mixing ratio of about ~ 3 ppmv in the tropical lower stratosphere, a poleward gradient at all times during the mission, and evidence of increasing mixing ratio with altitude at tropical and mid-latitudes. Perhaps even more interesting is the picture of the general two-dimensional stratospheric circulation suggested by the data. The strongest circulation appears to be toward the winter pole at high altitudes as theory would predict and there is evidence of lower altitude stratospheric transport toward the summer pole. This picture is reinforced in CH_4 and N_2O data from the SAMS experiment which shows mixing ratio enhancements or depressions that tend to coincide with areas where the LIMS H_2O would suggest strong or weak circulations.

In other studies using SME data, results show that ozone density in the mesosphere changes from day to day and with the seasons (Barth et al., 1983). The largest variations appear to be temperature induced. Ozone density and temperature are inversely related, i.e., when temperatures are high, ozone levels are low and vice versa. This dependence is also seen in seasonal patterns and orbit-to-orbit variations. In the lower mesosphere (1-0.1 mb), maximum mesospheric ozone occurs in the winter hemisphere and the variations are greater in winter than in summer (Thomas et al., 1983). Ozone time series from SME for 45°S show greater variability in Southern Hemisphere winter and less in summer. In the upper mesosphere (near 0.01 mb), a systematic semiannual cycle is observed, with maximum O_3 occurring at the equinoxes. This interesting feature probably reflects the influence of breaking small scale gravity waves, and shows the important role of mesospheric transport processes (Thomas et al., 1984; Garcia and Solomon, 1985). Comparison of ozone levels with the latest model calculations at 1 mb and 0.1 mb show observations by SME to be higher by 10 percent to 30 percent. This is the case for all other satellite results as well.

Perhaps one of the most exciting results to date from SME is the measurement of ozone during a solar proton event in July 1982 (Thomas et al., 1983). The ozone levels were observed to decrease by up to 60 percent at 76 km and 70°N latitude. These changes are well outside the natural variability observed by SME prior to and after that time. Solomon et al. (1983a) have carried out coupled ion-neutral chemistry 1-D model calculations (time scales are short so transport effects can be neglected) and obtain good agreement with the observed O_3 depletion. A similar event was observed previously by the Backscatter Ultraviolet (BUV) experiment on Nimbus 4 (Heath et al., 1977). The primary cause for this effect is believed to be production of odd hydrogen ($H+OH+HO_2$) which catalytically destroys ozone. The proton flux leading to ionization rates used in the calculations was measured by instrumentation on the NOAA-6 satellite.

There have also been several investigations published or submitted for publication which show great potential for using existing data to calculate the mixing ratios of some gases not measured directly. Pyle et al. (1983)

showed a calculation of the hydroxyl radical (OH) altitude versus latitude distribution using LIMS NO_2 and HNO_3 data which qualitatively compares well with theory. Similarly, Solomon et al. (1983b) have used SME NO_2 results to infer an N_2O_5 latitudinal distribution. More recently, Callis et al. (1986) conducted studies using LIMS and SAMS data to infer altitude versus latitude cross sections of $\text{O}(^3\text{P})$, $\text{O}(^1\text{D})$, OH, HO_2 , H_2O_2 , NO, NO_3 , N_2O_5 , HNO_4 , total odd nitrogen, and total odd hydrogen.

The purpose of this paper is to provide a collection of satellite results obtained to date in the form of monthly zonal mean cross sections and polar stereographic projections, to provide a description of the data and their limitations, and to point out salient features of the morphology of constituent distributions. An overview of measurements, latitude coverage, altitude coverage, vertical resolution, accuracy, and precision is provided in Table 2. It is intended that this paper be a convenient reference document for use in comparing observations with two-dimensional model results and for crude checks of three-dimensional models. These data also provide improved background information for chemical and dynamical studies. The data period presented will cover the first year after the Nimbus 7 launch and the first 12 months of SME data. The focus of the results is on minor constituents. Ozone and temperature results are included since both are needed in photochemical studies; however, detailed discussion of these variables is not presented since these will be discussed in three concurrent activities sponsored by COSPAR and MAP. These efforts include generation of a COSPAR International Reference Atmosphere (CIRA) for ozone, the MAP project--OZMAP, to analyze variability, and the Pre-MAP Project, PMP-1, to intercompare satellite and in situ temperature results (Rodgers, 1984; Grose and Rodgers, 1986). The next section of this paper provides a brief description of each experiment including instrument description, measurement approach, altitude range, vertical resolution, latitude coverage, data accuracy, and data precision. This section is followed by a description of the data highlighting significant features.

Experiment Descriptions

Limb Infrared Monitor of the Stratosphere (LIMS)

The LIMS experiment used a thermal infrared limb scanning radiometer with six channels centered at wavelengths ranging from 6.2 μm to 15.0 μm [see Russell and Gille (1978), Gille et al. (1980), Gille and Russell (1984) and Russell, 1984]]. The experiment was turned on in orbit on October 24, 1978, and it operated nearly flawlessly for the planned 7-1/2 month lifetime until May 28, 1979, measuring vertical radiance profiles across the atmospheric limb of the Earth. These profiles were later processed on the ground to infer middle atmosphere temperature profiles and the concentrations of key compounds believed to be important in the stratospheric ozone photochemistry. The experiment lifetime was limited by the $\text{NH}_3 - \text{CH}_4$ solid cryogen cooler used to cool the six HgCdTe-detectors to a temperature of 64°K. The six channels included two in the 15 μm CO_2 band for two color temperature-pressure sensing, and others at 11.3 μm for nitric acid (HNO_3) retrieval, 9.6 μm for ozone (O_3), 6.9 μm for water vapor (H_2O), and 6.2 μm for nitrogen dioxide (NO_2). The standard approach for thermal infrared remote sensing was used. First, by measuring emission in the band of a gas whose mixing ratio is known (i.e.,

TABLE 2 - MIDDLE ATMOSPHERE COMPOSITION MEASUREMENTS AND COVERAGE

EXPERIMENT	CONSTITUENT	MEAS. RANGE (KM)	ACC.* (%)	PREC. (%)	VERT. RES. (KM)	LATITUDE COVERAGE
LIMS	O ₃	10-65	±15-40	3	2.8	64°S-84°N
	NO ₂	10-50	±20-50	3	5	
	H ₂ O	10-50	±18-36	6	5	
	HNO ₃	10-50	±17-45	4	2.8	
SAMS	CH ₄	28-52	±17-50	3-15	>8	50°S-70°N**
	N ₂ O	28-58	±20-50	6-20	>8	
	CO	45-100	-57+130	25	>8	
SAGE/ SAM II	O ₃	10-50	± 6-40	5-40	1	80°S-80°N (SAGE)
	NO ₂	25-45	± 30	10	3	64°-80° N & S
	aerosols	10-35	± 5-20	5	1	(SAM II)
SME	O ₃	50-90	± 8-50	6-20	3.5	84°S-85°N
	NO ₂	20-40	±20-60	2-25	3.5	(SUNLIT PORTION)
SBUV	O ₃	25-55	± 7-9	8	8	80°S-80°N (SUNLIT PORTION)

*Root Sum Square of Systematic and Random Errors

**CO data are averaged over 6-month time period and 35° wide latitude bands

COLLECTIVE LIST - O₃, NO₂, N₂O, HNO₃, CH₄, H₂O, CO, and AEROSOLS

CO₂), the temperature profile was inferred and then by measuring emission in other bands, the unknown mixing ratios were retrieved. Since the observed parameter was horizon thermal emission, data were collected both night and day providing a data base for diurnal change investigations to be conducted and allowing the high latitude polar night region of the Northern Hemisphere to be sounded. This region of the globe has been of particular interest recently because of questions and theories that have arisen concerning storage of NO_x compounds in the polar night, the possibility of a high altitude polar night source of NO_x for the stratosphere, build-up of water vapor at low altitudes, and mesospheric ozone increases with time. The LIMS measurements were made nearly continuously during the mission with a duty cycle of 11 days on and 1 day off.

The LIMS radiometer scanned the atmospheric horizon vertically once every 12 seconds (≈ 84 km along the ground track) obtaining radiance profiles in each of six spectral bands as a function of tangent height (H). Tangent height is defined as the point of closest approach of a ray path to the Earth's surface (Fig. 1). The instrument view direction was 33.5° east of the negative spacecraft velocity vector so as to provide uniform coverage (Fig. 2) in the Northern Hemisphere for the $\approx 99.3^\circ$ orbital Sun synchronous inclination. The geometry provided daily coverage from 64°S to 84°N . The upward and downward arrows in Fig. 2 denote ascending (generally daytime data) and descending (generally nighttime data) nodes for the 14 orbits which occurred each day. The repeat cycle over a given latitude and longitude was ≈ 6 days. The altitude coverage varied for each channel depending mostly on signal-to-noise (S/N). The range for temperature and ozone was ≈ 10 km to 65 km, and for NO_2 , HNO_3 , and H_2O it was ≈ 10 km to 50 km. The lower altitude limit varied with latitude being highest in the Tropics due to interference by high clouds and lowest in the high latitudes. Also, at certain times, mostly in the high latitude deep winter period, the signal-to-noise (S/N) became too low in the NO_2 and H_2O channels for certain regions where the temperatures were cold. This comment applies mostly to latitudes greater than about 60°N and for pressures greater than about 10 mb. The vertical resolution of the measurements was ≈ 2.5 km in the temperature channels, 2.8 km in the O_3 and HNO_3 channels, and ≈ 5 km for NO_2 and H_2O . Horizontal resolution is much more coarse and is dictated by the limb geometry and atmospheric absorption characteristics to be ≈ 300 km.

The instrument was subjected to a thorough ground calibration prior to launch, which included among other things, characterization of noise levels, field of views, the optical encoder that provided precise relative angular measurements of radiance points on the horizon, and a primary radiometric calibration to the 1 percent accuracy level. Details of these measurements as well as other tests done on the instrument before launch are presented in Gille and Russell (1984). The LIMS scan mirror scanned the limb of the Earth at a rate of $0.25^\circ/\text{sec}$ starting at an altitude of ≈ 150 km and scanning down to a point ≈ 38 km below the hard horizon. At the top of every other scan (\approx

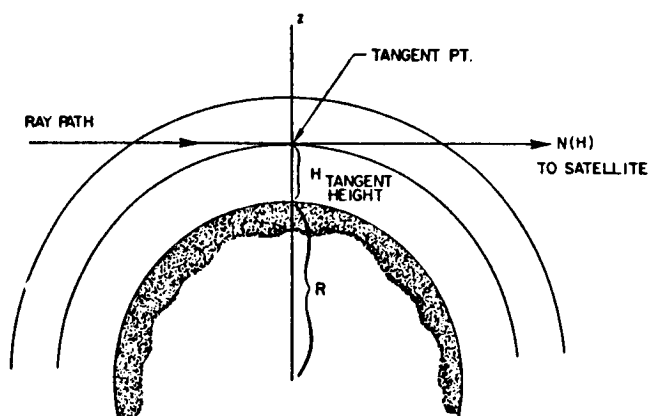


Figure 1 - LIMS Viewing Geometry.

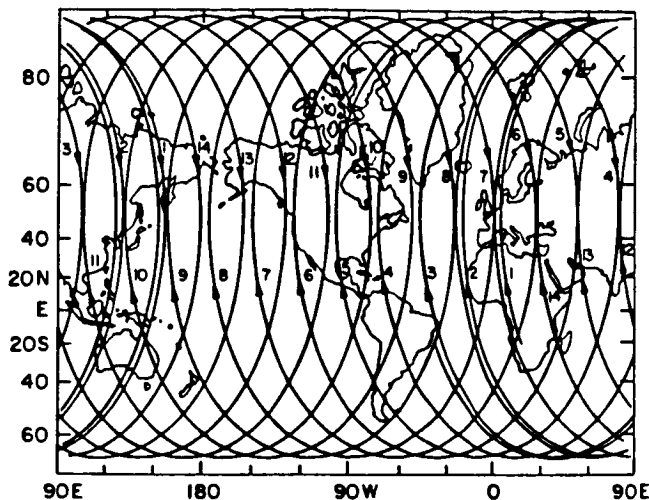


Figure 2 - LIMS Daily latitude-longitude coverage.

every 48 seconds), the detectors viewed radiation from a small cavity blackbody operating at 308°K. This in-flight calibration (IFC) blackbody served as a transfer standard to provide nearly continuous updates to the ground calibration in orbit to insure that any scale factor changes were accounted for in data reduction. The IFC temperature was stable to a small fraction of a degree, and the changes in scale factor over the entire mission were small. These results provided a sound and complete data base to gage experiment precision and accuracy in orbit.

An extensive program of correlative balloon underflights was carried out to aid in validation of LIMS data. The intent of the program was to obtain comparative data under a variety of atmospheric conditions at low, mid, and high latitudes. The general coincidence criteria were for the LIMS and correlative data to both occur within 3 hours time and 2° great arc distance from each other. These criteria could be met in some cases, but not all. Temperature data from rockets, for example, could be obtained with even smaller time and space differences. The extreme was for NO₂ where all data were collected from balloon remote sensors using the occultation technique. In this case, the time differences were on the order of 4-1/2 hours. Comparisons were made with 60 rocket temperature profiles, 14 rocket ozone profiles, 28 balloon ozone sondes, 13 H₂O balloon profiles, 7 NO₂ balloon profiles, and 14 HNO₃ balloon profiles. Further comparisons have been made with the Nimbus 7 SAMS temperature results, SBUV ozone data, and SAGE ozone and NO₂ results.

The validation criterion was that the error bars of the correlative and LIMS data overlap. It is recognized that since the balloon data also have errors, they cannot be used to assess LIMS accuracy. This was done through detailed computer simulations using all the systematic error estimates for the

experiment. Measurement precision was calculated using computer simulations that included the known experiment random error components as well as the orbital data. In using orbital data to assess precision, the standard deviation of six sequential retrievals (covering $\pm 2^\circ$ of latitude) about the six-scan mean was calculated at a series of latitudes to obtain an upper limit on precision. This is the worst case value since there will be some component of variation due to atmospheric changes. The results of the correlative measurement comparisons, accuracy calculations, and precision estimates are given in Table 3. In all cases, the error bars overlap for LIMS and correlative data. Accuracies range from $\leq 2^\circ\text{K}$ in temperature to 10 to ≈ 20 percent for gases. The measurement precision is $\approx 0.4^\circ\text{K}$ for temperature and 0.15 ppbv to 0.25 ppmv for constituents, depending on the channel. Details of the comparisons, descriptions of accuracy studies, and discussion of methods

TABLE 3 - LIMS ACCURACY, PRECISION, AND CORRELATIVE COMPARISON RESULTS

<u>PARAMETER</u>	<u>ESTIMATED*</u> <u>ACCURACY</u>	<u>CORRELATIVE</u> <u>COMPARISON</u>	<u>ESTIMATED</u> <u>PRECISION</u>
Temperature	<2 K**	$\leq 2\text{ K}$	< $0.2^\circ\text{K} - 0.6^\circ\text{K}$
Ozone	16-41%	< 10%	< 0.25 ppmv
Water Vapor	18-36%	< 20%	< 0.25 ppmv
Nitric Acid	17-45%	20-50%	< 0.15 ppbv
Nitrogen Dioxide	20-50%	< 20%	< 0.25 ppbv

*Range is Variation over Altitude
 **For Pressure $> 1\text{ mb}$

for estimating precision are presented in a series of LIMS validation papers. [Remsberg et al. (1984a), Russell et al. (1984a, b), and Gille et al. (1984a, b)]. The mapping procedure and discussions of the maps are included in papers by Haggard et al. (1986a, b) and Remsberg et al., 1986.

Stratospheric and Mesospheric Sounder (SAMS)

The SAMS instrument is a multichannel limb scanning infrared radiometer which measured thermal limb radiances that were ground processed to provide vertical profiles of atmospheric temperature versus pressure and the mixing ratios of methane (CH_4), nitrous oxide (N_2O), and carbon monoxide (CO). The $15\text{ }\mu\text{m}$ CO_2 band was used for temperature and the 1200 cm^{-1} ($8.3\text{ }\mu\text{m}$) to 1340 cm^{-1} ($7.5\text{ }\mu\text{m}$) spectral region was used for CH_4 (ν_4 band) and N_2O (ν_1 band) (e.g. Jones and Pyle, 1984). Carbon monoxide data were obtained using measurements of resonant fluorescent scattering of sunlight near $4.7\text{ }\mu\text{m}$. Although data are not yet available, SAMS also had channels for measuring the

vertical mixing ratio profiles of water vapor (H_2O), and nitric oxide (NO). Measurements were made using the method of pressure modulation radiometry (PMR). Energy from the atmospheric CH_4 and N_2O bands was passed through two PMR cells in tandem; one containing CH_4 and the other N_2O . These cells then acted as selective optical filters (see Drummond et al., 1980). Temperature was measured using CO_2 cells. The scanning geometry was the same as for LIMS (Fig. 1) except that the view direction was on the beam of the spacecraft velocity vector giving a different geographical coverage (Fig. 3). The orbit configuration and viewing geometry provided latitude coverage from $50^\circ S$ to $70^\circ N$ each day.

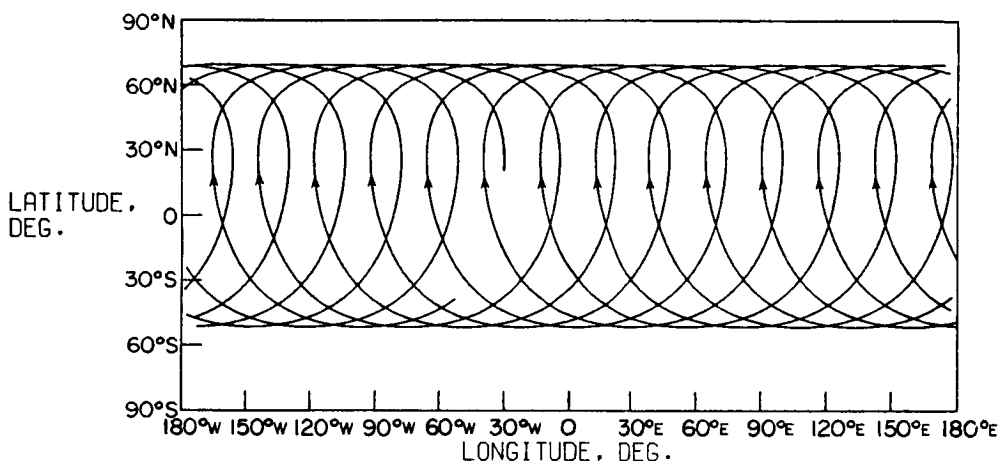


Fig. 3 - Typical SAMS daily latitude versus longitude coverage.

The use of a common optical chain and detector for both the CH_4 and N_2O channels meant that these gases could not be observed simultaneously, so the instrument was set to measure either one or the other gas in time blocks of 1 day. The SAMS duty cycle of 3 days on and 1 day off meant that each gas was measured about 12 days per month. The signal-to-noise ratios were not sufficient to measure individual profiles. Therefore, the approach taken was to zonally average radiance and temperature profiles before retrieval. Radiances were averaged over 10° latitude bands and ≈ 1.4 km in the vertical. This provided signal-to-noise ratios of about 30 in the low stratosphere.

The noise level for CO measurement was high, and it was necessary to average the data over long time periods (6 months) and wide latitude bands (30° to 50°). Consequently, the total number of "profiles" obtained was small. It should be noted that because of the geometry of the orbit, the density of observations is greatest at 50° and $70^\circ N$. As a result, averages for bands that include this range are biased towards the highest 20° of latitude.

A statistical method was used to retrieve temperature and mixing ratio from the radiance data. Details of this method and the instrument calibration procedures are discussed by Rodgers et al. (1984) and Wale and Peskett (1984), respectively. The instantaneous vertical field of view was ≈ 8 km for all channels. Temperature measurements covered the range from ≈ 10 km to ≈ 100 km. The useful altitude range for monthly zonal mean cross sections of CH_4 includes from 28 km (≈ 20 mb) to 52 km (≈ 0.6 mb) and for N_2O from 28 km to about 58 km (≈ 0.3 mb).

A detailed investigation of the sources of errors in the SAMS CH_4 and N_2O observations has been described by Jones and Pyle (1984). They found that systematic errors in the retrieved CH_4 fields fell into four main categories: uncertainties in the spectroscopy of the primary gases and of any other overlapping gases (mainly N_2O for the CH_4 measurement and vice versa), instrumental and calibration uncertainties, limitations and simplifications in the retrieval method and algorithm, and inaccurate knowledge of the atmospheric state (mainly the temperature structure).

To estimate the impacts of these various systematic error sources, a synthetic radiance profile was computed using typical mixing ratio and temperature profiles with all the uncertain parameters set to their nominal values. The simulated data set was then retrieved with the uncertain parameters offset in turn to their uncertainty limits, and the profiles thus obtained were compared each time with the original.

There was a significant random component to the error budget even when zonal means were considered. The effects of this on the retrieved profiles were quantified during the retrieval process by means of an error covariance matrix. In practice, only the diagonal elements of this matrix are used. This simplification, which ignores correlations between measurement errors at different levels of the atmosphere, tends to over estimate the random error at all levels.

Overall, the most important CH_4 and N_2O error sources are thought to be due to uncertainties in spectroscopy, effects due to retrieval using zonal radiance averaging and zonally averaged temperatures, and uncertainties in the line of sight altitude and atmospheric temperature. According to Jones and Pyle (1984), the CH_4 measurements appear to be superior to those of N_2O over much of the stratosphere. The estimated CH_4 RSS accuracy is < 20 percent as compared with 20 to 50 percent for N_2O . This occurs mainly because of the N_2O signal sensitivity to unwanted Doppler shifts and CH_4 interference, and it is worsened by the more rapid decrease of N_2O with increasing altitude. Random errors or precision is much better and is ≈ 3 -15 percent for CH_4 and 6-20 percent for N_2O below the 0.6 mb level.

The carbon monoxide signal levels are much lower and, therefore, the precision (≈ 25 percent) is worse than for N_2O and CH_4 . Also, the accuracy (-57 to 130 percent) is considerably worse. There were no simultaneous correlative measurements of CH_4 and N_2O to aid in validation. The investigators have, however, compared annual mean profiles to the few in situ profiles that exist. In general, the SAMS data reproduce the general features seen by other measurements quite well, i.e., vertical gradients, the low stratosphere, low latitude maxima, the essentially linear CH_4 decrease with

altitude, and the more rapid N_2O decrease. There appears to be a positive bias in N_2O by $\approx 20 - 30$ percent relative to in situ data at 30 km and below.

Stratospheric Aerosol Measurement II (SAM II)

The SAM II measurement uses the method of solar occultation to provide vertical profiles of aerosol extinction. The instrument is a single spectral channel Sun photometer with a passband centered at $1.0\text{-}\mu\text{m}$. Solar radiation is reflected by a scan mirror and collected by a Cassegrainian telescope to produce an image of the solar disk on the telescope's focal plane. On the focal plane is a circular aperture that defines a 0.6 arcmin instantaneous field of view (IFOV). This provides an instantaneous vertical field of view on the horizon of approximately 0.5-km altitude. Sunlight passing through the aperture is directed by a lens through a bandpass filter to a silicon photodiode used for measurement of atmospheric extinction.

Immediately before a satellite sunrise or sunset event, the SAM II instrument is activated by a sun-presence sensor indicating that the Sun is within the instrument's field of view. The instrument then locks onto the Sun in azimuth and scans in elevation until the Sun is acquired by the IFOV. The scan mirror then scans vertically, with respect to the Earth's horizon, across the solar disk at a rate of 15 arcmin per second, reversing the scan direction each time a Sun edge crossing occurs. The orbit of the Nimbus 7 satellite is a high-noon Sun-synchronous one, so SAM II performs 14 sunset and 14 sunrise measurements each day, with all sunsets occurring in the Arctic region and all sunrises occurring in the Antarctic region. In the course of a single day, measurements of the stratospheric aerosol will be obtained at 14 points spaced 26° apart in longitude in the Northern Hemisphere, and similarly for the Southern Hemisphere. All of the points obtained during 1 day in a given hemisphere will be at very nearly the same latitude, but as time progresses, the latitude of the measurements will slowly change with the season from 1 to 2 degrees per week, gradually sweeping from 64° to 80° . During a whole year, lowest latitude coverage occurs at the solstices, whereas the highest latitudes are measured at the equinoxes. The orbital viewing geometry and latitude versus time coverage is shown in Fig. 4.

The basic data product generated from each measurement is an aerosol extinction profile (extinction as a function of altitude) at $1.0\text{ }\mu\text{m}$ wavelength. Using a typical size distribution for stratospheric aerosols, their concentration as a function of altitude, longitude, latitude, and time can be determined. Since the measurements are confined to high latitudes ($64^\circ\text{--}80^\circ$) in both hemispheres, the results have provided the most detailed data set of stratospheric aerosol behavior ever obtained in the polar regions.

The altitude range for the aerosol extinction profile is typically from cloud top to approximately 35 km altitude covering all of the stratospheric aerosol layer in the polar regions. The vertical resolution for the inverted aerosol extinction profile is one km, with an accuracy of 10 percent and precision of about 5 percent. The accuracy at higher altitudes ($>20\text{ km}$) generally decreases due to the lower content of aerosols in that region of the stratosphere. The SAM II data have been validated by comparing to near simultaneous measurements by lidar and balloonborne dustsondes. Details of

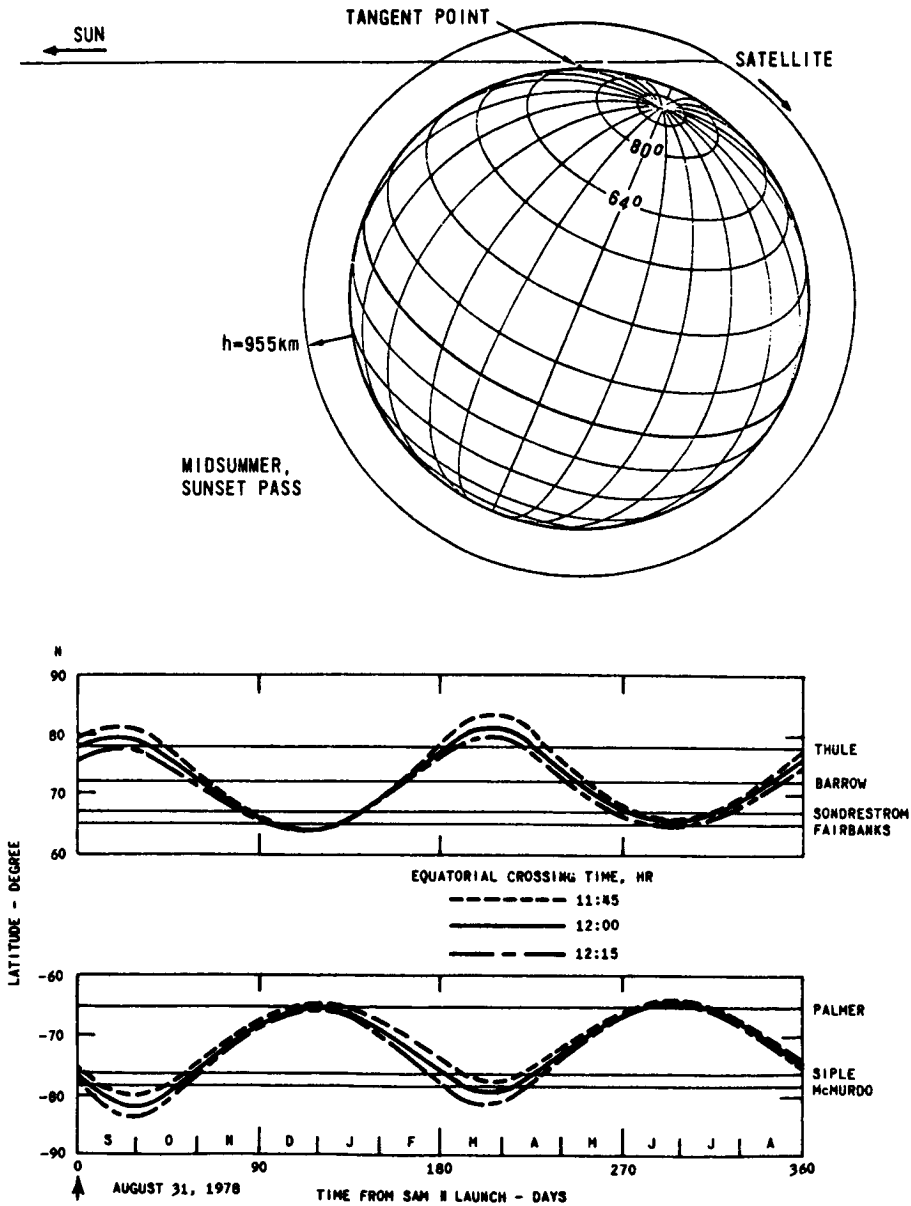


Figure 4 Latitude Coverage of SAM II Tangent Points For Sun-Synchronous High-Noon Orbit (Effect of changing equatorial crossing time on tangent location dates is shown by dashed curves)

the comparisons have been presented in two of the SAM II validation papers (Russell et al., 1981a, b).

Stratospheric Aerosol and Gas Experiment (SAGE)

The SAGE measurement is a direct follow-on to SAM II and is also based on the method of solar occultation. SAGE measures aerosol extinction as well as vertical profiles of O_3 and NO_2 .

The SAGE instrument is a four-channel Sun photometer and is very similar to the SAM II instrument. Spectral discrimination for SAGE is achieved by using a holographic diffraction grating which disperses the incoming sunlight in different directions depending on wavelength. By placing four sensors at appropriate locations along the Rowland circle, one can measure the sunlight intensity at four different wavelengths. The wavelengths selected are 0.385, 0.45, 0.60, and 1.00 μm . These were selected for the following reasons: at 0.385, 0.45 and 1.00 μm , absorption by stratospheric gases is quite small below 25 km, and solar extinction in these channels is almost entirely due to scattering by aerosol particles and air molecules. At higher stratospheric altitudes, attenuation at 0.60 μm is primarily due to ozone. Above an altitude of about 25 km, the extinction at 0.385 and 0.45 μm is mainly due to absorption by nitrogen dioxide.

In operation, the instrument is similar to SAM II, and is activated just before a sunrise or sunset is encountered by the satellite. The instrument searches for the Sun and nulls the center of intensity of the solar image. A scan mirror then begins scanning up and down across the face of the Sun. This mirror reverses in direction each time a limb crossing occurs. Solar light is reflected from the scan mirror to the aperture of a small Cassegrainian telescope which defines about a 1/2 km instantaneous field of view on the horizon and focuses this light onto the diffraction grating. The intensity of light dispersed by the grating at the four wavelengths of interest is measured by the four sensors. The data are inverted in ground processing to yield extinction as a function of altitude for each spectral channel at each location and time of a SAGE measurement.

The SAGE instrument was launched on February 18, 1979, on a dedicated orbit-tailored Applications Explorer Mission (AEM-2) satellite and obtained 34 consecutive months of data. The orbit is inclined at 55° with an apogee of 660 km, a perigee of 548 km, and a period of 96.8 minutes. This highly precessing orbit provided measurement opportunities distributed around the earth for latitudes from about 80°N to 80°S (depending on season). Unlike the emission experiments and SBUV, SAGE measurements are made over a wide range of longitudes but relatively small (< 1°) latitude ranges each day; generally one in the Southern Hemisphere and one in the Northern Hemisphere. Latitude versus time coverage for the period from launch to December 31, 1980, is shown in Fig. 5. The measurements were made each time the satellite entered or left the Earth's shadow, that is, during each sunrise and sunset encountered by the satellite. Due to the orbital motion of the satellite, the rotation of the Earth, and the motion of the Earth around the Sun, successive measurements are separated by about 24° in longitude and occurred at slightly different values of latitude.

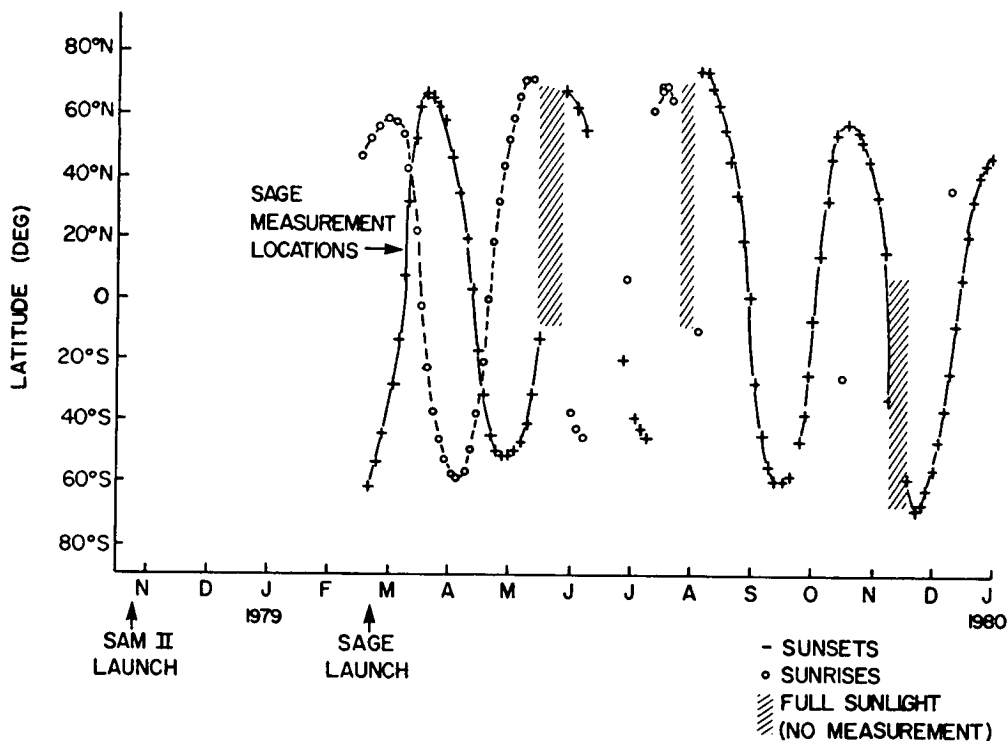


Fig. 5 - SAGE latitude versus time coverage for 1978 - 1979.

The basic data product generated from each SAGE measurement is an extinction profile (extinction as a function of altitude) for each of the four spectral channels. These contain information on the concentrations of stratospheric aerosols, ozone, and nitrogen dioxide as a function of altitude, longitude, latitude, and time. A corresponding temperature profile is provided by the National Meteorological Center (NMC) of the National Oceanic and Atmospheric Administration (NOAA) for the same time and location of each SAGE measurement. These profiles were constructed by interpolation from the NMC gridded global sets and used to convert SAGE derived gas concentrations to mixing ratios.

The altitude range for the four data products varies due to the difference in signal level for the four spectral channels. Vertical resolution for the inverted products is typically 1 km except for the nitrogen dioxide profile and the aerosol extinction at $0.45 \mu\text{m}$, where vertical smoothing to 3 km has been performed. Table 4 summarizes the altitude range, vertical resolution, estimated accuracy, and precision of the four SAGE data products. An extensive program of validation for the SAGE aerosol and ozone data has been carried out. The comparison of SAGE aerosol data with

correlative measurements has been reported by Russell et al. (1984) and Yue et al. (1984). The comparison of SAGE ozone data with balloon ozonesondes, rocketsondes, and SBUV data has been reported in a series of papers (Reiter and McCormick, 1982; McCormick et al., 1984; Cunnold et al., 1984).

The Solar Backscatter Ultraviolet (SBUV) Experiment

The SBUV is a nadir-viewing double monochromator which measures radiances backscattered from the atmosphere at 12 discrete wavelengths from 255 nm to 340 nm with a 1-nm bandpass (Heath et al., 1975; McPeters et al., 1984; Fleig et al., 1982). It is an extension, with modification, of the BUV measurement

TABLE 4 - SAGE ALTITUDE, RANGE, RESOLUTION, ACCURACY, AND PRECISION

<u>DATA</u>	<u>ALTITUDE RANGE</u>	<u>VERTICAL RESOLUTION</u>	<u>ESTIMATED ACCURACY</u>	<u>PRECISION</u>
Aerosol Extinction at 1.0 μm	Cloud Top to 35 km	1 km	10%	5%
Aerosol Extinction at 0.45 μm	10-35 km	3 km	20%	5%
Ozone	Cloud Top to 50 km	1 km	<35 km 5-10% >35 km 20-40%	5%
Nitrogen Dioxide	25-45 km	3 km	30%	10%

system flown on Nimbus 4 (1970-1977). Radiances between 255 nm and 206 nm are used to infer the ozone vertical profile distribution, while radiances between 312 nm and 340 nm are used to calculate total ozone. In order to calculate backscattered albedo, the ratio of backscattered radiance to extraterrestrial solar irradiance must be measured daily by deploying a diffuser plate. The scan-to-scan precision of the albedo measurement is very high--a few tenths of a percent.

Inferred of an ozone profile is possible because light at a given wavelength originates mostly in a limited-altitude region of the atmosphere, and this altitude region varies with wavelength. Thus, a wavelength scan is equivalent to an altitude scan. As sunlight penetrates the atmosphere, the scattering term increases exponentially with increasing density of air molecules, but the increasing depth of ozone causes the transmission of direct and backscattered sunlight to exponentially decrease. The balance between an exponentially increasing source term and exponentially decreasing transmission term produces a well-defined scattering layer of about 14 km half width. The wavelength of maximum ozone absorption, 255 nm, produces a scattering layer (contribution function) at the maximum possible altitude--50 km to 55 km, depending on solar zenith angle. Light at wavelengths longer than 310 nm

penetrates the ozone layer to be scattered by the troposphere and reflected by the ground and clouds. These wavelengths are useful for inferring the total ozone content of the atmosphere.

The inferral of an ozone profile from a set of measured backscattered albedos is done by using a partial derivative inversion algorithm that was described by Schneider et al. (1981). The optimum statistical concepts of Rodgers (1976) are used in the algorithm. Because of the width of the contribution functions, there is a limit to the altitude resolution that can be obtained in the retrieved profile. The inversion uses a-priori information in the form of climatological profiles (as a function of season and latitude) and an associated covariance matrix containing standard deviations and expected correlations between layers. Total ozone calculated from the longer wavelengths channels represents a strong additional constraint. A solution profile is obtained by minimizing the differences between the observed and calculated albedos and total ozone. The constraints are imposed in a statistically optimum manner by including the full covariance matrix of radiance errors and errors in estimating the a-priori profile. Two or three iterations normally suffice. It is estimated that an altitude resolution of approximately 8 km is achieved in the retrieved profiles. The limit to the altitude resolution from an inversion is set by the width of the contribution functions, the accuracy of the albedo measurement, and the magnitude of the off-diagonal elements of the a-priori covariance matrices.

The SBUV makes only daytime measurements since it uses backscattered sunlight. Measurements are made continuously over a broad latitude range at a spacing of 200 km along the orbit track and in longitude at the orbit spacing $\sim 26^\circ$ (Fig. 6). The upper and lower altitude limits vary with season depending on the Sun angle, but over the course of the year, the coverage is from $\sim 80^\circ\text{S}$ to $\sim 80^\circ\text{N}$. As an example, Fig. 6 shows coverage for mid-January. The estimated accuracy of ozone profile measurements is ~ 8 percent. The precision is estimated to be ~ 8 percent.

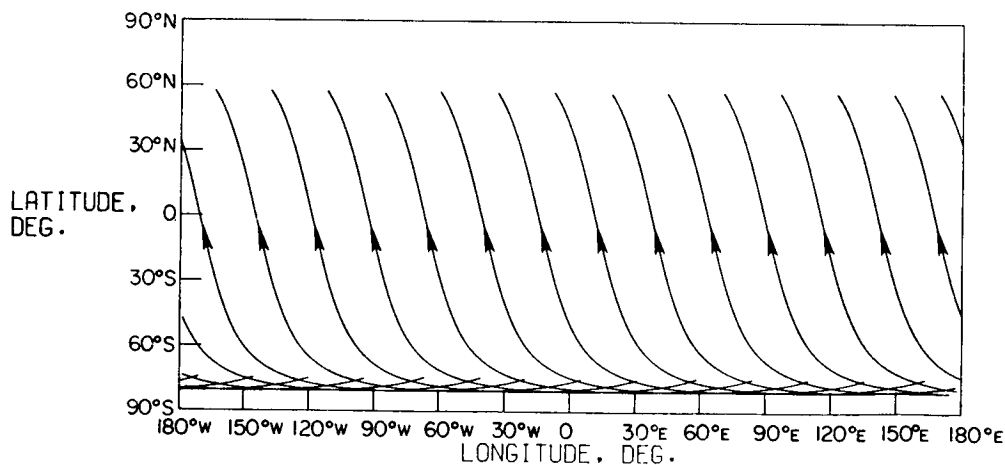


Fig. 6 - SBUV daily latitude versus longitude coverage for mid-January and a sun elevation angle $> 10^\circ$.

Total ozone measurements made by the SBUV have been compared with those from over 60 Dobson stations (Bhartia et al., 1984a). The result is that SBUV is lower, on average, by about 8 percent and the standard deviation of the differences is consistent with the estimates of 2 percent precision on each instrument type.

With respect to comparisons of SBUV profiles, Bhartia et al. (1984b) have compared the results with Umkehr and balloon ozonesonde information. The biases are generally less than 10 percent, but are functions of layer height and latitude. The standard deviation of the differences between SBUV and in situ measurements is found to be better than 8 percent for pressures between 1 and 64 mbar and better than 15 percent from 64 to 253 mbar.

The biases between SBUV and the ground-based observations, discussed above, are believed to be largely due to inconsistencies in the ozone absorption cross sections used for the various measurement systems. This comparison has recently been reexamined using data from SBUV obtained with the new absorption coefficients derived by Bass and Paur (private communication). This study has resulted in a recommendation by the International Ozone Commission that the new absorption data be used for reduction of satellite data.

Solar Mesosphere Explorer Satellite (SME)

Instruments on the Solar Mesosphere Explorer have been used to measure the ozone density in the Earth's atmosphere from about 1.0 to 0.001 mb and the NO₂ density from about 10.0 to 2.0 mb starting January 1, 1982, until the present. A full description of the mission objectives can be found in Thomas et al. (1980) and Barth et al. (1983). In this report, we present ozone data for all of 1982 and NO₂ data for the first 3 months of 1982.

The three instruments involved are spectrometers; one operating in the ultraviolet (UVS), one in the visible (VS), and one in the infrared (IRS). The UVS and the IRS measure ozone and the VS measures NO₂. Altitude coverage for ozone is from ~ 50 km to 90 km and for NO₂, it is from 20 km to about 60 km. The vertical resolution of the measurements is 3.5 km, and the latitude coverage is from 85°S to 85°N.

Instrument descriptions, data analysis techniques, and early results have been published for each instrument: For the UVS see Rusch et al. (1984); for the IRS see Thomas et al. (1984); and for the VS see Mount et al. (1984).

All atmospheric instruments on SME take data in the limb scanning mode. The satellite spins once in 12 seconds and the forward limb is sampled once each spin as the spin axis is perpendicular to the orbital plane. The satellite is in a near polar, Sun-synchronous orbit with the local time of the ascending mode near 3 p.m. Data are collected daily in four orbits centered in the ~ 50°W and ~ 100°W range.

The UVS measures Rayleigh scattered sunlight at two wavelengths, one where ozone efficiently absorbs (265 nm) and one where the ozone absorption is less efficient (296.5 nm). The shape of the limb profile of Rayleigh

scattered intensity is determined by the distribution of ozone in the atmosphere. The profiles are inverted to produce a profile of ozone mixing ratio as a function of pressure from 1.0 mb to 0.1 mb.

The uncertainties in a single inversion of six merged limb profiles are about 18 percent at all altitudes. About 65 percent of this uncertainty is due to systematic errors and the remainder to the statistical uncertainties. The complete error analysis is presented in Rusch et al. (1984).

The IRS measures radiation from the $O_2(^1\Delta_g)$ molecules at 1.27 μm resulting from the photolysis of ozone. A knowledge of the mechanisms of $O_2(^1\Delta_g)$ production and loss allows the ozone density to be inferred in the 1.0 to 0.001 mb region of the atmosphere. Random errors vary from about 4 percent at 1.0 mb to about 20 percent at 0.001 and systematic errors are about 15 percent at all pressures. The complete error analysis is given in Thomas et al. (1984).

NO_2 is measured by the VS using a differential absorption technique. The Rayleigh scattered signal is measured as a function of altitude at a wavelength where NO_2 absorption is low and at another nearby wavelength where it is several times larger. The NO_2 density is determined by a comparison of the ratio of the intensities of the two wavelengths measured to that expected if no NO_2 were present. The total RMS error varies from 21 percent at 28 km to about 60 percent at 38 km. The complete error analysis is given in Mount et al. (1984).

Satellite Data Description

All of the satellite data collected thus far for the time period of this report are displayed in subsequent figures in terms of monthly zonal mean pressure versus latitude cross sections or polar stereographic projections. In some cases, seasonal means are presented to allow a better comparison to be made with SAGE results, which are limited in coverage. The discussion which follows is divided according to the parameter measured. Intercomparison of results are discussed where data overlap occurs (i.e., temperature, O_3 , and NO_2) and significant features of the plots are described.

Temperature

As already indicated, the focus of this paper is on constituents; but since temperature is such a fundamental quantity needed in photochemical studies and for numerous other reasons, monthly zonal mean cross sections and the 10 mb polar stereographic projections are included in Figs. T1-T14 for LIMS and Figs. T15-T38 for SAMS. Both LIMS and SAMS temperatures have been compared to many rocketsonde/rawinsonde profiles (see Gille et al., 1984b and Barnett and Corney, 1984). In addition, LIMS and SAMS results have been extensively compared with each other and SSU satellite data, and with analyses from the Berlin Free University, the U.S. National Meteorological Center analyses, and the European Centre for Medium Range Forecasting. This work was done by a Pre-MAP Working Group, PMP-1, which compared daily zonal means and

polar stereographic projections at various pressure levels. Results were published in MAP Handbook No. 12, July 1984 (Rodgers, 1984). In a second workshop of the group, monthly zonal means and polar stereographic projections were compared using similar data sources and these results will be published in a future MAP handbook (Grose and Rodgers, 1986). The agreement between LIMS and SAMS is excellent under most conditions. Usually, the largest differences occur in regions where sharp horizontal and or vertical gradients occur such as in high latitude warming situations. The working group attributed this as being probably caused by the vast differences in vertical resolution of the two experiments and the fact that in the LIMS processing, horizontal gradients were accounted for to first order in the retrieval, whereas they were not included in the SAMS processing. The conclusion was that over most of the globe and most of the time, the two data sets agree to within a few degrees Kelvin.

Variations in monthly cross sections show the expected features of the cold tropopause and warm stratopause. The latter feature occurs at about the 1 mb level during all months at virtually all latitudes. The most noticeable exception is during October through January at high latitudes when the stratopause moves up to about the 0.6 mb level. The steepest latitudinal gradient in the stratopause region always occurs in the winter hemisphere with temperature decreasing poleward. There are transition periods in April and August when gradients are reduced. Maximum changes occur in June and December. Warmest temperatures at the 1 mb level occur at high latitudes of the summer hemisphere in accord with the other observations and theory which predicts a mean flow from the summer to winter hemisphere. During December and January, there is a wave-like temperature structure as a function of latitude at the highest levels of the data which is not present at other times. The month of February 1979 shows significant differences from previous winter months due to occurrence of a major stratospheric warming. Note in January the cold temperatures northward of about 60° which extend to the 10 mb level. In February, there are major changes from the January pattern and the temperature has increased by 20° K in this region. Significant changes are also seen in the polar stereographic projections.

Ozone (O₃)

Ozone was measured by four experiments for the time period covered by this report. These included LIMS, SAGE, SBUV, and SME. The first three experiments were operating simultaneously during February to May of 1979 while SME was launched much later. Extensive comparisons with in situ and Umkehr profiles have been done for LIMS, SAGE, and SBUV and reported on in the literature (Remsberg et al., 1984; McCormick et al., 1985; and Bhartia et al., 1984a). In addition, a preliminary effort has been made to intercompare data from these experiments (Fleig et al., 1984). One such comparison is shown in Fig. O3-1 for the March zonal mean LIMS and SBUV results and the 2-day zonal mean for SAGE at 42°N. In this comparison, the LIMS and SBUV agree better with each other than with SAGE above about 4 mb with SAGE values being higher than LIMS and SBUV. Below 10 mb, LIMS and SBUV data differ from SAGE values by about the same amount but with opposite sign. The differences reach ~ 25 percent at the highest altitudes but are only 10-15 percent below the 10 mb level. This is not a typical result, however, and in general, the agreement

of the data for the three experiments is much better. Even in this case, differences among the results are well within the error bars of the individual data sets. There have not been enough detailed analyses done at this point to draw conclusions concerning patterns of differences in various altitude ranges. This level of agreement is considered to be very good in view of the vastly different measurement approaches, i.e., thermal emission, solar occultation, and solar backscatter observations. There has been some limited reprocessing of SBUV data using new UV absorption coefficients (Bhartia, private communication, 1985) but there have not been enough comparisons to evaluate the statistical significance of changes. There appears to be very little difference in the results except at lower altitudes where the SBUV now agrees better with SAGE results than does LIMS. Final judgment on the new SBUV data must await a more detailed and careful study.

Only very limited comparisons have been performed with SME results in the region from 1 mb to 0.1 mb where LIMS and SME data overlap. At higher levels, the only satellite data are from SME. It is possible to extend LIMS results higher with special radiance averaging processing, but this has not yet been done. A January comparison of zonal mean latitude variations at 0.56 mb and 0.134 mb (Fig. 03-2) shows good SME/LIMS agreement (within 15 percent) at the lower altitude, but large discrepancies at 0.1 mb where the LIMS values are higher than SME by as much as a factor of two. A recent study by Solomon et al. (1986) shows that the 9.6 μm ozone band is not in local thermodynamic equilibrium (LTE) at the higher altitude and that large errors occur if LTE is assumed in the retrieval. When the effect of non-LTE is accounted for, the agreement between LIMS and SME at 0.136 mb is within the error bars of the two experiments. This is particularly encouraging in light of the fact that LIMS data were collected in 1979, and SME results were obtained in 1982. This suggests that the small interannual variability in ozone, indicated by SME during the time it has been operating, extends to other years as well. There still is a difference in shape of the latitude variation at 0.136 mb between LIMS and SME, which is not currently understood. A wave-like oscillation in temperature with latitude appears in the satellite derived temperature cross sections for December and January and the photochemically expected ozone oscillation accompanying the temperature changes is present in both LIMS and SME data sets at 0.56 mb but is seen only in LIMS at 0.134 mb. The true causes for these differences are not known at present, but they may be related still to the non-LTE effect in LIMS results. Monthly zonal mean cross sections and polar stereographic projections are shown in Figs. 03-3 to 03-30 for LIMS and in Figs. 03-31 to 03-86 for SBUV.

Monthly and seasonal zonal mean cross sections are shown in Figs. 03-87 to 03-96 for SAGE sunset data. All contour plots are in units of parts-per-million by volume (ppmv), and all polar stereographic projections are for the Northern Hemisphere. As already noted, the SAGE data coverage is sparse in some months because of the occultation experiment coverage; and since there were only sunset data taken after June, coverage was even less. During those months where SAGE data are particularly sparse, no contour plots are shown. For the months where all three experiments (i.e. LIMS, SBUV, SAGE) were operating, the general contour shapes are similar and the same features are apparent. The maximum March mixing ratio occurs at about the 10 mb level. At the Equator, the latitudinal gradients in each hemisphere are similar, and the vertical gradients at various latitudes are comparable.

There are some noticeable differences when details are examined. The March 1979 maximum mixing ratio is about 10.2 ppmv for LIMS (Fig. 03-7), 10.7 ppmv for SBUV (Fig. 03-35), and 11.5 ppmv for SAGE (Fig. 03-87). This is in accord with zonal mean profile comparisons already discussed. There are also some differences in contour shapes. The LIMS and SBUV 7 ppmv contours in April for example (Figs. 03-8 and 03-36), extend to a higher southern latitude and higher altitude. In August 1979 (Figs. 03-40 and 03-90), the SBUV and SAGE latitudinal gradients are quite different in some altitude regions. In general, the SBUV and LIMS contour shapes agree better with each other than with SAGE. This may be related to the sampling level associated with the occultation experiment. There are, however, some important LIMS/SBUV differences. Perhaps the most significant points to note are the differences in January and February contours (Figs. 03-5 and 03-6 for LIMS and 03-33 and 03-34 for SBUV). It should be recalled that February was a month when there was a major stratospheric warming. Note first that in January, the maximum mixing ratio levels occur in the same location for the two experiments but the levels are different by almost 2 ppmv. The contour shapes at 10 mb and 60°S are noticeably different and the 8 ppmv contour at the same level in the Northern Hemisphere extends to only $\approx 28^\circ\text{N}$ for LIMS but to $\approx 45^\circ\text{N}$ for SBUV. The most significant differences occur in February below the 10 mb level. Here there is a large change in the LIMS poleward gradient at 60°N and 20 mb, for example, and the "ozone hole" suggested by the contour fills in; but in the SBUV results, there is essentially no change in the gradient. These differences are made more evident in the 10 mb polar plot which shows the SBUV ozone gradient (Fig. 03-62) remaining essentially constant to the pole whereas the LIMS gradient changes significantly at about 30°N (Fig. 03-20). Downward propagation associated with a warming event which would bring higher ozone levels downward is expected. It could be that the differences are caused by the higher vertical resolution provided by LIMS (≈ 3 km versus ≈ 8 km for SBUV). Also, at this time, there were sharp horizontal temperature gradients present at high latitudes which are difficult to include in a limb experiment retrieval. Thus, some LIMS ozone error is expected due to temperature errors at the highest latitudes. There are noticeable LIMS/SBUV differences present in horizontal ozone gradients revealed by polar stereographic projections at all levels and months. The reasons for the LIMS/SBUV differences are unclear at present. Other features can be compared and differences noted, but in general, the nature of the important differences for all months are essentially characterized by these major points.

The ozone cross sections show the expected qualitative features of an equatorial mid-stratosphere maximum in mixing ratio due to chemical activity and downward and poleward slopes of the isolines in the lower stratosphere due to the mean circulation. There is also a hemispheric asymmetry present in the ≈ 2 mb to 7 mb range where elongated contours emanating in the Tropics extend upward and poleward at certain times of year mostly in one hemisphere (see e.g. LIMS Figs. 03-7 and 03-9). There is still some uncertainty about the relative importance of photochemistry and transport in this region, but the correlation with dry water vapor contours (e.g. Figs. 03-9 and CHN-31) suggests that transport plays a definite role in controlling the distribution in this region. All of the cross sections show rather low latitudinal gradients above the 4 mb level. The SME data shown in Figs. 03-97 to 03-108 for the UV and 03-109 to 03-120 for the IR extend to a much higher altitude than SBUV, LIMS, or SAGE, but they extend downward only to about 1 mb

pressure. SME results show a rather uniform vertical slope at all latitudes and only small latitudinal gradients. Since the climatology and variations of ozone will be treated in depth by another MAP project, no more will be said here.

Nitrogen Dioxide (NO_2)

Nitrogen compounds arise in the stratosphere primarily from a sequence of chemical reactions initiated by the reaction of nitrous oxide (N_2O) transported up from the surface with atomic oxygen in an excited state [$\text{O}(^1\text{D})$]. Nitrogen dioxide results from the combination of nitric oxide (NO) (which is an initial product of the $\text{N}_2\text{O} - \text{O}(^1\text{D})$ reaction) and ozone. Therefore, it is a central molecule in the chain of ozone destroying chemical reactions, and it is of great importance to our understanding of ozone temporal and spatial variations. At night, after NO has essentially all converted to NO_2 through reaction with O_3 , NO_2 further reacts with O_3 and NO_3 to form the radical N_2O_5 . This reaction and subsequent photolysis which dissociates N_2O_5 is highly temperature sensitive and altitude dependent. Therefore, measurement of NO_2 variations provide some revealing, important, and stringent tests to theory.

As noted earlier, NO_2 measurements have been obtained by three different instruments; LIMS, SAGE, and SME, all of which use different experiment approaches. The measurements represent a remarkable scientific achievement in view of the importance of the data and the very low NO_2 mixing ratio which is in the ppbv range. These three experiments, combined, provide measurements at five different times of day, i.e., LIMS measured at approximately 11:00 p.m. and 1:00 p.m. local time over a wide range of latitudes, SAGE made measurements at sunrise and sunset, and SME conducted observations at ≈ 3 p.m. In addition, LIMS provided data at a variety of local times at high latitudes where the terminator was crossed. Therefore, there is a wealth of data available for conducting diurnal change and solar zenith angle dependent investigations.

Since NO_2 varies significantly over the diurnal cycle, it is difficult to intercompare results from the three experiments. In addition, SME data were collected about 3 years later in time. Therefore, the approach for intercomparing these data which we will take here is to briefly describe the nature of the zonal mean cross sections for each experiment and include in the discussion a mention of similarities and differences. There are a few cases at high latitudes where LIMS and SAGE took data at essentially the same time and these comparisons will be discussed. Finally, comparisons of results will be made through the medium of a model.

The LIMS monthly zonal mean cross sections are shown in Figs. N-1 to N-7 for daytime and in Figs. N-8 to N-14 for nighttime. A detailed discussion of the " NO_2 climatology" as observed by LIMS is in preparation (Russell et al., 1986). The low latitude boundary of stippled areas in the high latitudes represents the region where the terminator is crossed and the measurement period changes from day to night or vice versa. The cross-hatched area below the 40 mb level reflects the fact that starting at about that level, an NO_2 "climatology" was used according to the degree of molecular oxygen interfer-

ence in the NO_2 channel. At the 100 mb level, for example, the result is almost all climatology since under most circumstances at those levels, emission by O_2 made up nearly 100 percent of the radiance used for retrieval. Thus, little NO_2 information was available. Several features in the data stand out. The contours tend to slope poleward and downward, and there is evidence of upward motion at the Equator bringing NO_2 poor air into the stratosphere. The diurnal differences are obvious with maximum daytime values reaching ~ 6 ppbv and night values reaching ~ 19 ppbv. The altitude of the peak mixing ratio occurs at the 10 mb level during the day and ~ 5 mb at night. In both time periods, the region of maximum NO_2 is biased toward the Tropics and Southern Hemisphere through most of the mission. The daytime contours become almost symmetrical about the Equator by May. Nighttime results are never as symmetrical but are more so in May than previous months. The distributions exhibit a layered structure in altitude and there are distinct latitudinal gradients which are largest in the altitude region of the peak mixing ratio. The night distribution in January (Fig. N-10) shows a particularly sharp gradient which is indicative of the so called "Noxon cliff," a term used to describe very rapid decreases in mixing ratio with latitude which were first observed from the ground by Noxon (1979). This feature has been carefully analyzed and is believed to be due to chemistry-dynamics interactions associated with the polar vortex and NO_2 conversion to N_2O_5 (see e.g. Solomon and Garcia, 1983 and Callis et al., 1983). The gradient is not as steep during the day due to already depressed NO_2 levels resulting from photolysis. Examination of descending (nighttime) polar stereographic projections at 3 mb in Figs. N-15 to N-17 for November through January show that the NO_2 decrease occurs over a broad longitude region. These maps were made using Kalman filtering. In doing this, since NO_2 has large diurnal changes, it was assumed that the nighttime distribution does not change over a 36-hour time period. Therefore, in analyzing higher wave number features of the maps, this assumption should be considered. As a minimum, the mapping allows a more accurate determination of the 36-hour zonal mean distribution. Another feature of the data which is not obvious from the contours is the effect of mesospheric NO_2 on the stratosphere levels. Russell et al. (1984c) performed special processing of LIMS data using radiance averaging methods to show that the polar night mesosphere can lead to significant increases in upper stratosphere NO_2 levels.

SAGE monthly zonal mean sunset pressure versus latitude cross sections are shown in Figs. N-22 to N-28 and sunrise plots are shown in Figs. N-29 to N-31. Seasonal sunset zonal means are shown in Figs. N-32 to N-34. The mixing ratio patterns based on seasonal zonal means are similar to those for LIMS. The NO_2 mixing ratio is a maximum in equatorial regions and decreases toward the poles in both hemispheres. The maximum mixing ratio contour of 8 ppbv typically covers altitudes from ~ 32 km to 36 km and like LIMS, there is a bias in location toward the Southern Hemisphere in winter months becoming essentially symmetric about the Equator in spring and then the bias shifts toward the Northern Hemisphere in summer and fall. SAGE also observes an NO_2 "cliff" type behavior in the winter hemisphere, which is somewhat steeper than LIMS daytime latitude gradients and as expected, it is less than the nighttime gradients. The behavior of the NO_2 column content at mid to high northern latitudes during the local winter season has been investigated with the SAGE observations (Chu and McCormick, 1986) and variations were found to be strongly correlated with the large scale horizontal flow pattern.

Daytime LIMS and SAGE data for winter and spring are compared in Figs. N-35 and N-36 for 31°N. The LIMS results are for January and May, respectively, and SAGE data are 3-year seasonal means for winter and spring. Therefore, these comparisons are more qualitative in nature, but nevertheless, they are instructive. Note that in both periods, the profile shapes agree very well. LIMS is biased low relative to SAGE by about 15-20 percent as expected based on diurnal change considerations. The error bars of the two data sets overlap in both cases and, therefore, lend credence to the combined data set.

SME monthly zonal mean NO₂ cross sections are shown in Figs. N-37 to N-39. Unlike LIMS and SAGE, these cross sections show several distinct regions of an NO₂ maximum and they show considerable variability. Maximum values of 12 ppbv occur at about the 10 mb level and the regions of maximum NO₂ persist through the period January to March. Part of the reason for the difference of the SME cross sections compared to those from LIMS and SAGE may be due to the fact that SME covers only a small longitude range whereas the other experiments cover a full 360° range. The signal contamination caused by aerosol loading associated with eruption of the El Chichon volcano prevented NO₂ data collection in later months. The tendency for there to be a bias of maximum NO₂ toward the summer hemisphere that was seen in LIMS and SAGE data is not seen in SME results. Also, there is no indication of poleward and downward sloping of contours as was the case in LIMS and to some degree in SAGE. There is a move towards symmetry of the cross section as the summer is approached in agreement with the other two data sets.

Another way to compare these three data sets is through use of a time dependent photochemical model. Solomon et al. (1986b) have used LIMS and SAGE observations of O₃ and temperature to study expected NO₂ diurnal variations. The calculations use the daytime LIMS NO₂ data to constrain the amount of NO_x. In this case, the daytime LIMS data are assumed to be exact, but the calculated diurnal variations around this value depend strongly on photochemistry and therefore provide a means of comparing daytime LIMS data to SME at 3 p.m., SAGE data at sunrise and sunset, and LIMS data at night. A typical comparison of this type for the month of March using zonally averaged results at the Equator and the 10 mb level is shown in Fig. N-40. The general conclusion is that the satellite results are in good agreement with one another and with the model.

In summary, the available satellite NO₂ data base reveals that:

1. This gas is highly variable diurnally and with altitude, latitude, longitude, and time.
2. There are strong photochemical-dynamics interactions associated with winter conditions when a polar vortex is established. This leads to formation of the "Noxon Cliff."
3. The mesosphere is a source for stratospheric NO₂ in the polar night region.
4. Peak zonal mean mixing ratios of 18 ppbv at night and 8 ppbv in the day occur in the Tropics mostly south of the Equator.

5. The three satellite data sets are in good agreement with time dependent photochemical theory.

Methane (CH_4), Nitrous Oxide (N_2O), and Water Vapor (H_2O)

The SAMS satellite instrument has yielded the first global observations of the long-lived tracers, N_2O and CH_4 . These constituents are believed to be produced exclusively in the troposphere, and their stratospheric distributions therefore directly reflect a balance between transport processes and photochemical destruction. If these chemical processes are well known, then the observed distributions of these species can be used to critically evaluate our understanding of stratospheric transport.

Chemical destruction of N_2O takes place via photodissociation and by reaction with $\text{O}(^1\text{D})$, a species produced in turn by ozone photolysis. Thus, its loss rate is relatively well known, although it should be noted that the N_2O photolysis cross section exhibits important temperature sensitivity as a function of wavelength. The chemical destruction of methane takes place by reaction with $\text{O}(^1\text{D})$, Cl and particularly OH ; this latter species has not yet been measured directly in the lower stratosphere below about 30 km. Further, the OH densities are tightly coupled to those of other poorly characterized species such as HNO_4 and HOCl . These chemical uncertainties must be considered in the interpretation of CH_4 and N_2O as tracers.

The chemical loss of CH_4 results in the production of H_2O , a constituent which has now been observed globally by LIMS and currently by SAGE II. H_2O is also long-lived at stratospheric altitudes and can, therefore, provide information on transport. It also plays a strong role in the photochemistry of stratospheric ozone through production of odd hydrogen radicals.

With these considerations in mind, we will briefly review what has been learned from the satellite observations of these constituents and discuss their general comparison to models. Monthly zonal mean cross sections for CH_4 are shown in Figs. CHN-1 to CHN-12 and for N_2O in Figs. CHN-13 to CHN-24. The morphology of these first satellite observations of N_2O and CH_4 have supported trends suggested by the available limited balloon data. In particular, the global distributions of these species exhibit a "vaulted" structure, with much higher mixing ratios observed in the Tropics than at high latitudes. Such structure suggests that most, if not all, of the air entering the stratosphere from the N_2O and CH_4 rich troposphere must enter in the Tropics. The lower abundances observed at high latitudes probably reflect downward transport of air photochemically depleted in these tracers. Model calculations by Jones and Pyle (1984), Guthrie et al. (1984), Ko et al. (1984), Solomon and Garcia (1984), Gray and Pyle (1985), and Solomon et al. (1985a) are in general agreement with the SAMS observations in this respect.

The model by Jones and Pyle (1984) is a classical Eulerian model while the other three cited above are formulated in the diabatic or residual Eulerian frameworks. Comparison of the SAMS observed tracer distributions to the latter model calculations suggest mean vertical (K_{zz}) and horizontal (K_{yy}) mixing (dispersion) coefficients of the order of $1 \times 10^3 \text{ cm}^2 \text{ s}^{-1}$ and $1-3 \times 10^3 \text{ cm}^2 \text{ s}^{-1}$, respectively, in fair agreement with theoretical estimates

of the approximate globally averaged strength of mixing by Kida (1983) and Tung (1984). On the other hand, McIntyre and Palmer (1983) and Plumb and Mahlman (1984) have suggested that locally much more vigorous mixing may be important in tracer transport at particular points and times. Further analysis of SAMS observations and comparison to model gradients is likely to yield important information on the strength of dispersive processes.

Perhaps the most surprising aspect of the SAMS observations of N_2O and CH_4 was the discovery of "double-peaks" in both constituents as a function of latitude, particularly in spring. Thus, rather than exhibiting a single "vaulted" peak near the Equator as is generally found during solstice, the spring observations tend to display a double maximum, one near $20^\circ S$ and another near perhaps $10^\circ N$. These peaks generally coincide with the occurrence of double minima in the LIMS H_2O distribution (see e.g. CHN-30 and CHN-31). This tendency is not apparent in any of the published two-dimensional model studies, but recent work by Pyle and co-workers (Gray et al., 1984) suggests that this feature may be related to the semiannual oscillation of zonal winds in the tropical lower stratosphere, possibly forced by Kelvin waves.

In summary, then, the SAMS N_2O and CH_4 data have thus far led to the following interpretations:

1. Confirmation of balloon observations that suggest strong net upward transport in the Tropics, and largely descending motion at extra-tropical latitudes (the "Brewer-Dobson") net circulation pattern)
2. suggestion of relatively small globally averaged mixing (dispersion) coefficients in the mean, and
3. indications of the importance of large scale circulation modulation associated with the semiannual forcing of the tropical circulation.

Finally, we briefly discuss the LIMS observations of H_2O . Monthly zonal mean descending node cross sections and polar stereographic plots for the 10 mb level are shown in Figs. CHN-25 to CHN-38. H_2O is of particular interest because of balloon observations by Kley et al. (1979), that suggest that a "hygropause" is found near 20 km in the Tropics. These observations have called into question the traditional belief (Brewer, 1949) that the stratospheric water vapor content is limited by condensation at the tropical tropopause (which is located substantially lower, near 16 km). Johnston and Solomon (1979) and Danielsen (1982), suggested that transport via cumulus towers that penetrate into the lower stratosphere might result in colder temperatures (and lower water vapor mixing ratios) than those of the mean tropical tropopause. Such processes could also result in an elevation of the location of the mixing ratio minimum above the tropopause level. Thus, it becomes important to ask what fraction of troposphere - stratosphere exchange occurs via such towers. Newell and Gould-Stewart (1981) suggested that preferentially enhanced transport may occur over Micronesia during the monsoon season.

The LIMS observations of H_2O have been discussed by Remsberg et al. (1984) and a more detailed presentation of "climatology of H_2O " as seen by

LIMS is in preparation (Remsberg et al., 1986). These data do indeed display a hypopause, most pronounced in the Tropics, where the observed water vapor minimum is about 2-2.5 ppmv. Interestingly, however, the results show little longitudinal variability in the Tropics even during the monsoon season. This suggests that large-scale upward transport of water vapor may be important in addition to localized convection, or the effects of localized convection as viewed by LIMS are blurred, either by real atmospheric mixing or because of the field of view of the limb-sounding experiment. It is also conceivable that some detail is lost due to the smoothing effects of the Kalman filtering process.

Remsberg et al. (1984) also examined the quantity $R = \Delta\text{CH}_4/\Delta\text{H}_2\text{O}$ and noted that the observed increase in H_2O with respect to altitude is roughly consistent with the observed decrease in CH_4 relative to the values obtained near the tropical tropopause. While this method has merit for examining the role of methane oxidation in the hydrogen budget of the stratosphere, there are limitations. It implicitly assumes that air enters the stratosphere with a constant hydrogen content or otherwise, transport processes would invalidate the procedure. Also, since the quantity $\Delta\text{CH}_4/\Delta\text{H}_2\text{O}$ is computed by taking differences of mixing ratios of similar size, the technique is rather sensitive to random measurement error. An alternate approach taken by Jones et al. (1986) is to study the sum of total hydrogen which they consider as $\hat{H} = 2x [\text{CH}_4] + [\text{H}_2\text{O}]$, where the $[\text{H}_2]$ component has been neglected or can be considered as a bias offset. This approach tends to be less sensitive to measurement errors and does not depend on the history of air parcels. They find an essentially uniform latitude versus altitude field for \hat{H} of ≈ 6 ppmv. This consistency of the field suggest that \hat{H} is conserved. Both approaches to analyzing the data give a similar conclusion, namely that the important role of CH_4 oxidation in producing stratospheric water vapor seems reasonably well established.

One of the most interesting aspects of the LIMS H_2O observations is the magnitude of the observed vertical gradients between about 100 and 50 mb in high latitudes. In winter at middle and high latitudes, for example, northward of $\approx 60^\circ\text{N}$, observed mixing ratios decrease abruptly from about 6.5 to 4.5 ppmv over this region. Because of the large abundances of H_2O in the upper troposphere, and because of the warm troposphere temperatures at middle and high latitudes, such a gradient would be difficult to reconcile with much appreciable net upward transport at these latitudes. As was shown by Brewer (1949), gradients of approximately this magnitude are consistent with downward velocities of the order of a few tenths cm s^{-1} coupled with very slow vertical mixing ($K_{zz} = 10^3 \text{ cm}^2 \text{ s}^{-1}$). Also, there is evidence that these high H_2O levels in the winter hemisphere lower stratosphere gradually decay as spring and summer approach. This can be clearly seen by examining the region north and south of 45° and below about 50 mb during the LIMS mission. Note that the high levels exist in the north in November (CHN-25) and the south in May (CHN-31).

Stordal et al. (1984) have presented a photochemical model employing a diagnostically derived diabatic circulation and $K_{zz} = 10^3 \text{ cm}^2 \text{ s}^{-1}$. This model yields large vertical gradients in H_2O near the upper troposphere - lower stratosphere region at middle and high latitudes, in approximate

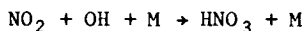
agreement with the LIMS observations. Similar results have been obtained by Guthrie and Jackman (private communication). These numerical model results coupled with the LIMS observations strongly support the suggestion of Brewer (1949) that the mean vertical profile of H_2O at extra-tropical latitudes is maintained principally by a net downward transport coupled with slow vertical mixing, although the possibility of locally important injection of H_2O at particular points cannot be ruled out.

The H_2O observations have, therefore, led to the following interpretation:

1. Confirmation of the existence of the hygropause in the Tropics on a global scale, but no suggestion of local exchange that exceeds large-scale exchange near the tropical tropopause.
2. Quantitative proof that a significant increase in H_2O mixing ratio occurs with altitude in the middle and upper stratosphere, and the increase is roughly consistent with the CH_4 oxidation mechanism.
3. Vertical profiles in the lowest part of the stratosphere at extratropical latitudes strongly suggest the importance of net downward motion (a "Brewer-Dobson" like circulation) and relatively slow vertical mixing.

Nitric Acid (HNO_3)

The LIMS instrument has provided the first global observations of HNO_3 ; a gas which is important as an end product and reservoir molecule in the chain of nitrogen related photochemical reactions that destroy ozone. Formation of nitric acid in the sunlit atmosphere takes place primarily through the reaction



Nitric acid transport to the troposphere and subsequent rainout is thought to be the primary mechanism for removal of NO_x from the stratosphere and, therefore, it plays a central role in the NO_x photochemistry. Further, its close link along with its precursor, NO_2 , to the critical hydroxyl radical (OH) makes HNO_3 an extremely important gas in the stratosphere.

Monthly zonal mean LIMS HNO_3 pressure versus latitude cross sections and 30 mb polar stereographic projections are shown in Figs. H-1 to H-14. A detailed discussion of " HNO_3 climatology" observed by LIMS is in preparation (Gille et al., 1986). The zonal mean altitude versus latitude distribution of HNO_3 is in general agreement with prior balloon and aircraft measurements which show low values in the Tropics and higher values at high latitudes. This picture is consistent with the idea of HNO_3 poor air entering the stratosphere from the troposphere at low latitudes. The high latitude buildup raises questions and at present is not adequately explained by theory, especially in the winter hemisphere. The data show considerable latitudinal variability during all months of the LIMS mission. There are persistently low mixing ratios in the Tropics (≈ 2 -3 ppbv) and high values in high winter latitudes (12 ppbv in November at 84°N). This distribution is suggestive of a

high latitude nighttime HNO_3 source (Austin et al., 1986). Other features of the data common to all periods is the downward slope of the contours toward each pole, and a significant hemispheric asymmetry. Although it is almost always present, the asymmetry changes during the LIMS mission with highest mixing ratios switching from the Northern Hemisphere to the Southern Hemisphere in May (Fig. H-7). There is essentially no asymmetry during February and March (Figs. H-4 and H-5). Models (both 2-D and 3-D) tend to show the HNO_3 downward slope with latitude rather well, but the asymmetry remains a problem. Also, models tend to show the HNO_3 peak mixing ratio occurring at a higher altitude (≈ 10 mb) than the 40 mb level shown by LIMS data.

It is interesting to note HNO_3 variations during the major sudden warming event of 1979. This warming, which occurred in late February and resulted in the main polar vortex splitting into two vortices, was preceded by a minor disturbance in late January. Thus, there was significant dynamical activity during this time. Figures H-10 and H-11 show HNO_3 polar stereographic projections on the 30 mb surface before and during the warming. It appears that the HNO_3 mixing ratio was conserved when the main polar vortex split with some of the gas being entrained in each resulting vortex. This can be seen by study of the 8 ppbv, 9 ppbv, and 10 ppbv contours in both periods. Note that the 8 ppbv contour is essentially unchanged, but the 9 ppbv contour shape has significantly changed to conform to regions of low temperatures associated with the two vortices, and the 10 ppbv contour has disappeared in February. A similar interpretation has been made for aerosols during the same event (McCormick et al., 1983). This picture of dynamical control of HNO_3 is reinforced by the strong correlations of HNO_3 and Ertel's potential vorticity calculated from LIMS temperatures (Grose and Russell, 1986). Potential vorticity and HNO_3 are positively correlated.

As a further test of the quality of HNO_3 data, Pyle et al. (1983), Gille et al. (1984a), and Callis et al. (1986) used LIMS NO_2 and HNO_3 to calculate the $[\text{OH}]$ global distribution. They calculated instantaneous $[\text{OH}]$ values with no consideration of the time required for photochemical equilibrium to be reached. The results from Pyle et al. (1983) which are typical are compared to in situ data in Fig. H-15. Many of the in situ measurements have been crudely adjusted to high Sun values. In view of these points, the agreement between derived and measured $[\text{OH}]$ is encouraging and suggests that the LIMS NO_2 and HNO_3 data are of high quality. One point to note is the divergence of the agreement above about 35 km altitude. This is due mostly to a bias in the LIMS HNO_3 values arising from an instrument artifact which causes high HNO_3 radiances. The LIMS team noted this bias in the HNO_3 validation paper [Gille et al. (1984a)] and since then have confirmed the bias which is only about one bit in size in the data stream. A study is underway to determine the best way to correct the data.

In summary, the LIMS HNO_3 data show features that are consistent with past balloon and aircraft data; they have been extensively validated, and they show some characteristics which differ rather markedly from model results. Most notable of these are the altitude of peak mixing and the hemispheric asymmetry. The data suggest that HNO_3 is under strong dynamical control as expected from chemical time constants for HNO_3 formation and the known mechanisms for HNO_3 removal from the stratosphere. The general features of the distribution are:

1. Low mixing ratios persist in the Tropics ($\approx 2-4$ ppbv);
2. mixing ratio contours which slope downward and poleward;
3. an interhemispheric asymmetry with winter high latitude mixing ratios that are ≈ 50 percent higher than for the opposite hemisphere;
4. significant longitudinal variability;
5. HNO_3 features that correlate positively with Ertel potential vorticity, and
6. suggestion from the data that the HNO_3 source region is in the high latitudes.

Carbon Monoxide (CO)

Carbon monoxide is of interest in the middle atmosphere primarily because of its role as a tracer for study of transport. This is so because CO is largely inert, and it is only in the mesosphere that its photochemical lifetime becomes comparable to transport time scales. Ground-based observations using microwave techniques (Clancy et al., 1984) and 2-D model calculations (Solomon et al., 1985b) suggest that CO mixing ratios are higher in the winter mesosphere than in summer primarily because of downward transport by the mean meridional circulation.

Details of the SAMS carbon monoxide measurement have been reported by Murphy (1985). Although the random errors are high, the SAMS data reveal marked variations in CO (Fig. CO-1). Note that the dotted line is the a-priori profile used in the retrieval, and it is identical in all cases. The most significant feature is that mixing ratios are very high in the mesosphere during the Northern Hemisphere winter in accord with ground-based observations and model results. This effect is clearly seen in the retrievals for the 1978/79 and 1979/80 winters for 35°N to 70°N . There is a difference of well over a factor of 10 between summer and winter mixing ratios at some levels. This difference is far too large to be attributed to errors in the measurements or the retrieval process. There is some evidence for a similar effect in the Southern Hemisphere, at about 85 km (12 pressure scale heights), but the most southerly latitude zone extends only to 50°S . The variations between the remaining profiles are generally comparable with the level of errors on the retrievals. The central latitude band shows a profile which exhibits little variation between the data periods, and the mixing ratios are comparable with summertime values in the Northern and Southern Hemisphere zones.

Aerosols

Prior to the satellite measurements by the SAM II and SAGE instruments, stratospheric aerosols were monitored primarily with either a lidar system (McCormick et al., 1978), or in situ devices onboard aircraft (Lem et al., 1979), and balloons (Rosen, 1964). These measurements are generally restricted to a single locality, and extrapolation of the results in order to

describe the stratospheric aerosol on a global scale is very difficult to do satisfactorily. Also, the poor sampling (both spatial and temporal) of these measurements is inadequate for the study of special events such as volcanic injections with their subsequent dispersion and decay.

SAM II and SAGE measurements have now provided us with a global picture of the behavior of stratospheric aerosols. The seasonal variation at all latitudes from the Tropics to the high polar region has been surveyed. During the nearly 3-year lifetime of the SAGE instrument, several volcanic injection events with their dispersion and decay have been measured. Another example of the usefulness of this new aerosol data base is the discovery of polar stratospheric clouds (PSC's) by the SAM II instrument. This new data and the volcanic set have contributed significantly to our understanding of stratospheric aerosol formation mechanisms and their effects on the radiation balance.

Monthly pressure versus latitude aerosol extinction ratio cross sections from SAGE are shown in Figs. A-1 to A-7. Seasonal means are shown in Figs. A-8 through A-10. Extinction ratio is the ratio of aerosol extinction to molecular extinction at $1\ \mu\text{m}$ wavelength. The data are consistent with the idea of a tropical source for aerosols. Here, the extinction ratio is a maximum and decreases poleward in both hemispheres. These data represent near-background stratospheric aerosol conditions, since the last major volcanic stratospheric enhancement occurred in 1974 after the eruption of Volcan De Fuego (Hofmann and Rosen, 1981), which was 5 years prior to the SAGE launch.

The ability to observe volcanic injections of material into the stratosphere by SAGE was first demonstrated during April 1979, when the La Soufriere volcano on St. Vincent Island (13.3°N , 61.2°W) erupted several times sending a small amount of material into the stratosphere. SAGE observations shortly after the volcanic eruption indicated enhanced aerosol extinction at about an altitude of 20 km at locations near the volcano and extending northeast over the Atlantic Ocean and the western shore of Africa. About a 2 percent global enhancement was recorded (McCormick et al., 1982).

In addition to the observations of the La Soufriere volcanic injection, SAGE has observed at least five other stratospheric volcanic injection events; the Sierra Negra volcano (0.8°N , 91°W) which erupted in late November 1979, the Mt. St. Helens volcano (46°N , 125°W) which erupted violently on May 18, 1980, the Ulawun volcano (5.0°S , 151.3°E) which erupted on October 7, 1980, the Alaid volcano (50.8°N , 155.5°E) which erupted on April 17, 1981, and the Pagan volcano (18.1°N , 145.8°E) which erupted on May 15, 1981. All five eruptions were accompanied by large amounts of volcanic materials (ash and gas) injected into the stratosphere.

The polar stratospheric aerosol has been thoroughly mapped by the SAM II measurements. The time histories for 1 year of stratospheric aerosols for the Arctic and Antarctic regions are illustrated in Figs. A-11 and A-12 (McCormick et al., 1981). Figure A-11b shows isopleths of weekly averaged aerosol extinction, as a function of altitude and time, for the Northern Hemisphere for October 29, 1978, through October 27, 1979. The dashed quasi-horizontal line near 10 km shows the position of the average tropopause for each week. Figure A-11c shows the corresponding isopleths of temperature in Kelvins.

The SAM II results have indicated that the seasonal behavior of the stratospheric aerosol in the two polar regions are similar and that there are strong correlations with temperature. In the winter period, increased aerosol extinction is found in both hemispheres. The large increases in extinction occurring during periods of particularly cold temperatures are manifestations of stratospheric clouds thought to be made up of ice crystals. These are occasionally sighted in the arctic winter but are ubiquitous in the antarctic winter. Toward the end of winter, the aerosol layer descends in both polar regions, followed by a rapid ascent in early spring. Following this period, the top of the aerosol layer falls steadily throughout the summer and stays nearly constant through the fall season. Interesting dynamics are seen which appear to be associated with the polar vortex (McCormick et al., 1983; Kent et al., 1985; and Wang and McCormick, 1985).

Summary

We have shown, in this report, a series of plots that describe the state of the stratosphere and to some degree, the mesosphere as revealed by satellite observations. The pertinent instrument features, spatial and temporal coverage, and details of accuracy and precision for the experiments providing the data have been described. The main features of zonal mean cross sections and polar stereographic projections have been noted and intercomparisons have been discussed where a parameter was measured by more than one experiment. It was not our attempt to be exhaustive in this or to present detailed results of scientific investigations. The main purpose was to collect the available data in one place and provide enough information on limitations or cautions about the data so that they could be used in model comparisons and science studies. Without a doubt, when these data are used, numerous questions will arise that were not addressed here. In such cases, the reader is encouraged to contact the experimenters for proper clarification.

ACKNOWLEDGMENTS

The authors acknowledge the assistance of Tom Marshall who collected the data for this paper on tape, Sukdee Storaasli who carefully plotted the data and assisted in report preparation, and Sheila D. Johnson who patiently and carefully typed the manuscript.

REFERENCES

- Austin, John, R. Garcia, J. M. Russell III, and Susan Solomon, 1986: On the Atmospheric Photochemistry of HNO_3 , Accepted by J. Geophys. Res.
 Barnett, J. J. and M. Corney, 1984: Temperature Comparisons Between the NIMBUS 7 SAMS, Rocket/Radiosondes and the NOAA 6 SSU, J. Geophys. Res., 89, No. D4, June 30, p. 5294.

- Barth, C. A., D. W. Rusch, R. J. Thomas, G. H. Mount, G. J. Rottmon, G. E. Thomas, R. W. Saunders, and G. M. Lawrence, 1983: Solar Mesosphere Explorer: Scientific Objectives and Results, Geophys. Res. Lett., 10, p. 237.
- Bhartia, P. K., K. F. Klenk, A. J. Fleig, C. G. Wellemeyer, and D. Gordon, 1984a: Intercomparison of NIMBUS 7 Solar Backscattered Ultraviolet Ozone Profiles with Rocket, Balloon, and Umkehr Profiles, J. Geophys. Res., 89, pp. 5227-5238.
- Bhartia, P. K., K. F. Klenk, C. K. Wong, B. Gordon, and A. J. Fleig, 1984b: Intercomparison of the Nimbus 7 SBUV/TOMS Total Ozone Data Set with Dobson and M83 Results, J. Geophys. Res., 89, pp. 5239-5248.
- Brewer, A. W., 1949: Evidence for a World Circulation Provided by Measurements of Helium and Water Vapor Distribution in the Stratosphere, Q. J. Royal Met. Soc., 75, p. 731.
- Callis, Linwood B., M. Natarajan, R. E. Boughner, J. M. Russell III, and J. D. Lambeth, 1986: Stratospheric Photochemical Studies Using NIMBUS 7 Data Part II: Development of Inferred Trace Specie Distributions, J. Geophys. Res., 91, No. C1, January 20.
- Callis, Linwood B., James M. Russell III, K. V. Haggard, and Murali Natarajan, 1983: Examination of Wintertime Latitudinal Gradients in Stratospheric NO₂ Using Theory and LIMS Observations, Geophys. Res. Lett., 10, No. 10, October, pp. 945-948.
- Clancy, R. T., D. O. Muhleman, and M. Allen, 1984: Seasonal Variability of Carbon Monoxide in the Terrestrial Mesosphere, J. Geophys. Res., 89, No. D6, October 20, pp. 9673-9676.
- Chu, W. P. and M. P. McCormick, 1986: SAGE Observations of Stratospheric Nitrogen Dioxides, J. Geophys. Res., to be published.
- Cunnold, D. M., M. C. Pitts, and C. R. Trepte, 1984: An Intercomparison of SAGE and SBUV Ozone Observations for March and April 1979, J. Geophys. Res., 89, p. 5249.
- Danielsen, E. F., 1982: A Dehydration Mechanism for the Stratosphere, Geophys. Res. Lett., 9, p. 605.
- Drummond, J. R., J. T. Houghton, G. D. Peskett, C. D. Rodgers, M. J. Wale, J. Whitney, and E. J. Williamson, 1980: The Stratospheric and Mesospheric Sounder on NIMBUS 7, Phil. Trans. R. Soc., London, Ser. A, 296, pp. 219-241.
- Fleig, A., J. C. Gille, M. P. McCormick, D. W. Rusch, J. M. Russell III, and J. M. Lindsay, 1984: Intercomparison of Satellite Ozone Measurements, Paper presented at the Quadrennial Ozone Symposium, Thessaloniki, Greece, August.
- Fleig, A. J., K. F. Klenk, P. K. Bhartia, D. Gordon, and W. H. Schneider, 1982: Users' Guide for the Solar Backscatter Ultraviolet (SBUV) Instrument First Year Ozone-S Data Set. NASA-RP 1095.
- Garcia, R. R. and S. Solomon, 1985: The Effect of Breaking Gravity Waves on the Dynamics and Chemical Composition of the Mesosphere and Lower Thermosphere, J. Geophys. Res., 90, No. D2, p. 3850.
- Gille, J. C., P. L. Bailey, and J. M. Russell III, 1980: Temperature and Composition Measurements from the LRIR and LIMS Experiments on NIMBUS 6 and 7. Phil. Trans. R. Soc., 293, pp. 205-218.
- Gille, John C., Paul L. Bailey, James M. Russell III, E. E. Remsberg, and L. L. Gordley, 1986: The Climatology of Stratospheric HNO₃ Measured by LIMS, To be submitted to J. Geophys. Res.

- Gille, J. C., and J. M. Russell III, 1984: The Limb Infrared Monitor of the Stratosphere (LIMS): Experiment Description, Performance and Results. J. Geophys. Res., **89**, No. D4, pp. 5125-5140.
- Gille, J. C., J. M. Russell III, P. L. Bailey, E. E. Remsberg, L. L. Gordley, W. F. J. Evans, H. Fischer, B. W. Gandrud, A. Girard, J. E. Harries, and S. A. Beck, 1984a: Accuracy and Precision of the Nitric Acid Concentrations Determined by the Limb Infrared Monitor of the Stratosphere (LIMS) Experiment on NIMBUS 7, J. Geophys. Res., **89**, No. D4, June 30, pp. 5179-5190.
- Gille, J. C., J. M. Russell III, P. L. Bailey, L. L. Gordley, E. E. Remsberg, J. H. Lienesch, W. G. Planet, F. B. House, L. V. Lyjak, and S. B. Beck, 1984b: Validation of Temperature Retrievals Obtained by the Limb Infrared Monitor of the Stratosphere (LIMS), J. Geophys. Res., **89**, No. D4, June 30, pp. 5147-5160.
- Gray, L., J. D. Haigh, R. L. Jones, J. A. Pyle, R. J. Wells, and A. M. Zavody, 1984: Paper presented at the Quadrennial Ozone Symposium, Thessaloniki, Greece, August.
- Gray, L. G. and J. A. Pyle, 1985: Submitted to the Q. J. Royal Met. Soc.
- Grose, W. L., and C. D. Rodgers, Editors, 1986: Coordinated Study of the Behavior of the Middle Atmosphere in Winter: Monthly Mean Comparisons of Satellite and Radiosonde Data and Derived Quantities, To be published in a future MAP Handbook.
- Grose, William L., and James M. Russell III, 1986: The Use of Isentropic Potential Vorticity in Conjunction With Quasi-Conserved Species in the Study of Stratospheric Dynamics and Transport, To be submitted to J. Geophys. Res.
- Guthrie, P. D., C. H. Jackman, J. R. Herman, and C. J. McQuillan, 1984: A Diabatic Circulation Experiment in a Two-Dimensional Photochemical Model, J. Geophys. Res., **89**, p. 9589.
- Haggard, K. V., E. E. Remsberg, W. L. Grose, J. M. Russell III, B. T. Marshall, and G. Lingenfelter, 1986a: The Nimbus 7 LIMS MAP Archive Tape, Part I - Temperature and Geopotential. NASA TP, in review.
- Haggard, K. V., B. T. Marshall, R. J. Kurzeja, E. E. Remsberg, and J. M. Russell III, 1986b: The Nimbus 7 LIMS Map Archive Tape, Part II - Water Vapor and Nitrogen Dioxide. NASA TP, in preparation.
- Heath, D. F., A. J. Krueger, and P. J. Crutzen, 1977: Solar Proton Event: Influence on Stratospheric Ozone, Science, **197**, pp. 886.
- Heath, D. F., A. J. Krueger, H. A. Roder, and B. D. Henderson, 1975: The Solar Backscatter Ultraviolet and Total Ozone Mapping Spectrometer (SBUV/TOMS) for Nimbus 6. Opt. Eng., **14**, p. 323.
- Hoffman, D. J. and J. M. Rosen, 1981: On the Background Stratospheric Aerosol Layer, J. Atmos. Sci., **38**, p. 168-181.
- Johnston, H. S., and S. Solomon, 1979: Thunderstorms as Possible Micrometeorological Sink for Stratospheric Water, J. Geophys. Res., **84**, p. 3155.
- Jones, R. L., and J. A. Pyle, 1984: Observations of CH₄ and N₂O by the NIMBUS 7 SAMS: A Comparison with In-Situ Data and Two-Dimensional Numerical Model Calculations, J. Geophys. Res., **89**, p. 5263.
- Jones, R. L., J. A. Pyle, J. E. Harries, A. M. Zavody, J. M. Russell III, and J. C. Gille, 1986: The Water Vapor Budget of the Stratosphere Studied Using LIMS and SAMS Satellite Data, Submitted to the Q. J. of Royal Meteor. Soc.

- Kent, G. S., C. R. Trepte, V. O. Farrukh, and M. P. McCormick, 1985: Variations in the Stratospheric Aerosol Associated with the North Cyclonic Polar Vortex as Measured by the SAM II Satellite Sensor, J. Atmos. Sci., **42**, p. 1536.
- Kida, H., 1983: General Circulation of Air Parcels and Transport Characteristics Derived From a Hemispheric GCM Part I. A Determination of Advective Mass Flow in the Lower Stratosphere, J. Met. Soc. Jap., **61**, p. 171.
- Kley, D., E. J. Stone, W. R. Henderson, J. W. Drummon, W. Harrop, A. L. Schmeltekopf, T. L. Thompson, and R. W. Winkler, 1979: In Situ Measurements of the Mixing Ratio of Water Vapor in the Stratosphere, J. Atmos. Sci., **96**, p. 2513.
- Ko, M. K. W., K. K. Tung, D. K. Weisenstein, and N. D. Sze, 1984: A Zonal Mean Model of Stratospheric Tracer Transport in Isentropic Coordinates: Numerical Simulations for Nitrous Oxide and Nitric Acid, Submitted to J. Geophys. Res.
- Lem, H. Y., N. H. Farlow, 1979: Efficiency of Aerosol Collection on Wires Exposed in the Stratosphere, NASA TM-81147, Ames Research Center.
- McCormick, M. P., T. J. Swissler, W. P. Chu, W. H. Fuller, Jr., 1978: Post-Volcanic Stratospheric Aerosol Decay as Measured by Lidar, J. Atmos. Sci., **35**, pp. 1296-1303.
- McCormick, M. P., W. P. Chu, G. W. Grams, P. Hamil, B. M. Herman, L. R. McMaster, T. J. Pepin, P. B. Russell, H. M. Steele, and T. J. Swissler, 1981: High-Latitude Stratospheric Aerosols Measured by the SAM II Satellite System in 1978 and 1979, Science, **214**, Oct. 16, pp. 328-331.
- McCormick, M. P., C. S. Kent, G. K. Yue, D. M. Cunnold, 1982: Stratospheric Aerosol Effects from Soufriere Volcano as Measured by the SAGE Satellite System, Science, **216**, pp. 1115-1118.
- McCormick, M. P., C. R. Trepte, and G. S. Kent, 1983: Spatial Changes in the Stratospheric Aerosol Associated with the North Polar Vortex, Geophys. Res. Lett., **10**, pp. 941-944.
- McCormick, M. P., T. J. Swissler, E. Hilsenrath, A. J. Krueger, and M. T. Osborn, 1984: Satellite and Correlative Measurements of Stratospheric Ozone: Comparison of Measurements Made by SAGE, ECC Balloons, Chemiluminescent, and Optical Rocketsondes, J. Geophys. Res., **89**, No. D4, June 30, p. 5315.
- McIntyre, M. E., and T. N. Palmer, 1983: Breaking Planetary Waves in the Stratosphere, Nature, **305**, p. 593.
- McPeters, R. D., D. J. Heath, and P. K. Bhartia, 1984: Average Ozone Profiles for 1979 from the Nimbus 7 SBUV Instrument, J. Geophys. Res., **89**, pp. 5199-5214.
- Mount, G. H., D. Rusch, J. F. Noxon, J. M. Zawodny, and C. A. Barth, 1984: Measurements of Stratospheric NO₂ from the Solar Mesosphere Explorer Satellite. 1. An Overview of the Results, J. Geophys. Res., **89**, pp. 1327-1340.
- Murphy, A. K., 1985: Satellite Measurements of Atmospheric Trace Gases, D. Phil. Thesis, Oxford University.
- Newell, R. E. S., and A. Gould-Stewart, 1981: A Stratospheric Fountain?, J. Atmos. Sci., **38**, p. 2789.
- Noxon, J. F., 1979: NO₂ 2, Global Behavior, J. Geophys. Res., **84**, pp. 7883-7888.
- Plumb, A., and T. D. Mahlman, 1984: Presented at the NASA Workshop on Stratospheric Processes, Feldafing, W. Germany, June.

- Pyle, J. A., A. M. Zavody, J. E. Harries, and P. H. Modfot, 1983: Derivation of OH Concentration from Satellite Infrared Measurements of NO_2 and HNO_3 , Nature, 305, pp. 690-692.
- Reiter, R. and M. P. McCormick, 1982: SAGE-European Ozone-sonde Comparisons, Nature, 300, p. 337.
- Remsberg, E. E., J. M. Russell III, J. C. Gille, L. L. Gordley, P. L. Bailey, W. G. Planet, and J. E. Harries, 1984a: The Validation of Nimbus 7 LIMS Measurements of Ozone, J. Geophys. Res., 89, pp. 5161-5178, June 30.
- Remsberg, E. E., J. M. Russell III, L. L. Gordley, J. C. Gille, and P. L. Bailey, 1984b: Implications of the Stratospheric Water Vapor Distribution as Determined from the NIMBUS 7 LIMS Experiment, J. Atmos. Sci., 41, No. 19, pp. 2934-2945, October.
- Remsberg, E. E., James M. Russell III, L. L. Gordley, John C. Gille, and Paul L. Bailey, 1986: The Climatology of Stratospheric H_2O Measured by LIMS, To be submitted to J. Geophys. Res.
- Remsberg, E. E., R. J. Kurzeja, K. V. Haggard, J. M. Russell III, and L. L. Gordley, 1986: Description of the Nimbus 7 LIMS Map Archive Tape, Ozone and Nitric Acid. NASA TP, in preparation.
- Rodgers, C. D., Editor, 1984: Coordinated Study of the Behavior of the Middle Atmosphere in Winter (PMP-1 Workshops: May 1982, Boulder; April 1983, U. Oxford; August 1983, Hamburg, MAP Handbook No. 12, July.
- Rodgers, C. D., 1976: Retrieval of Atmospheric Temperature and Composition from Remote Measurements of Thermal Radiation, Rev. Geophys. Space Phys., 14, pp. 609-624.
- Rodgers, C. D., R. L. Jones, and J. J. Barnett, 1984: Retrieval of Temperature and Composition From NIMBUS 7 SAMS Measurements, J. Geophys. Res., 89, No. D4, June 30, p. 5280.
- Rosen, J. M., 1964: J. Geophys. Res., 69, pp. 4673-4676.
- Rusch, D. W., G. H. Mount, C. A. Barth, R. J. Thomas, and M. T. Callan, 1984: Solar Mesosphere Explorer Ultraviolet Spectrometer: Measurements of Ozone in the 1.0 to 0.1 mb Region, J. Geophys. Res., 89, pp. 11,677-11,687.
- Russell, James M. III and John C. Gille, 1978: The Limb Infrared Monitor of the Stratosphere (LIMS) Experiment in the NIMBUS 7 Users's Guide, edited by C. R. Madrid, NASA, Goddard Space Flight Center, Greenbelt, Maryland, pp. 71-103.
- Russell, J. M. III, 1984: The Global Distribution and Variability of Stratospheric Constituents Measured by LIMS, Adv. Space Res., 4, No. 4, pp. 107-116.
- Russell, J. M. III, J. C. Gille, E. E. Remsberg, L. L. Gordley, P. L. Bailey, S. R. Drayson, H. Fischer, A. Girard, J. E. Harries, and W. F. J. Evans, 1984a: Validation of Nitrogen Dioxide Results Measured by the Limb Infrared Monitor of the Stratosphere (LIMS) Experiment on NIMBUS 7, J. Geophys. Res., 89, No. D4, June 30, pp. 5099-5107.
- Russell, J. M., J. C. Gille, E. E. Remsberg, L. L. Gordley, P. L. Bailey, H. Fischer, A. Girard, S. R. Drayson, W. F. J. Evans, and J. E. Harries, 1984b: Validation of Water Vapor Results Measured by the Limb Infrared Monitor of the Stratosphere (LIMS) Experiment on NIMBUS 7, J. Geophys. Res., 89, No. D4, June 30, pp. 5115-5124.
- Russell, J. M. III, S. Solomon, L. L. Gordley, E. E. Remsberg, L. B. Callis, 1984c: The Variability of Stratospheric and Mesospheric NO_2 in the Polar Winter Night Observed by LIMS, J. Geophys. Res., 89, No. C8, August 20, pp. 7267-7275.

- Russell, James M. III, E. E. Remsberg, L. L. Gordley, John C. Gille, and Paul L. Bailey, 1986: The Climatology of Stratospheric NO_2 Measured by LIMS, to be submitted to J. Geophys. Res.
- Russell, P. B., T. J. Swissler, M. P. McCormick, W. P. Chu, J. M. Livingston, and T. J. Pepin, 1981a: Satellite and Correlative Measurements of the Stratospheric Aerosol I: An Optical Model for Data Conversion, J. Atmos. Sci., **36**, p. 1279.
- Russell, P. B., M. P. McCormick, T. J. Swissler, W. P. Chu, J. M. Livingston, W. H. Fuller, J. M. Rosen, D. J. Hofmann, L. R. McMaster, D. C. Wood, and T. J. Pepin, 1981b: Satellite and Correlative Measurements of the Stratospheric Aerosol II: Comparison of Measurements Made by SAM II, Dustsondes, and an Airborne Lidar, J. Atmos. Sci., **38**, p. 1295.
- Russell, P. B., M. P. McCormick, T. J. Swissler, L. R. McMaster, J. M. Rosen, and D. J. Hofmann, 1984: Satellite and Correlative Measurements of the Stratospheric Aerosol III: Comparison of Measurements by SAM II, SAGE, Dustsondes, Filters, Impactors, and Lidar, J. Atmos. Sci., **41**, p. 11.
- Schneider, W. H., P. K. Bhartia, K. F. Klenk, and C. L. Mateer, 1981: An Optimum Statistical Technique for Ozone Profile Retrieval From Backscattered UV Radiances, Paper presented at Fourth Conference on Atmospheric Radiation, Am. Meteorol. Soc., Toronto Ontario, Canada, June 16-18.
- Solomon, S. and R. R. Garcia, 1983: Simulation of NO_x Partitioning Along Isobaric Parcel Trajectories, J. Geophys. Res., **88**, No. C9, pp. 5497-5501.
- Solomon, S. and R. R. Garcia, 1984: On the Distributions of Long Lived Tracers and Chlorine Species in the Middle Atmosphere, J. Geophys. Res., **89**, 11,633-11,644, 1984.
- Solomon, S., G. C. Reid, D. W. Rusch, and R. J. Thomas, 1983a: Mesospheric Ozone Depletion During the Solar Proton Event of July 13, 1982, Part II: Comparison Between Theory and Measurements, Geophys. Res. Lett., **10**, No. 4, p. 249.
- Solomon, S., G. H. Mount, and J. M. Zawodny, 1983b: Measurements of Stratospheric NO_2 from Solar Mesospheric Explorer Satellite 2 - General Morphology of Observed NO_2 and Derived N_2O_5 , J. Geophys. Res., **89**, p. 7317.
- Solomon, S., J. T. Kiehl, R. R. Garcia, and W. L. Grose, 1985a: Tracer Transport by the Diabatic Circulation Deduced from Satellite Observations. Submitted to J. Geophys. Res.
- Solomon, S., R. R. Garcia, J. J. Olivero, R. M. Bevilacqua, P. R. Schwartz, R. T. Clancy, and D. O. Muhleman, 1985b: Photochemistry and Transport of Carbon Monoxide in the Middle Atmosphere, J. Atmos. Sci., **42**, No. 10, pp. 1072-1083.
- Solomon, S., J. T. Kiehl, B. J. Kerridge, E. E. Remsberg, and J. M. Russell III, 1986a: Evidence for Non-Local Thermodynamic Equilibrium in the ν_3 Mode of Mesospheric Ozone. Submitted to J. Geophys. Res.
- Solomon, S., James M. Russell III, and M. P. McCormick, 1986b: On the Atmospheric Photochemistry of NO_3 , To be submitted to J. Atmos. Sci.
- Stordal, F., I. S. A. Isaksen, and K. Horntveth, 1984: A Diabatic Circulation Two-Dimensional Model with Photochemistry: Simulations of Ozone and Ground Released Tracers, Submitted to J. Geophys. Res.
- Thomas, G. E., C. A. Barth, E. R. Hansen, C. W. Hord, G. M. Lawrence, G. H. Mount, G. J. Rottman, D. W. Rusch, A. I. Stewart, R. J. Thomas, J. London, P. L. Bailey, P. J. Crutzen, R. E. Dickenson, J. C. Gille, S. C. Liu, J. F. Noxon, and C. B. Farmer, 1980: Scientific Objectives of the Solar Mesosphere Explorer Mission, Pageoph, **118**, pp. 591-615.

- Thomas, R. J., C. A. Barth, G. J. Rottmon, D. W. Rusch, G. H. Mount, G. M. Lawrence, R. W. Saunders, G. E. Thomas, and L. E. Clemens, 1983: Ozone Density Distribution in the Mesosphere (50 - 90 km) Measured by the SME Limb Scanning Near Infrared Spectrometer, Geophys. Res. Lett., 10, p. 245.
- Thomas, R. J., C. A. Barth, D. W. Rusch, and R. W. Sanders, 1984: Solar Mesosphere Explorer Near-Infrared Spectrometer: Measurements of $1.27\mu\text{m}$ Radiance and the Inference of Mesospheric Ozone, J. Geophys. Res., pp. 9569-9580.
- Tung, K. K., 1984: Proceedings of the U.S.-Japan Seminar on Middle Atmosphere Dynamics, Terra Scientific Pub., (Tokyo).
- Yue, G. K., M. P. McCormick, and W. P. Chu, 1984: A Comparative Study of Aerosol Extinction Measurements made by the SAM II and SAGE Satellite Experiments, J. Geophys. Res., 89, p. 5321.
- Wale, M. J. and G. D. Peskett, 1984: Some Aspects of the Design and Behavior of the Stratospheric and Mesospheric Sounder, J. Geophys. Res., 89, No. D4, June 30, p. 5287.
- Wang, P. H. and M. P. McCormick, 1985: Variations in Stratospheric Aerosol Optical Depth During Northern Warmings, J. Geophys. Res., 90, p. 10597.

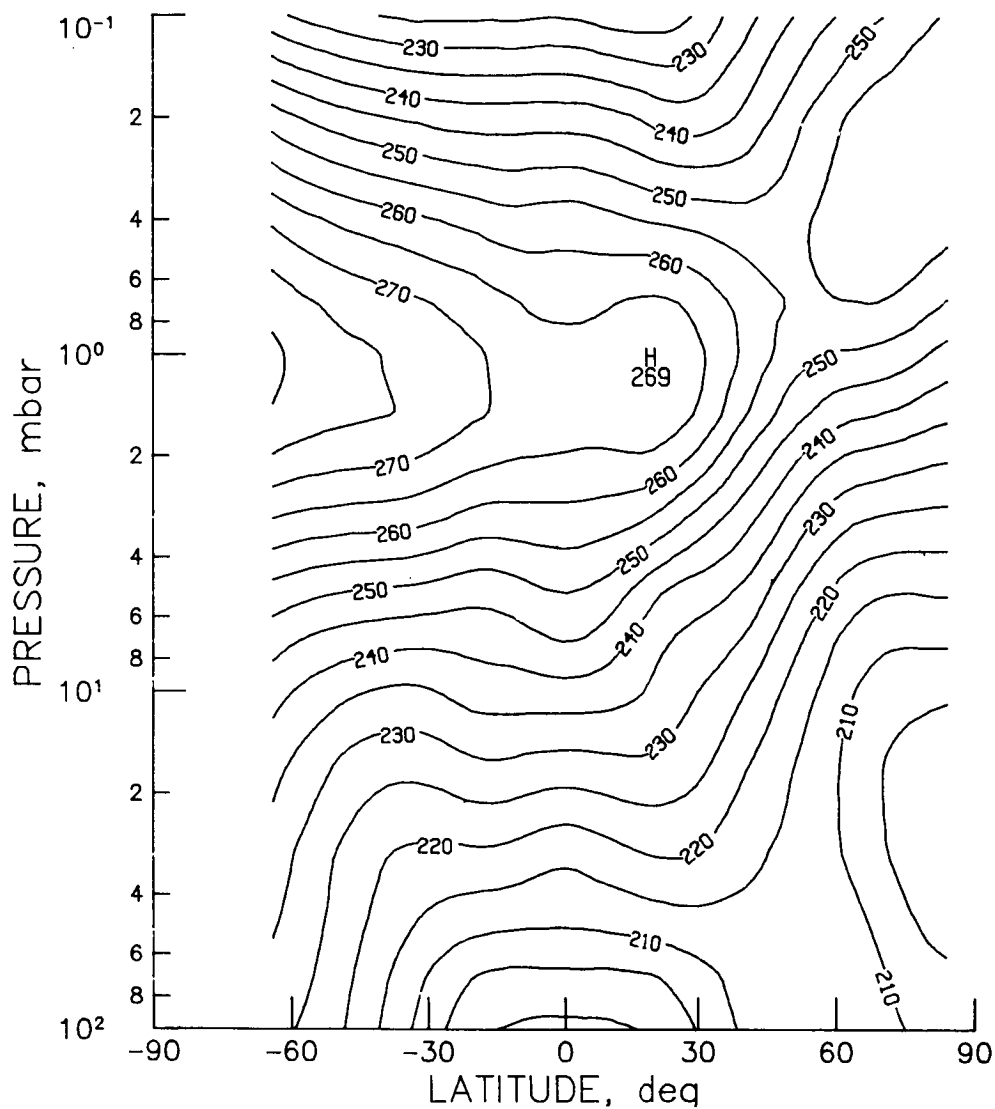


Figure T1 - LIMS monthly zonal mean temperature cross section for November 1978 (contour interval is 5.0°K).

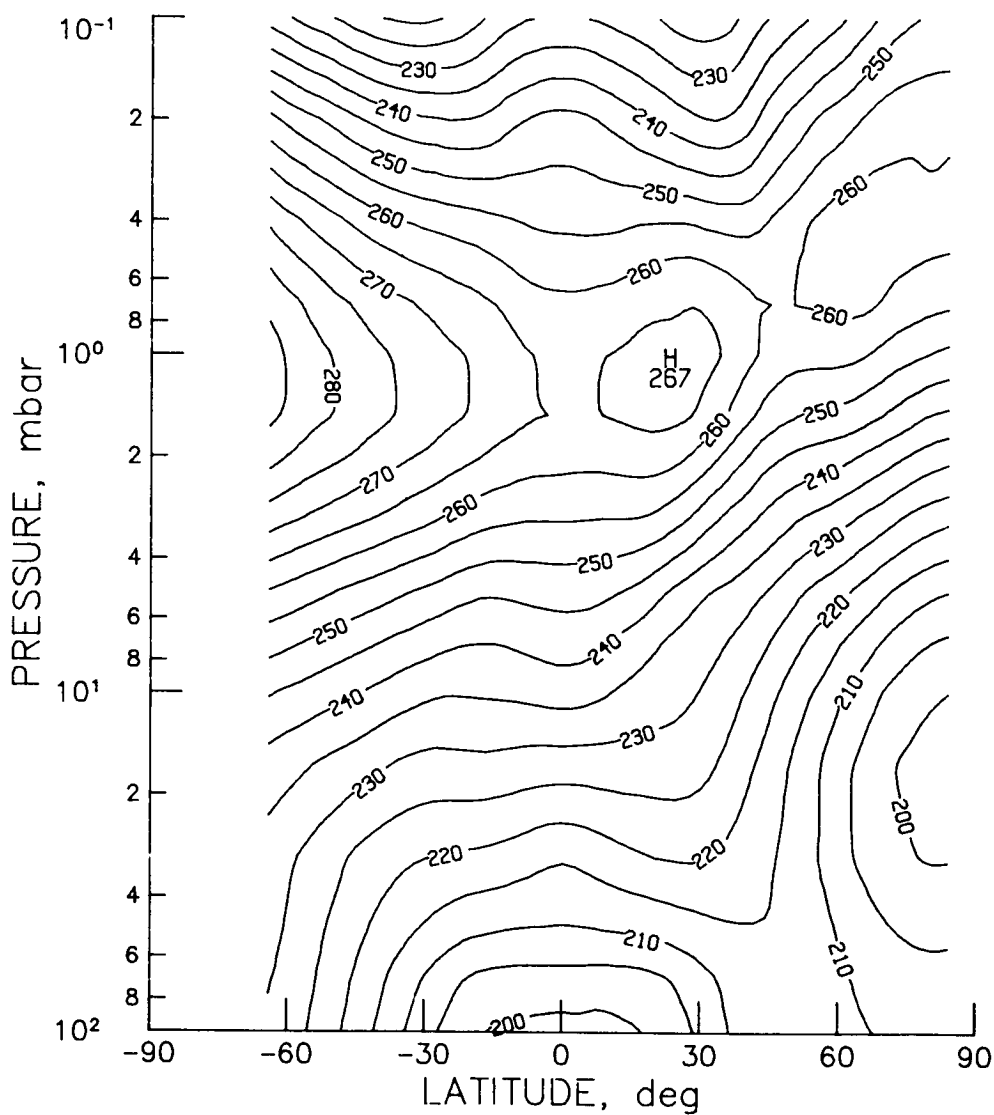


Figure T2 - LIMS monthly zonal mean temperature cross section for December 1978 (contour interval is 5.0°K).

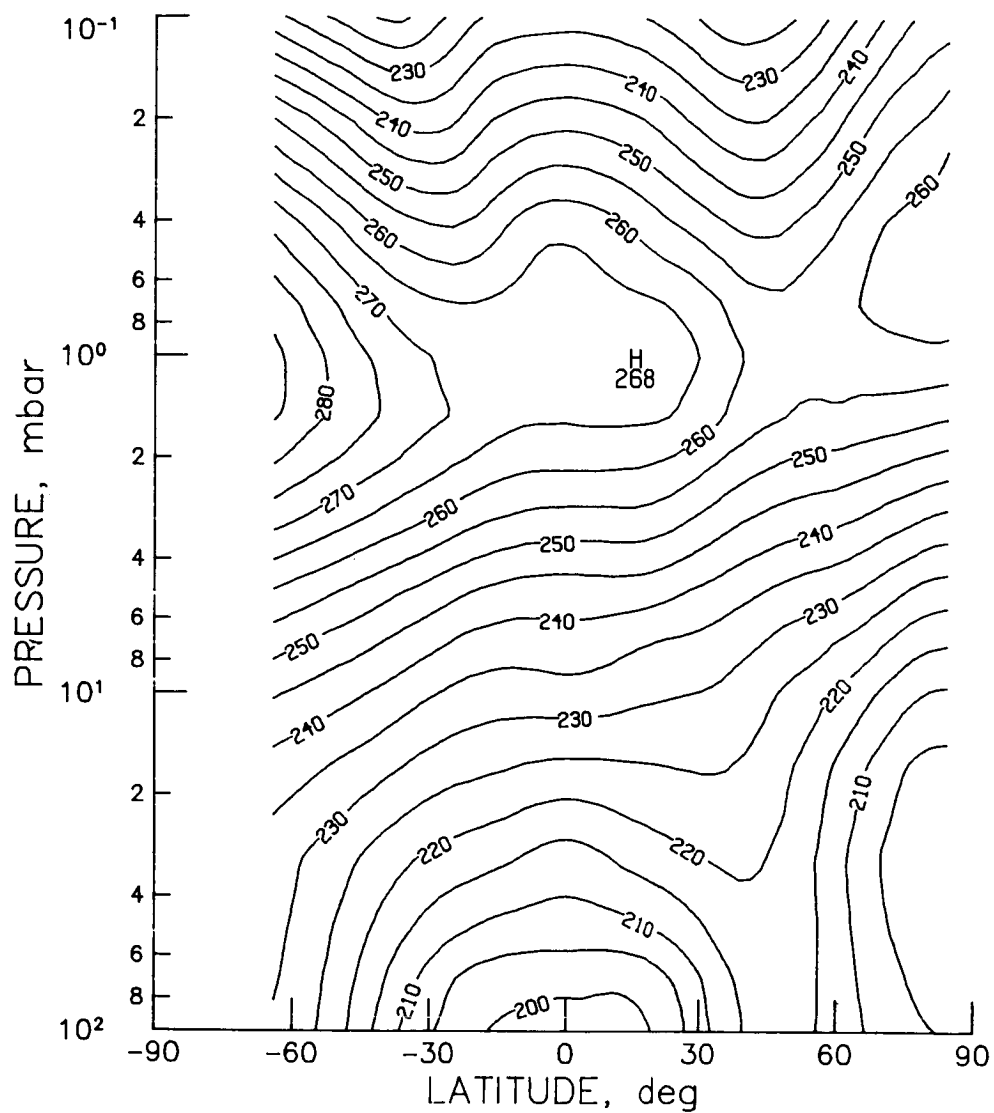


Figure T3 - LIMS monthly zonal mean temperature cross section for January 1979 (contour interval is 5.0°K).

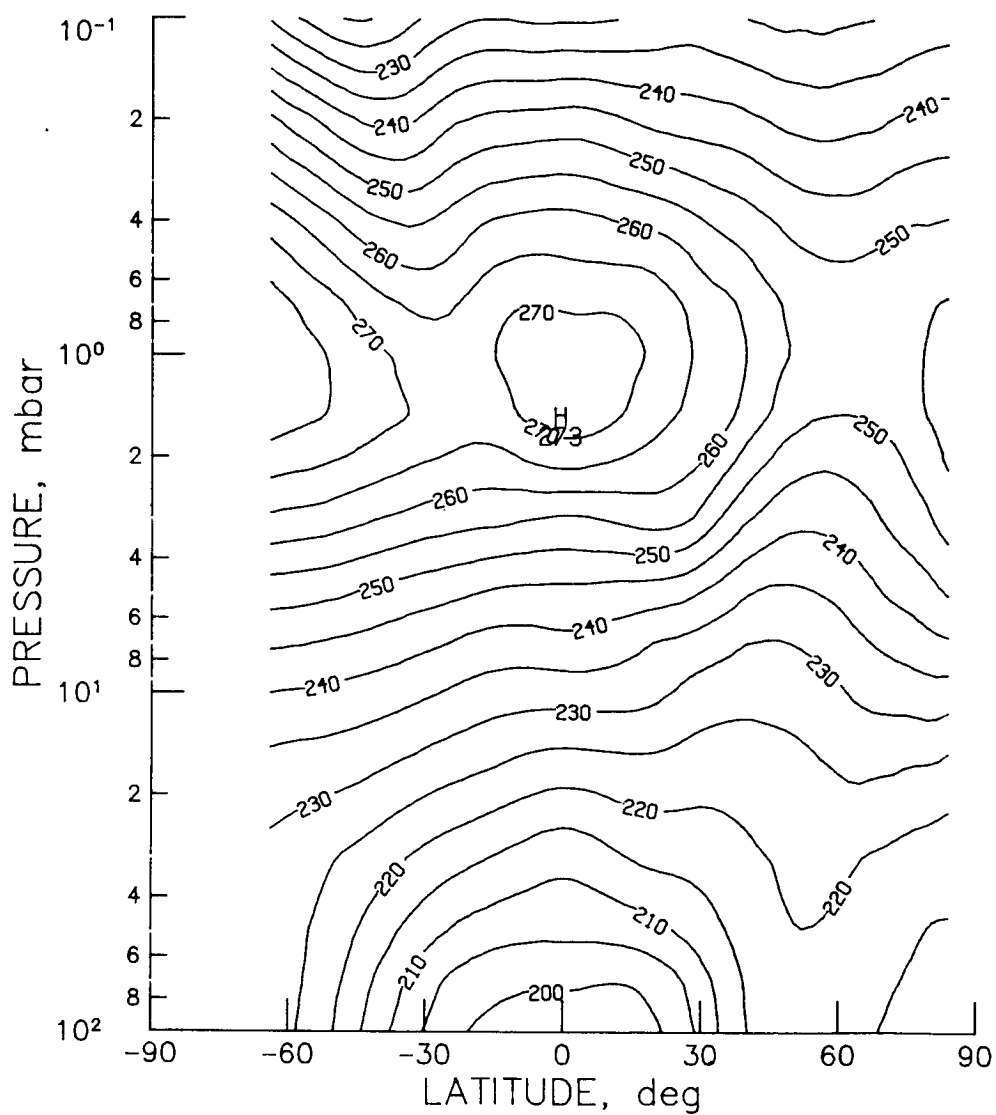


Figure T4 - LIMS monthly zonal mean temperature cross section for February 1979 (contour interval is 5.0°K).

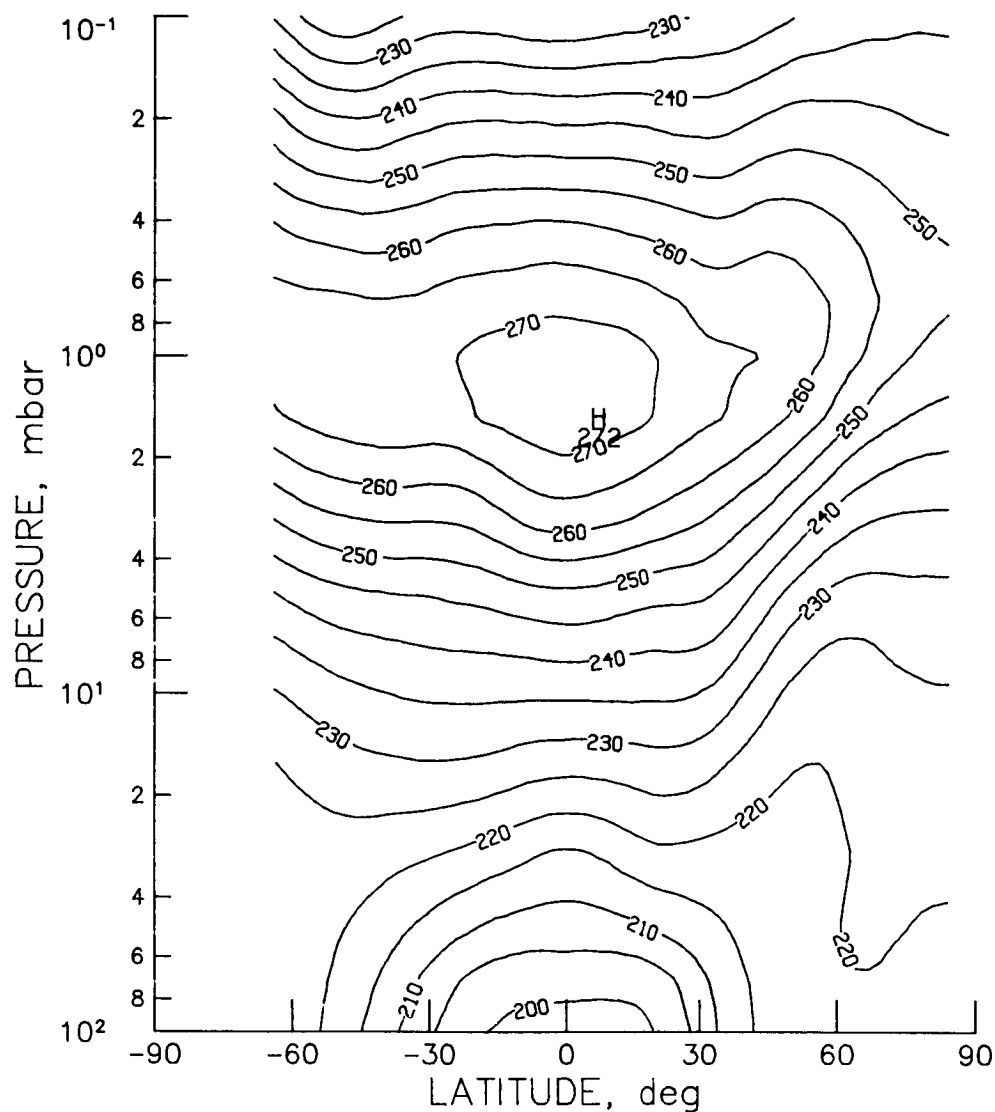


Figure T5 - LIMS monthly zonal mean temperature cross section for March 1979 (contour interval is 5.0°K).

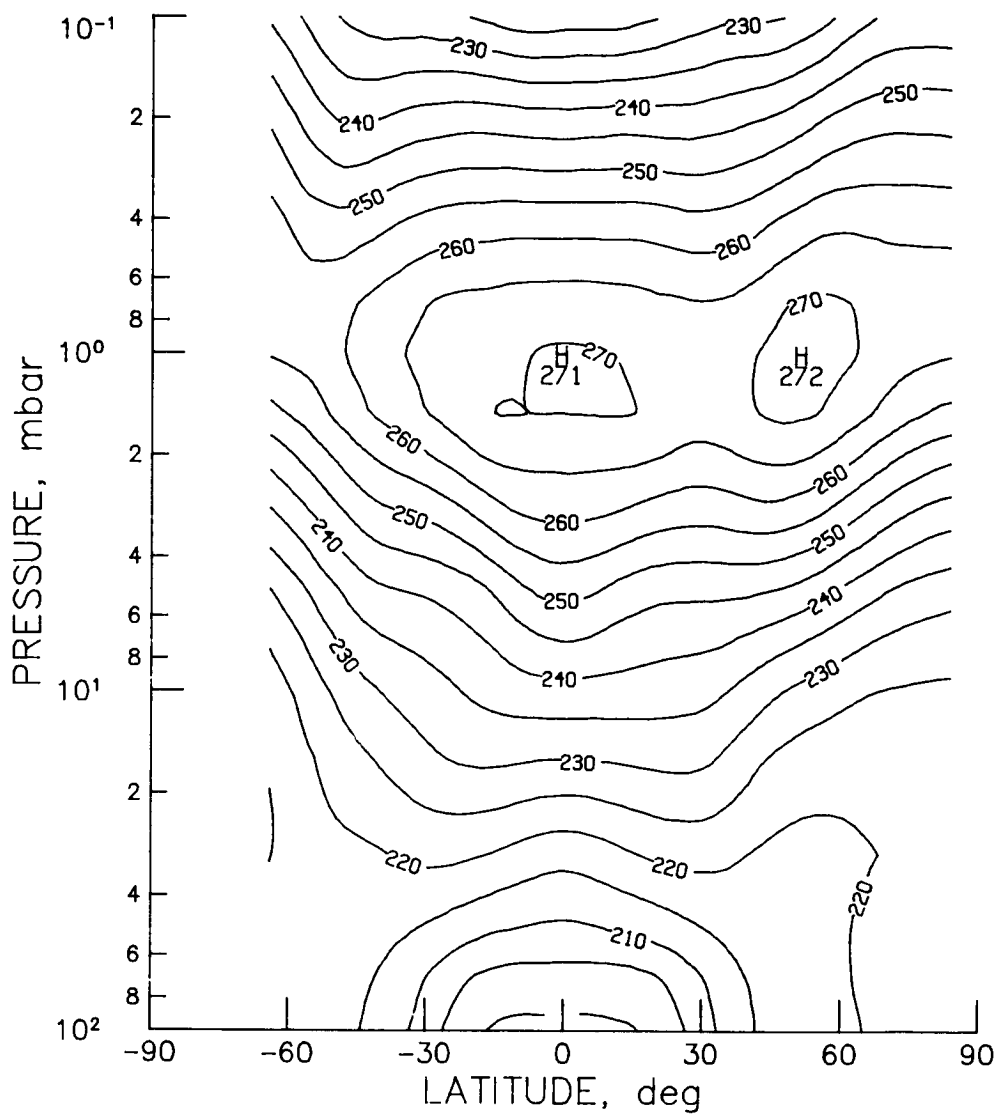


Figure T6 - LIMS monthly zonal mean temperature cross section for April 1979 (contour interval is 5.0°K).

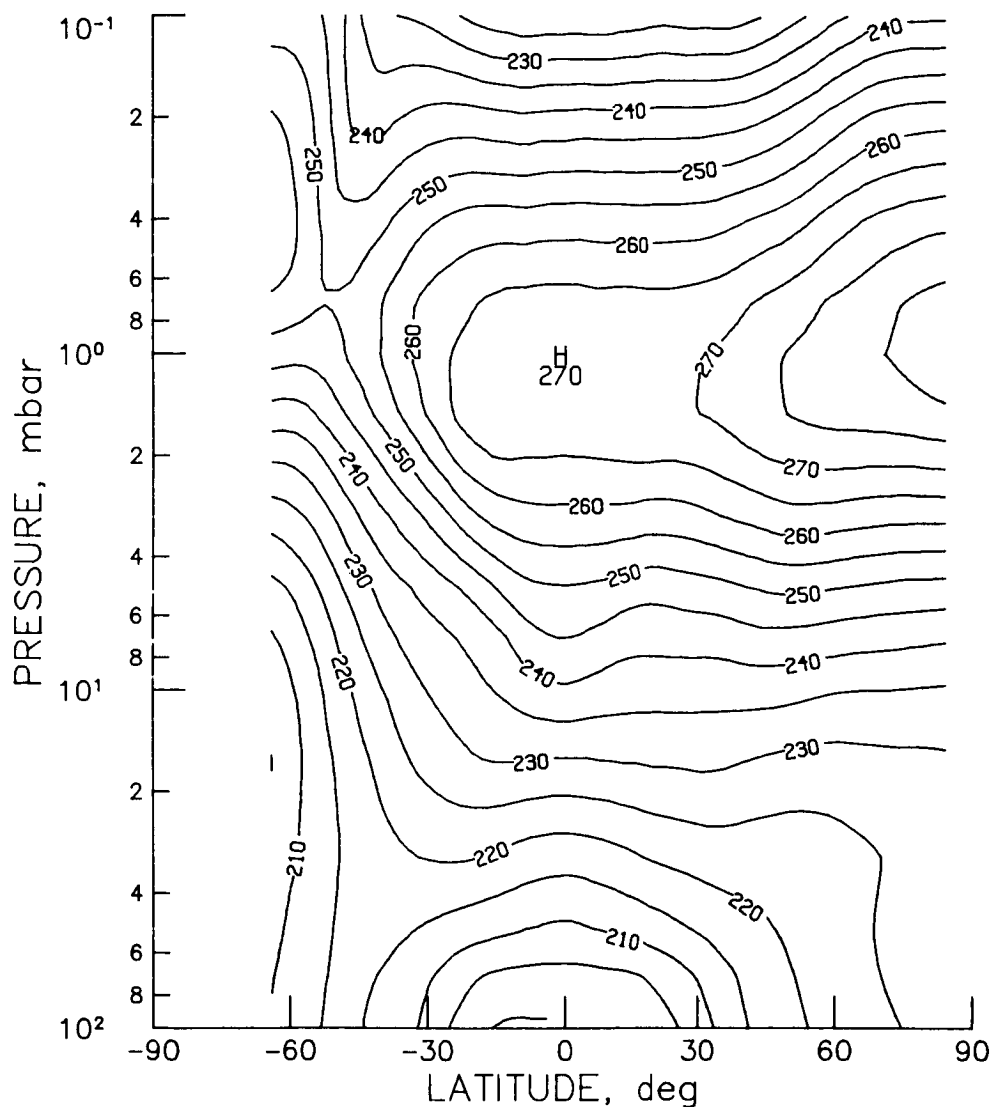
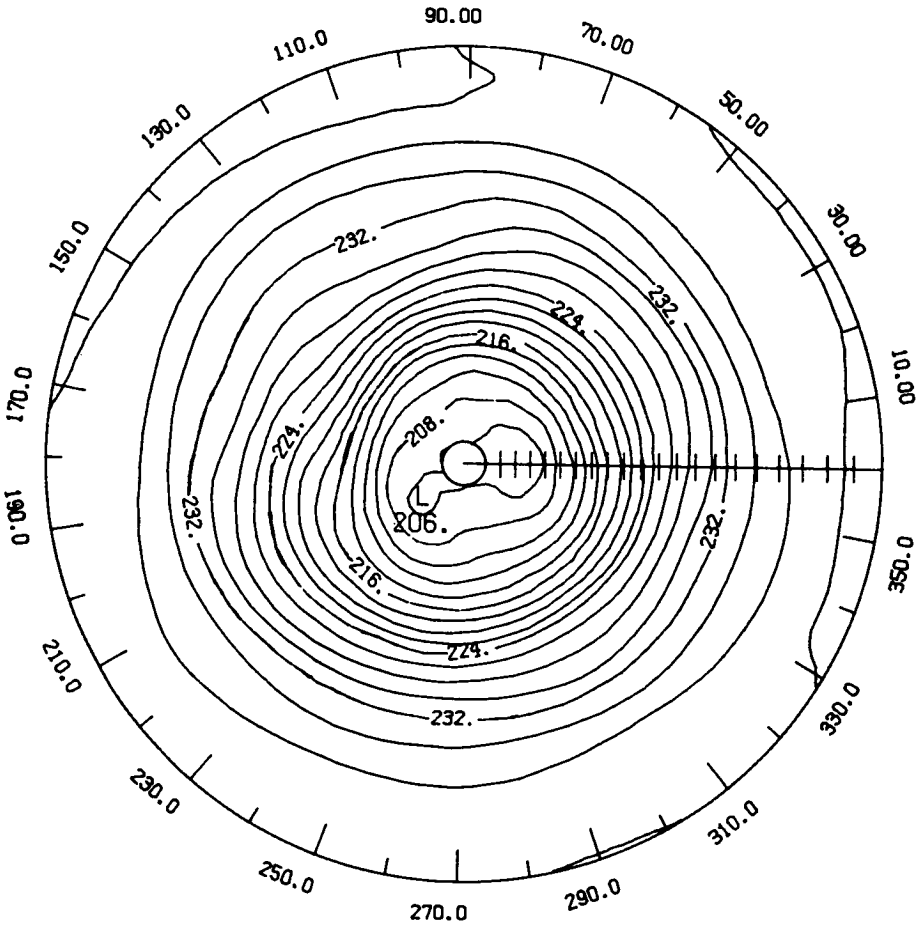
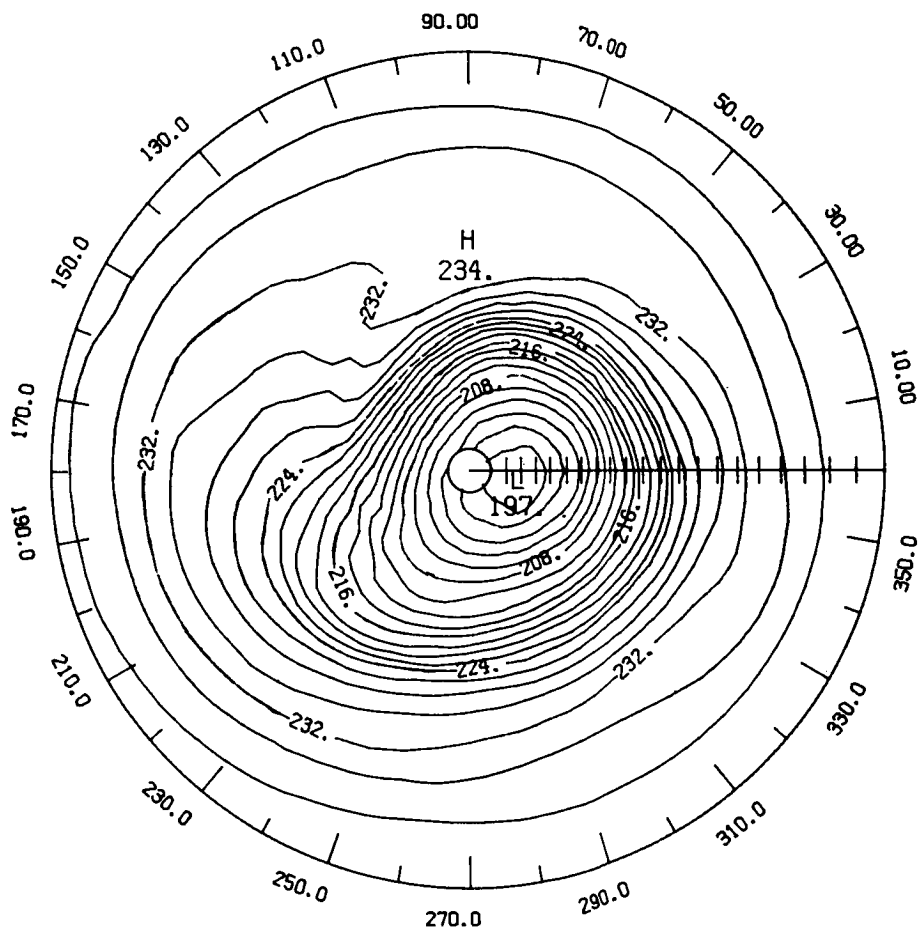


Figure T7 - LIMS monthly zonal mean temperature cross section for May 1979
(contour interval is 5.0°K).



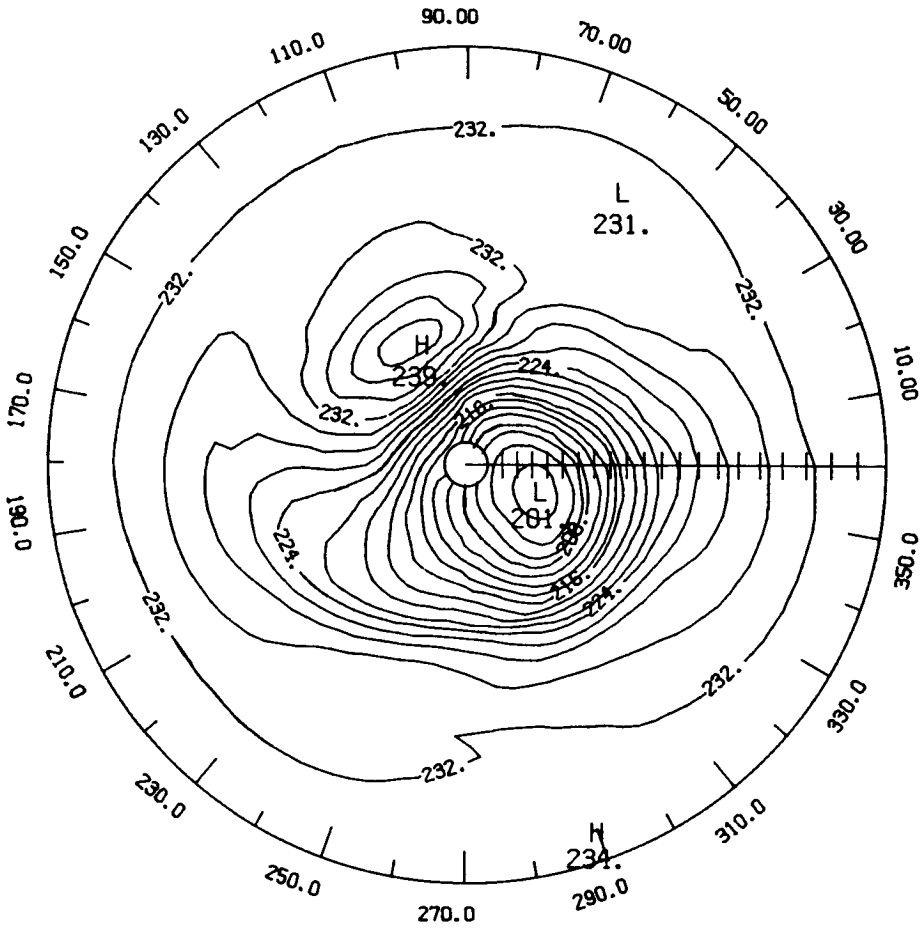
LATITUDE 0. TO 84.

Figure T8 - LIMS temperature monthly mean polar stereographic projection at 10 mb for November 1978 (contour interval is 2.0°K).



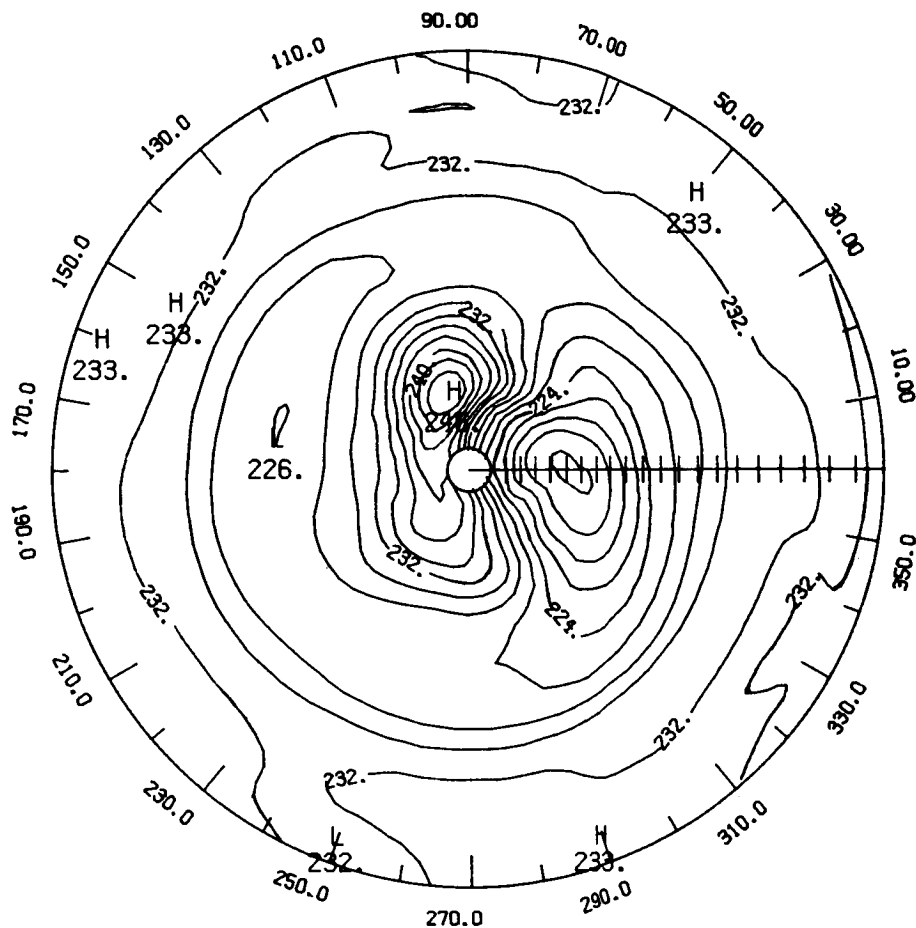
LATITUDE 0. TO 84.

Figure T9 - LIMS temperature monthly mean polar stereographic projection at 10 mb for December 1978 (contour interval is 2.0°K).



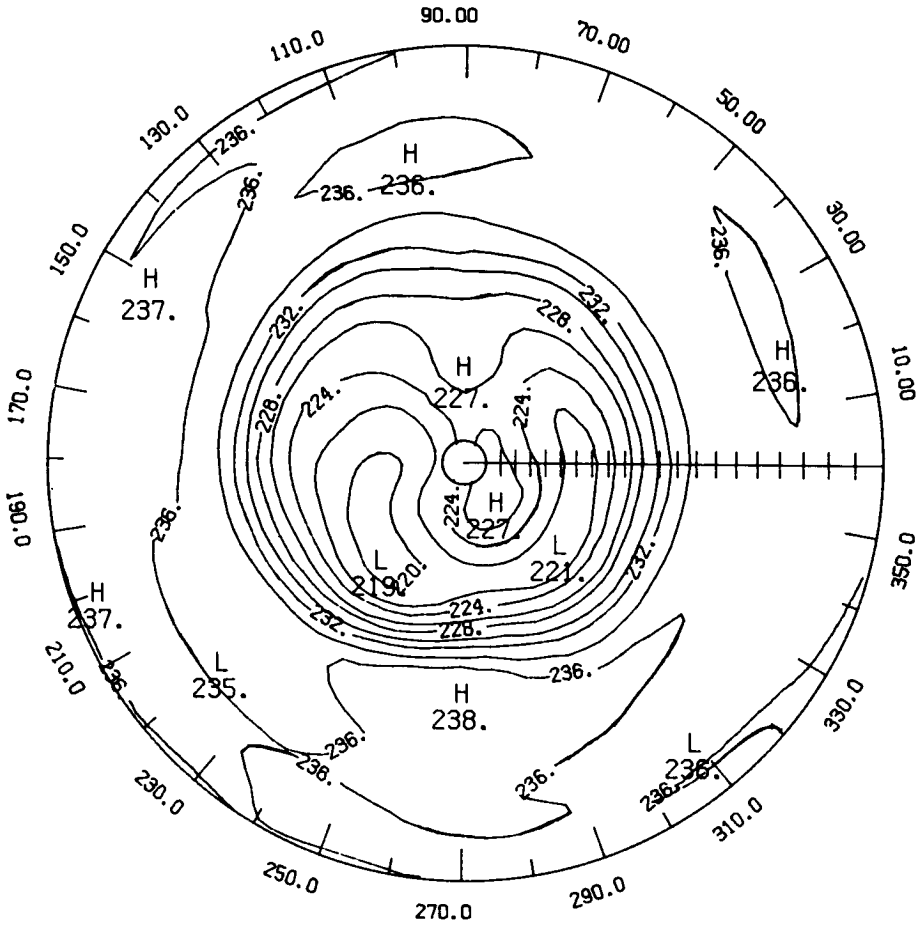
LATITUDE 0. TO 84.

Figure T10 - LIMS temperature monthly mean polar stereographic projection at 10 mb for January 1979 (contour interval is 2.0°K).



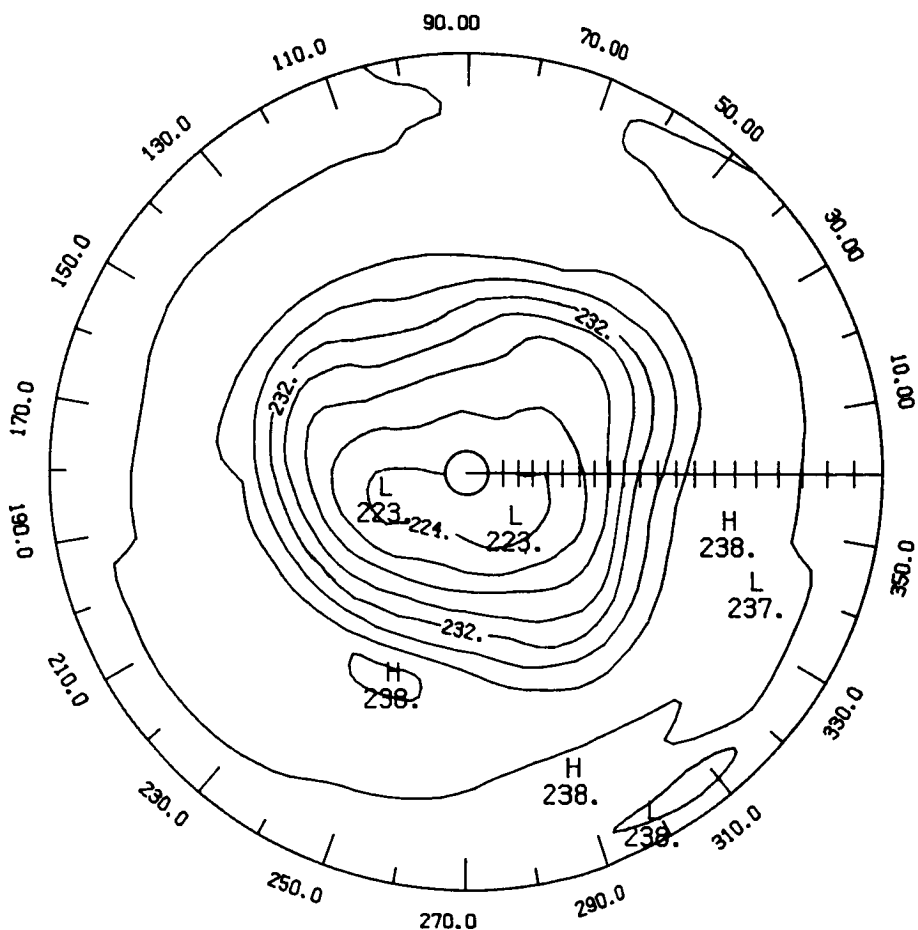
LATITUDE 0. TO 84.

Figure T11 - LIMS temperature monthly mean polar stereographic projection at 10 mb for February 1979 (contour interval is 2.0°K).



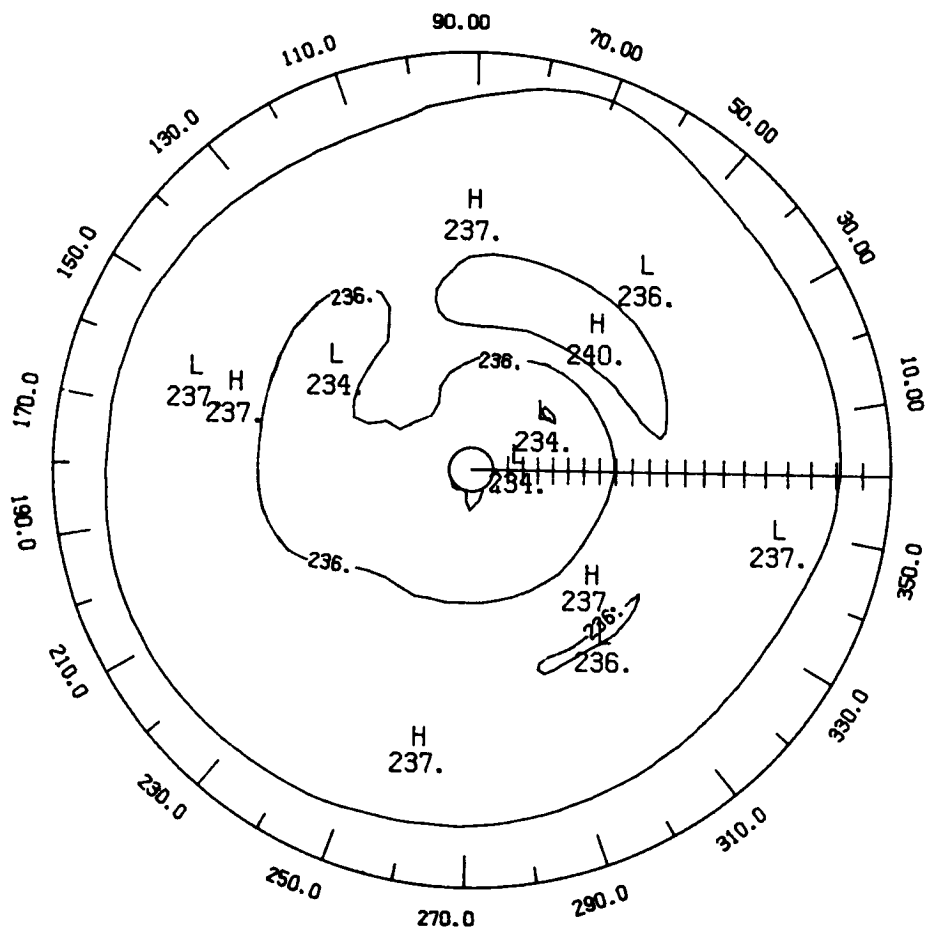
LATITUDE 0. TO 84.

Figure T12 - LIMS temperature monthly mean polar stereographic projection at 10 mb for March 1979 (contour interval is 2.0°K).



LATITUDE 0. TO 84.

Figure T13 - LIMS temperature monthly mean polar stereographic projection at 10 mb for April 1979 (contour interval is 2.0°K).



LATITUDE 0. TO 84.

Figure T14 - LIMS temperature monthly mean polar stereographic projection at 10 mb for May 1979 (contour interval is 2.0°K).

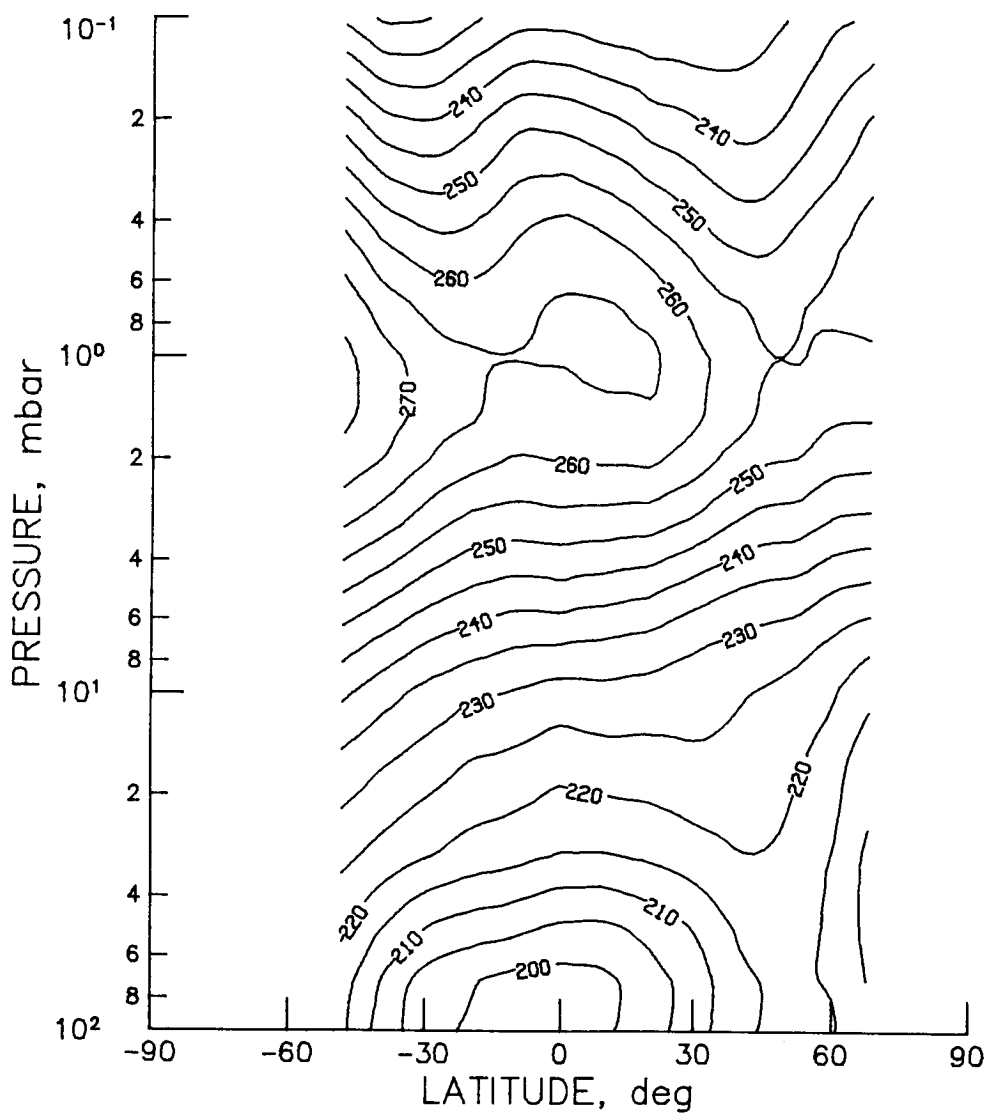


Figure T15 - SAMS monthly zonal mean temperature cross section for January 1979 (contour interval is 5.0°K).

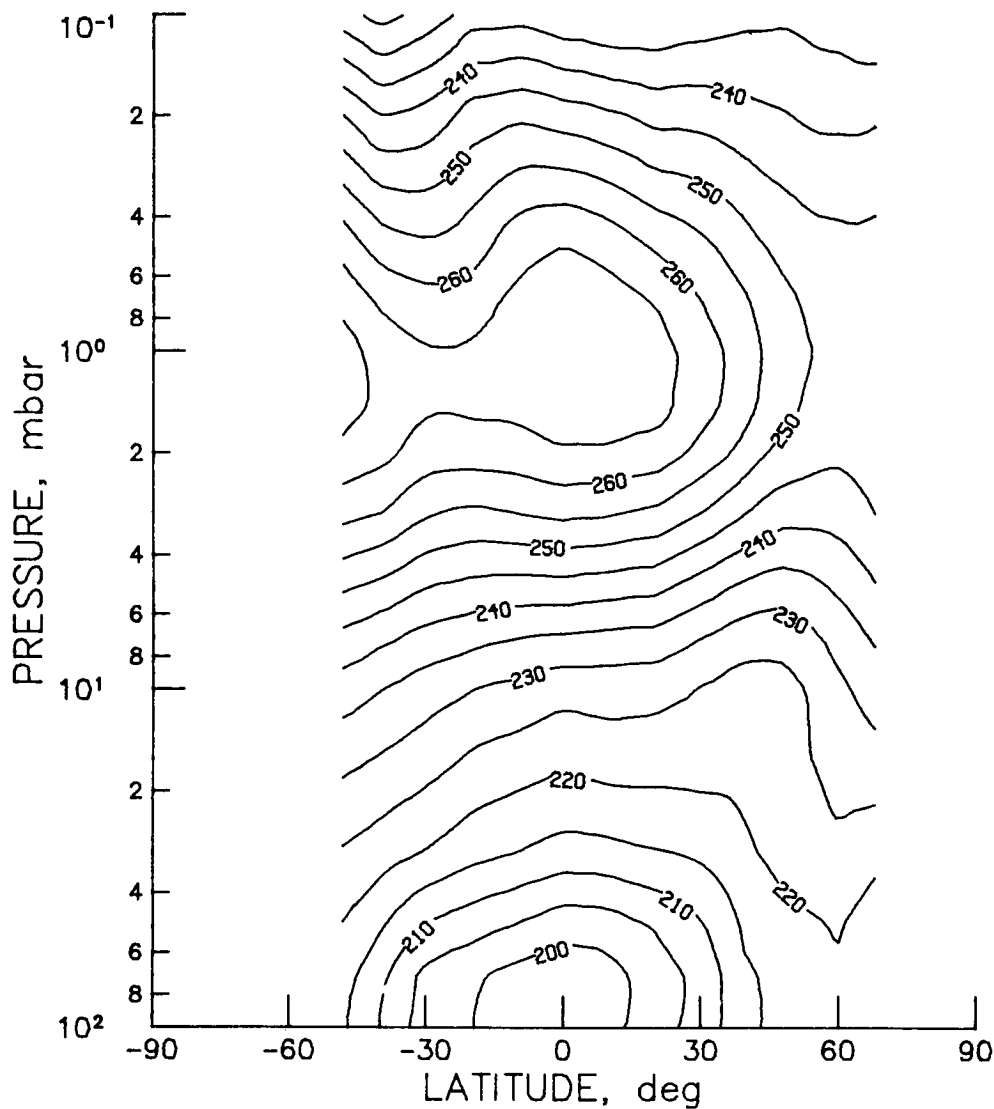


Figure T16 - SAMS monthly zonal mean temperature cross section for February 1979 (contour interval is 5.0°K).

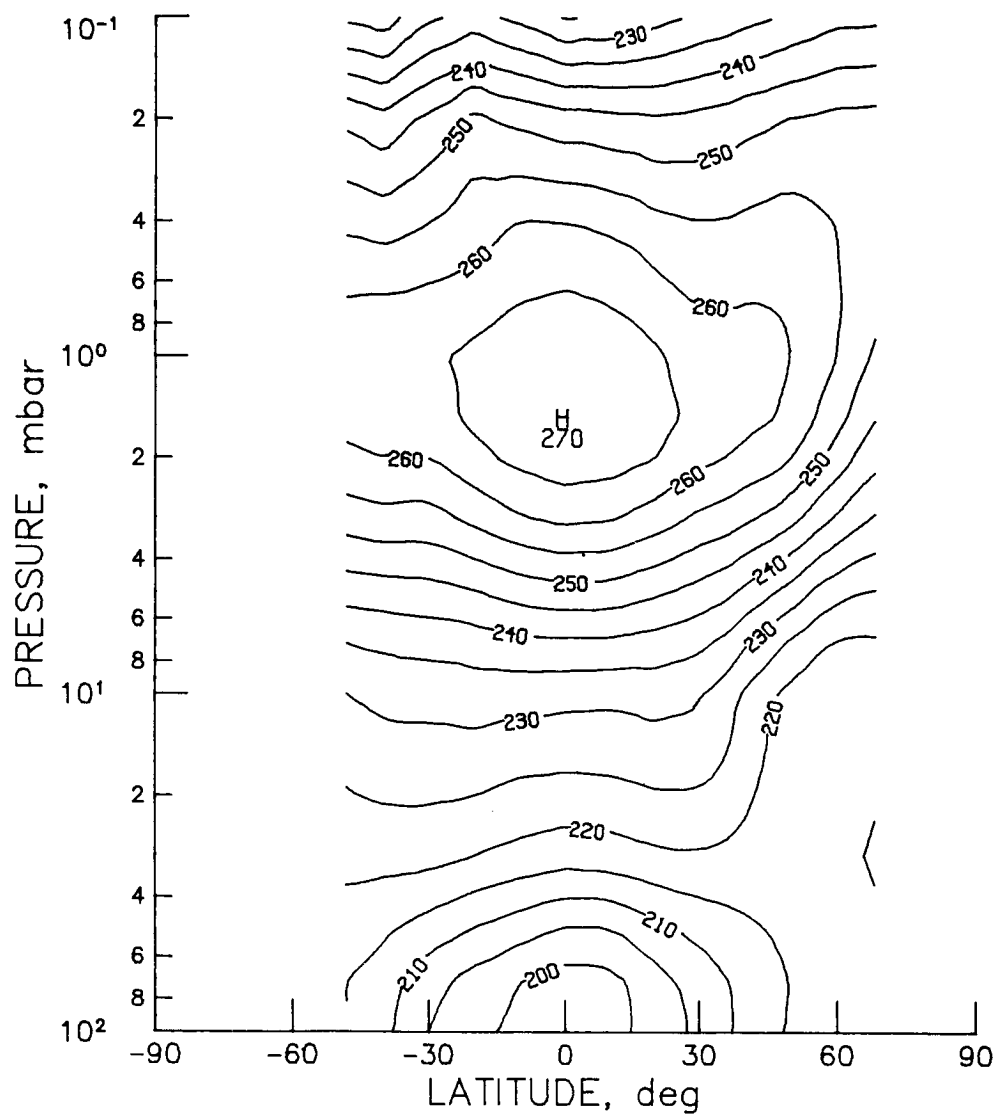


Figure T17 - SAMS monthly zonal mean temperature cross section for March 1979 (contour interval is 5.0°K).

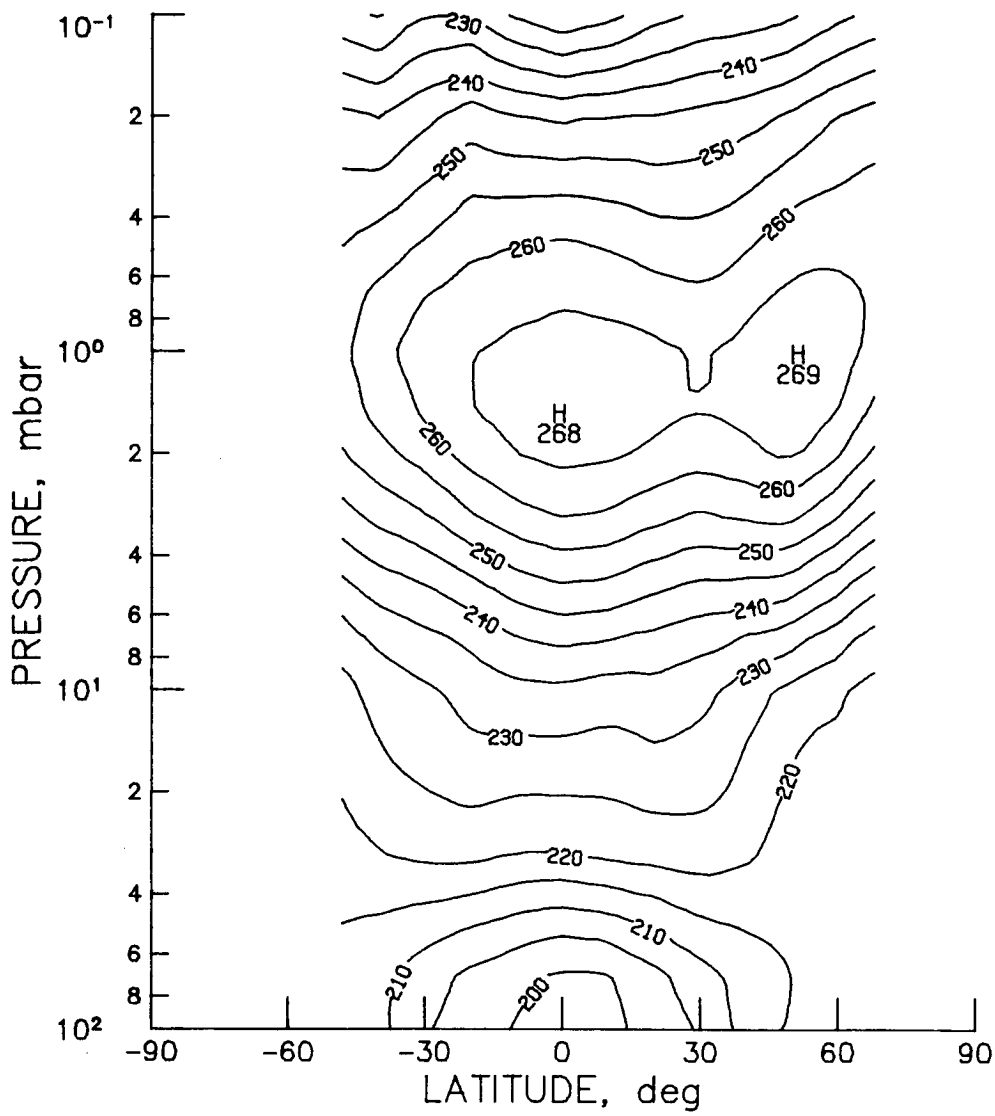


Figure T18 - SAMS monthly zonal mean temperature cross section for April 1979 (contour interval is 5.0°K).

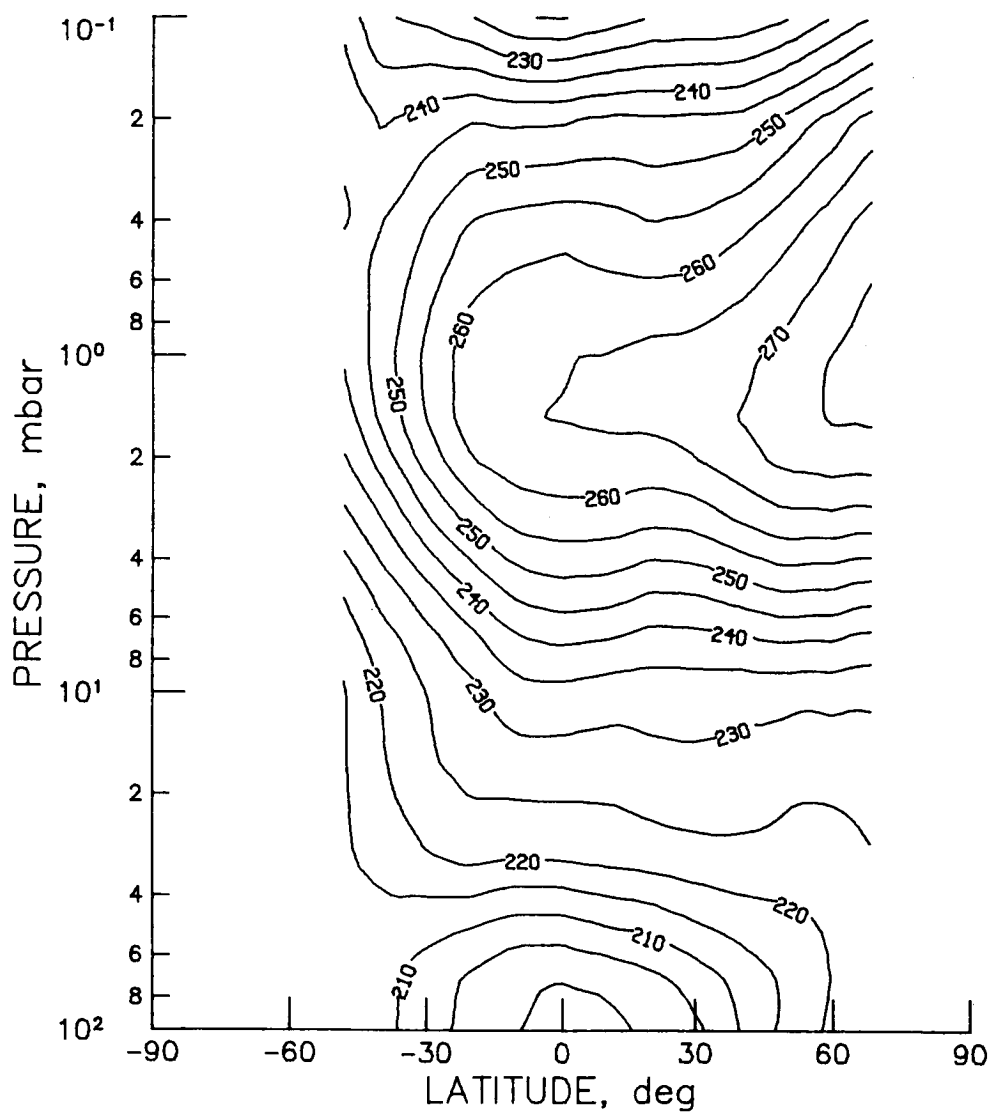


Figure T19 - SAMS monthly zonal mean temperature cross section for May 1979
(contour interval is 5.0°K).

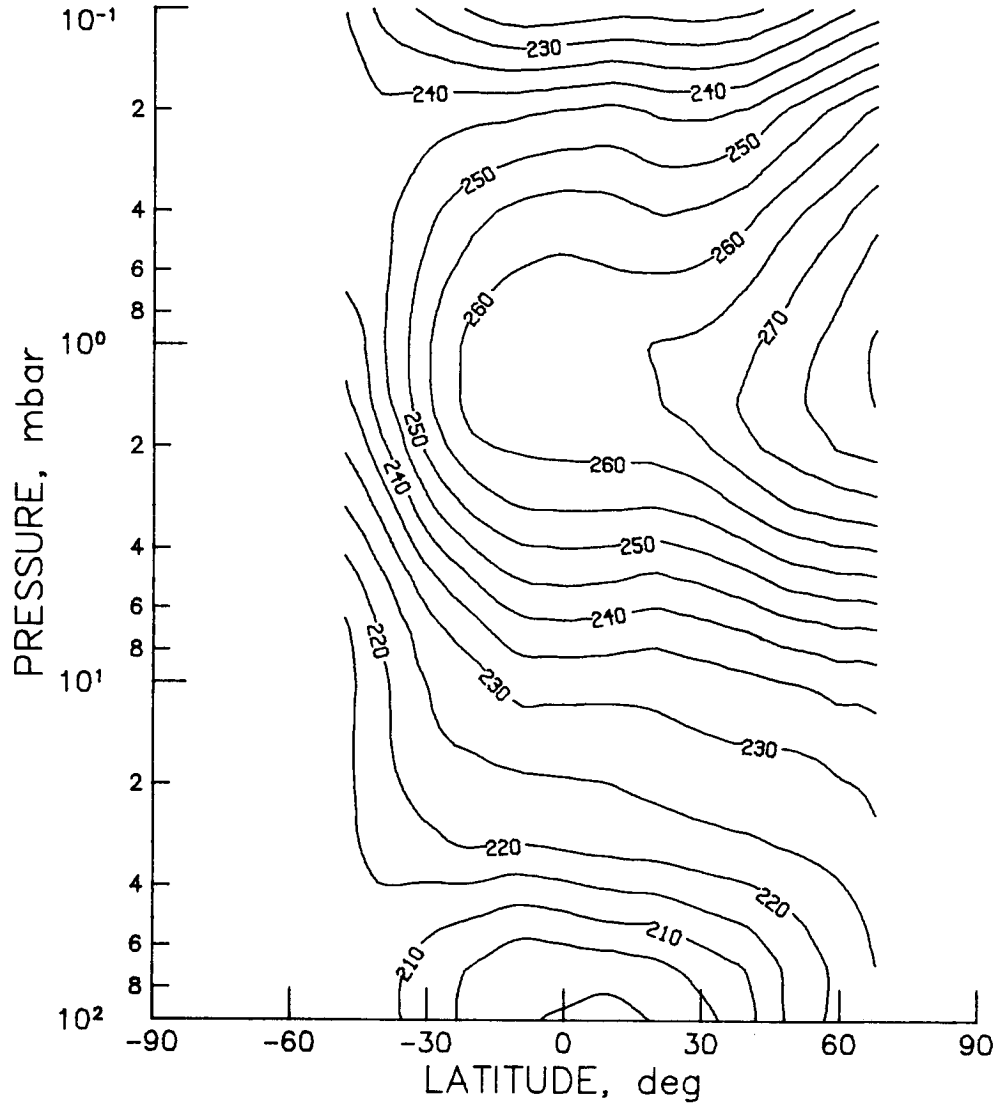


Figure T20 - SAMS monthly zonal mean temperature cross section for June 1979 (contour interval is 5.0°K).

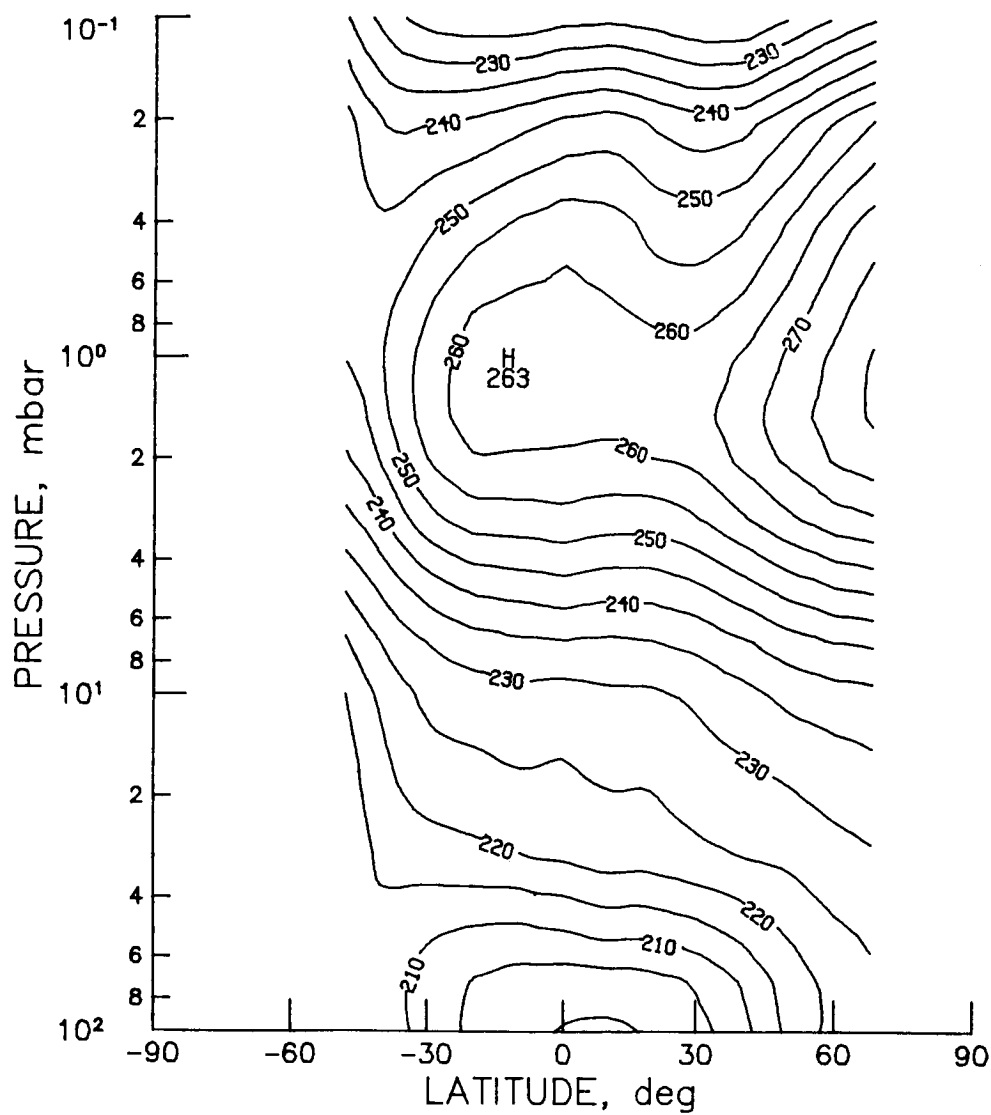


Figure T21 - SAMS monthly zonal mean temperature cross section for July 1979 (contour interval is 5.0°K).

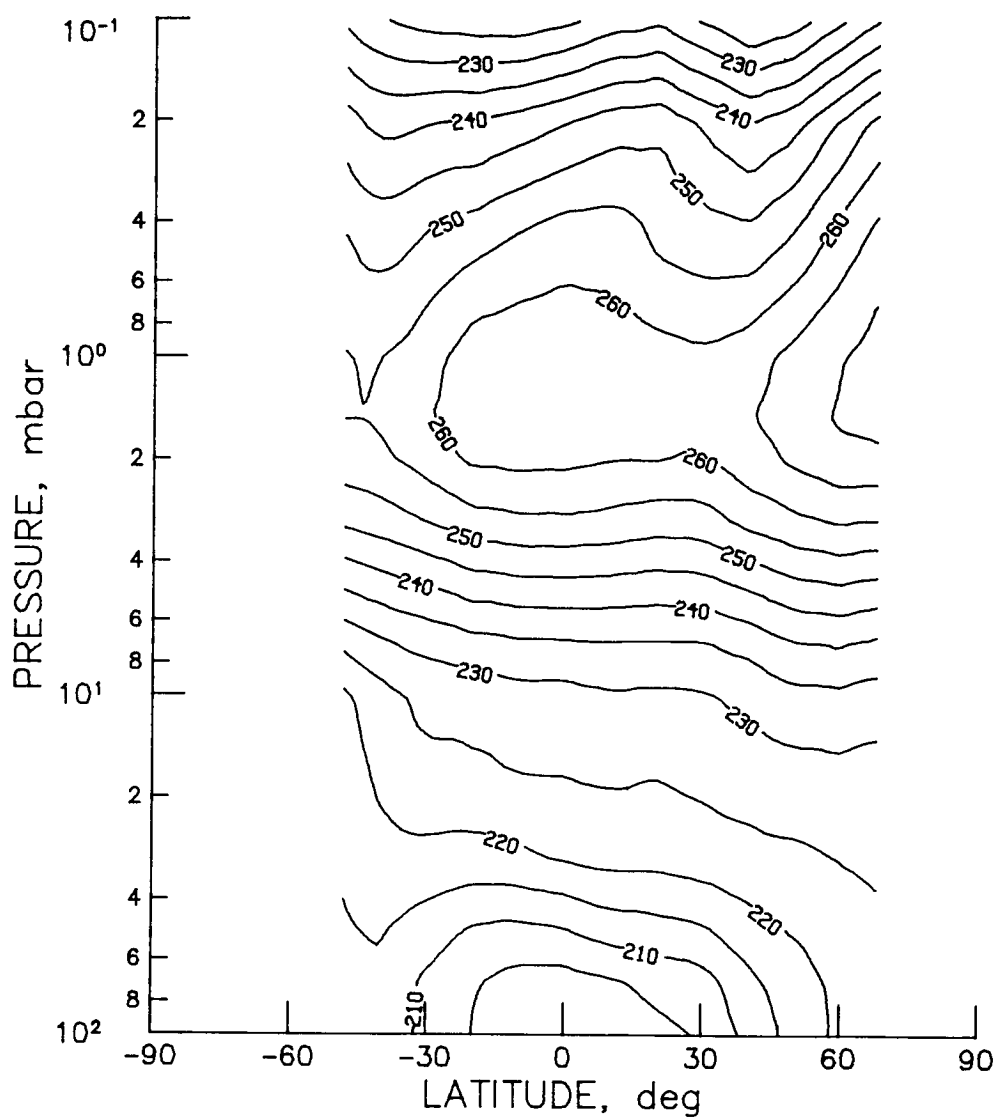


Figure T22 - SAMS monthly zonal mean temperature cross section for August 1979 (contour interval is 5.0°K).

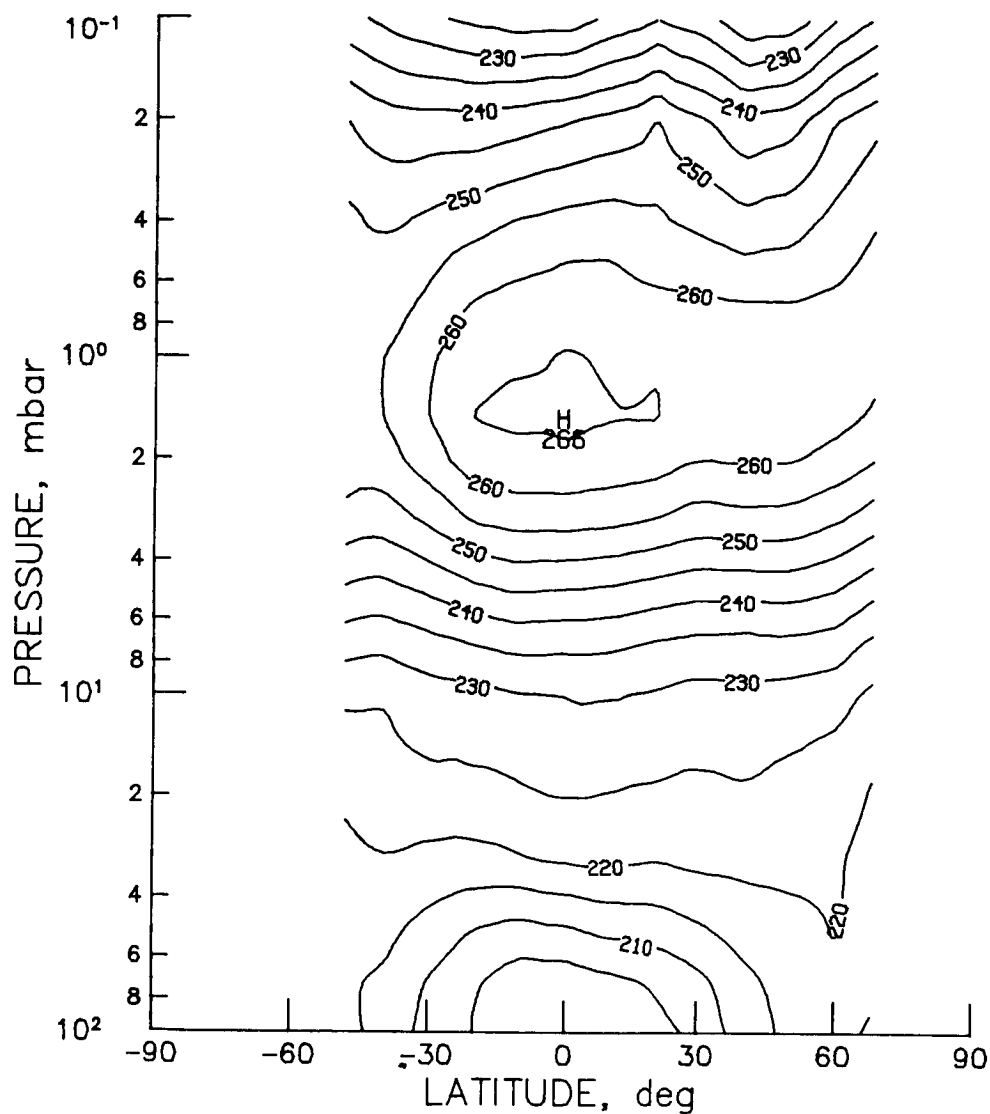


Figure T23 - SAMS monthly zonal mean temperature cross section for September 1979 (contour interval is 5.0°K).

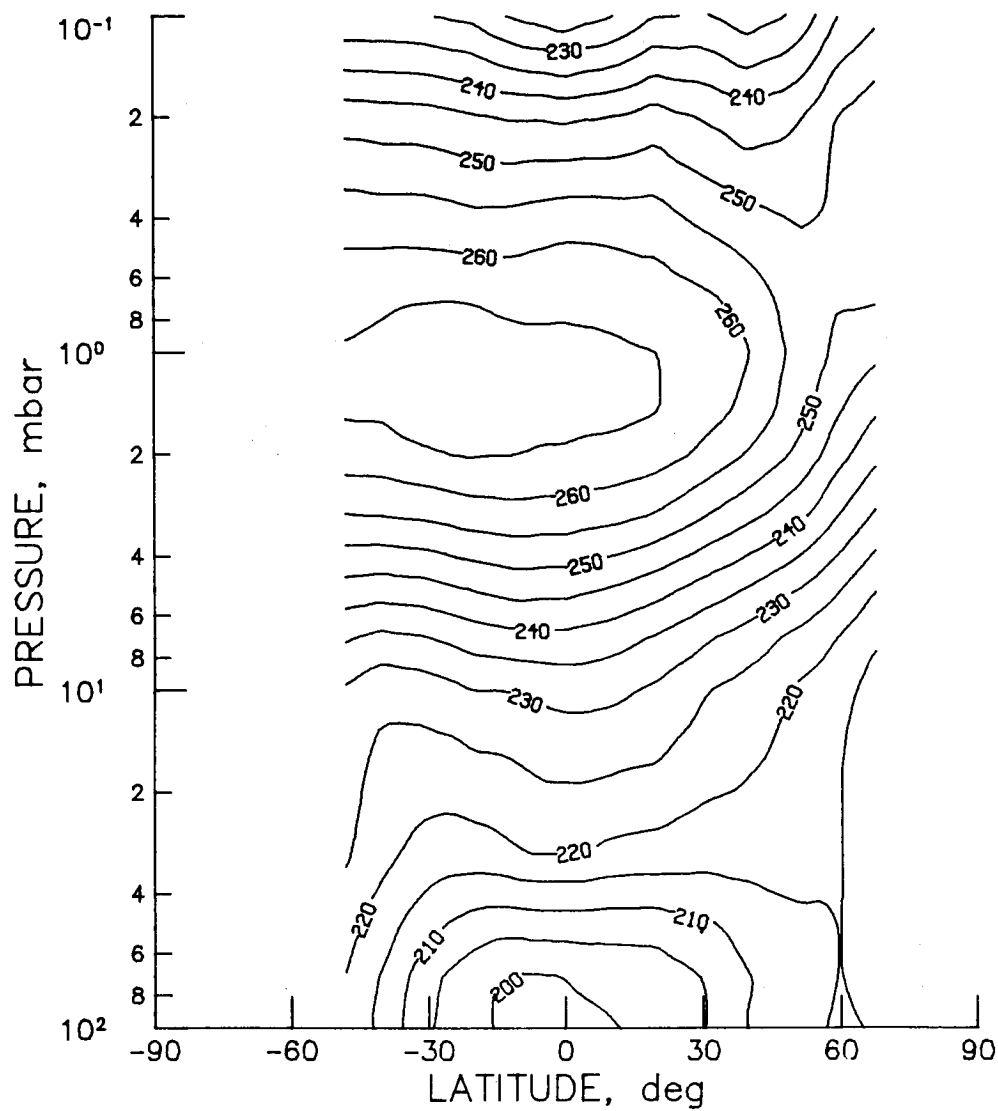


Figure T24 - SAMS monthly zonal mean temperature cross section for October 1979 (contour interval is 5.0°K).

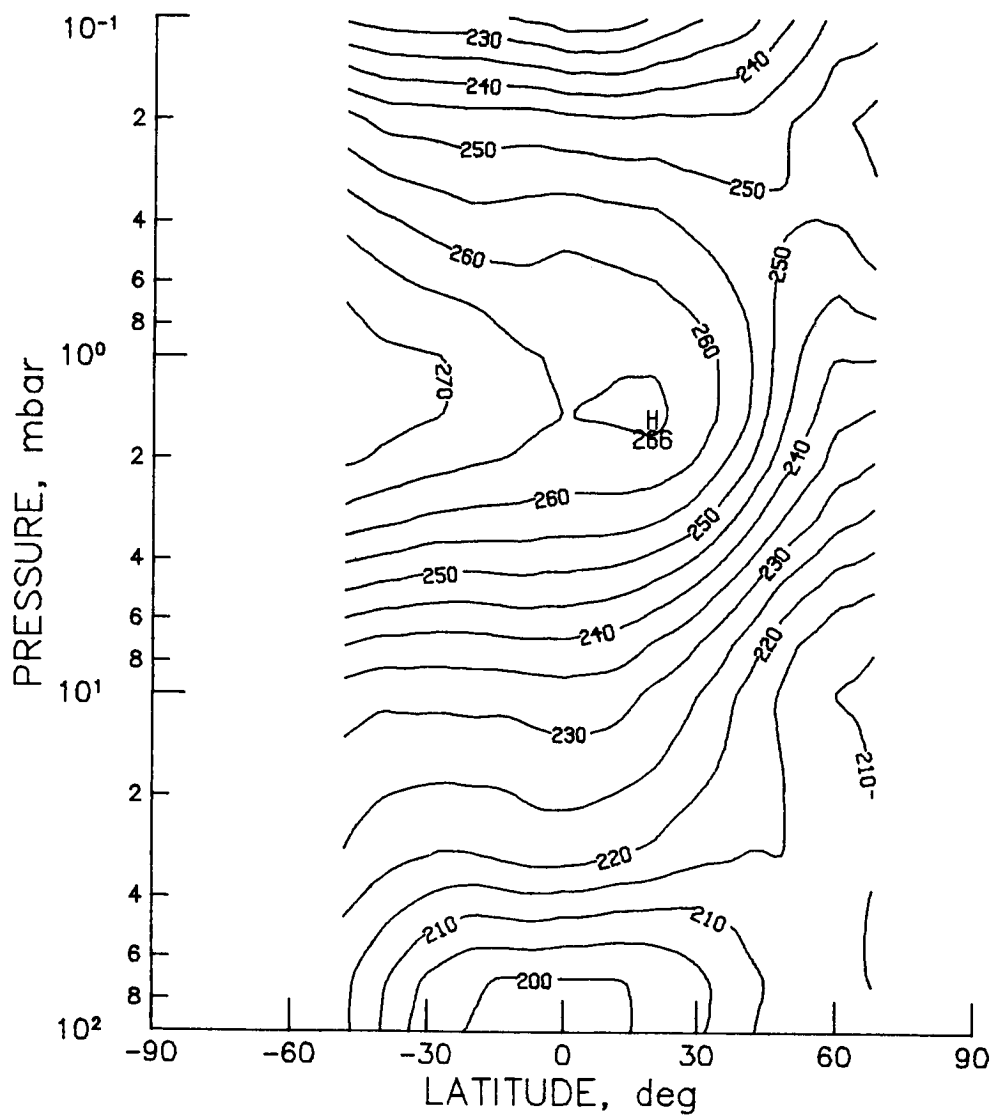


Figure T25 - SAMS monthly zonal mean temperature cross section for November 1979 (contour interval is 5.0°K).

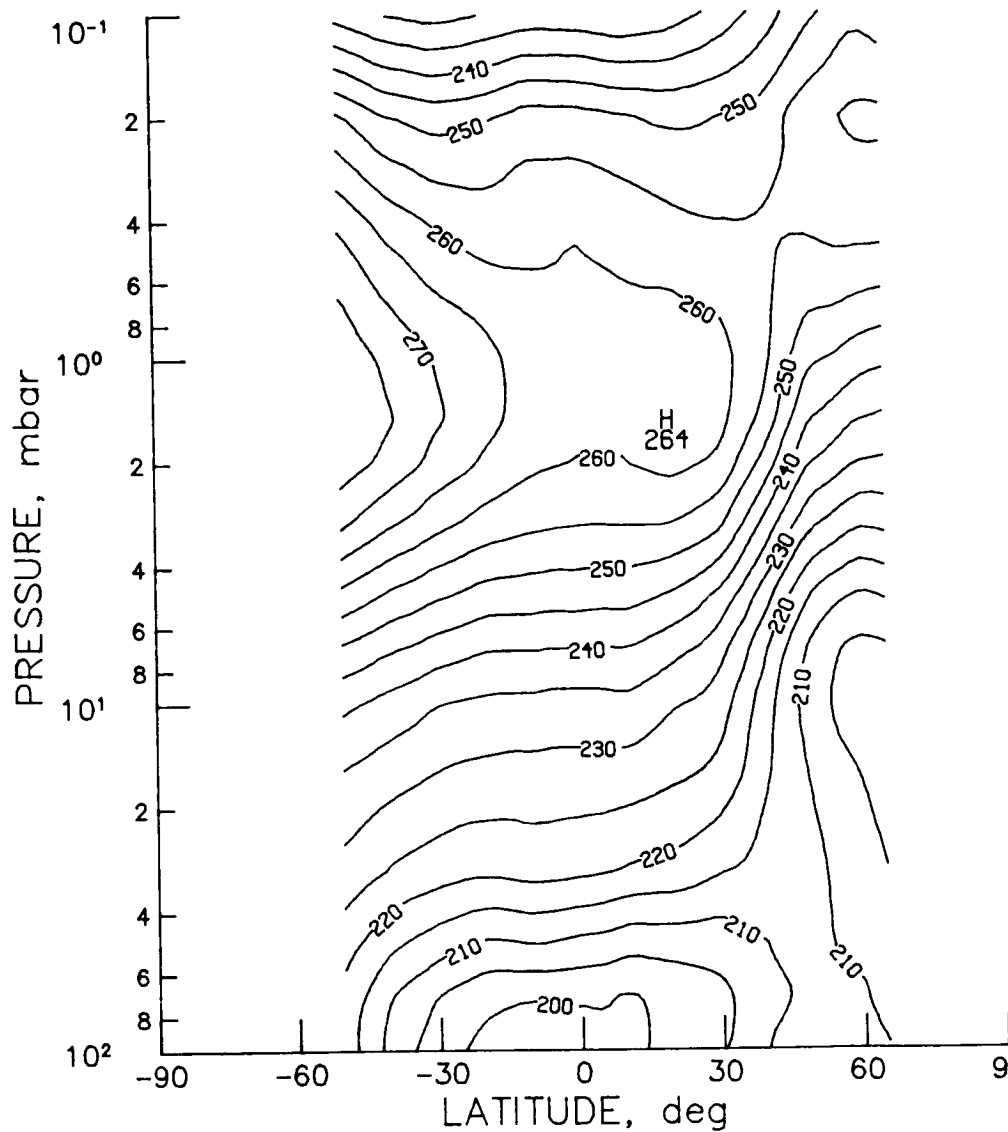
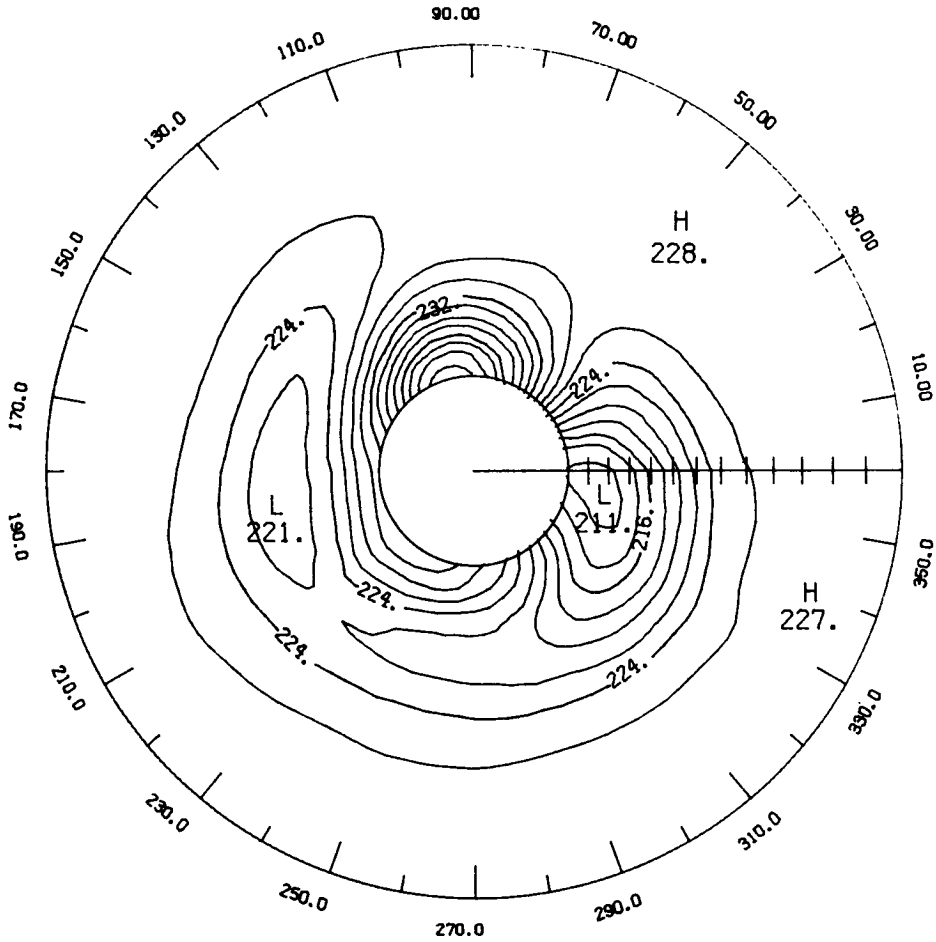
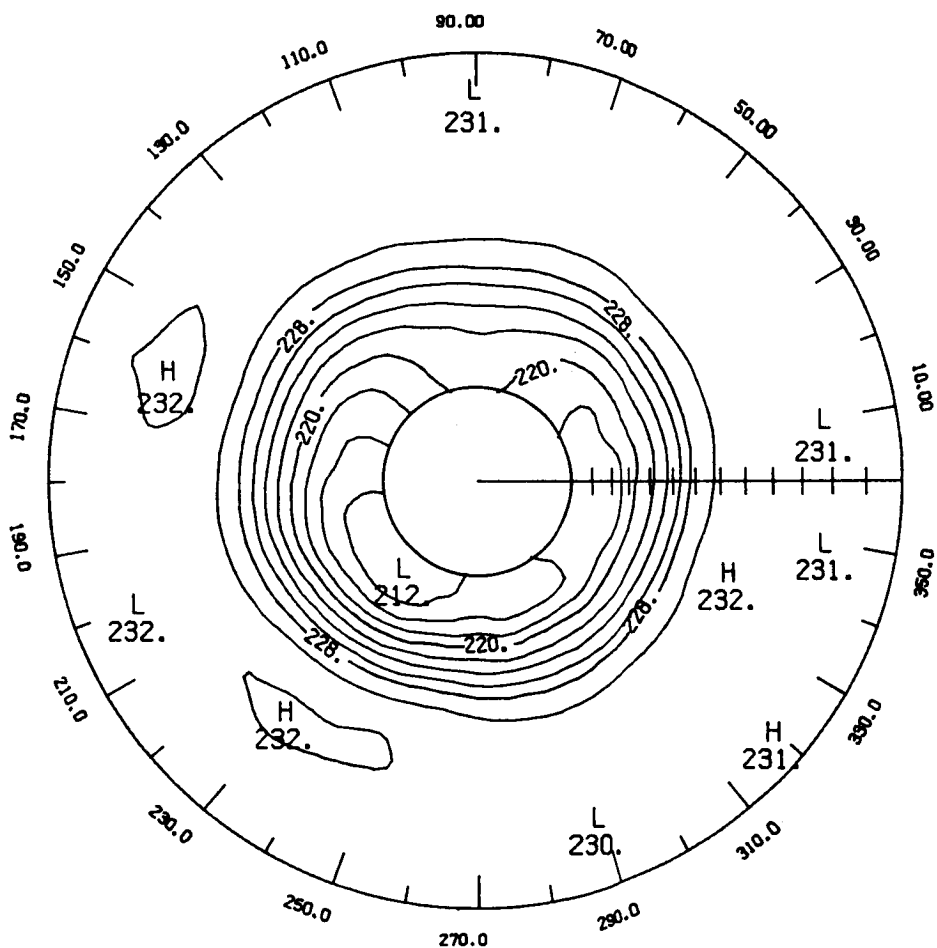


Figure T26 - SAMS monthly zonal mean temperature cross section for December 1979 (contour interval is 5.0°K).



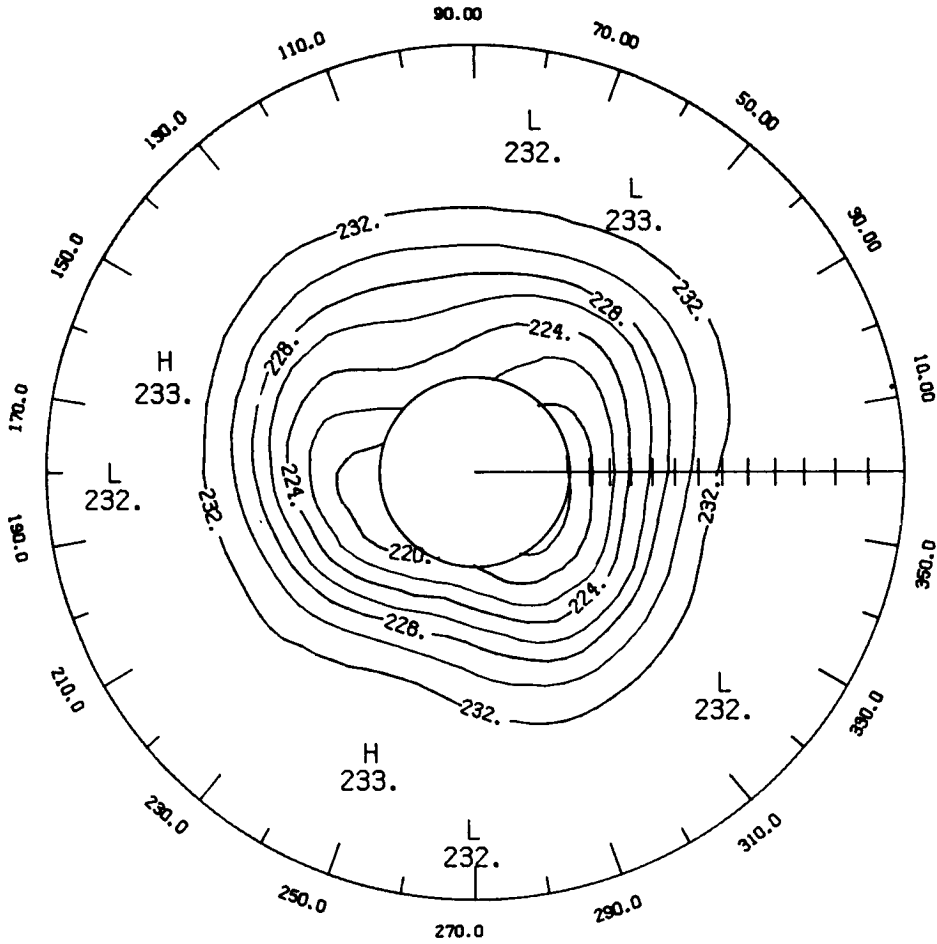
LATITUDE 0. TO 65.

Figure T28 - SAMS temperature monthly mean polar stereographic projection at 10 mb for February 1979 (contour interval is 2.0°K).



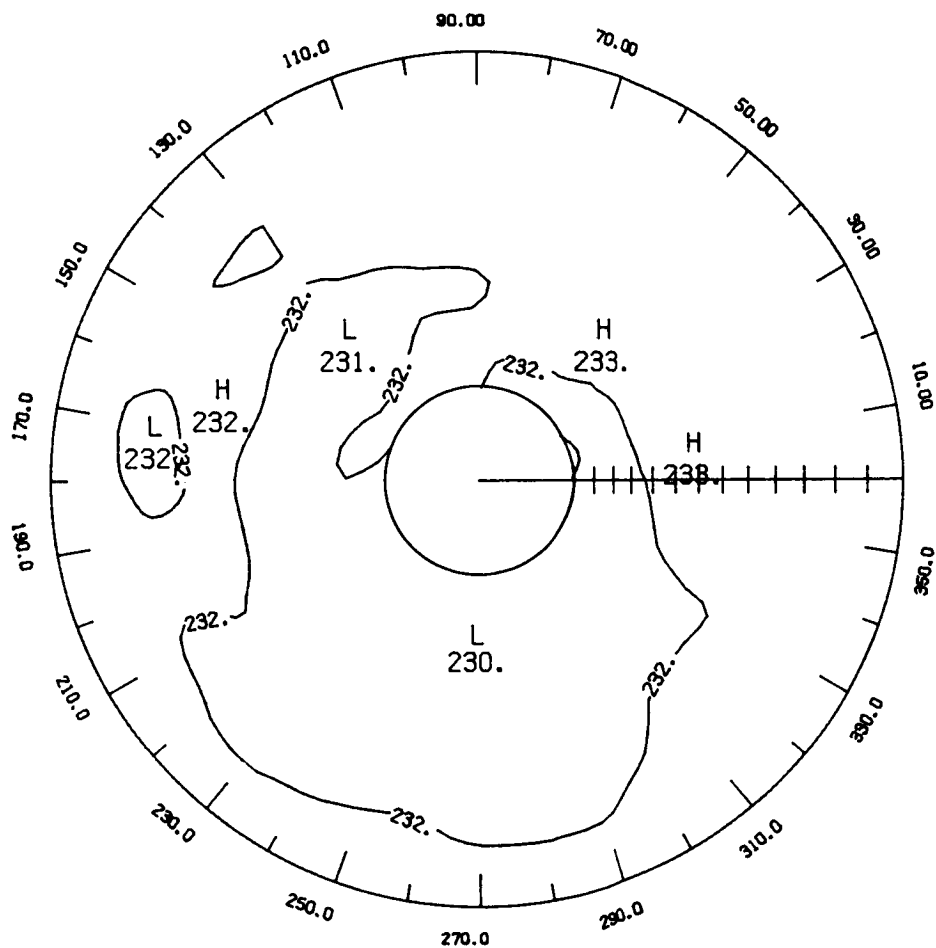
LATITUDE 0. TO 65.

Figure T29 - SAMS temperature monthly mean polar stereographic projection at 10 mb for March 1979 (contour interval is 2.0°K).



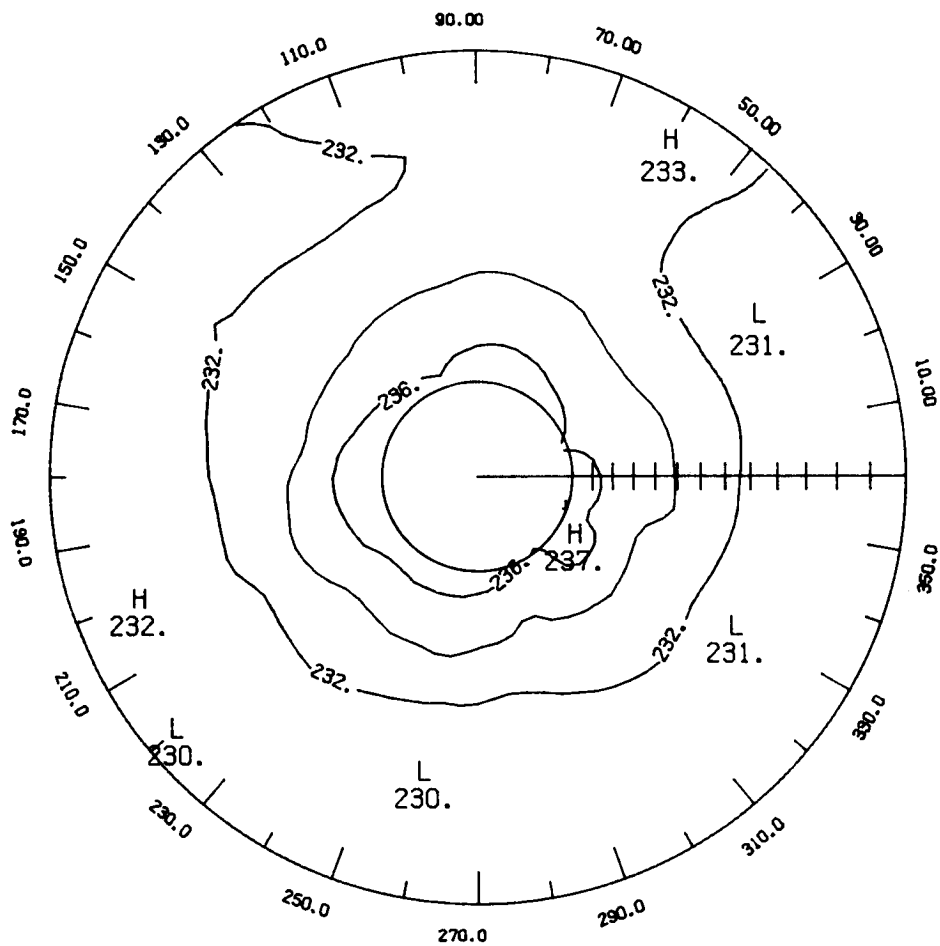
LATITUDE 0. TO 65.

Figure T30 - SAMS temperature monthly mean polar stereographic projection at 10 mb for April 1979 (contour interval is 2.0°K).



LATITUDE 0. TO 65.

Figure T31 SAMS temperature monthly mean polar stereographic projection at 10 mb for May 1979 (contour interval is 2.0°K).



LATITUDE 0. TO 65.

Figure T32 - SAMS temperature monthly mean polar stereographic projection at 10 mb for June 1979 (contour interval is 2.0°K).

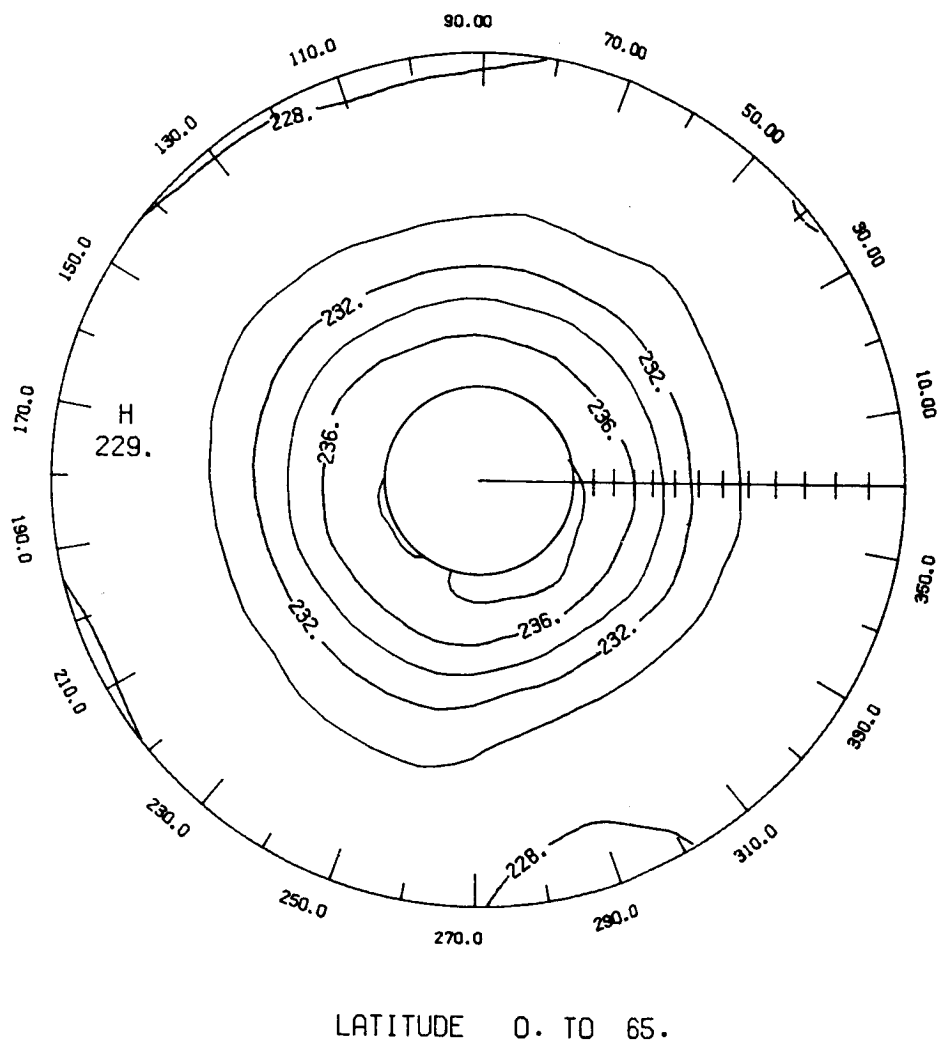
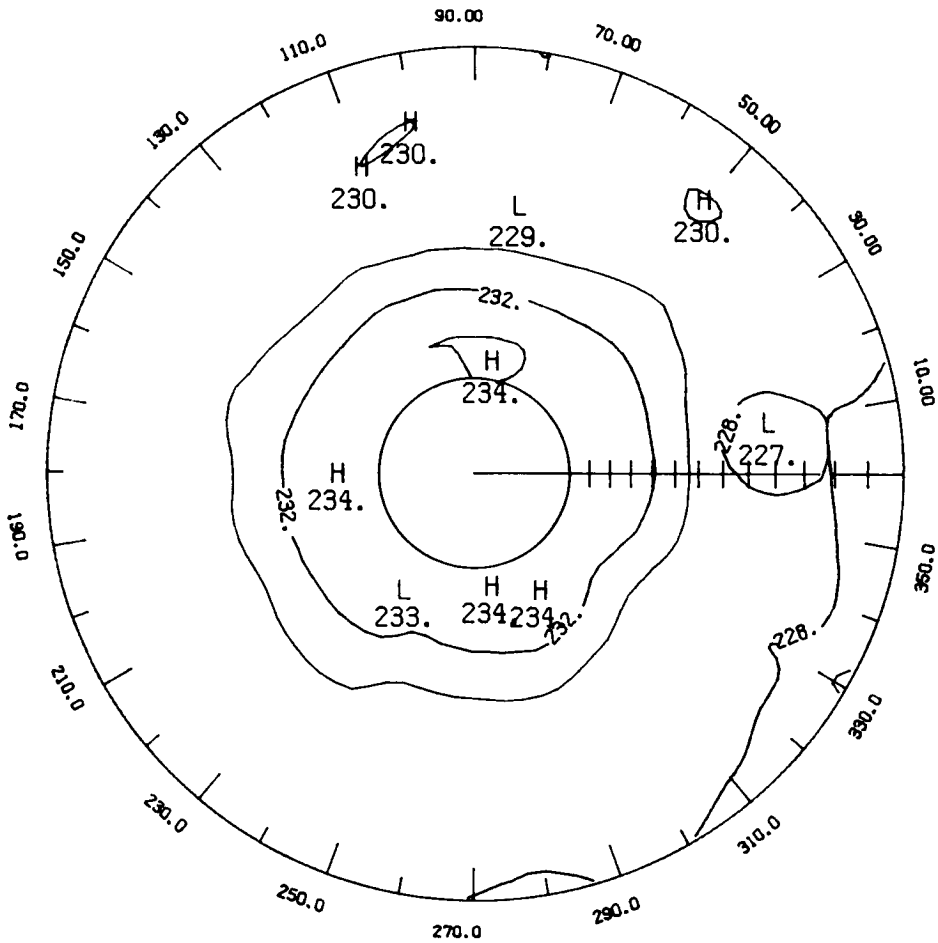
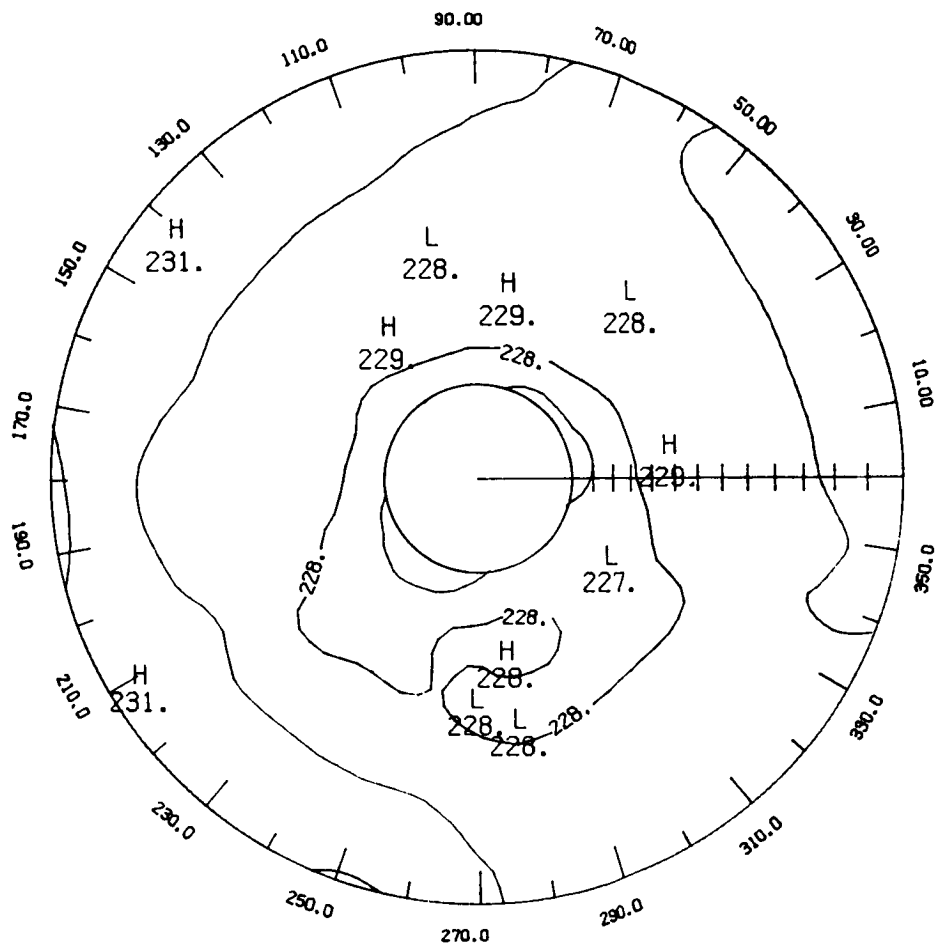


Figure T33 - SAMS temperature monthly mean polar stereographic projection at 10 mb for July 1979 (contour interval is 2.0°K).



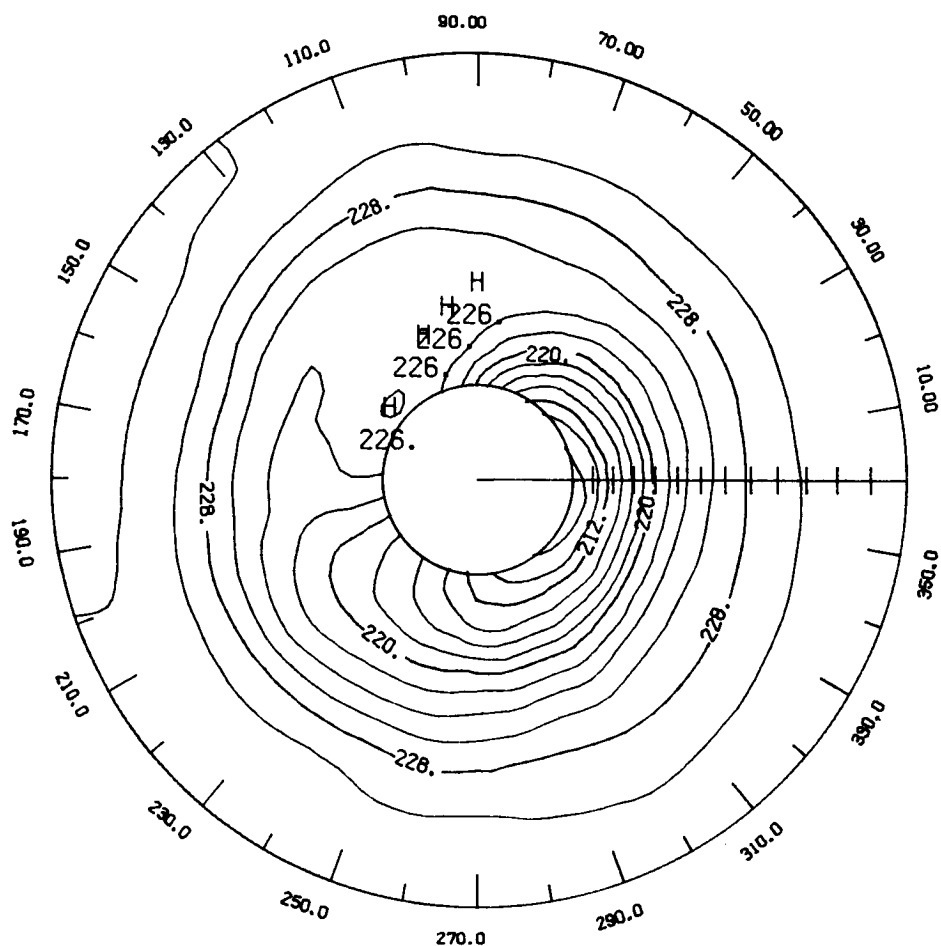
LATITUDE 0. TO 65.

Figure T34 - SAMS temperature monthly mean polar stereographic projection at 10 mb for August 1979 (contour interval is 2.0°K).



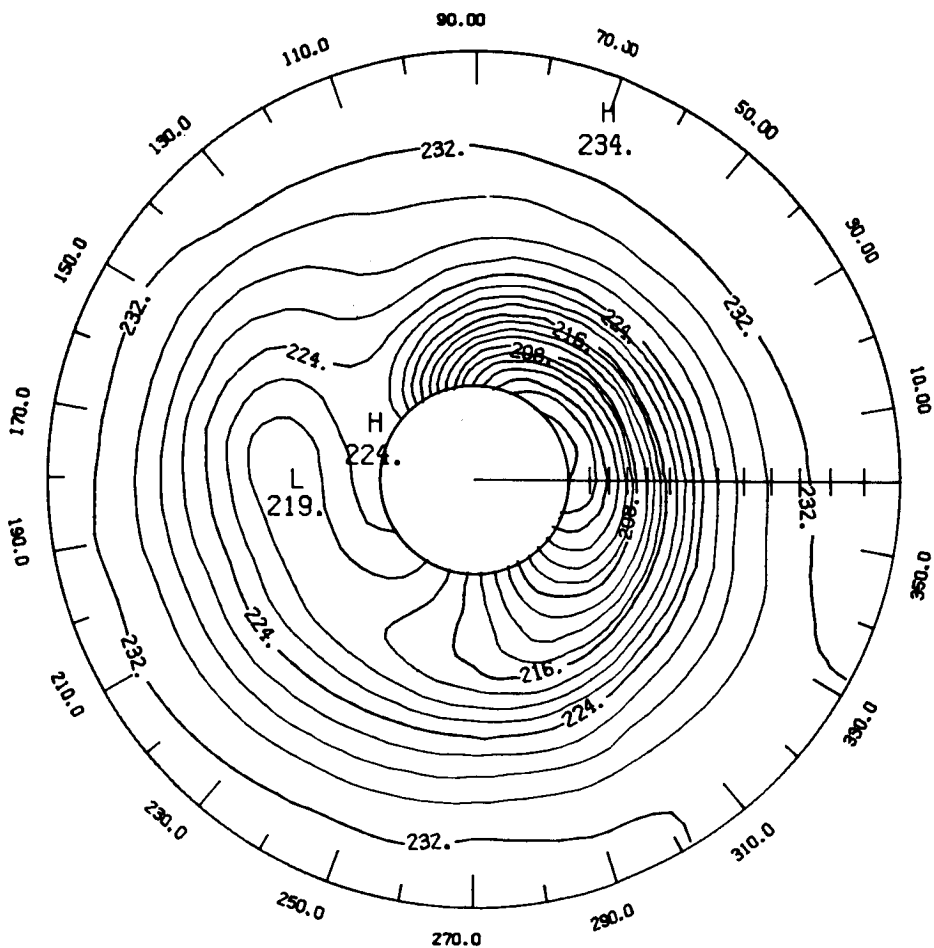
LATITUDE 0. TO 65.

Figure T35 - SAMS temperature monthly mean polar stereographic projection at 10 mb for September 1979 (contour interval is 2.0°K).



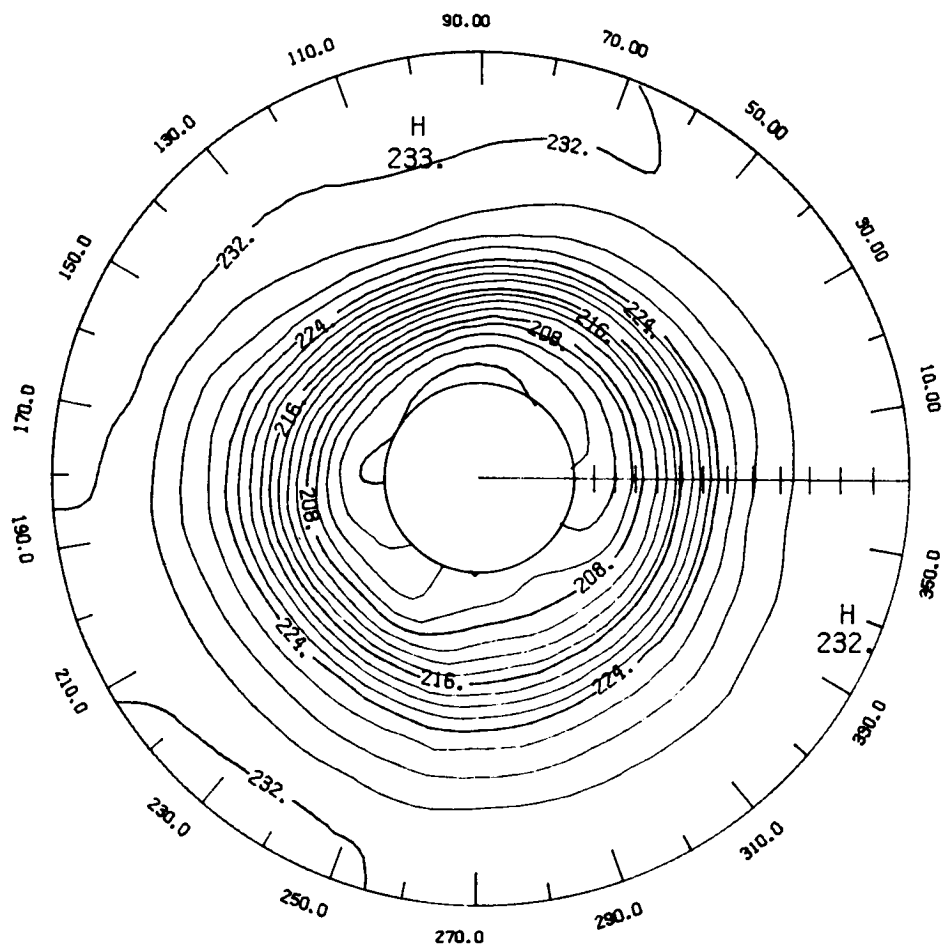
LATITUDE 0. TO 65.

Figure T36 - SAMS temperature monthly mean polar stereographic projection at 10 mb for October 1979 (contour interval is 2.0°K).



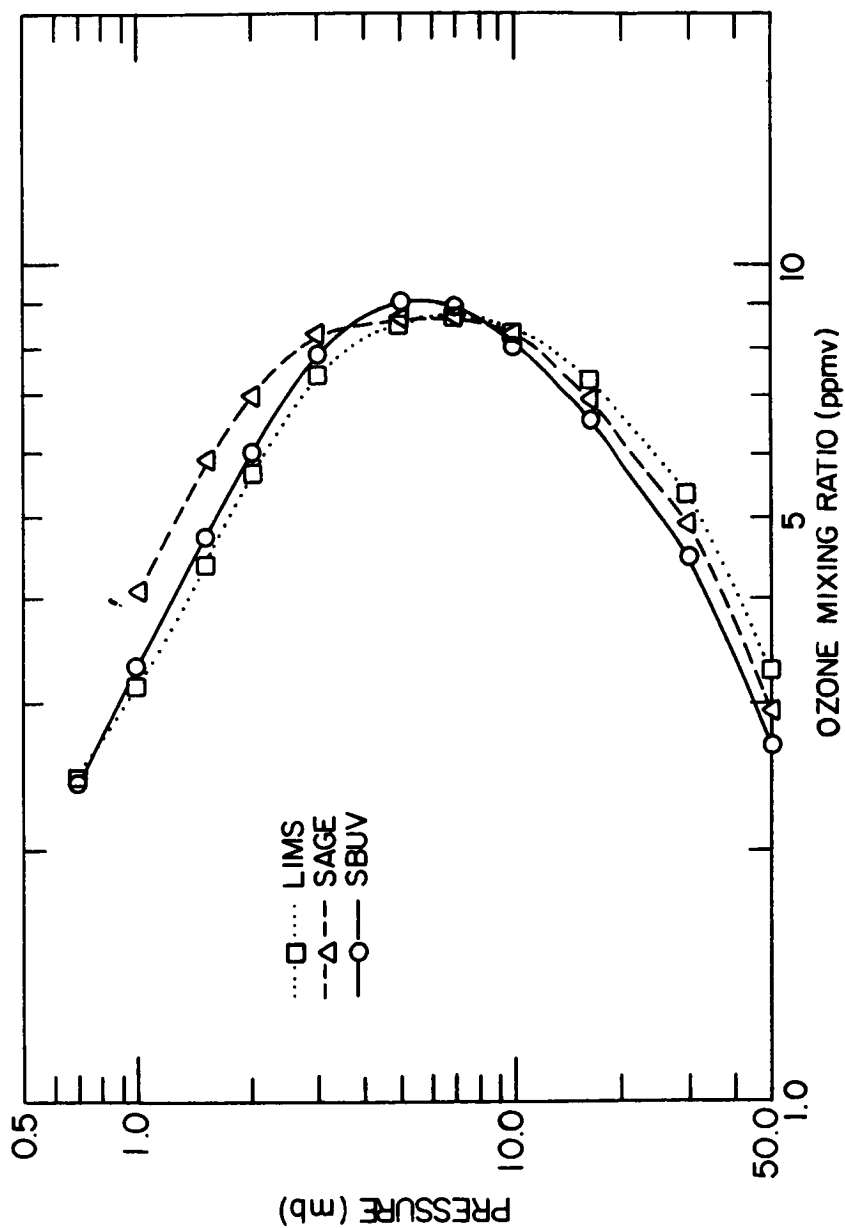
LATITUDE 0. TO 65.

Figure T37 - SAMS temperature monthly mean polar stereographic projection at 10 mb for November 1979 (contour interval is 2.0°K).



LATITUDE 0. TO 65.

Figure T38 - SAMS temperature monthly mean polar stereographic projection at 10 mb for December 1979 (contour interval is 2.0°K).



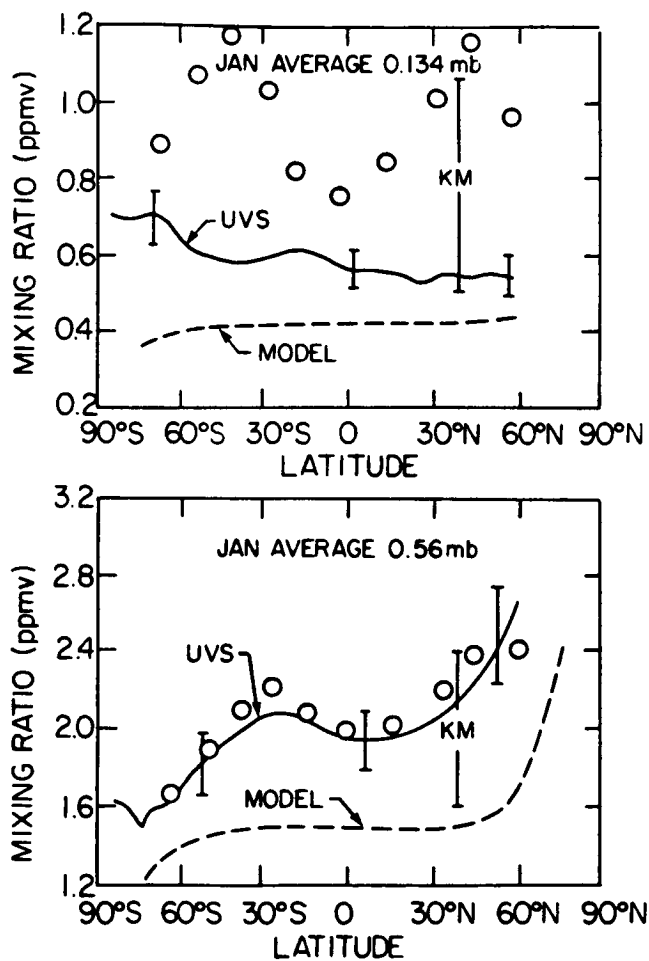


Figure O₃-2 - Comparison of zonal mean LIMS ozone (circles) for January 1979 with ozone from the ultraviolet spectrometer on the Solar Mesospheric Explorer (UVS-SME) for January 1982, with ozone from the Kreuger-Minzer (KM-vertical bars) annual mean ozone climatology, and with ozone from photochemical model calculations (adapted from Fig. 1 of Solomon et al., (1983)). Results are given for 0.134 mb and 0.560 mb in ppmv.

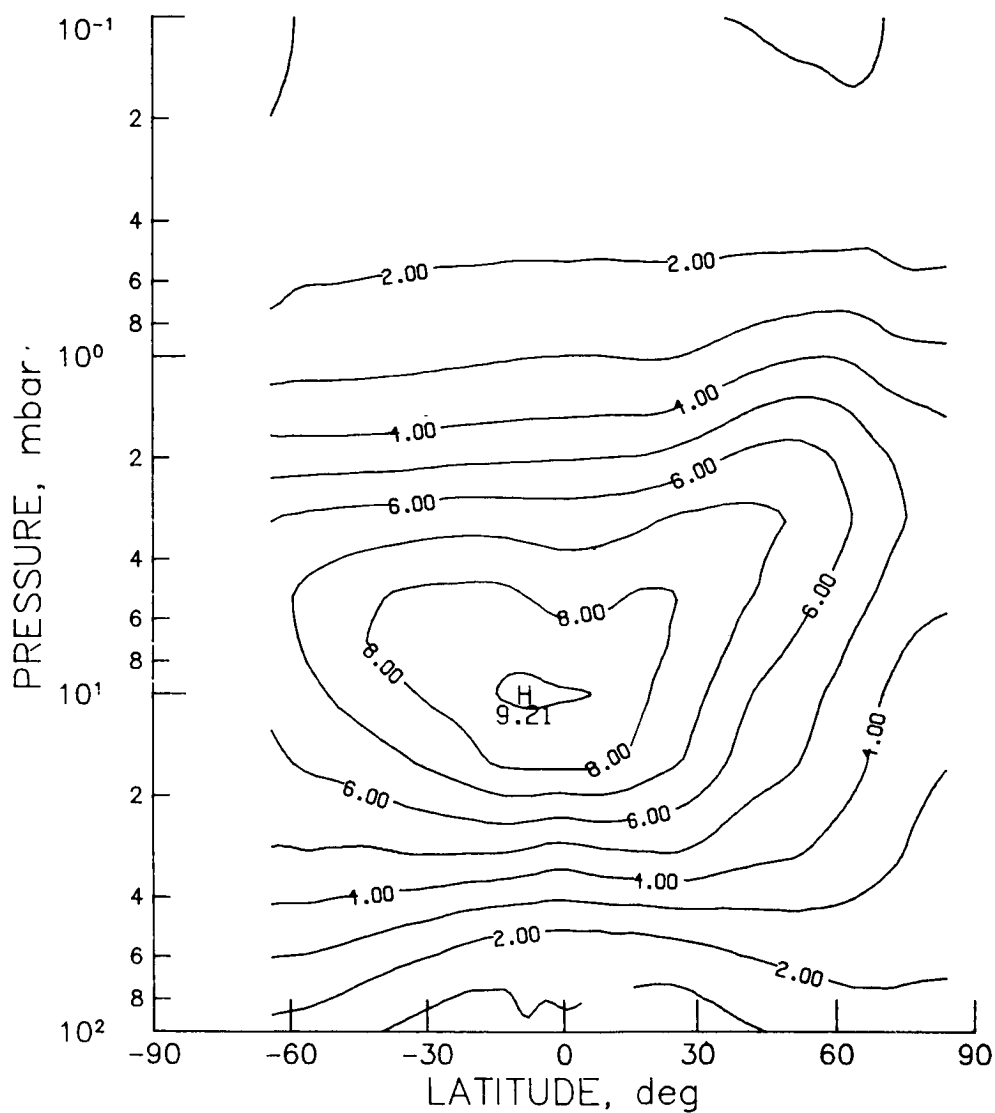


Figure O₃-3 - LIMS monthly zonal mean ozone cross section for November 1978 (contour interval is 1.0 ppmv).

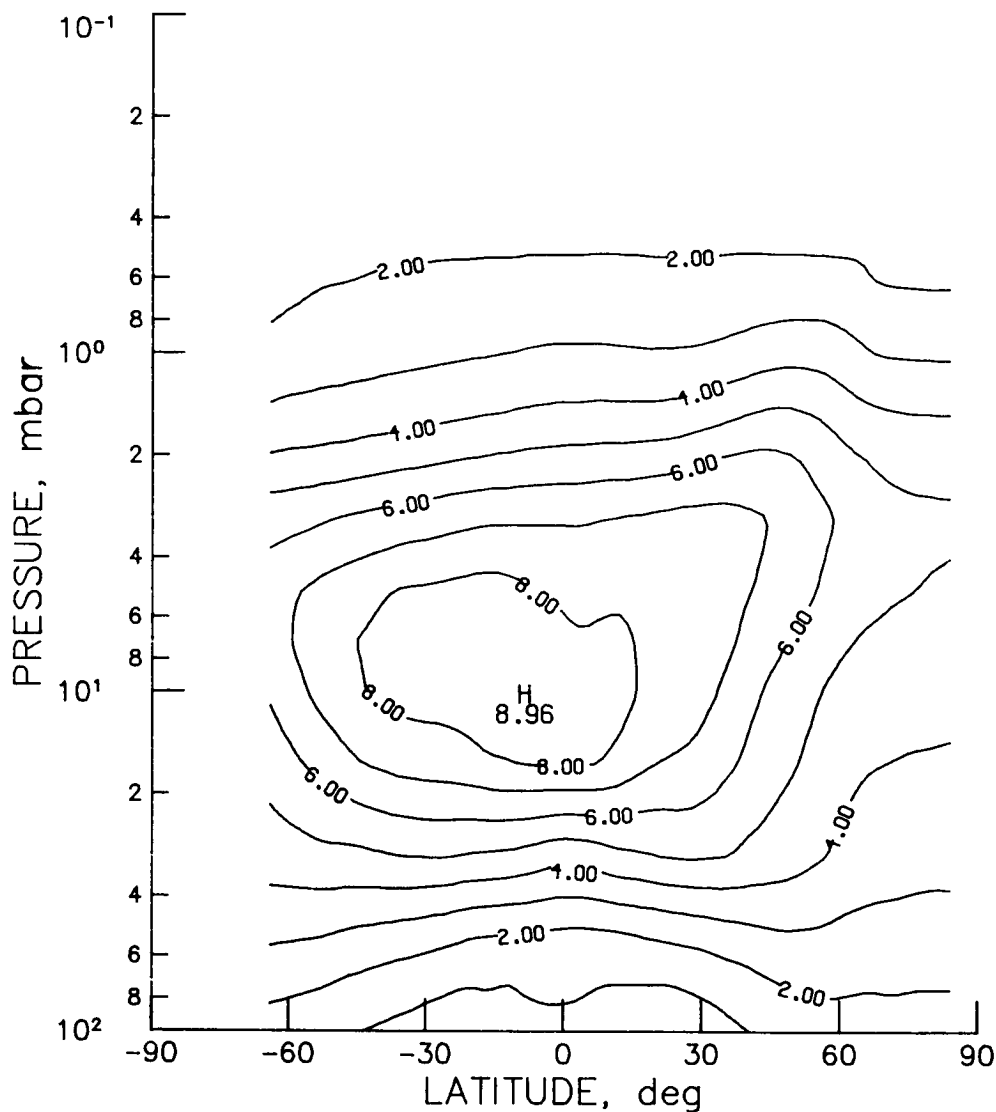


Figure 03-4 - LIMS monthly zonal mean ozone cross section for December 1978 (contour interval is 1.0 ppmv).

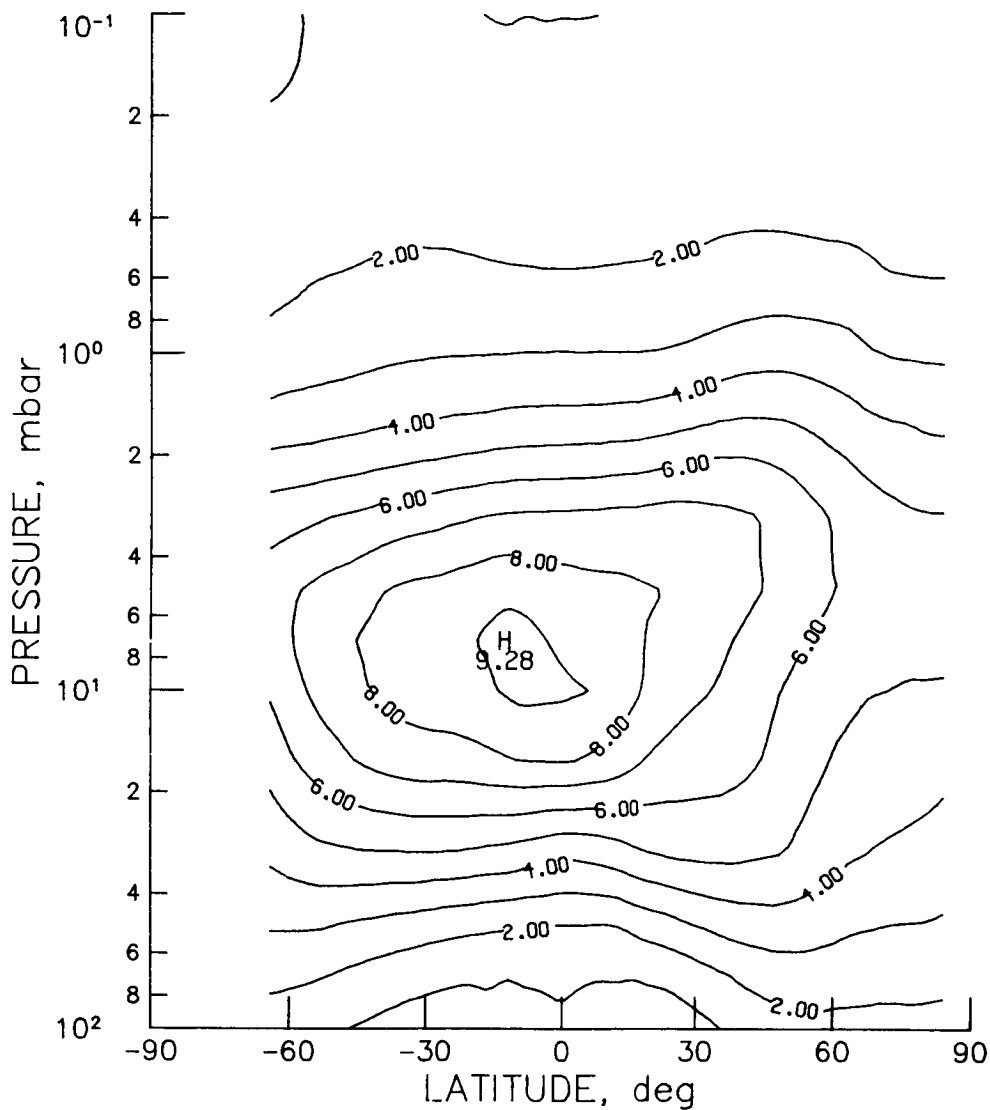


Figure 03-5 - LIMS monthly zonal mean ozone cross section for January 1979 (contour interval is 1.0 ppmv).

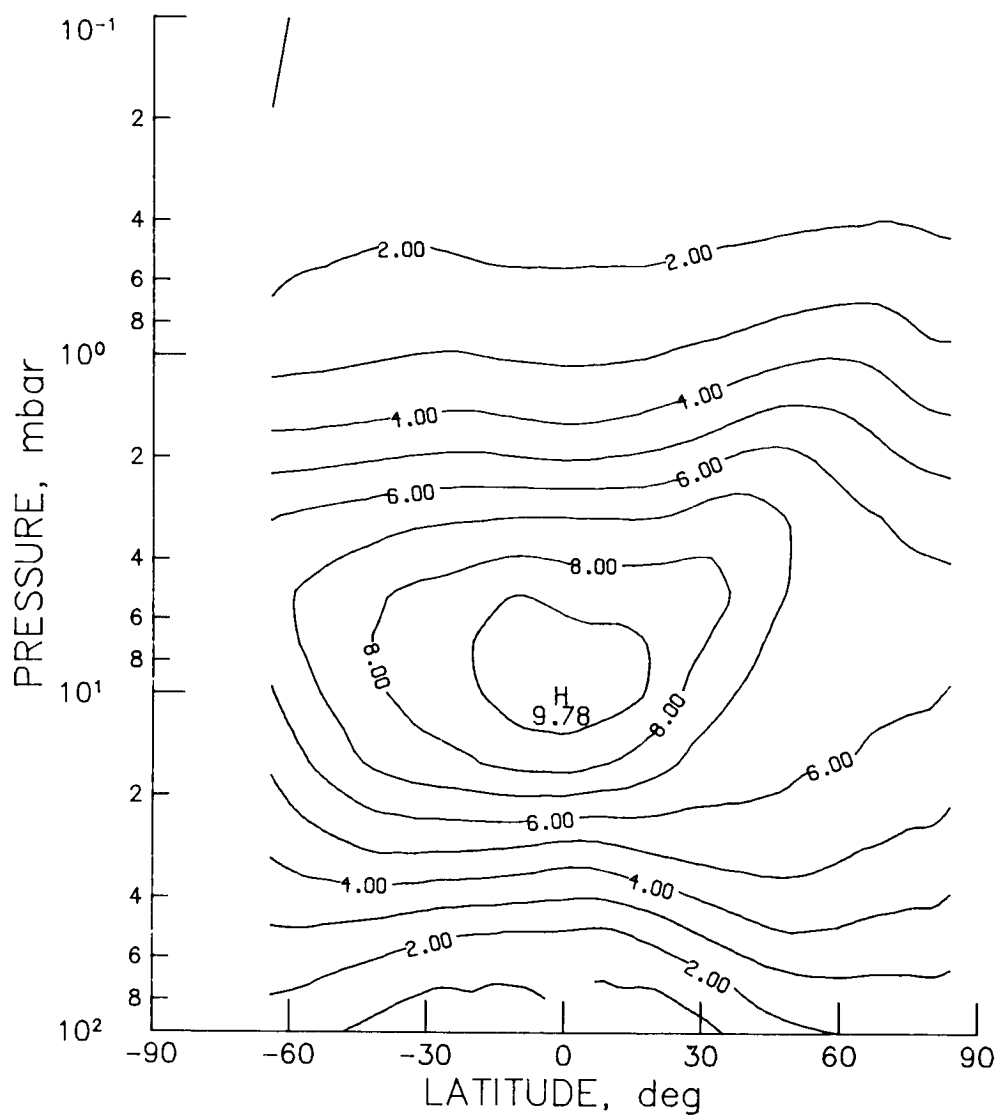


Figure 03-6 - LIMS monthly zonal mean ozone cross section for February 1979
(contour interval is 1.0 ppmv).

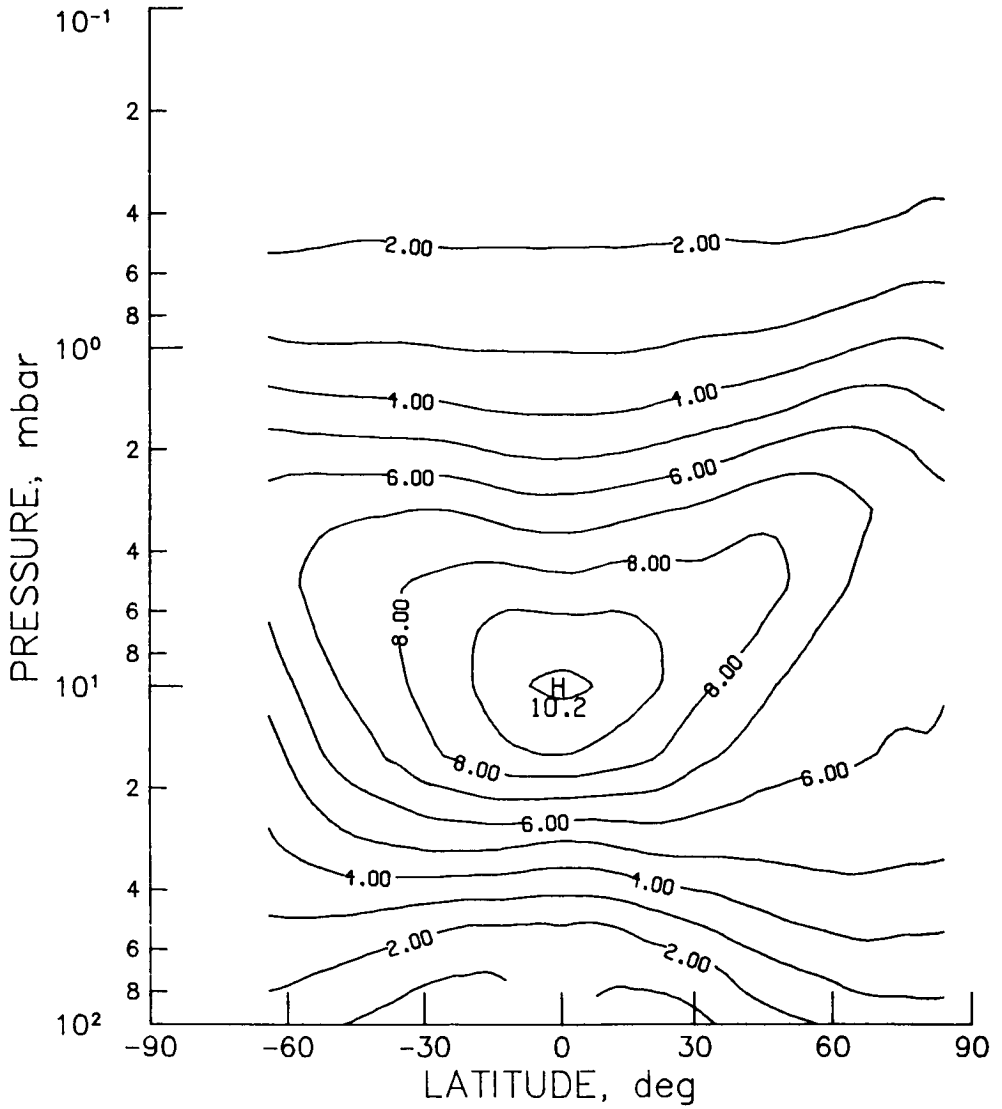


Figure 03-7 - LIMS monthly zonal mean ozone cross section for March 1979
(contour interval is 1.0 ppmv).

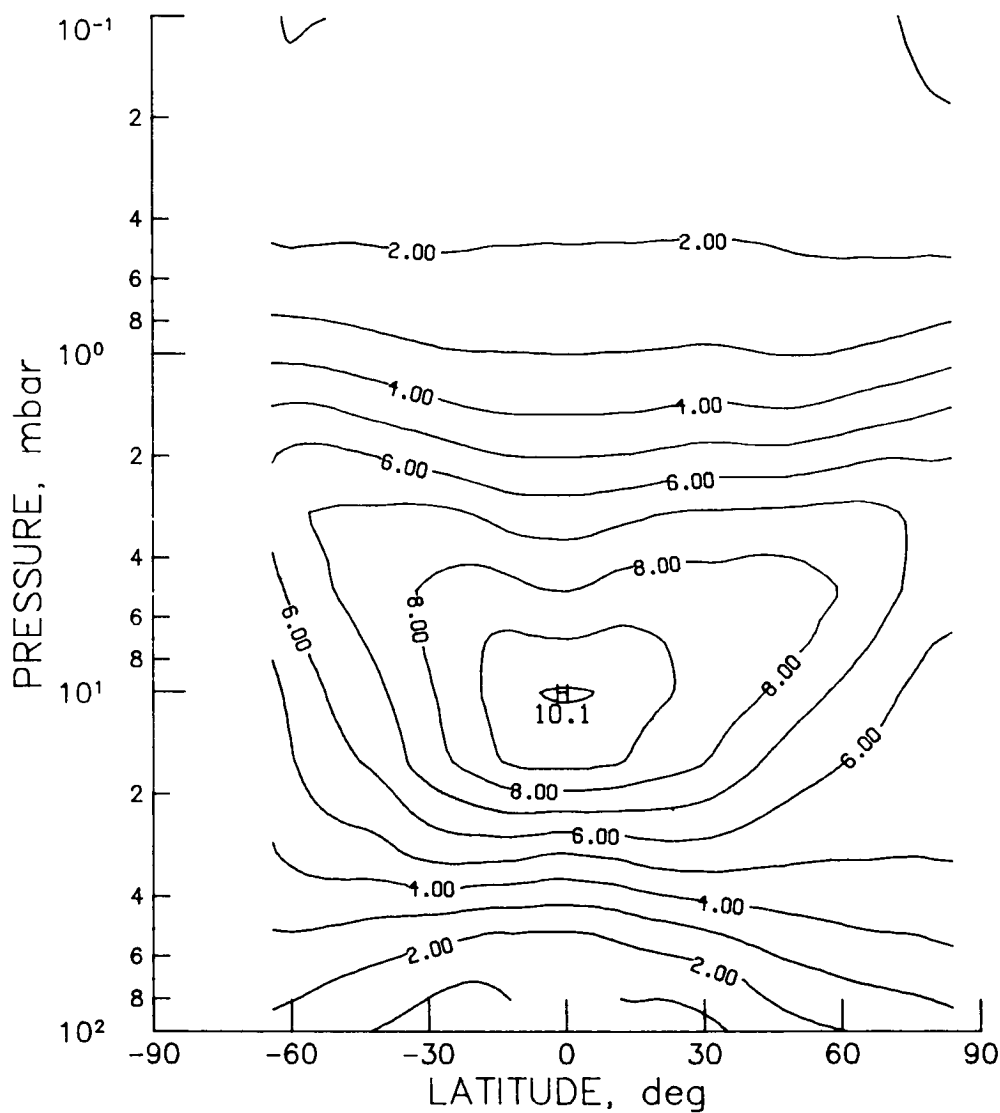


Figure 03-8 - LIMS monthly zonal mean ozone cross section for April 1979
(contour interval is 1.0 ppmv).

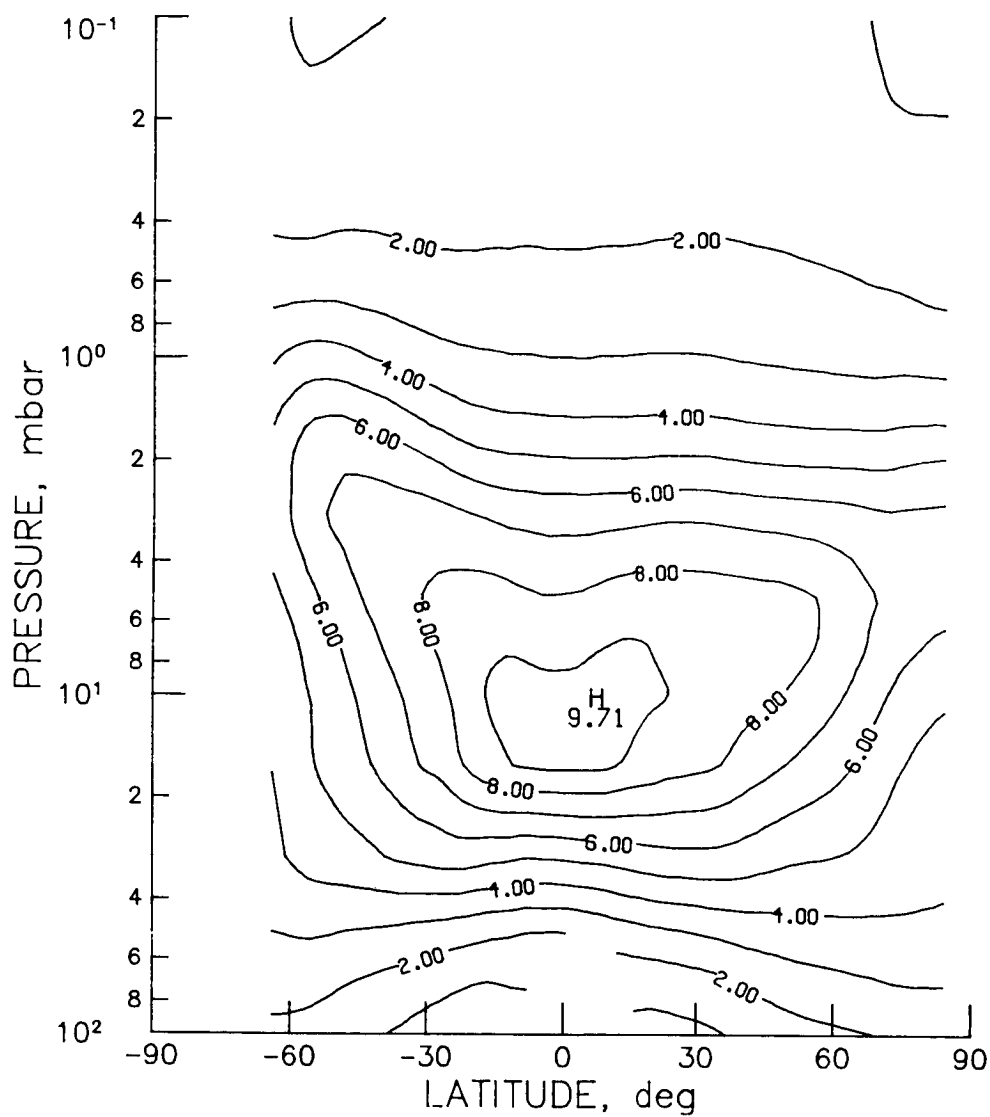


Figure 03-9 - LIMS monthly zonal mean ozone cross section for May 1979
(contour interval is 1.0 ppmv).

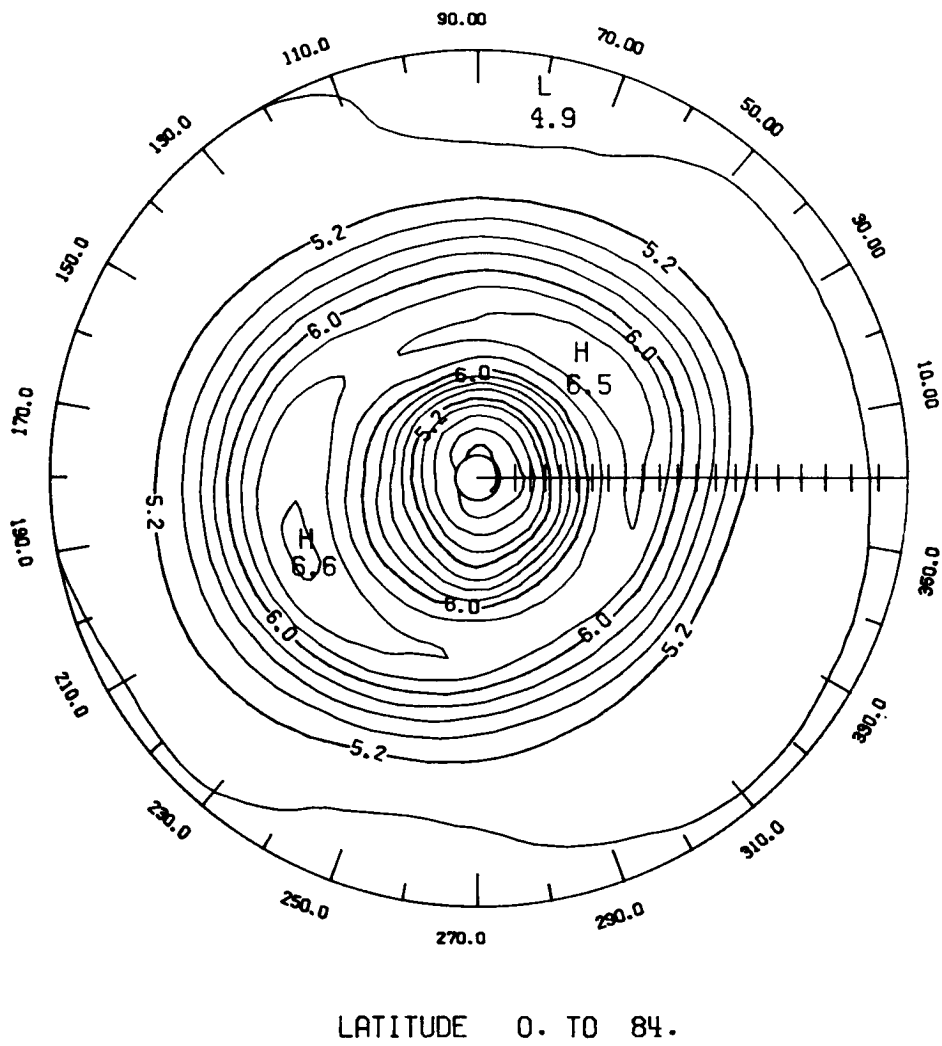


Figure 03-10 - LIMS ozone monthly mean polar stereographic projection at 2 mb for November 1978 (contour interval is 0.20 ppmv).

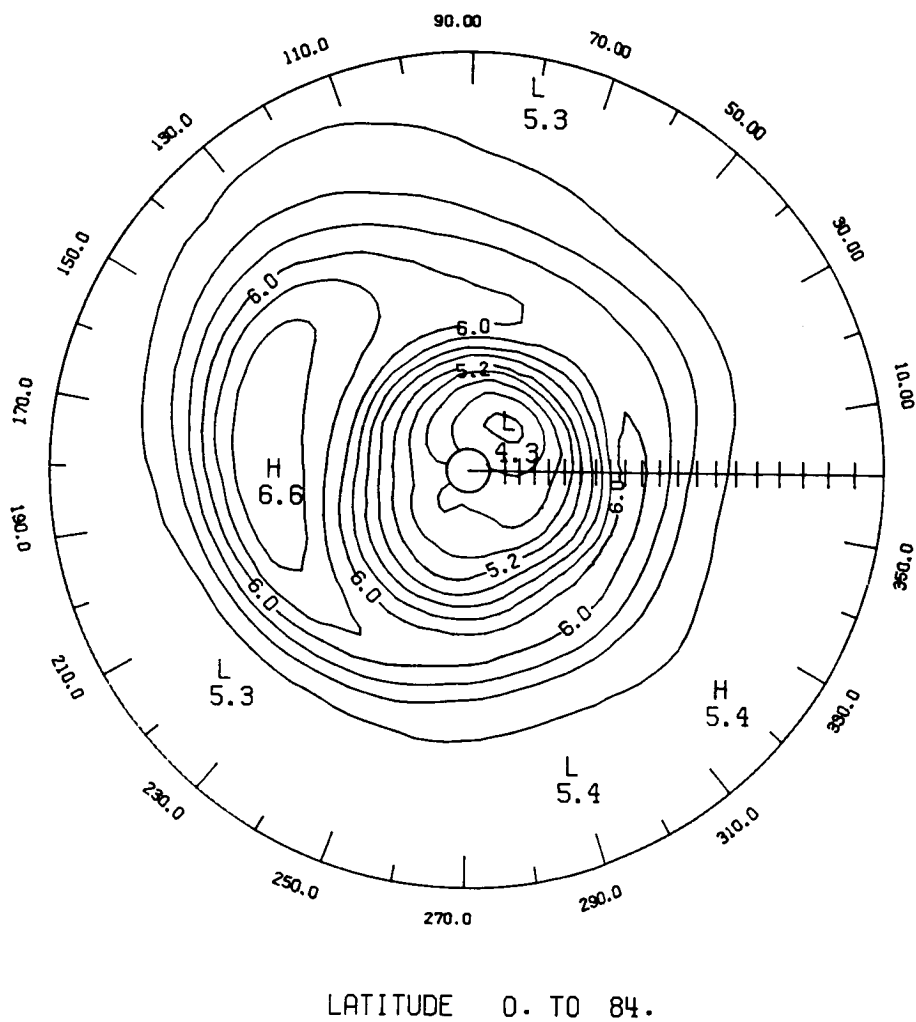
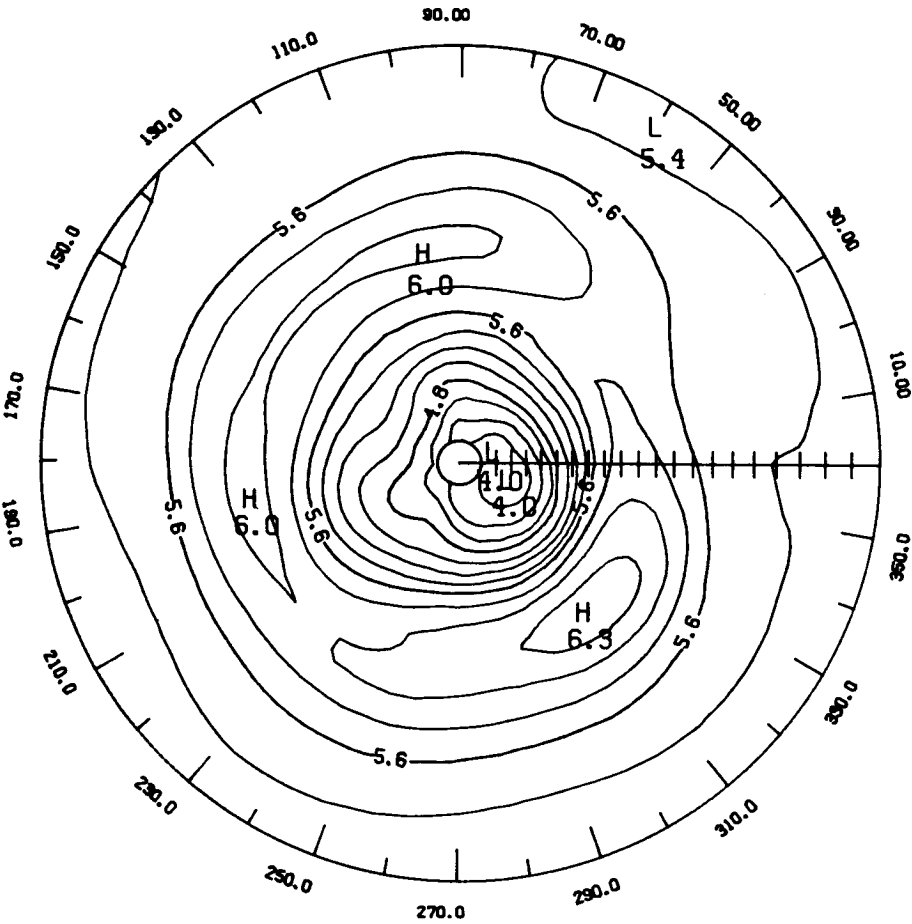
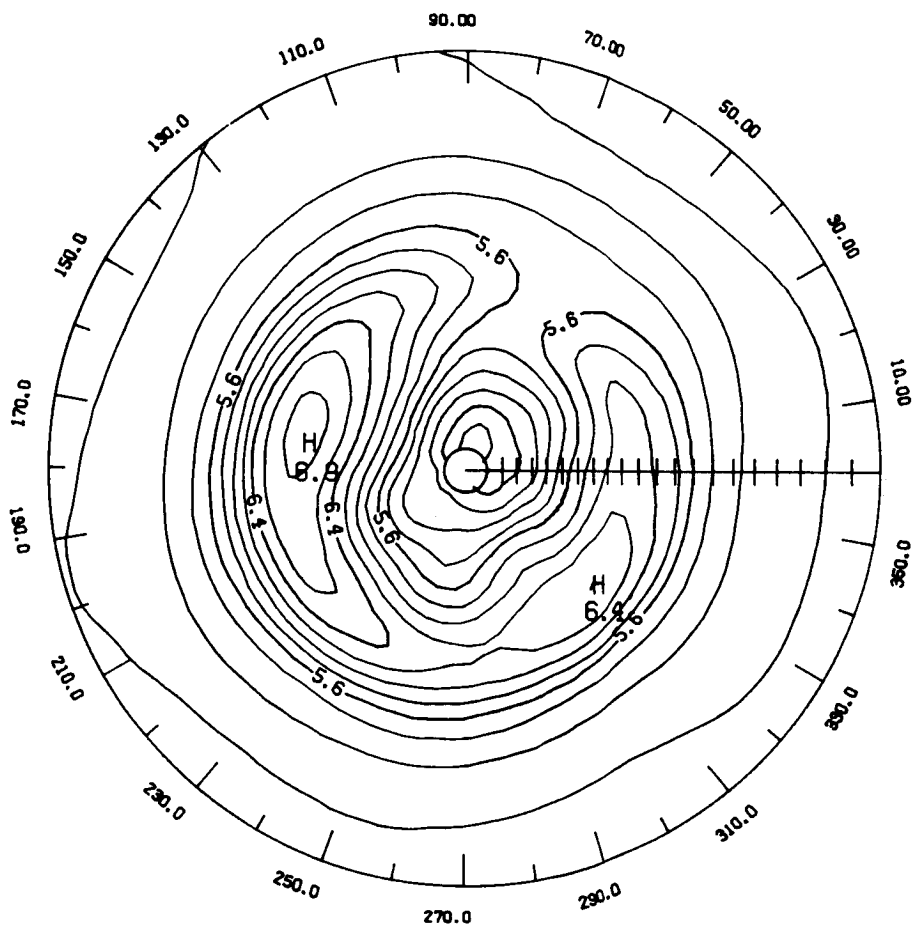


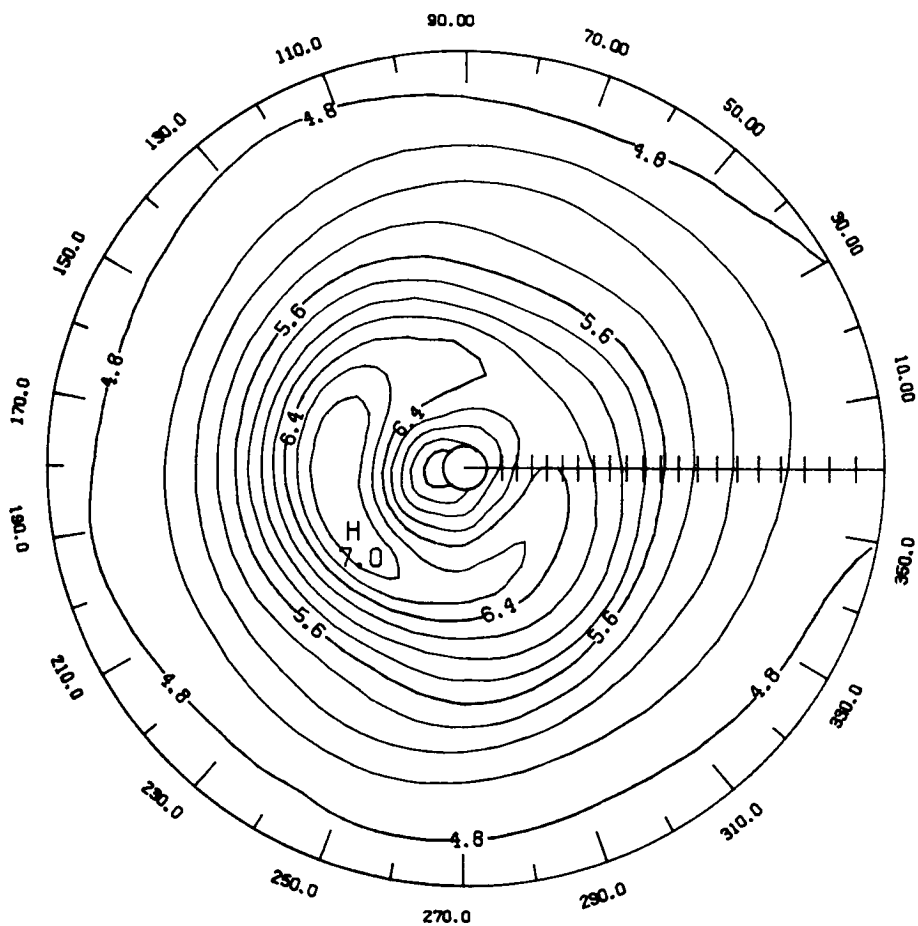
Figure 03-11 - LIMS ozone monthly mean polar stereographic projection at 2 mb for December 1978 (contour interval is 0.20 ppbv).





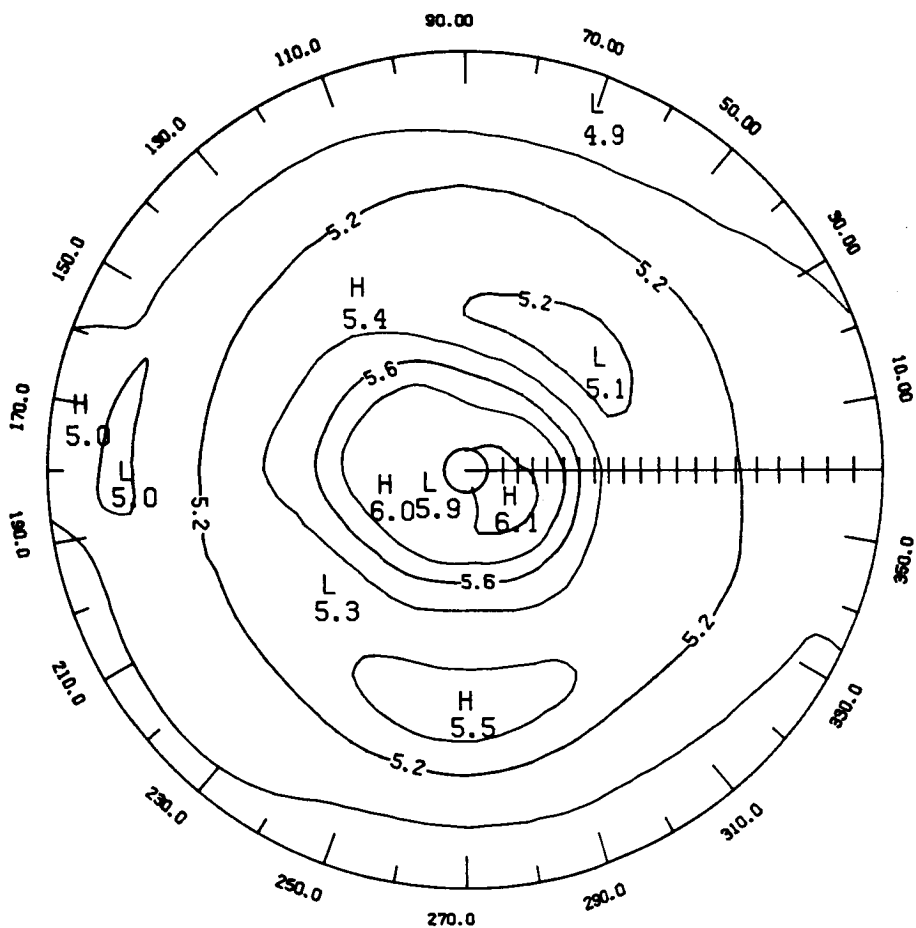
LATITUDE 0. TO 84.

Figure 03-13 - LIMS ozone monthly mean polar stereographic projection at 2 mb for February 1979 (contour interval is 0.20 ppmv).



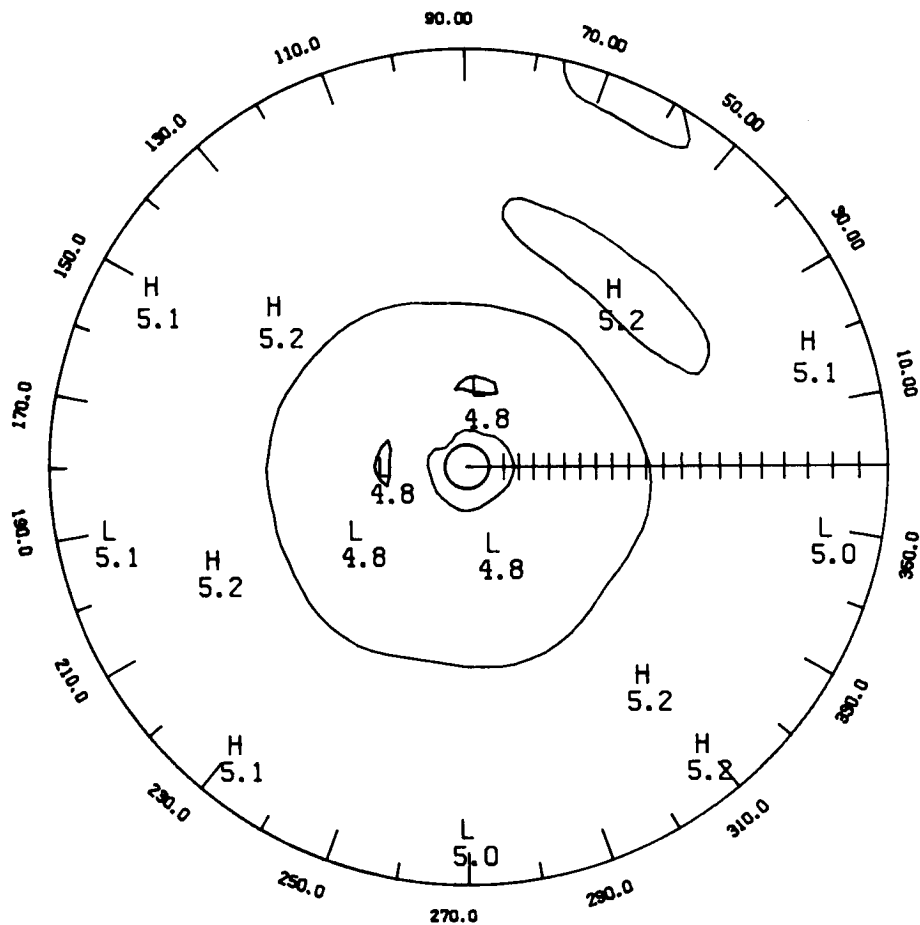
LATITUDE 0. TO 84.

Figure 03-14 - LIMS ozone monthly mean polar stereographic projection at 2 mb for March 1979 (contour interval is 0.20 ppmv).



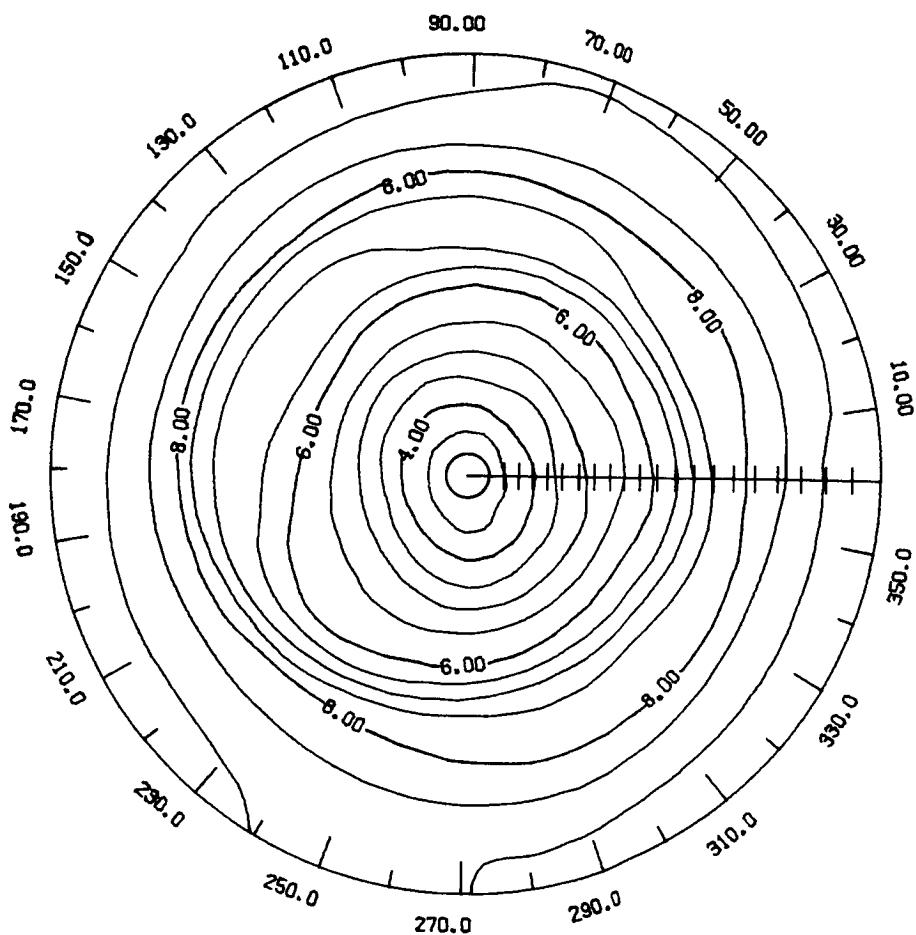
LATITUDE 0. TO 84.

Figure 03-15 - LIMS ozone monthly mean polar stereographic projection at 2 mb for April 1979 (contour interval is 0.20 ppbv).



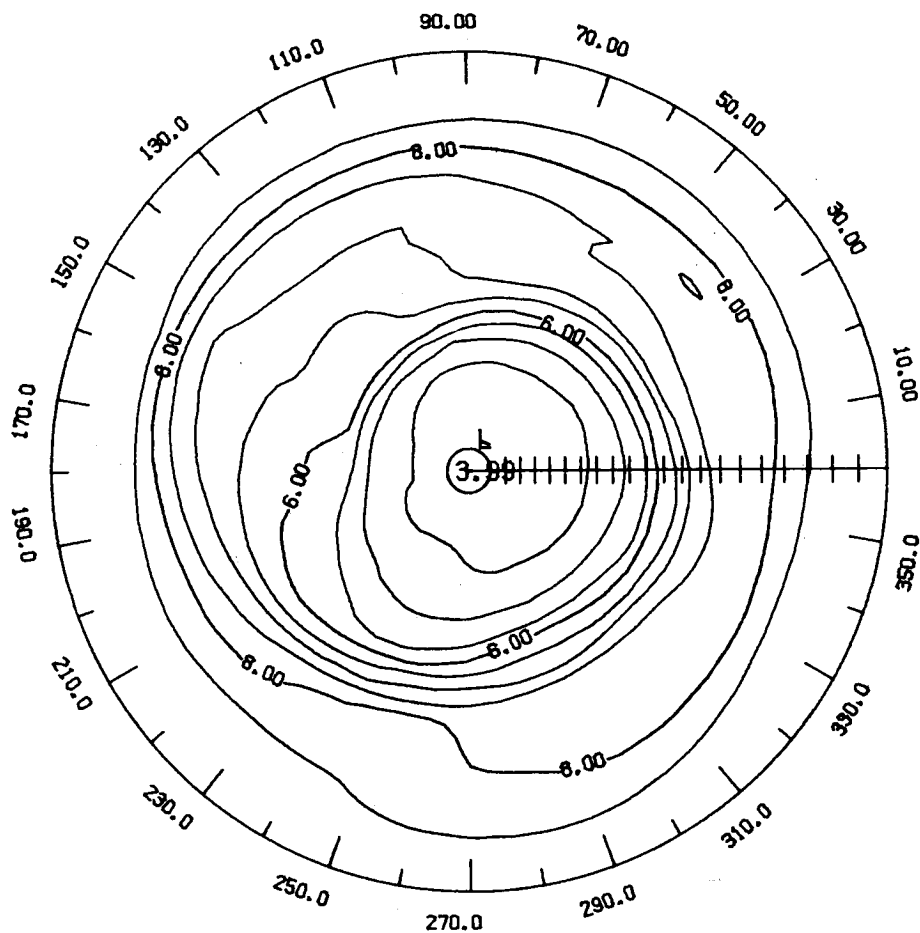
LATITUDE 0. TO 84.

Figure 03-16 - LIMS ozone monthly mean polar stereographic projection at 2 mb for May 1979 (contour interval is 0.20 ppmv).



LATITUDE 0. TO 84.

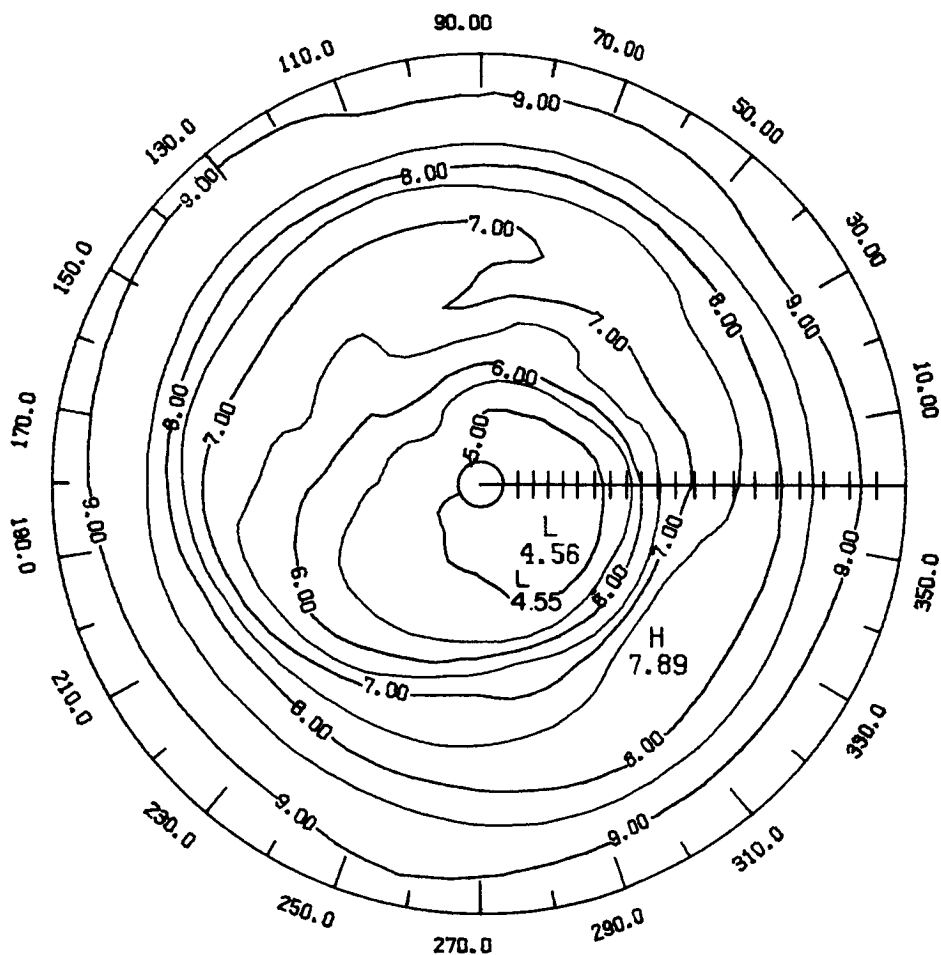
Figure 03-17 - LIMS ozone monthly mean polar stereographic projection at 10 mb for November 1978 (contour interval is 0.5 ppmv).



LATITUDE 0. TO 84.

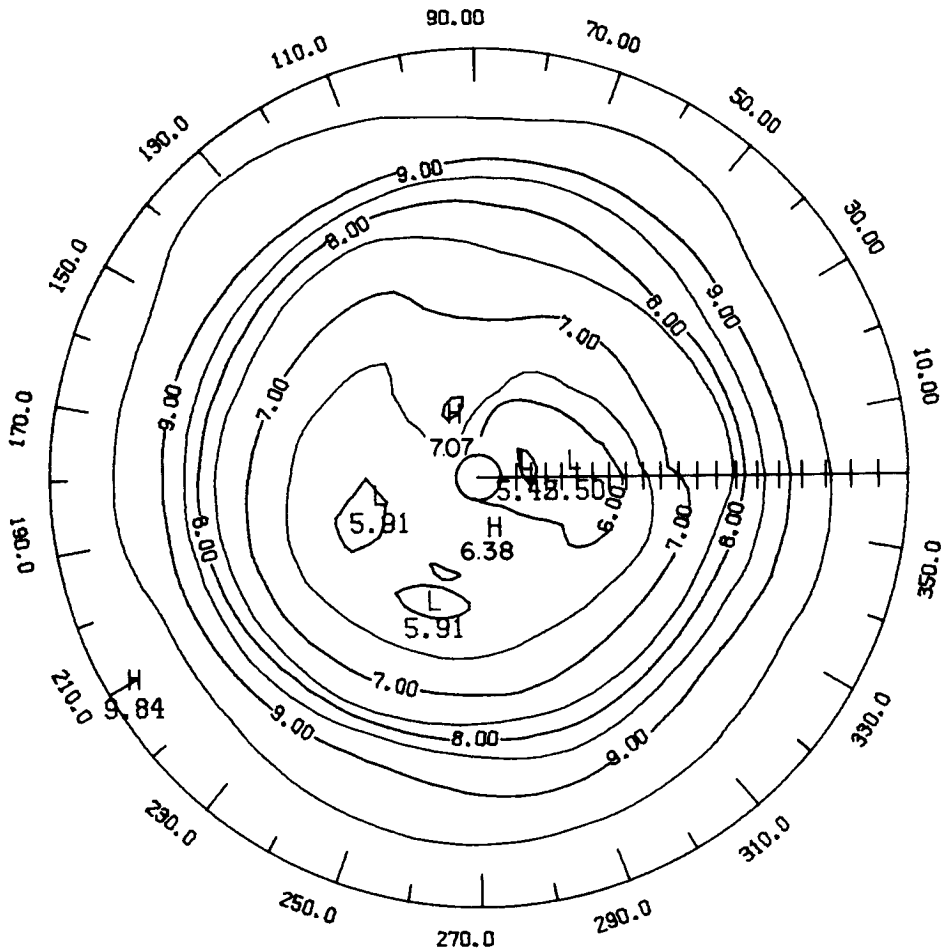
Figure 03-18 - LIMS ozone monthly mean polar stereographic projection at 10 mb for December 1978 (contour interval is 0.5 ppmv).

C-2



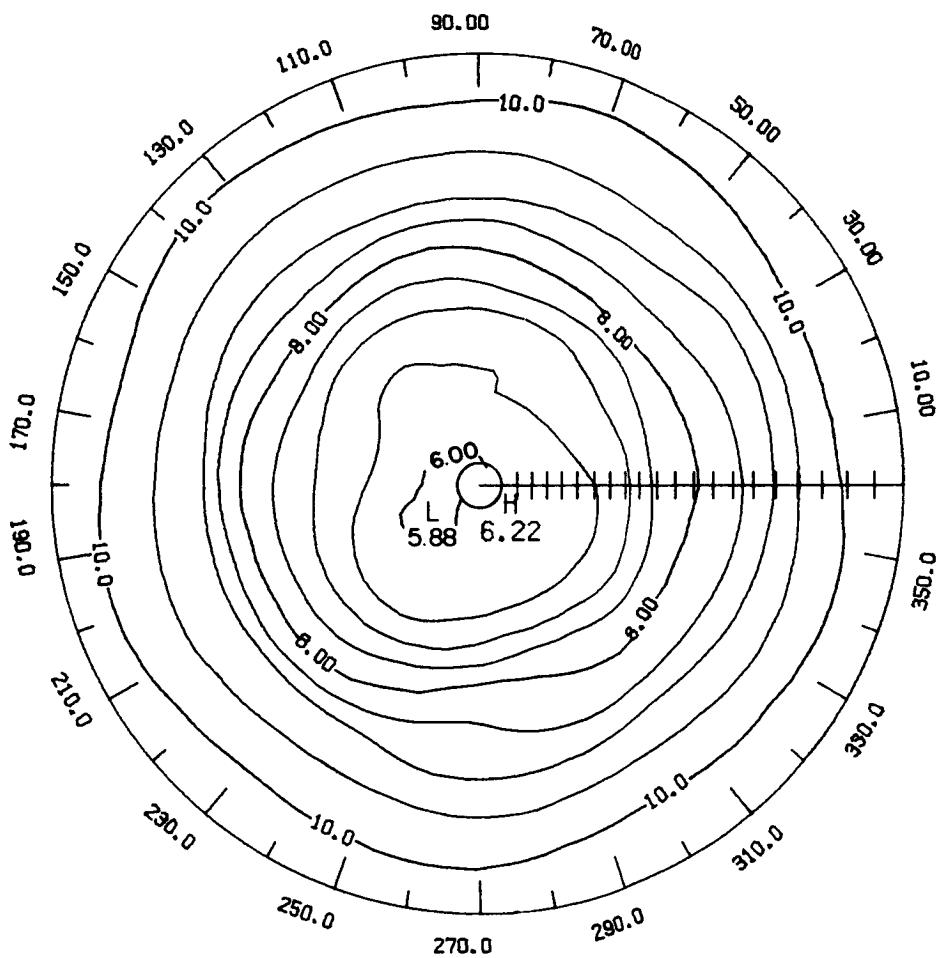
LATITUDE 0. TO 84.

Figure 03-19 - LIMS ozone monthly mean polar stereographic projection at 10 mb for January 1979 (contour interval is 0.5 ppmv).



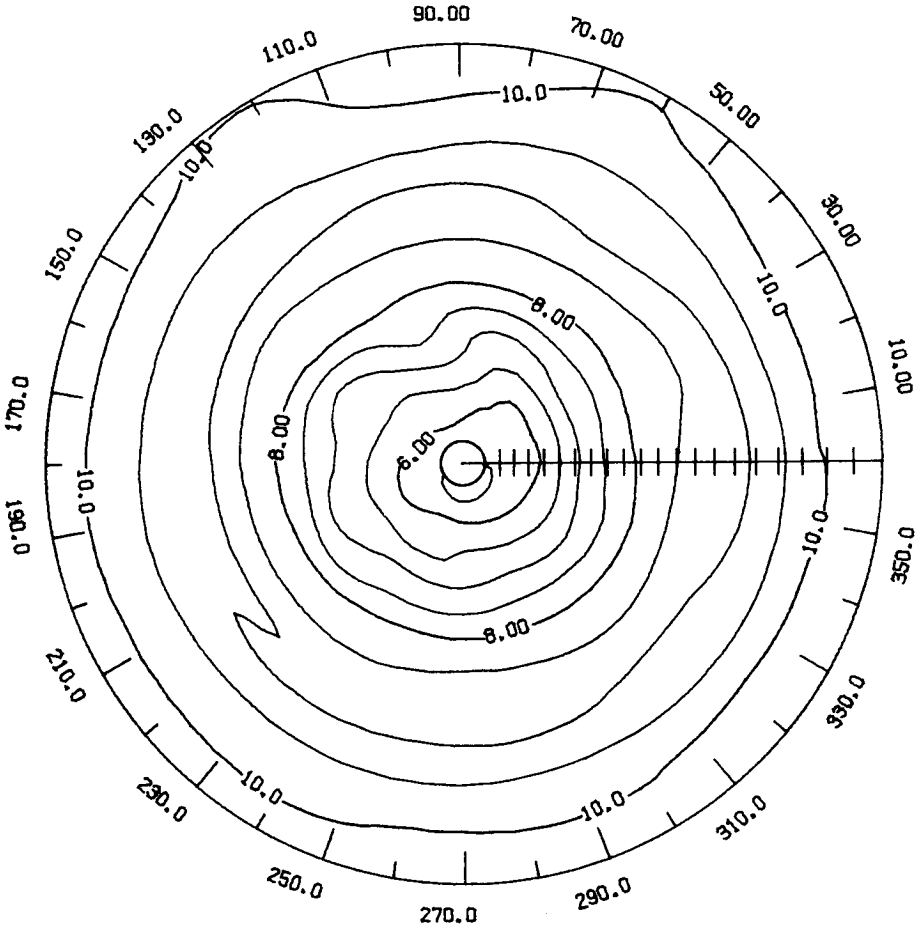
LATITUDE 0. TO 84.

Figure 03-20 - LIMS ozone monthly mean polar stereographic projection at 10 mb for February 1979 (contour interval is 0.5 ppmv).



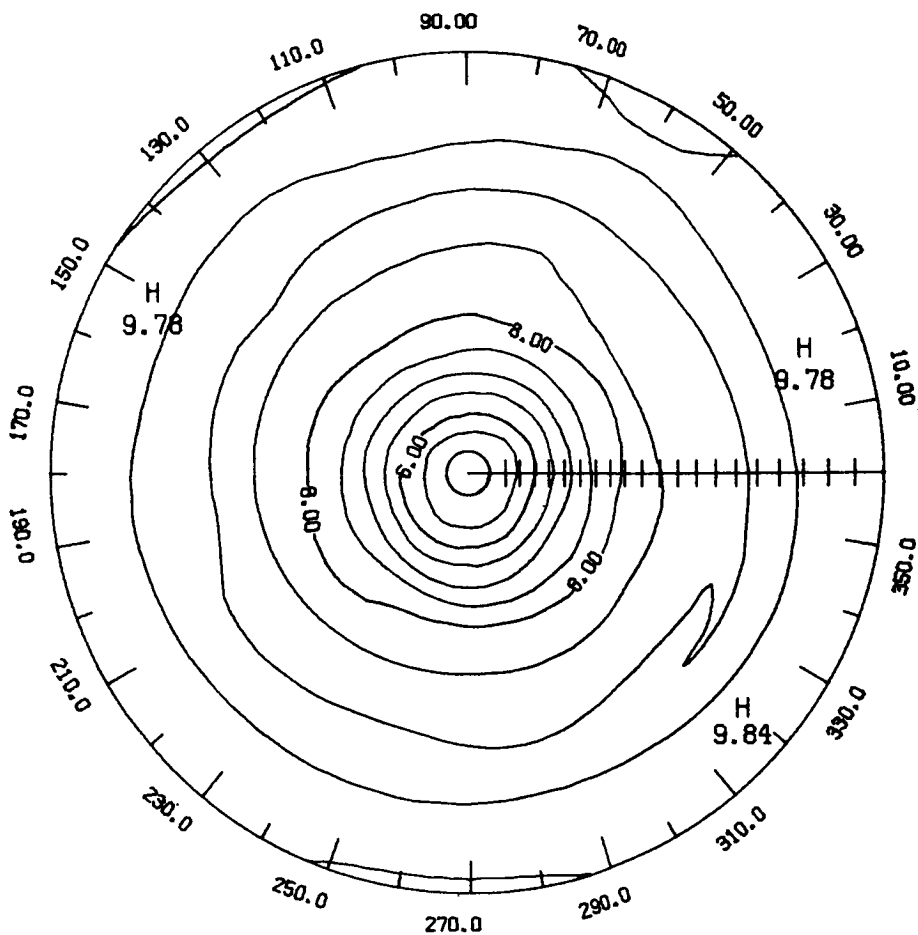
LATITUDE 0. TO 84.

Figure O3-21 - LIMS ozone monthly mean polar stereographic projection at 10 mb for March 1979 (contour interval is 0.5 ppmv).



LATITUDE 0. TO 84.

Figure 03-22 - LIMS ozone monthly mean polar stereographic projection at 10 mb for April 1979 (contour interval is 0.5 ppmv).



LATITUDE 0. TO 84.

Figure 03-23 - LIMS ozone monthly mean polar stereographic projection at 10 mb for May 1979 (contour interval is 0.5 ppmv).

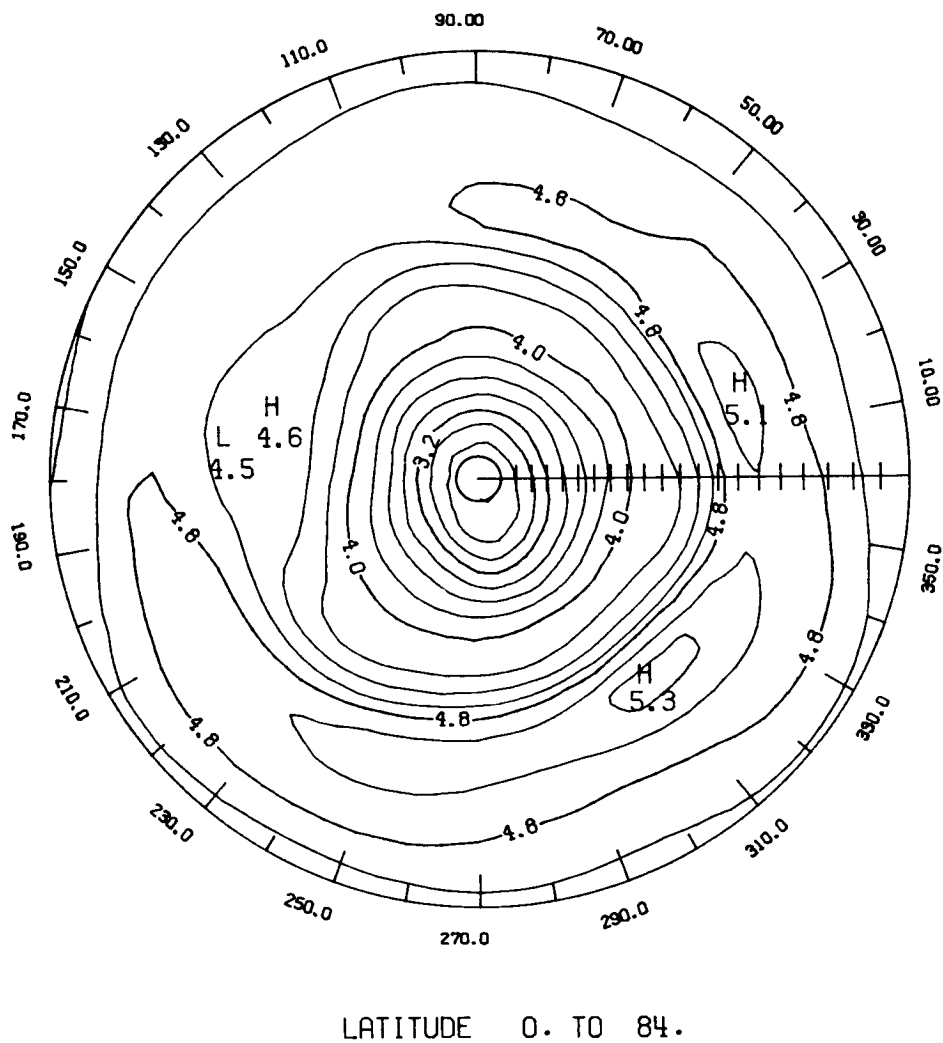
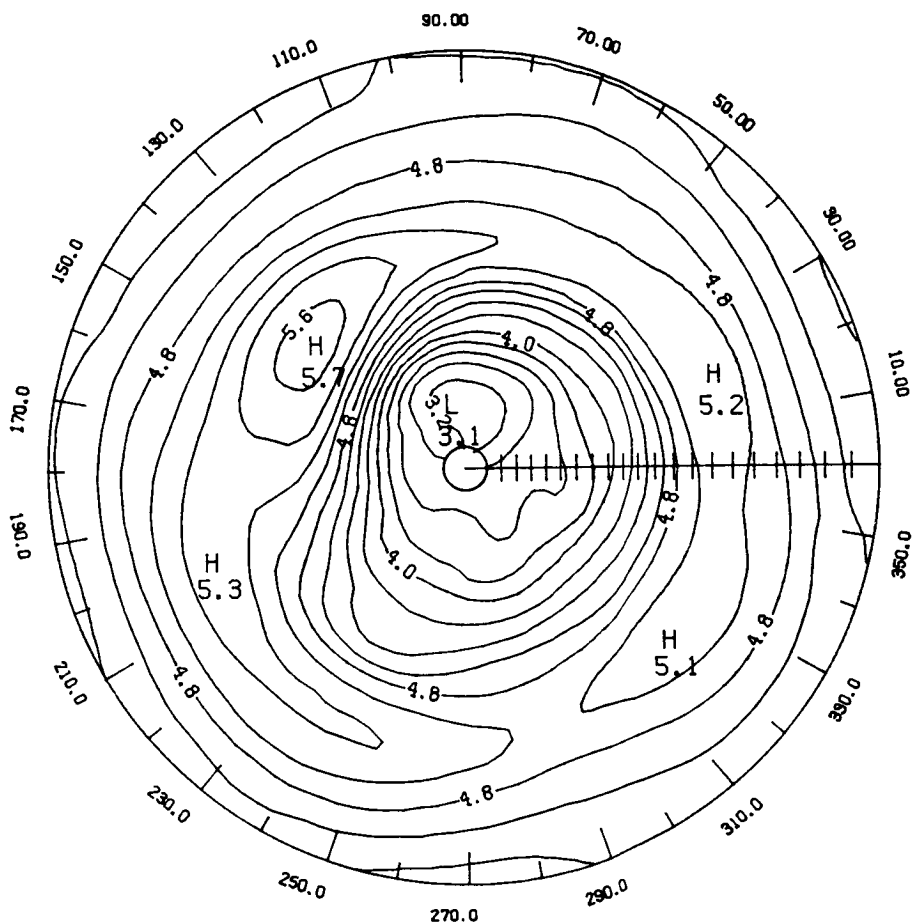


Figure 03-24 - LIMS ozone monthly mean polar stereographic projection at 30 mb for November 1978 (contour interval is 0.2 ppmv).



LATITUDE 0. TO 84.

Figure 03-25 - LIMS ozone monthly mean polar stereographic projection at 30 mb for December 1978 (contour interval is 0.2 ppmv).

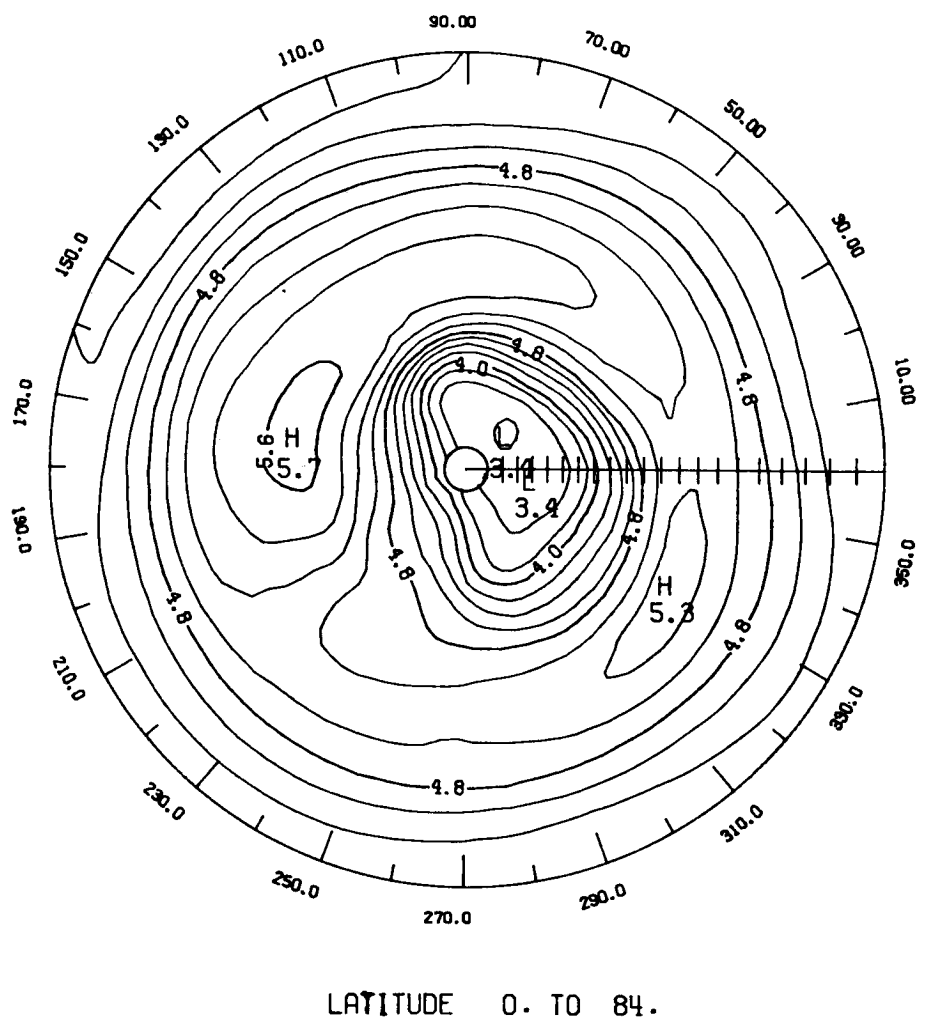
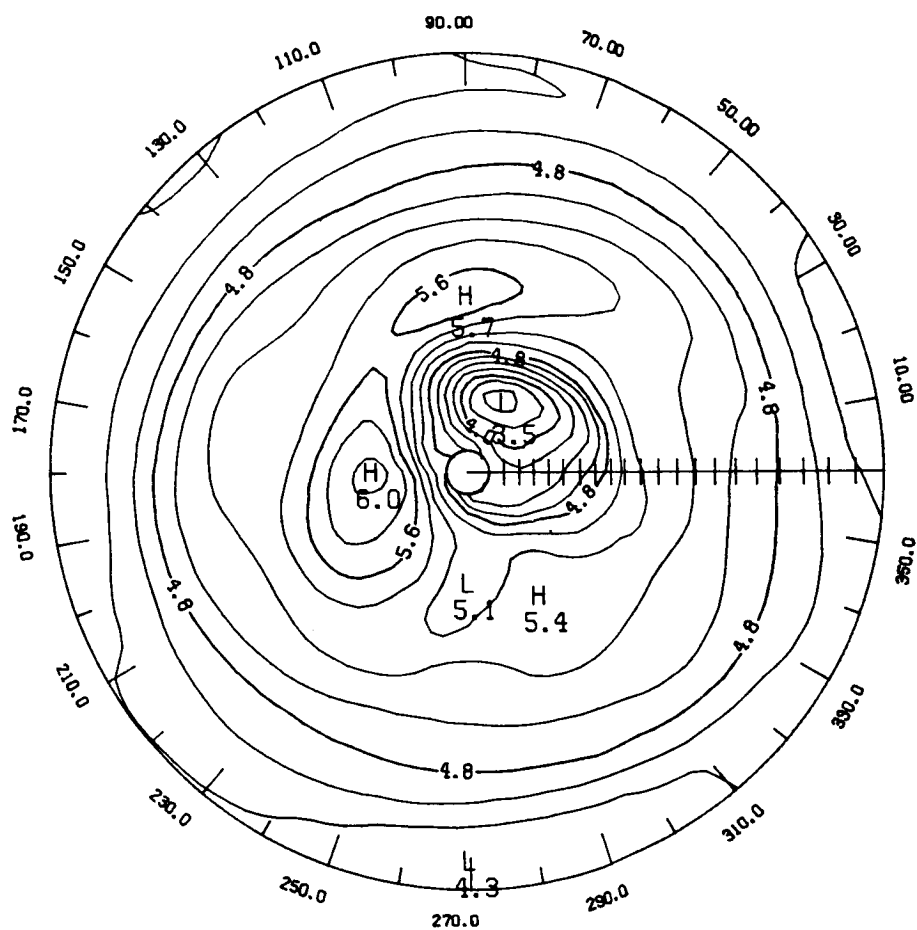
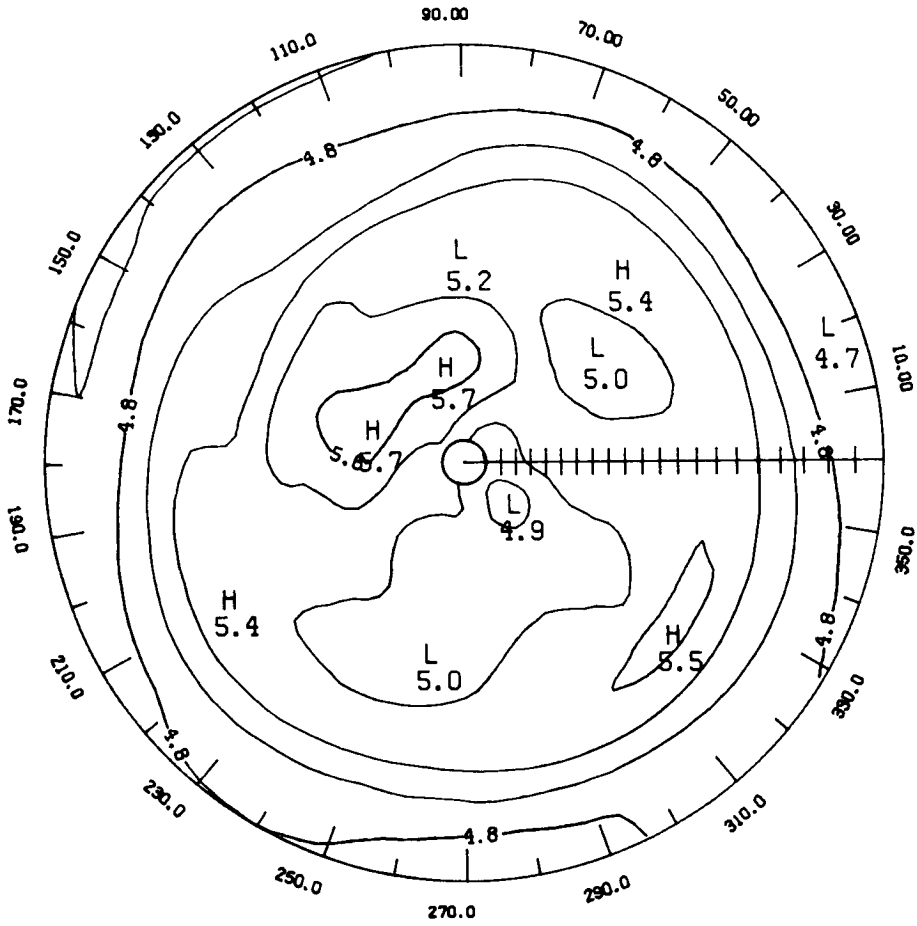


Figure 03-26 - LIMS ozone monthly mean polar stereographic projection at 30 mb for January 1979 (contour interval is 0.2 ppmv).



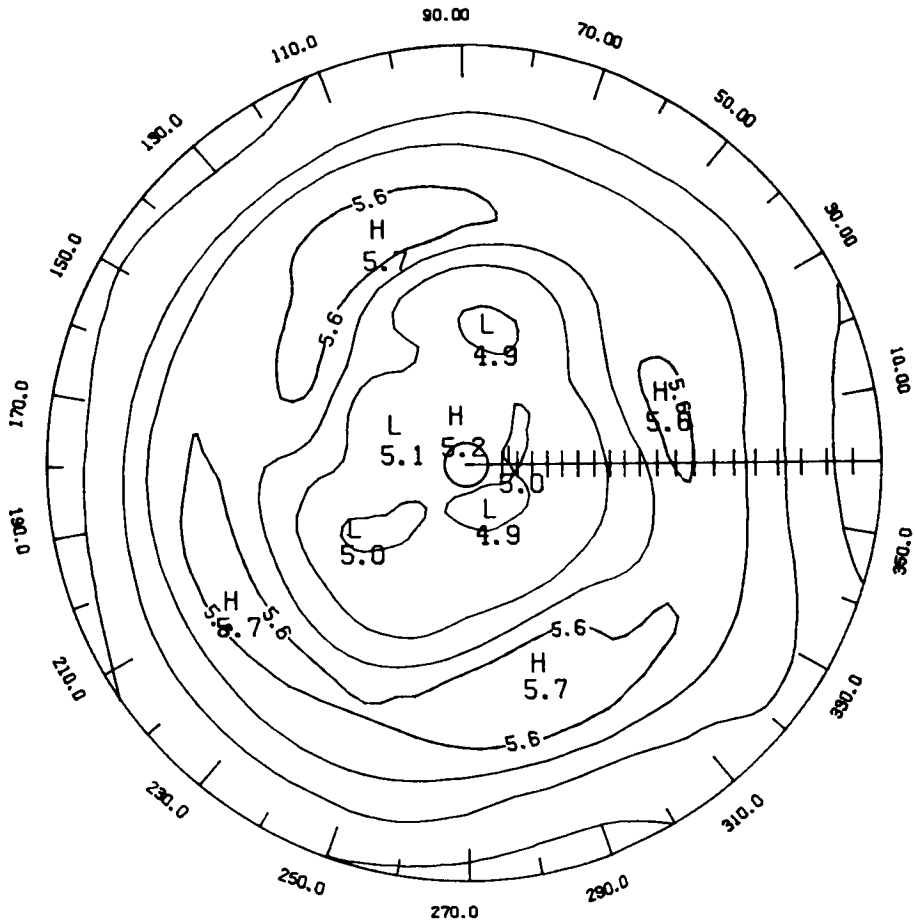
LATITUDE 0. TO 84.

Figure 03-27 - LIMS ozone monthly mean polar stereographic projection at 30 mb for February 1979 (contour interval is 0.2 ppmv).



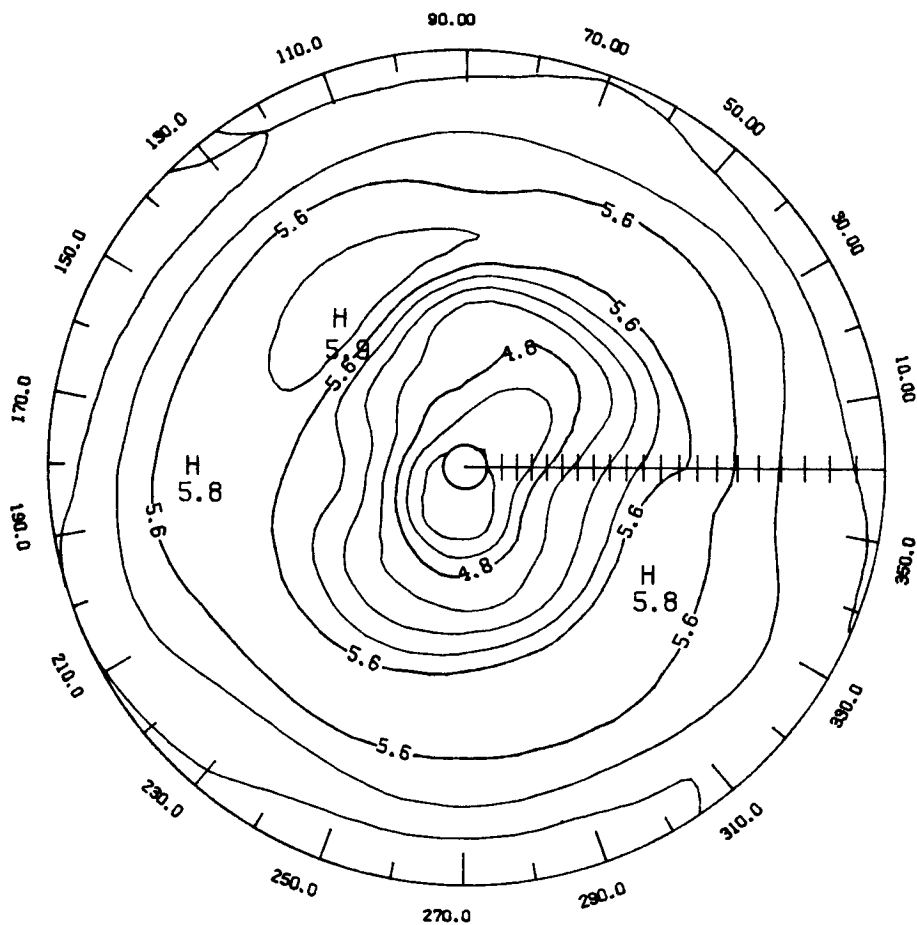
LATITUDE 0. TO 84.

Figure 03-28 - LIMS ozone monthly mean polar stereographic projection at 30 mb for March 1979 (contour interval is 0.2 ppmv).



LATITUDE 0. TO 84.

Figure 03-29 - LIMS ozone monthly mean polar stereographic projection at 30 mb for April 1979 (contour interval is 0.2 ppmv).



LATITUDE 0. TO 84.

Figure 03-30 - LIMS ozone monthly mean polar stereographic projection at 30 mb for May 1979 (contour interval is 0.2 ppmv).

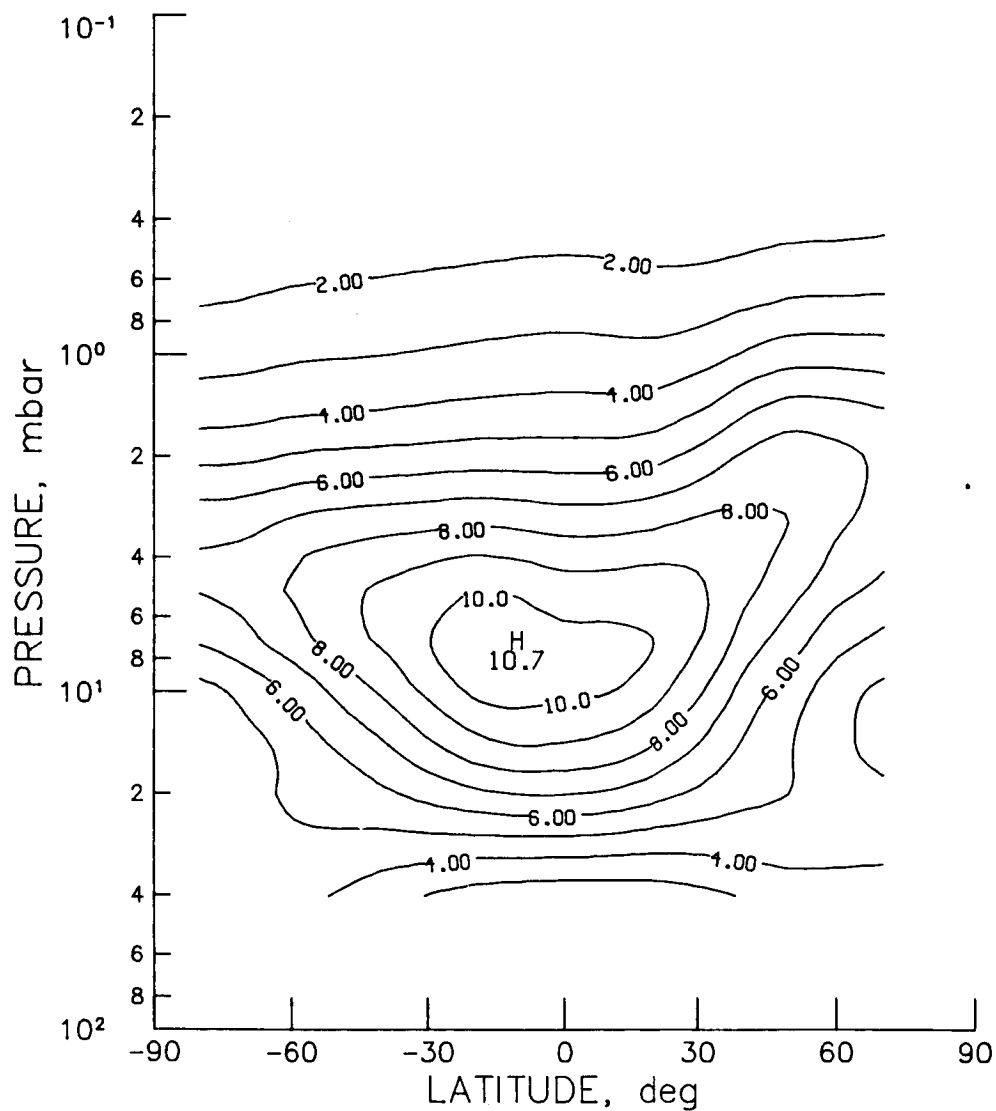


Figure O₃-31 - SBUV monthly zonal mean ozone cross section for November 1978
(contour interval is 1.0 ppmv).

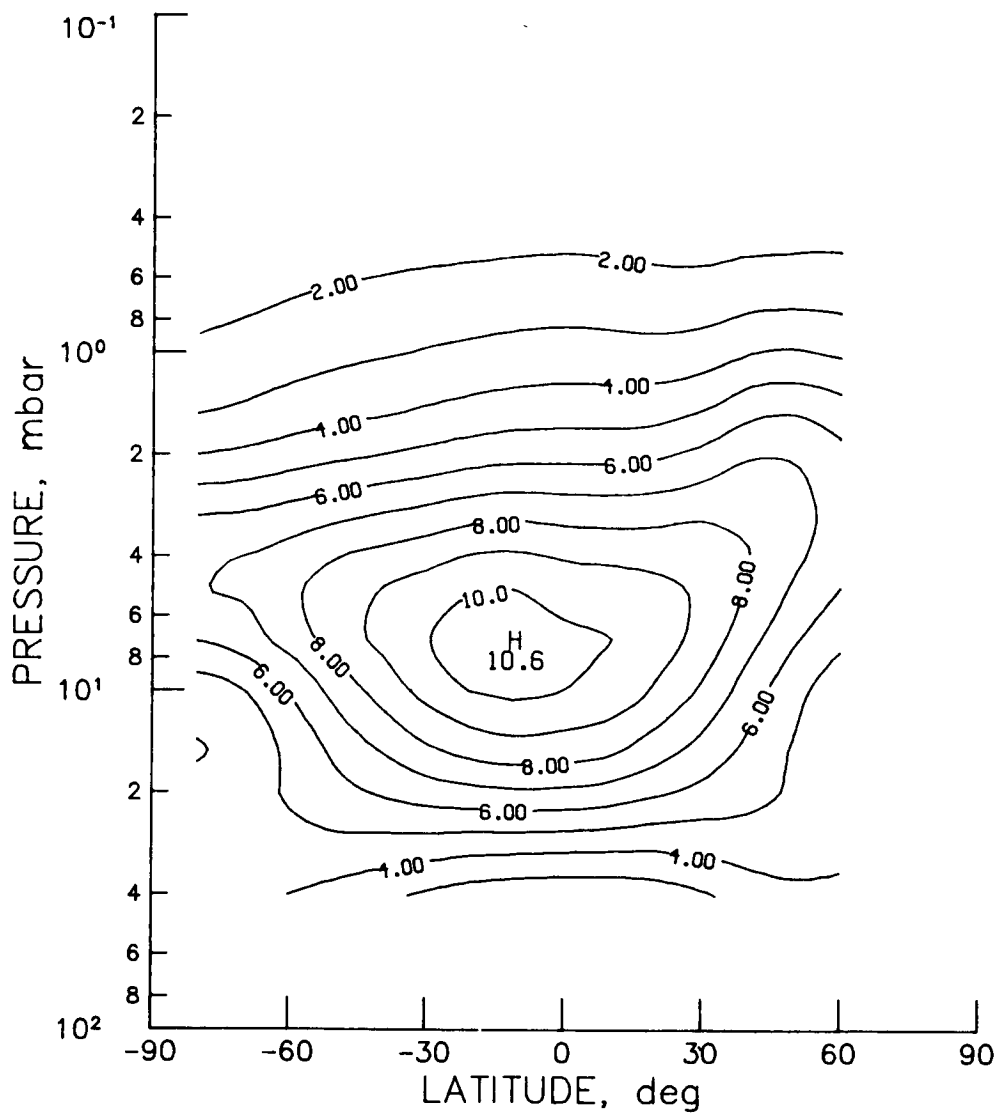


Figure 03-32 - SBUV monthly zonal mean ozone cross section for December 1978 (contour interval is 1.0 ppmv).

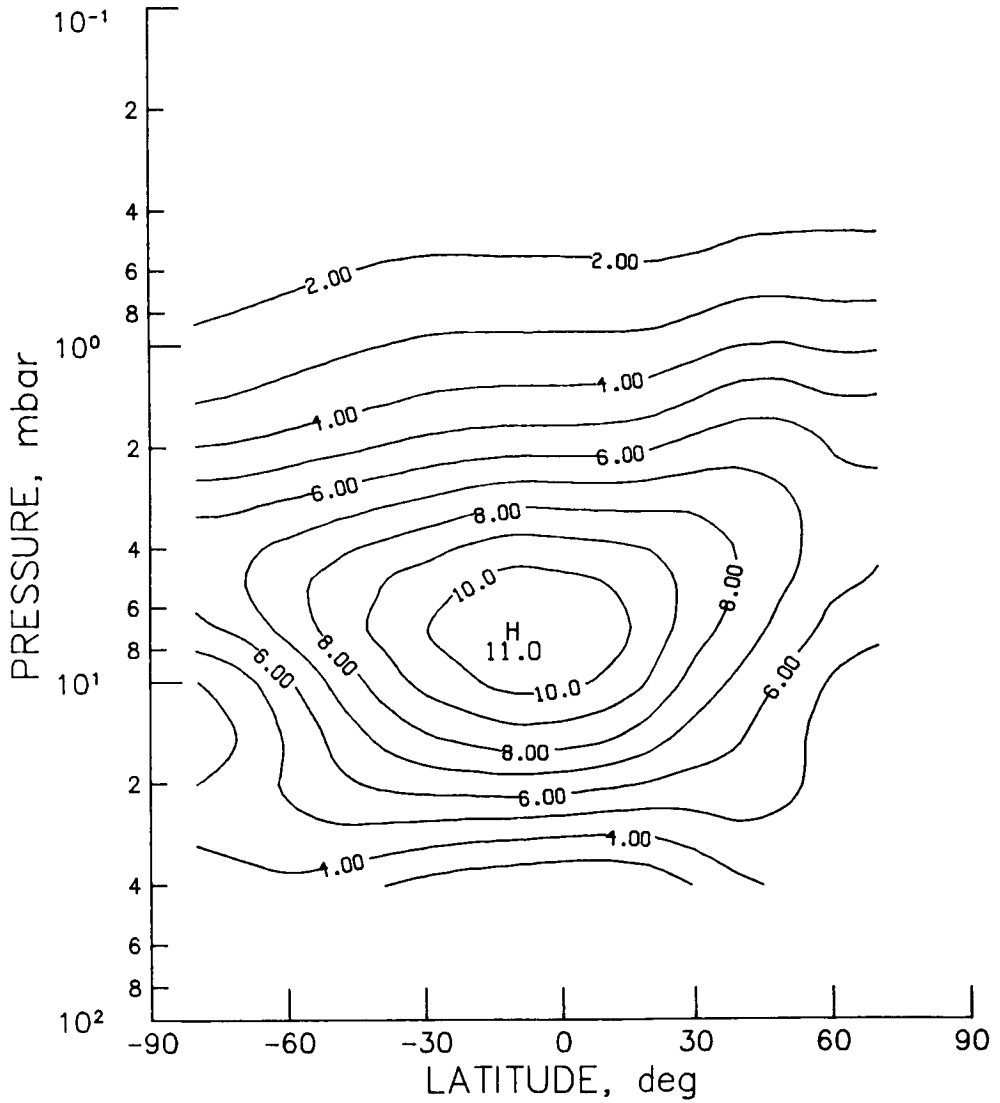


Figure 03-33 - SBUV monthly zonal mean ozone cross section for January 1979
(contour interval is 1.0 ppmv).

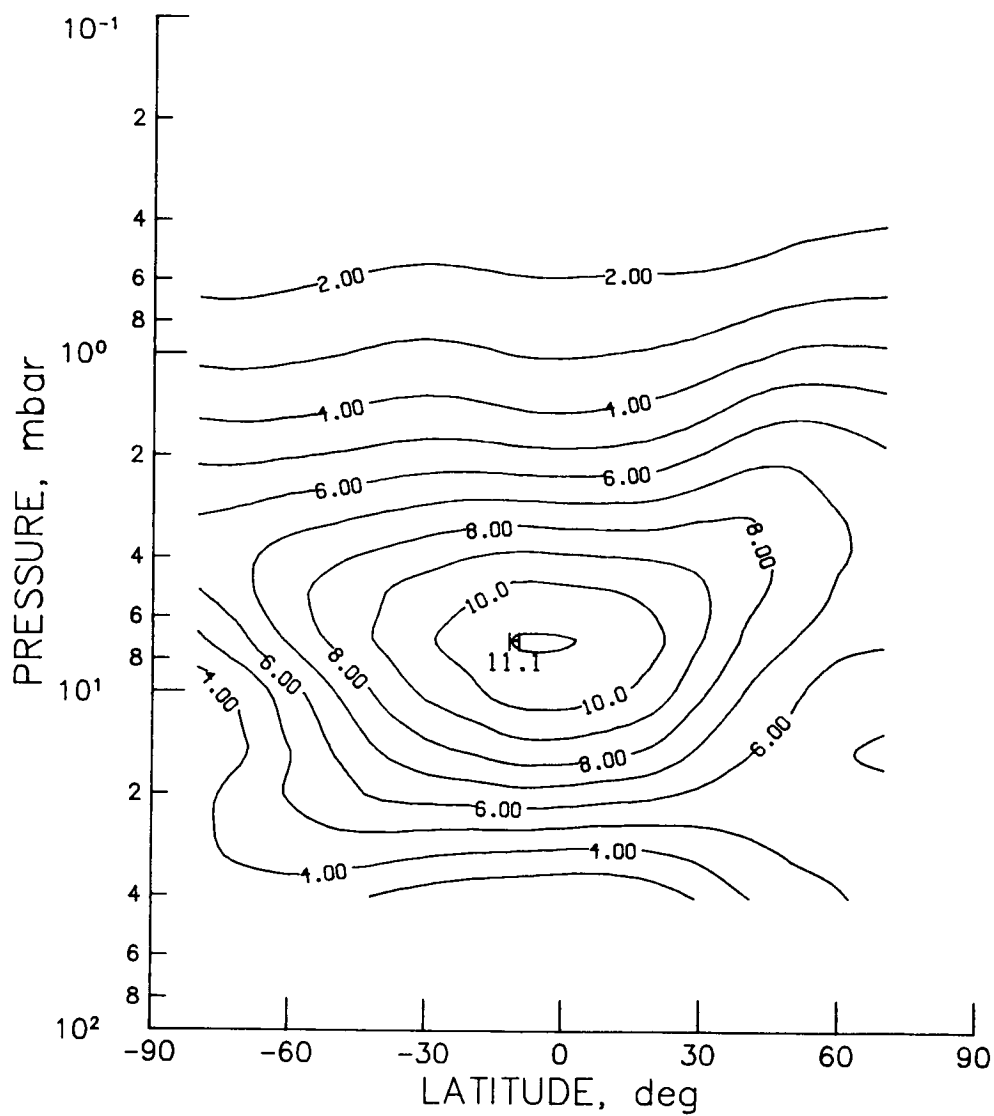


Figure 03-34 - SBUV monthly zonal mean ozone cross section for February 1979 (contour interval is 1.0 ppmv).

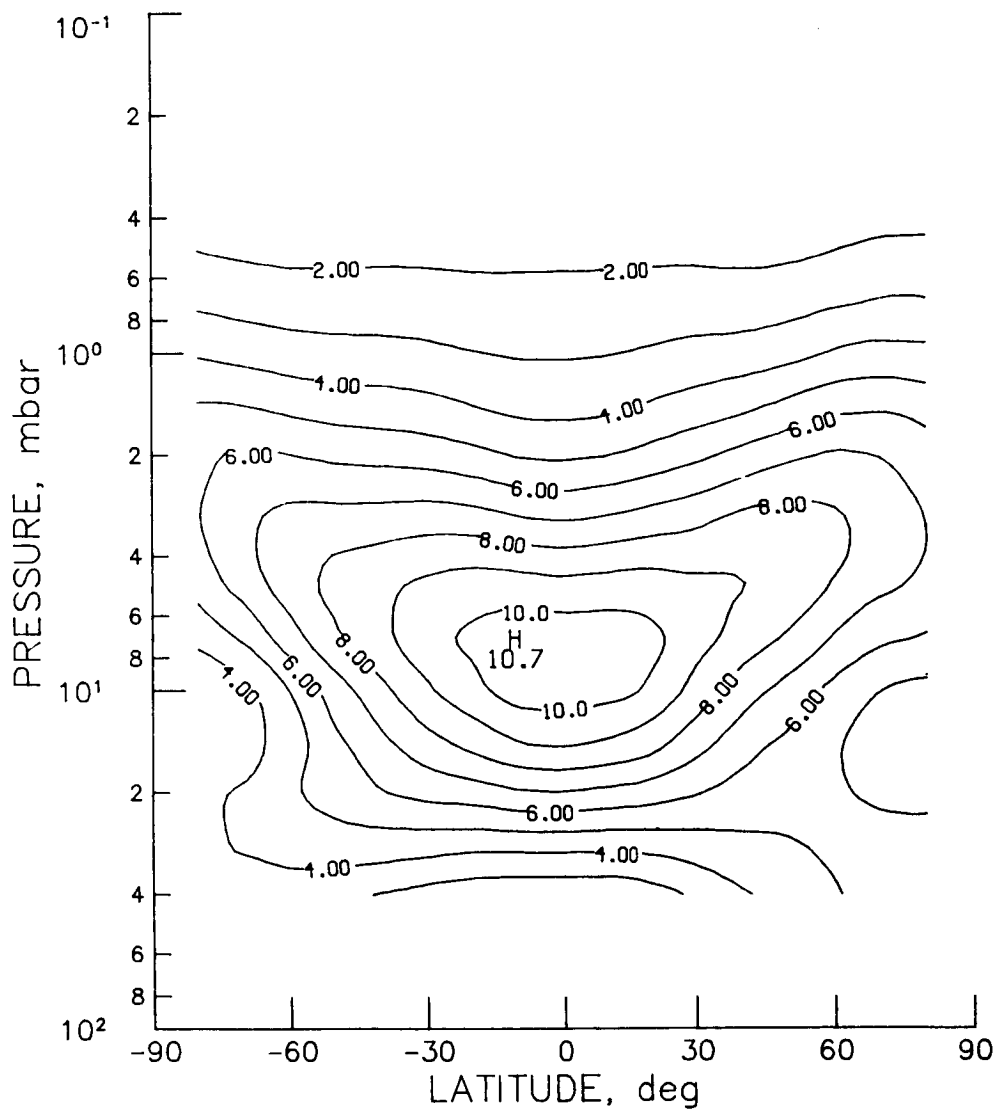


Figure 03-35 - SBUV monthly zonal mean ozone cross section for March 1979
(contour interval is 1.0 ppmv).

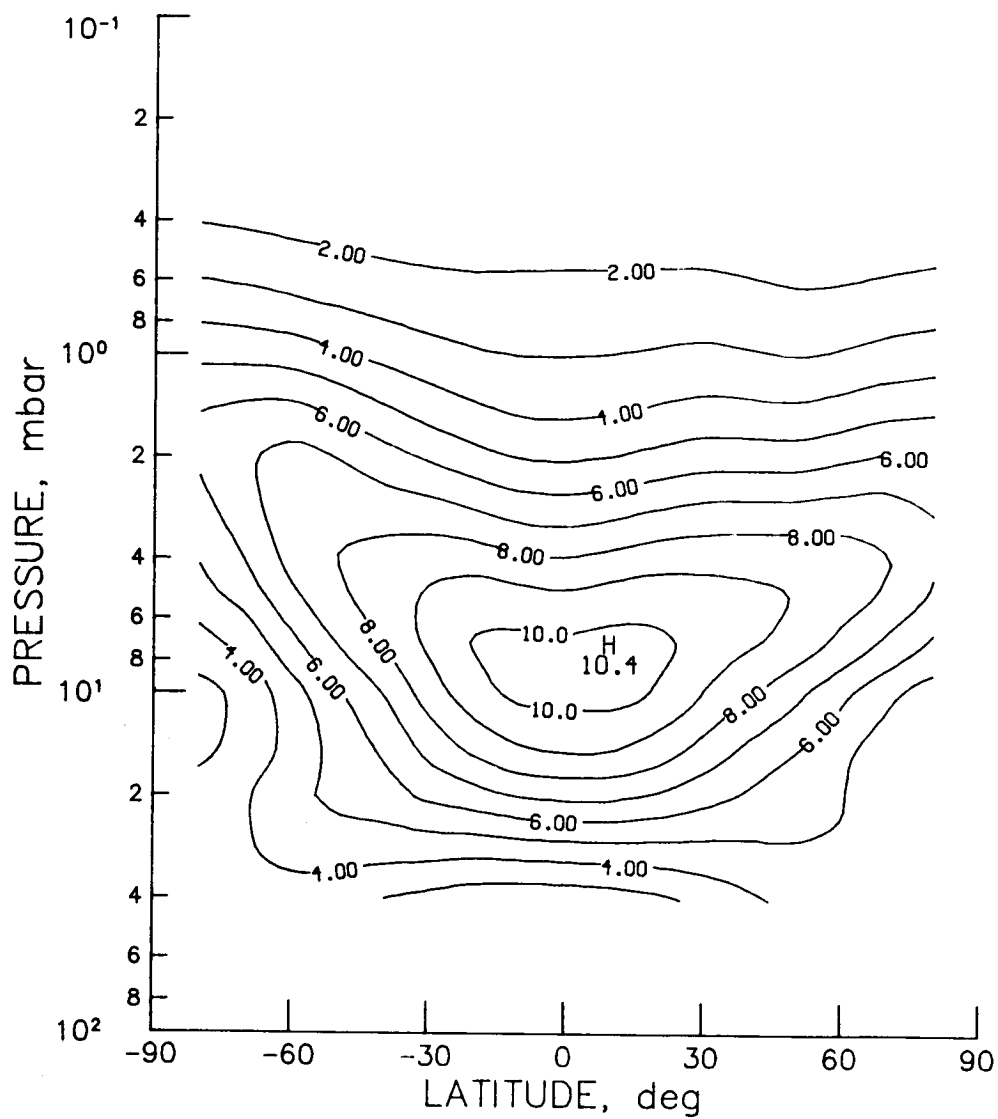


Figure 03-36 - SBUV monthly zonal mean ozone cross section for April 1979 (contour interval is 1.0 ppmv).

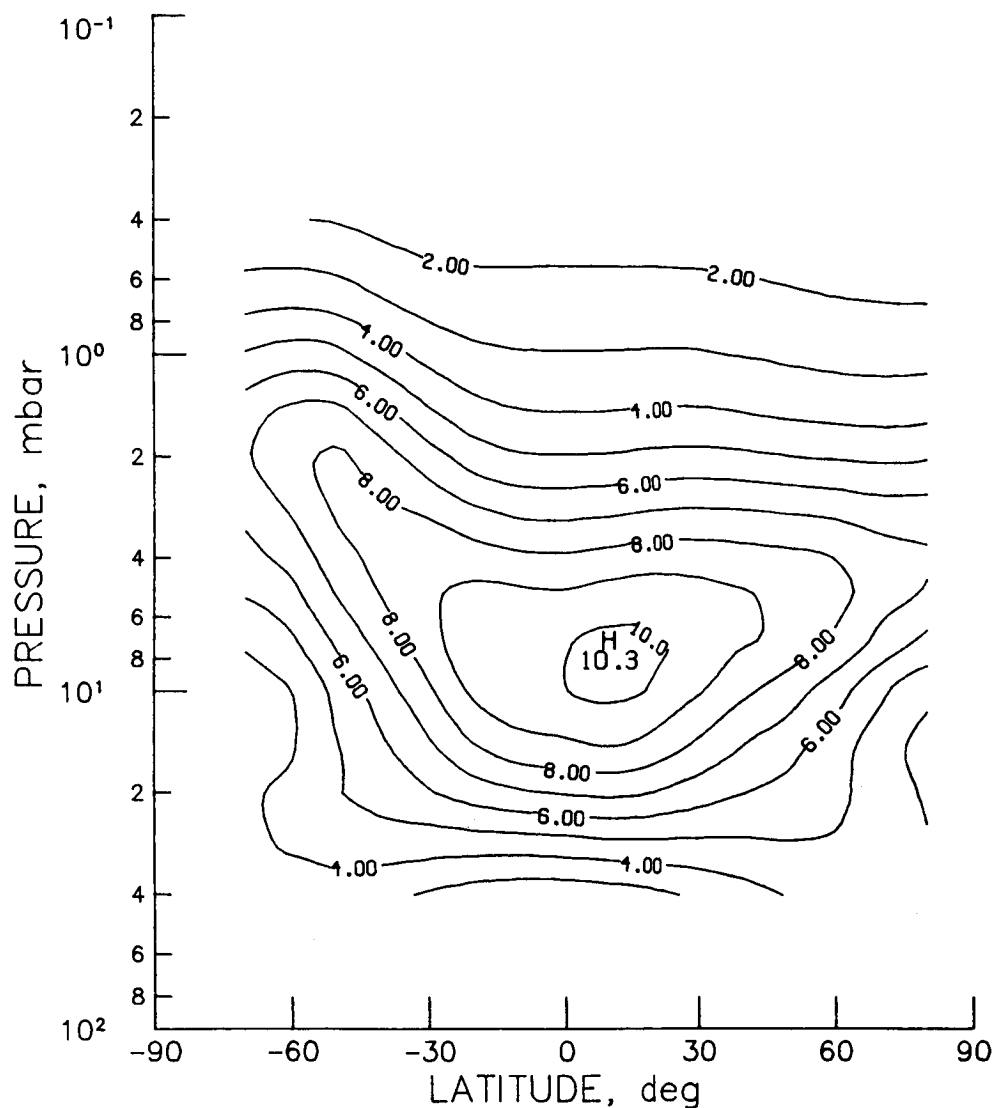


Figure 03-37 - SBUV monthly zonal mean ozone cross section for May 1979
(contour interval is 1.0 ppmv).

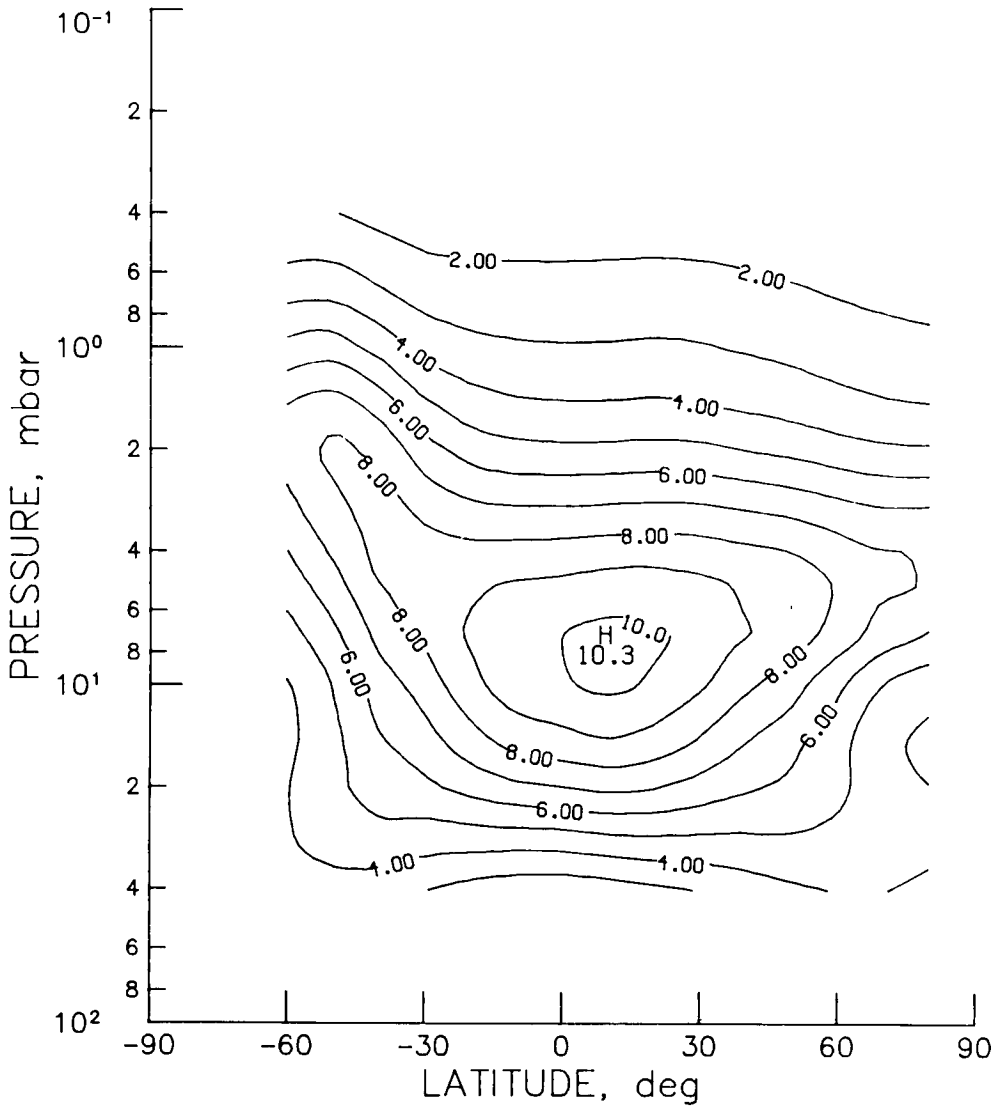


Figure 03-38 - SBUV monthly zonal mean ozone cross section for June 1979 (contour interval is 1.0 ppmv).

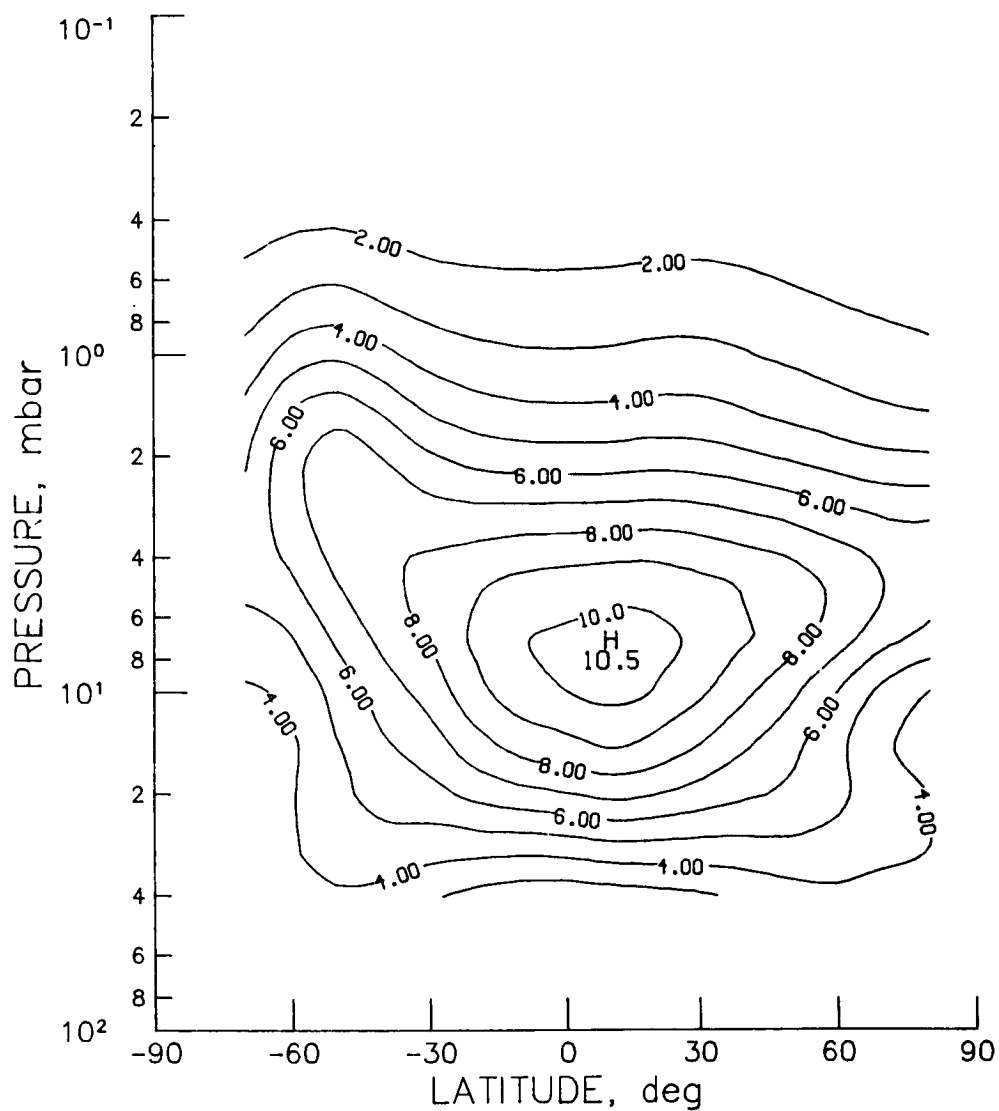


Figure 03-39 - SBUV monthly zonal mean ozone cross section for July 1979
(contour interval is 1.0 ppmv).

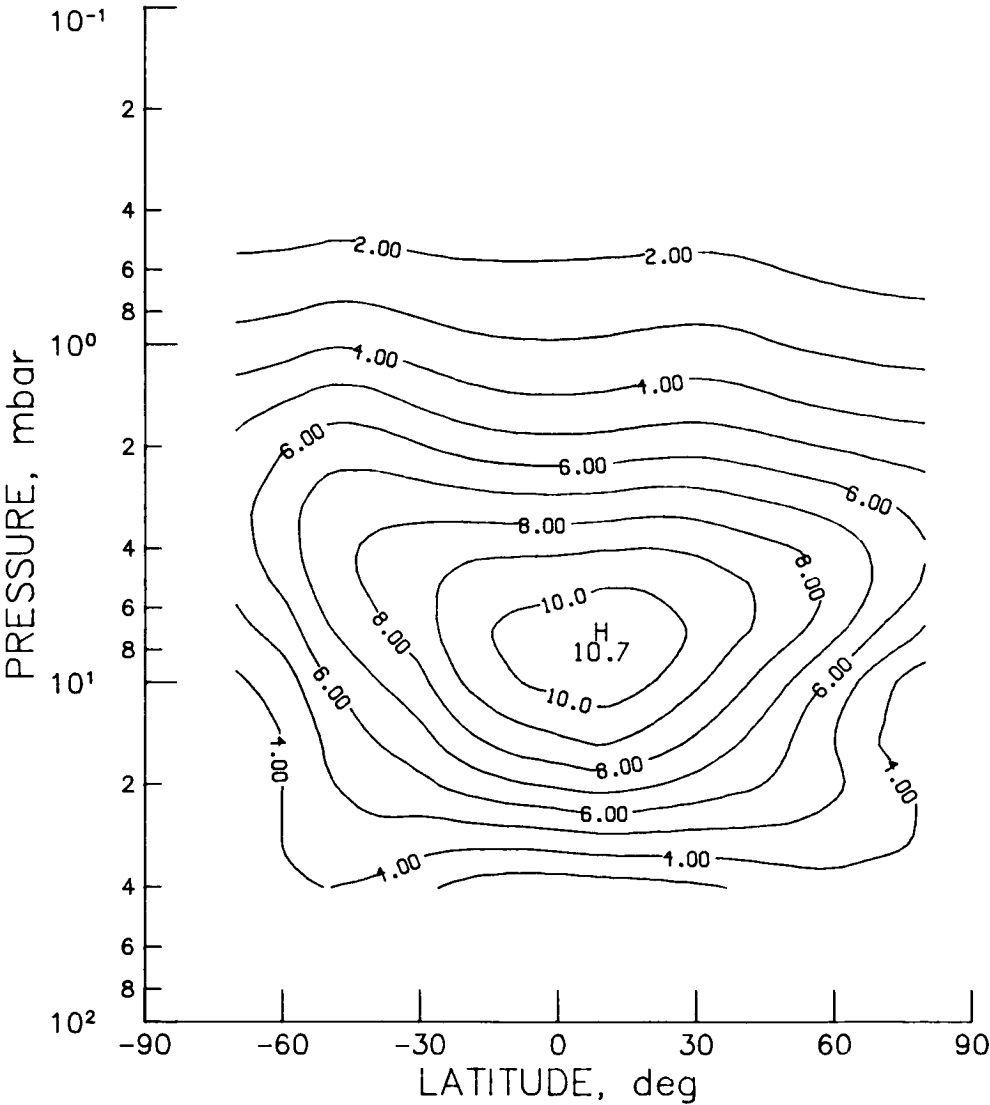


Figure O₃-40 - SBUV monthly zonal mean ozone cross section for August 1979 (contour interval is 1.0 ppmv).

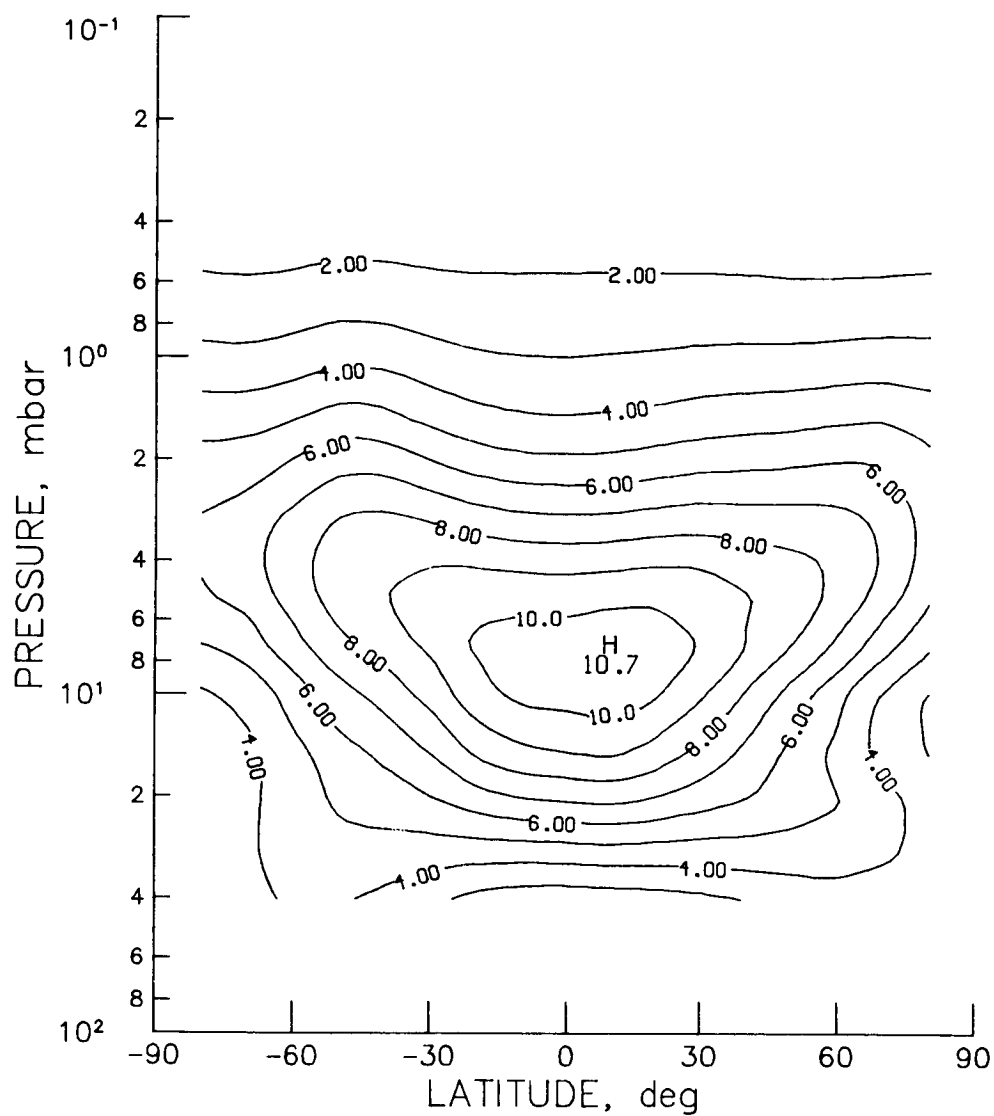


Figure 03-41 - SBUV monthly zonal mean ozone cross section for September 1979 (contour interval is 1.0 ppmv).

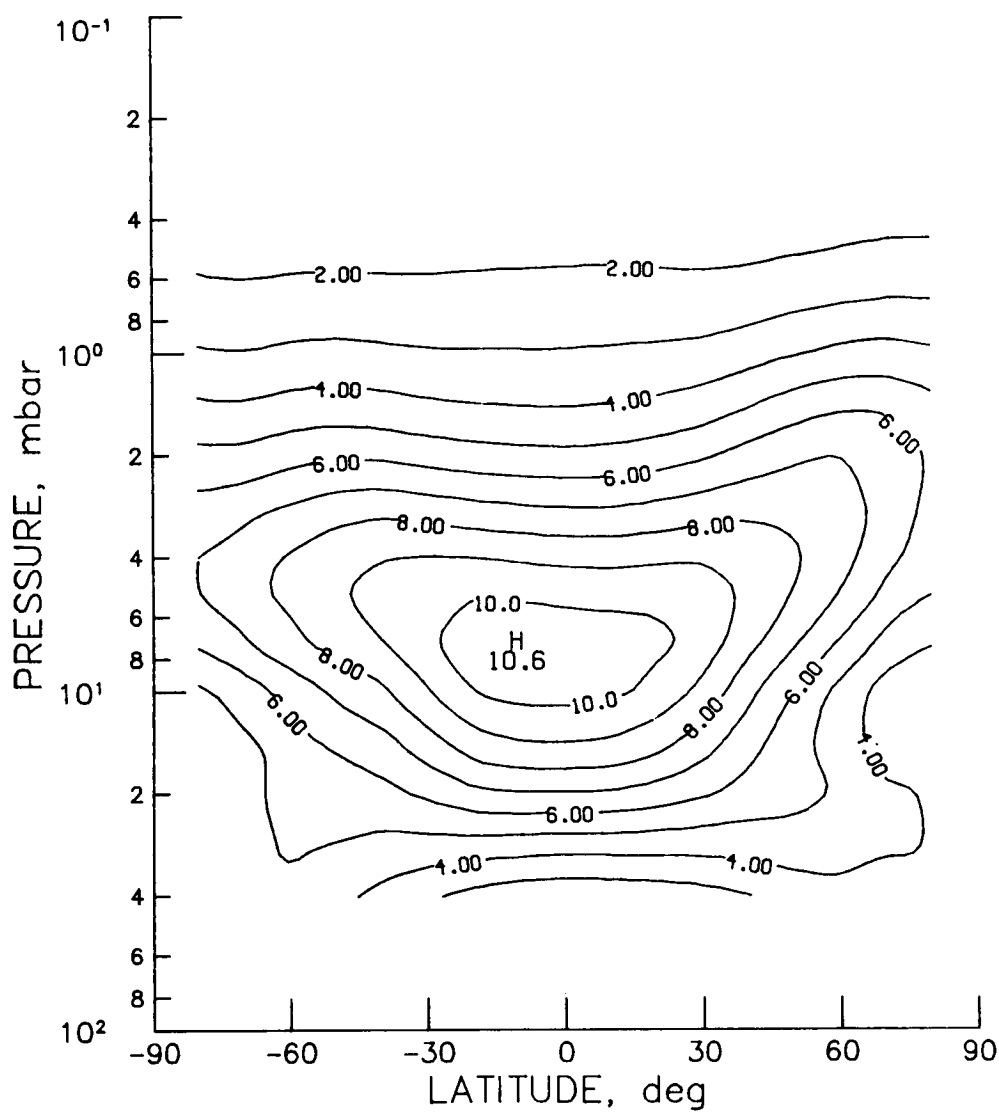


Figure O₃-42 - SBUV monthly zonal mean ozone cross section for October 1979 (contour interval is 1.0 ppmv).

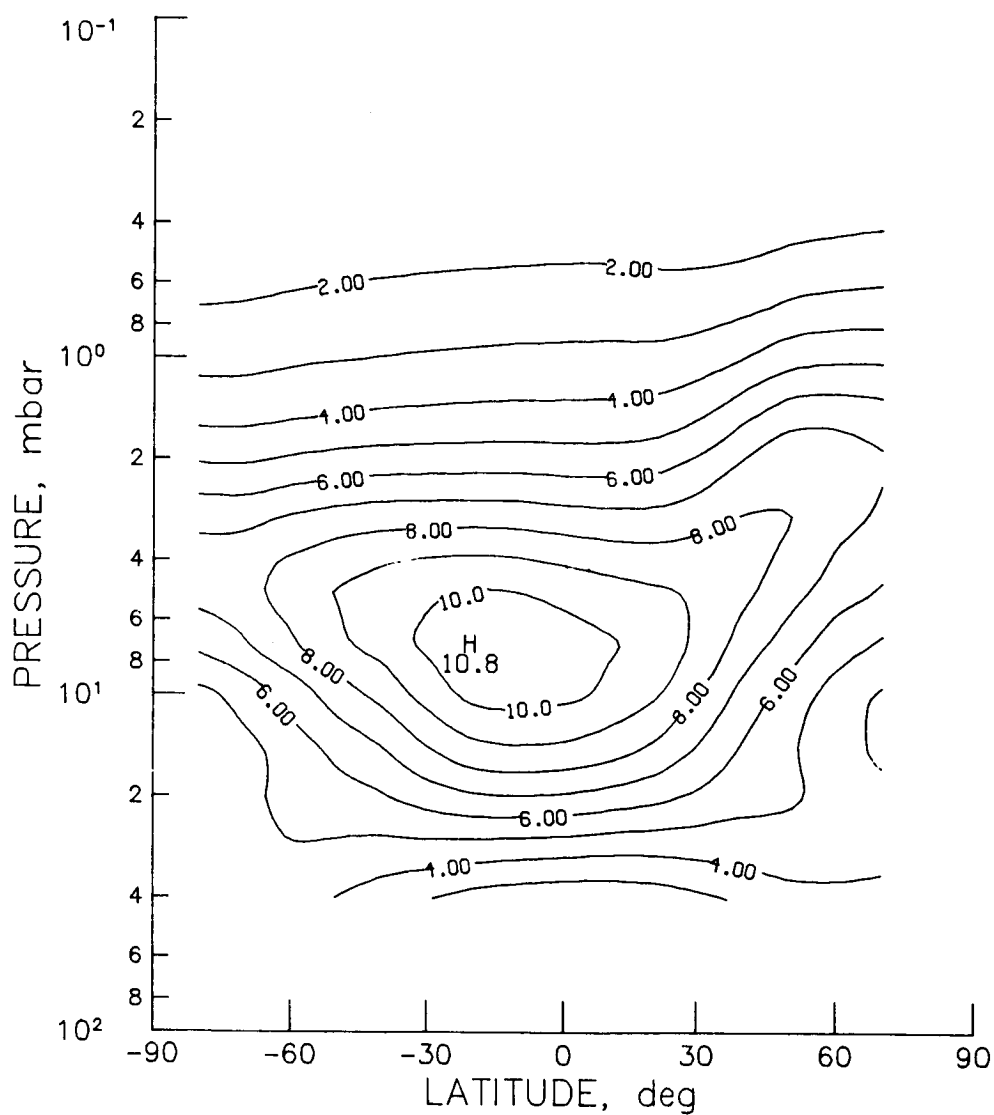


Figure 03-43 - SBUV monthly zonal mean ozone cross section for November 1979 (contour interval is 1.0 ppmv).

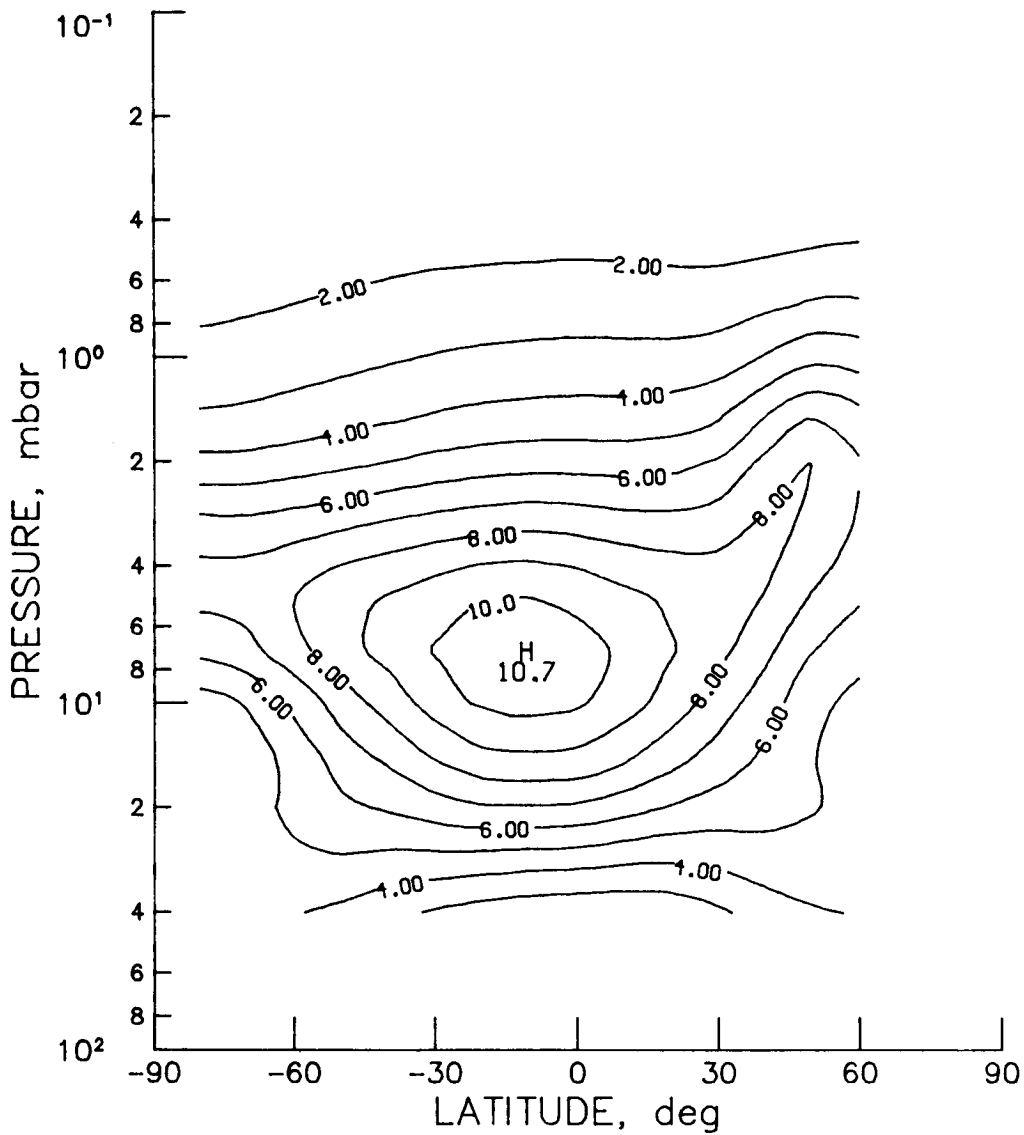
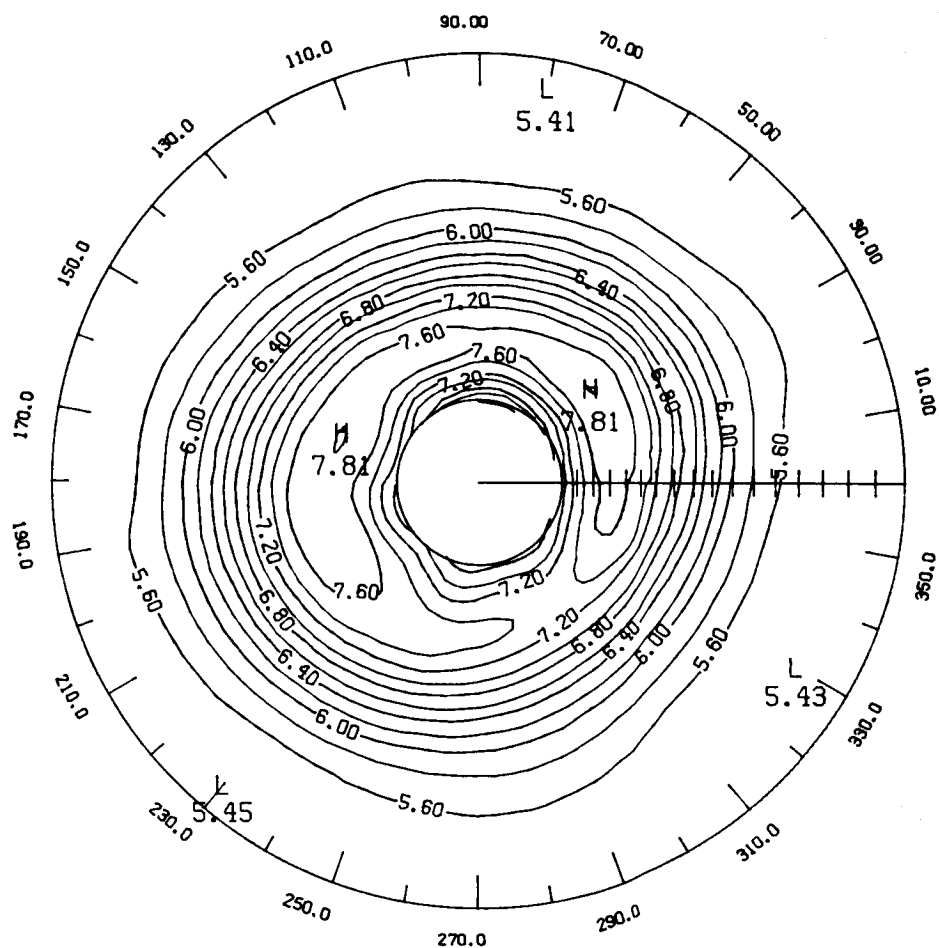
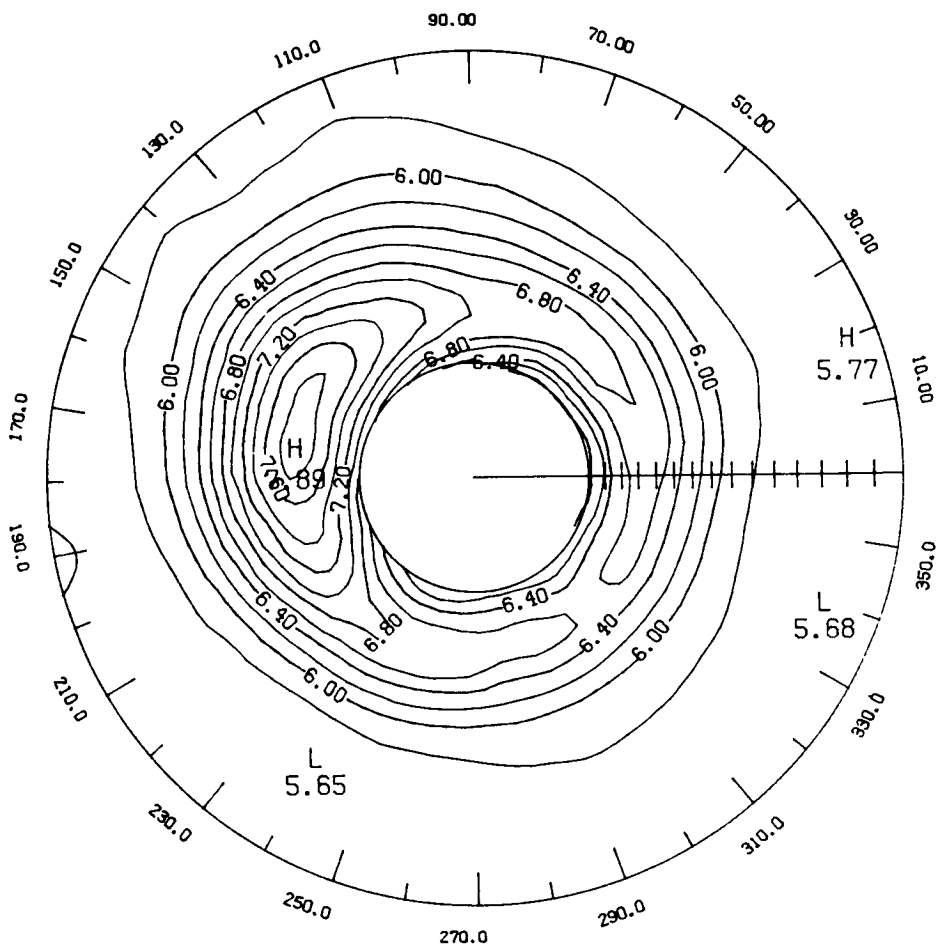


Figure 0₃-44 - SBUV monthly zonal mean ozone cross section for December 1979 (contour interval is 1.0 ppbv).



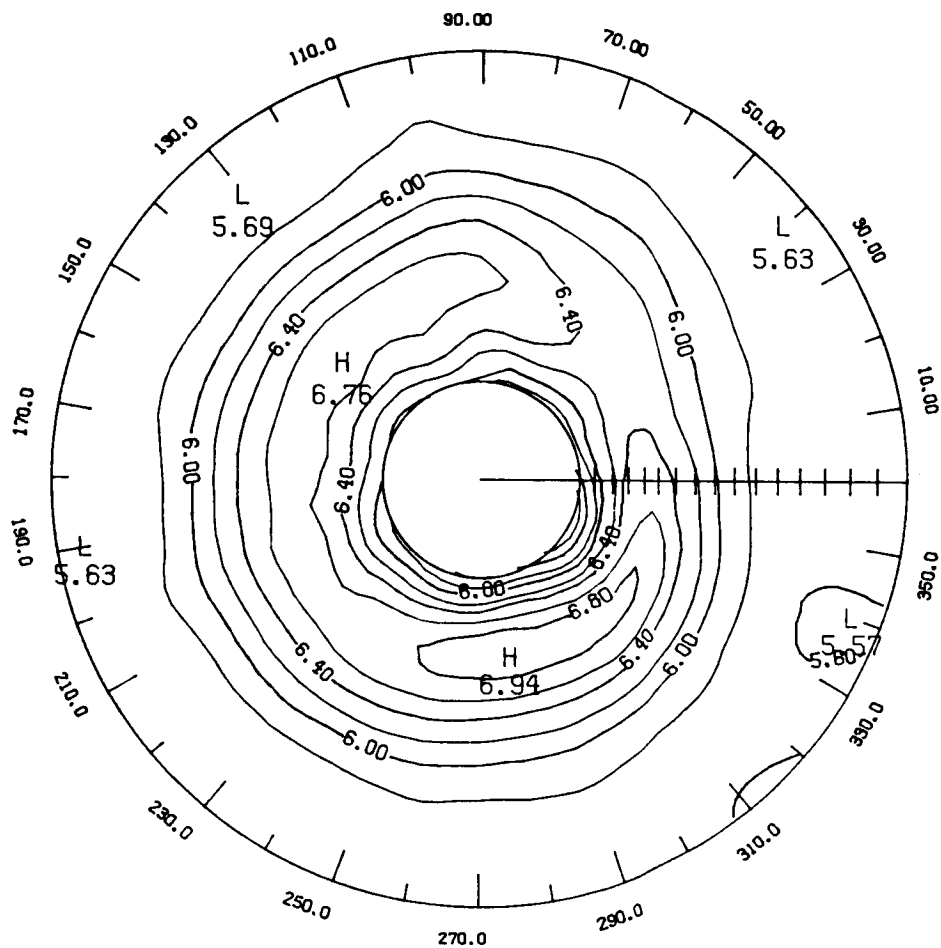
LATITUDE 0. TO 68.

Figure 03-45 - SBUV monthly mean ozone polar stereographic projection at 2 mb for November 1978 (contour interval is 0.2 ppbv).



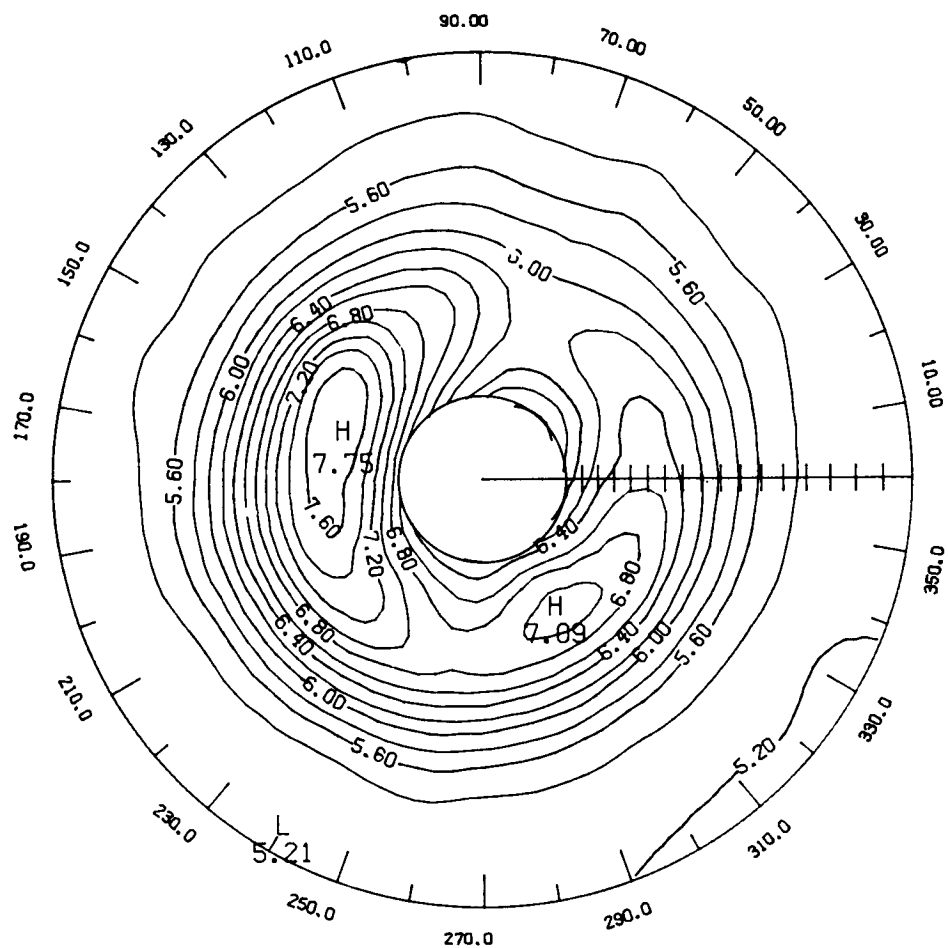
LATITUDE 0. TO 60.

Figure 03-46 - SBUV monthly mean ozone polar stereographic projection at 2 mb for December 1978 (contour interval is 0.2 ppbv).



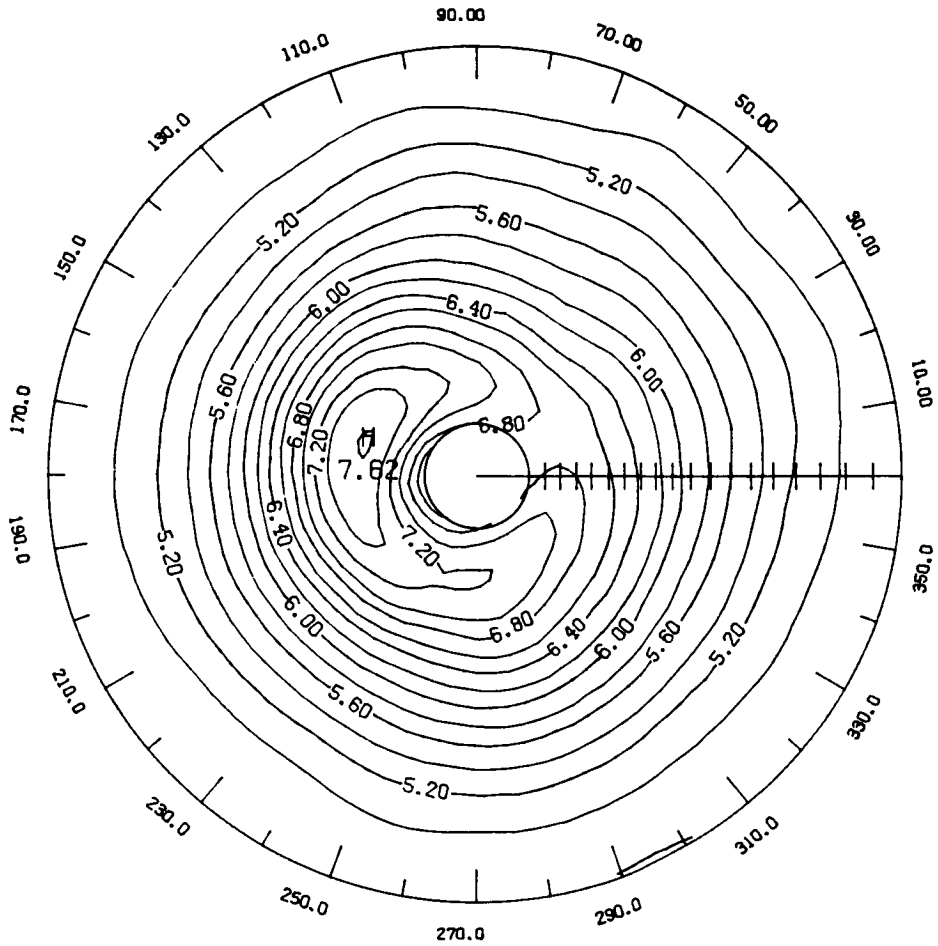
LATITUDE 0. TO 64.

Figure 03-47 - SBUV monthly mean ozone polar stereographic projection at 2 mb for January 1979 (contour interval is 0.2 ppbv).



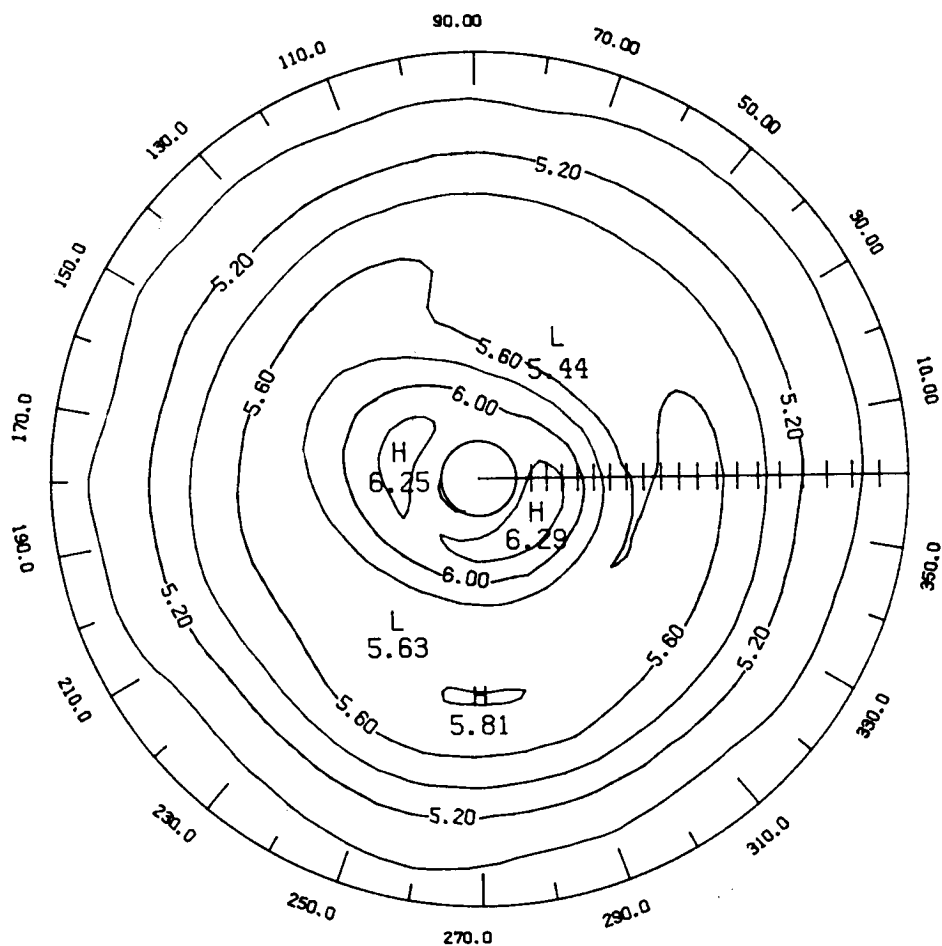
LATITUDE 0. TO 68.

Figure 03-48 - SBUV monthly mean ozone polar stereographic projection at 2 mb for February 1979 (contour interval is 0.2 ppmv).



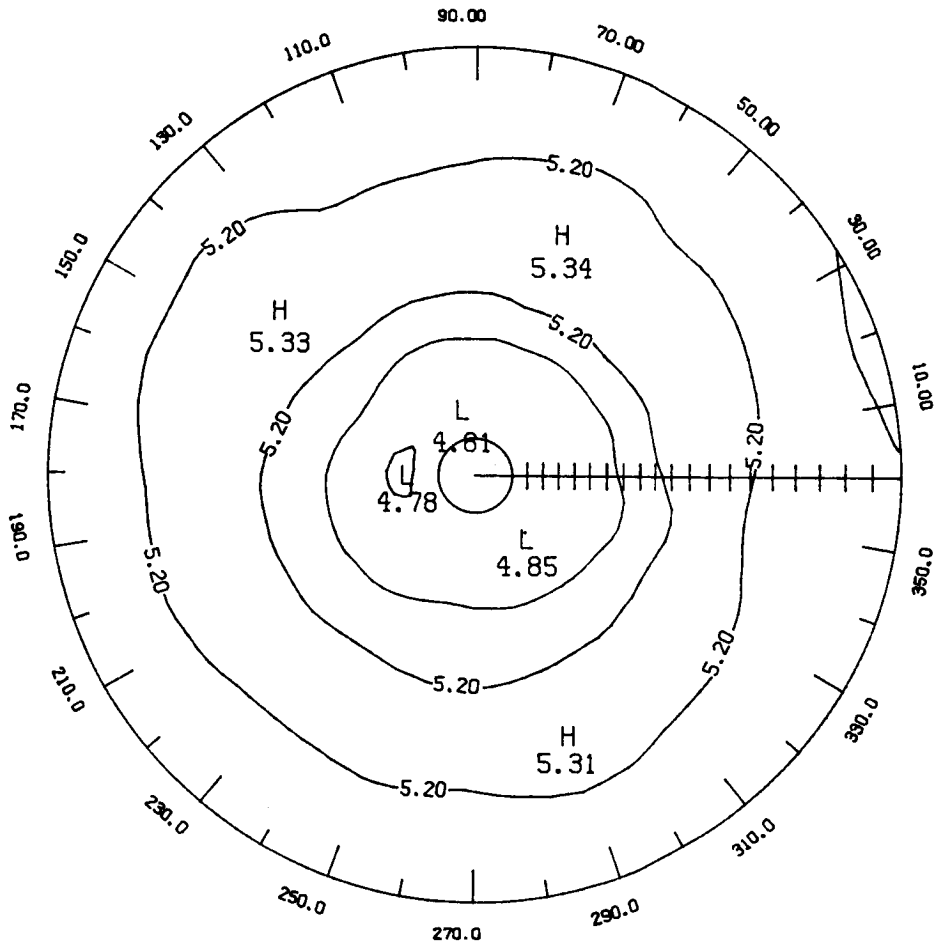
LATITUDE 0. TO 76.

Figure 03-49 - SBUV monthly mean ozone polar stereographic projection at 2 mb for March 1979 (contour interval is 0.2 ppmv).



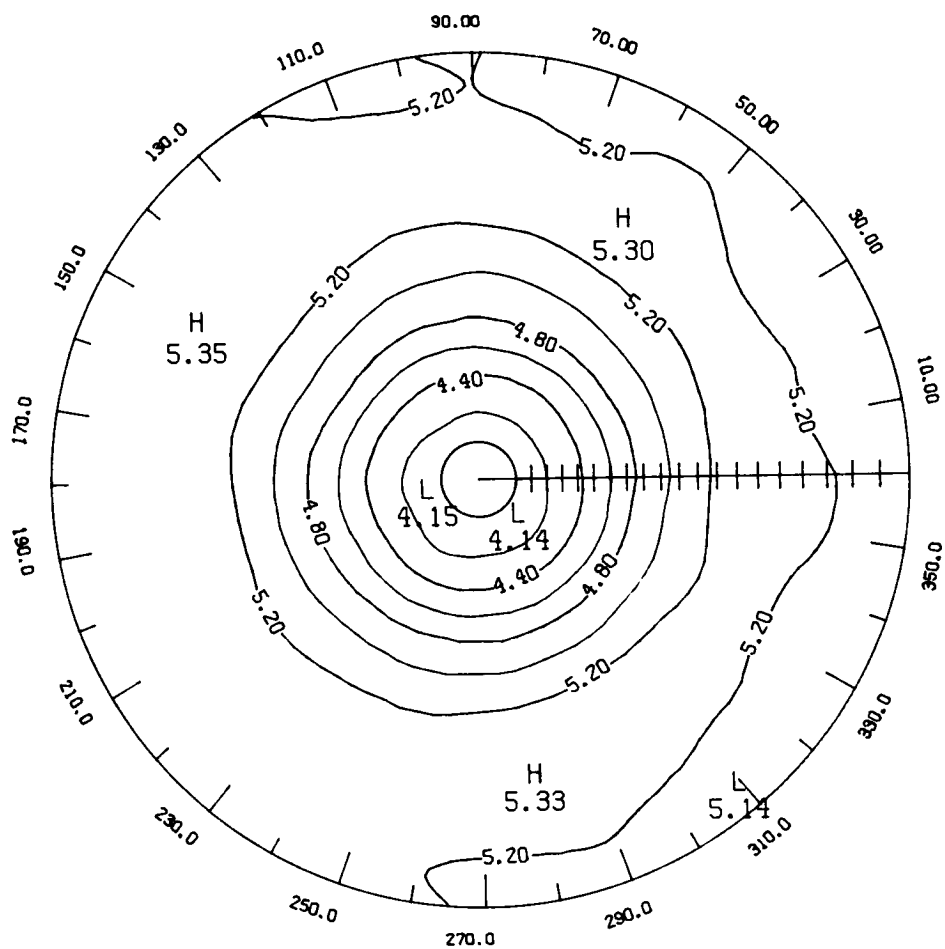
LATITUDE 0. TO 80.

Figure 03-50 - SBUV monthly mean ozone polar stereographic projection at 2 mb for April 1979 (contour interval is 0.2 ppmv).



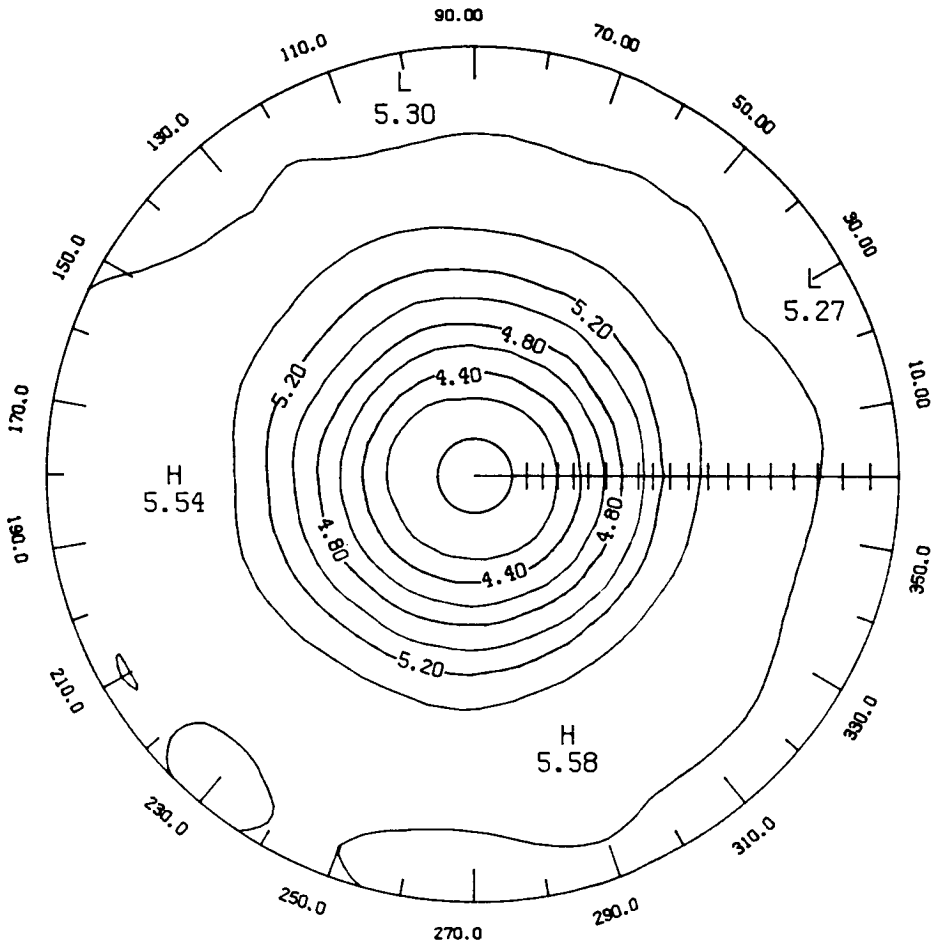
LATITUDE 0. TO 80.

Figure 03-51 - SBUV monthly mean ozone polar stereographic projection at 2 mb for May 1979 (contour interval is 0.2 ppmv).



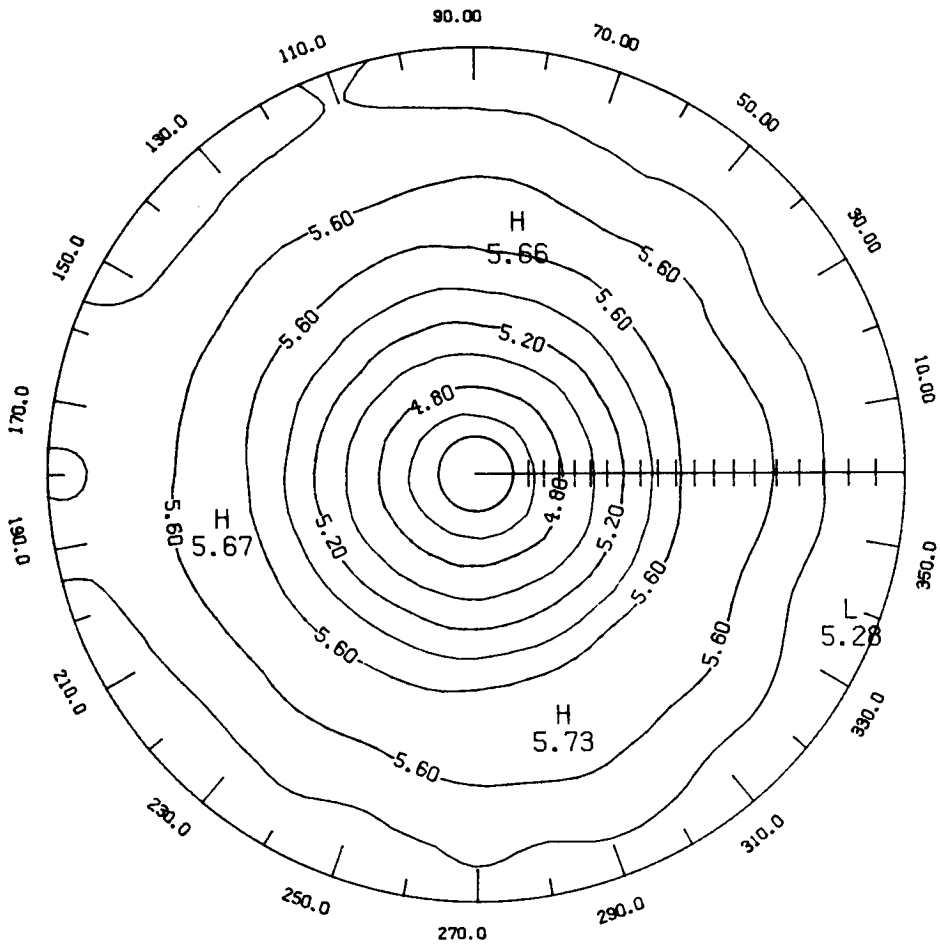
LATITUDE 0. TO 80.

Figure 03-52 - SBUV monthly mean ozone polar stereographic projection at 2 mb for June 1979 (contour interval is 0.2 ppmv).



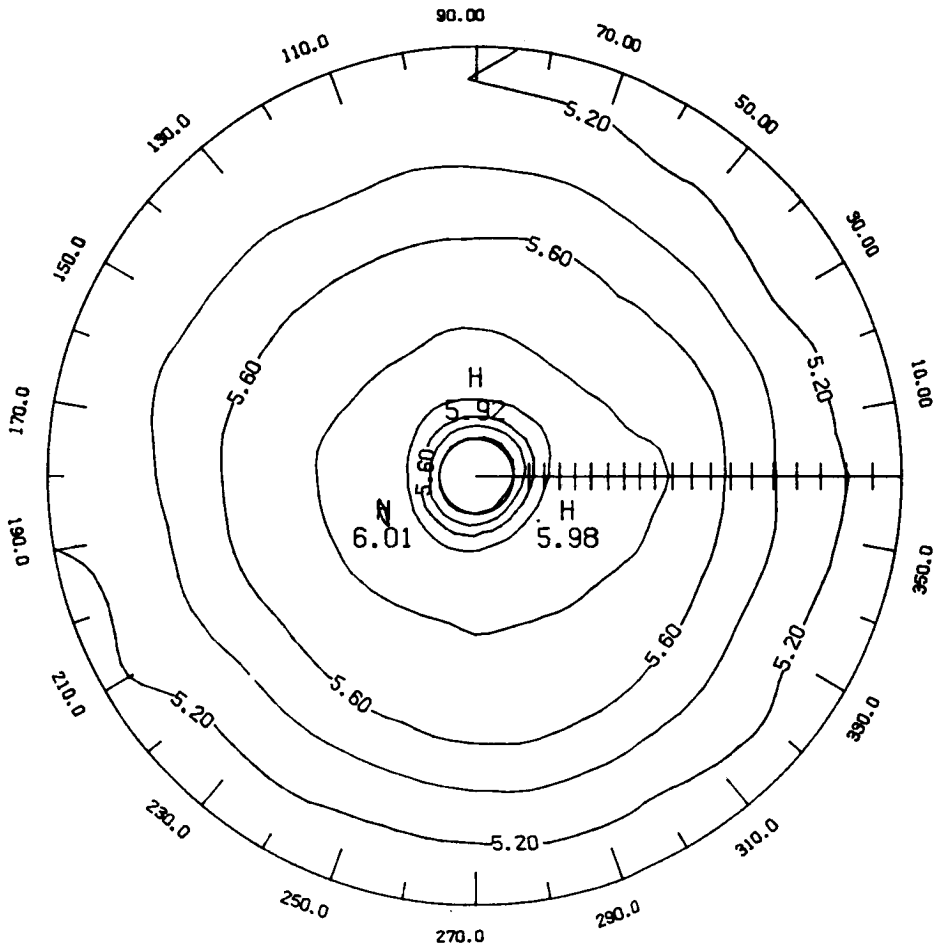
LATITUDE 0. TO 80.

Figure 03-53 - SBUV monthly mean ozone polar stereographic projection at 2 mb for July 1979 (contour interval is 0.2 ppmv).



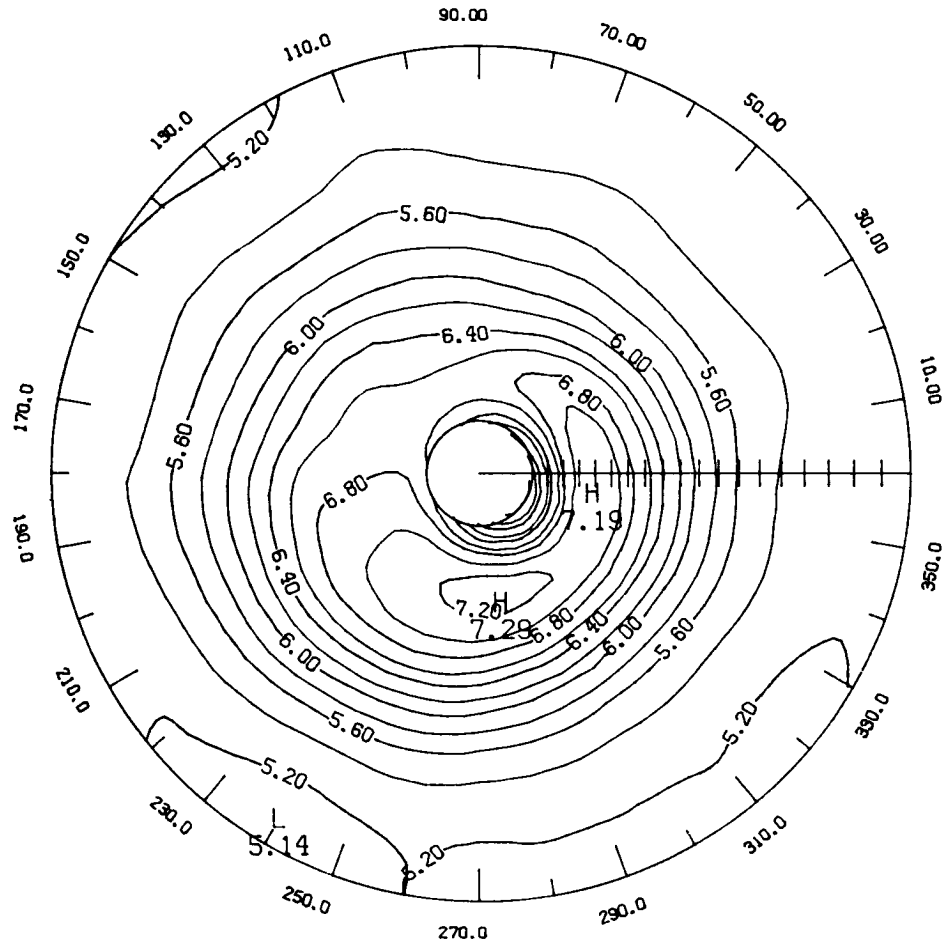
LATITUDE 0. TO 80.

Figure 03-54 - SBUV monthly mean ozone polar stereographic projection at 2 mb for August 1979 (contour interval is 0.2 ppmv).



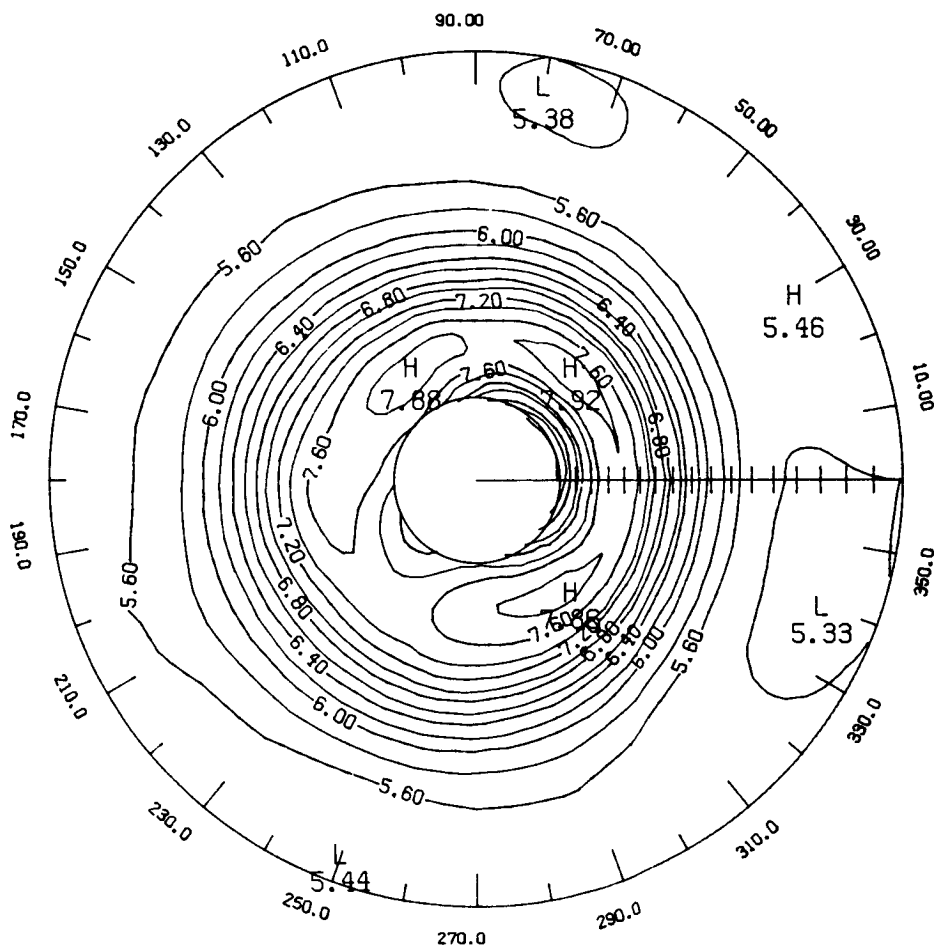
LATITUDE 0. TO 80.

Figure 03-55 - SBUV monthly mean ozone polar stereographic projection at 2 mb for September 1979 (contour interval is 0.2 ppmv).



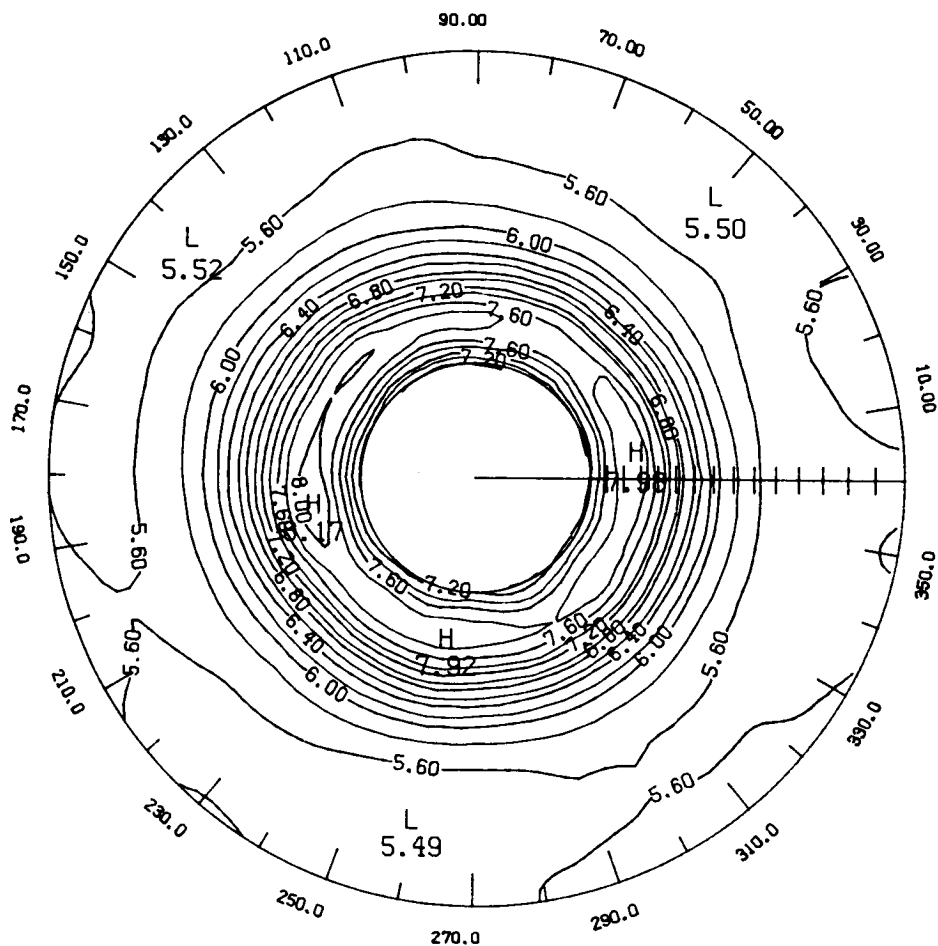
LATITUDE 0. TO 76.

Figure 03-56 - SBUV monthly mean ozone polar stereographic projection at 2 mb for October 1979 (contour interval is 0.2 ppmv).



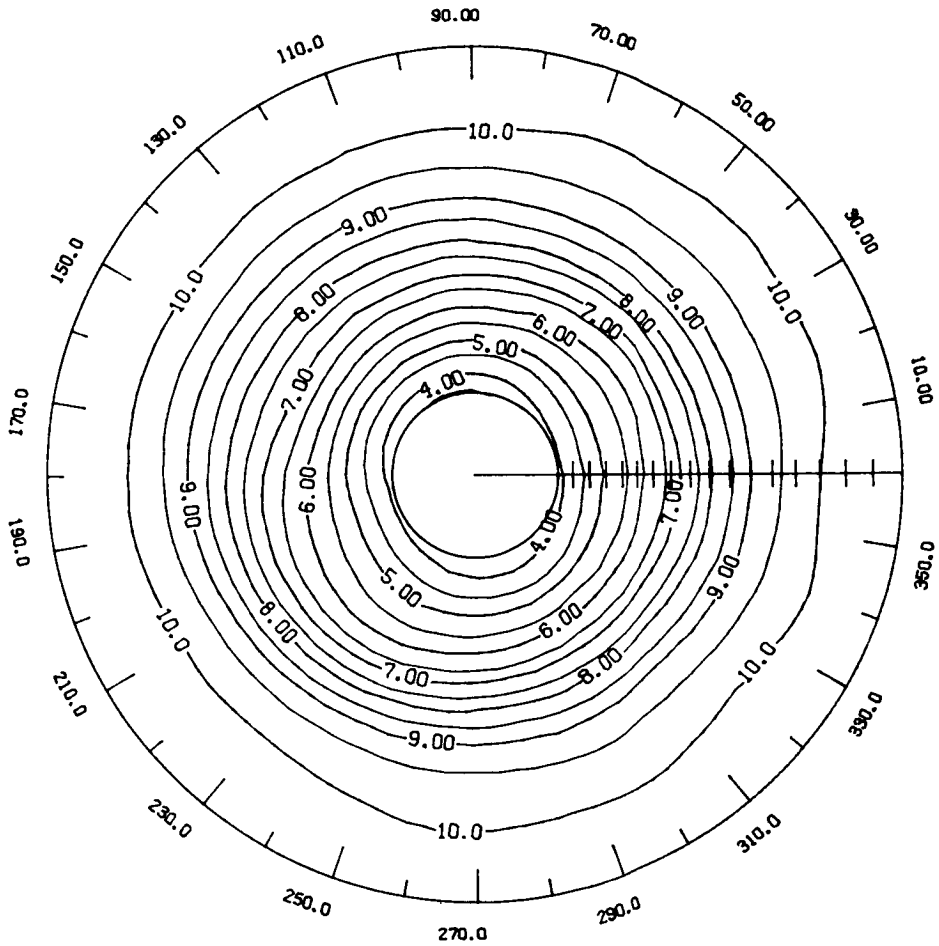
LATITUDE 0. TO 68.

Figure 03-57 - SBUV monthly mean ozone polar stereographic projection at 2 mb for November 1979 (contour interval is 0.2 ppmv).



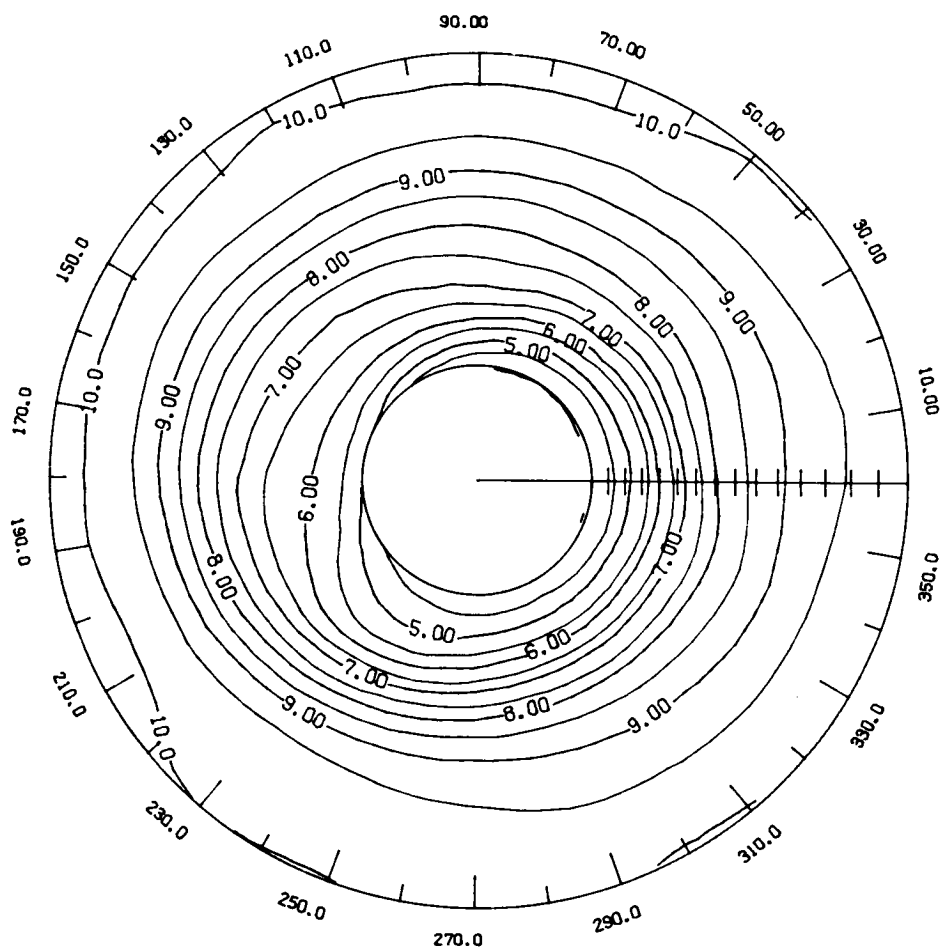
LATITUDE 0. TO 60.

Figure 03-58 - SBUV monthly mean ozone polar stereographic projection at 2 mb for December 1979 (contour interval is 0.2 ppmv).



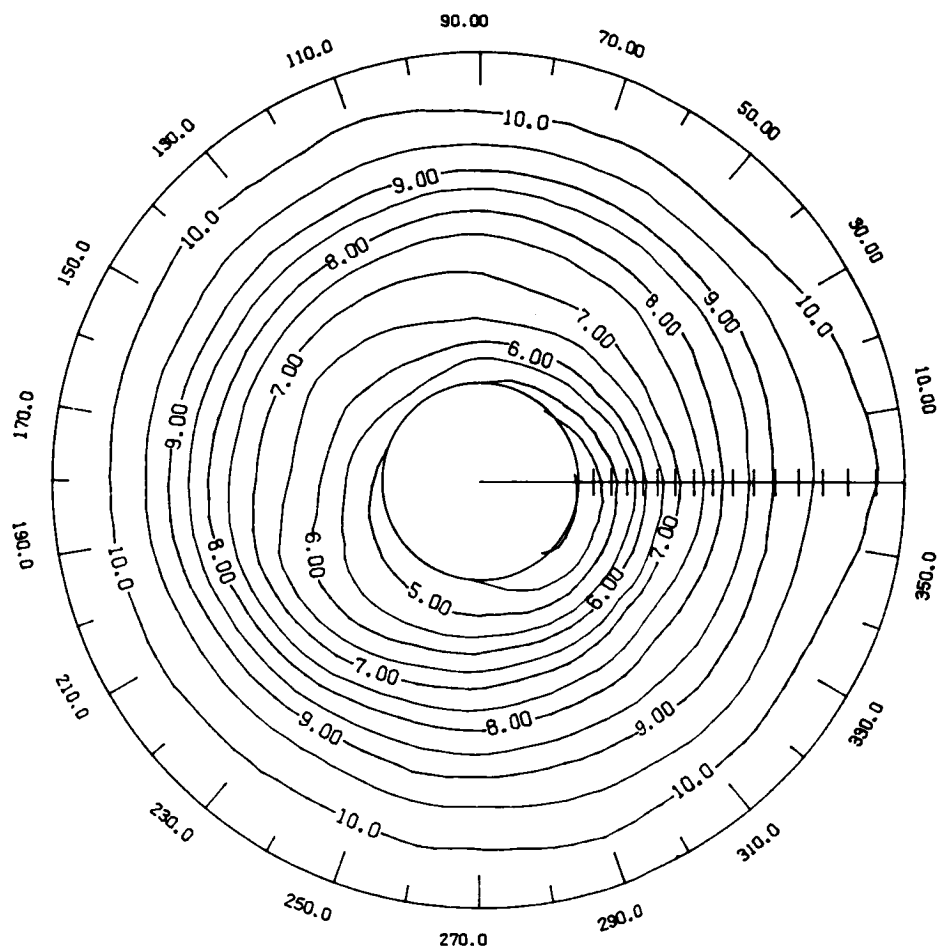
LATITUDE 0. TO 68.

Figure 03-59 - SBUV monthly mean ozone polar stereographic projection at 10 mb for November 1978 (contour interval is 0.5 ppmv).



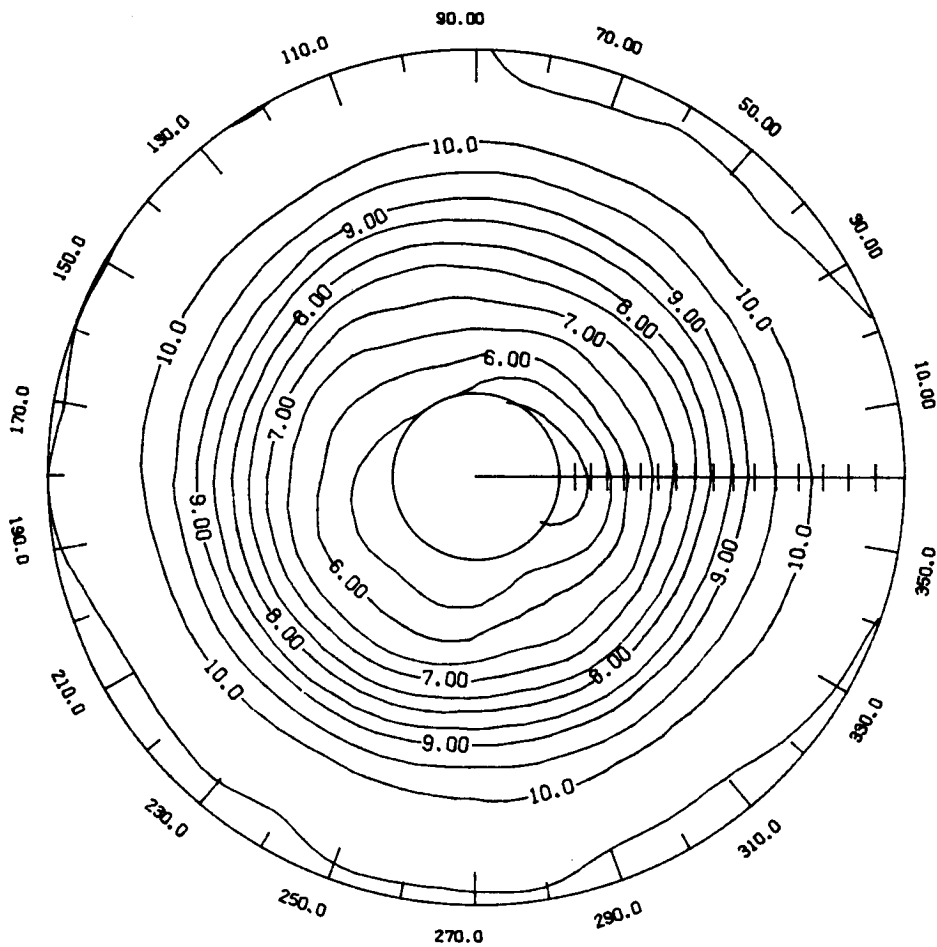
LATITUDE 0. TO 60.

Figure 03-60 - SBUV monthly mean ozone polar stereographic projection at 10 mb for December 1978 (contour interval is 0.5 ppmv).



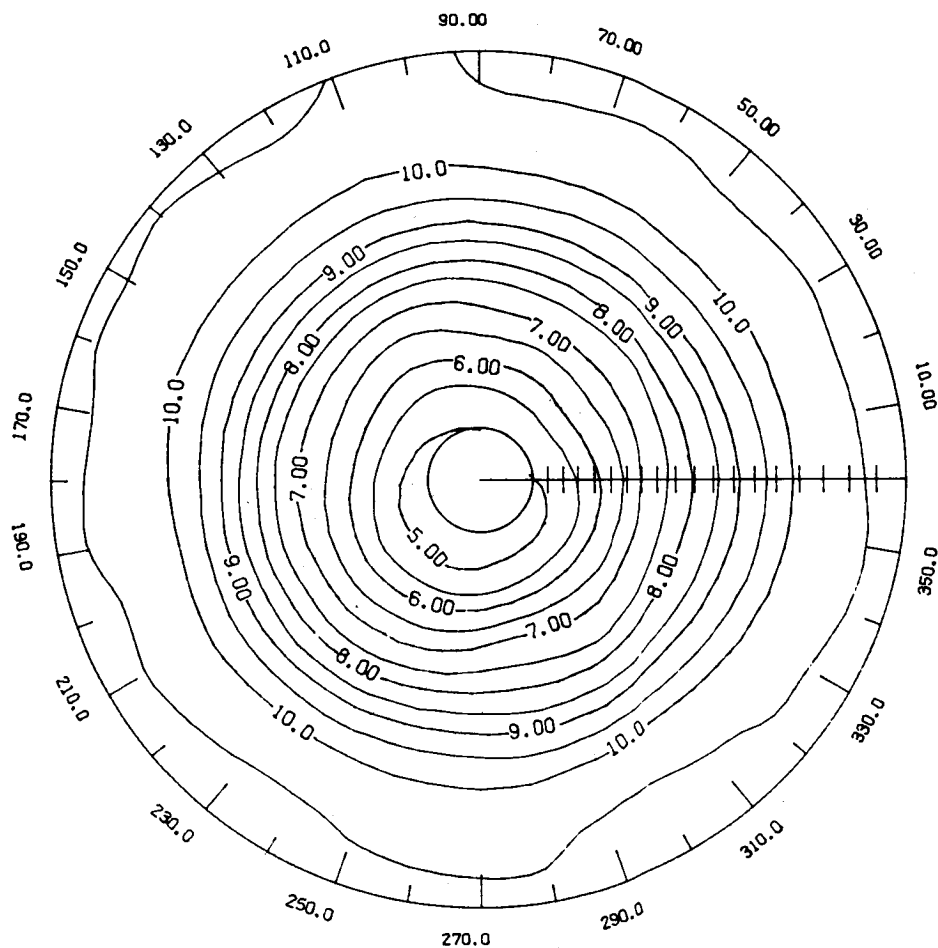
LATITUDE 0. TO 64.

Figure 03-61 - SBUV monthly mean ozone polar stereographic projection at 10 mb for January 1979 (contour interval is 0.5 ppmv).



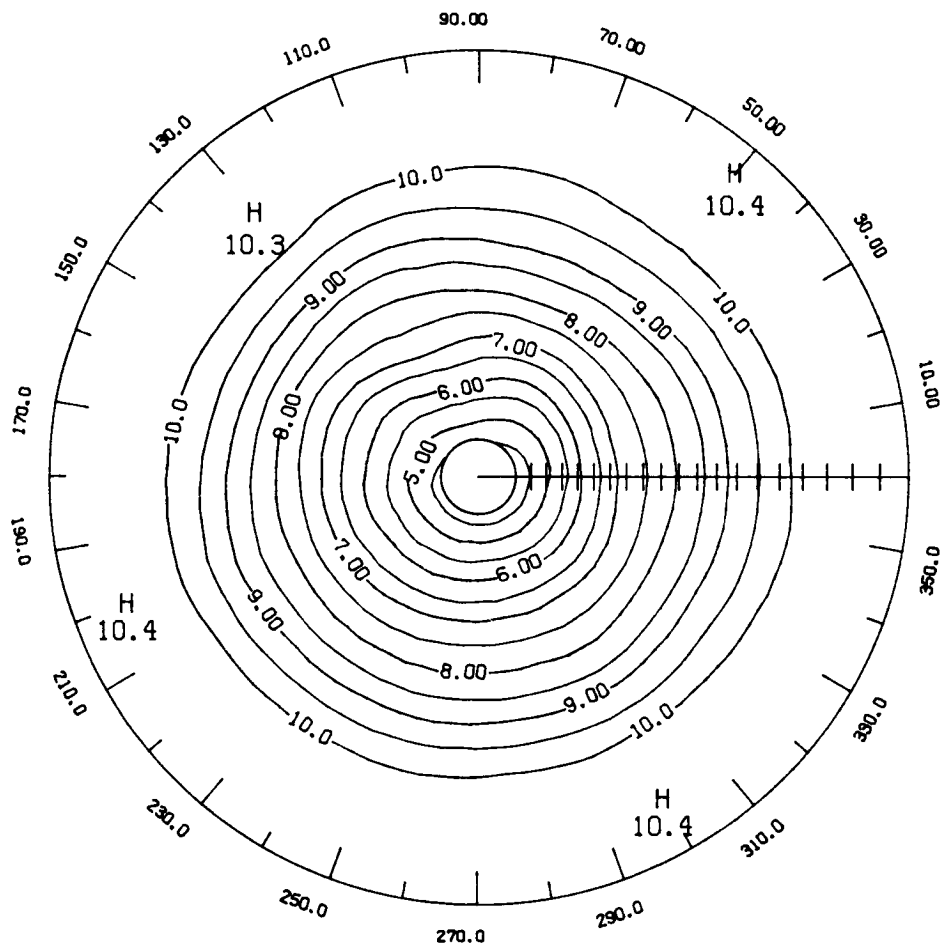
LATITUDE 0. TO 68.

Figure 03-62 - SBUV monthly mean ozone polar stereographic projection at 10 mb for February 1979 (contour interval is 0.5 ppmv).



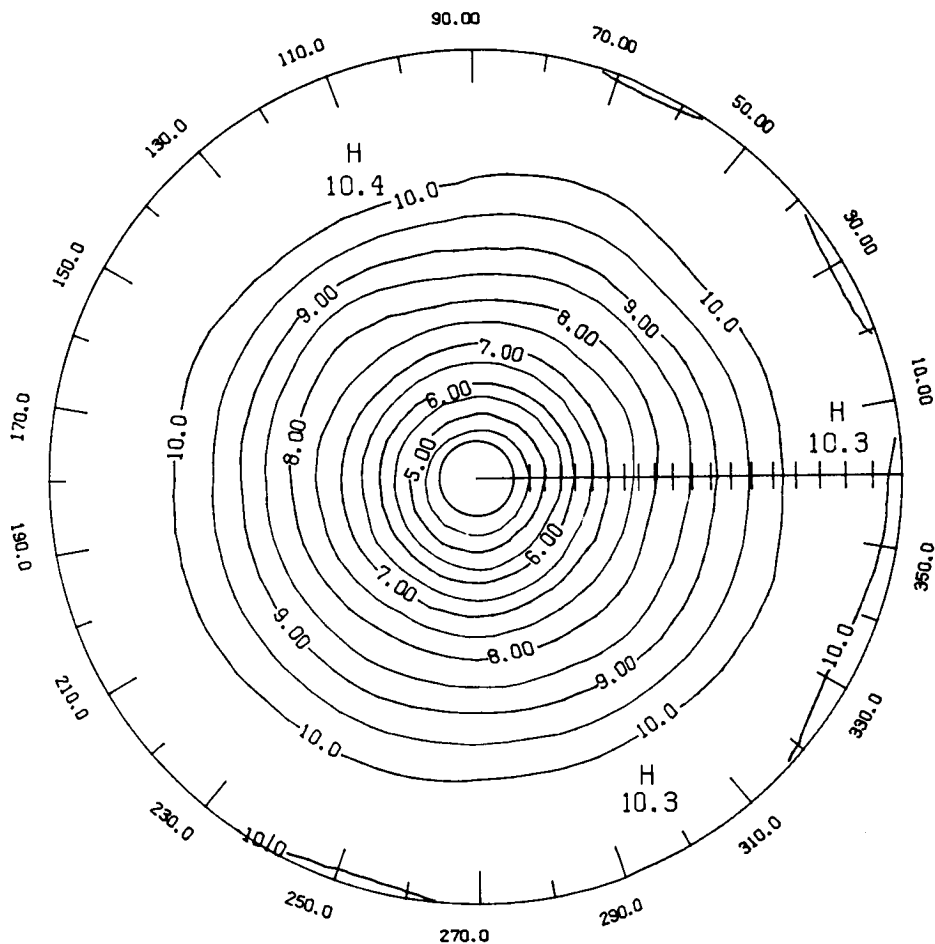
LATITUDE 0. TO 76.

Figure 03-63 - SBUV monthly mean ozone polar stereographic projection at 10 mb for March 1979 (contour interval is 0.5 ppmv).



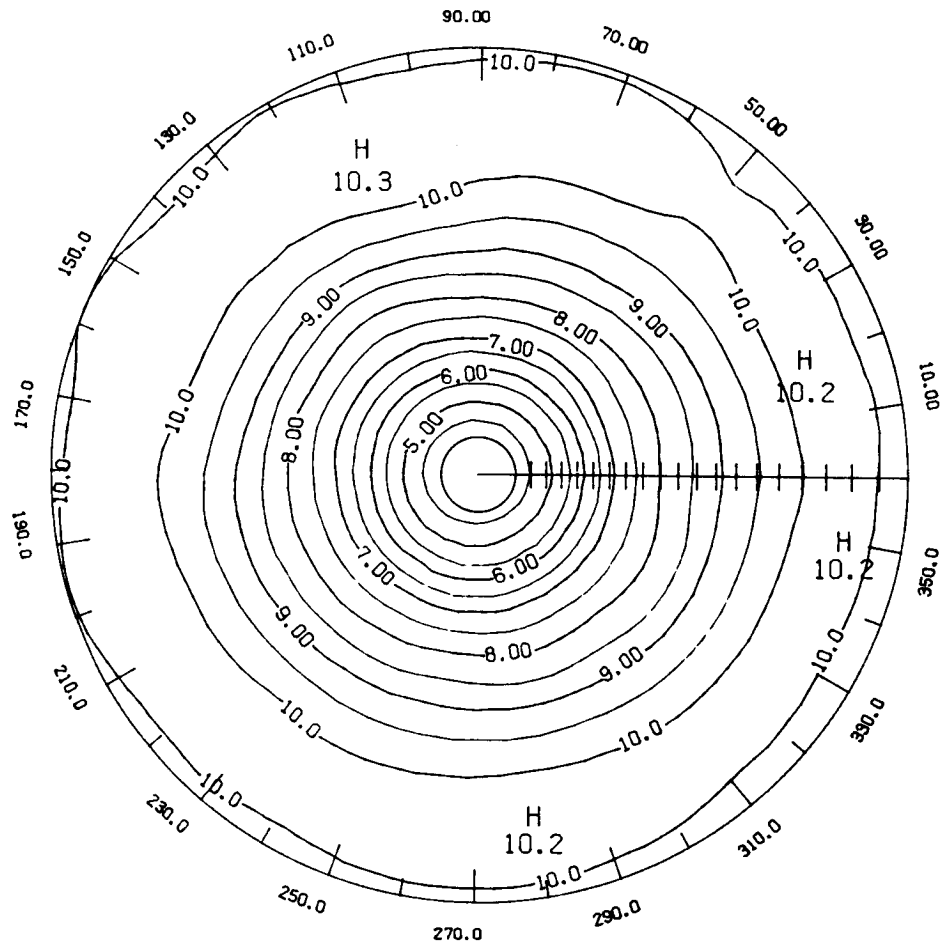
LATITUDE 0. TO 80.

Figure 03-64 - SBUV monthly mean ozone polar stereographic projection at 10 mb for April 1979 (contour interval is 0.5 ppmv).



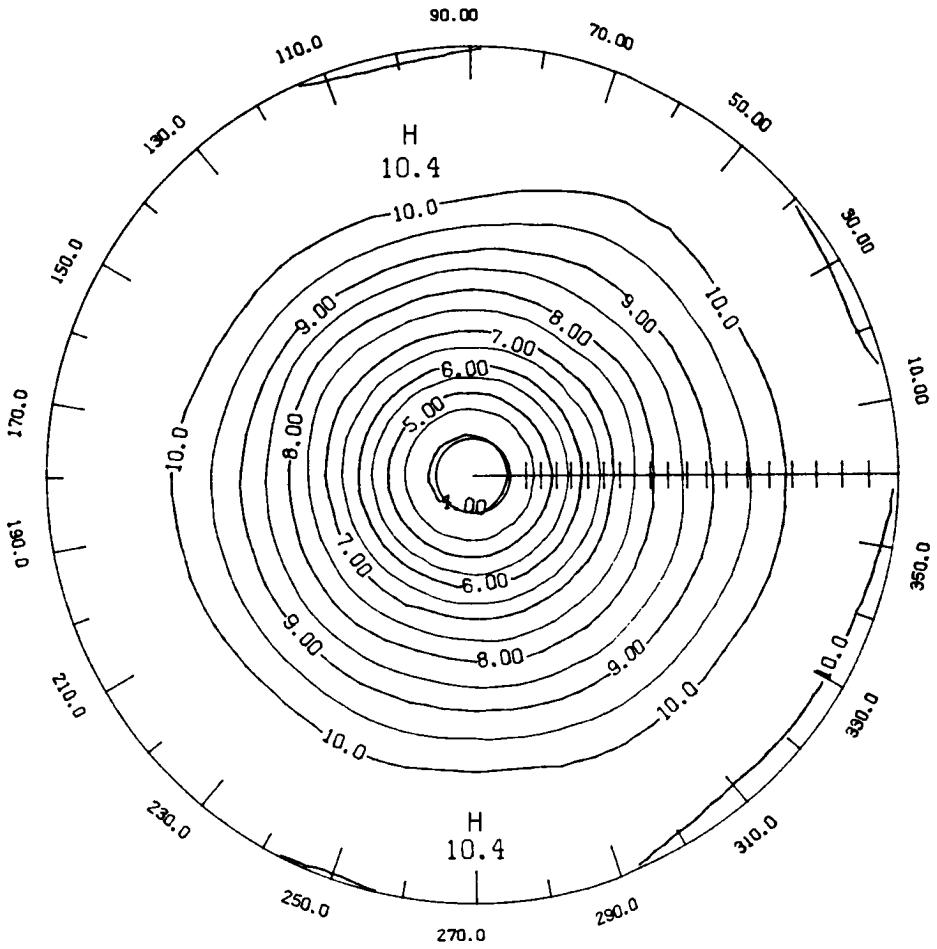
LATITUDE 0. TO 80.

Figure 03-65 - SBUV monthly mean ozone polar stereographic projection at 10 mb for May 1979 (contour interval is 0.5 ppmv).



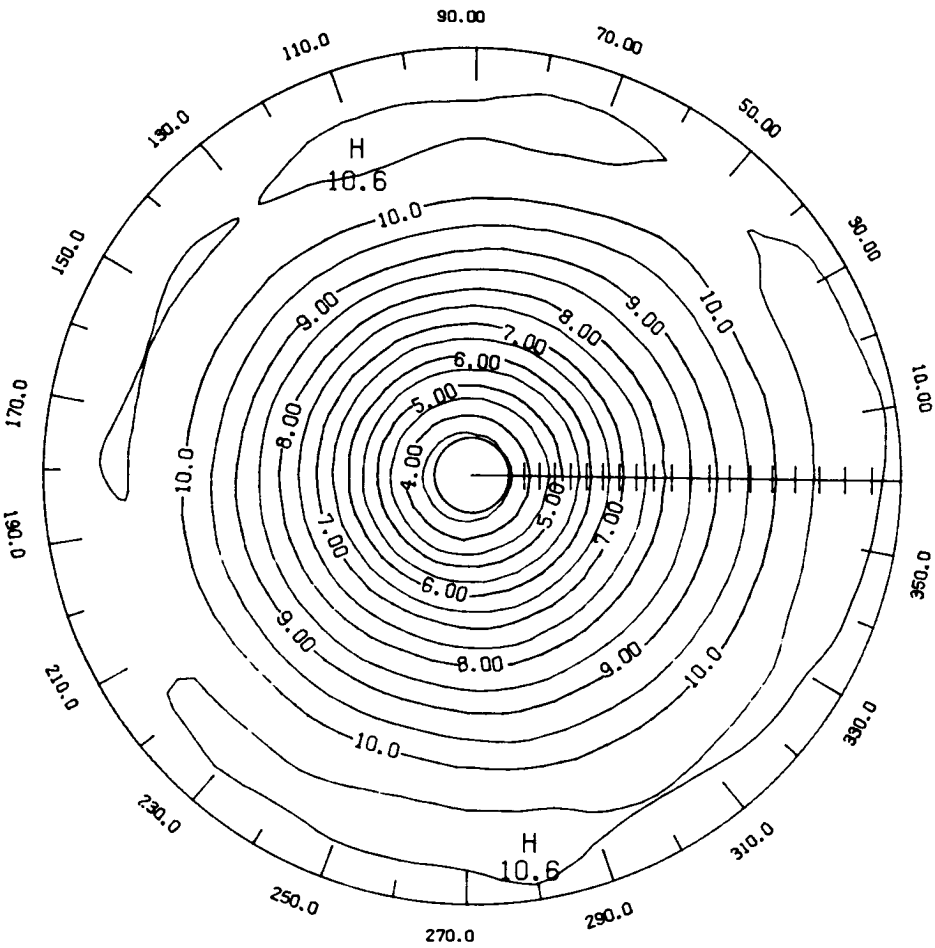
LATITUDE 0. TO 80.

Figure 03-66 - SBUV monthly mean ozone polar stereographic projection at 10 mb for June 1979 (contour interval is 0.5 ppmv).



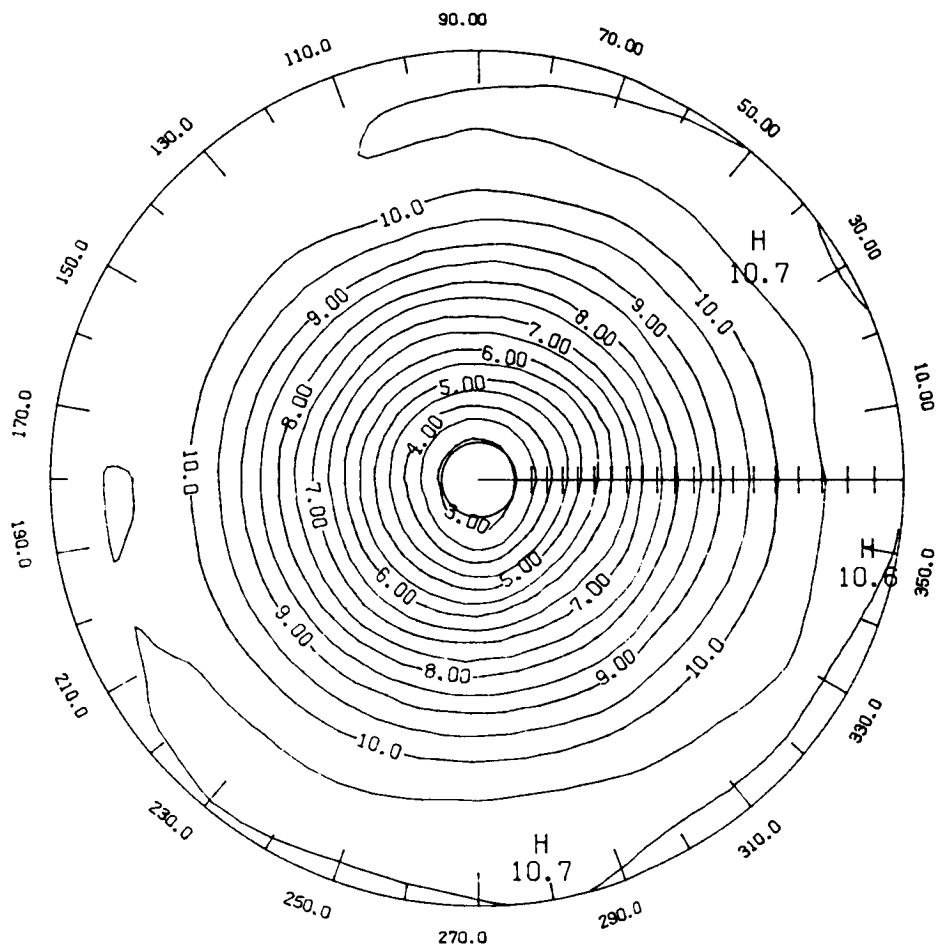
LATITUDE 0. TO 80.

Figure 03-67 - SBUV monthly mean ozone polar stereographic projection at 10 mb for July 1979 (contour interval is 0.5 ppmv).



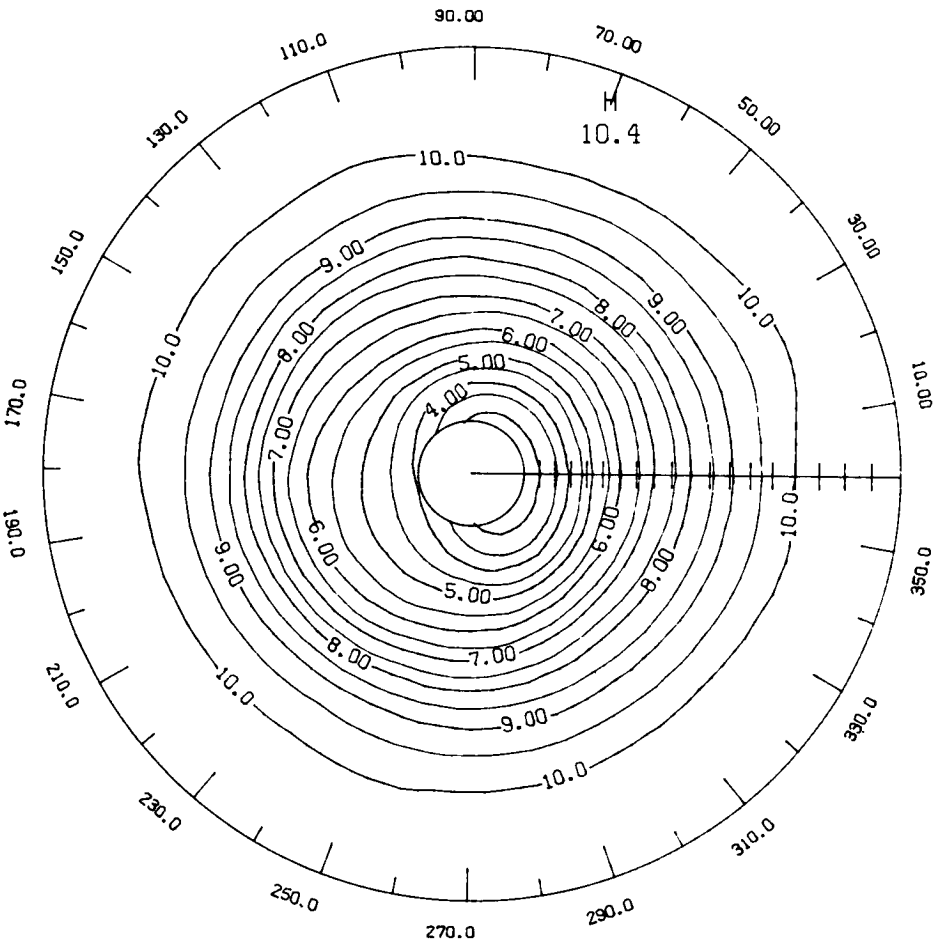
LATITUDE 0. TO 80.

Figure 03-68 - SBUV monthly mean ozone polar stereographic projection at 10 mb for August 1979 (contour interval is 0.5 ppmv).



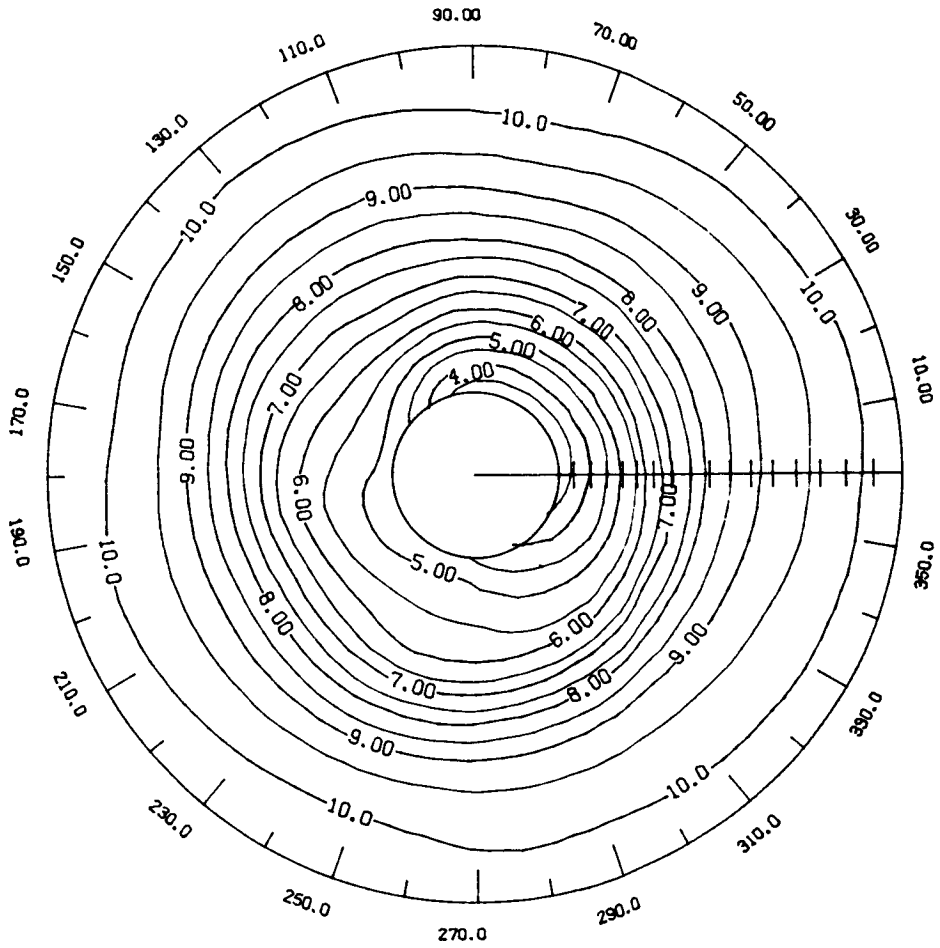
LATITUDE 0. TO 80.

Figure 03-69 - SBUV monthly mean ozone polar stereographic projection at 10 mb for September 1979 (contour interval is 0.5 ppmv).



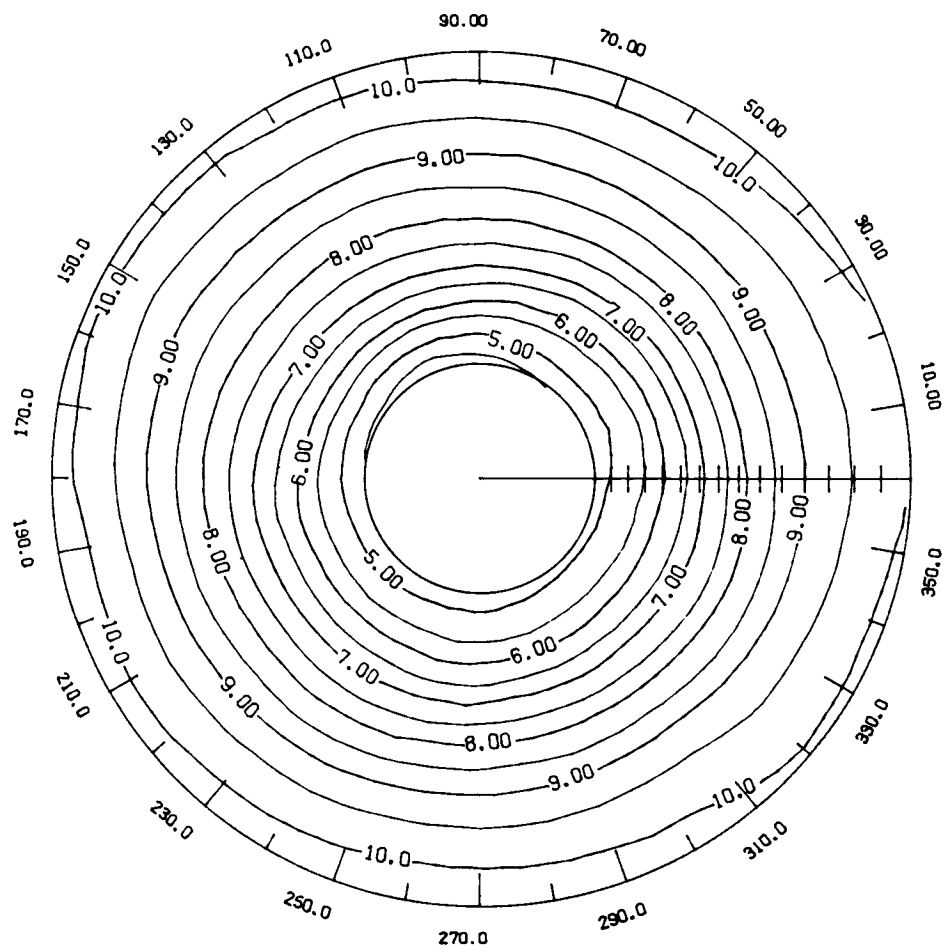
LATITUDE 0. TO 76.

Figure 03-70 - SBUV monthly mean ozone polar stereographic projection at 10 mb for October 1979 (contour interval is 0.5 ppmv).



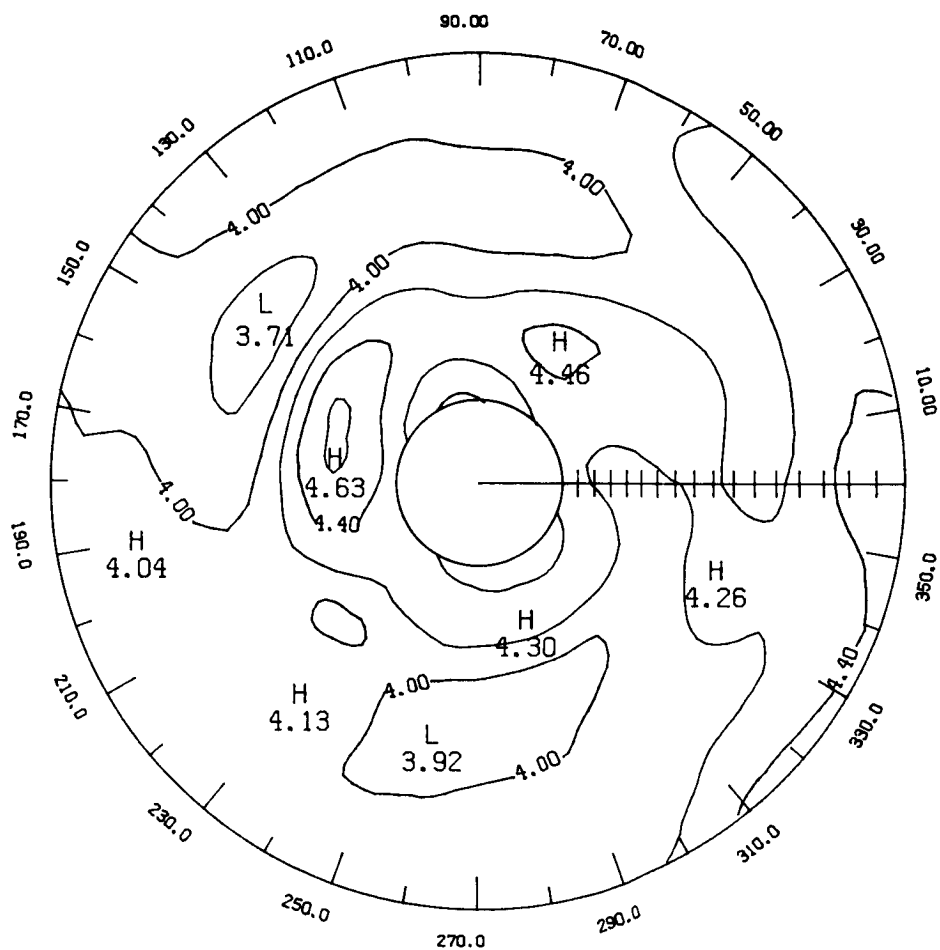
LATITUDE 0. TO 68.

Figure 03-71 - SBUV monthly mean ozone polar stereographic projection at 10 mb for November 1979 (contour interval is 0.5 ppmv).



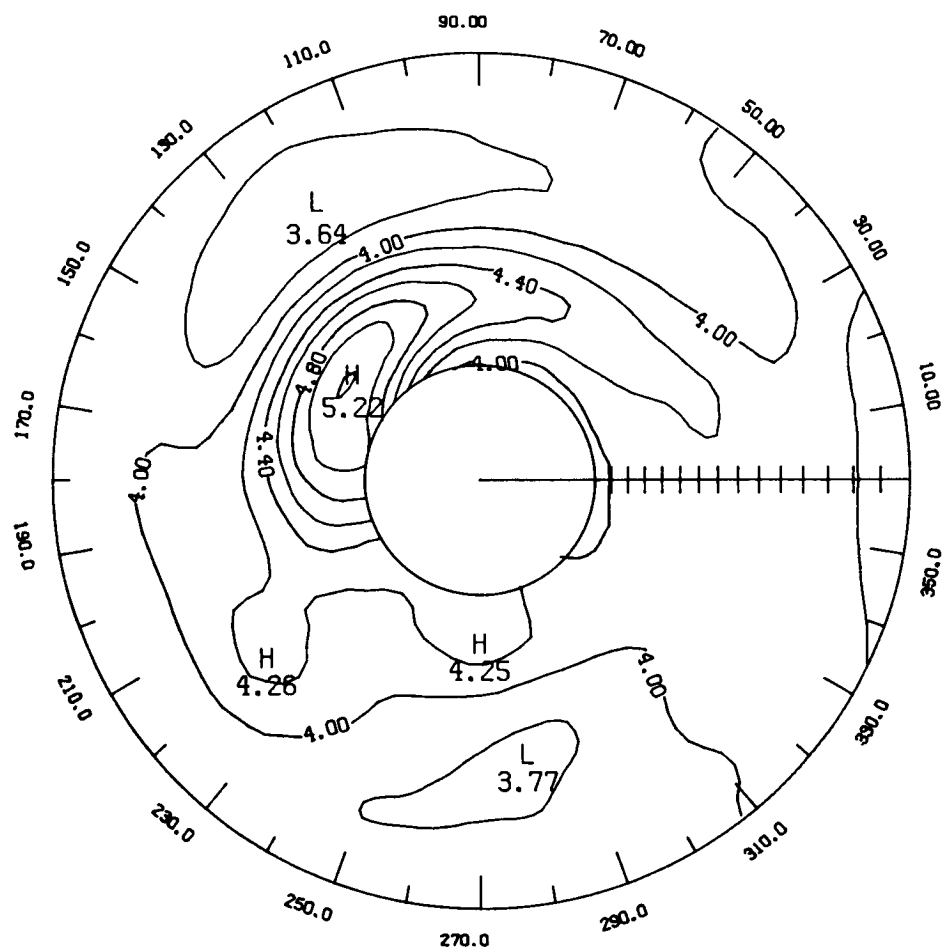
LATITUDE 0. TO 60.

Figure 03-72 - SBUV monthly mean ozone polar stereographic projection at 10 mb for December 1979 (contour interval is 0.5 ppmv).



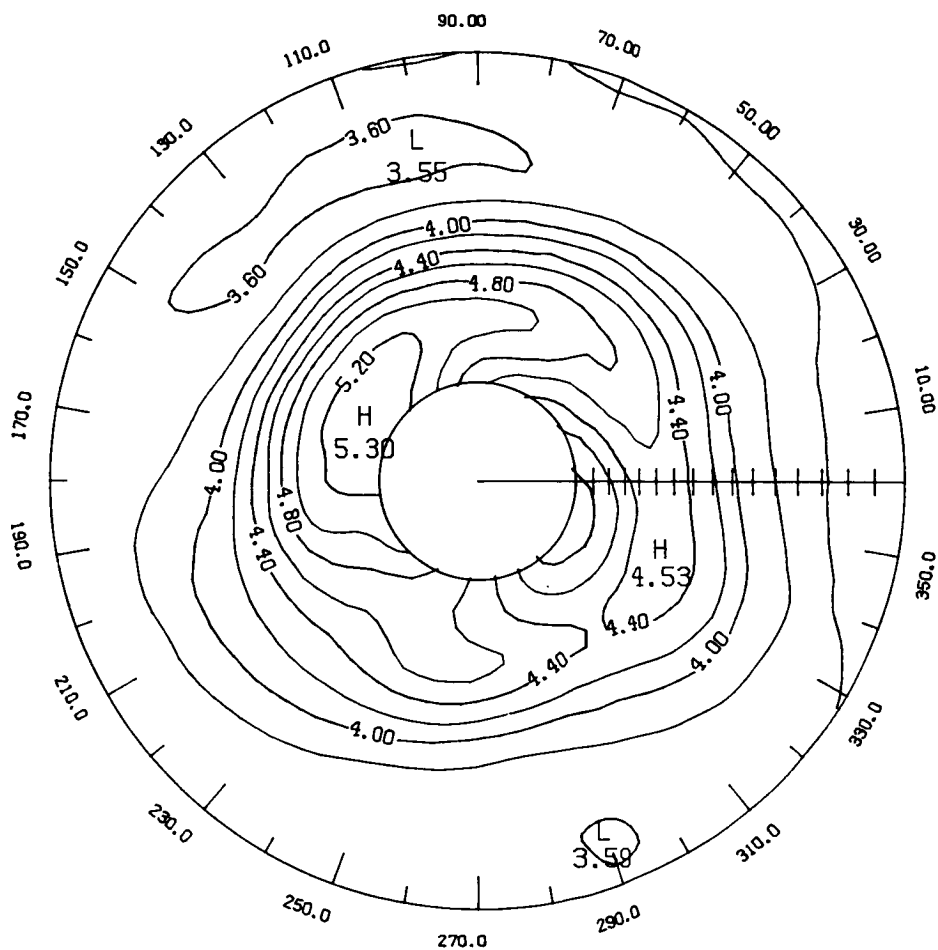
LATITUDE 0. TO 68.

Figure 03-73 - SBUV monthly mean ozone polar stereographic projection at 30 mb for November 1978 (contour interval is 0.2 ppmv).



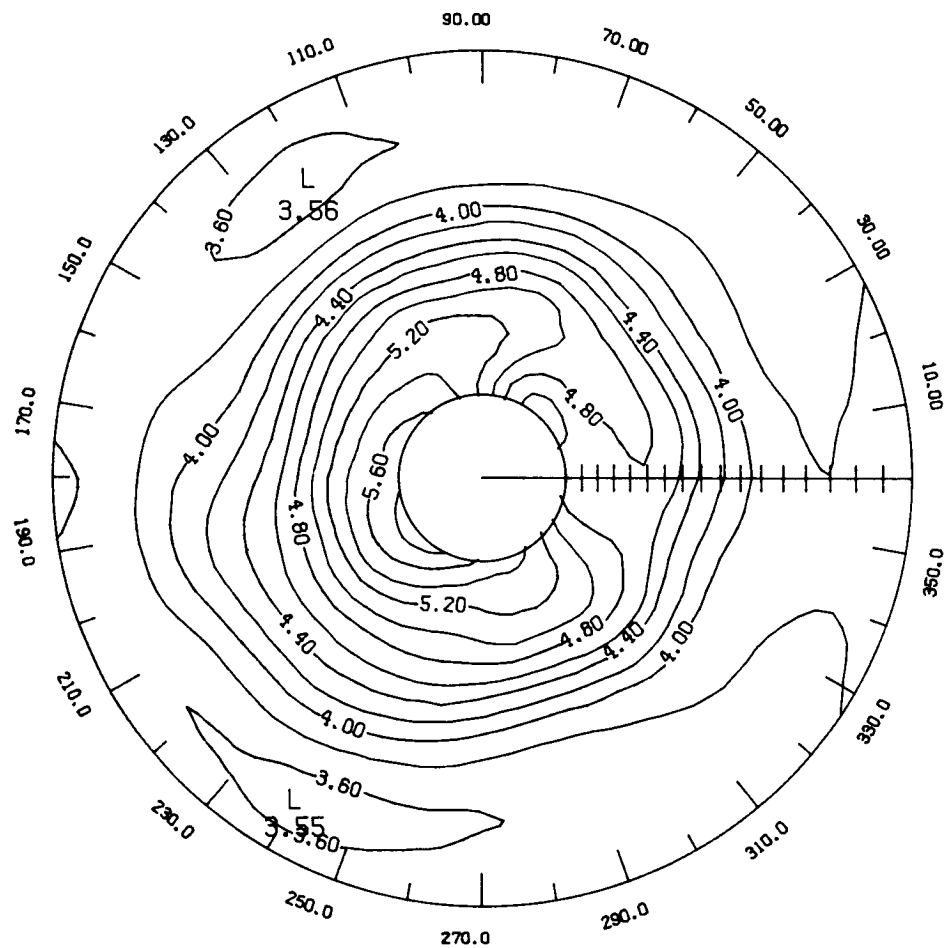
LATITUDE 0. TO 60.

Figure 03-74 - SBUV monthly mean ozone polar stereographic projection at 30 mb for December 1978 (contour interval is 0.2 ppbv).



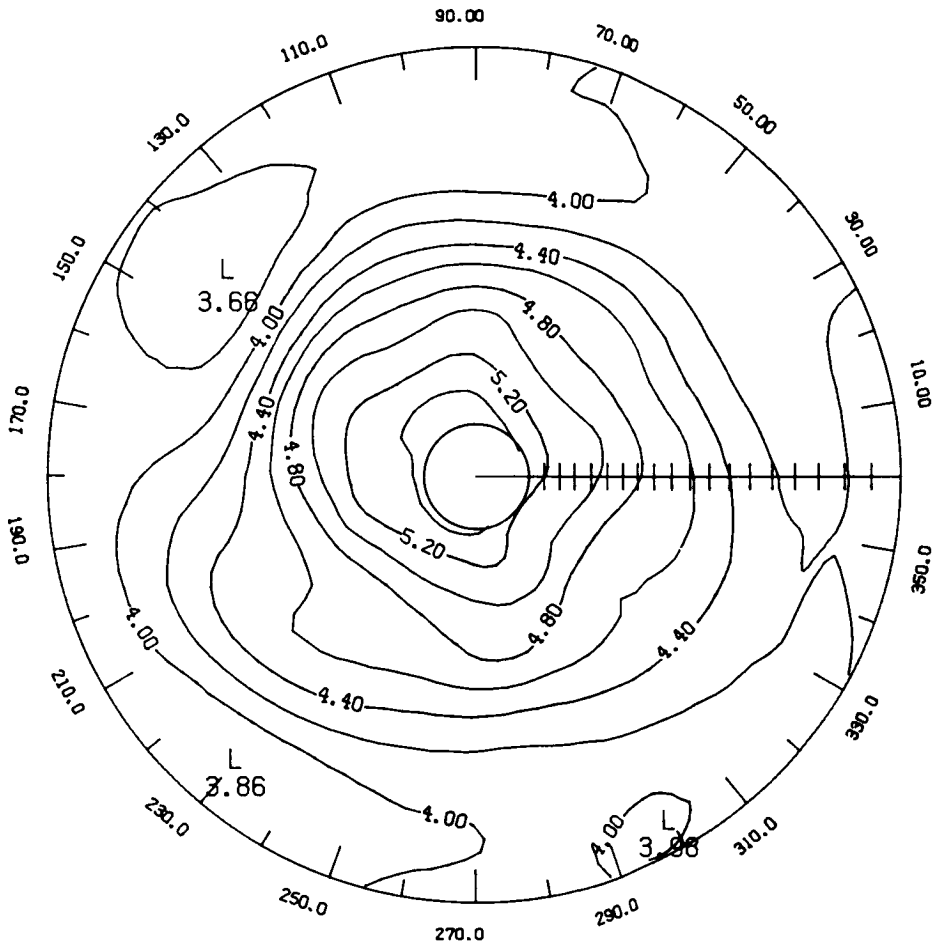
LATITUDE 0. TO 64.

Figure 03-75 - SBUV monthly mean ozone polar stereographic projection at 30 mb for January 1979 (contour interval is 0.2 ppmv).



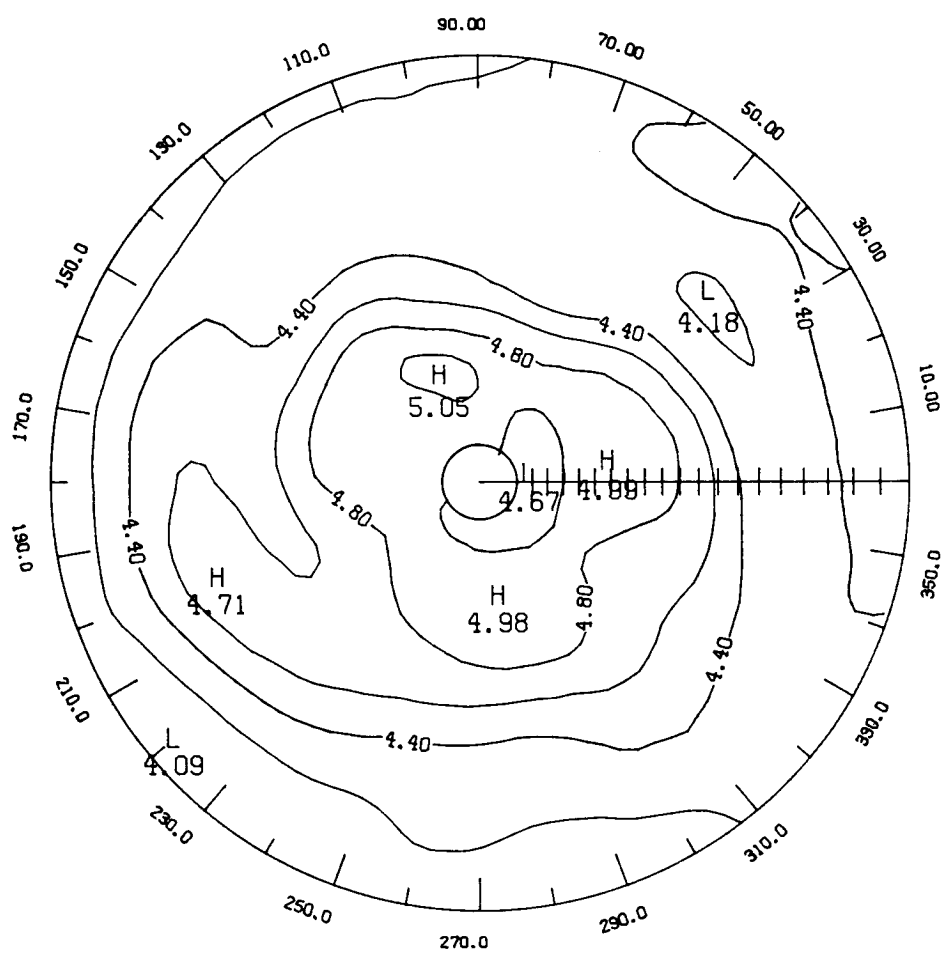
LATITUDE 0. TO 68.

Figure 03-76 - SBUV monthly mean ozone polar stereographic projection at 30 mb for February 1979 (contour interval is 0.2 ppmv).



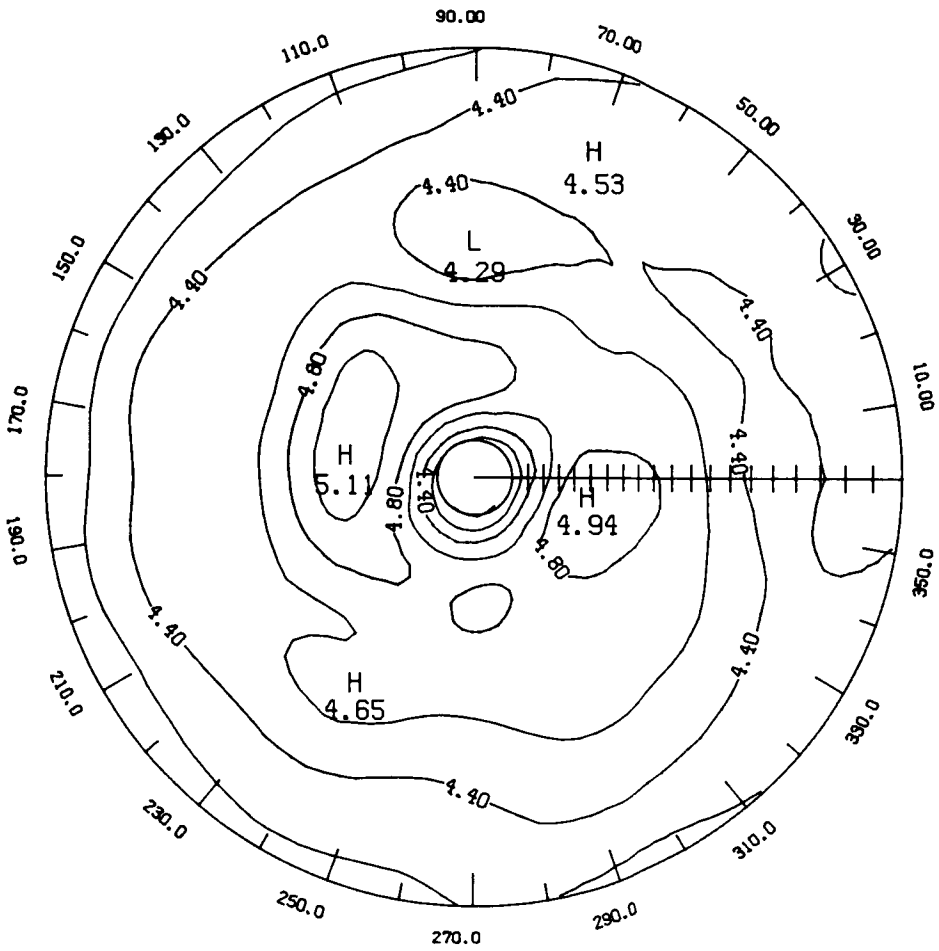
LATITUDE 0. TO 76.

Figure 03-77 - SBUV monthly mean ozone polar stereographic projection at 30 mb for March 1979 (contour interval is 0.2 ppmv).



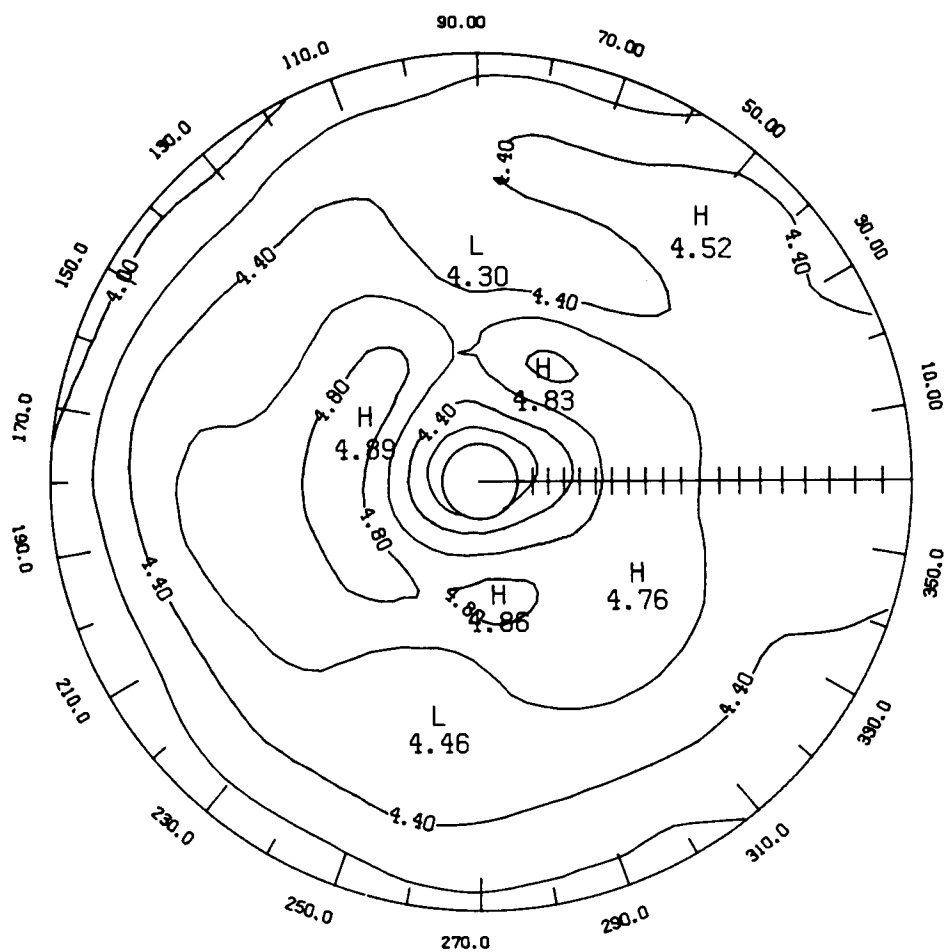
LATITUDE 0. TO 80.

Figure 03-78 - SBUV monthly mean ozone polar stereographic projection at 30 mb for April 1979 (contour interval is 0.2 ppmv).



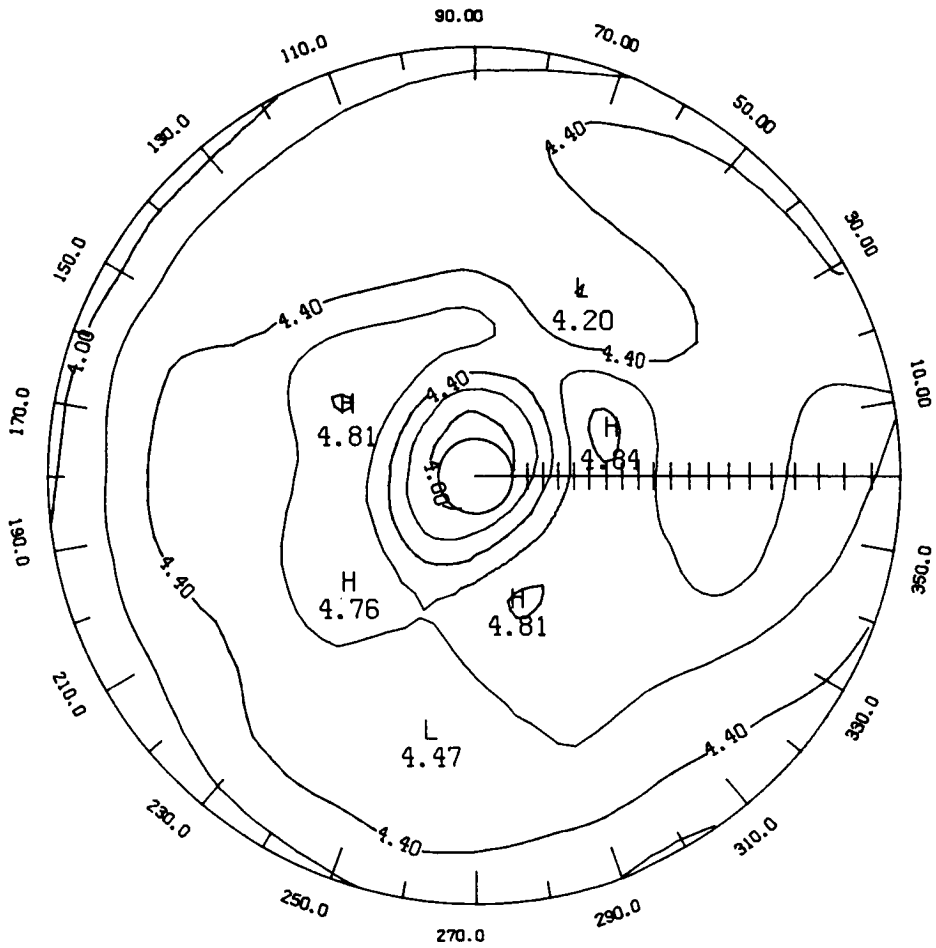
LATITUDE 0. TO 80.

Figure 03-79 - SBUV monthly mean ozone polar stereographic projection at 30 mb for May 1979 (contour interval is 0.2 ppmv).



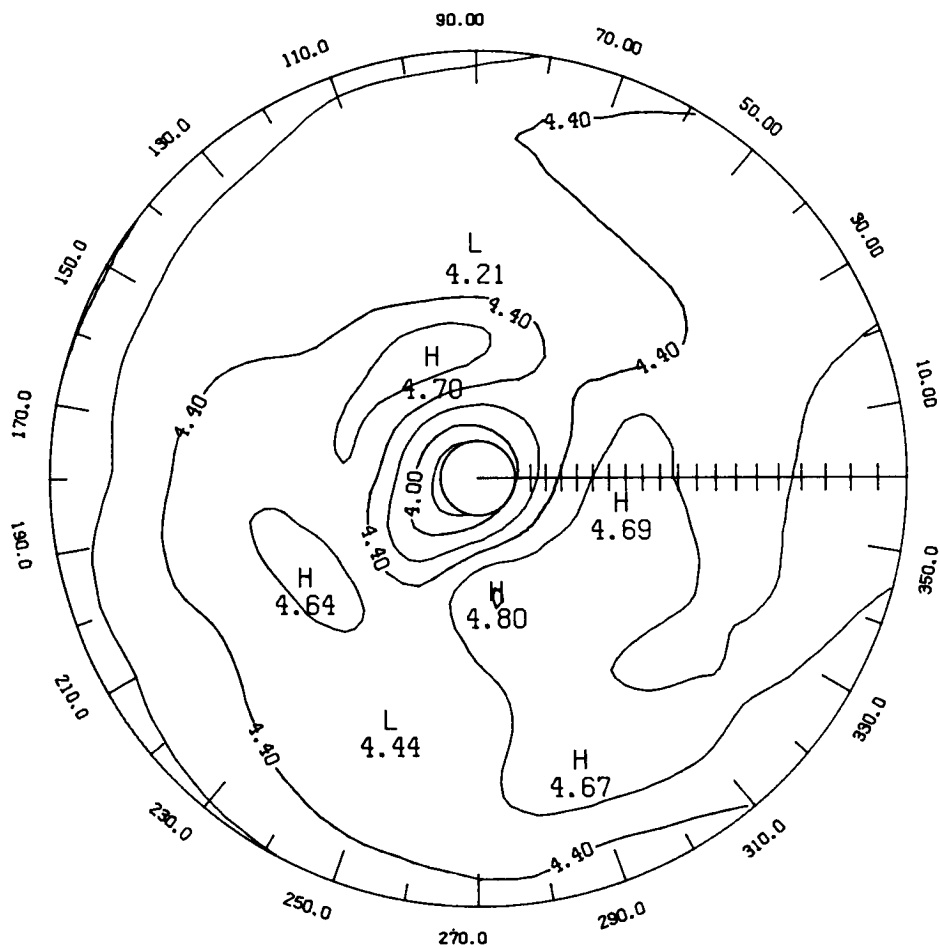
LATITUDE 0. TO 80.

Figure 03-80 - SBUV monthly mean ozone polar stereographic projection at 30 mb for June 1979 (contour interval is 0.2 ppmv).



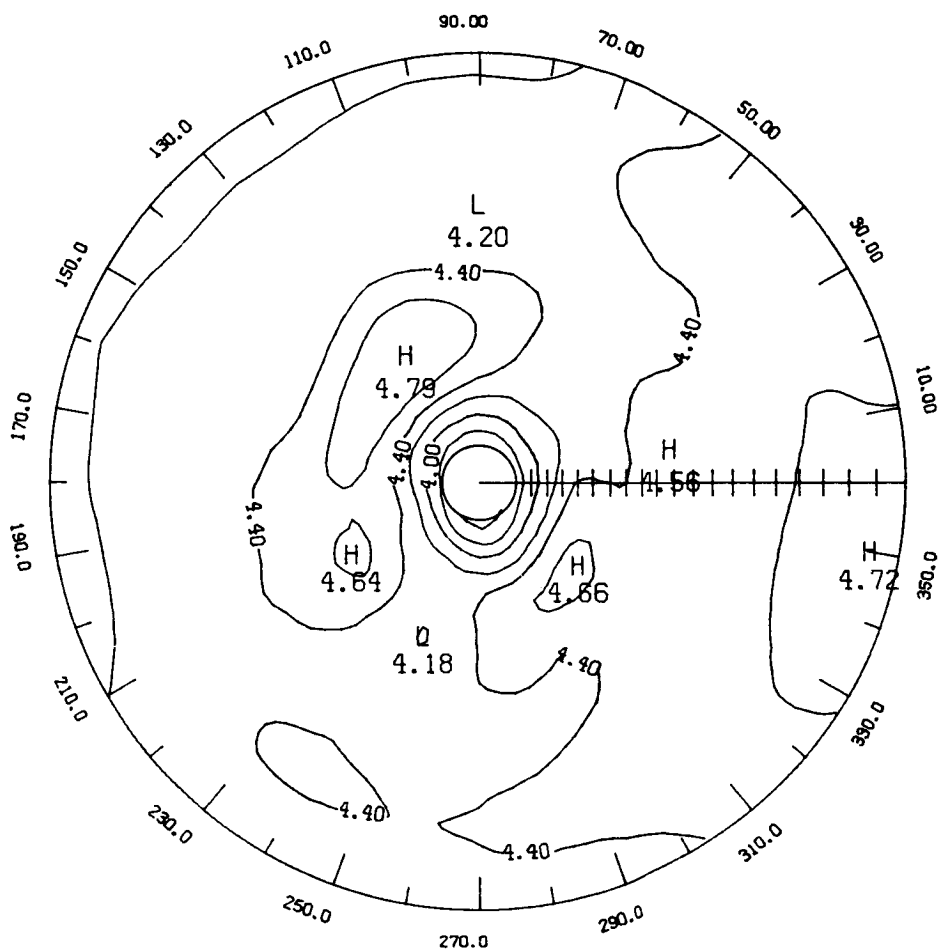
LATITUDE 0. TO 80.

Figure 03-81 - SBUV monthly mean ozone polar stereographic projection at 30 mb for July 1979 (contour interval is 0.2 ppmv).



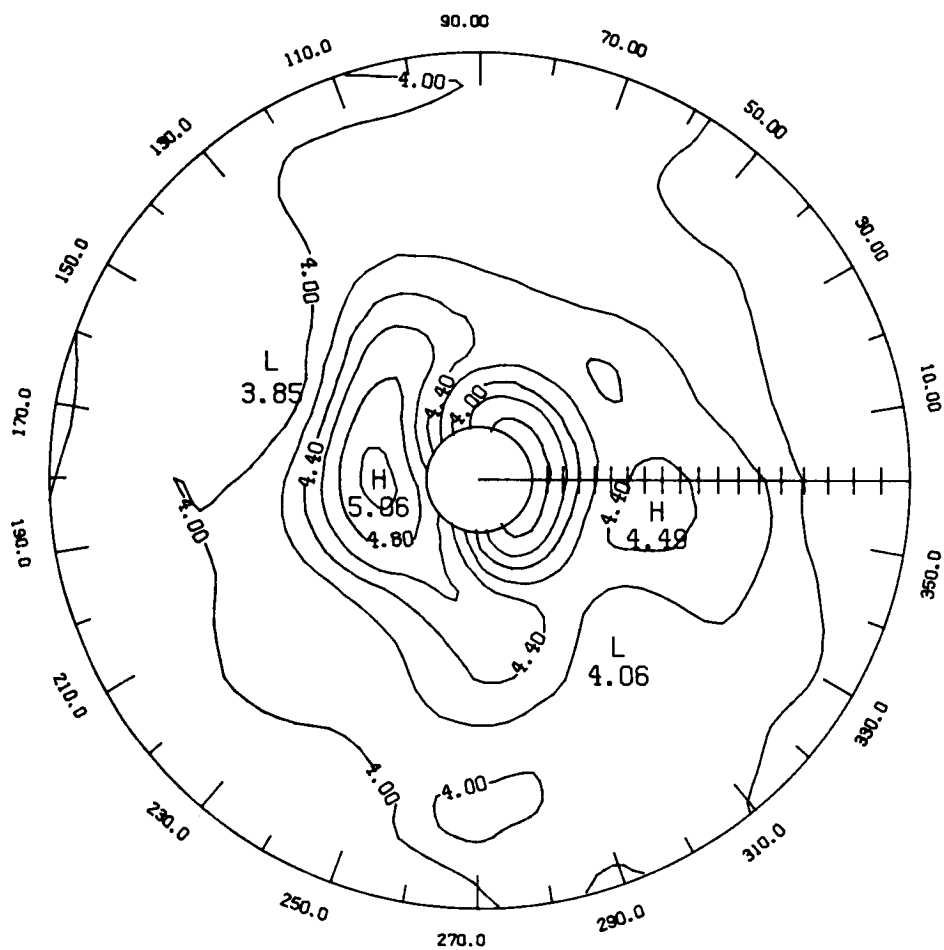
LATITUDE 0. TO 80.

Figure O₃-82 - SBUV monthly mean ozone polar stereographic projection at 30 mb for August 1979 (contour interval is 0.2 ppmv).



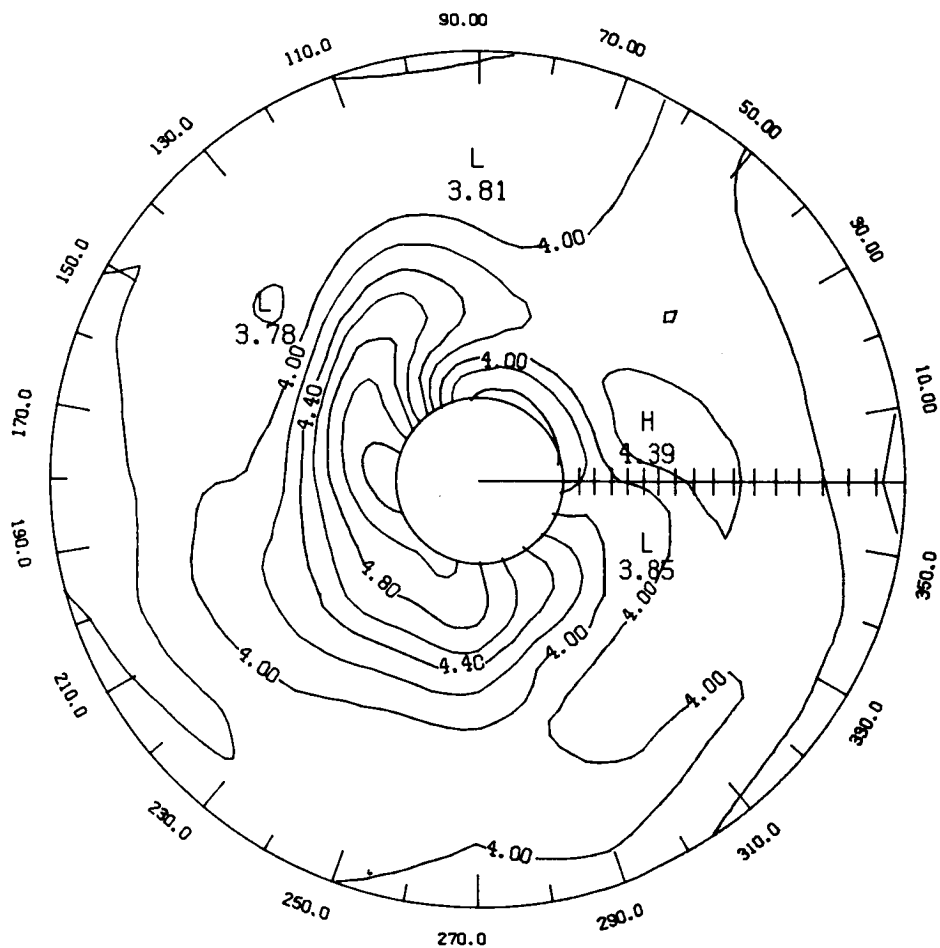
LATITUDE 0. TO 80.

Figure 03-83 - SBUV monthly mean ozone polar stereographic projection at 30 mb for September 1979 (contour interval is 0.2 ppmv).



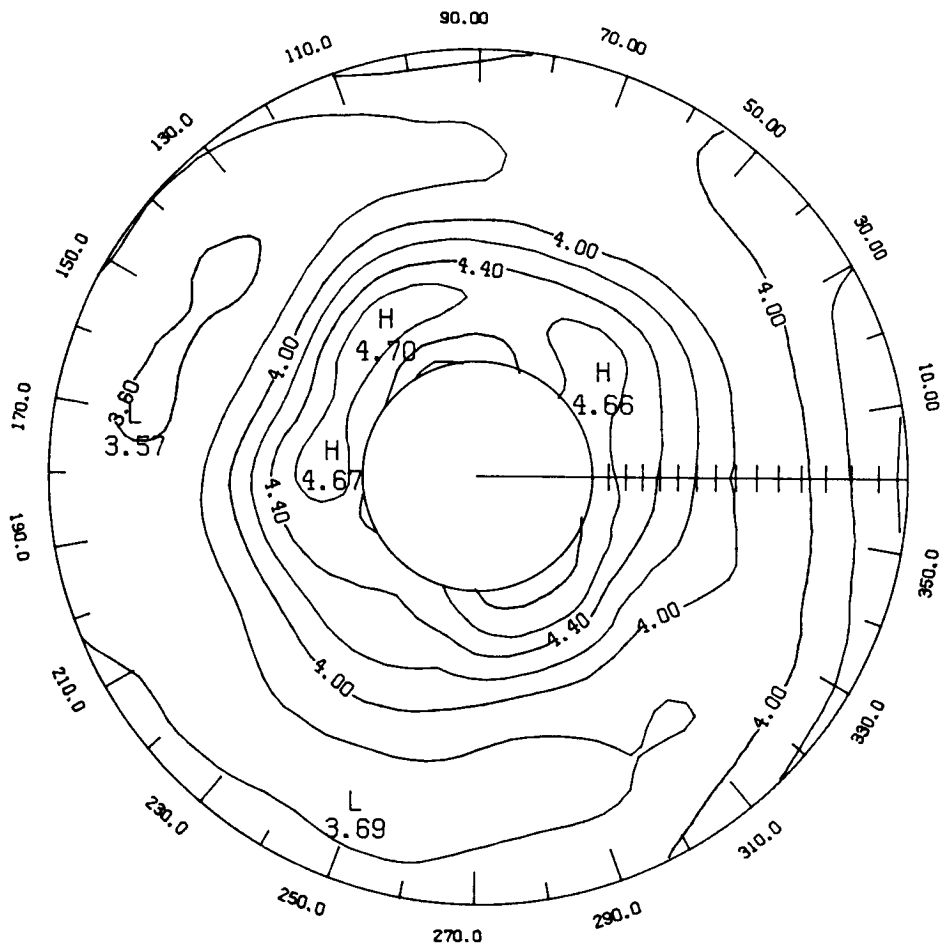
LATITUDE 0. TO 76.

Figure 03-84 - SBUV monthly mean ozone polar stereographic projection at 30 mb for October 1979 (contour interval is 0.2 ppmv).



LATITUDE 0. TO 68.

Figure 03-85 - SBUV monthly mean ozone polar stereographic projection at 30 mb for November 1979 (contour interval is 0.2 ppmv).



LATITUDE 0. TO 60.

Figure 03-86 - SBUV monthly mean ozone polar stereographic projection at 30 mb for December 1979 (contour interval is 0.2 ppmv).

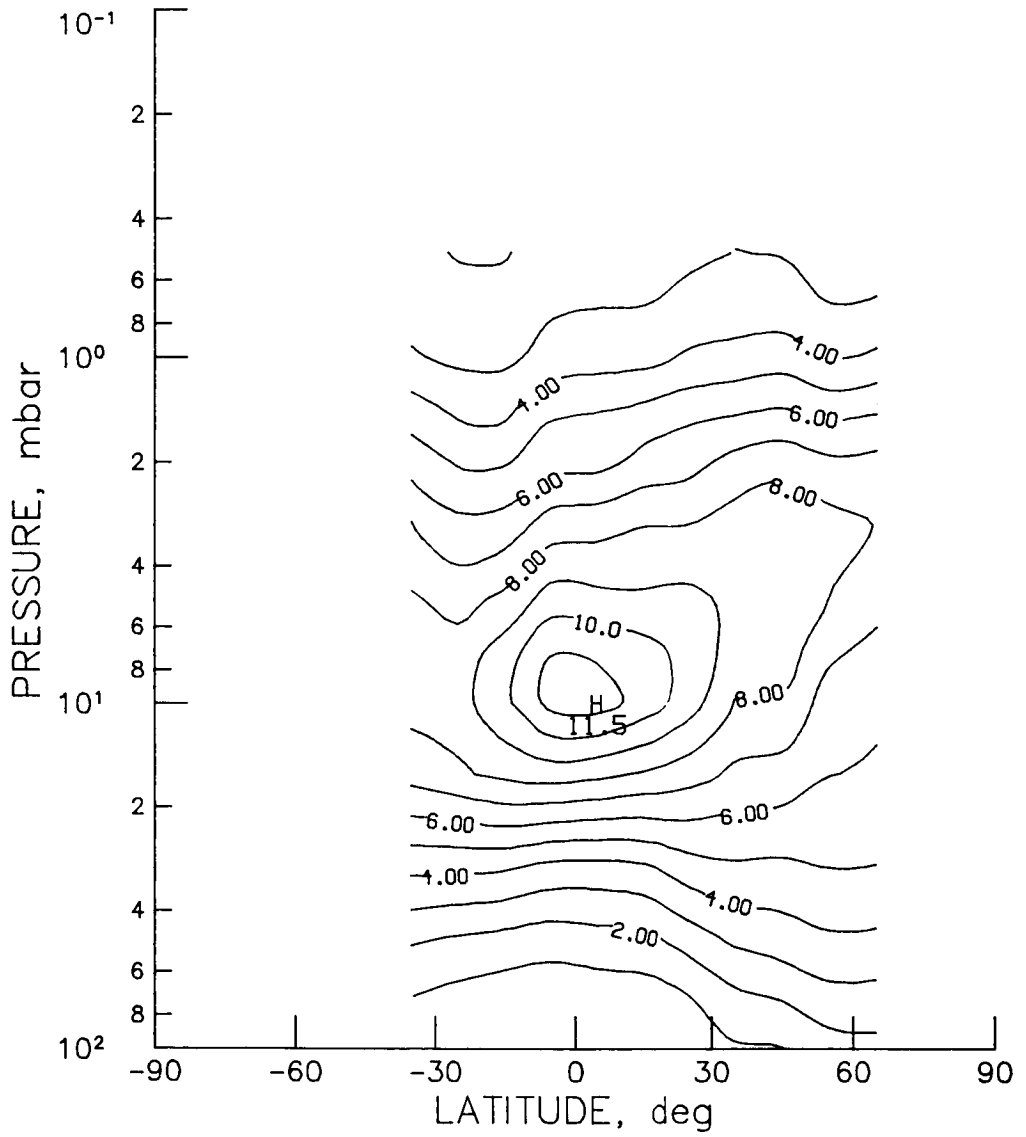


Figure O₃-87 - SAGE sunset monthly zonal mean ozone cross section for March 1979 (contour interval is 1.0 ppmv).

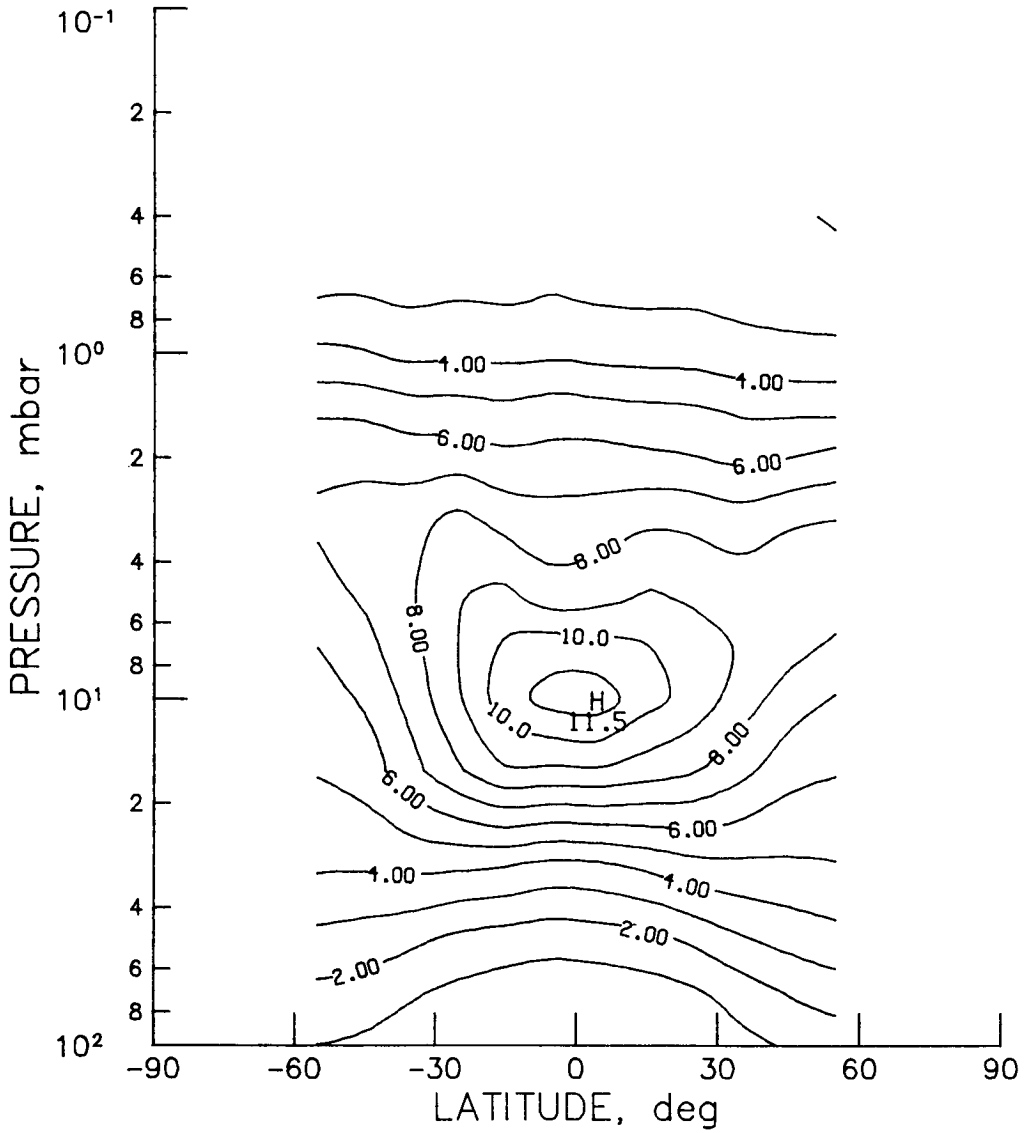


Figure O₃-88 - SAGE sunset monthly zonal mean ozone cross section for April 1979 (contour interval is 1.0 ppmv).

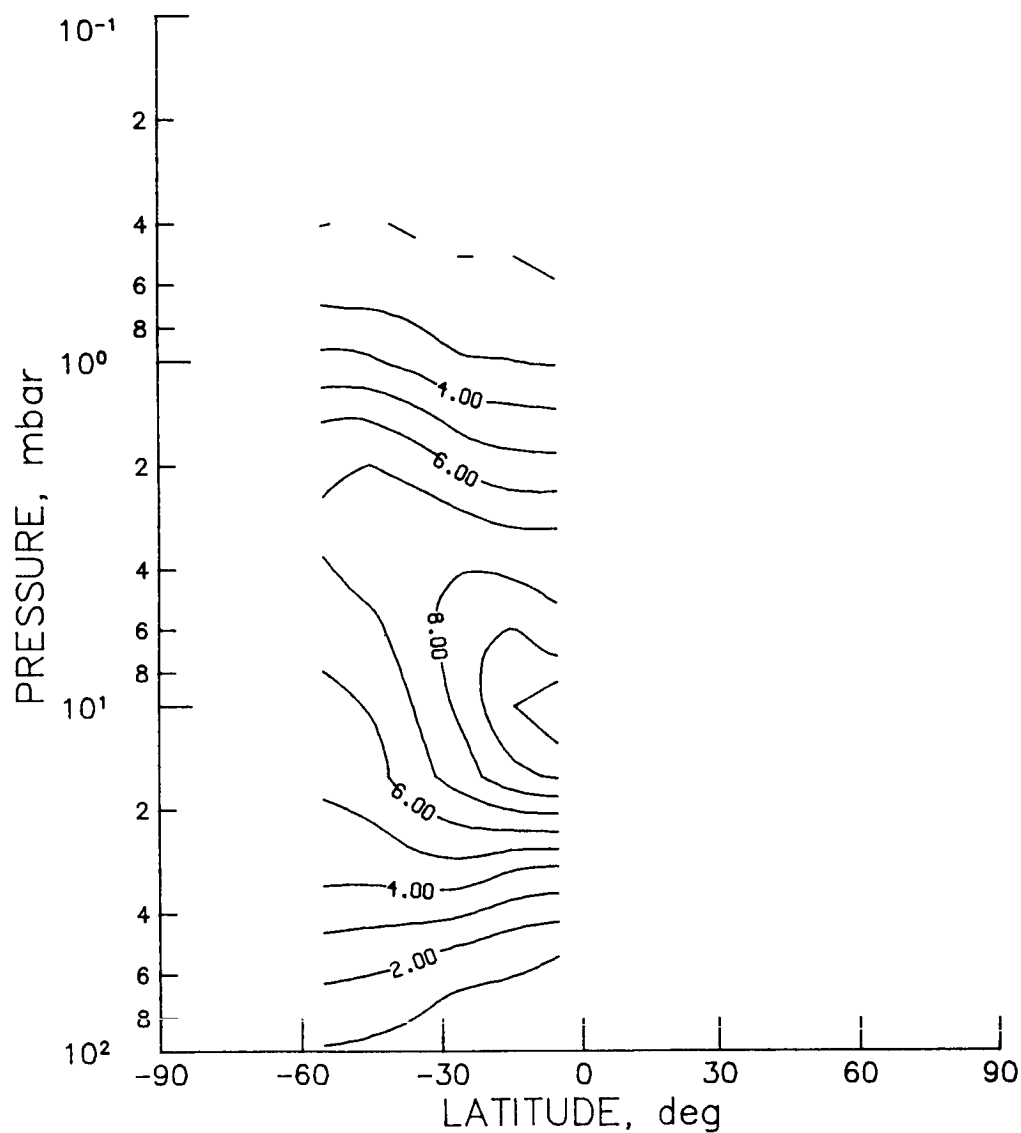
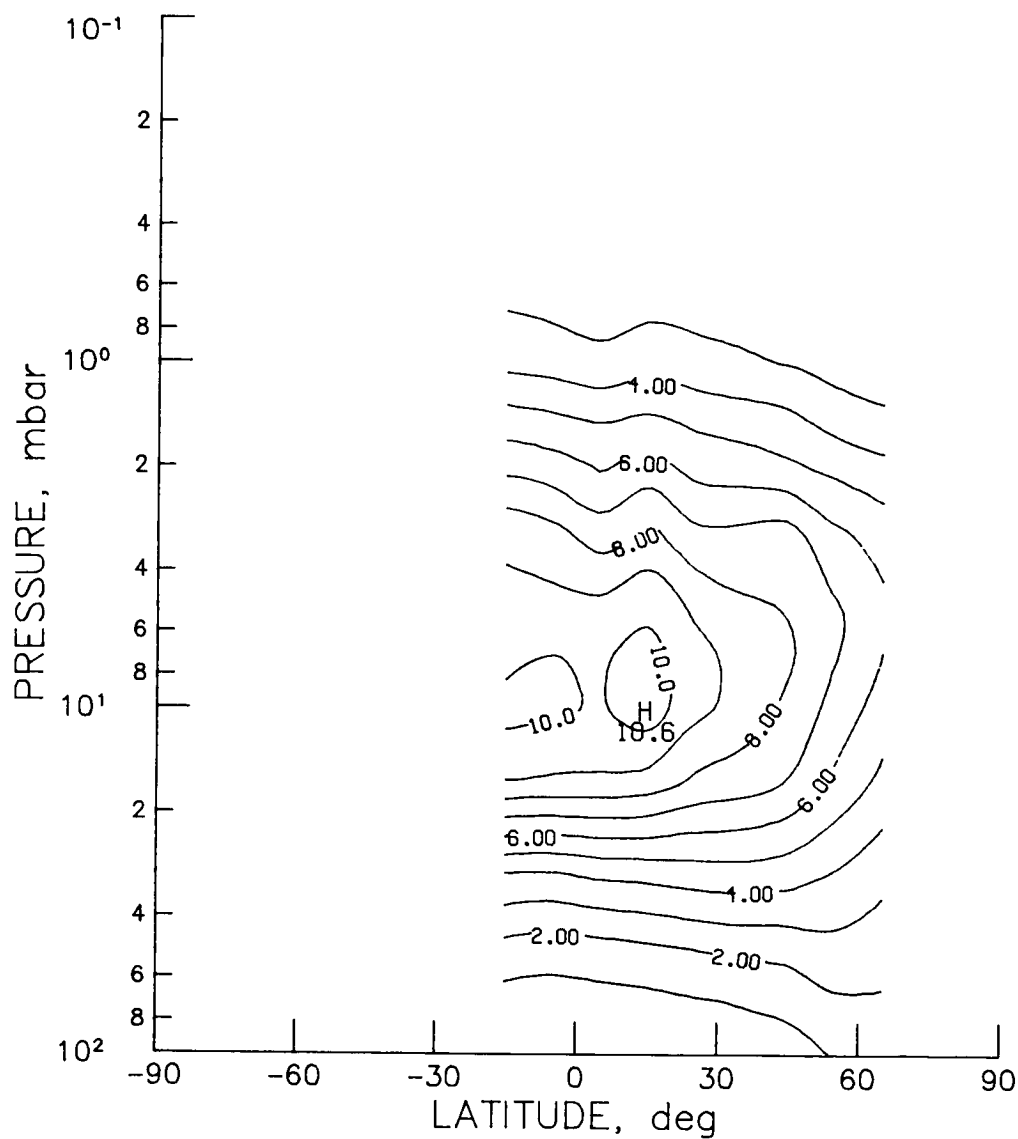


Figure 0₃-89 - SAGE sunset monthly zonal mean ozone cross section for May 1979
(contour interval is 1.0 ppmv).



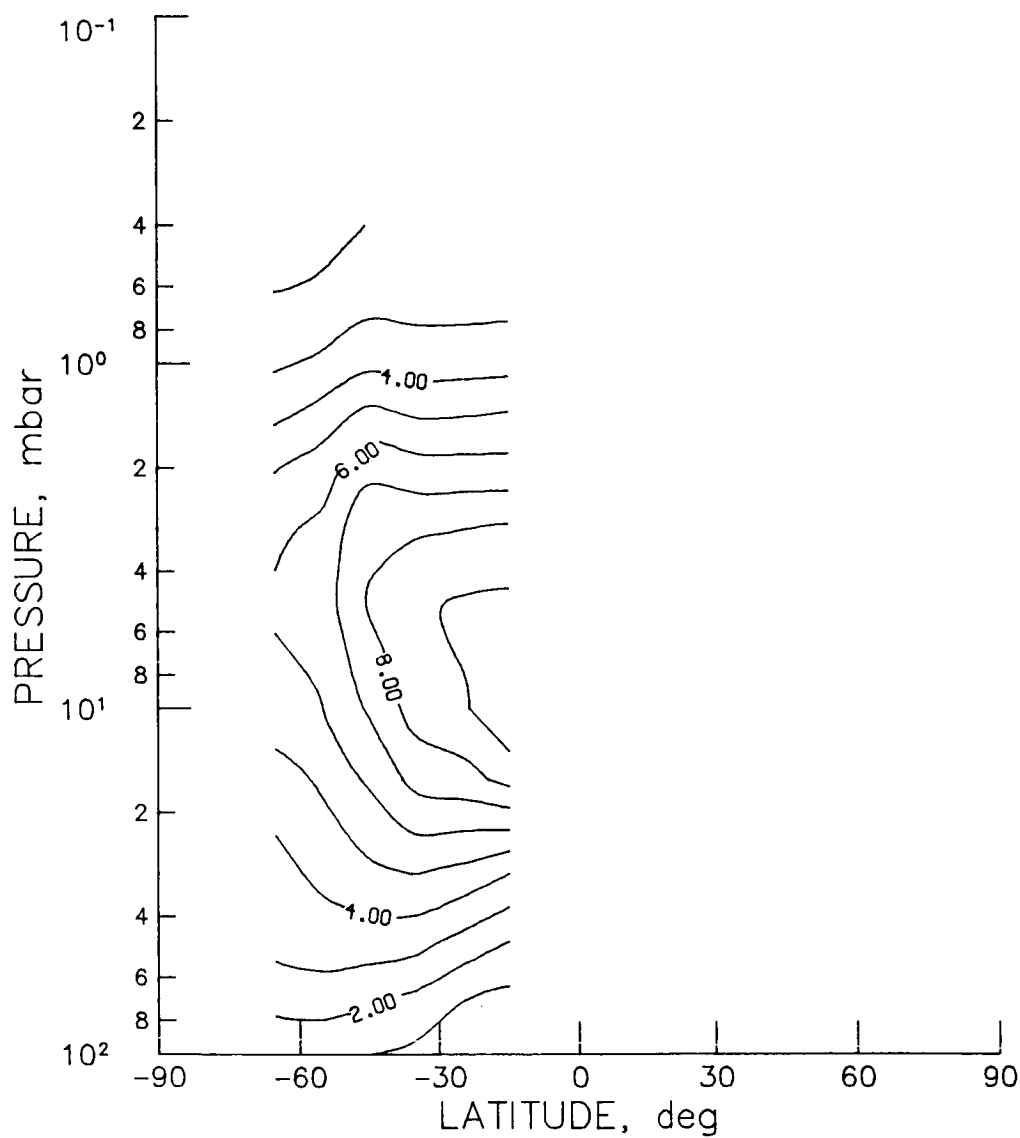


Figure O₃-91 - SAGE sunset monthly zonal mean ozone cross section for September 1979 (contour interval is 1.0 ppmv).

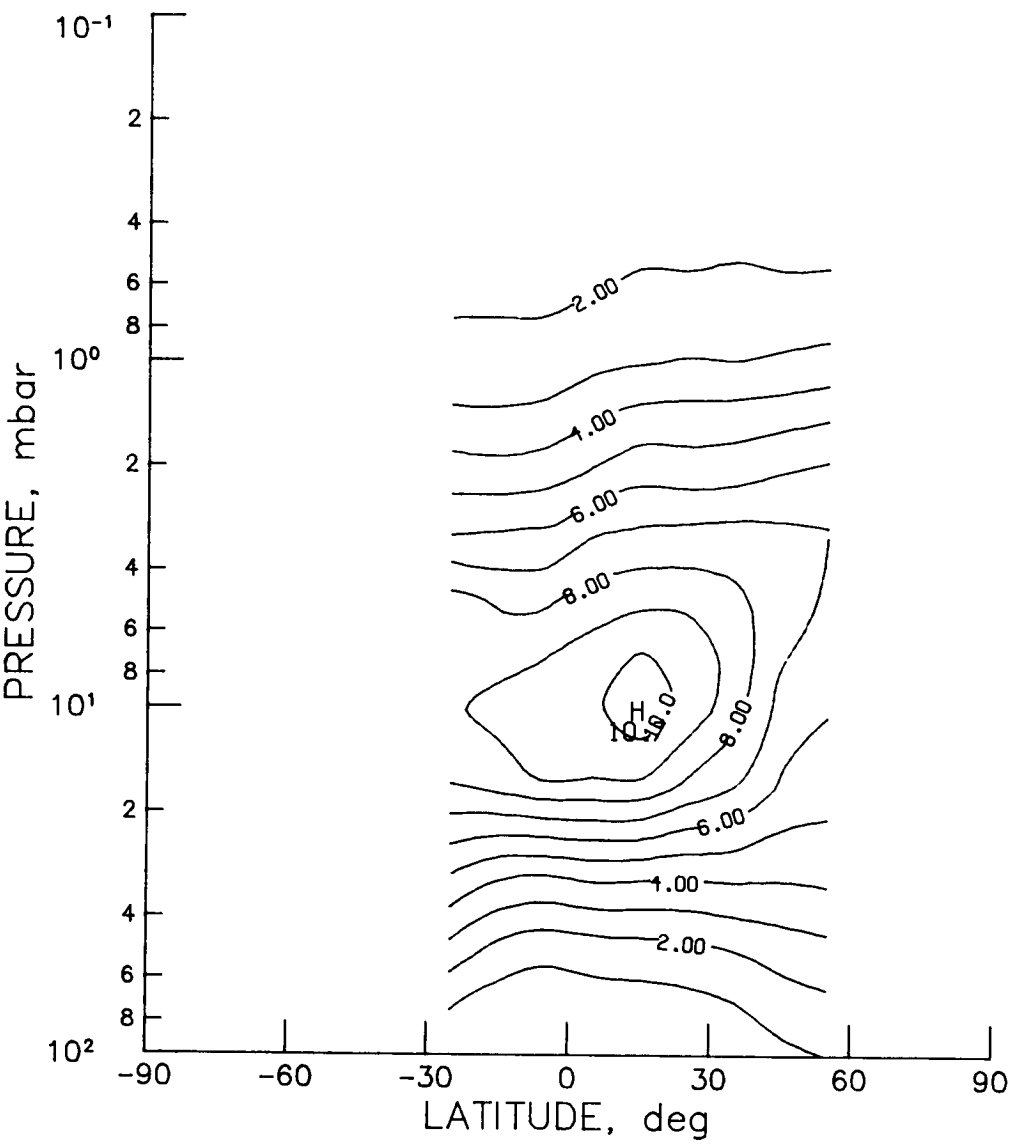


Figure 03-92 - SAGE sunset monthly zonal mean ozone cross section for October 1979 (contour interval is 1.0 ppmv).

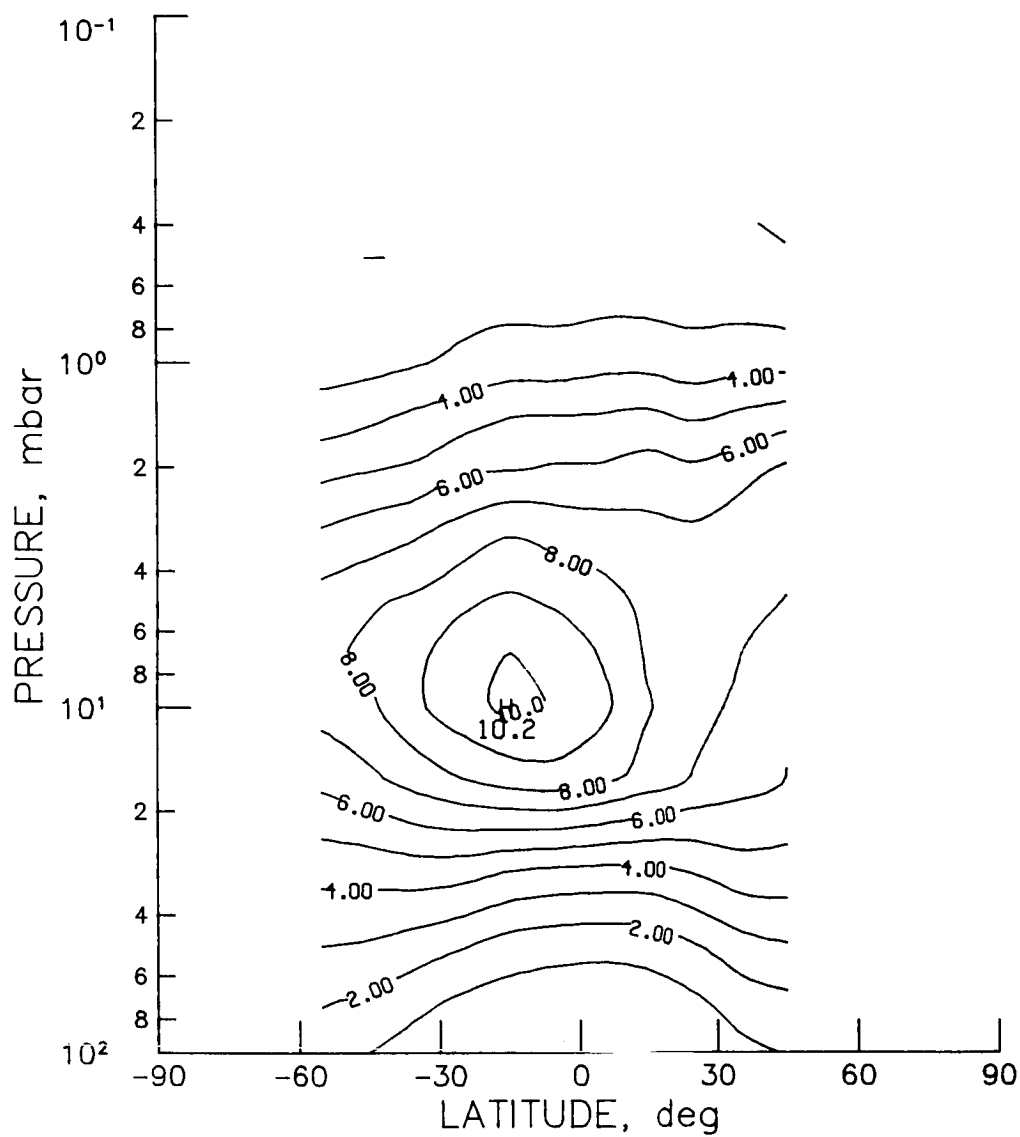


Figure 03-93 - SAGE sunset monthly zonal mean ozone cross section for December 1979 (contour interval is 1.0 ppmv).

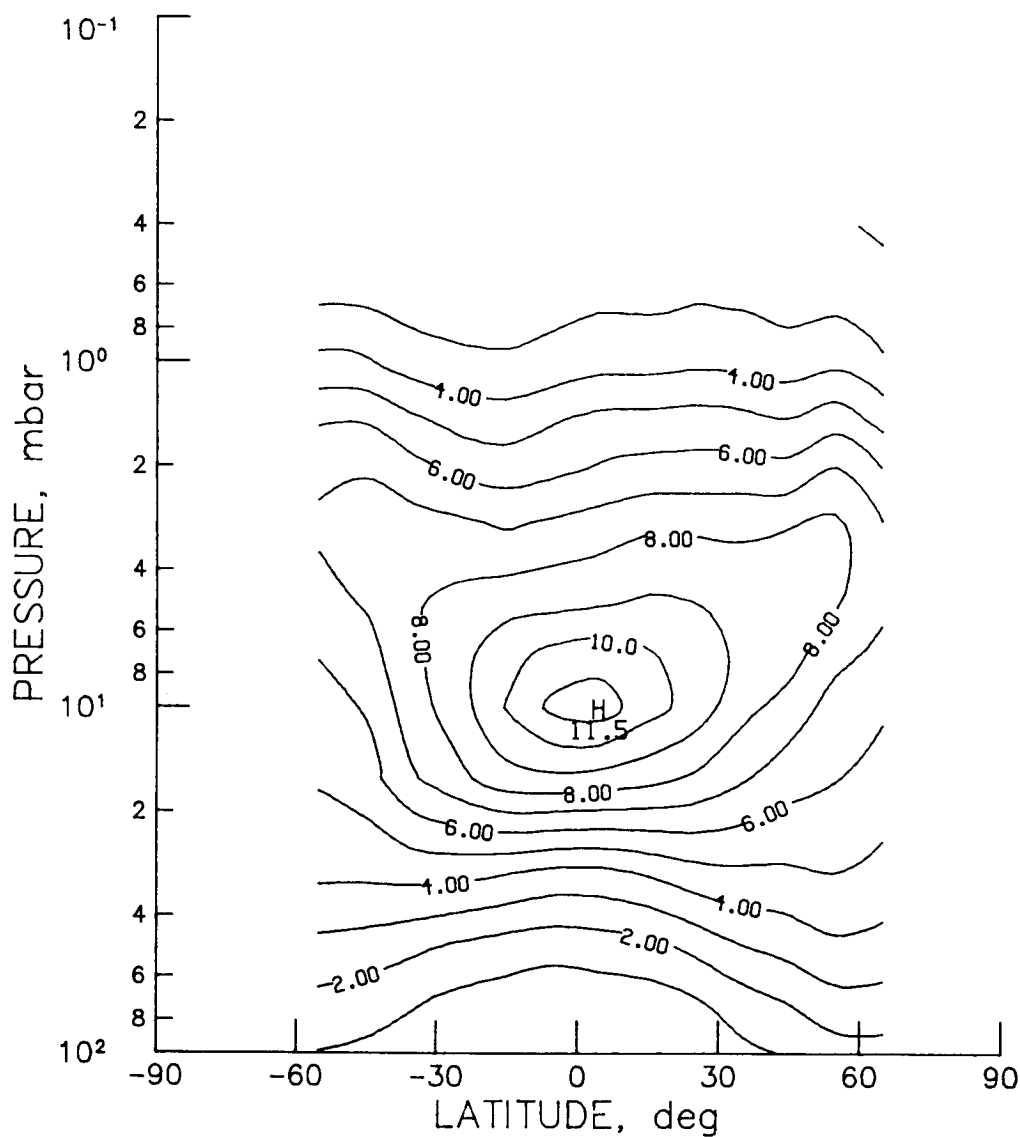


Figure 03-94 - SAGE seasonal sunset zonal mean ozone cross section for March, April, and May, 1979 (contour interval is 1.0 ppmv).

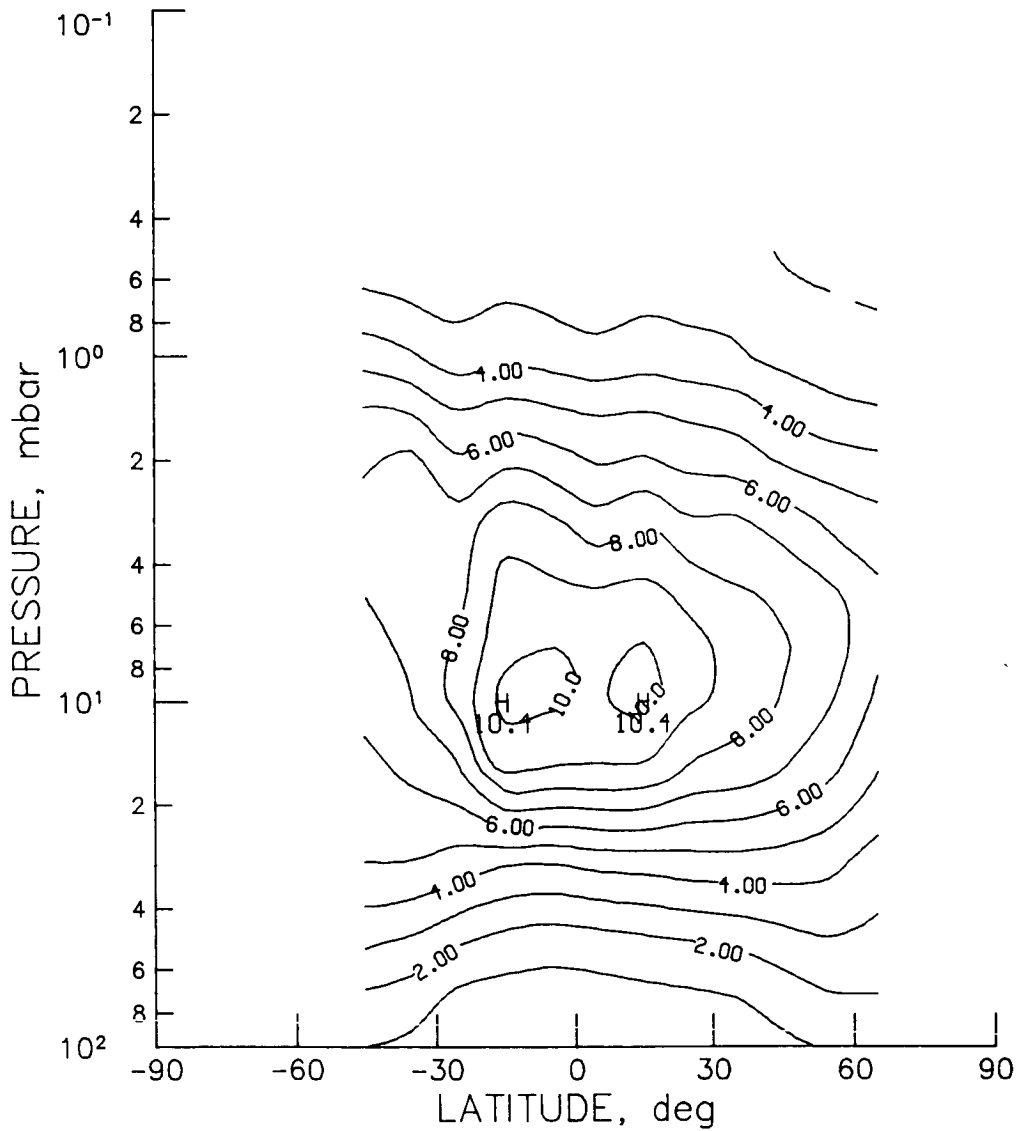


Figure 03-95 - SAGE seasonal sunset zonal mean ozone cross section for June, July, and August 1979 (contour interval is 1.0 ppmv).

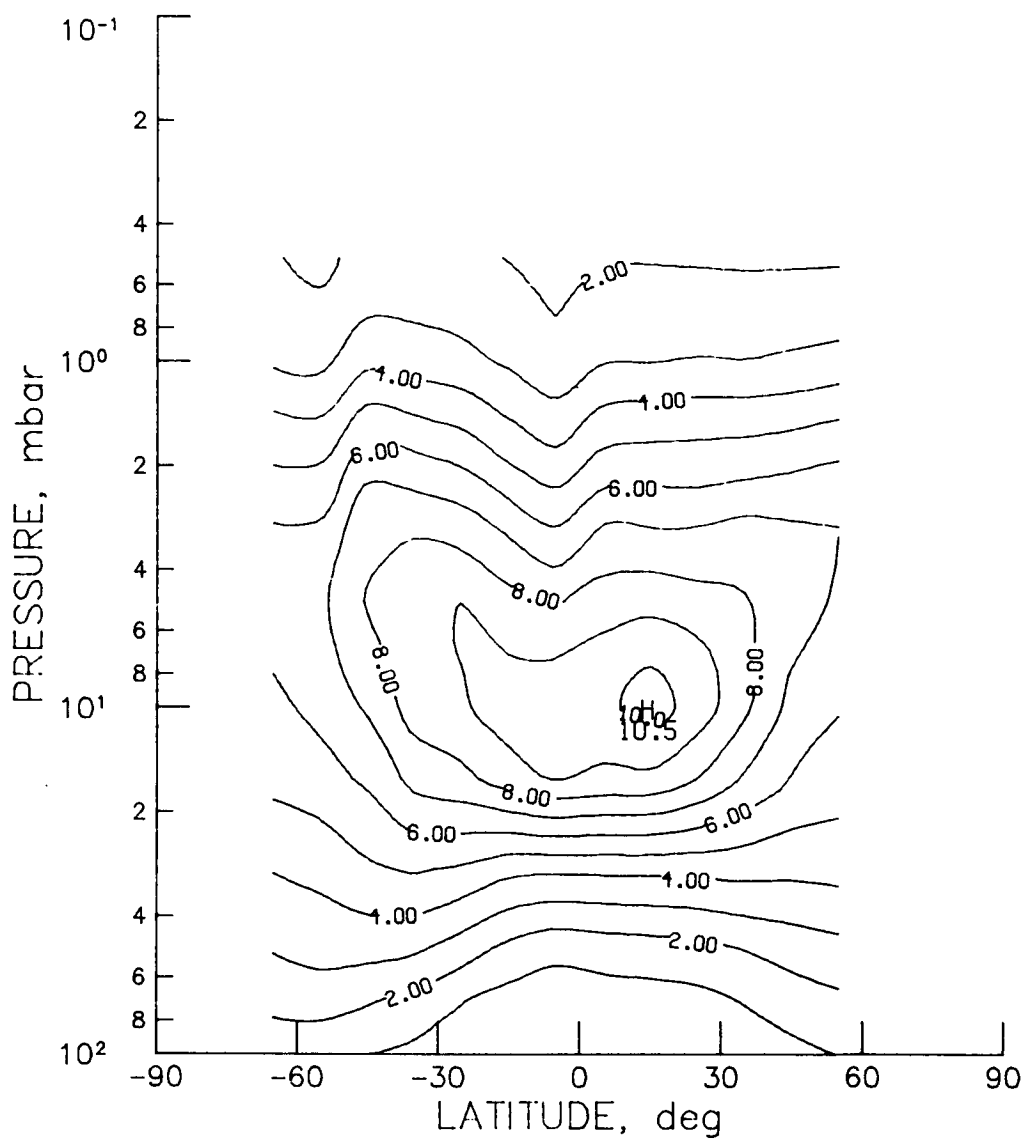


Figure 03-96 - SAGE seasonal sunset zonal mean ozone cross section for September, October, and November 1979 (contour interval is 1.0 ppmv).

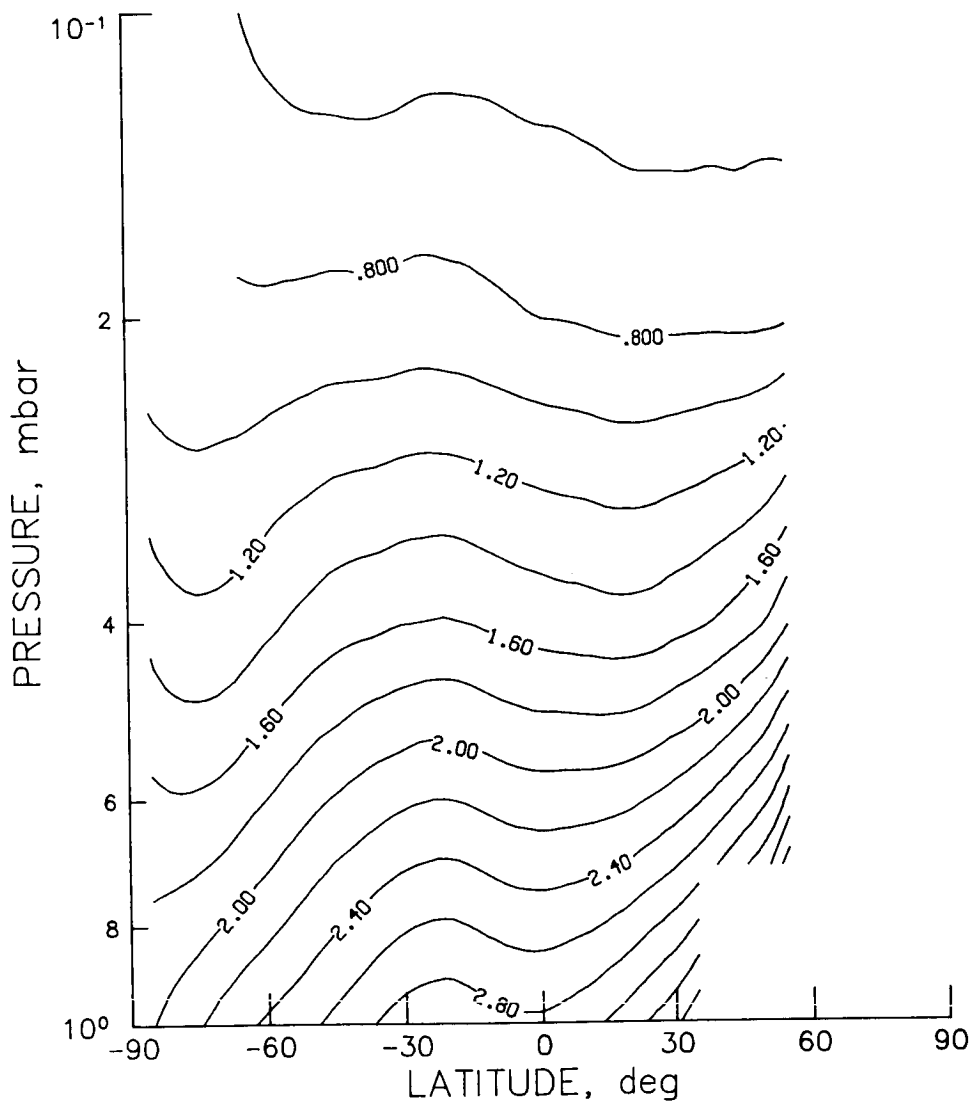


Figure 0₃-97 - SME monthly zonal mean ozone cross section for January 1982 obtained with the UV spectrometer (contour interval is 0.2 ppmv).

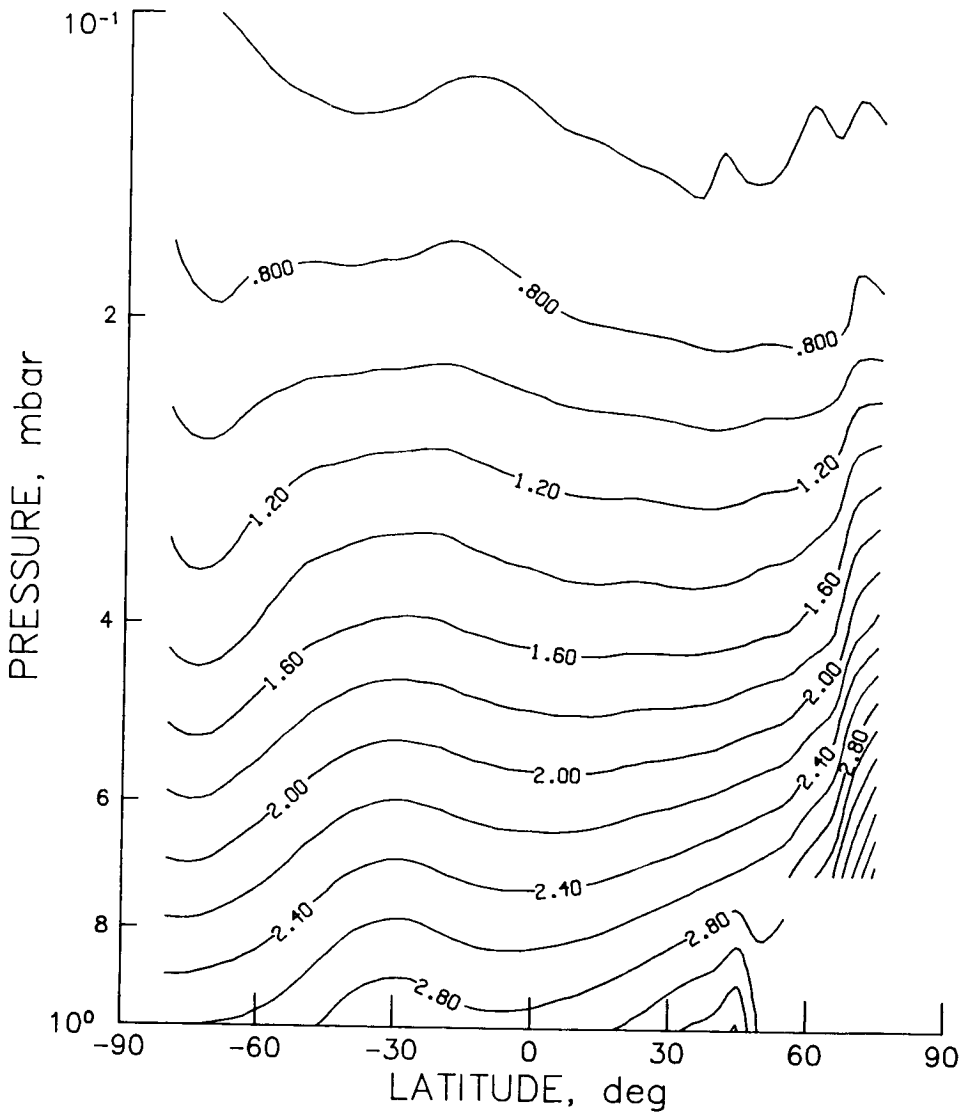


Figure 0₃-98 - SME monthly zonal mean ozone cross section for February 1982 obtained with the UV spectrometer (contour interval is 0.2 ppmv).

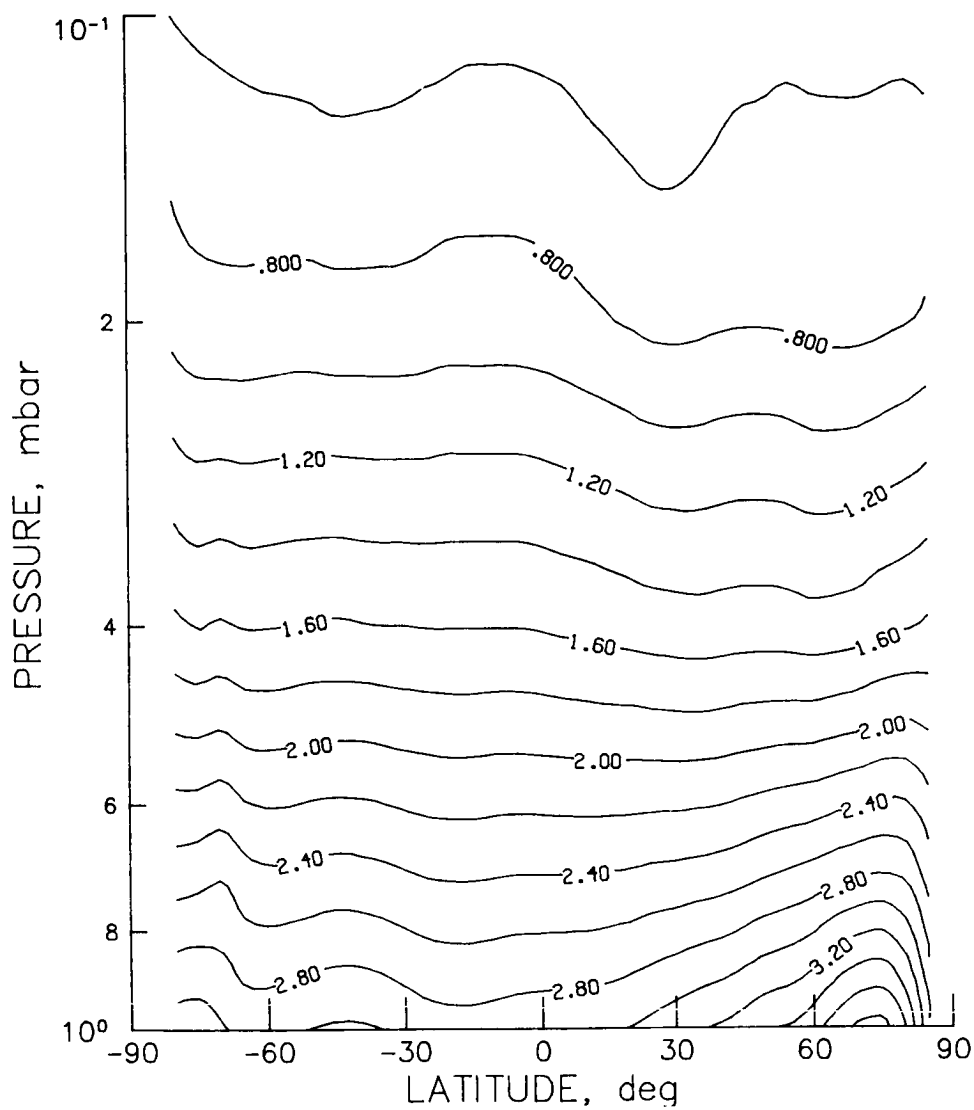


Figure O₃-99 - SME monthly zonal mean ozone cross section for March 1982 obtained with the UV spectrometer (contour interval is 0.2 ppmv).

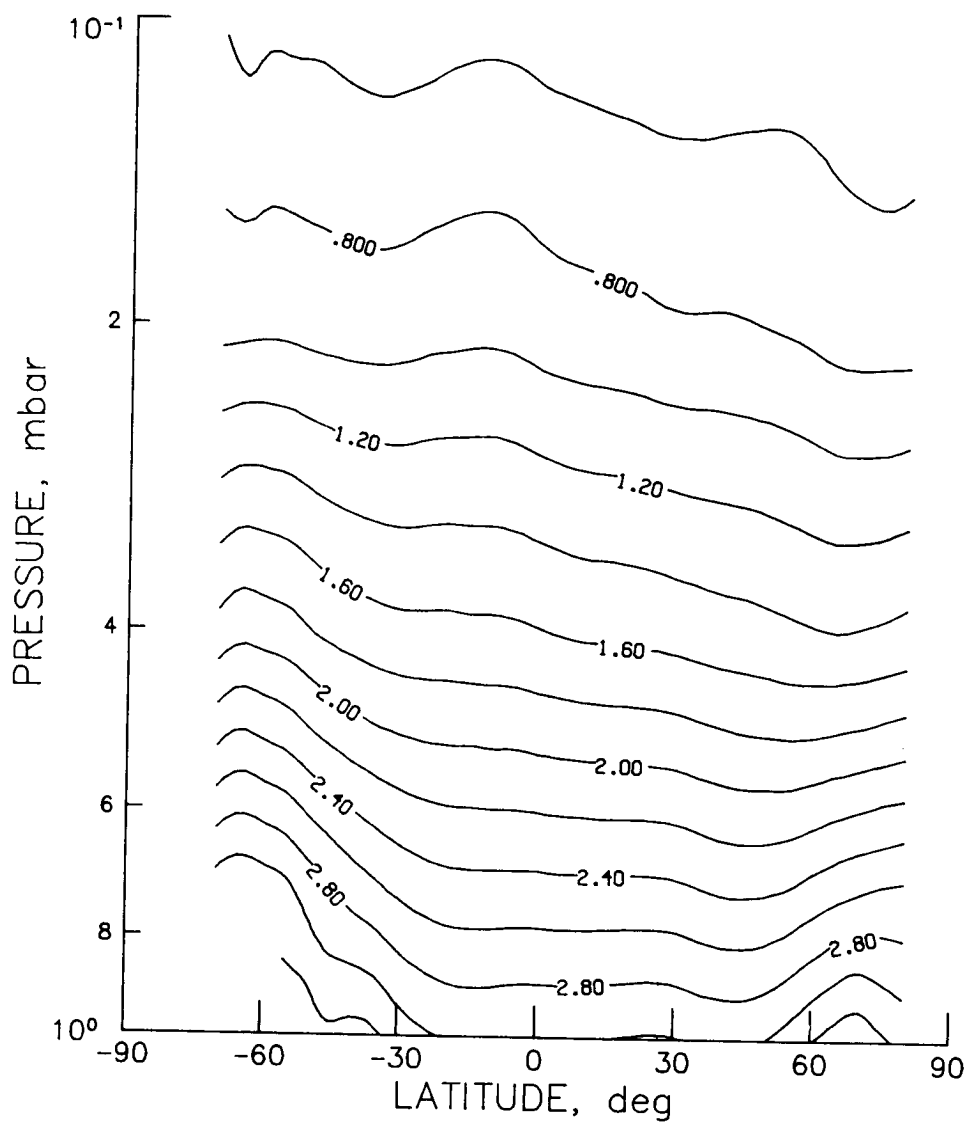


Figure 0₃-100 - SME monthly zonal mean ozone cross section for April 1982 obtained with the UV spectrometer (contour interval is 0.2 ppwv).

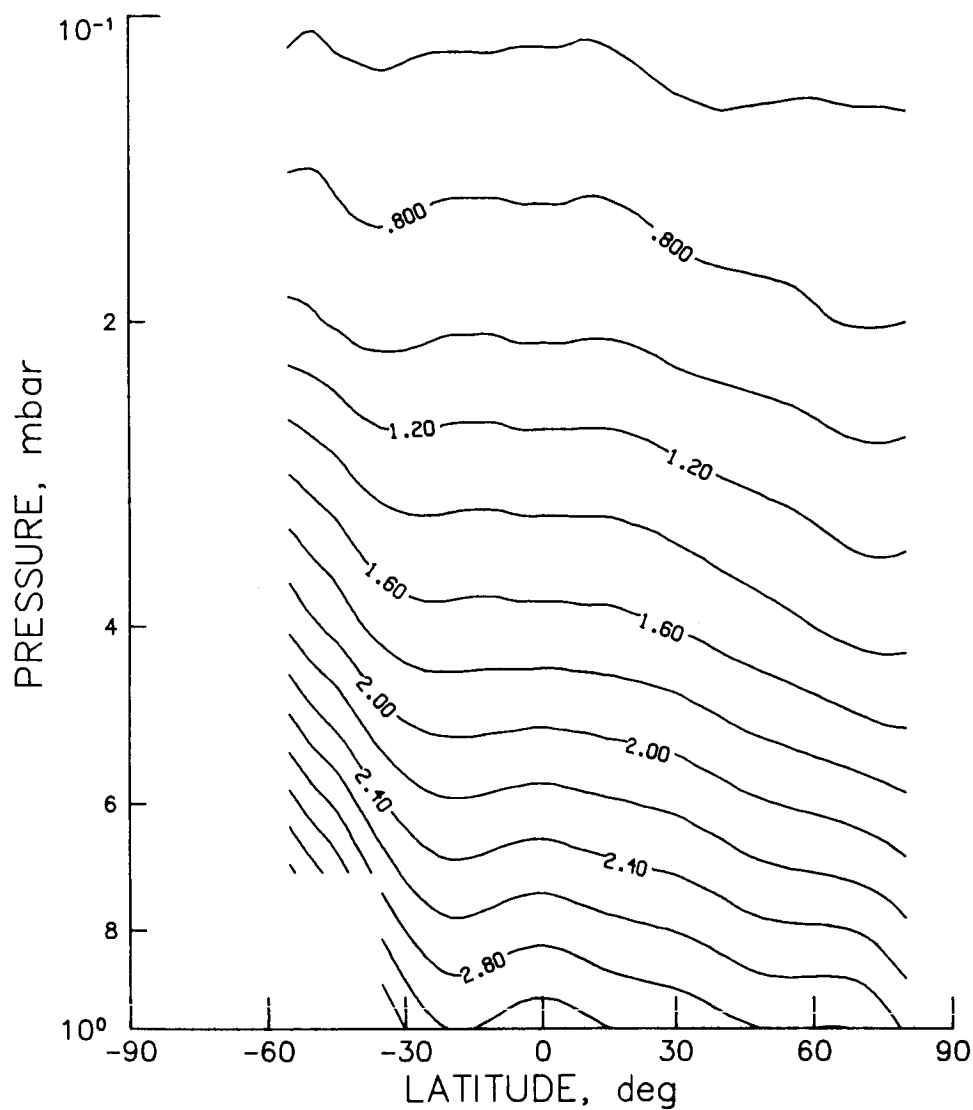


Figure 0₃-101 - SME monthly zonal mean ozone cross section for May 1982
obtained with the UV spectrometer (contour interval is 0.2
ppmv).

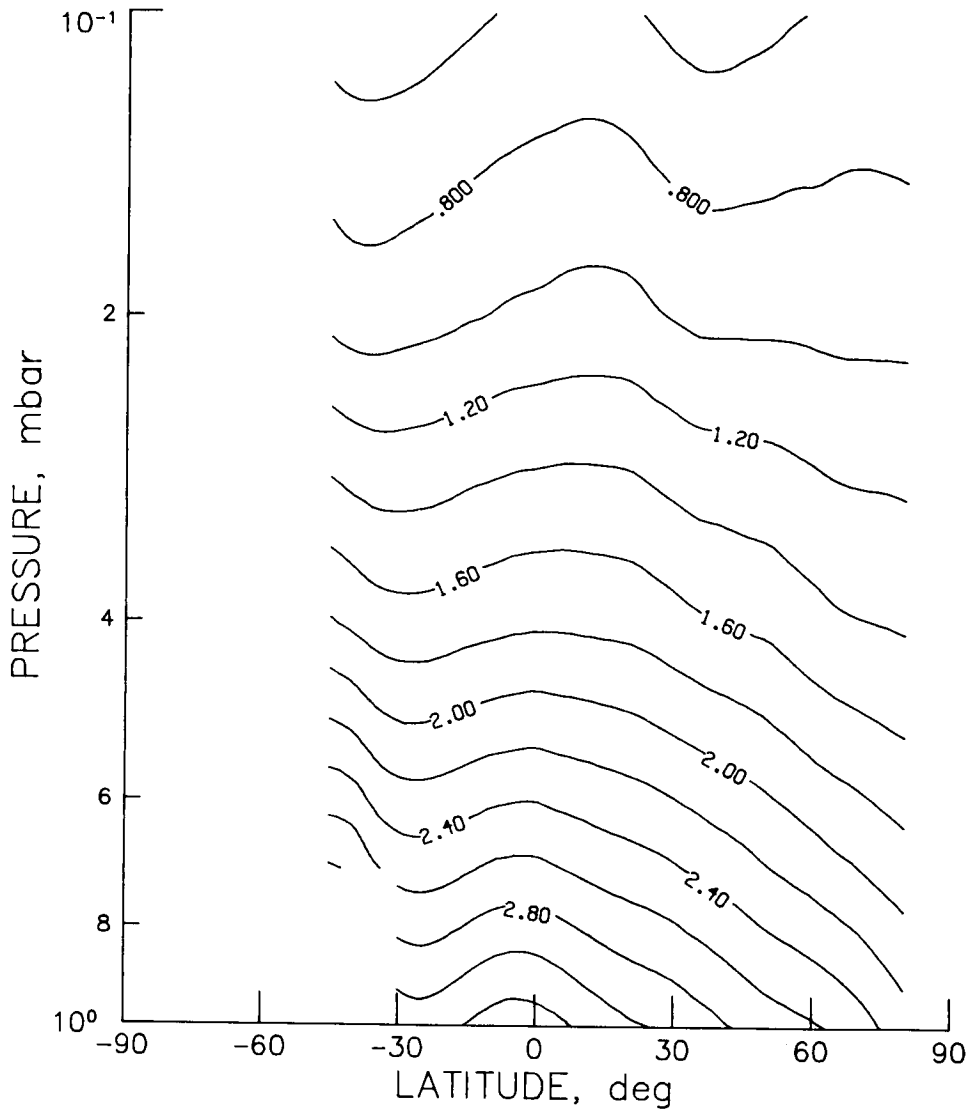


Figure 0₃-102 - SME monthly zonal mean ozone cross section for June 1982
obtained with the UV spectrometer (contour interval is 0.2
ppmv).

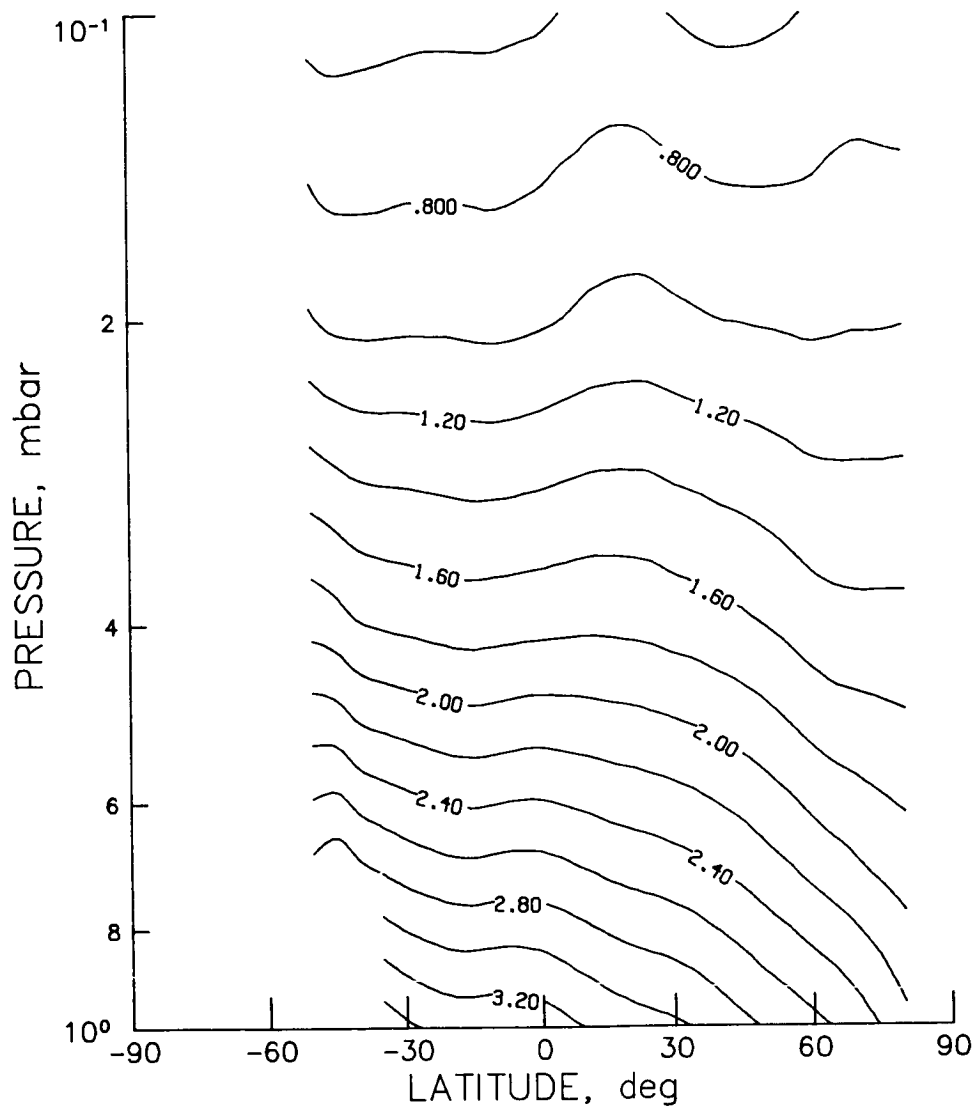


Figure 0₃-103 - SME monthly zonal mean ozone cross section for July 1982 obtained with the UV spectrometer (contour interval is 0.2 ppmv).

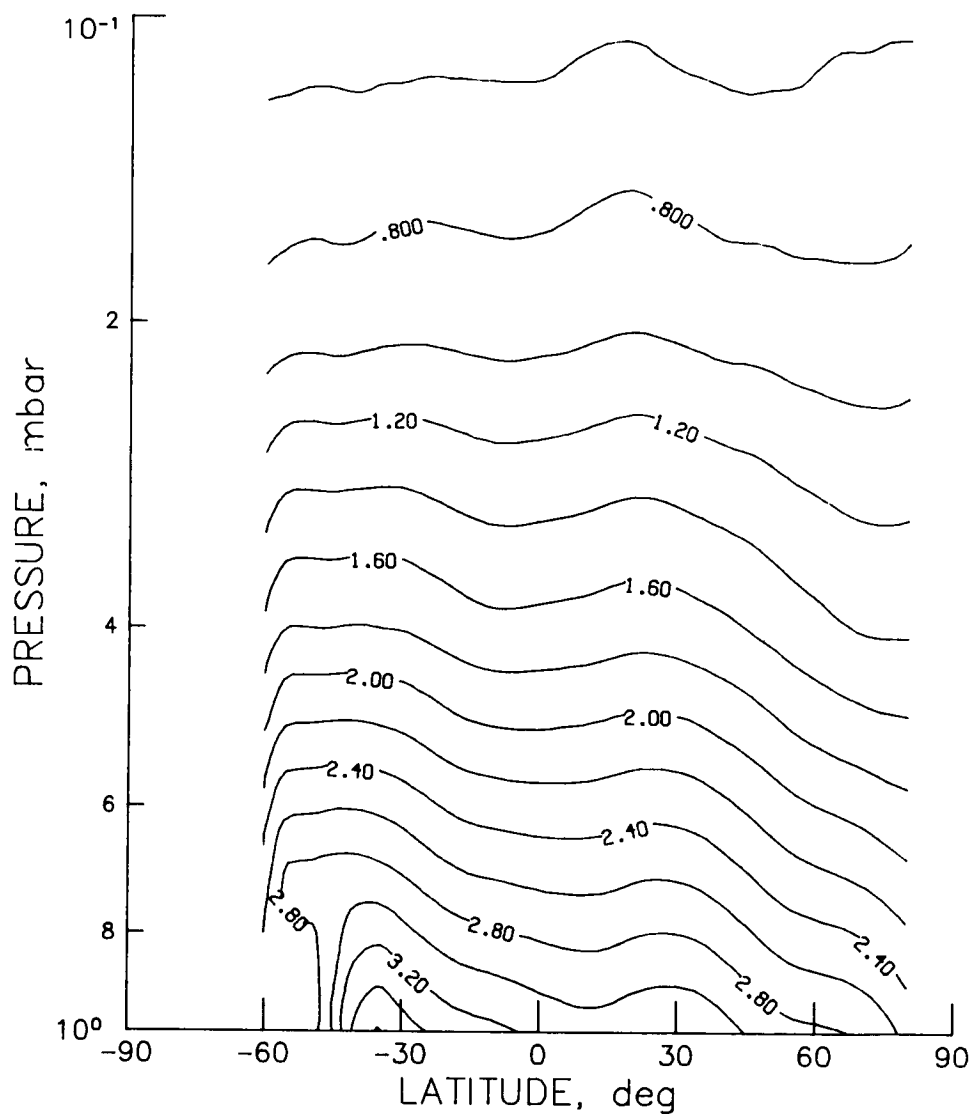


Figure 03-104 - SME monthly zonal mean ozone cross section for August 1982 obtained with the UV spectrometer (contour interval is 0.2 ppmv).

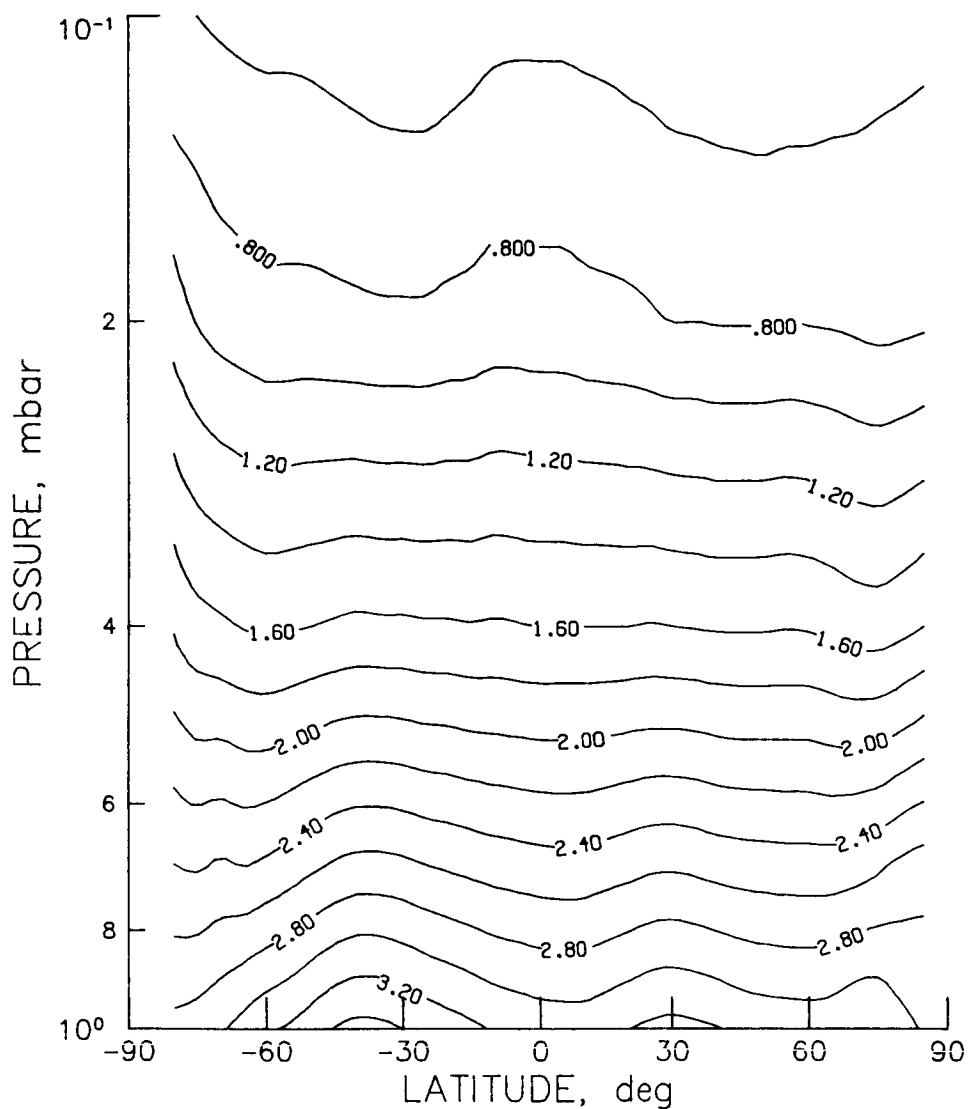


Figure 0₃-105 - SME monthly zonal mean ozone cross section for September 1982 obtained with the UV spectrometer (contour interval is 0.2 ppmv).

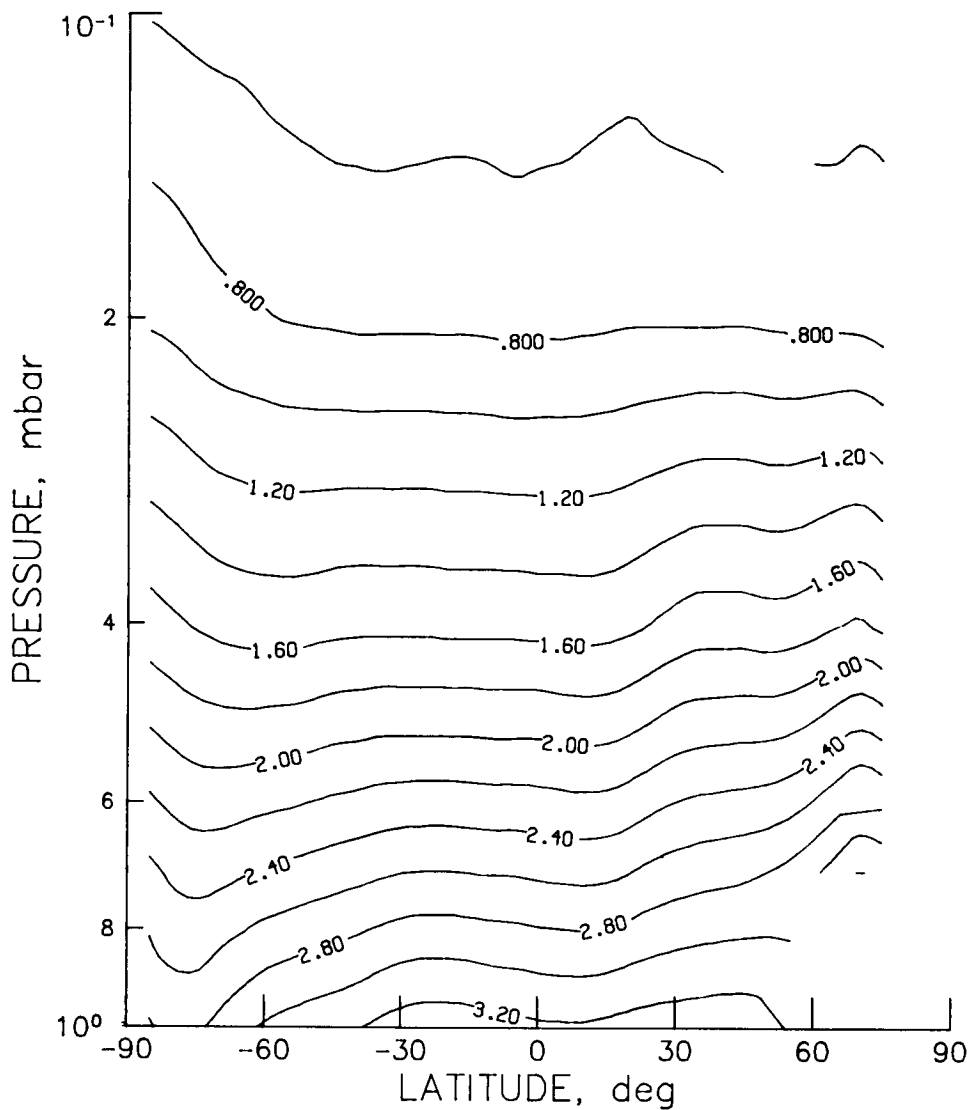


Figure O₃-106 - SME monthly zonal mean ozone cross section for October 1982 obtained with the UV spectrometer (contour interval is 0.2 ppmv).

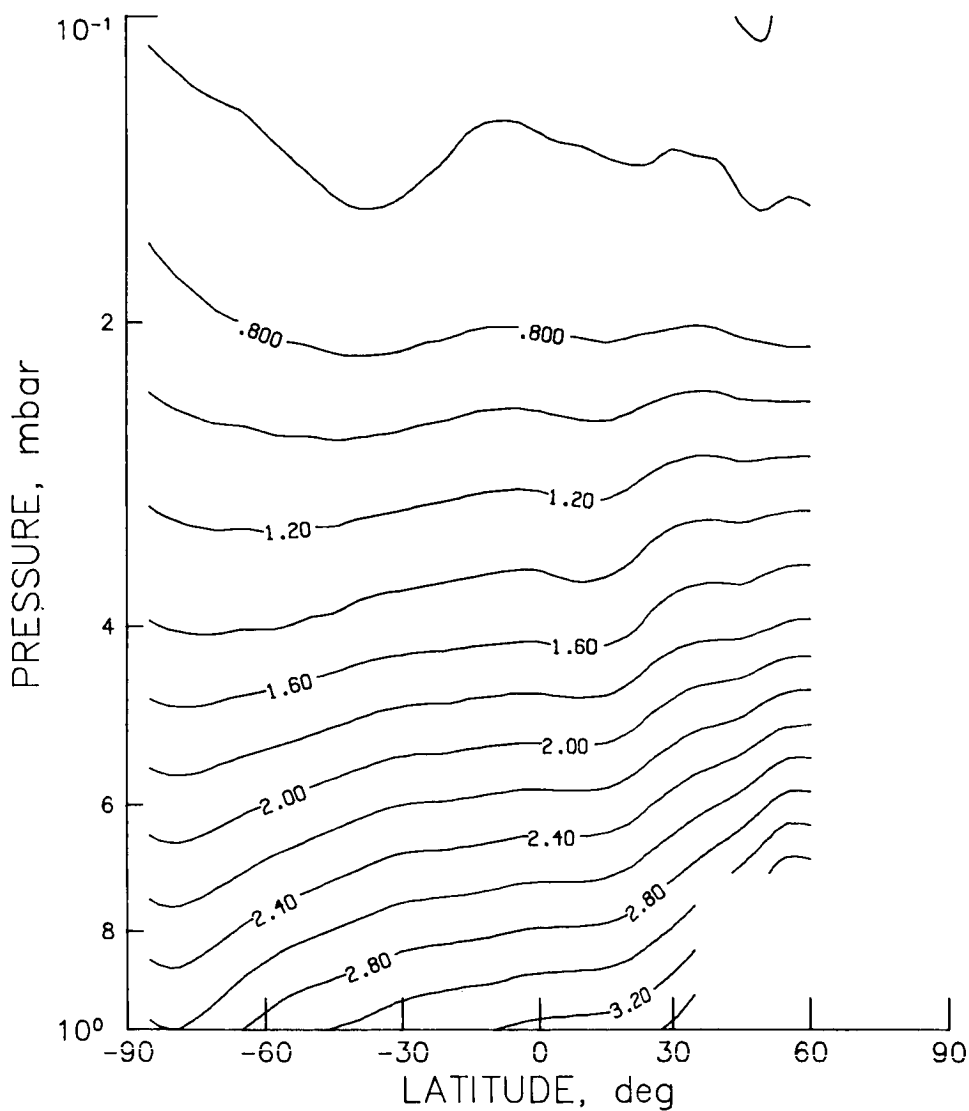


Figure 0₃-107 - SME monthly zonal mean ozone cross section for November 1982 obtained with the UV spectrometer (contour interval is 0.2 ppmv).

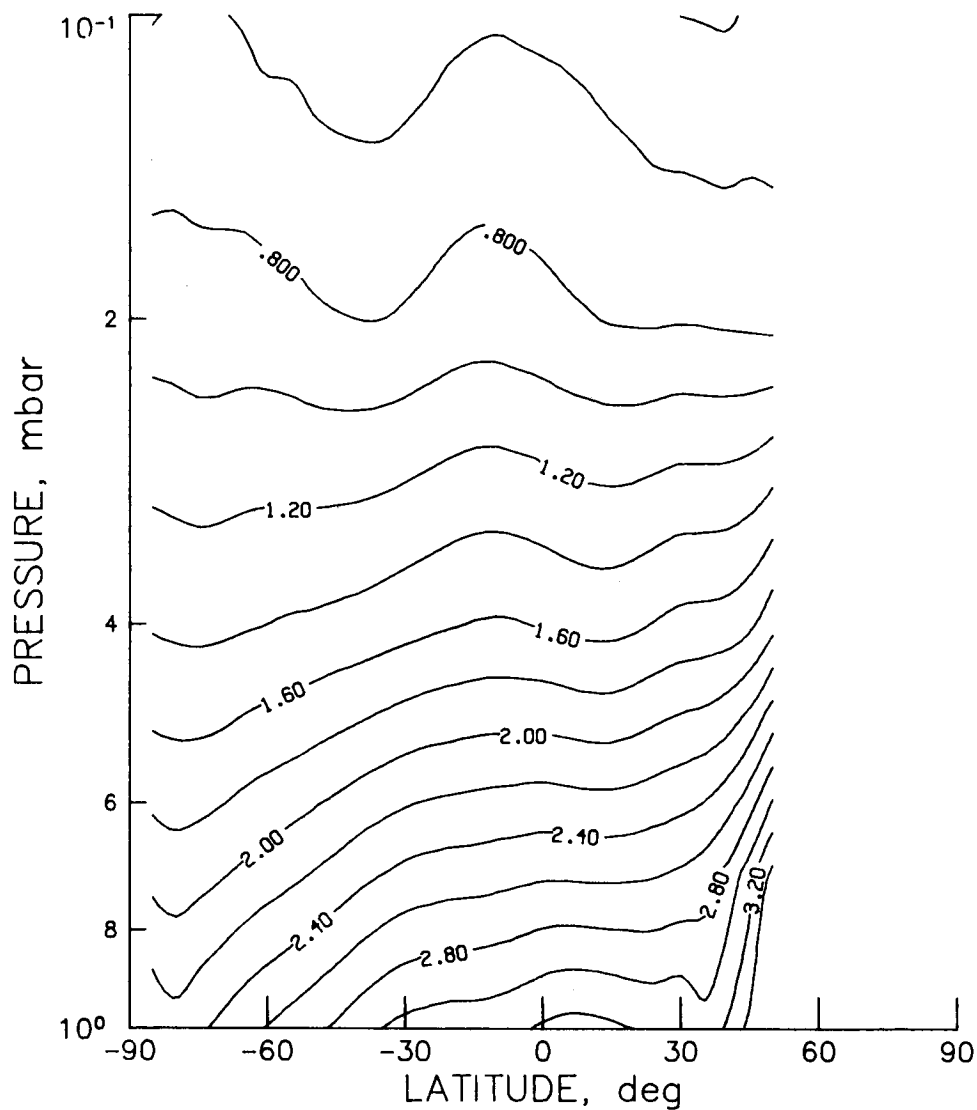


Figure 0₃-108 - SME monthly zonal mean ozone cross section for December 1982 obtained with the UV spectrometer (contour interval is 0.2 ppmv).

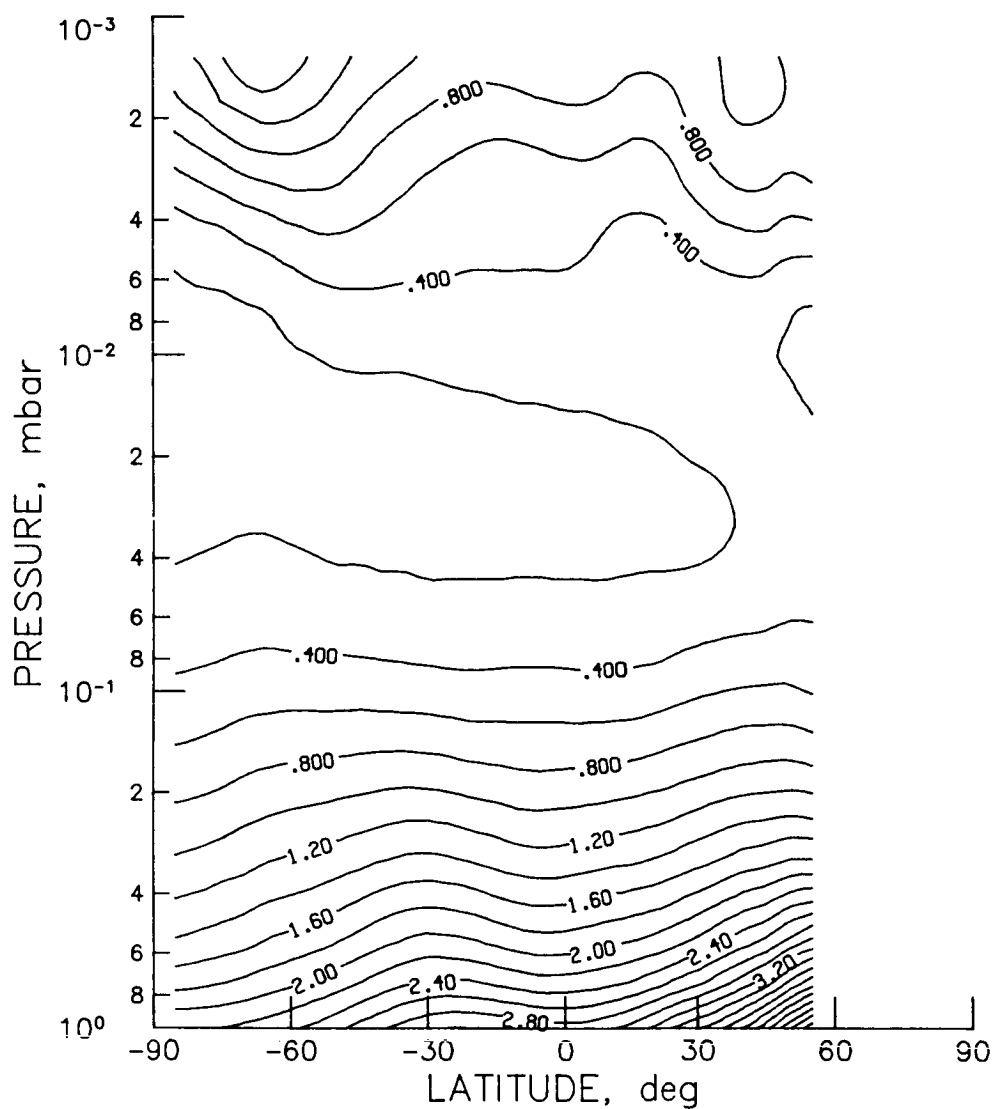


Figure 0₃-109 - SME monthly zonal mean ozone cross section for January 1982 using IR measurements (contour interval is 0.2 ppmv).

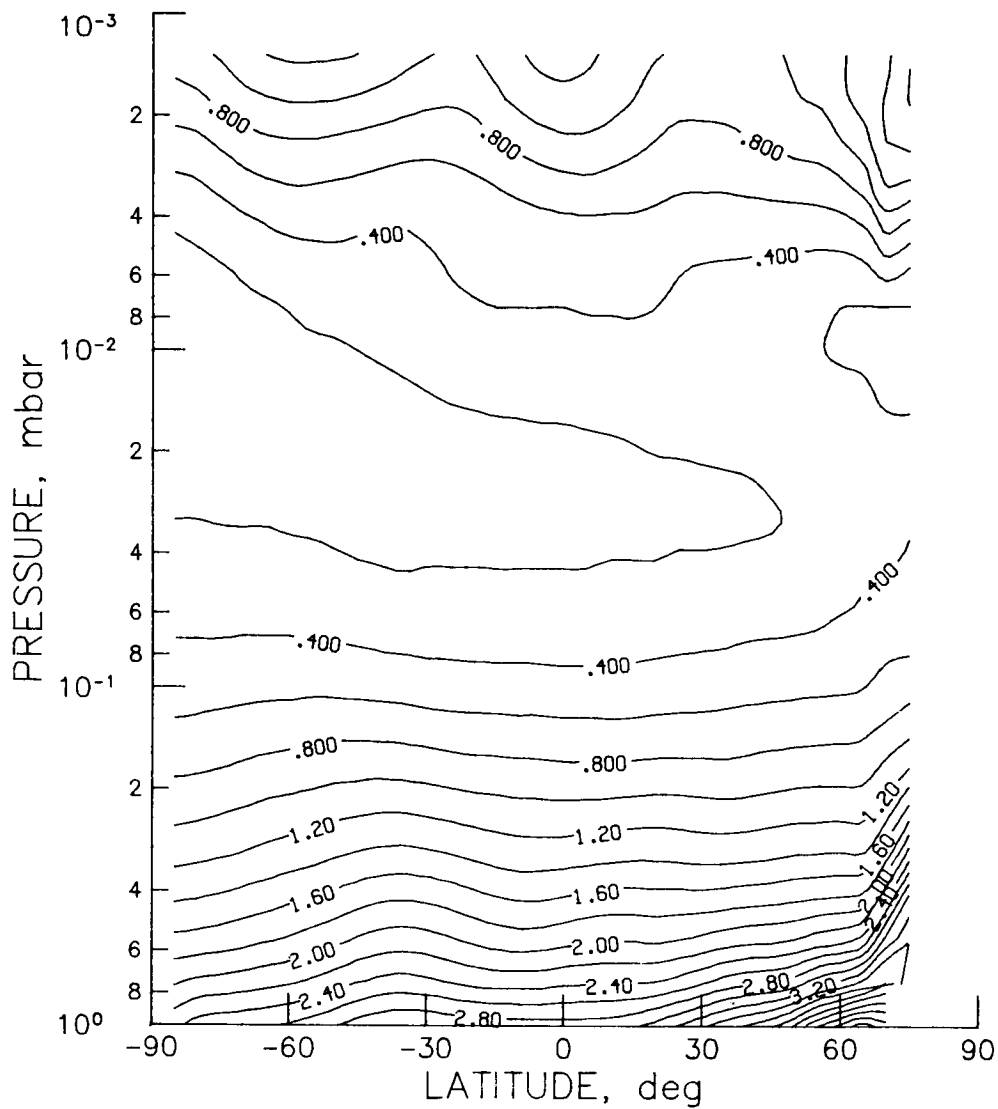


Figure 0₃-110 - SME monthly zonal mean ozone cross section for February 1982 using IR measurements (contour interval is 0.2 ppmv).

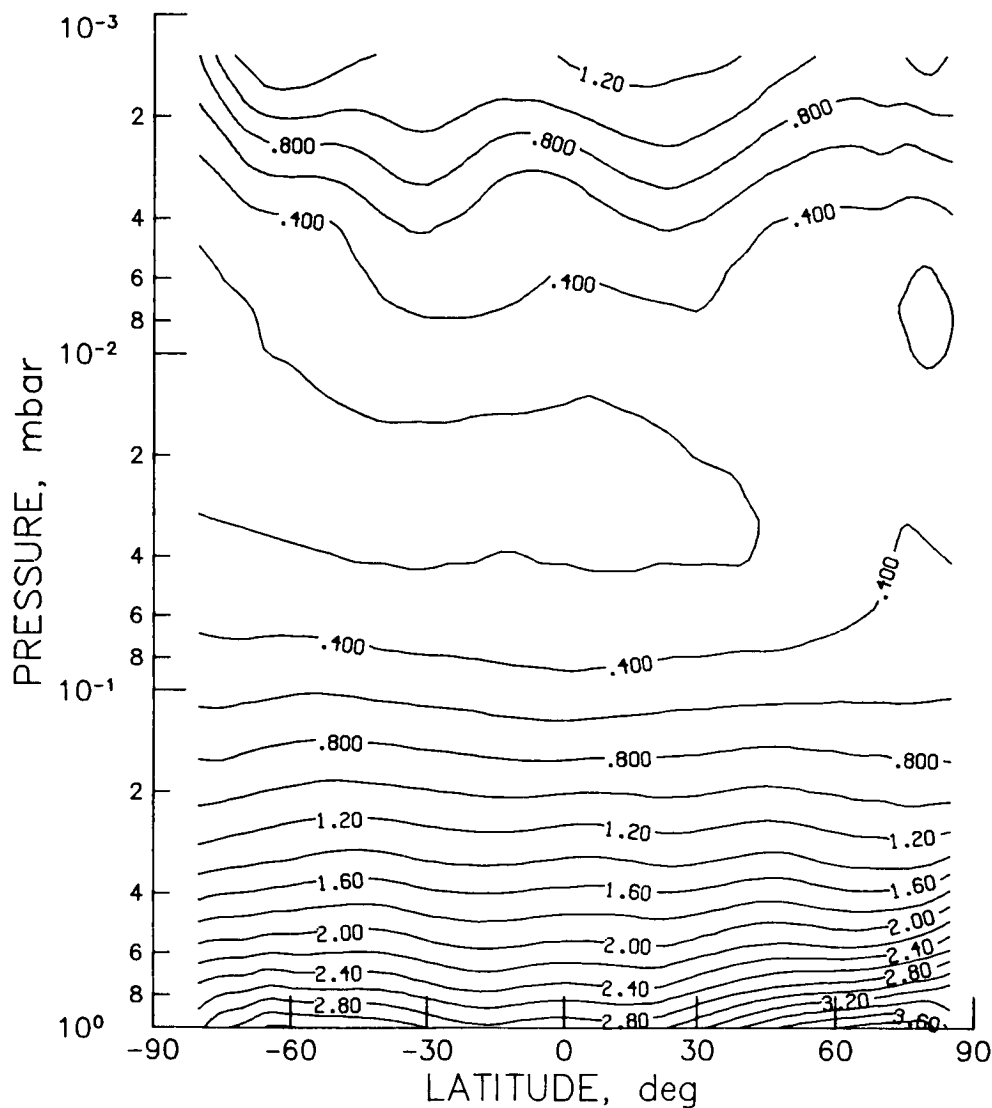


Figure 0₃-111 - SME monthly zonal mean ozone cross section for March 1982 using IR measurements (contour interval is 0.2 ppmv).

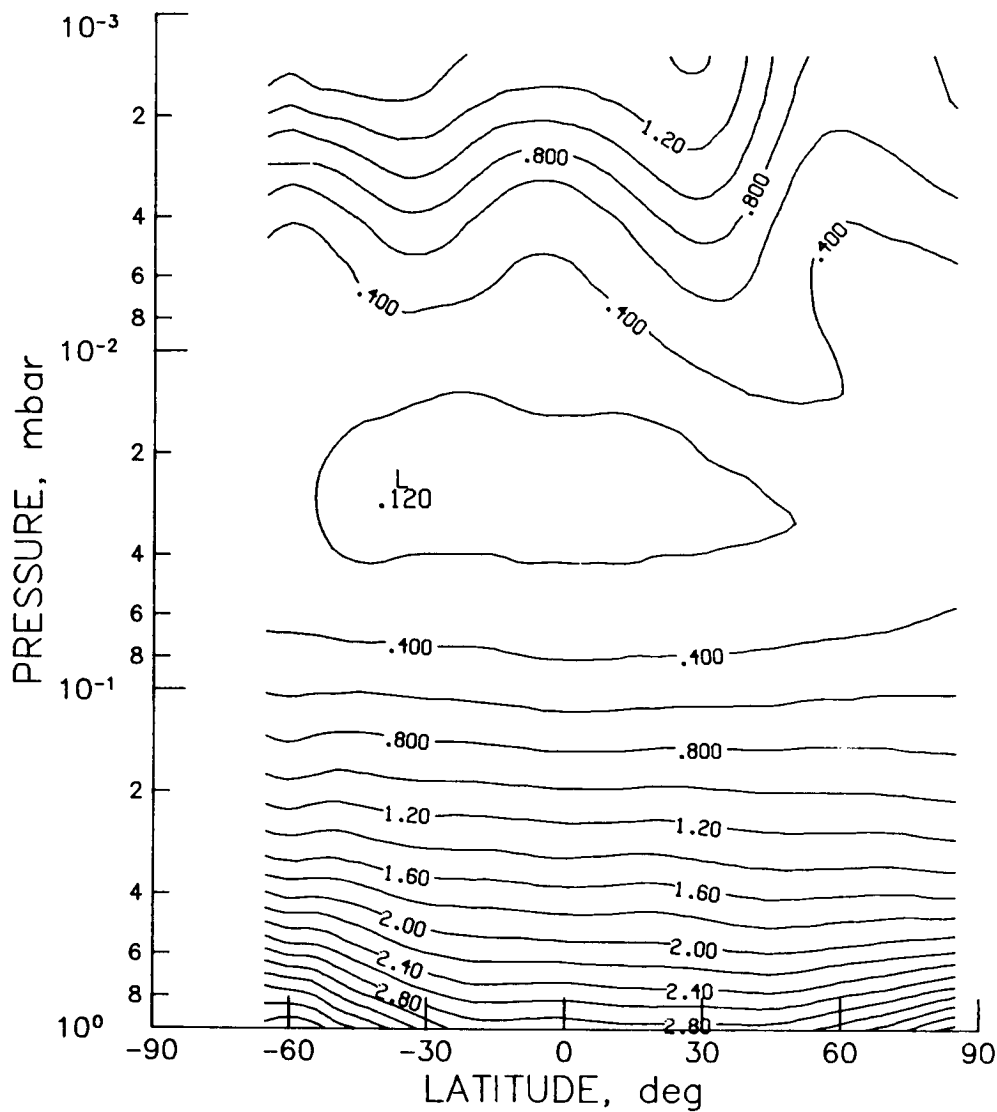


Figure O₃-112 - SME monthly zonal mean ozone cross section for April 1982 using IR measurements (contour interval is 0.2 ppmv).

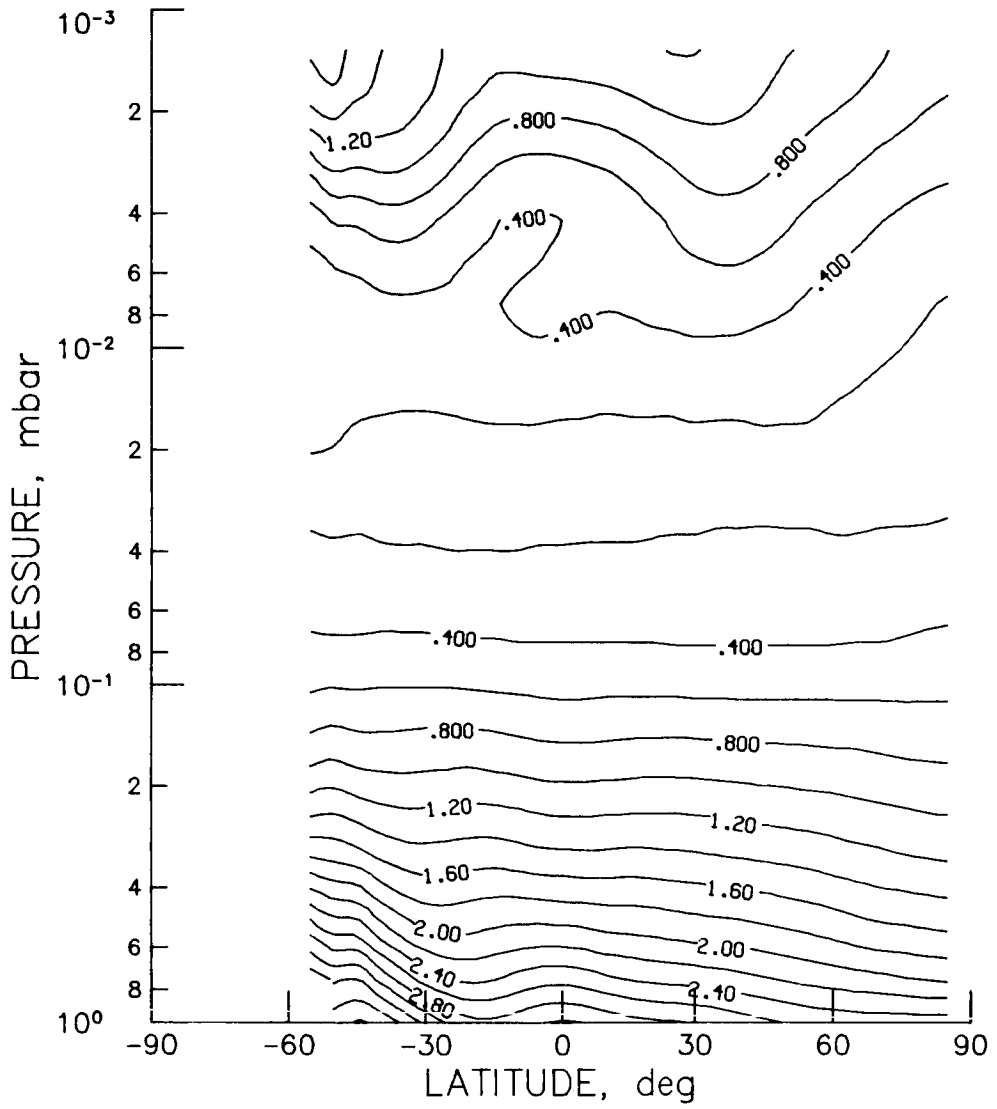


Figure 0₃-113 - SME monthly zonal mean ozone cross section for May 1982 using IR measurements (contour interval is 0.2 ppmv).

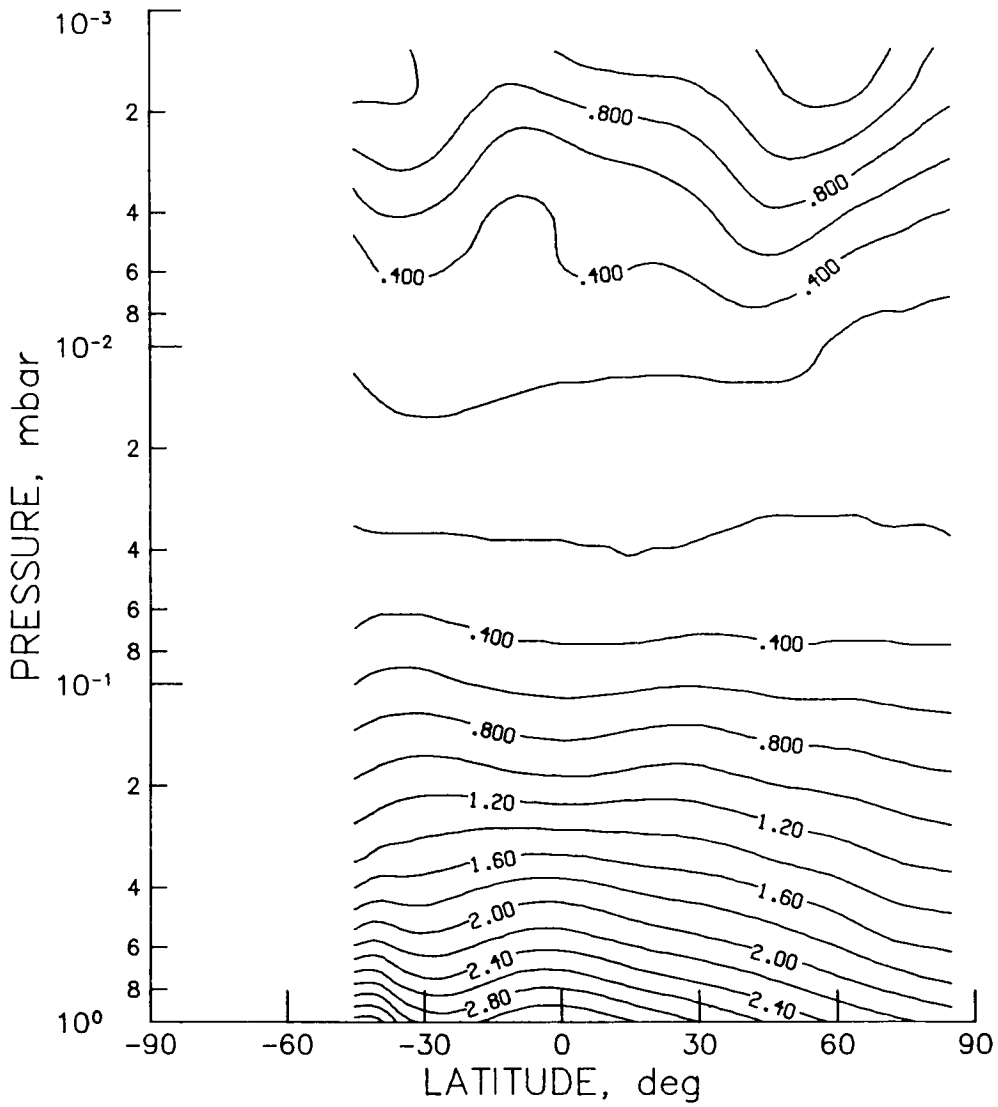


Figure O₃-114 - SME monthly zonal mean ozone cross section for June 1982 using IR measurements (contour interval is 0.2 ppmv).

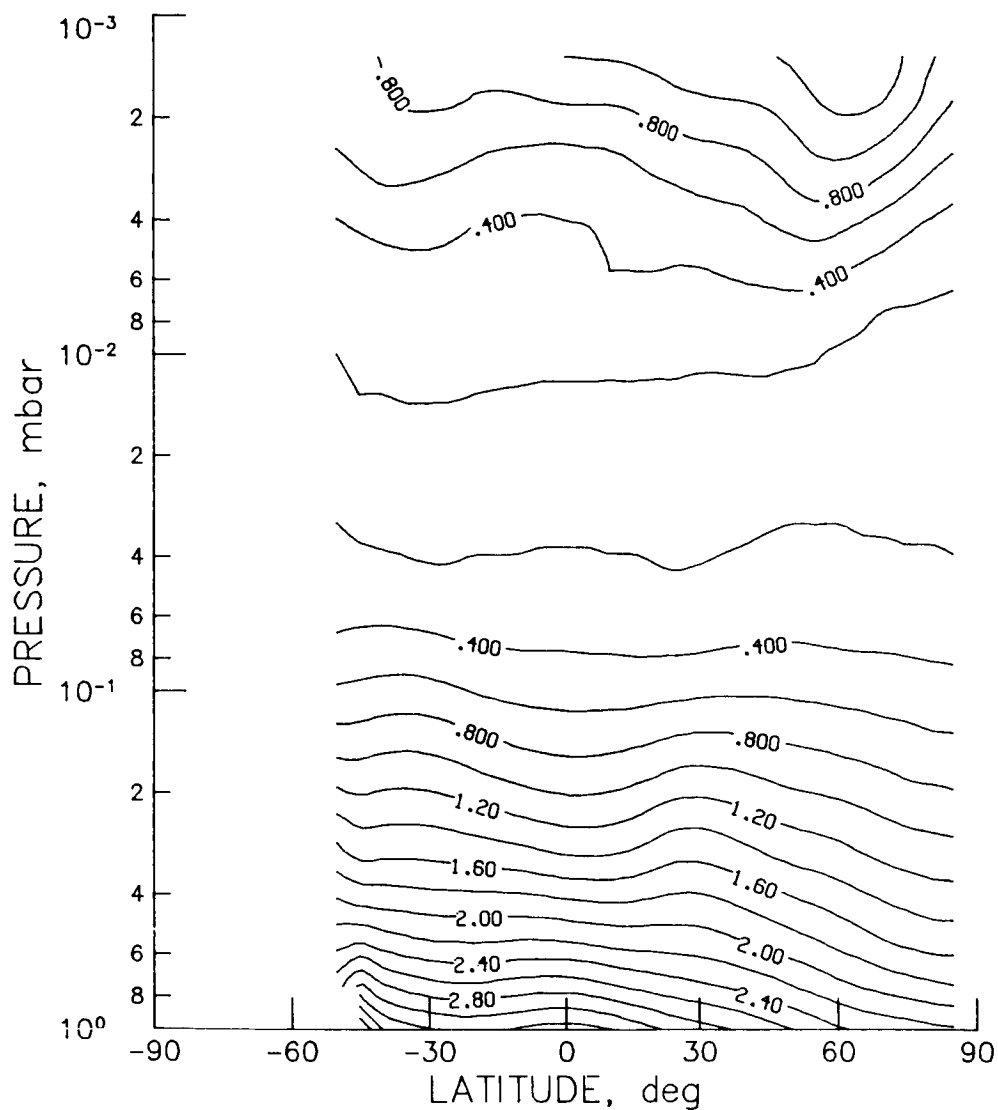


Figure O₃-115 - SME monthly zonal mean ozone cross section for July 1982 using IR measurements (contour interval is 0.2 ppmv).

C-3

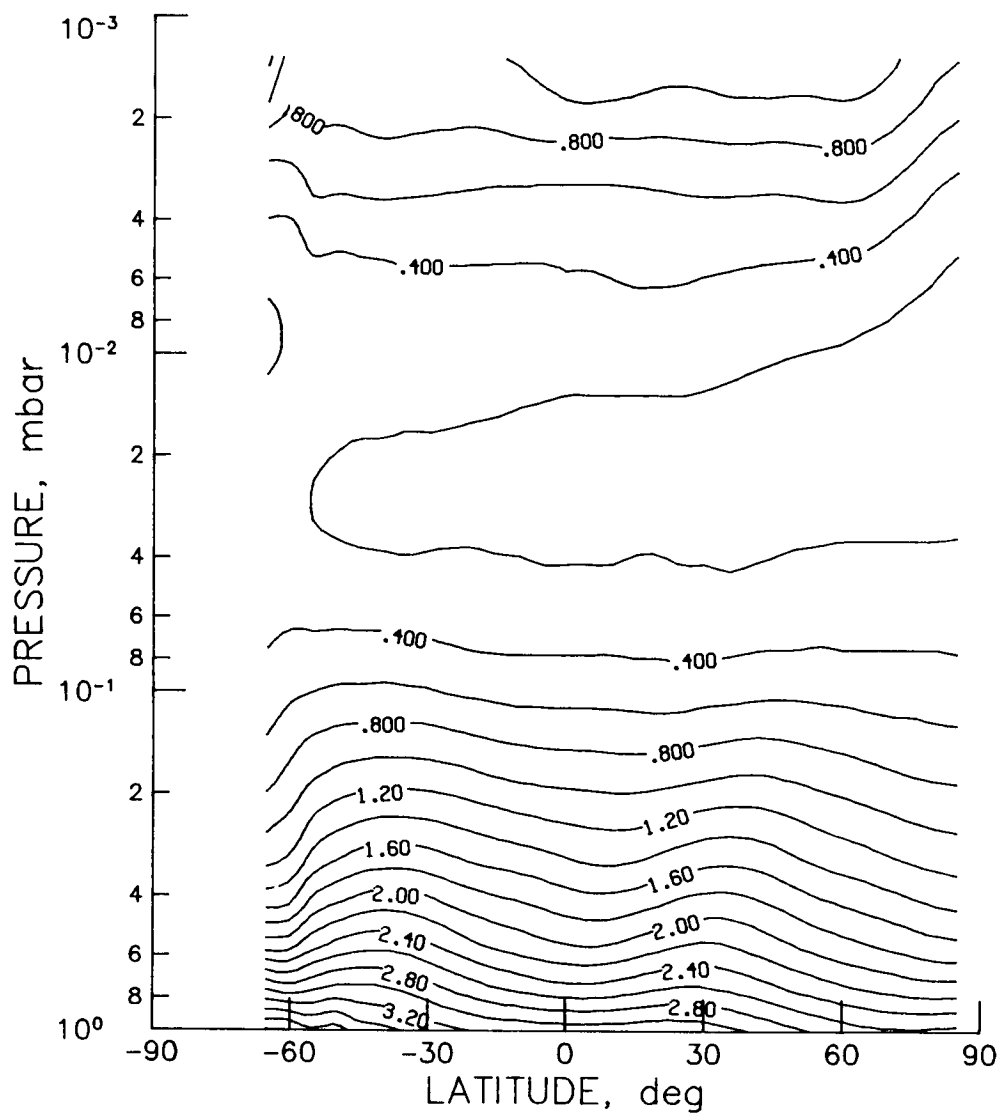


Figure 0₃-116 - SME monthly zonal mean ozone cross section for August 1982 using IR measurements (contour interval is 0.2 ppmv).

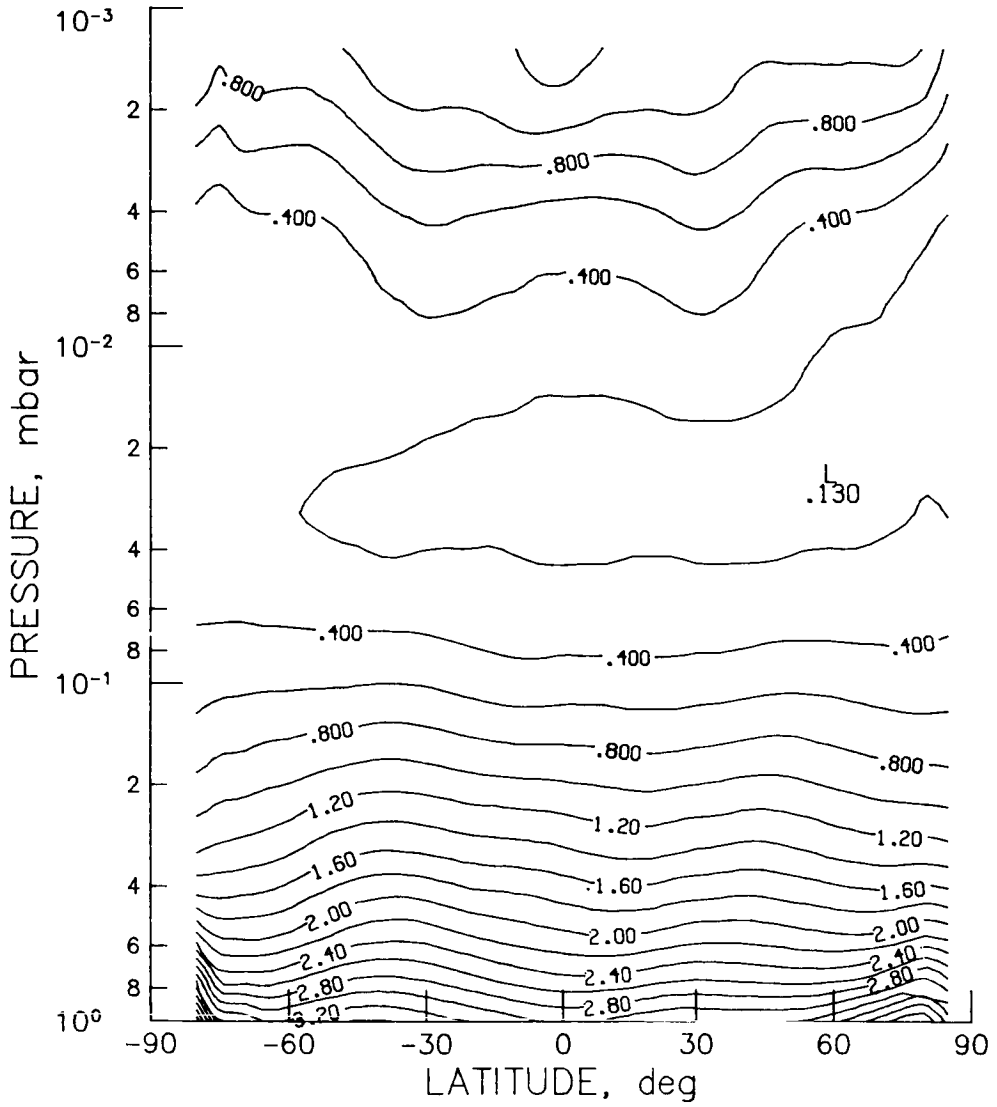


Figure 0₃-117 - SME monthly zonal mean ozone cross section for September 1982 using IR measurements (contour interval is 0.2 ppmv).

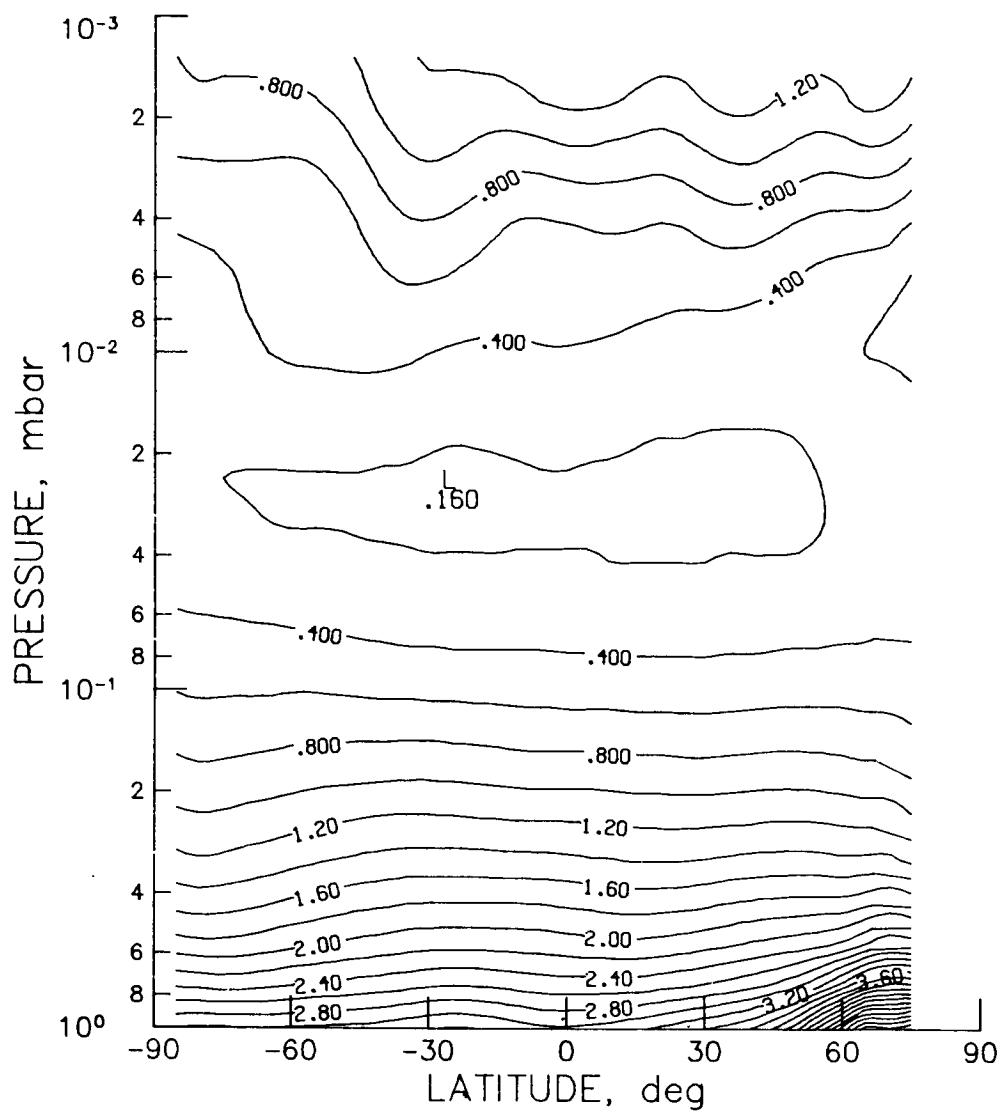


Figure 0₃-118 - SME monthly zonal mean ozone cross section for October 1982 using IR measurements (contour interval is 0.2 ppmv).

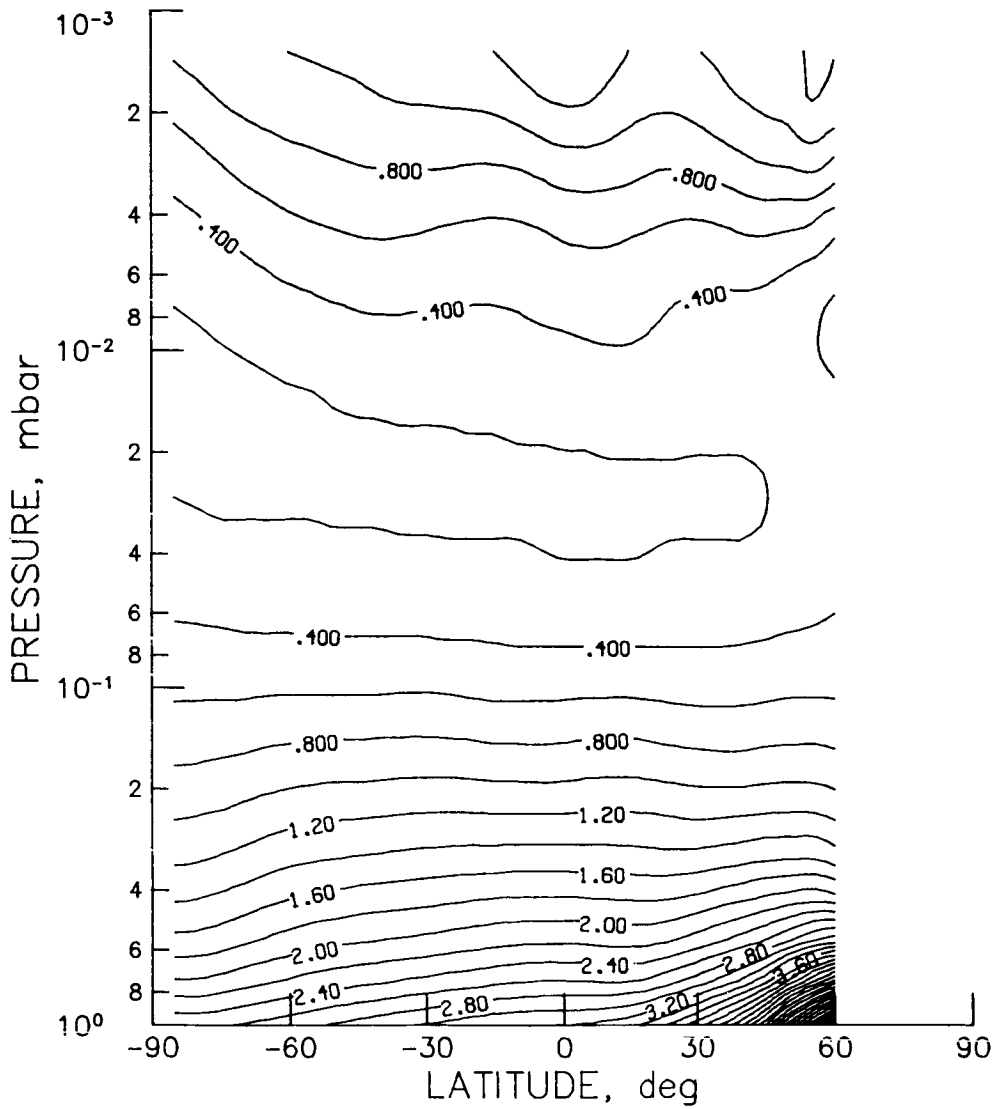


Figure 0₃-119 - SME monthly zonal mean ozone cross section for November 1982 using IR measurements (contour interval is 0.2 ppmv).

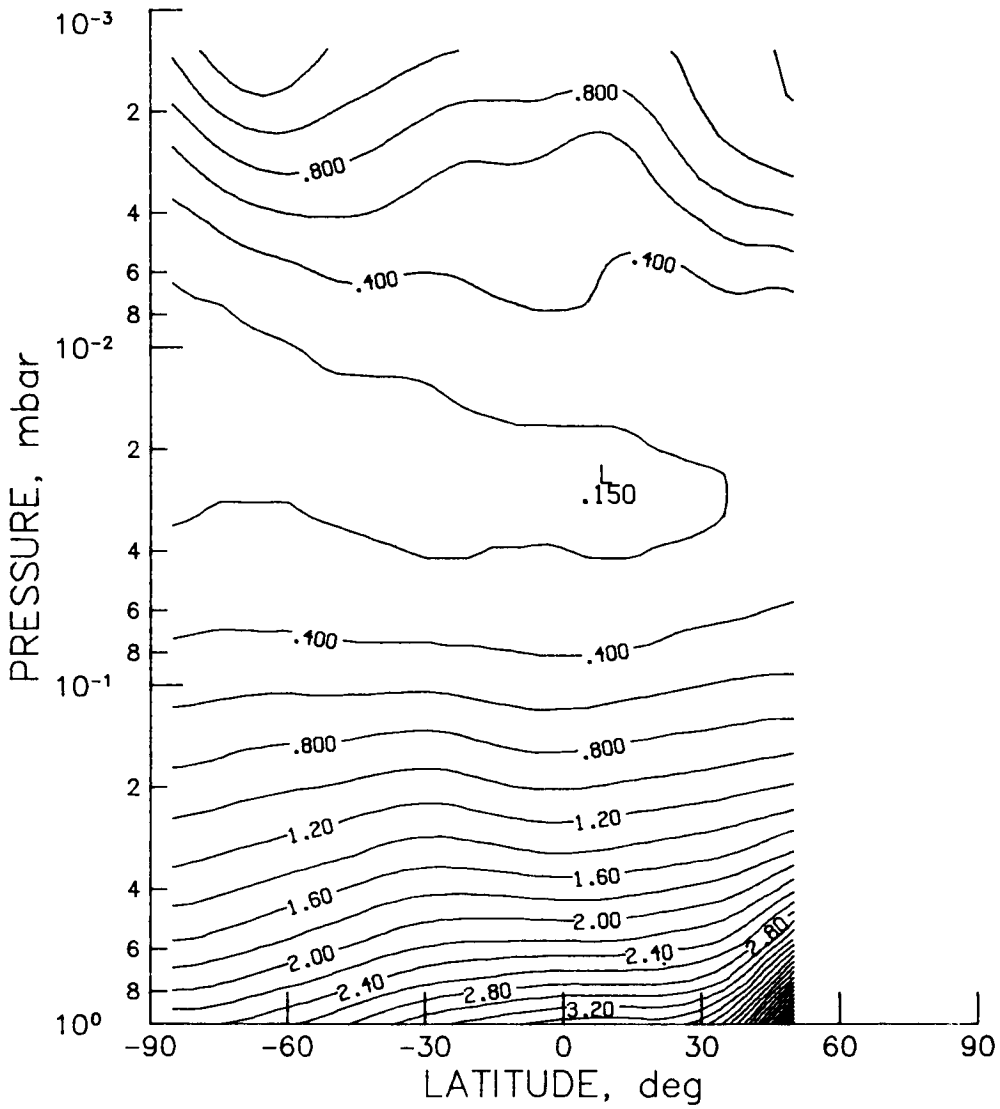


Figure 0₃-120 - SME monthly zonal mean ozone cross section for December 1982 using IR measurements (contour interval is 0.2 ppmv).

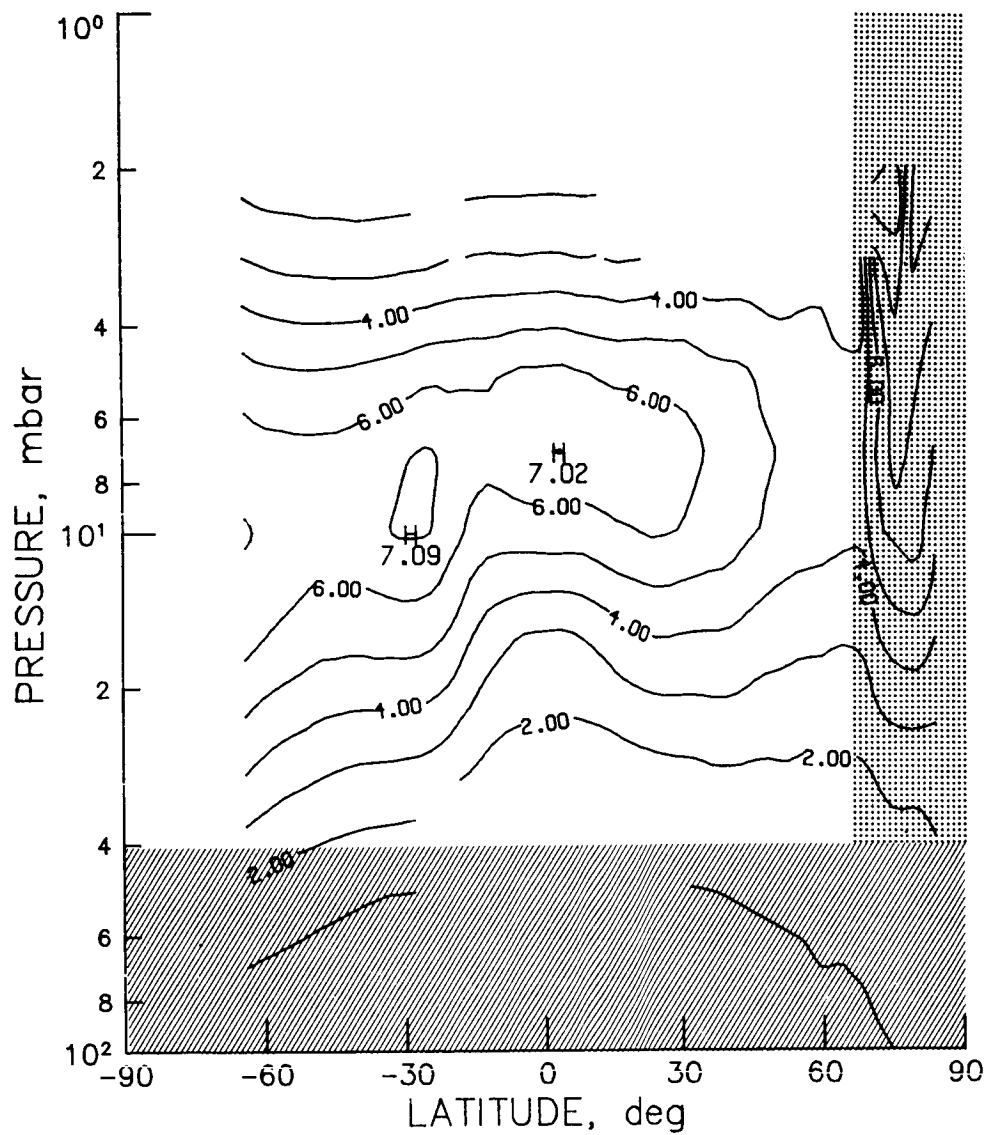


Figure N-1 - LIMS monthly zonal mean daytime NO₂ cross section for November 1978 (contour interval is 1.0 ppbv).

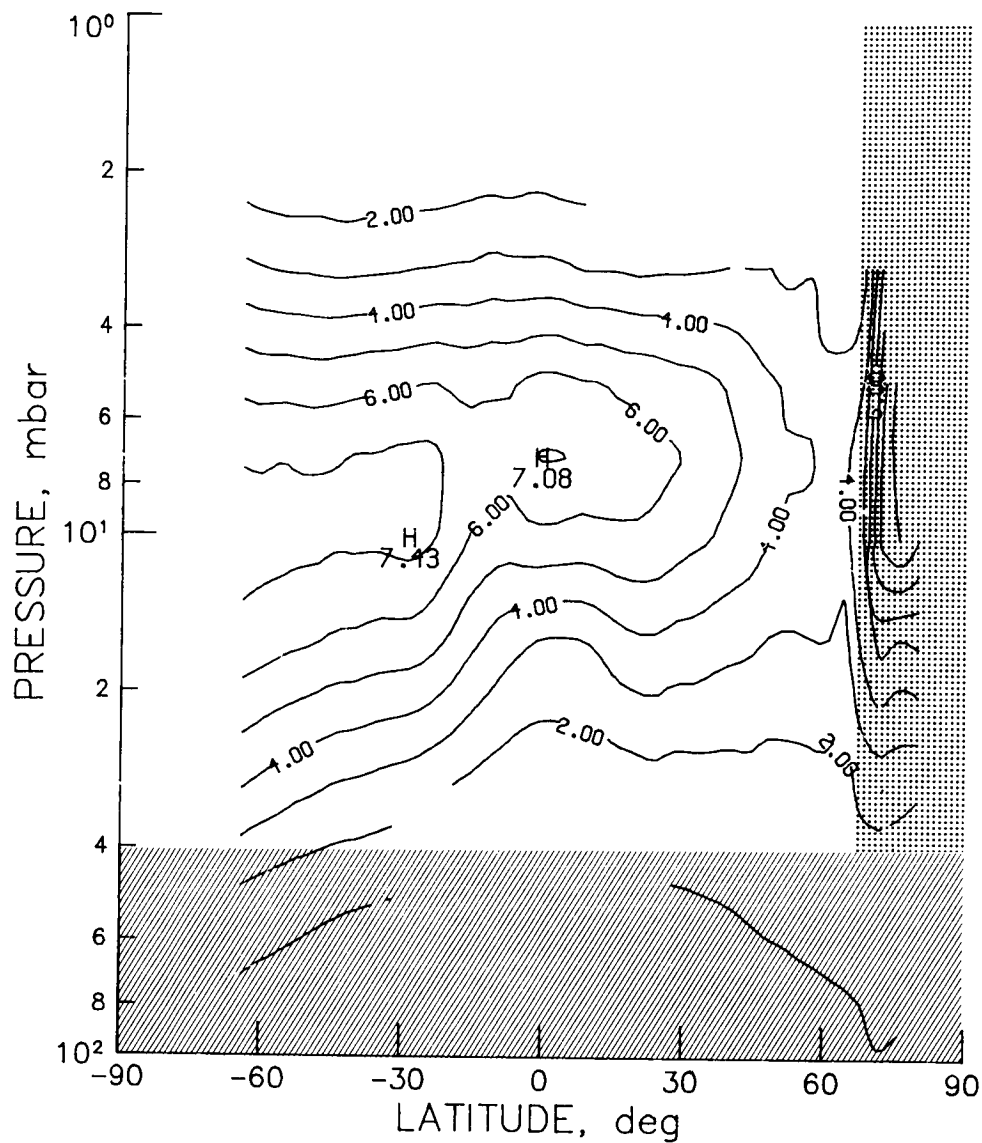


Figure N-2 - LIMS monthly zonal mean daytime NO_2 cross section for December 1978 (contour interval is 1.0 ppbv).

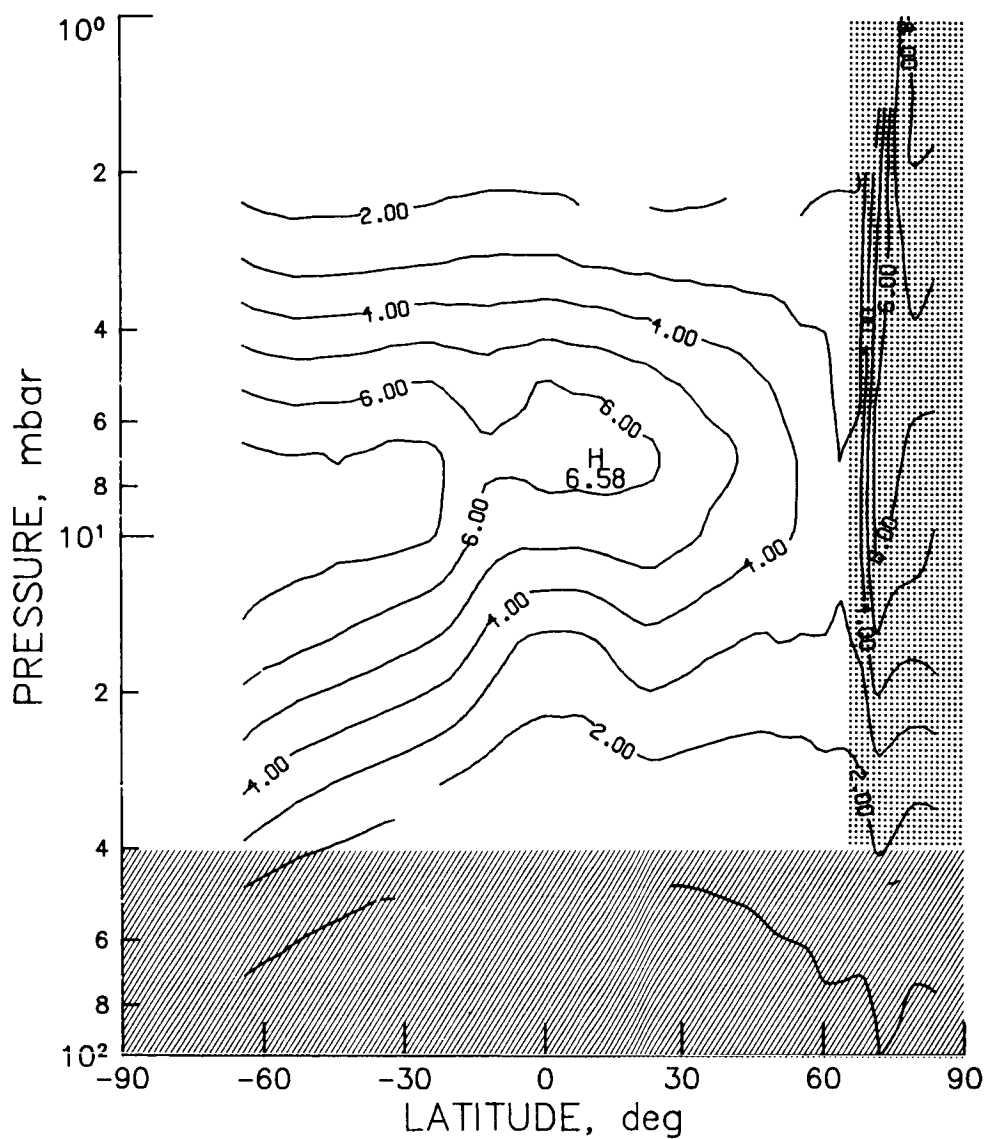


Figure N-3 - LIMS monthly zonal mean daytime NO_2 cross section for January 1979 (contour interval is 1.0 ppbv).

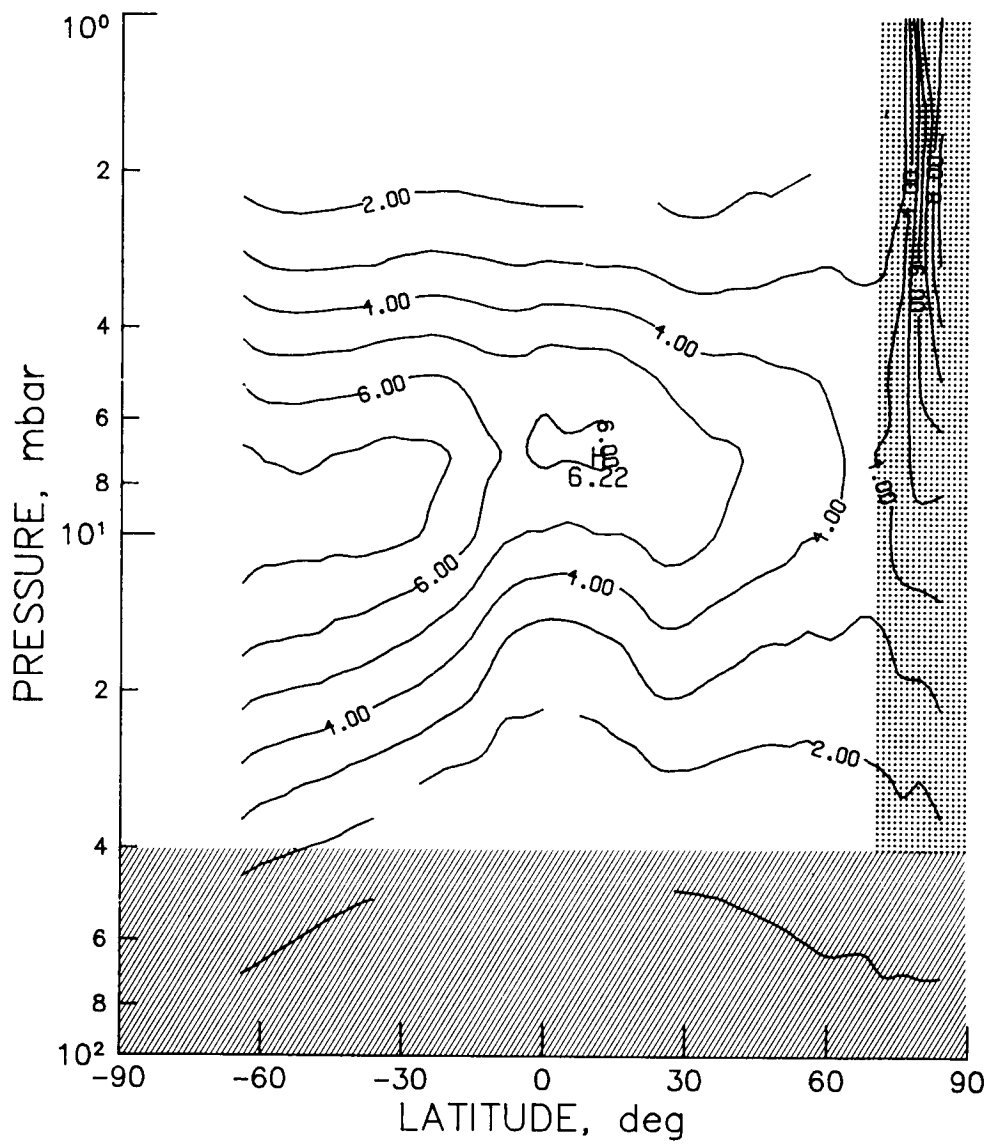


Figure N-4 - LIMS monthly zonal mean daytime NO₂ cross section for February 1979 (contour interval is 1.0 ppbv).

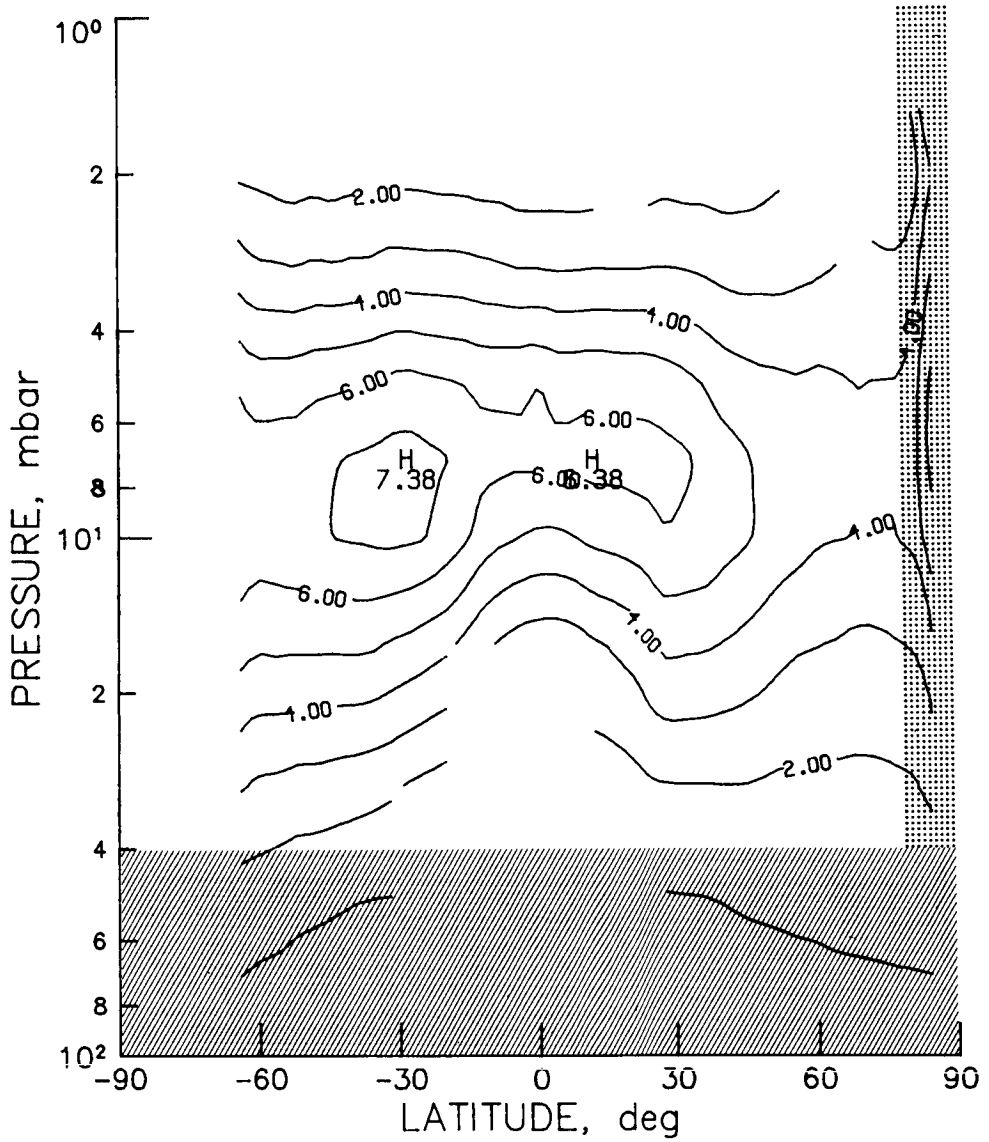


Figure N-5 - LIMS monthly zonal mean daytime NO₂ cross section for March 1979 (contour interval is 1.0 ppbv).

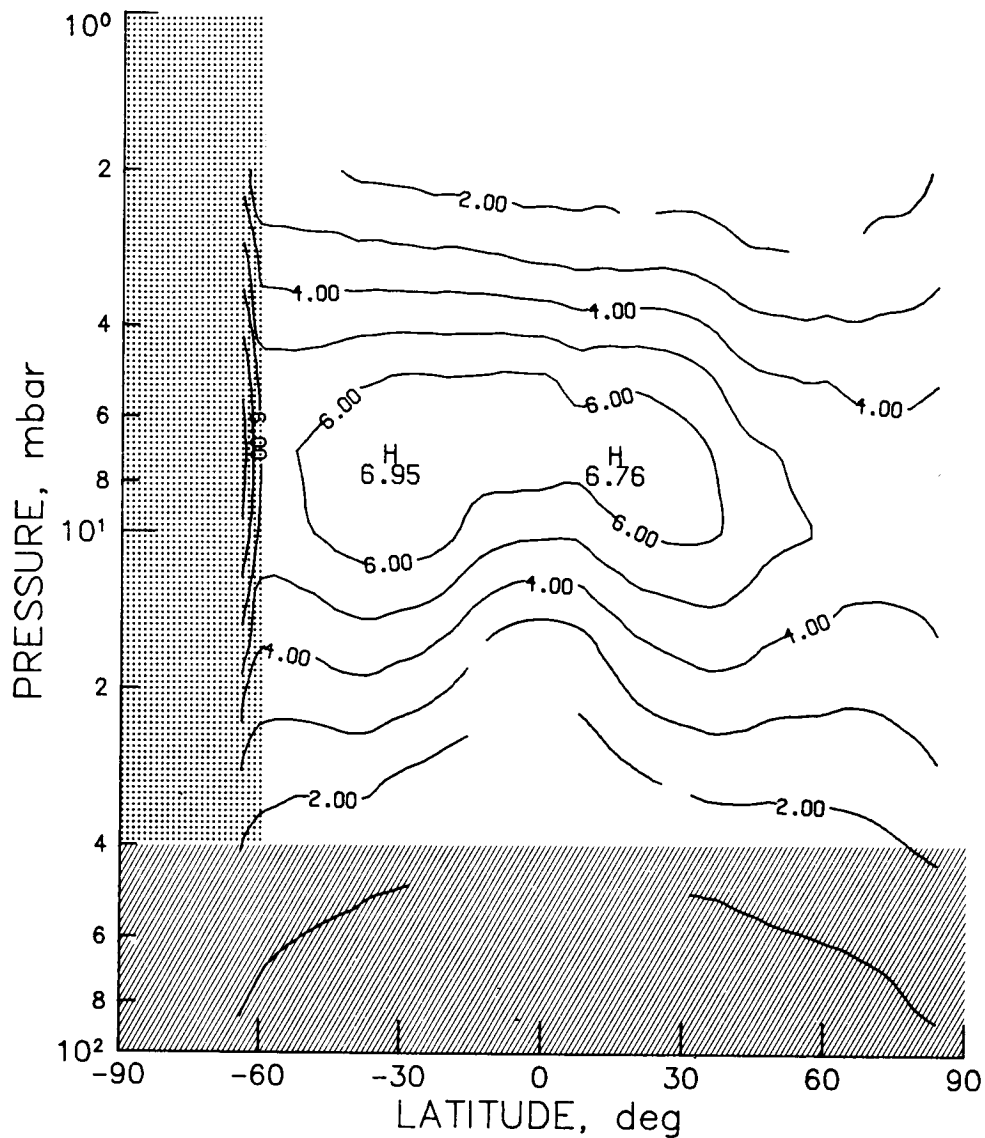


Figure N-6 - LIMS monthly zonal mean daytime NO_2 cross section for April 1979 (contour interval is 1.0 ppbv).

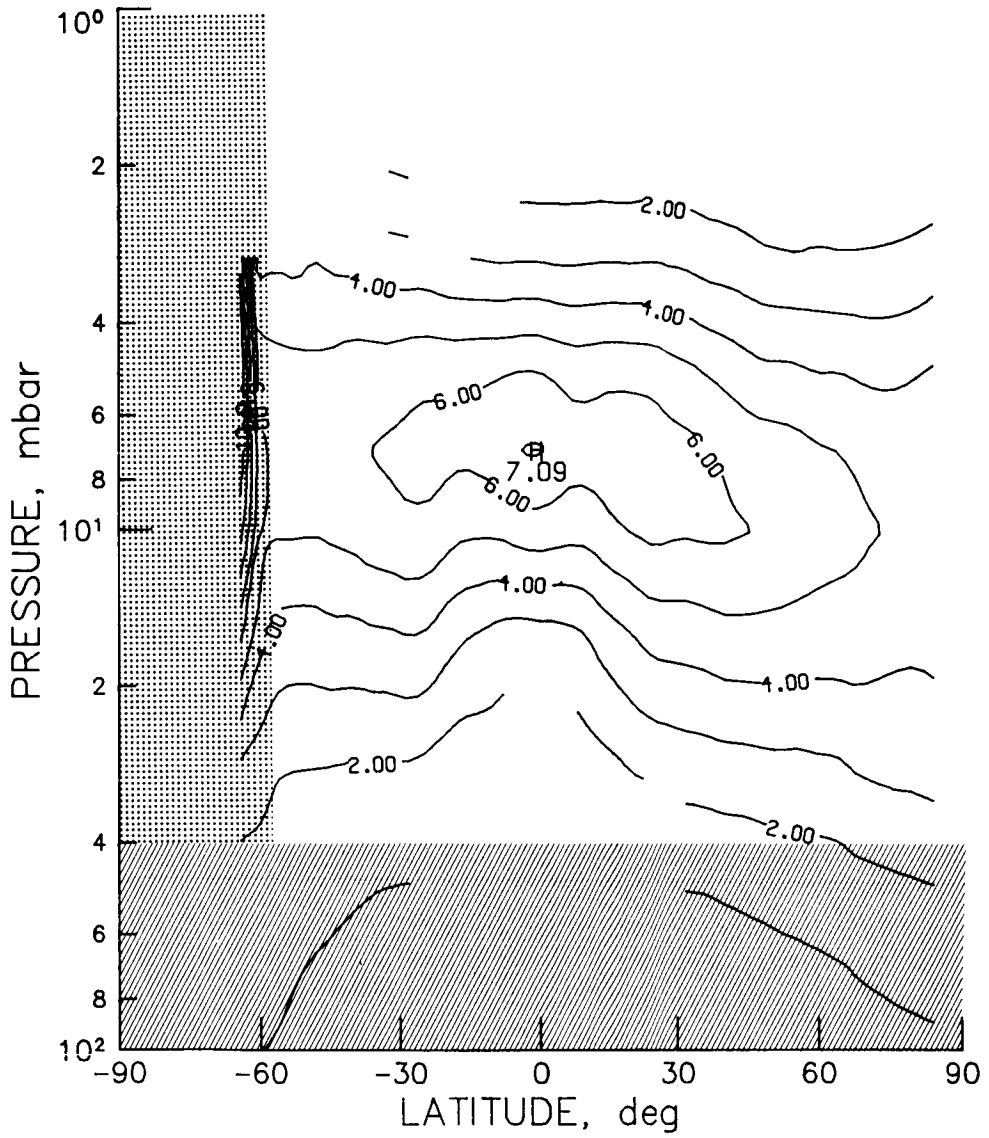


Figure N-7 - LIMS monthly zonal mean daytime NO_2 cross section for May 1979 (contour interval is 1.0 ppbv).

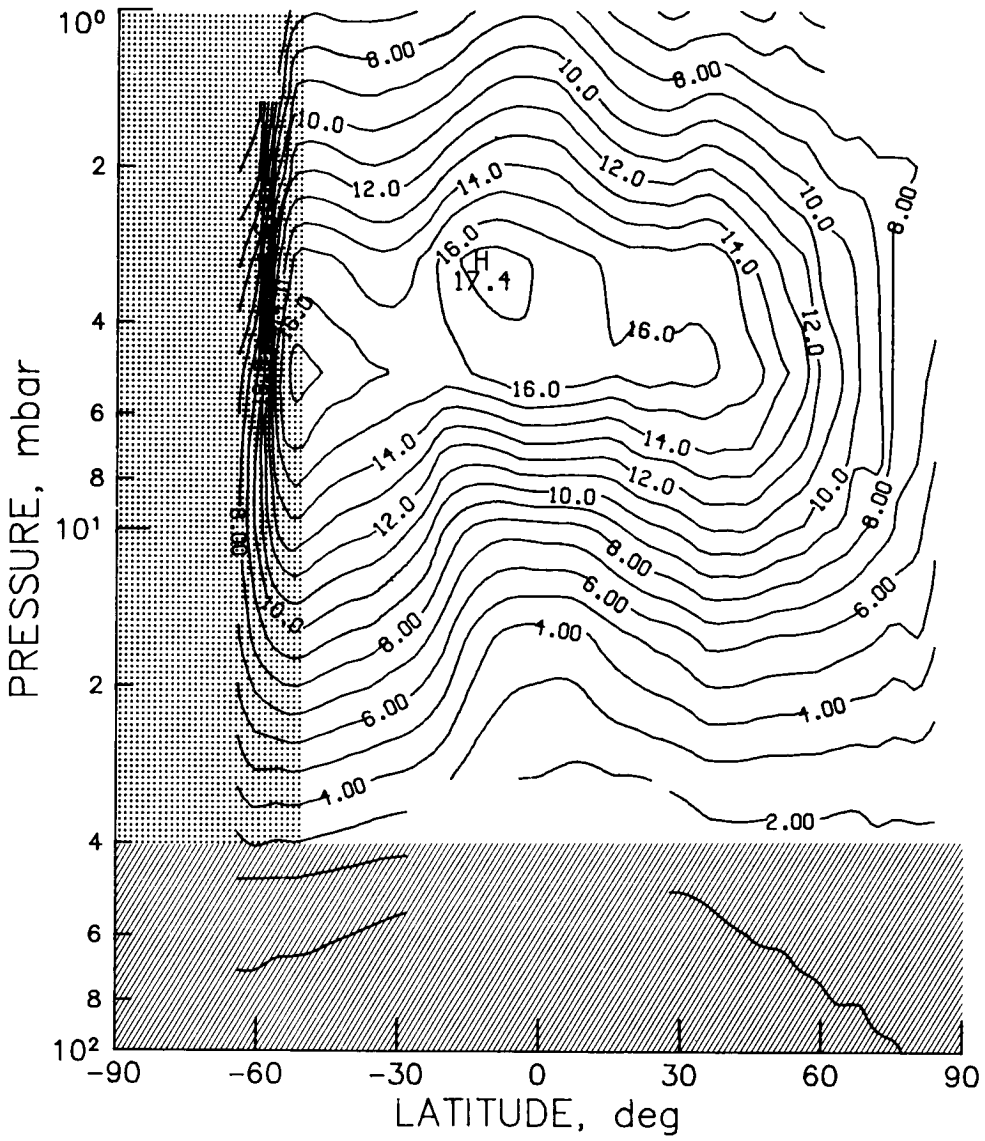


Figure N-8 - LIMS monthly zonal mean nighttime NO₂ cross section for November 1978 (contour interval is 1.0 ppbv).

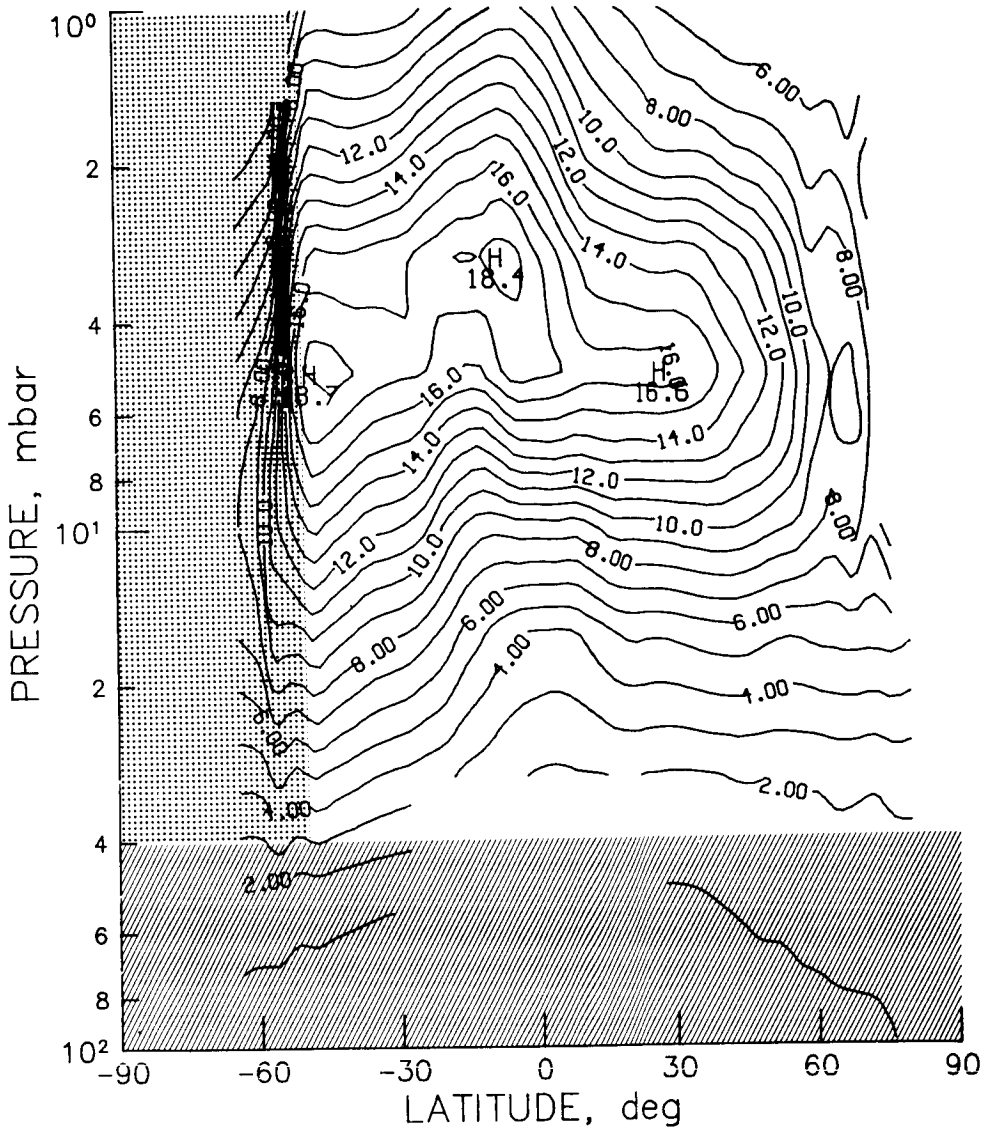


Figure N-9 - LIMS monthly zonal mean nighttime NO_2 cross section for December 1978 (contour interval is 1.0 ppbv).

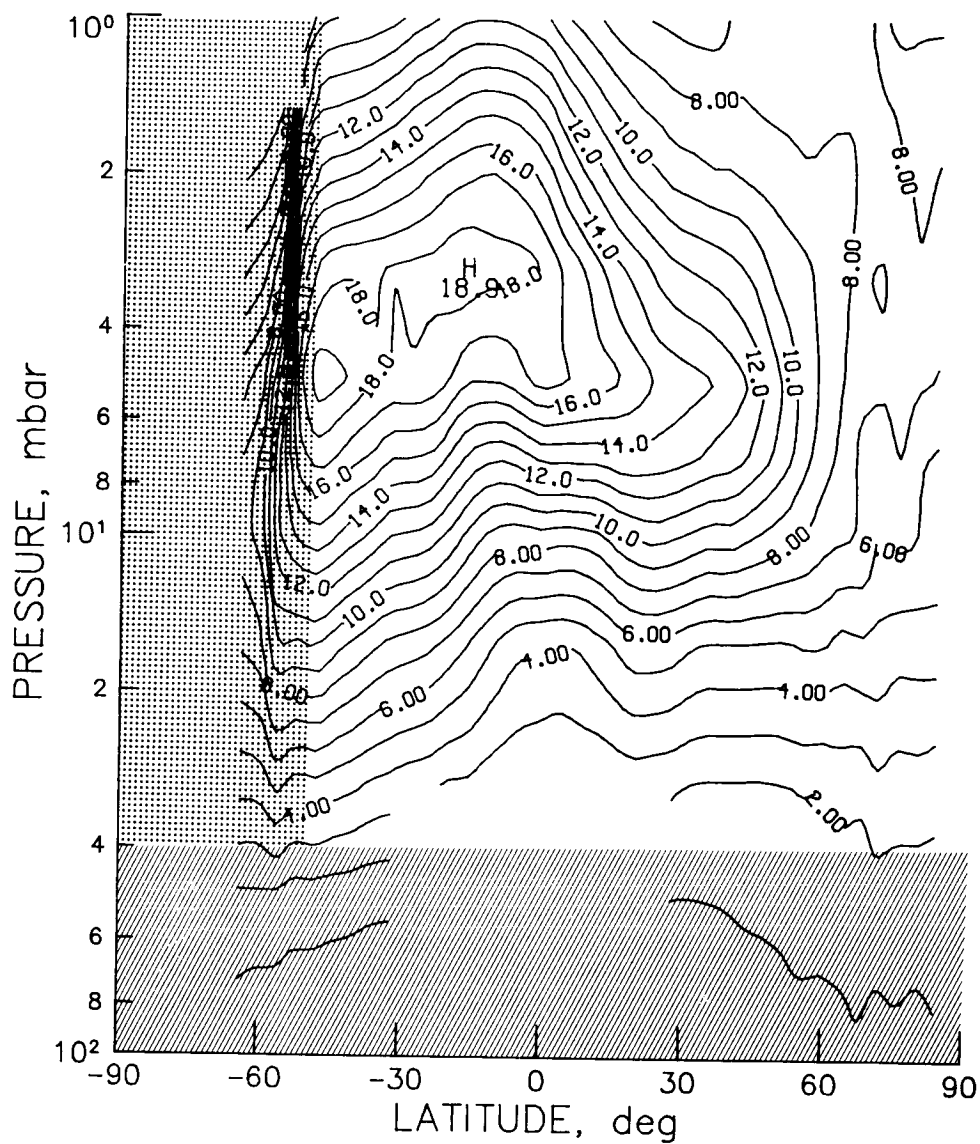


Figure N-10 - LIMS monthly zonal mean nighttime NO_2 cross section for January 1979 (contour interval is 1.0 ppbv).

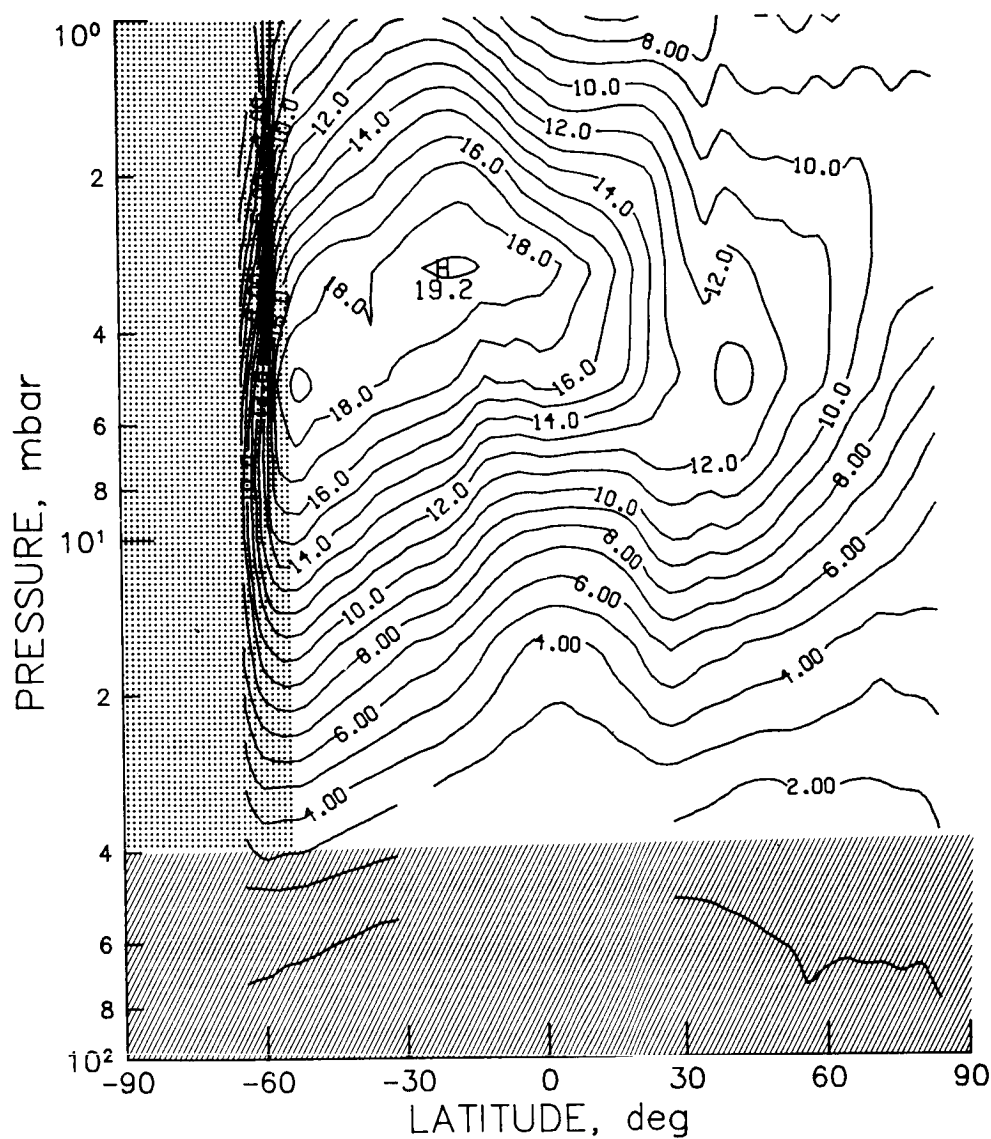


Figure N-11 - LIMS monthly zonal mean nighttime NO₂ cross section for February 1979 (contour interval is 1.0 ppbv).

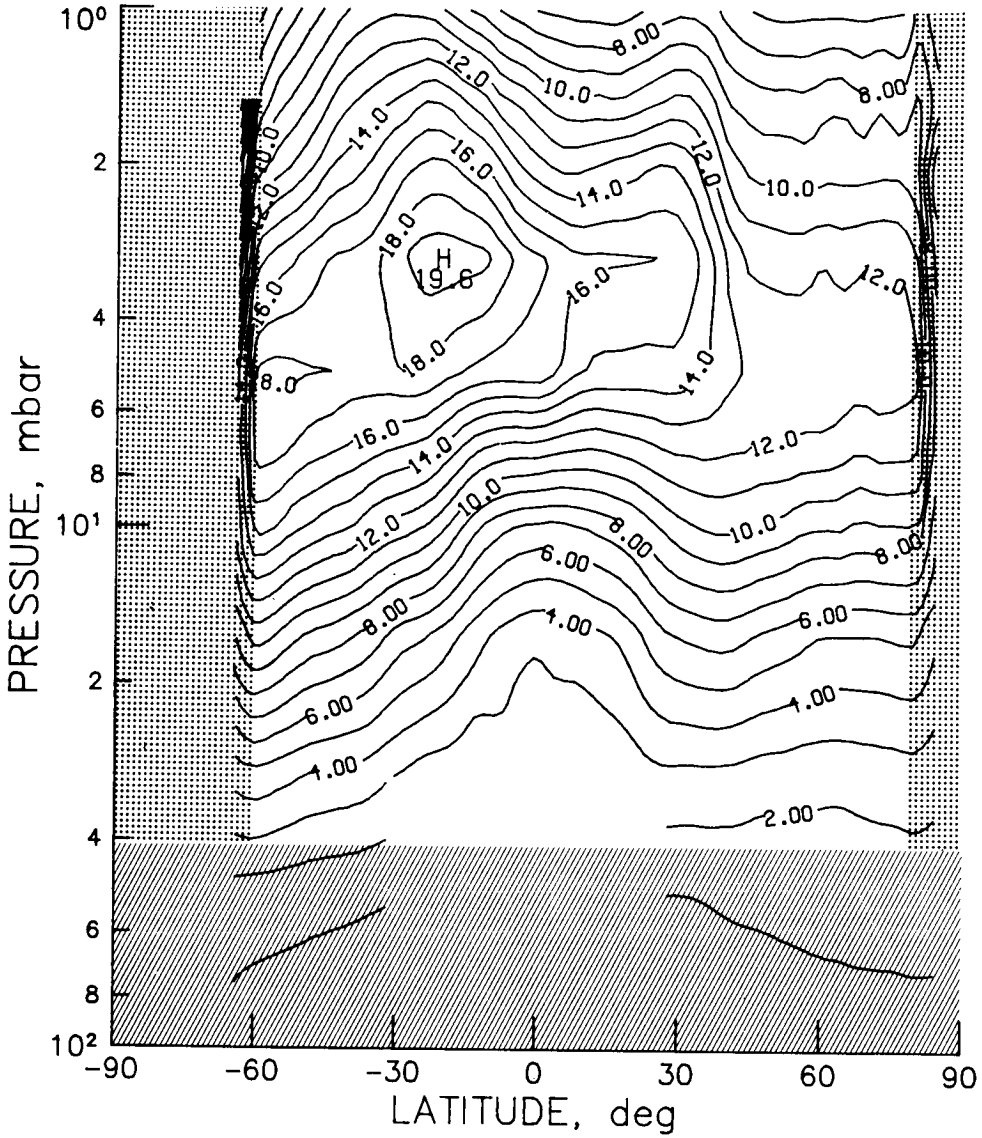


Figure N-12 - LIMS monthly zonal mean nighttime NO_2 cross section for March 1979 (contour interval is 1.0 ppbv).

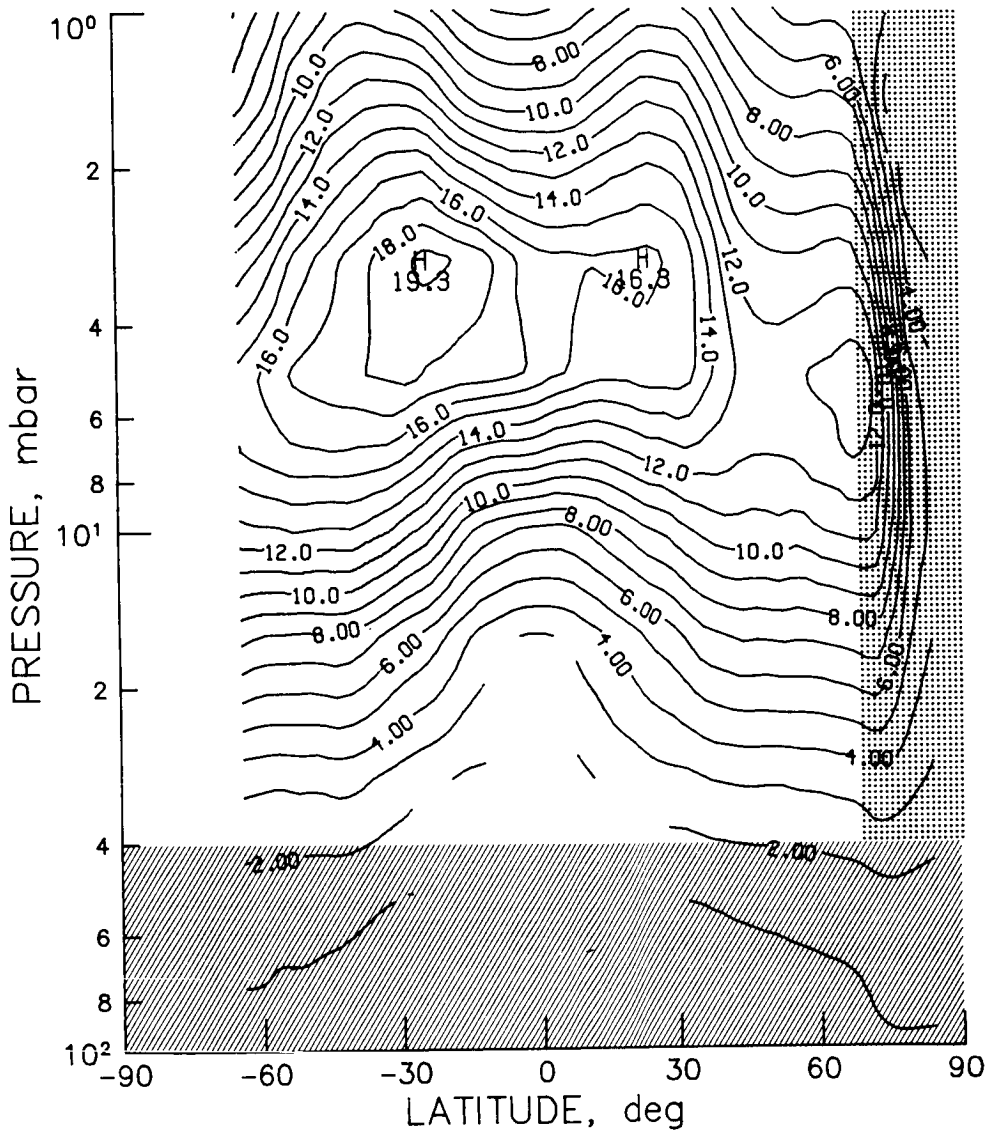


Figure N-13 - LIMS monthly zonal mean nighttime NO₂ cross section for April 1979 (contour interval is 1.0 ppbv).

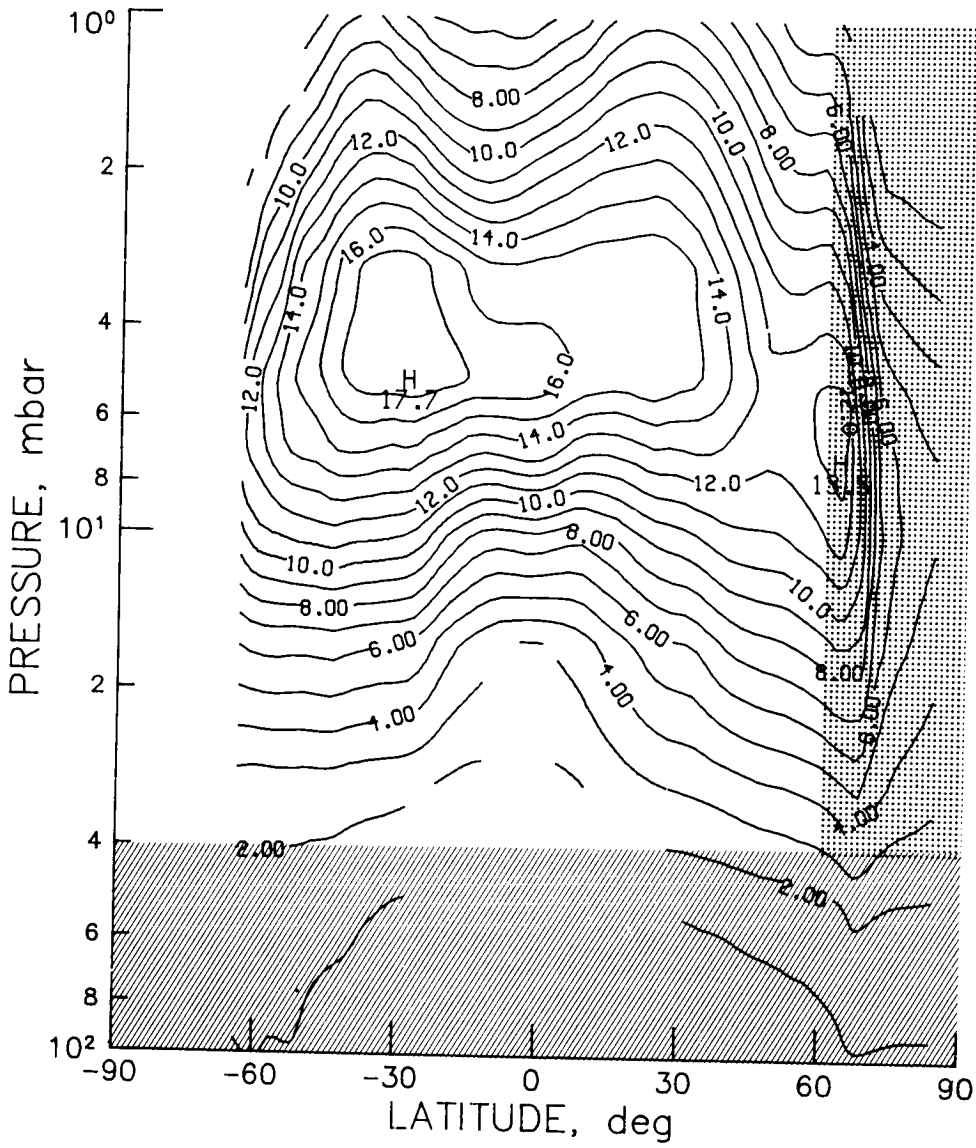
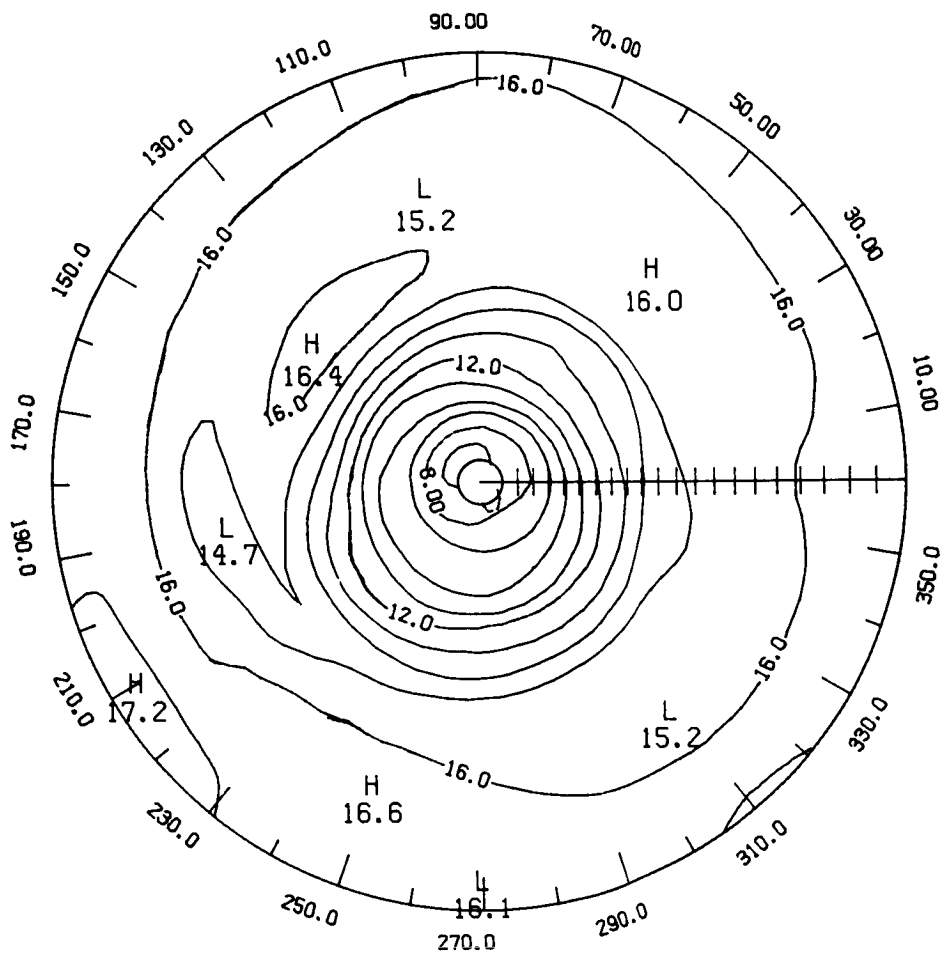
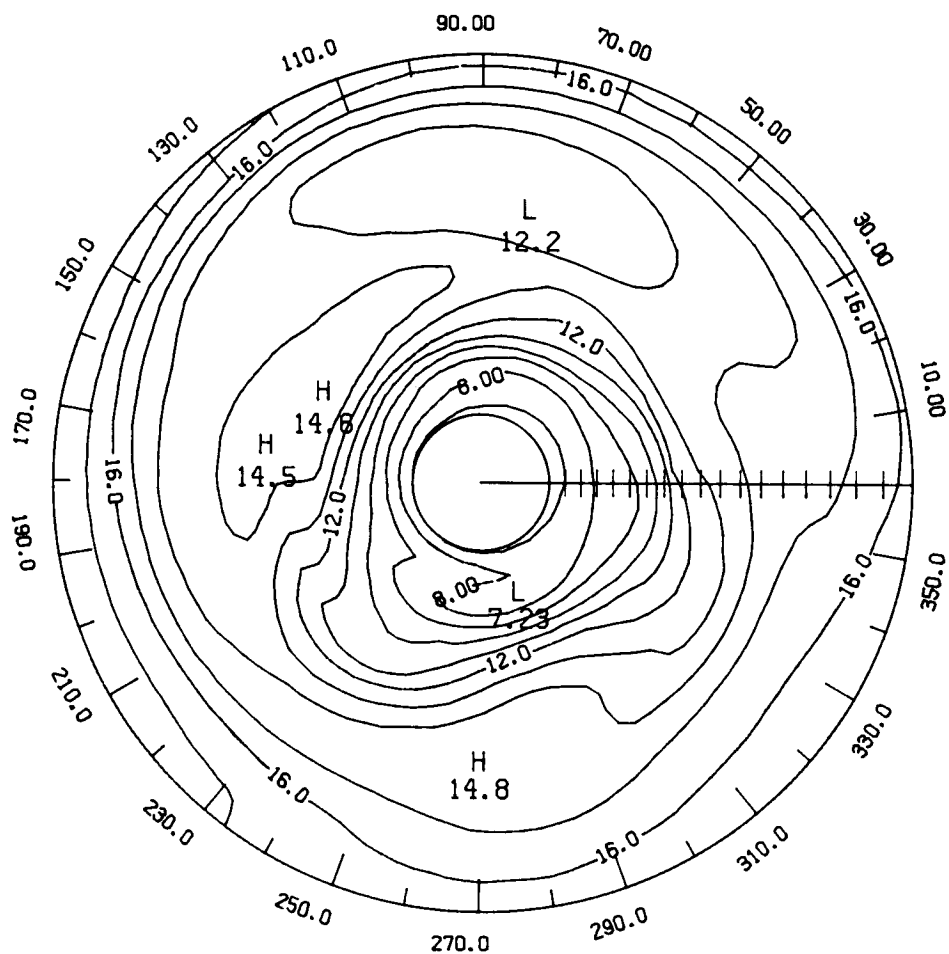


Figure N-14 - LIMS monthly zonal mean nighttime NO_2 cross section for May 1979 (contour interval is 1.0 ppbv).



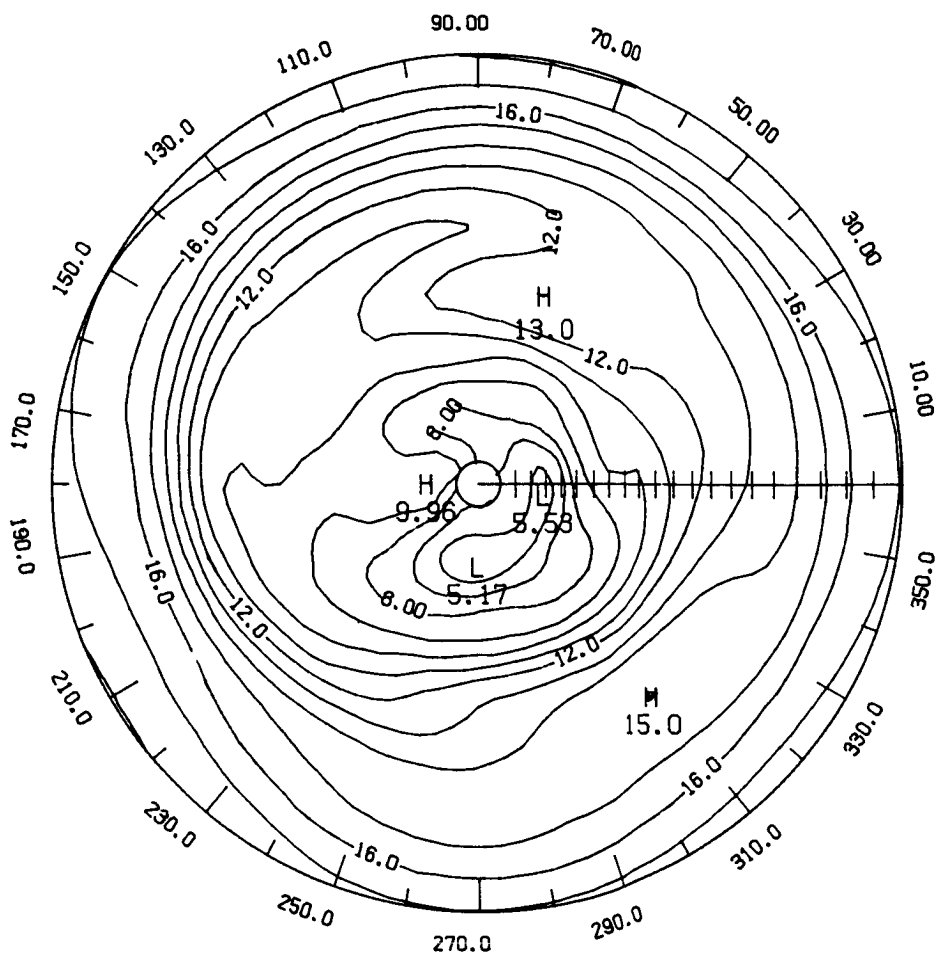
LATITUDE 0. TO 84.
1 2 1 LAT SMOOTHING

Figure N-15 - LIMS NO₂ monthly mean nighttime 3 mb polar stereographic plot for November 1978 (contour interval is 1.0 ppbv).



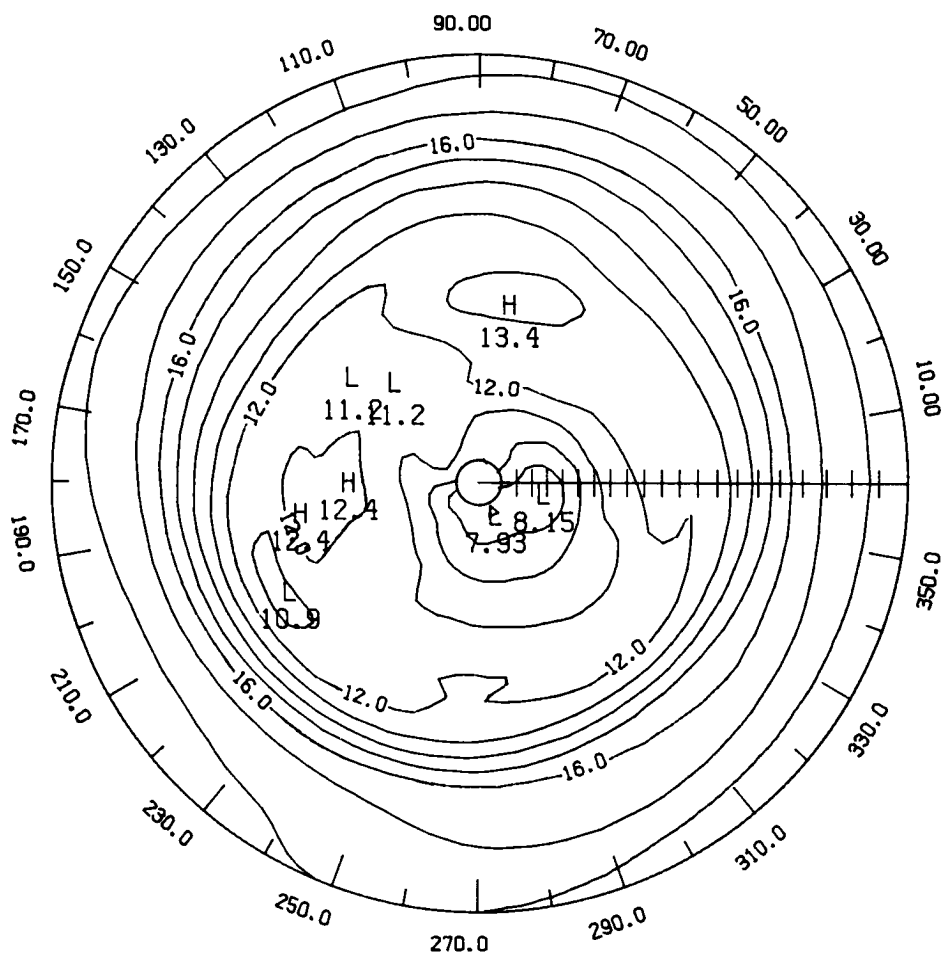
LATITUDE 0. TO 72.
1 2 1 LAT SMOOTHING

Figure N-16 - LIMS NO₂ monthly mean nighttime 3 mb polar stereographic plot for December 1978 (contour interval is 1.0 ppbv).



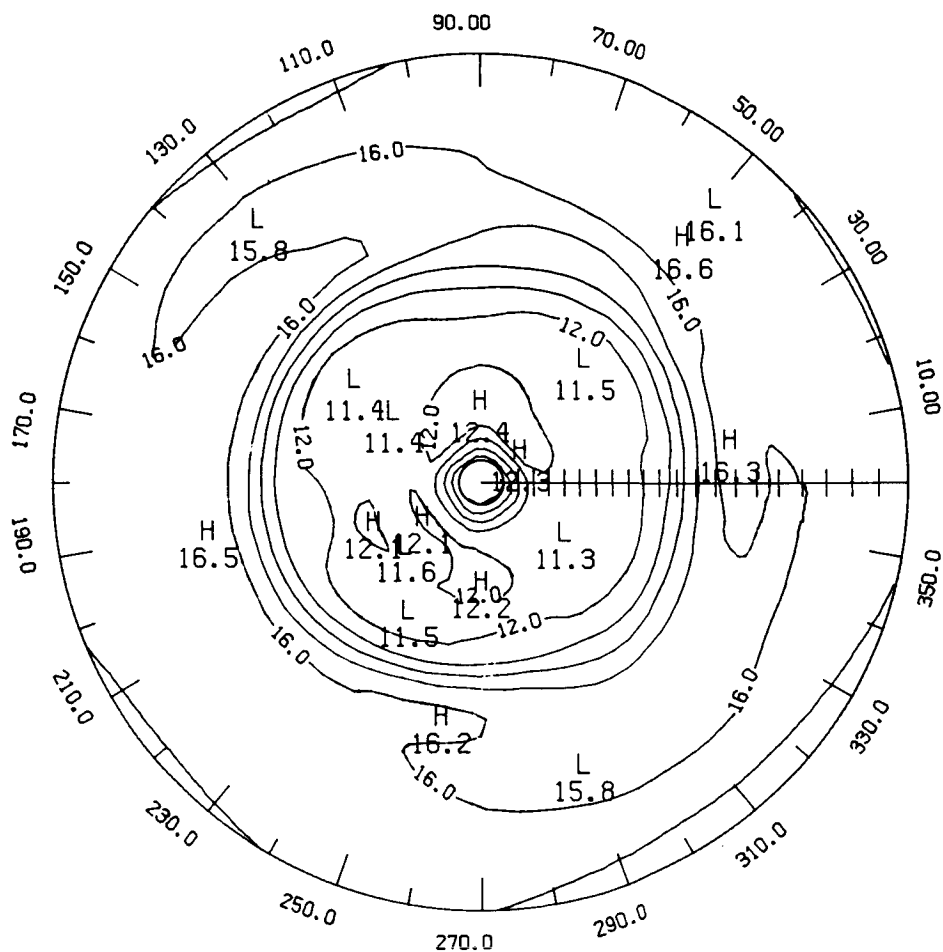
LATITUDE 0. TO 84.
1 2 1 LAT SMOOTHING

Figure N-17 - LIMS NO₂ monthly mean nighttime 3 mb polar stereographic plot for January 1979 (contour interval is 1.0 ppbv).



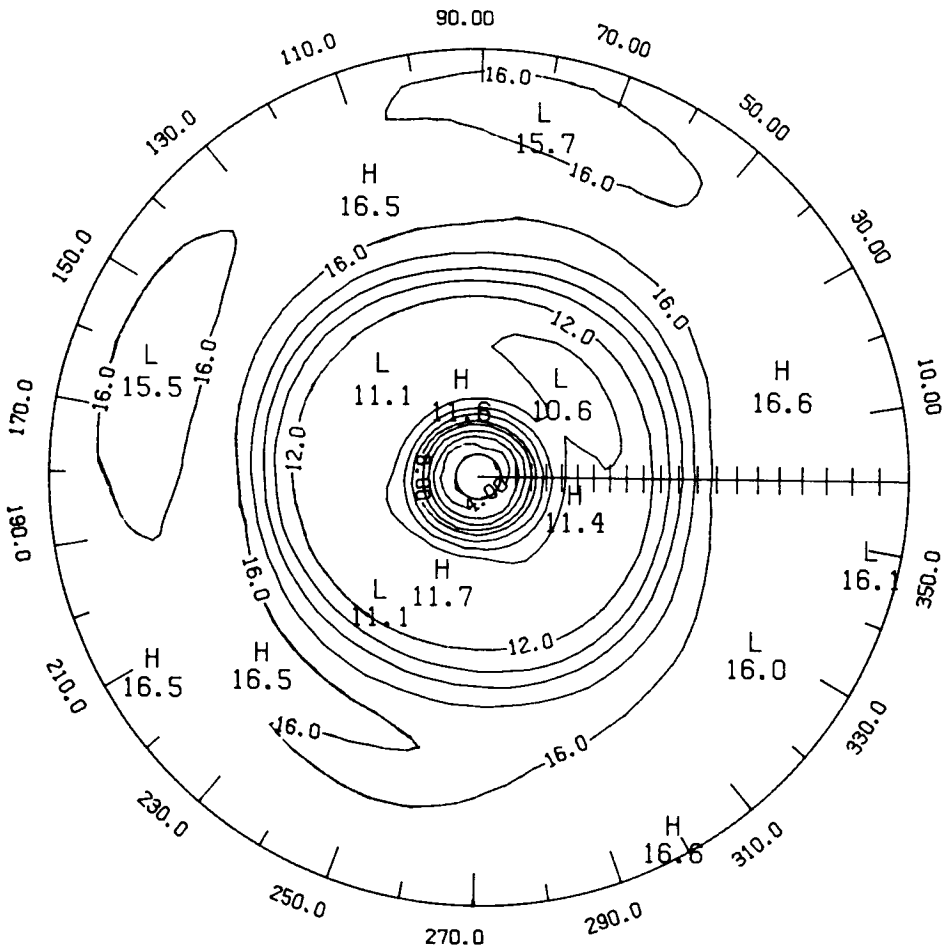
LATITUDE 0. TO 84.
1 2 1 LAT SMOOTHING

Figure N-18 - LIMS NO₂ monthly mean nighttime 3 mb polar stereographic plot for February 1979 (contour interval is 1.0 ppbv).



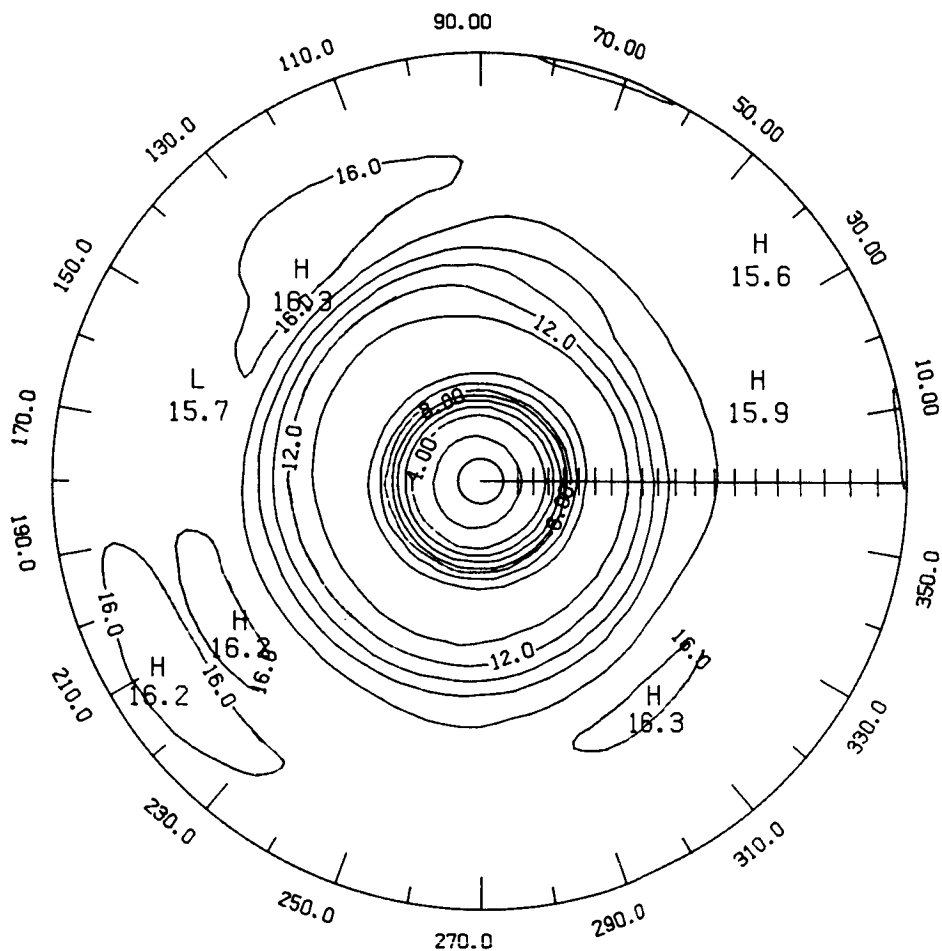
LATITUDE 0. TO 84.
1 2 1 LAT SMOOTHING

Figure N-19 - LIMS NO₂ monthly mean nighttime 3 mb polar stereographic plot for March 1979 (contour interval is 1.0 ppbv).



LATITUDE 0. TO 84.
1 2 1 LAT SMOOTHING

Figure N-20 - LIMS NO₂ monthly mean nighttime 3 mb polar stereographic plot for April 1979 (contour interval is 1.0 ppbv).



LATITUDE 0. TO 84.
1 2 1 LAT SMOOTHING

Figure N-21 - LIMS NO₂ monthly mean nighttime 3 mb polar stereographic plot for May 1979 (contour interval is 1.0 ppbv).

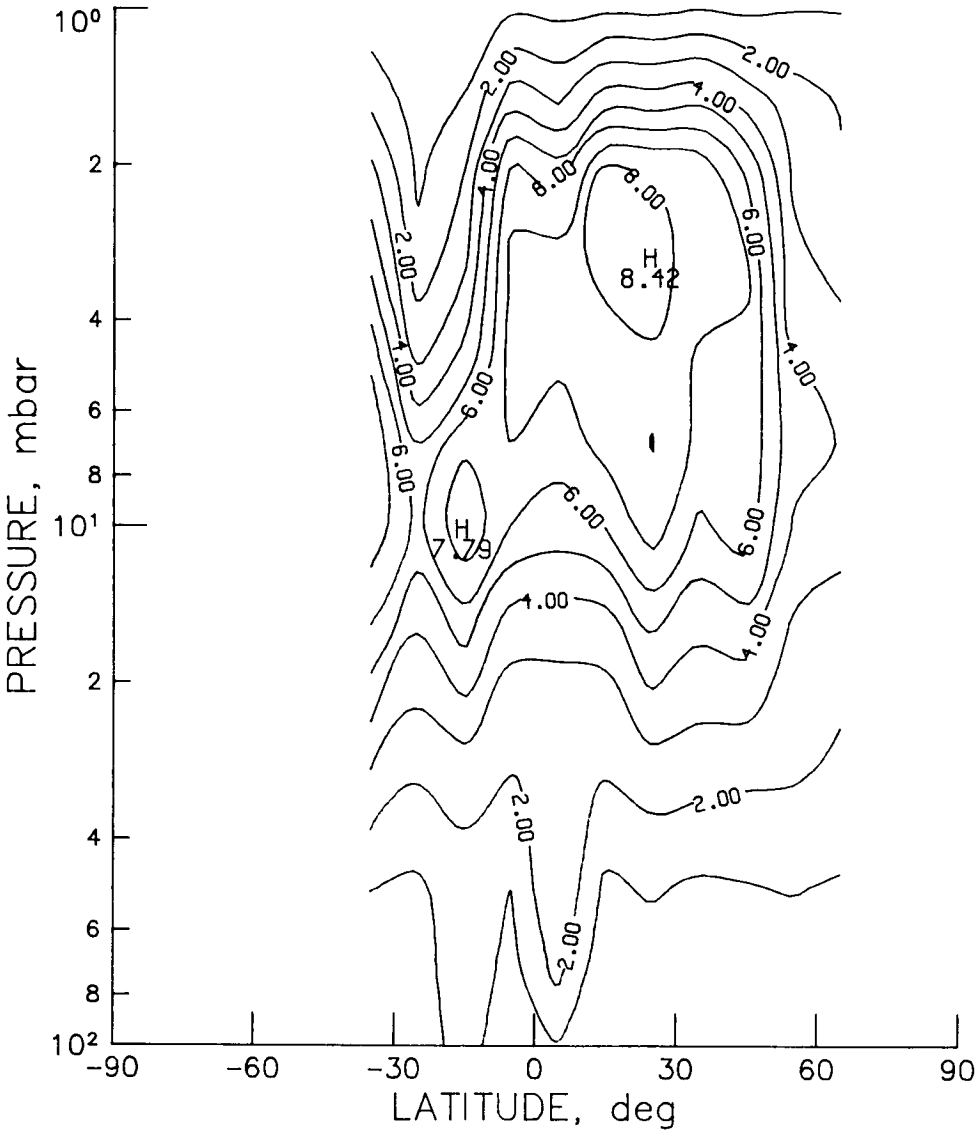


Figure N-22 - SAGE sunset monthly zonal Mean NO₂ cross section for March 1979 (contour interval is 1.0 ppbv).

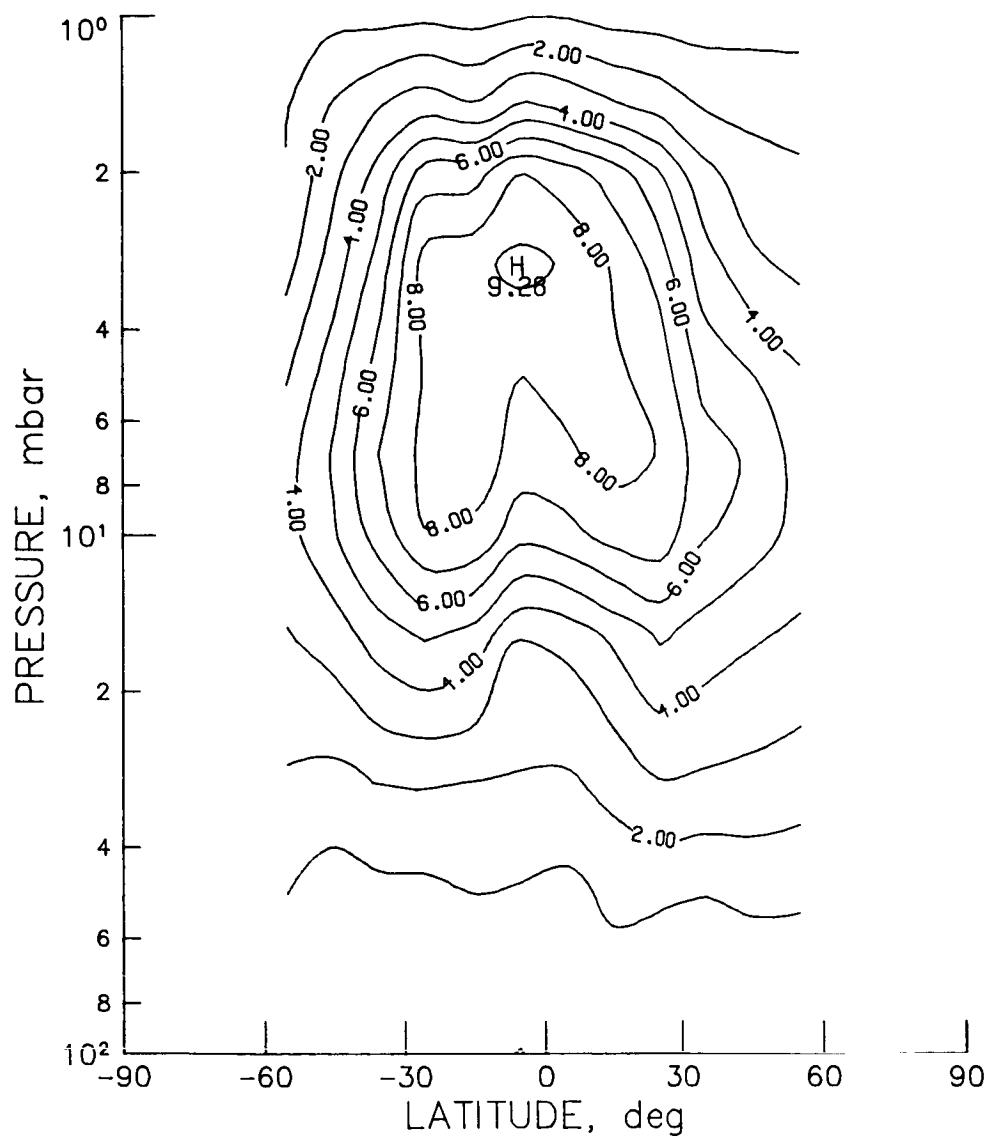


Figure N-23 - SAGE sunset monthly zonal mean NO_2 cross section for April 1979 (contour interval is 1.0 ppbv).

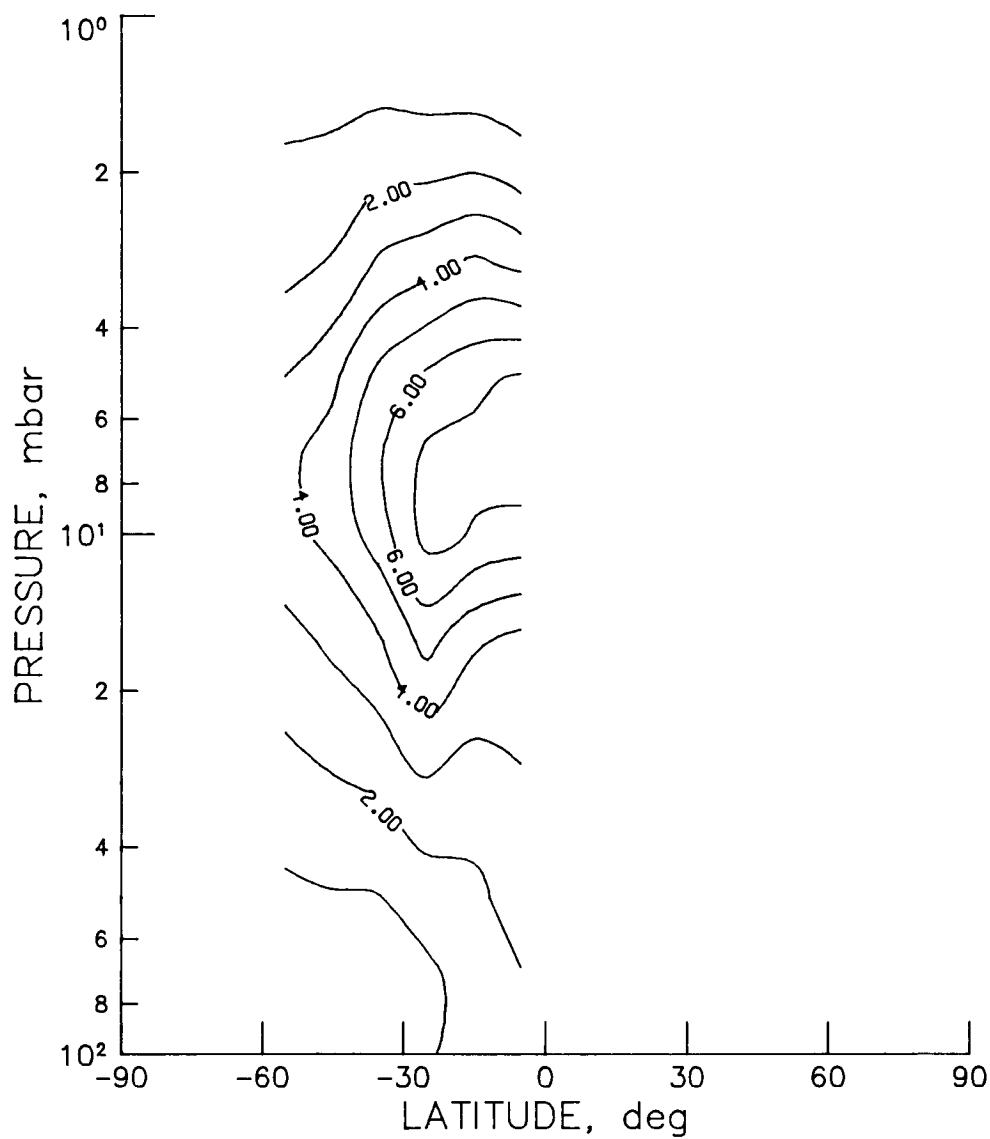


Figure N-24 - SAGE sunset monthly zonal mean NO_2 cross section for May 1979 (contour interval is 1.0 ppbv).

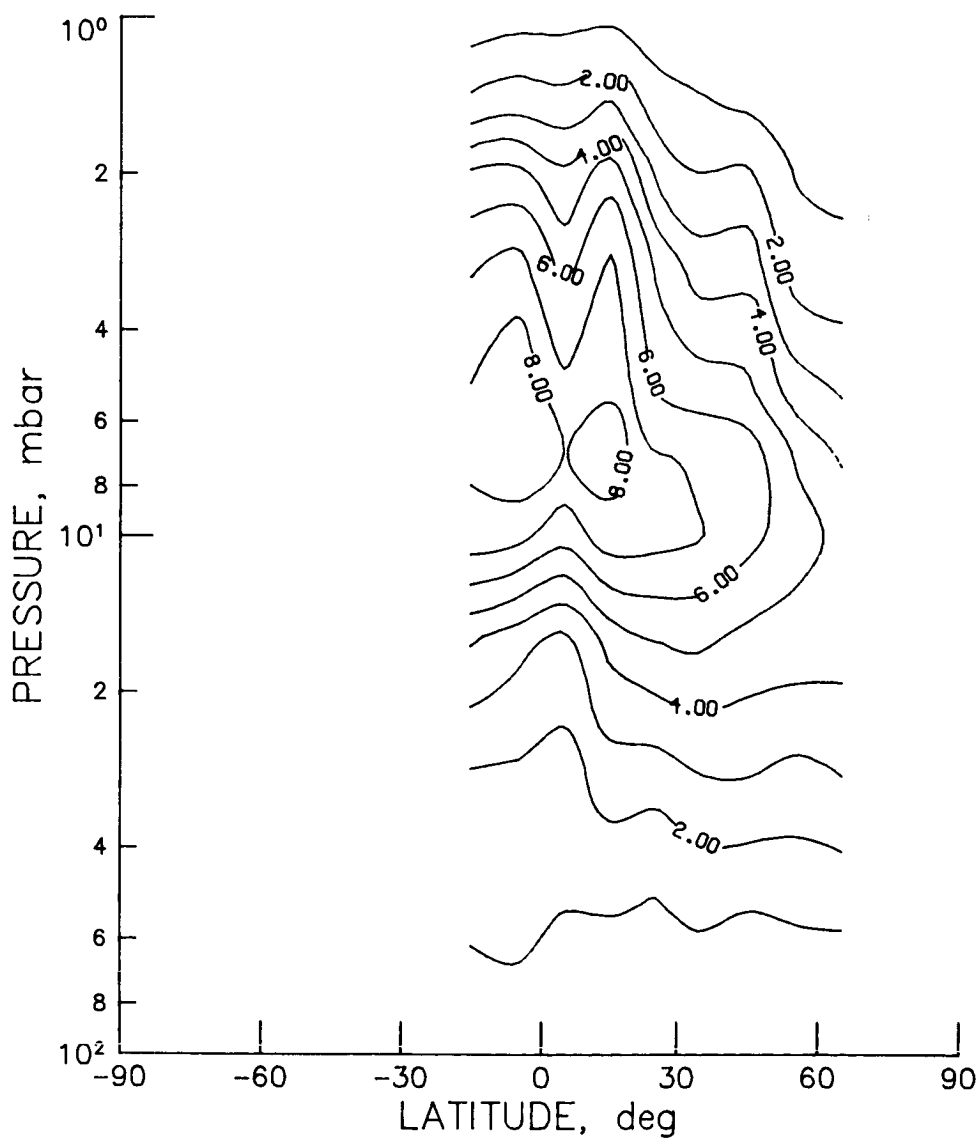


Figure N-25 - SAGE sunset monthly zonal mean NO_2 cross section for August 1979 (contour interval is 1.0 ppbv).

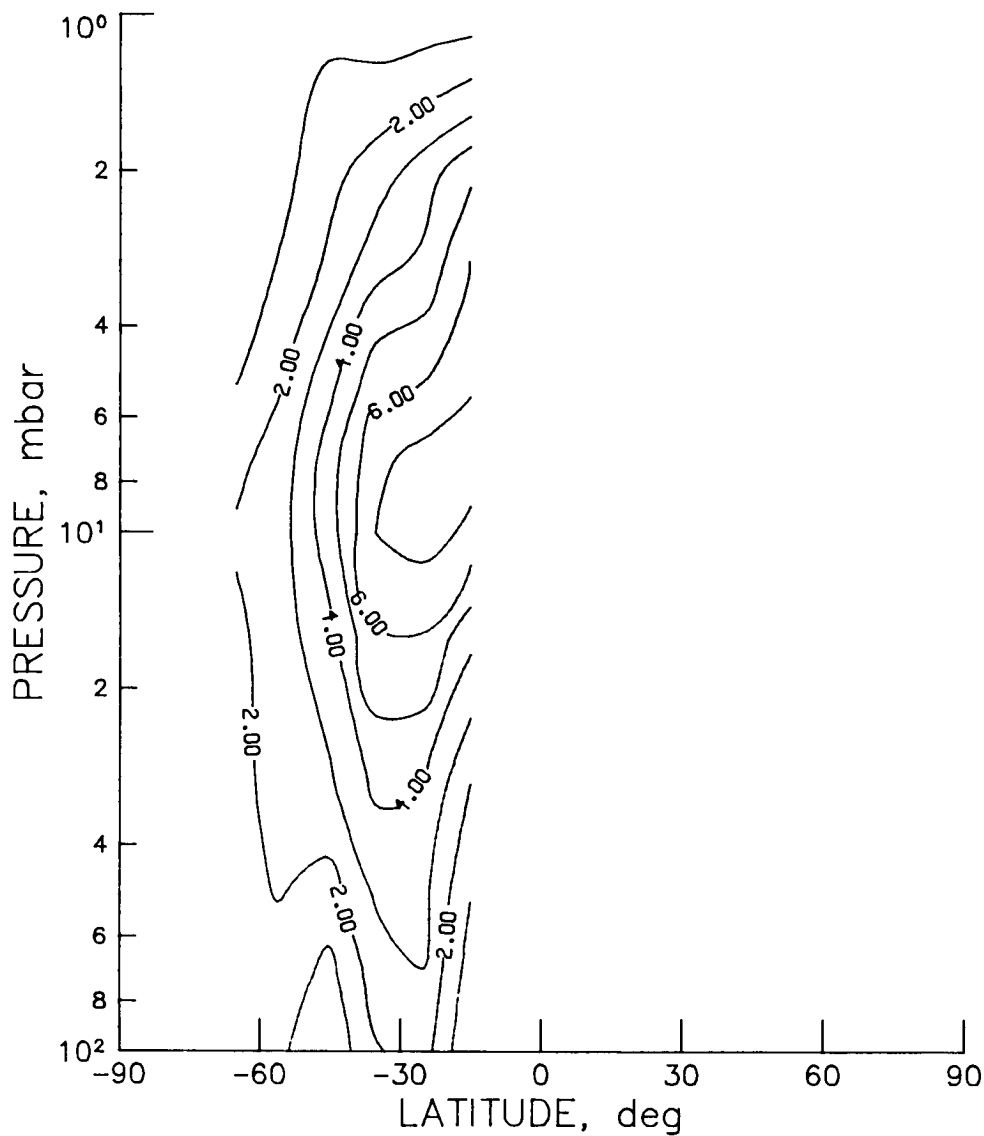


Figure N-26 - SAGE sunset monthly zonal mean NO_2 cross section for September 1979 (contour interval is 1.0 ppbv).

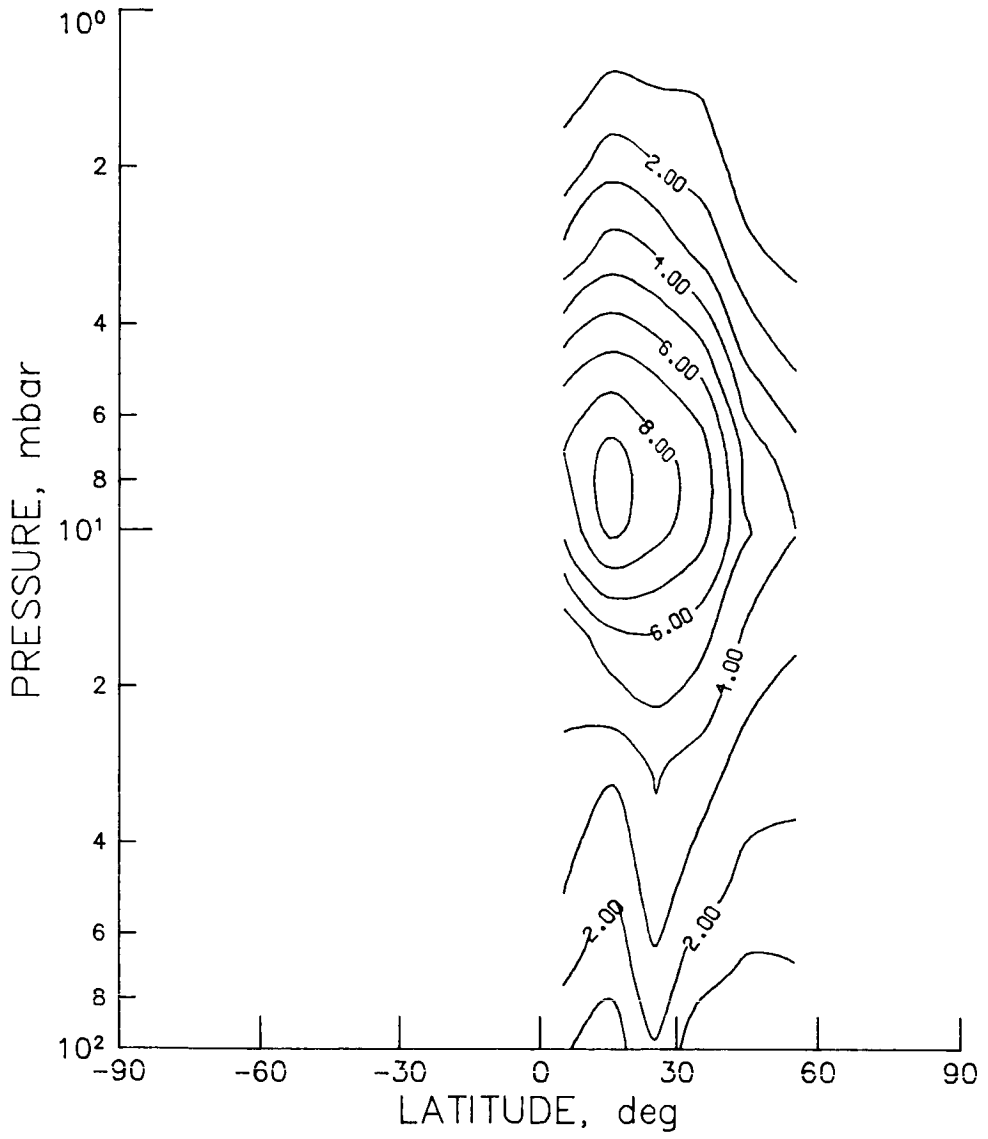


Figure N-27 - SAGE sunset Monthly Zonal Mean NO_2 cross section for October 1979 (contour interval is 1.0 ppbv).

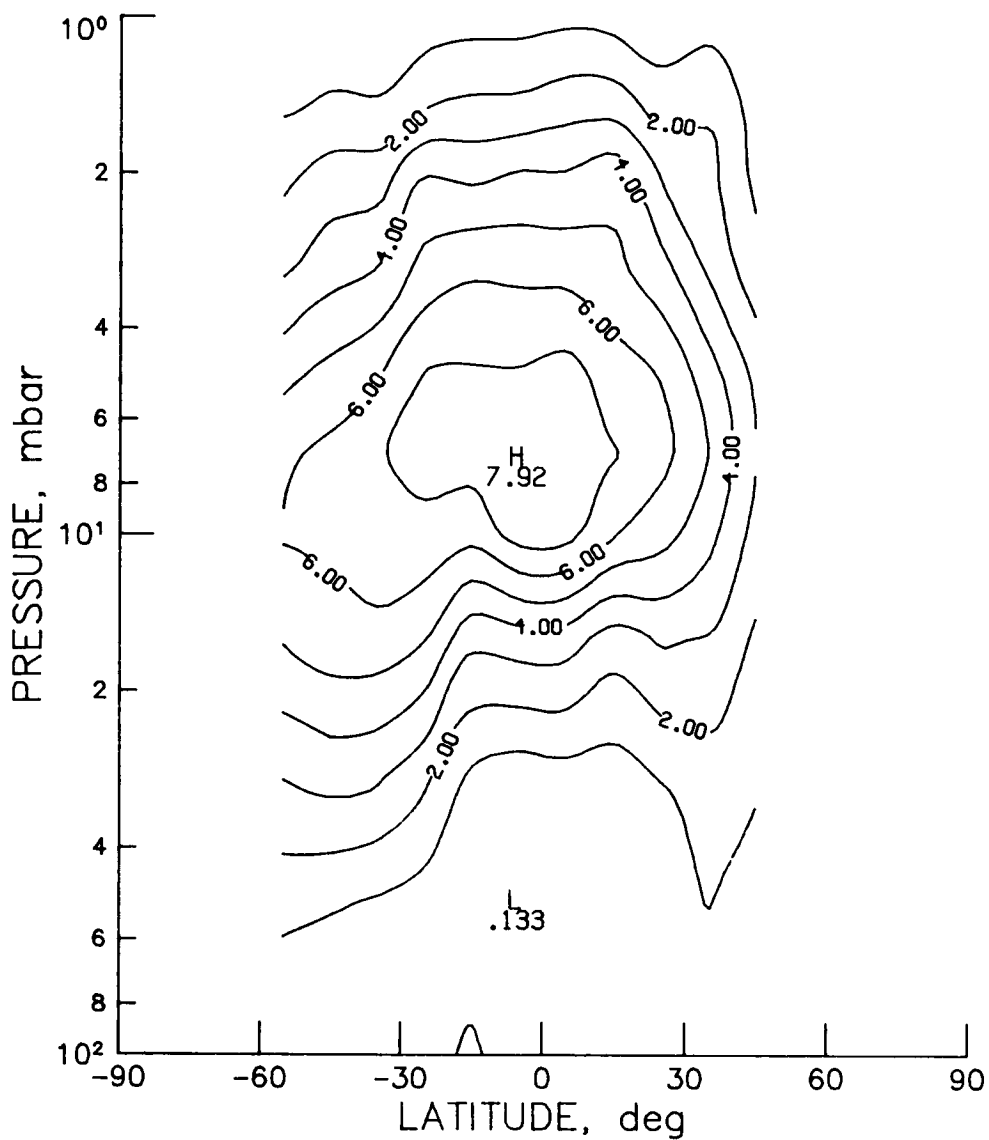


Figure N-28 - SAGE sunset monthly zonal mean NO_2 cross section for December 1979 (contour interval is 1.0 ppbv).

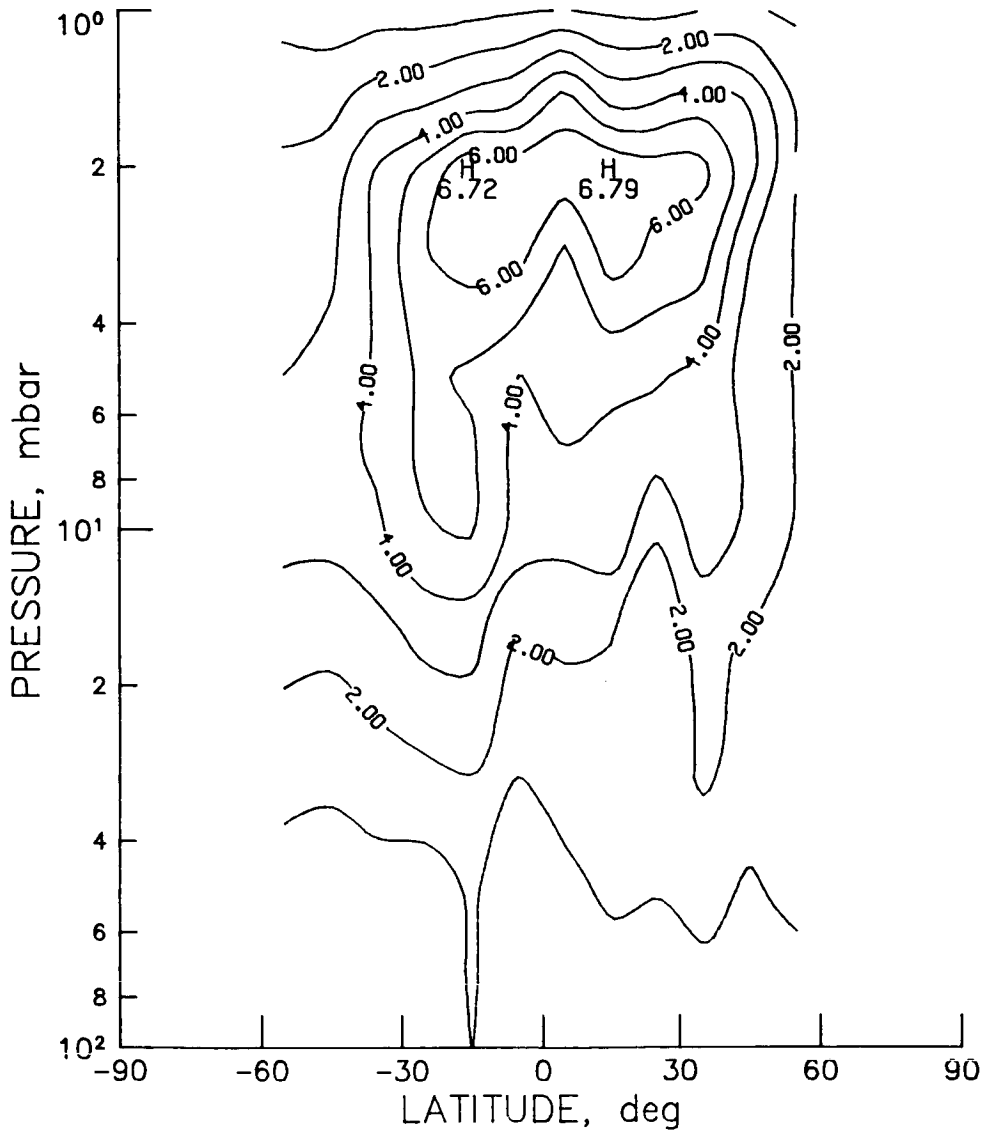


Figure N-29 - SAGE sunrise monthly zonal mean NO₂ cross section for March 1979 (contour interval is 1.0 ppbv).

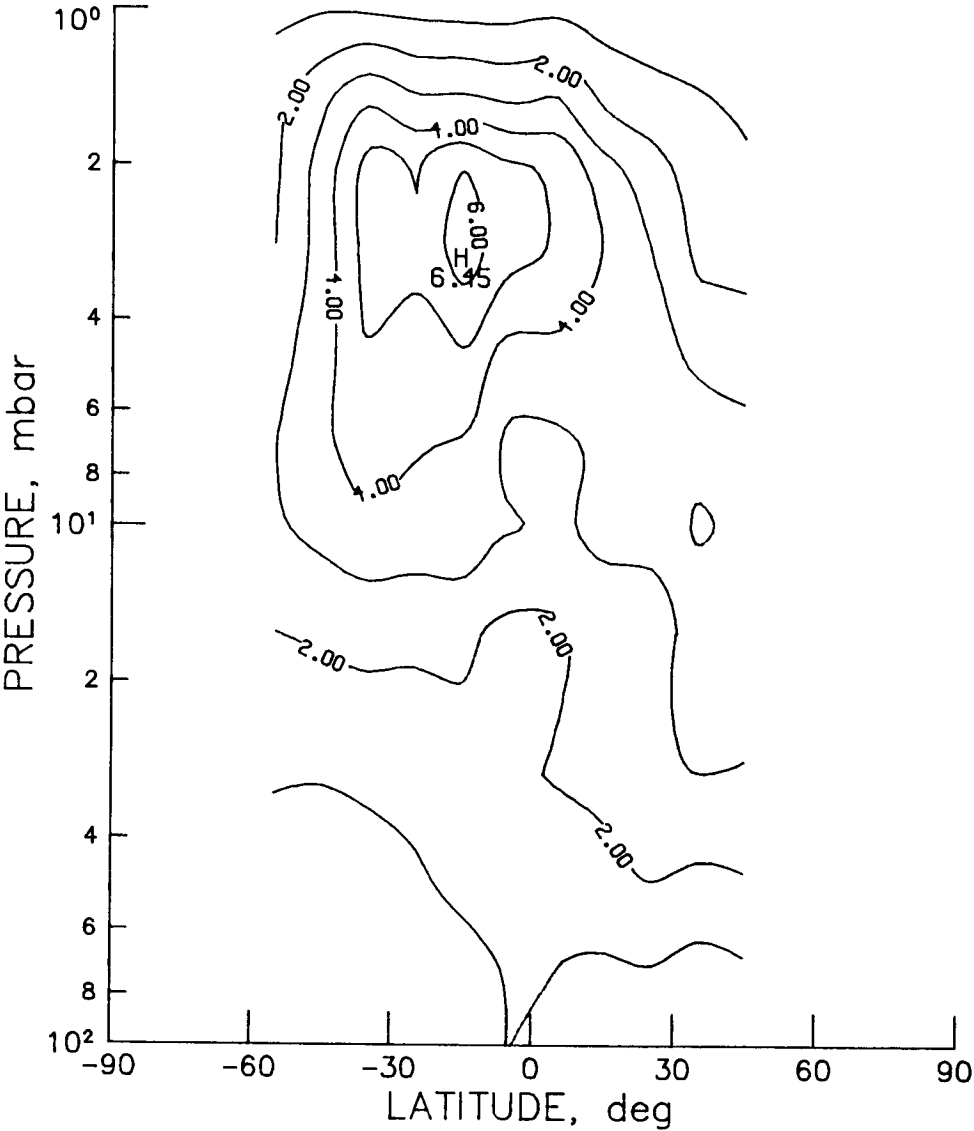


Figure N-30 - SAGE sunrise monthly zonal mean NO₂ cross section for April 1979 (contour interval is 1.0 ppbv).

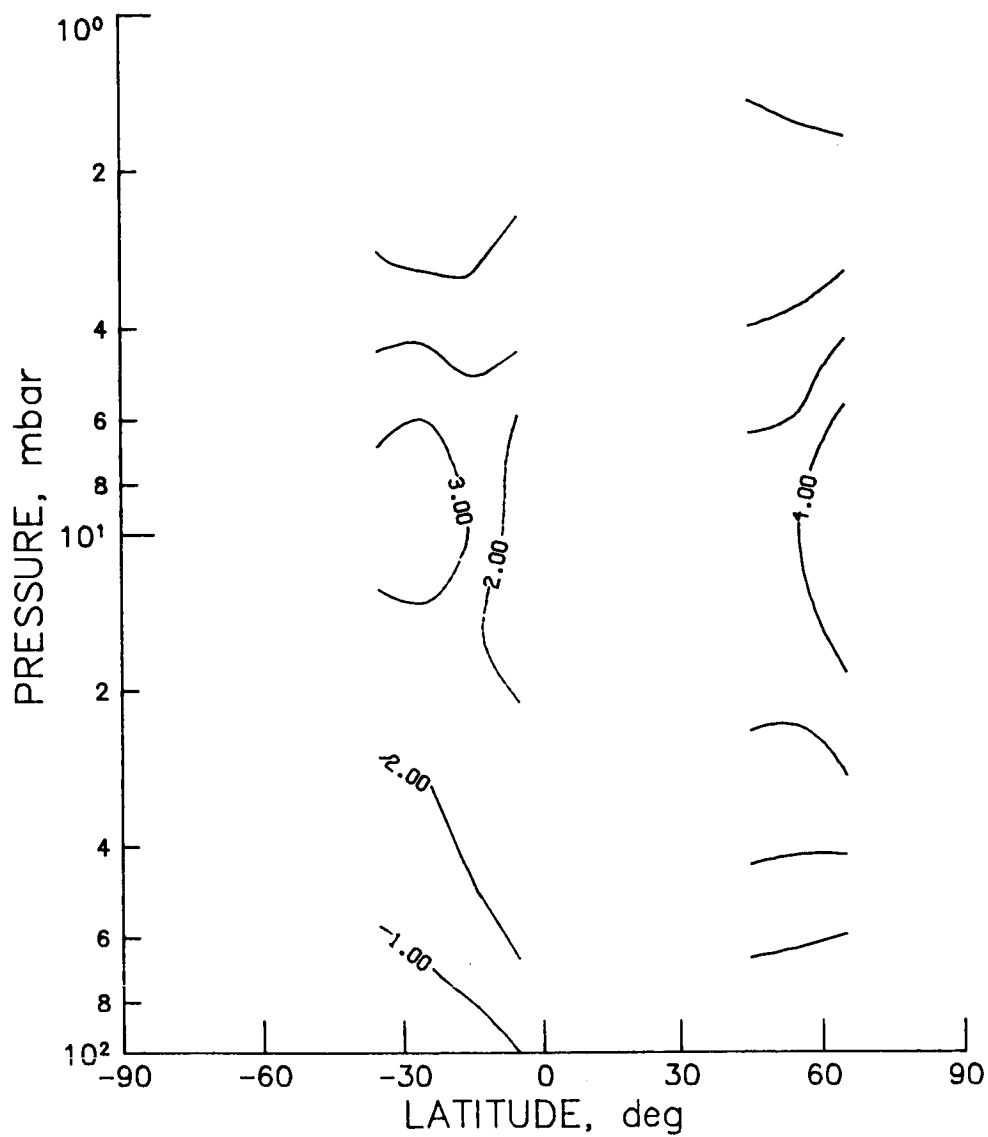


Figure N-31 - SAGE sunrise monthly zonal mean NO_2 cross section for May 1979 (contour interval is 1.0 ppbv).

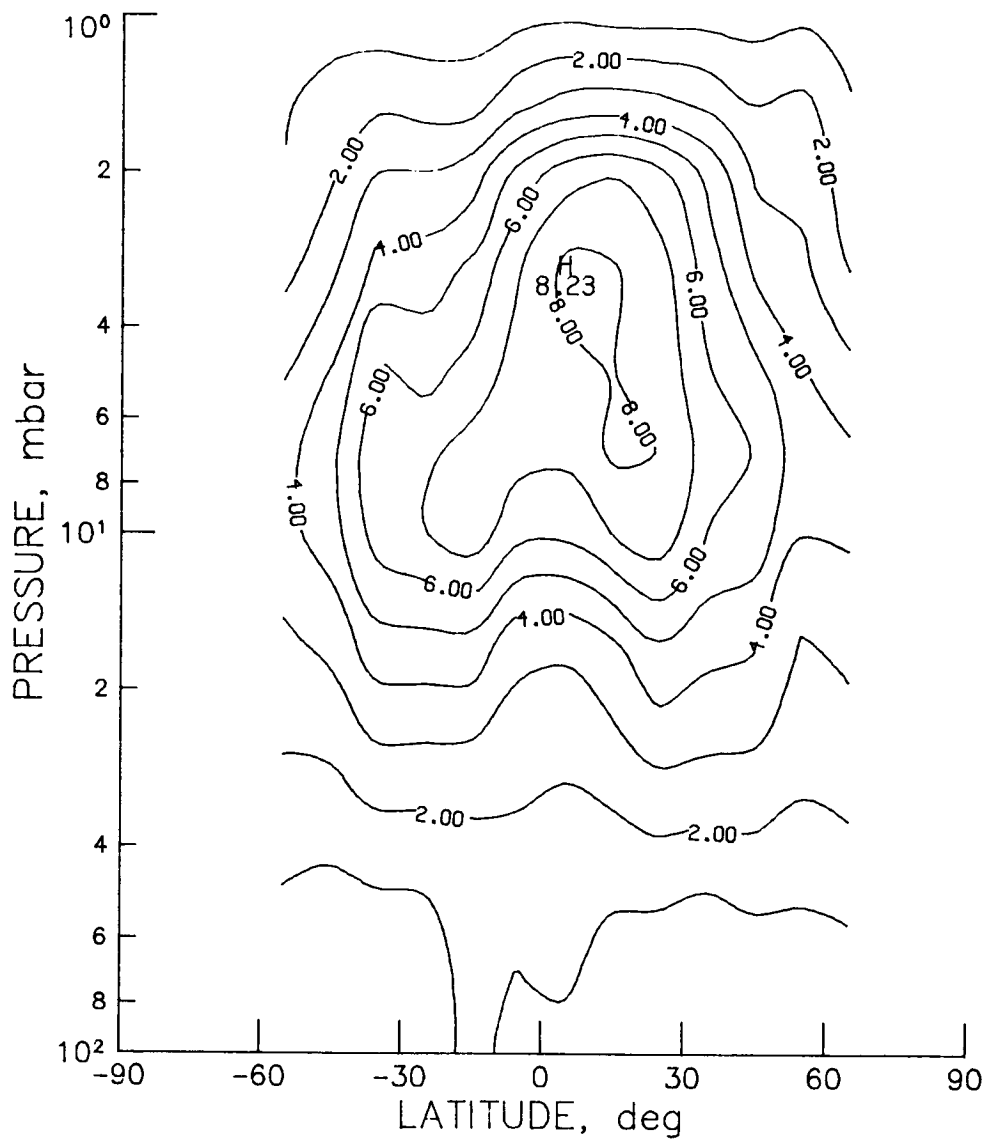


Figure N-32 - SAGE sunset seasonal zonal mean NO₂ cross section for March, April, and May 1979 (contour interval is 1.0 ppbv).

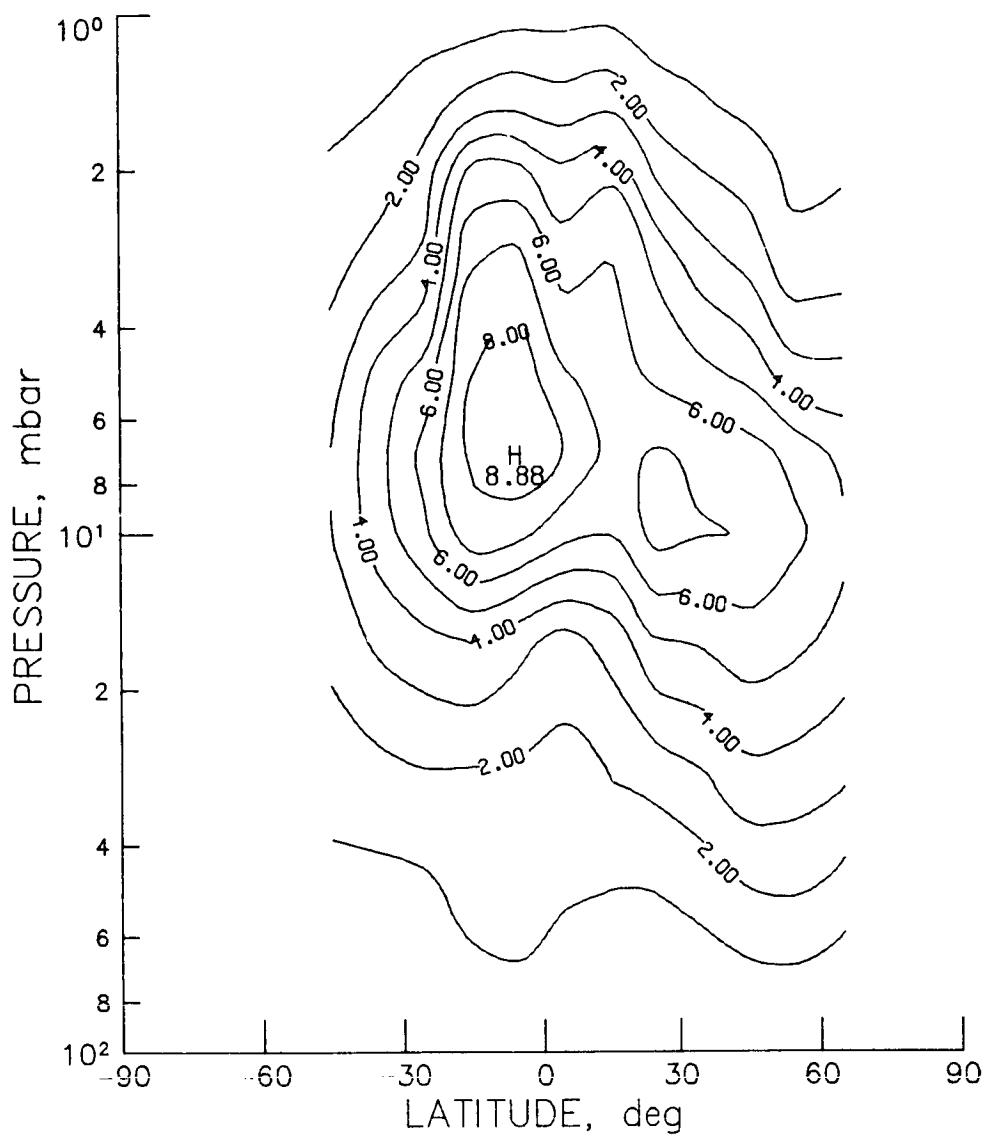


Figure N-33 - SAGE sunset seasonal zonal mean NO_2 cross section for June, July, and August 1979 (contour interval is 1.0 ppbv).

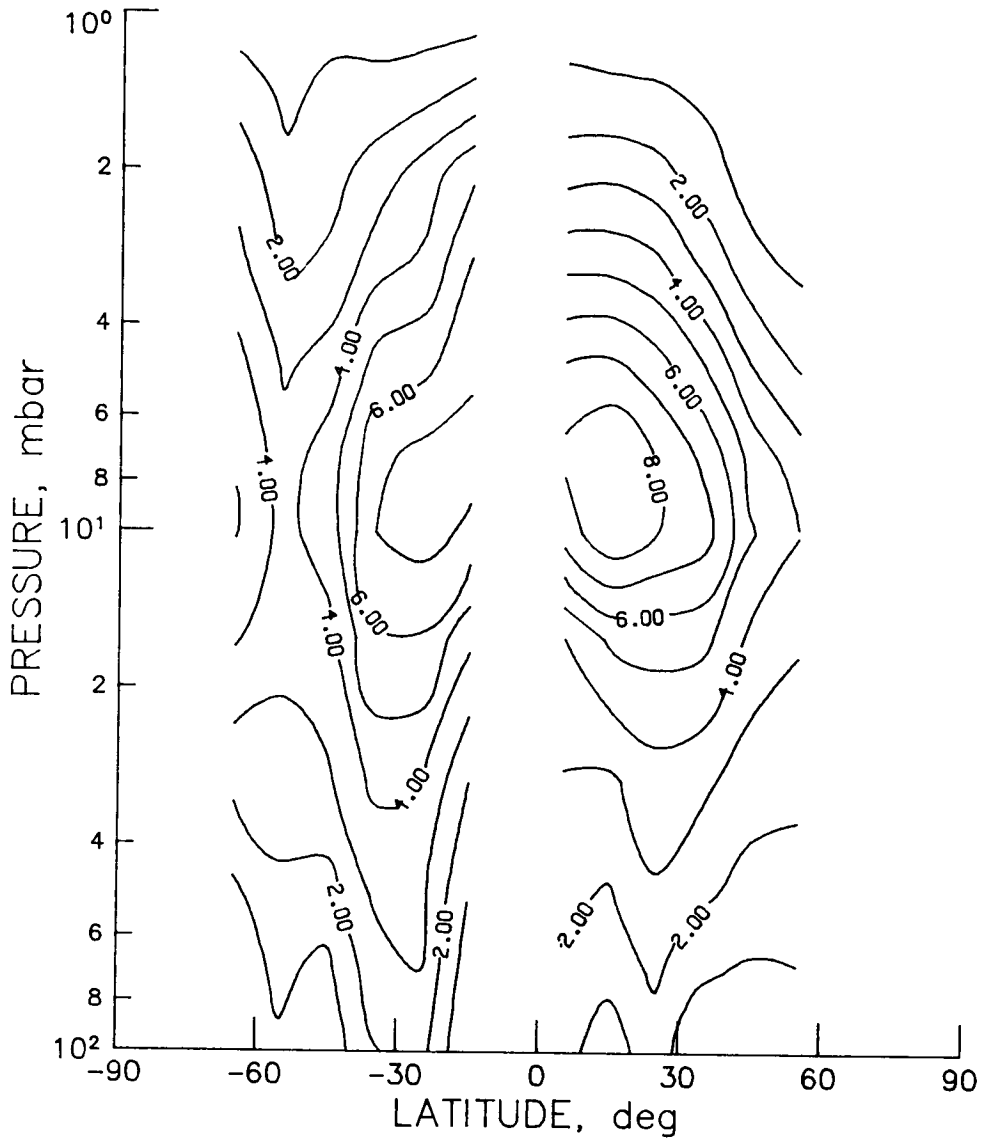


Figure N-34 - SAGE sunset seasonal zonal mean NO₂ cross section for September, October, and November 1979 (contour interval is 1.0 ppbv).

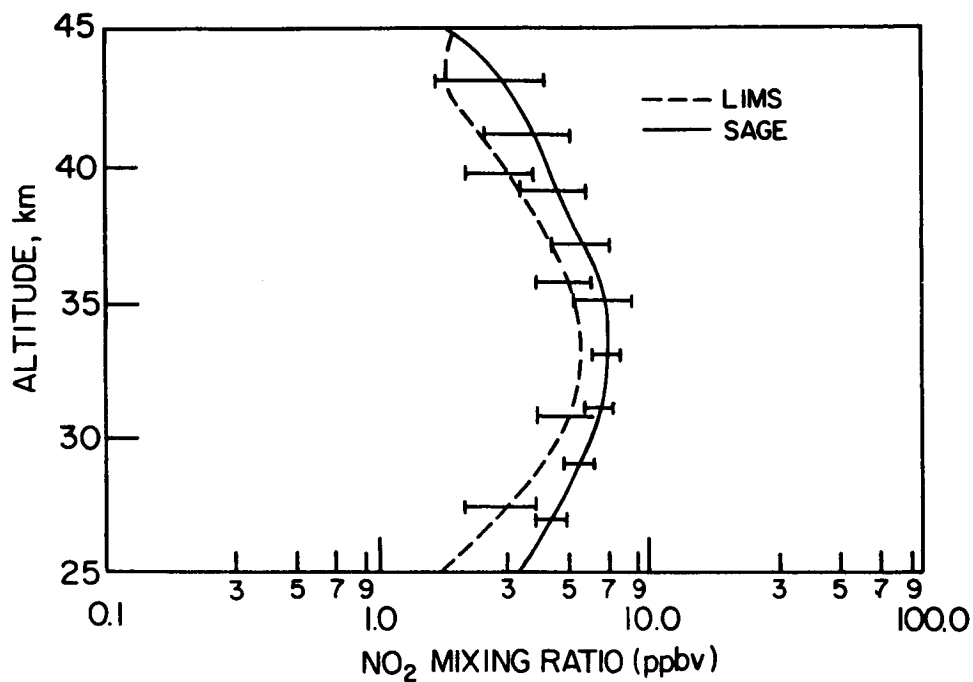


Figure N-35 - Comparison of LIMS monthly zonal mean daytime NO₂ mixing ratio with the SAGE sunset seasonal zonal mean for January and February at 31°N.

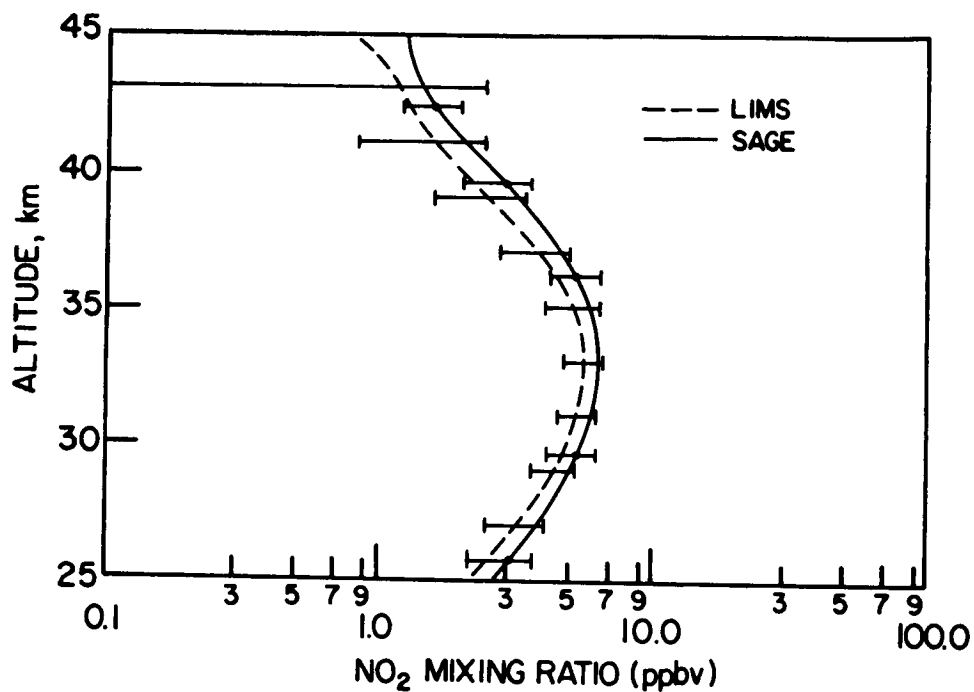


Figure N-36 - Comparison of LIMS monthly zonal mean daytime NO₂ mixing ratio with the SAGE sunset seasonal zonal² mean for March, April and May at 31°N.

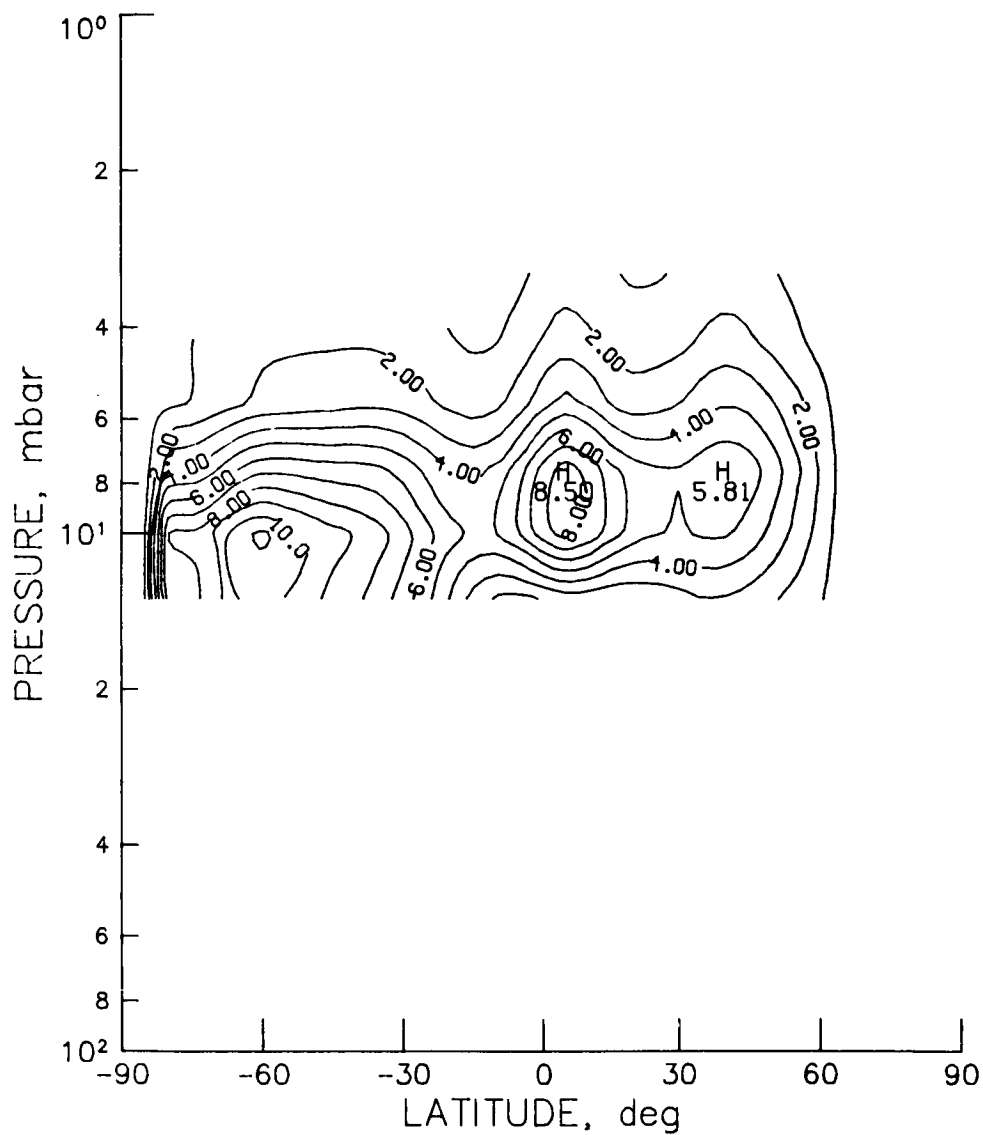


Figure N-37 - SME monthly zonal mean NO_2 cross section for January 1982 (contour interval is 1.0 ppbv).

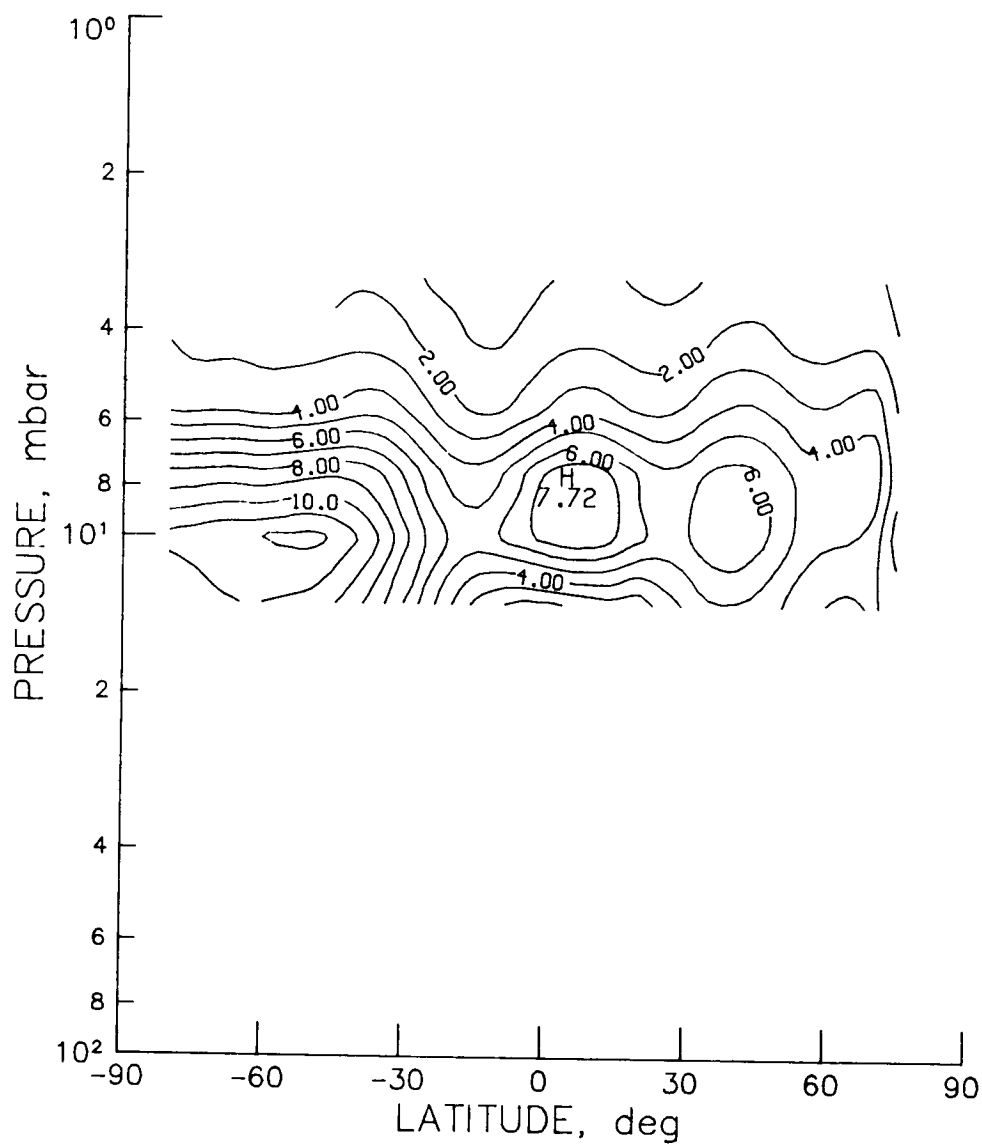


Figure N-38 - SME monthly zonal mean NO_2 cross section for February 1982 (contour interval is 1.0 ppbv).

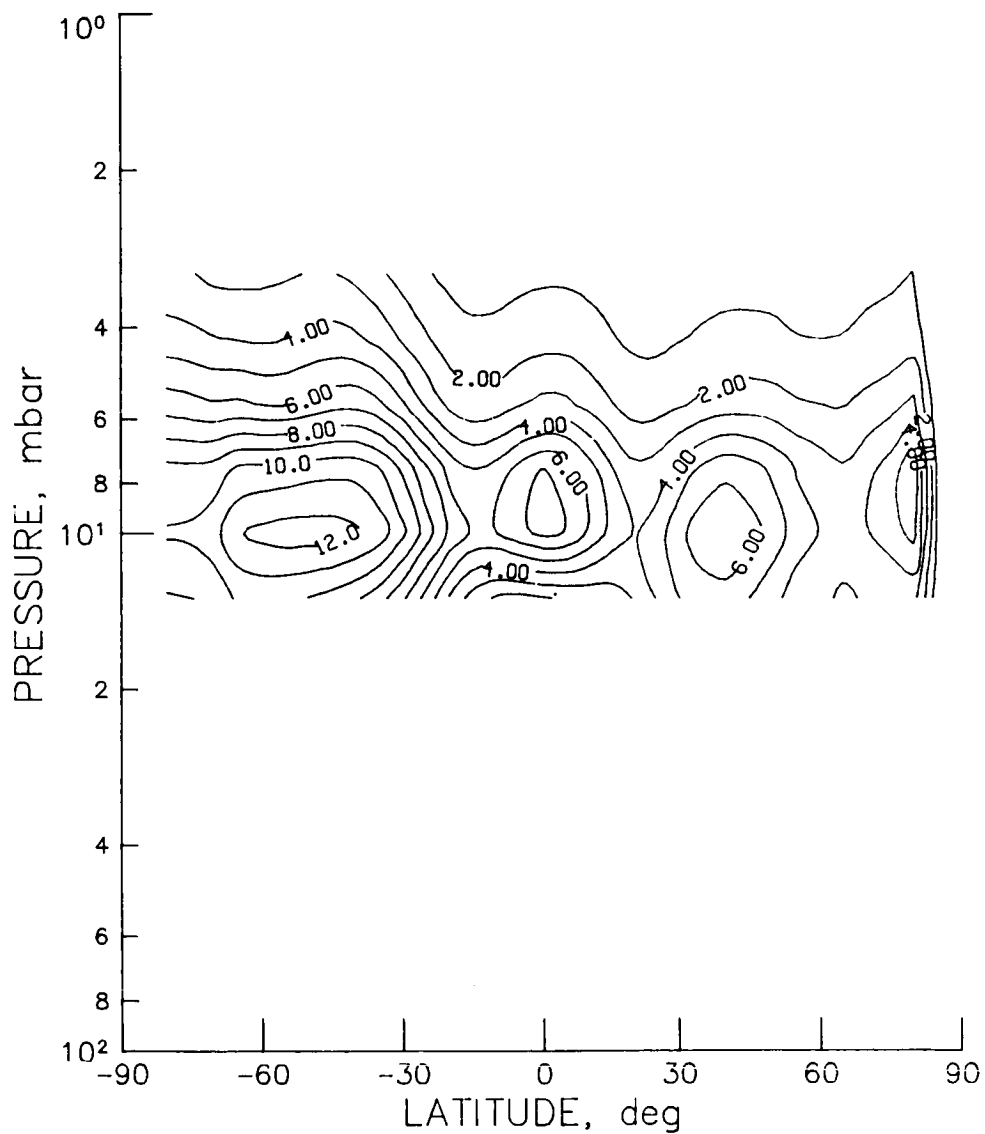


Figure N-39 - SME monthly zonal mean NO₂ cross section for March 1982
(contour interval is 1.0 ppbv).

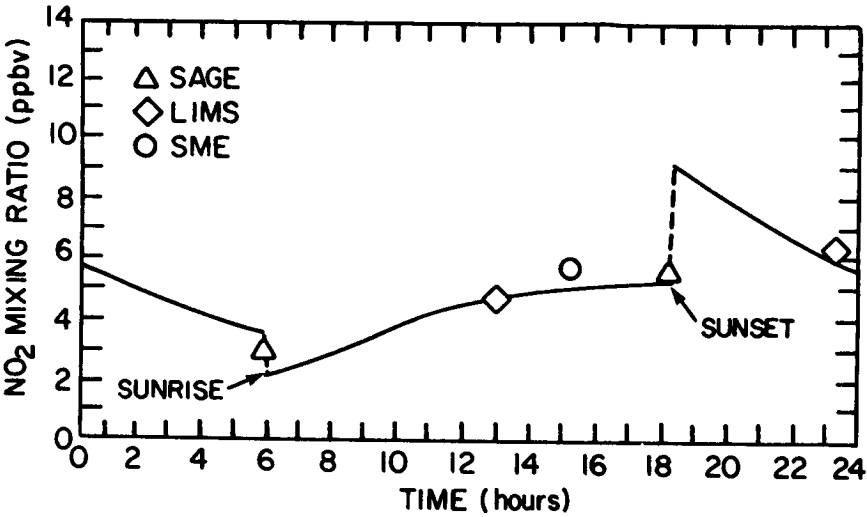


Figure N-40 - NO₂ diurnal calculations by Solomon et al (1985) using NO_x constrained to LIMS daytime NO₂ values compared to satellite measurements by LIMS, SAGE, and SME for March at the 10 mb level and the equator.

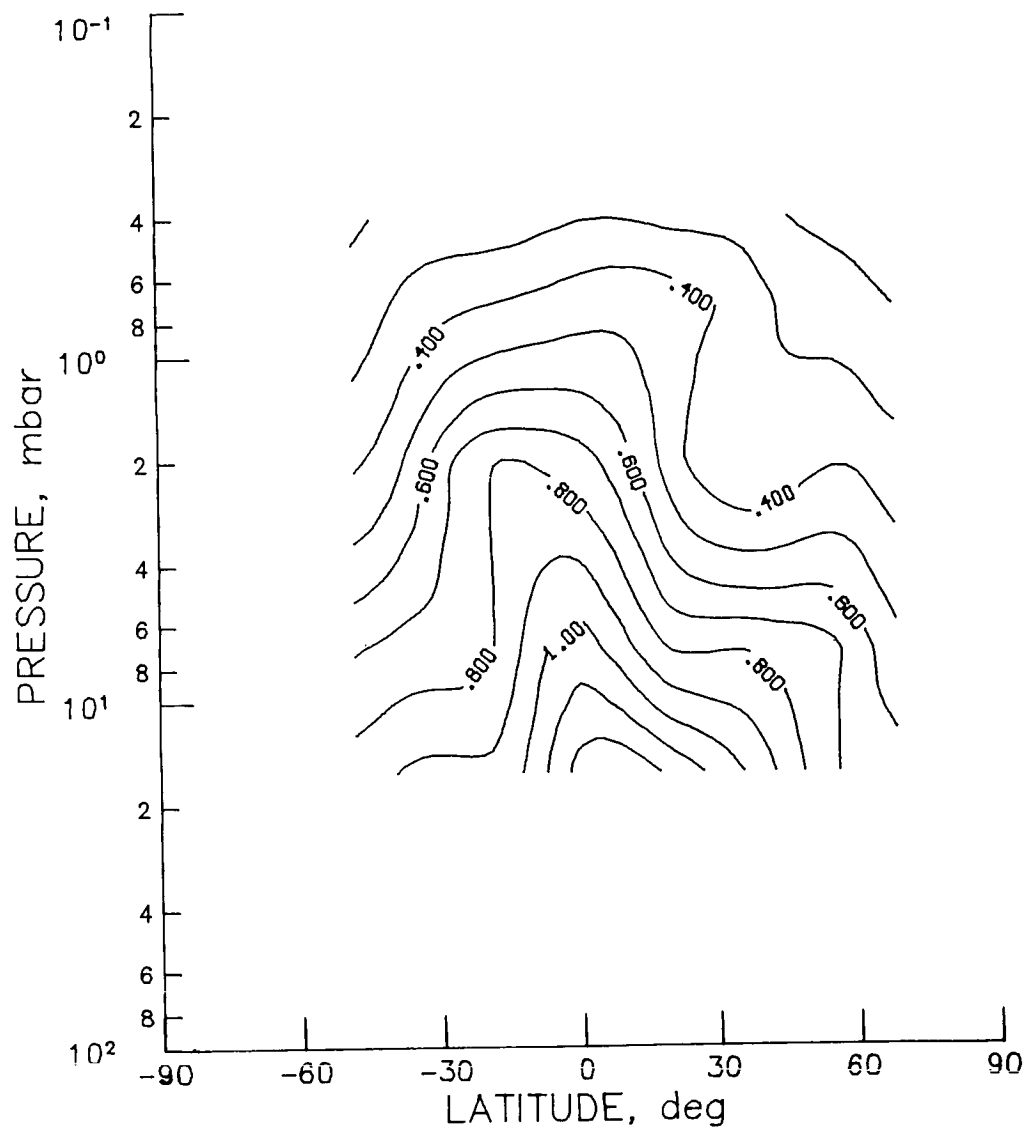


Figure CHN-1 - SAMS monthly zonal mean CH_4 cross section for January 1979
(contour interval is 0.10 ppmv).

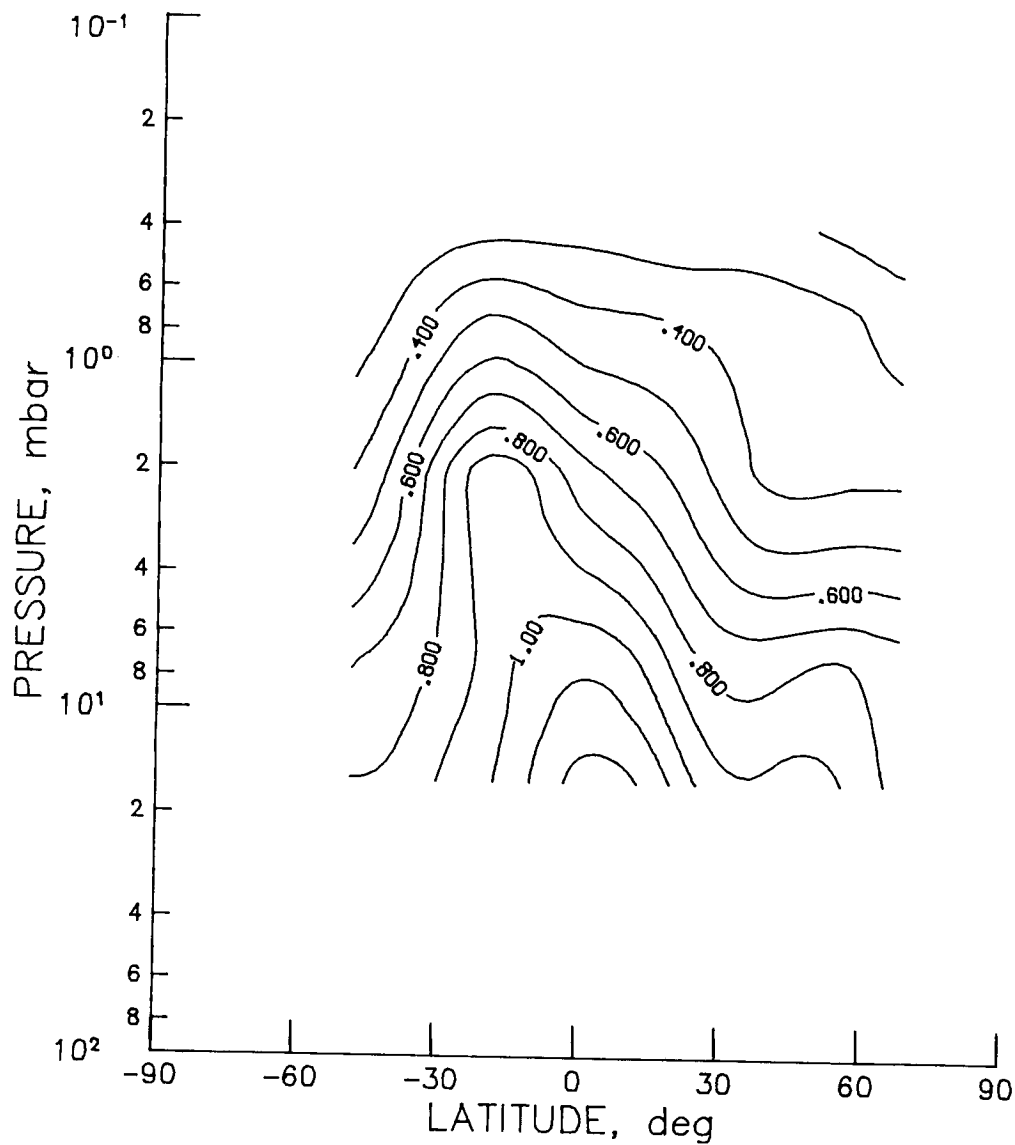


Figure CHN-2 - SAMS monthly zonal mean CH_4 cross section for February 1979 (contour interval is 0.10 ppmv).

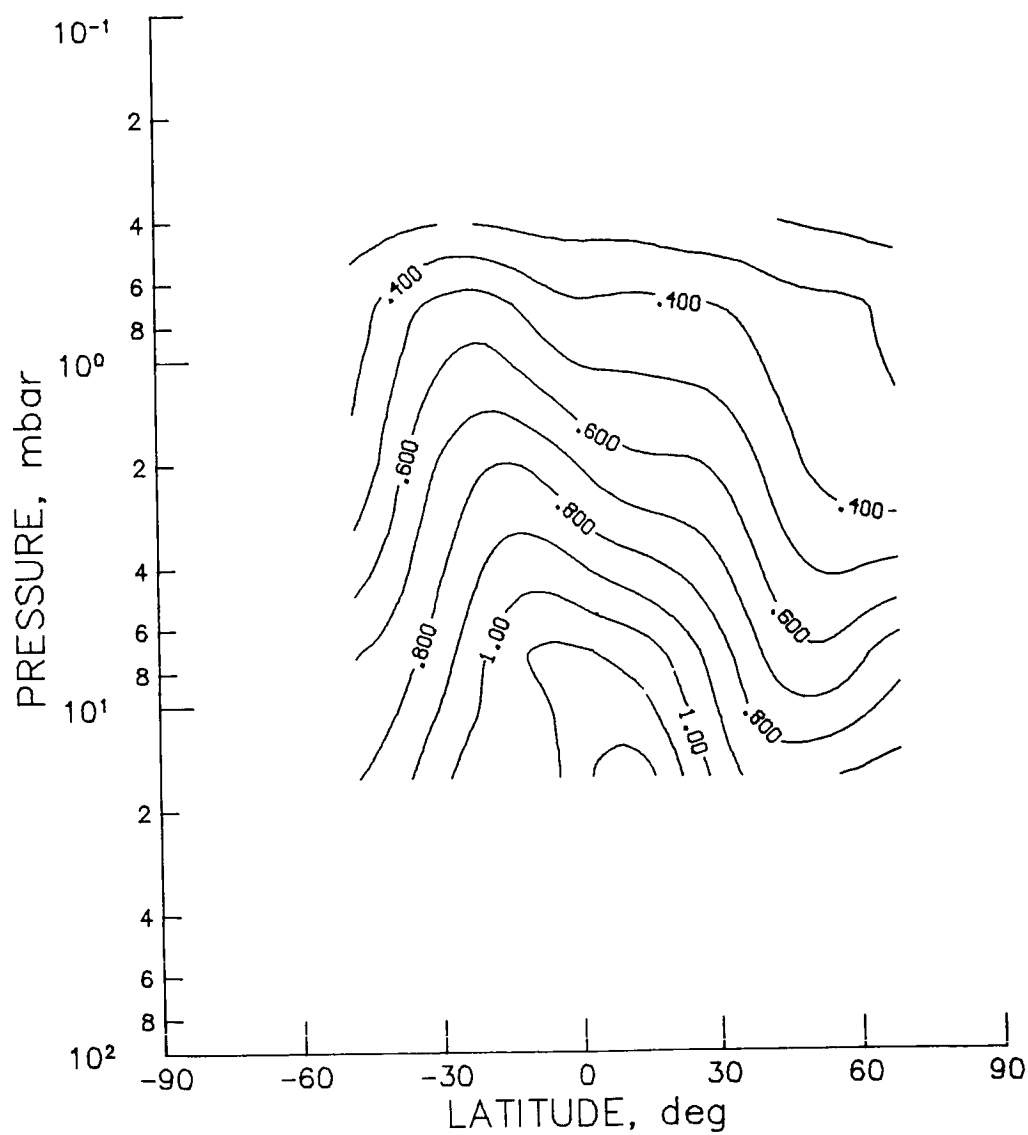


Figure CHN-3 - SAMS monthly zonal mean CH_4 cross section for March 1979
(contour interval is 0.10 ppmv).

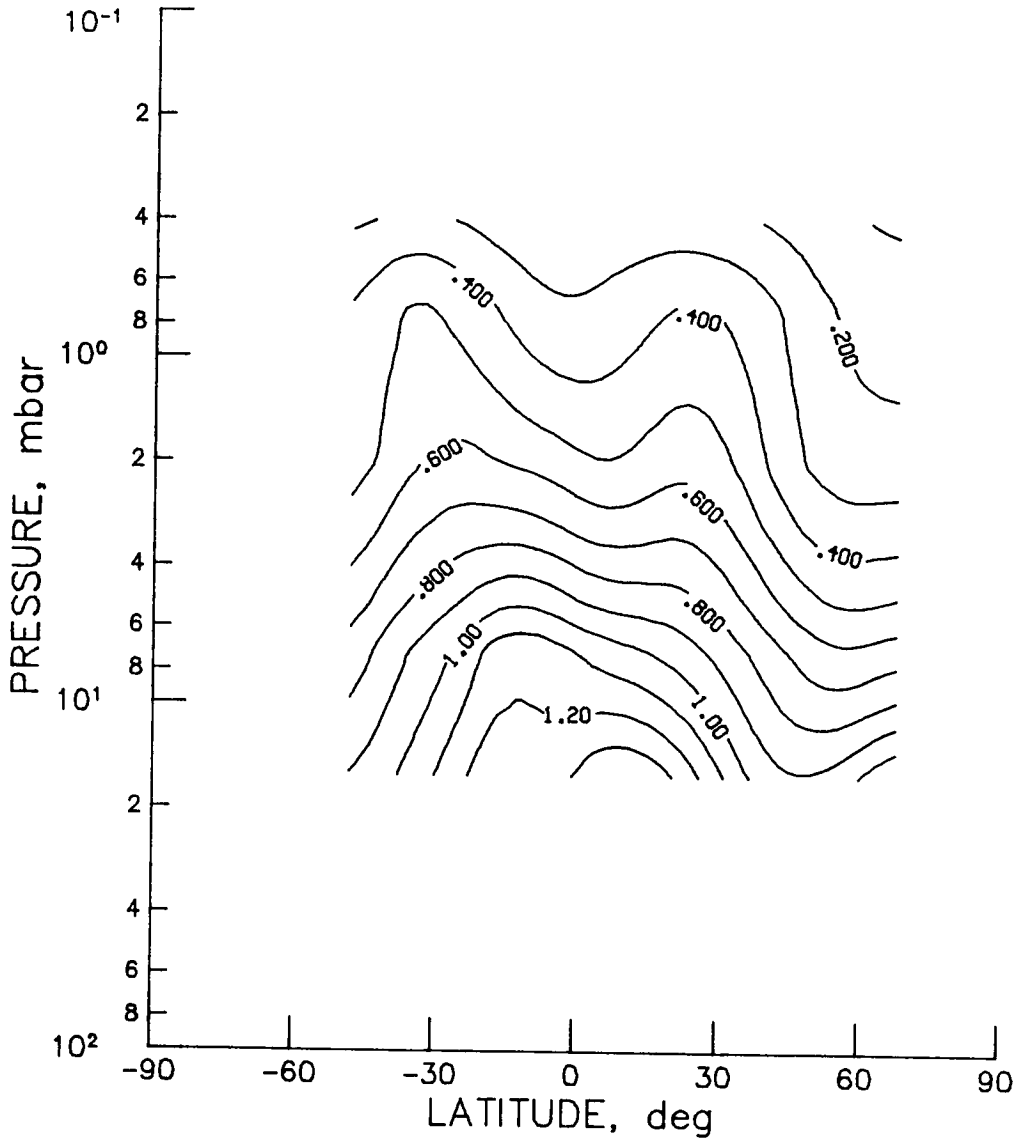


Figure CHN-4 - SAMS monthly zonal mean CH₄ cross section for April 1979
(contour interval is 0.10 ppmv).

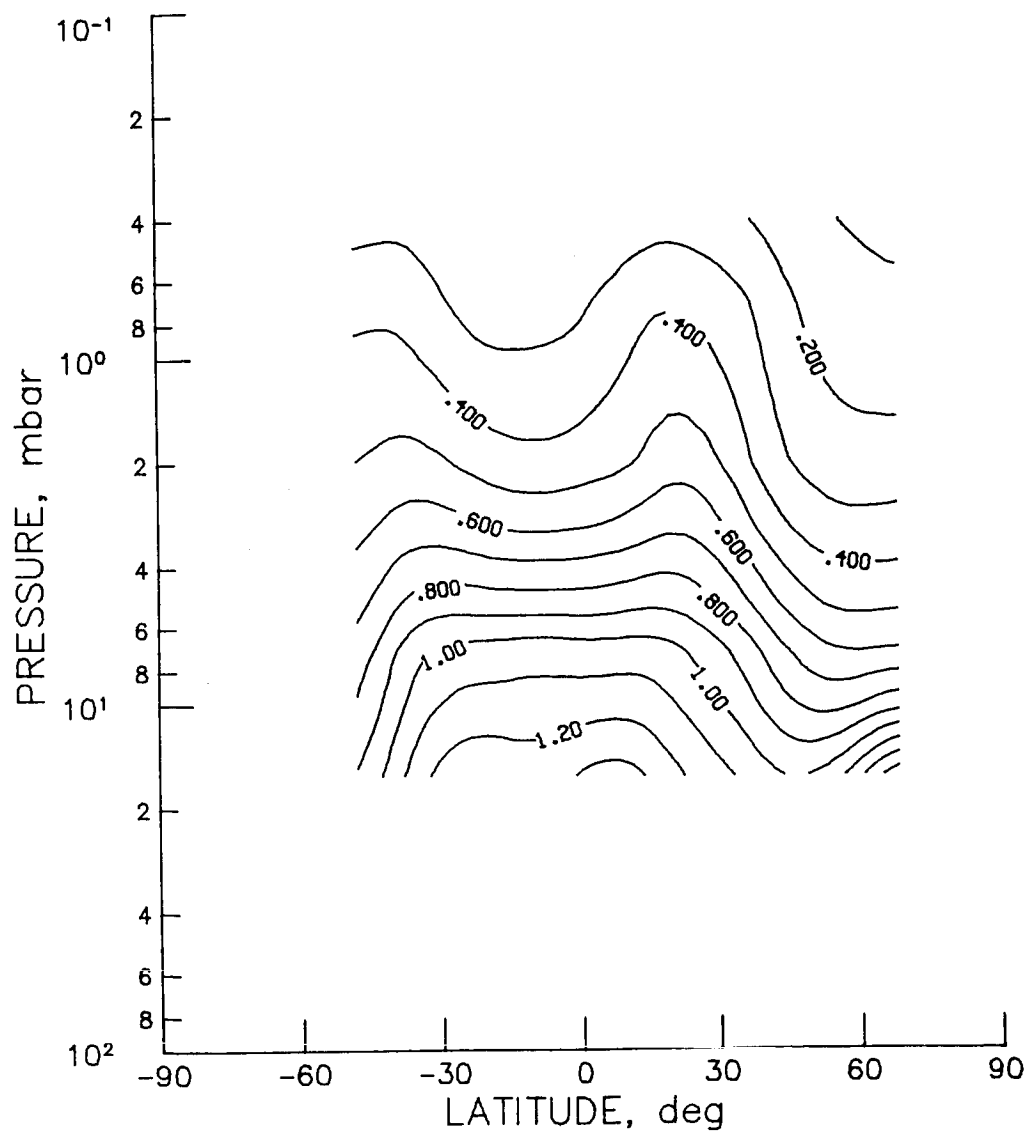


Figure CHN-5 - SAMS monthly zonal mean CH_4 cross section for May 1979
(contour interval is 0.10 ppmv).

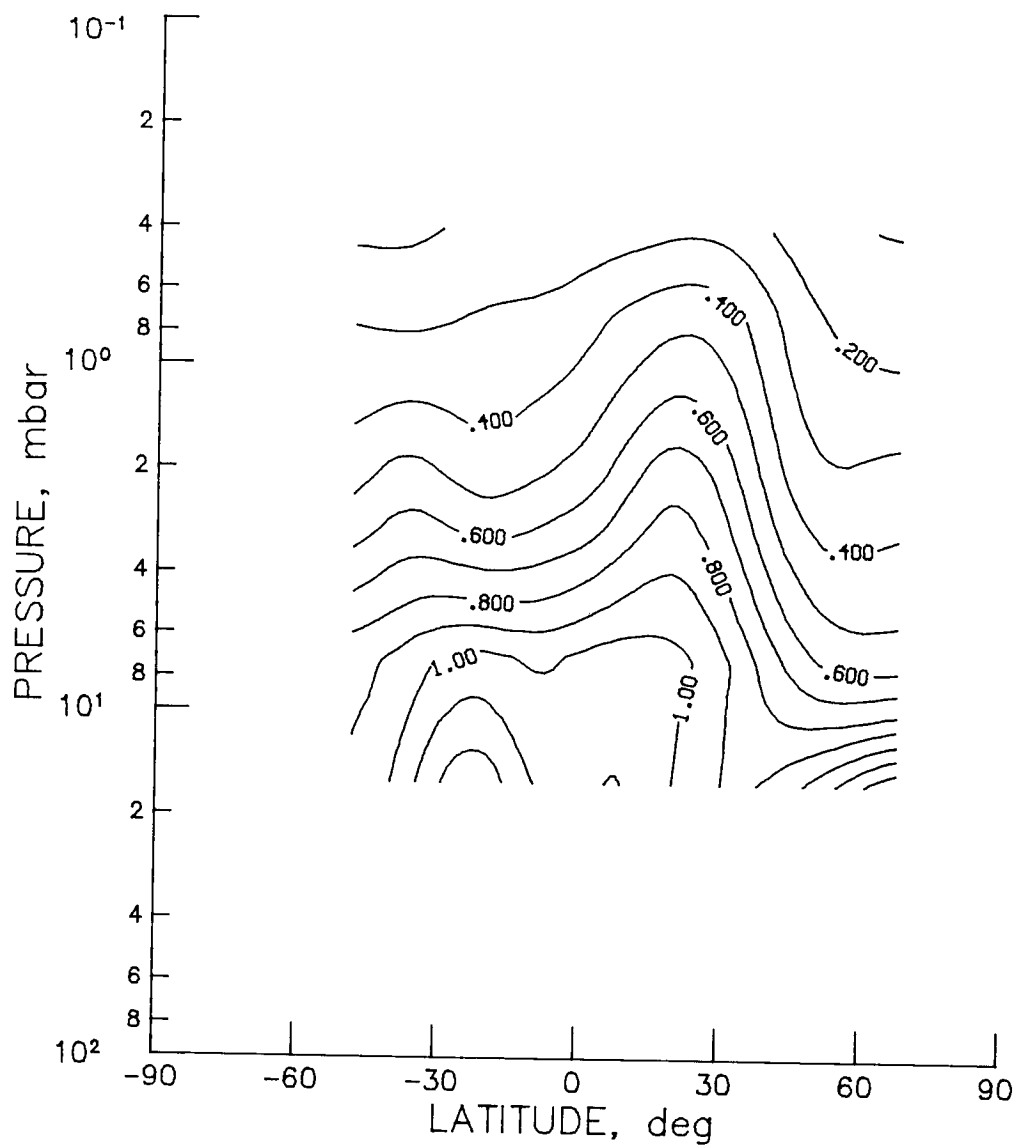


Figure CHN-6 - SAMS monthly zonal mean CH_4 cross section for June 1979 (contour interval is 0.10 ppmv).

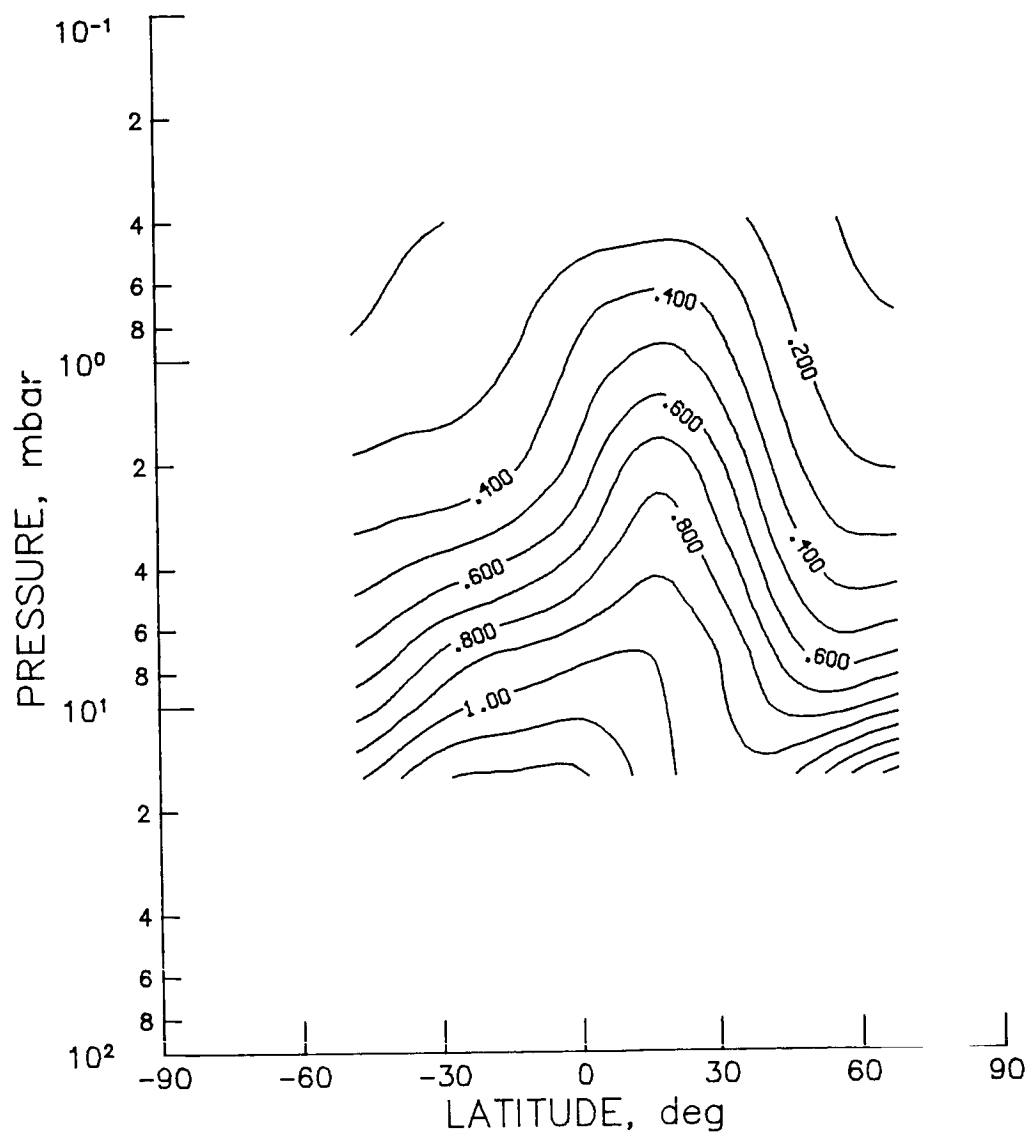


Figure CHN-7 - SAMS monthly zonal mean CH_4 cross section for July 1979
(contour interval is 0.10 ppmv).

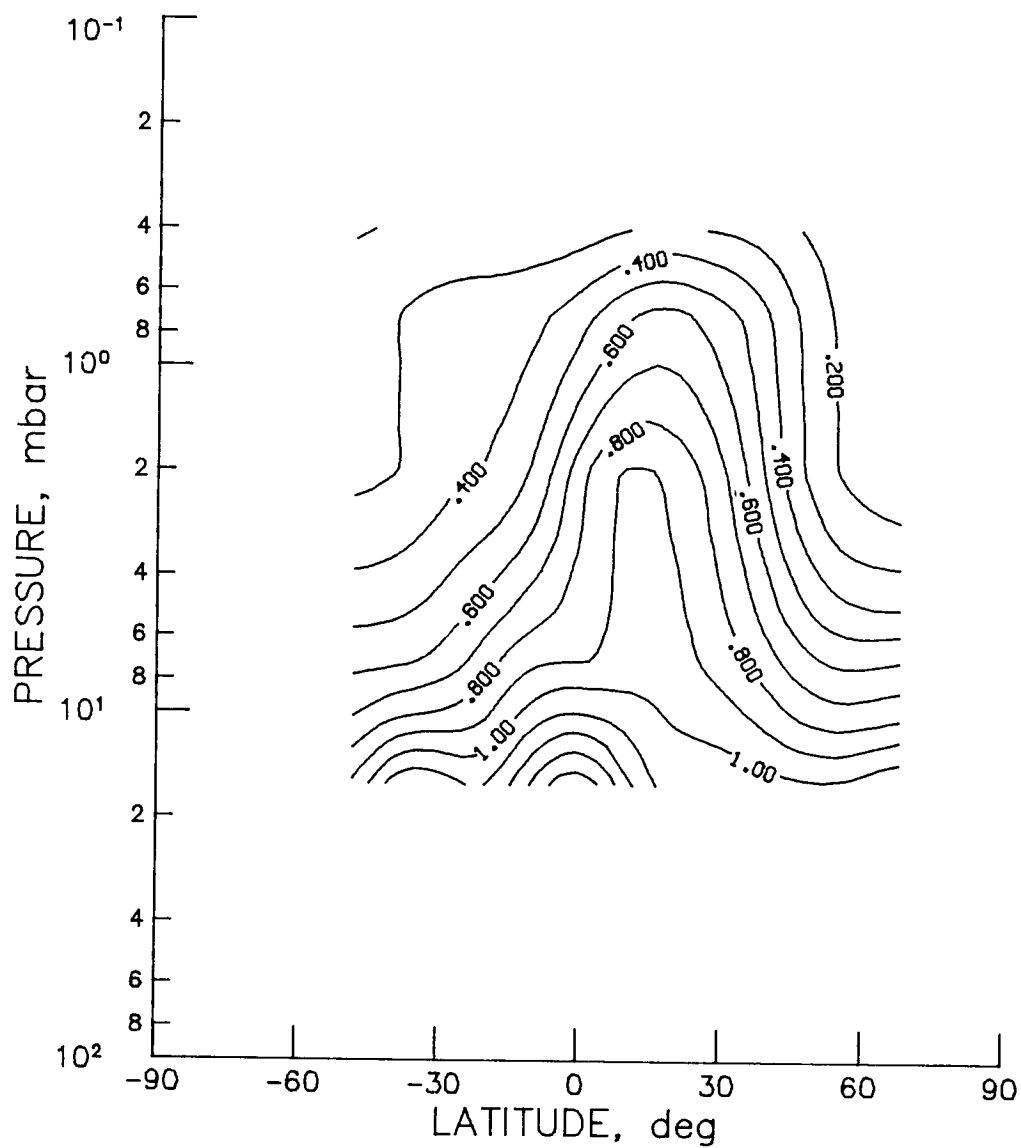


Figure CHN-8 - SAMS monthly zonal mean CH_4 cross section for August 1979
(contour interval is 0.10 ppmv).

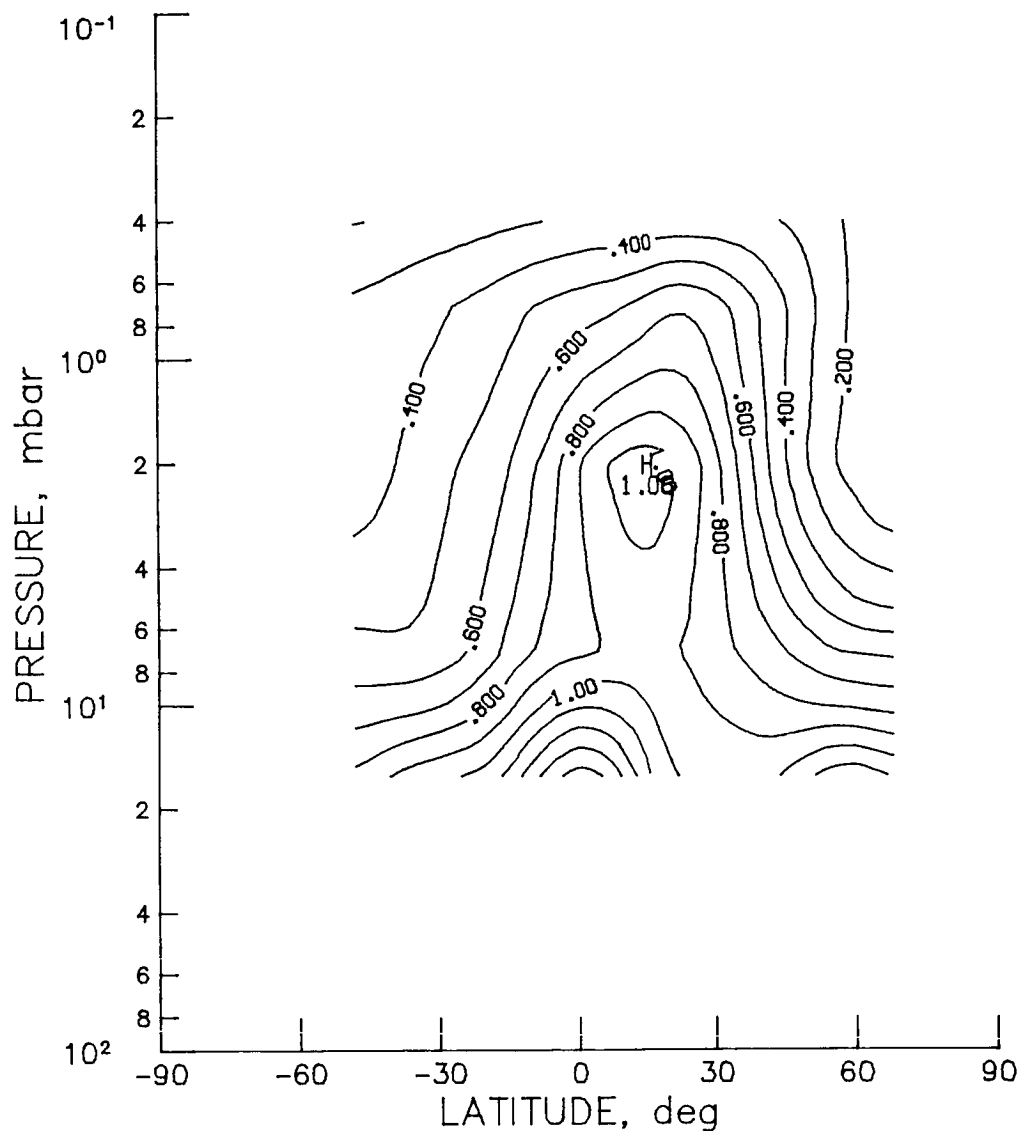


Figure CHN-9 - SAMS monthly zonal mean CH_4 cross section for September 1979
(contour interval is 0.10 ppmv).

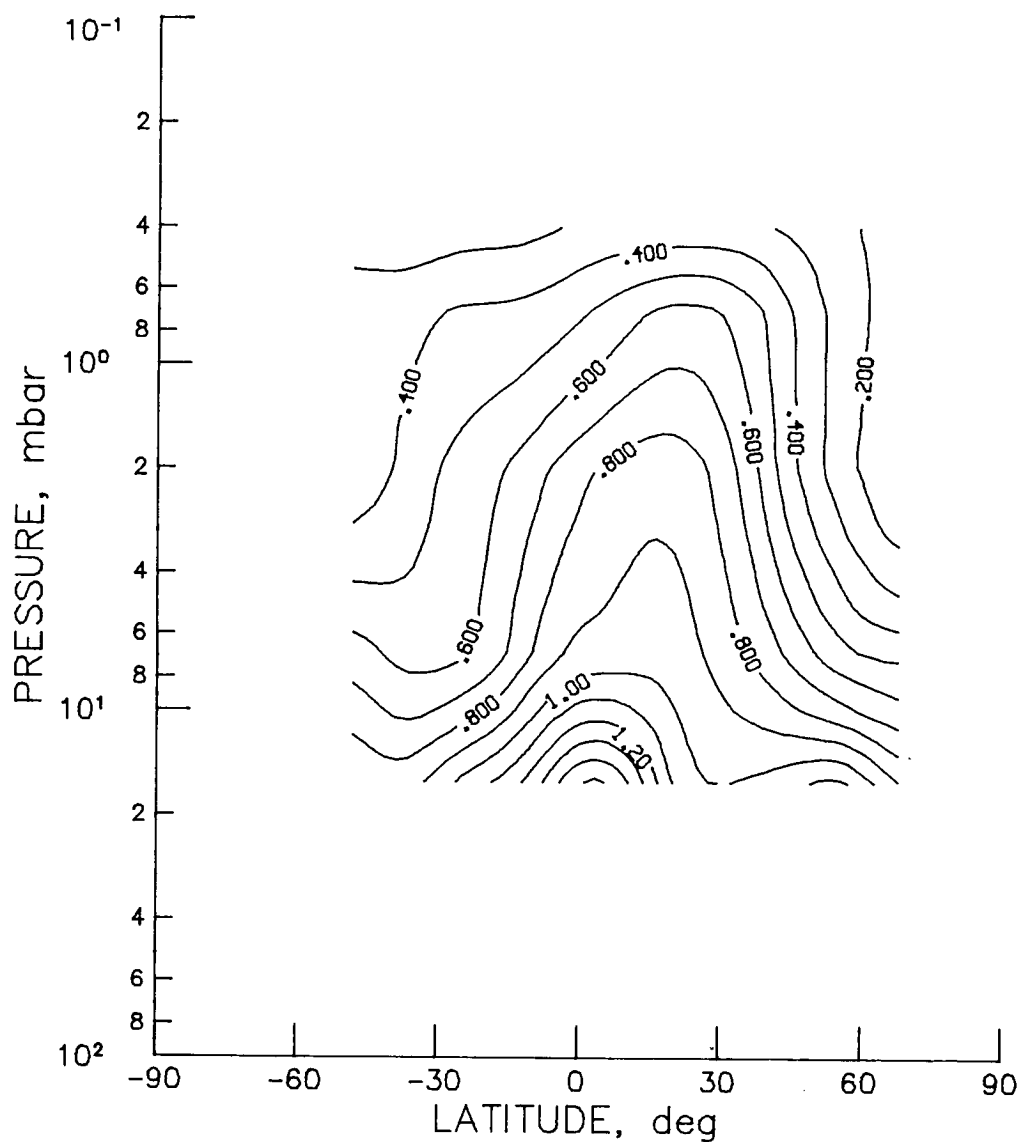


Figure CHN-10 - SAMS monthly zonal mean CH_4 cross section for October 1979
(contour interval is 0.10 ppmv).

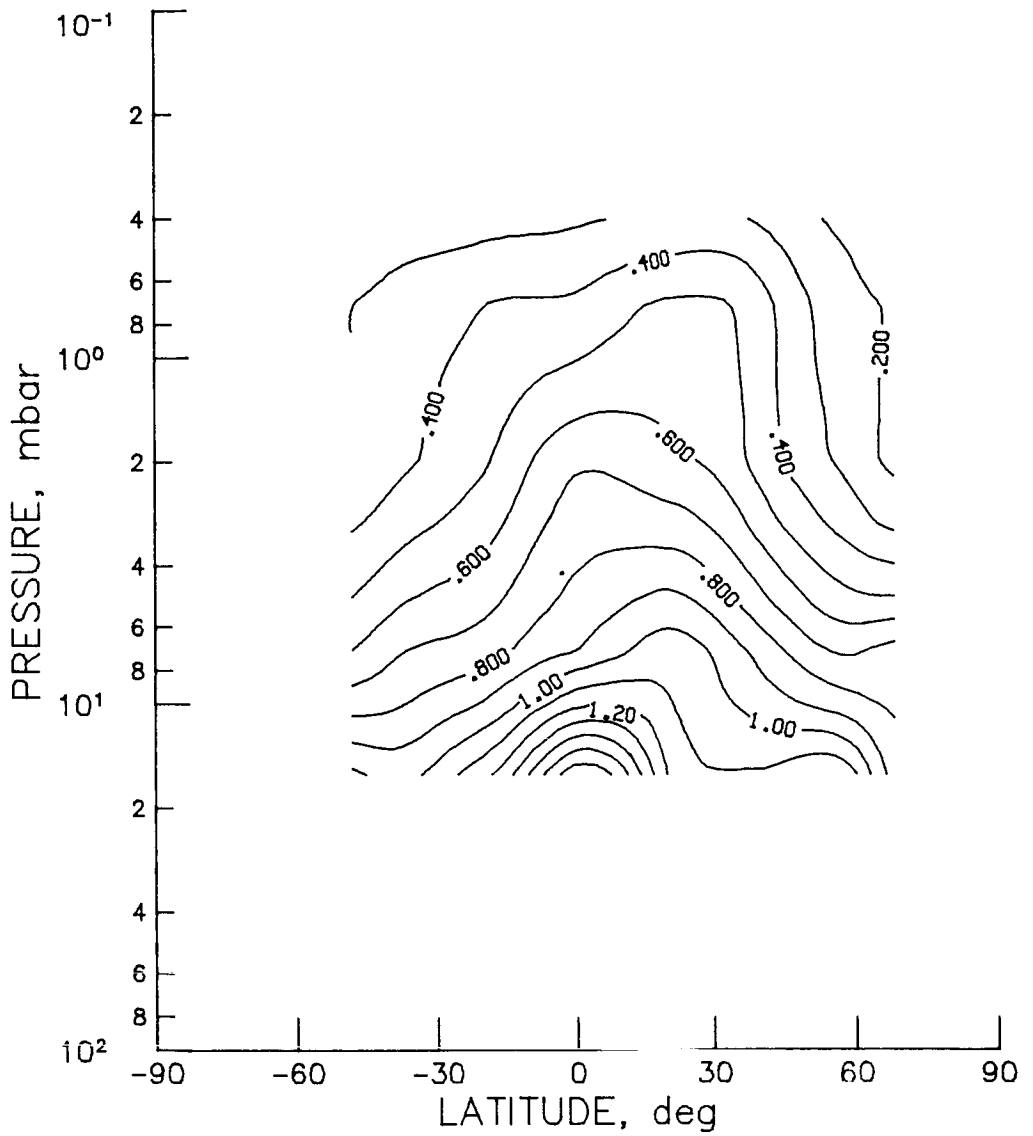


Figure CHN-11 - SAMS monthly zonal mean CH_4 cross section for November 1979
(contour interval is 0.10 ppmv).

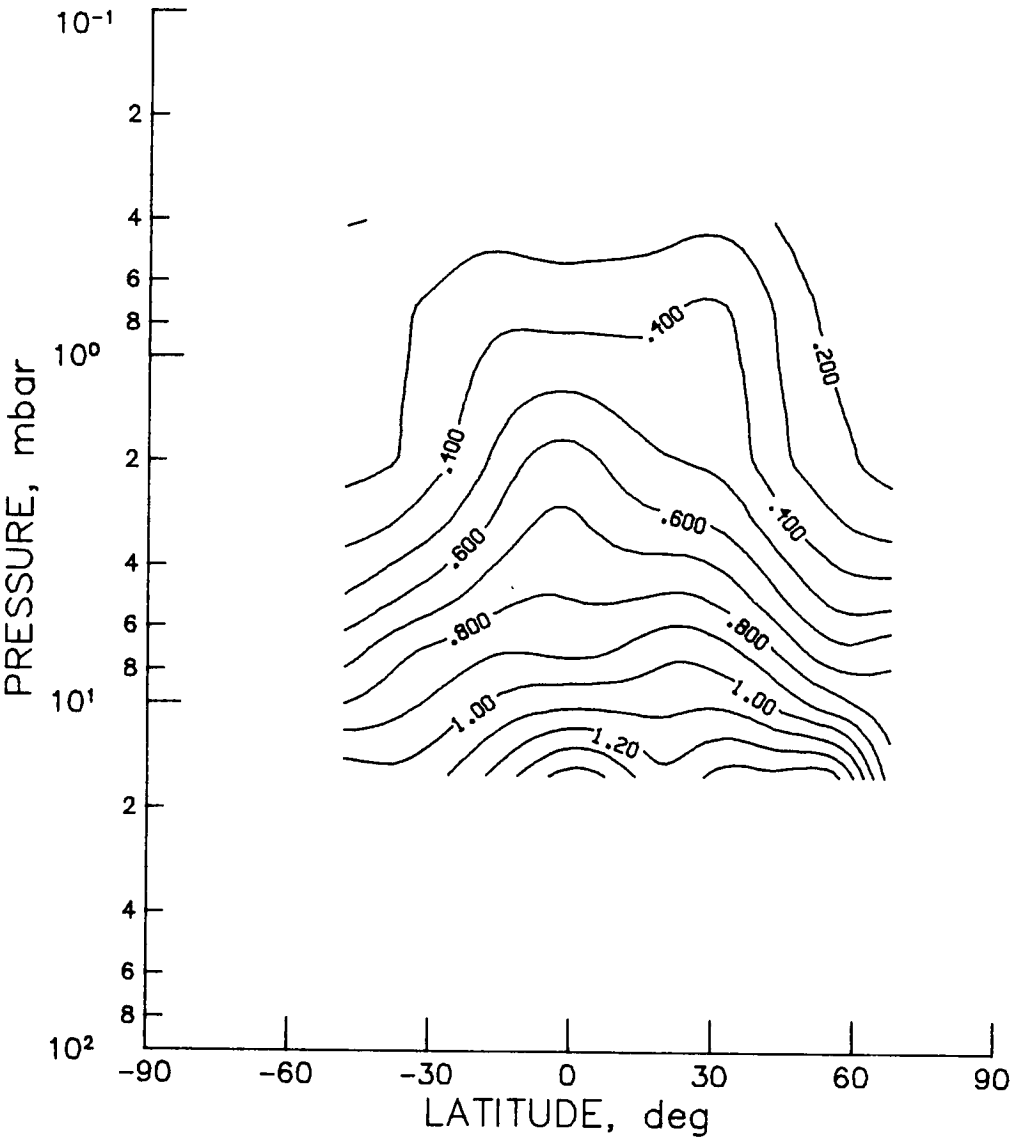


Figure CHN-12 - SAMS monthly zonal mean CH₄ cross section for December 1979 (contour interval is 0.10 ppmv).

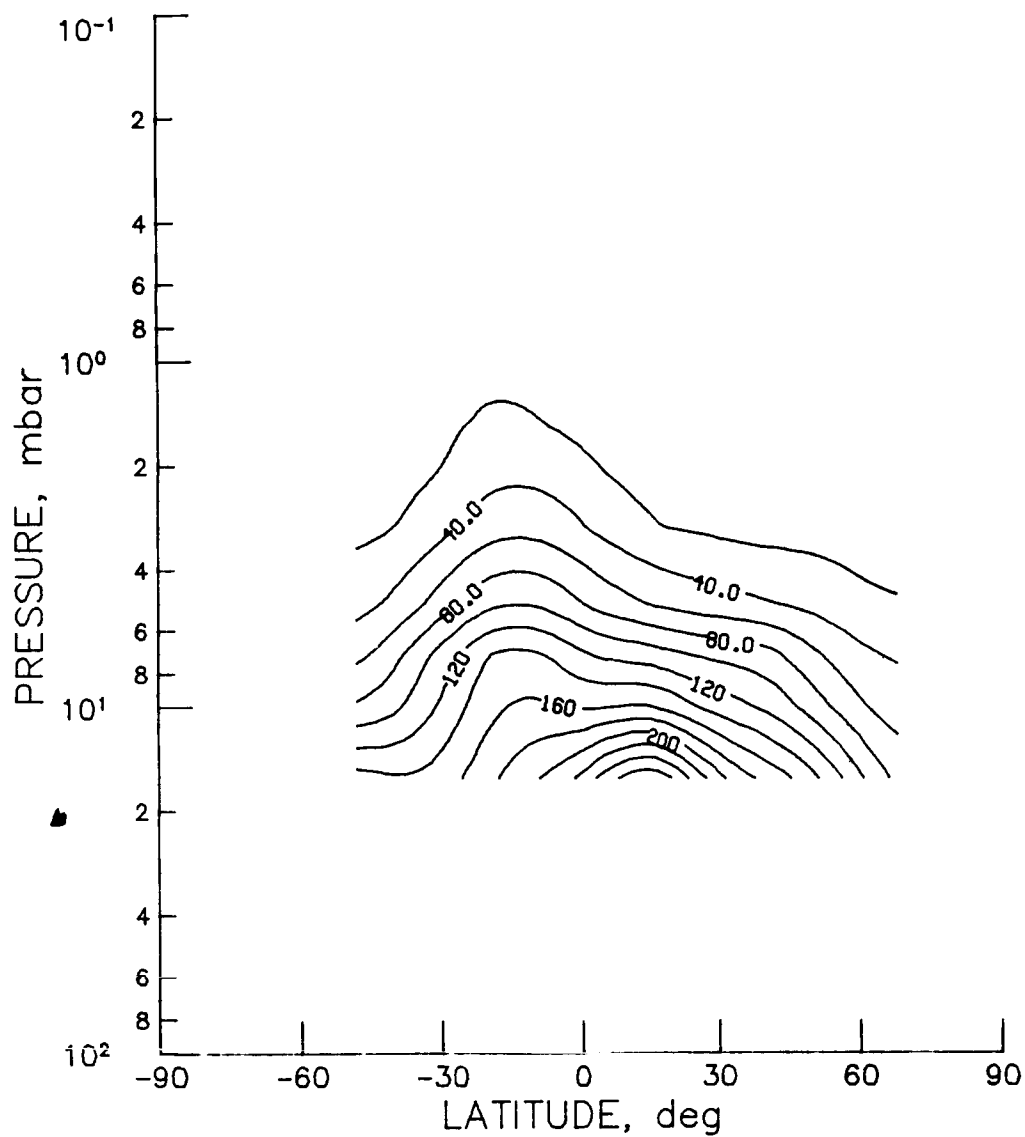


Figure CHN-13 - SAMS monthly zonal mean N_2O cross section for January 1979
(contour interval is 20.0 ppbv).

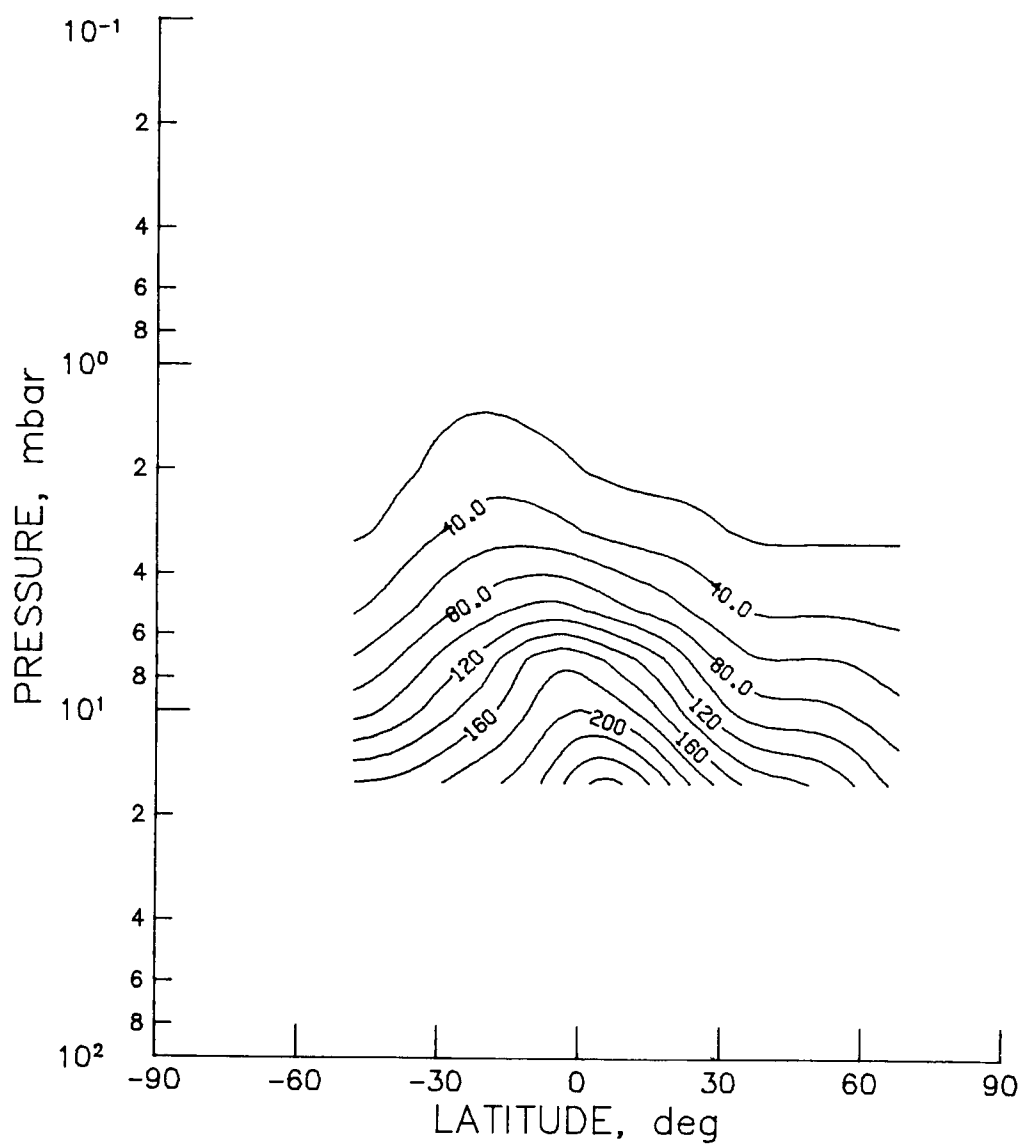


Figure CHN-14 - SAMS monthly zonal mean N_2O cross section for February 1979 (contour interval is 20.0 ppbv).

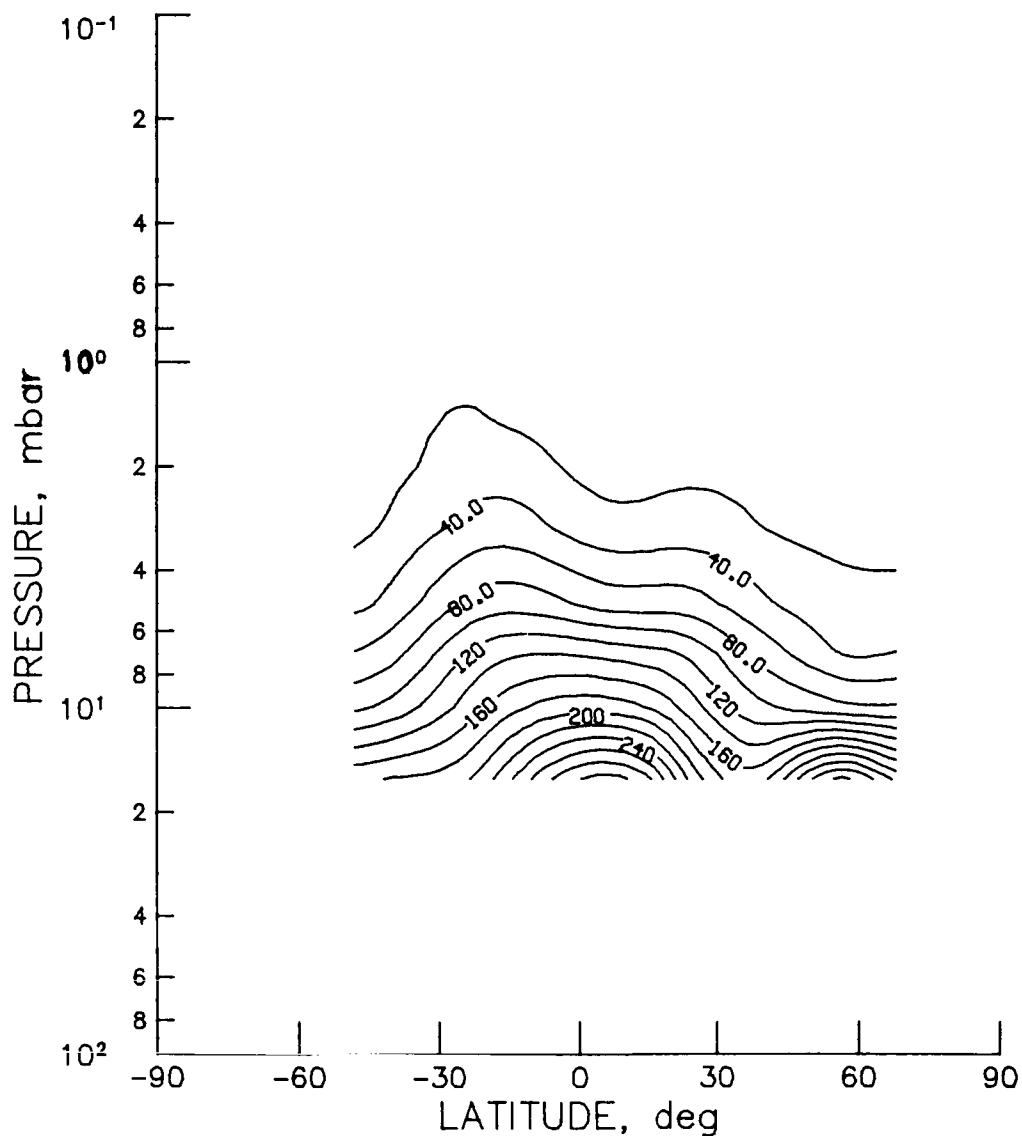


Figure CHN-15 - SAMS monthly zonal mean N_2O cross section for March 1979
(contour interval is 20.0 ppbv).

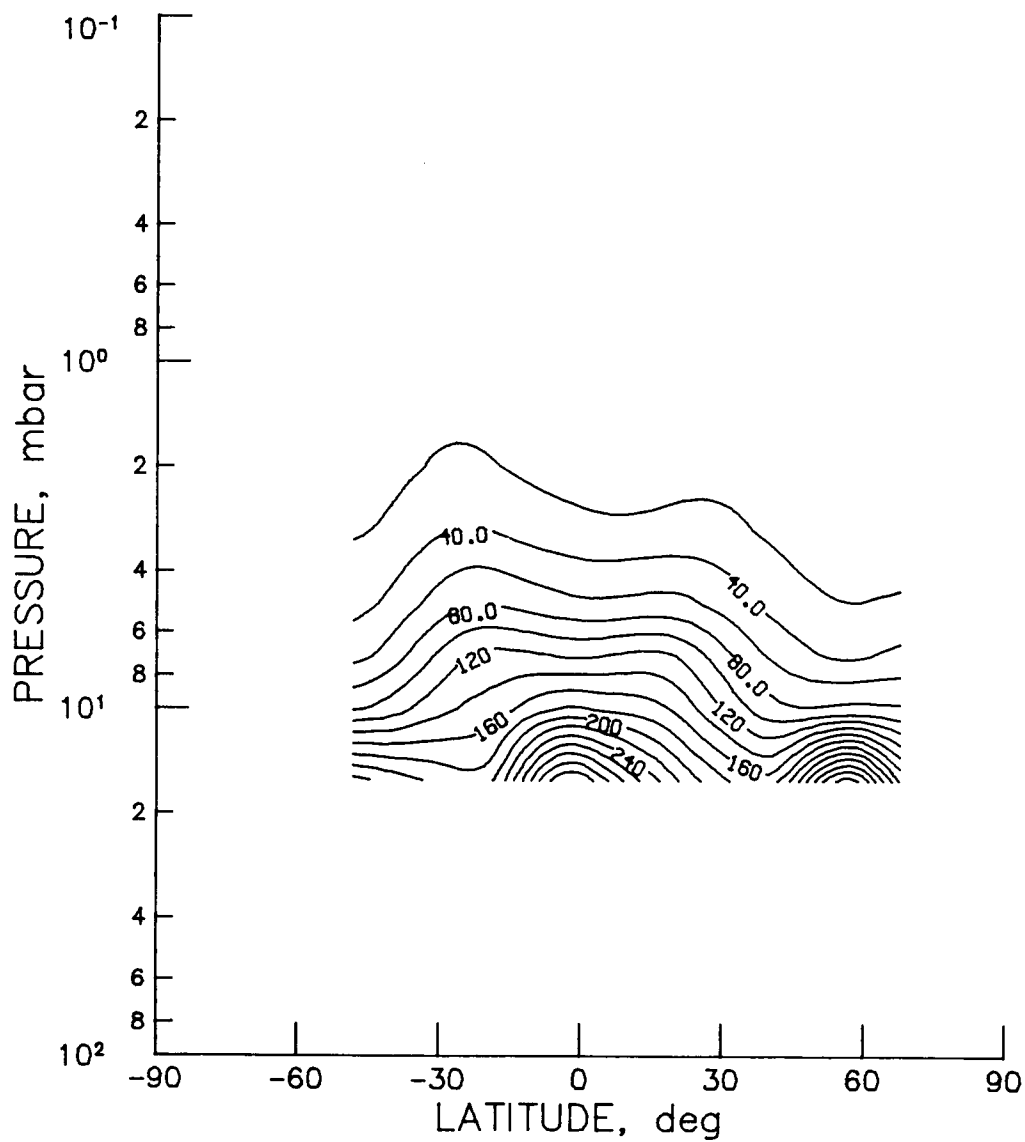


Figure CHN-16 - SAMS monthly zonal mean N_2O cross section for April 1979
(contour interval is 20.0 ppbv).

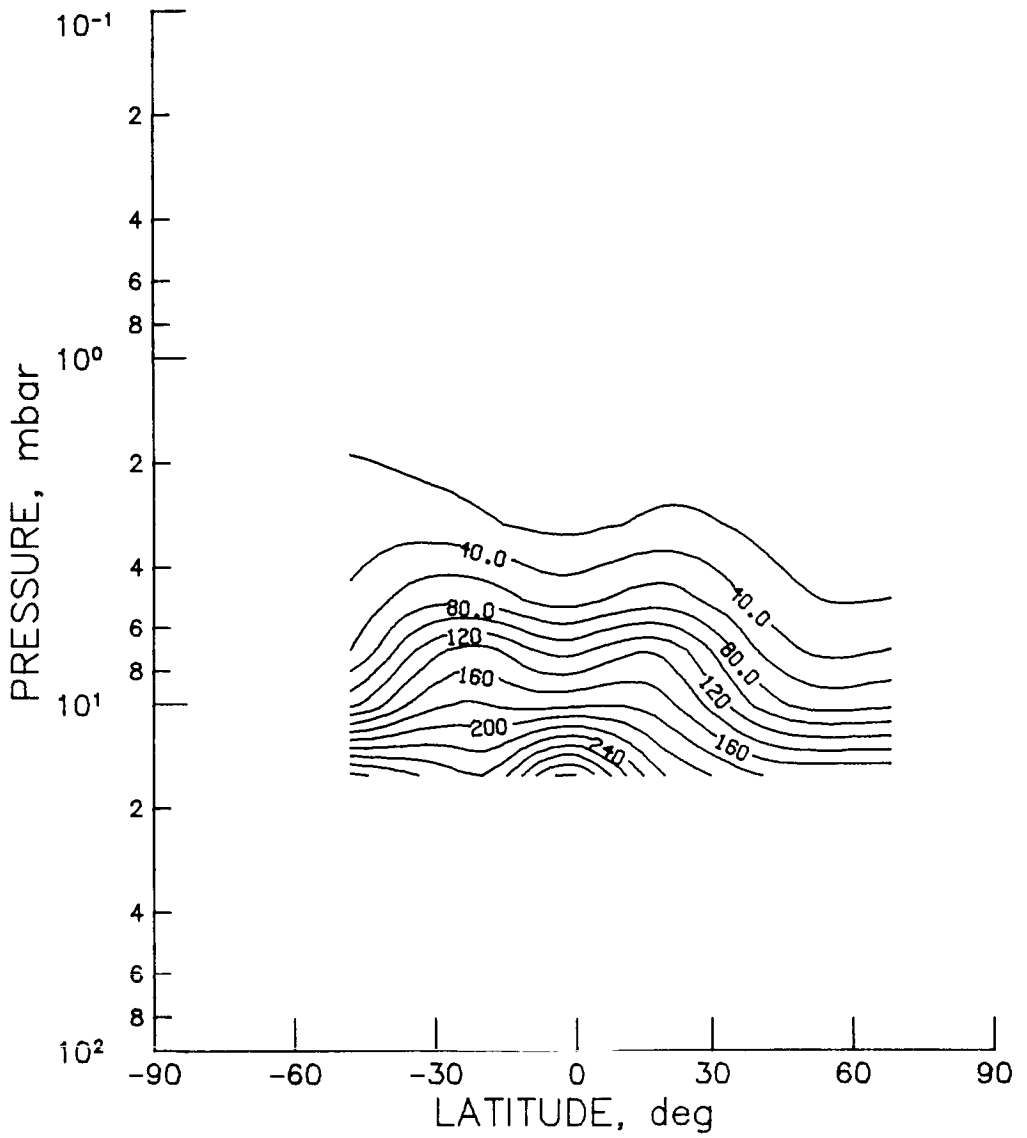


Figure CHN-17 - SAMS monthly zonal mean N_2O cross section for May 1979
(contour interval is 20.0 ppbv).

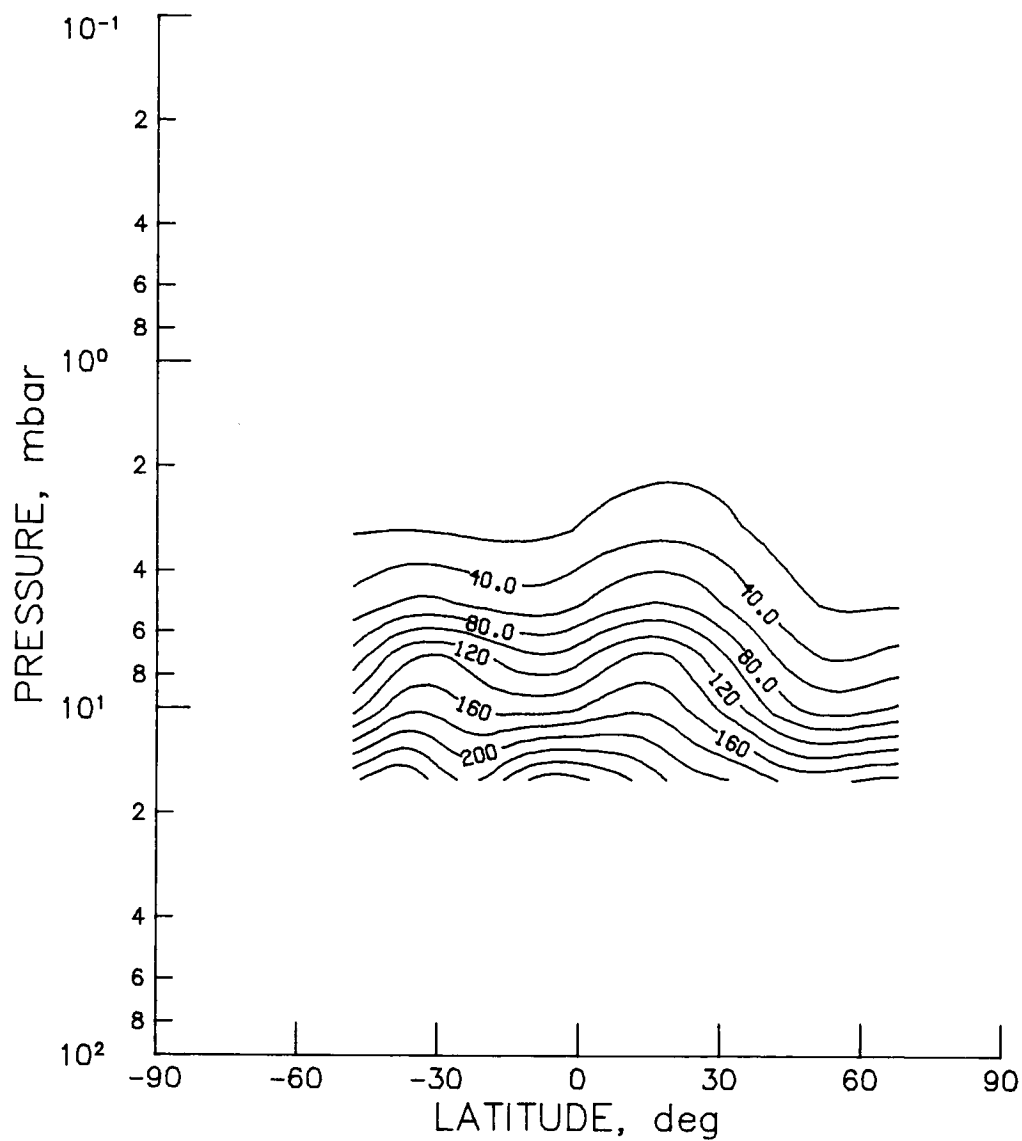


Figure CHN-18 - SAMS monthly zonal mean N_2O cross section for June 1979
(contour interval is 20.0 ppbv).

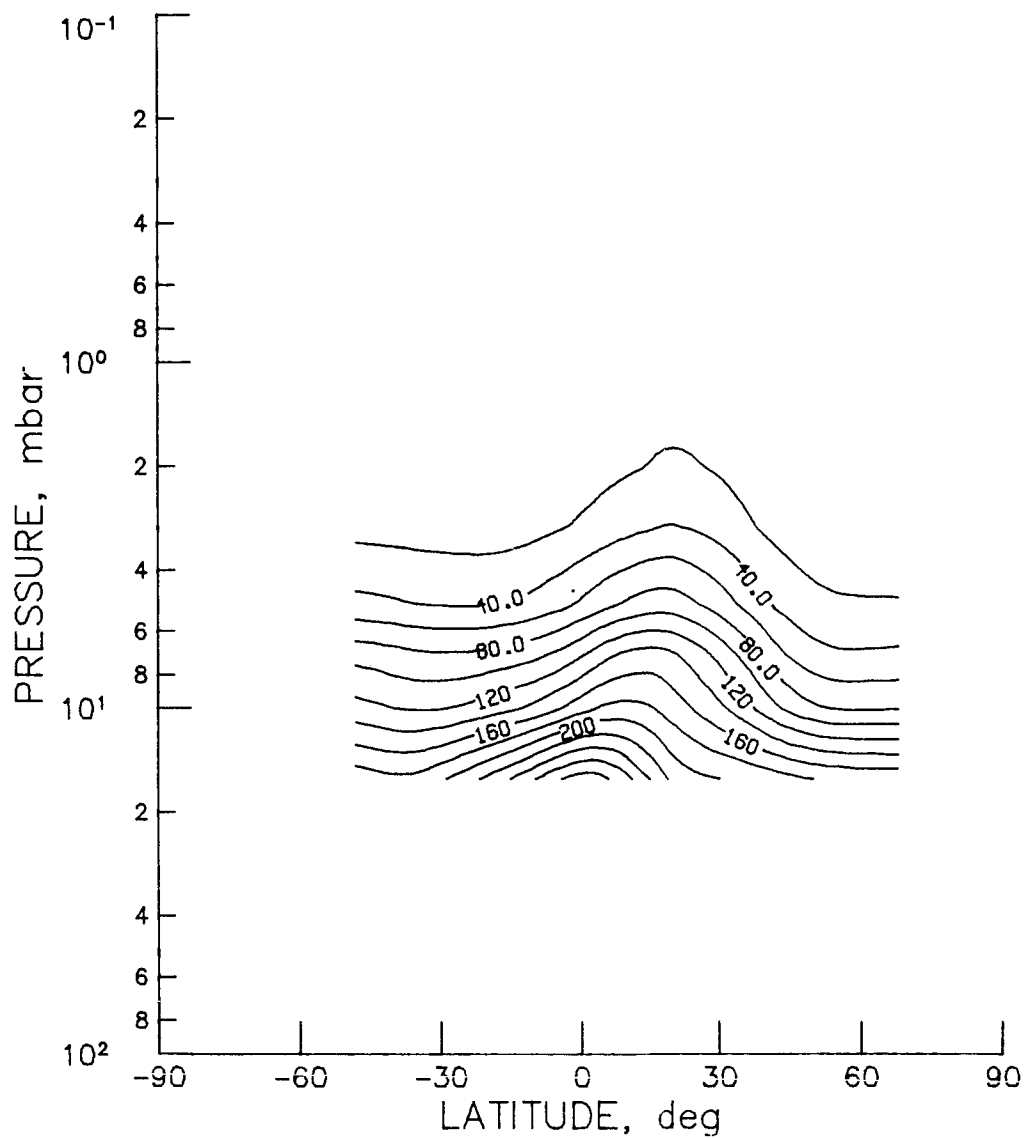


Figure CHN-19 - SAMS monthly zonal mean N_2O cross section for July 1979
(contour interval is 20.0 ppbv).

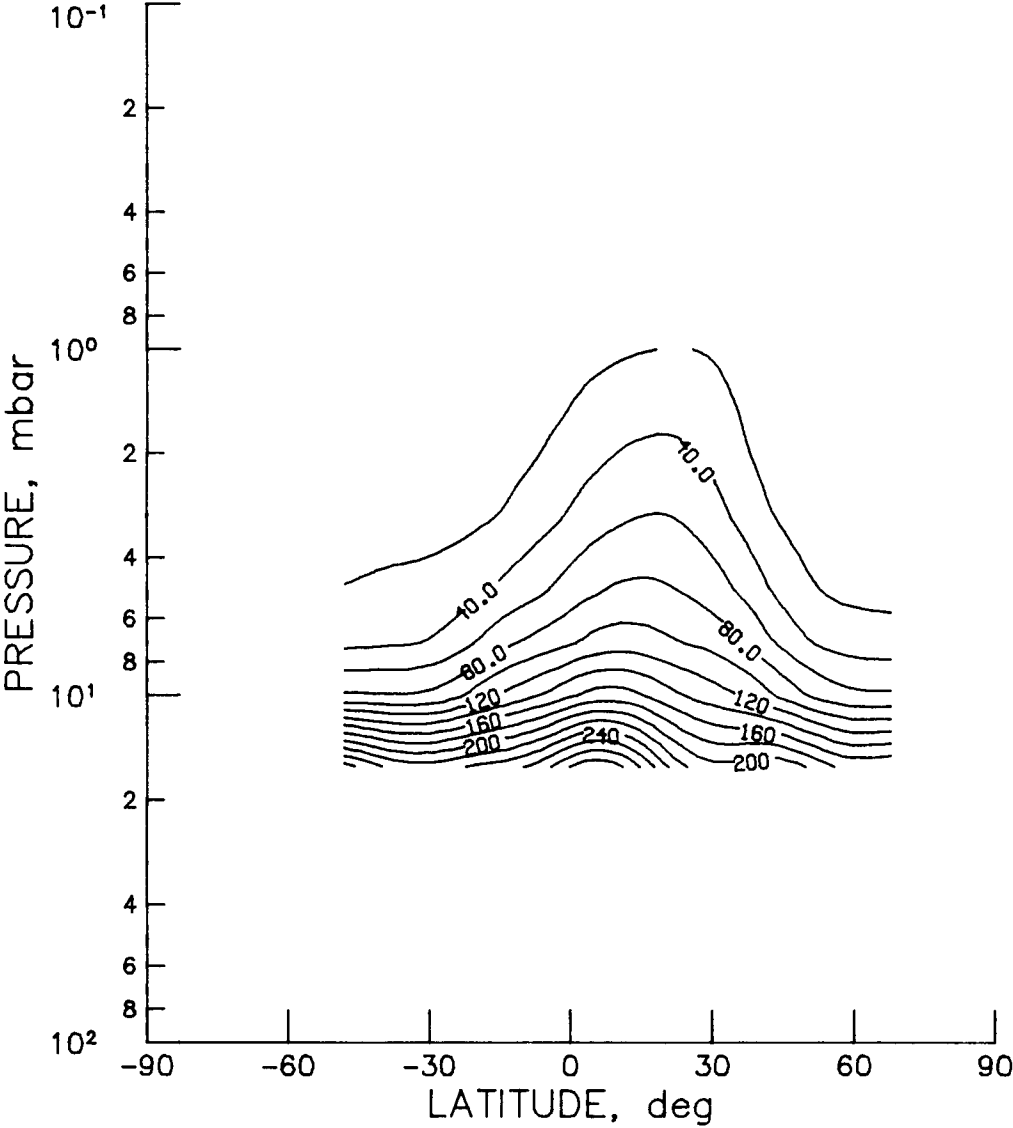


Figure CHN-20 - SAMS monthly zonal mean N₂O cross section for August 1979 (contour interval is 20.0 ppbv).

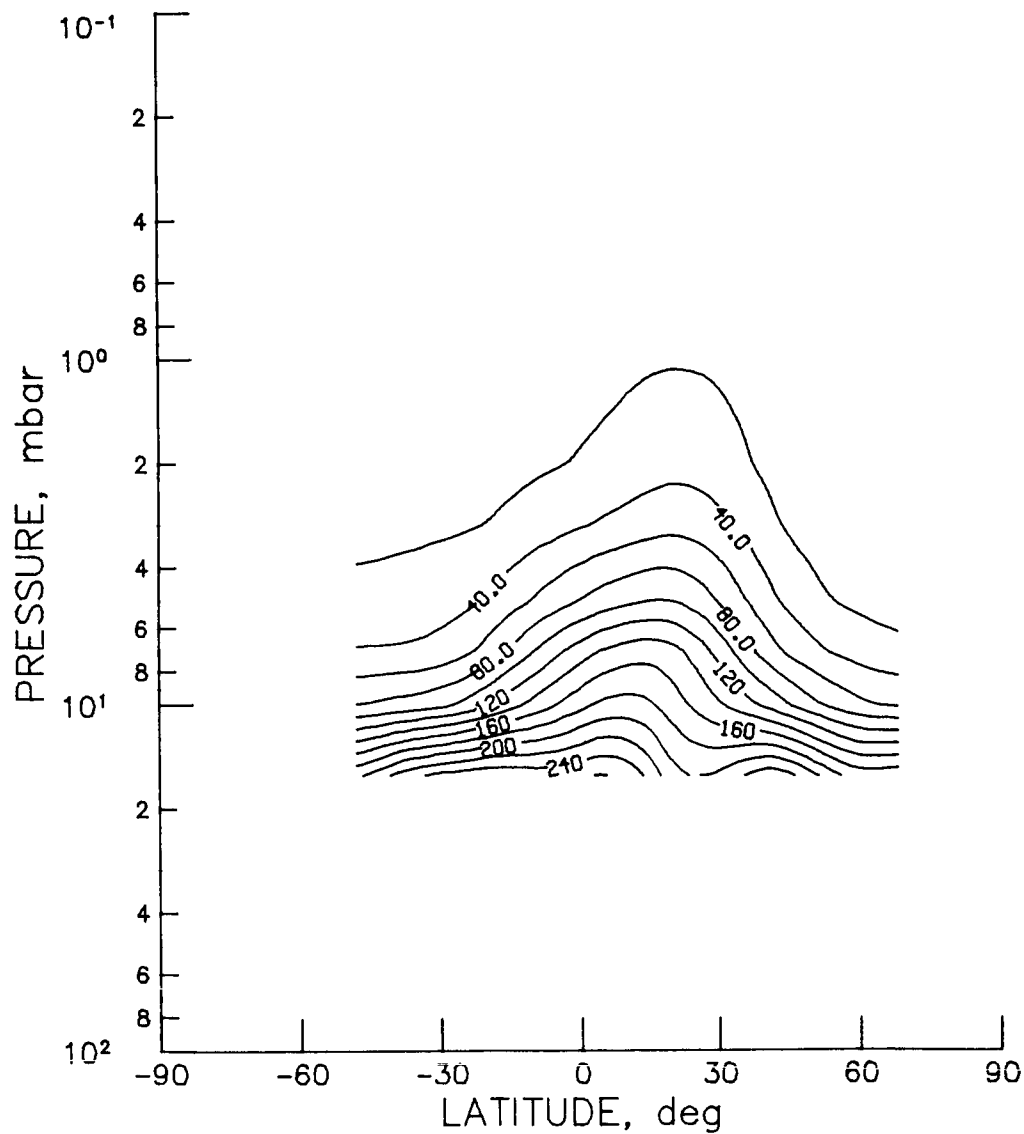


Figure CHN-21 - SAMS monthly zonal mean N_2O cross section for September 1979 (contour interval is 20.0 ppbv).

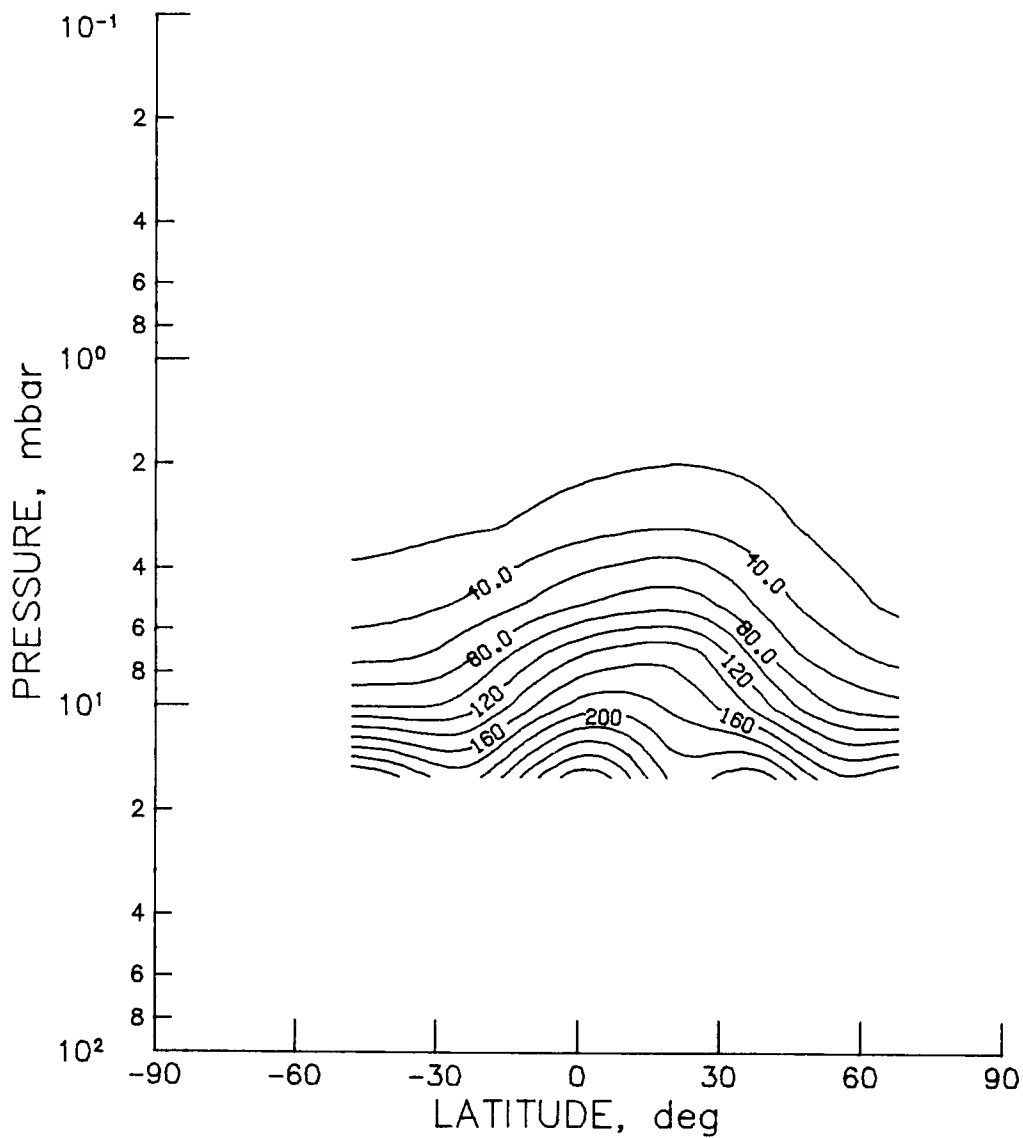


Figure CHN-22 - SAMS monthly zonal mean N_2O cross section for October 1979
(contour interval is 20.0 ppbv).

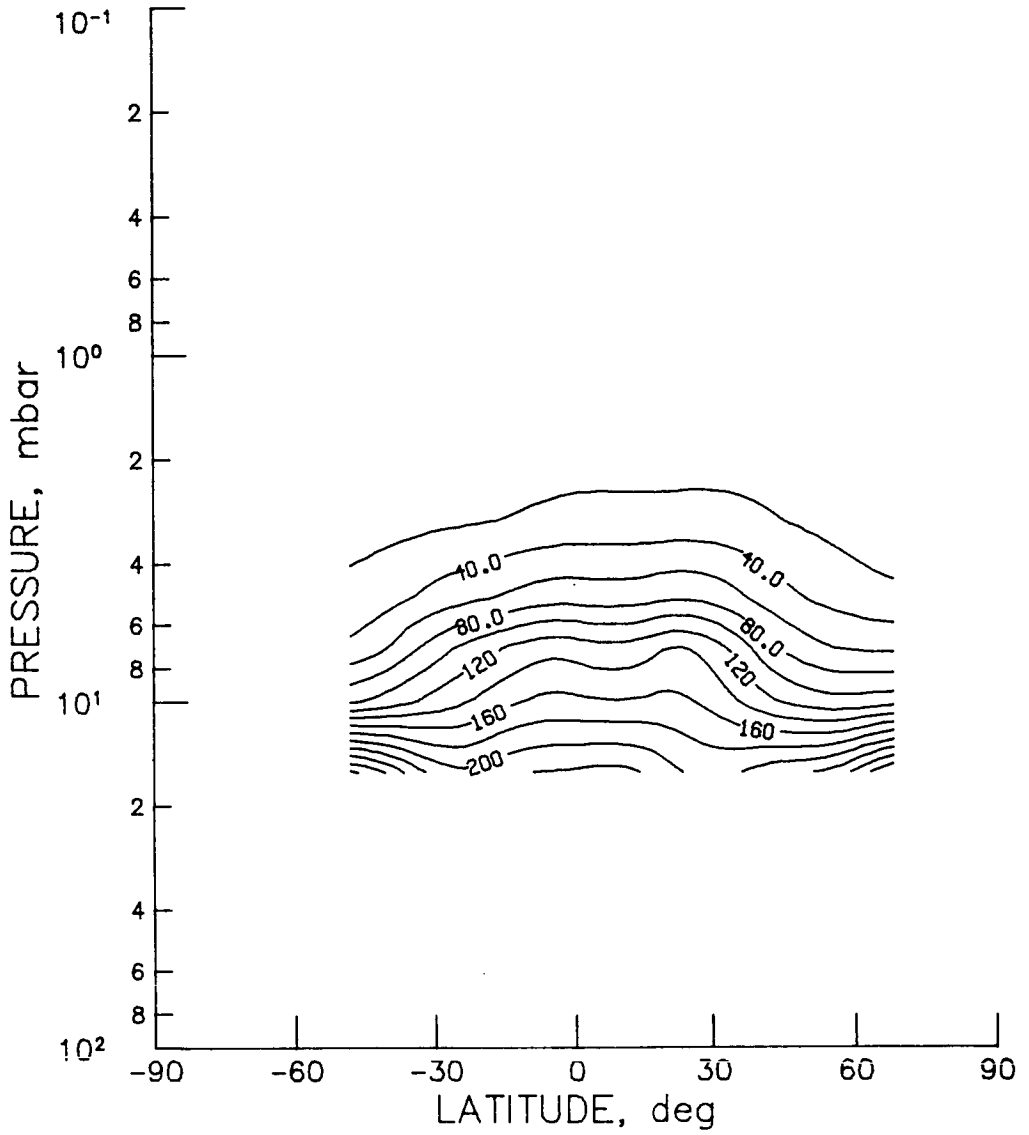


Figure CHN-23 - SAMS monthly zonal mean N_2O cross section for November 1979
(contour interval is 20.0 ppbv).

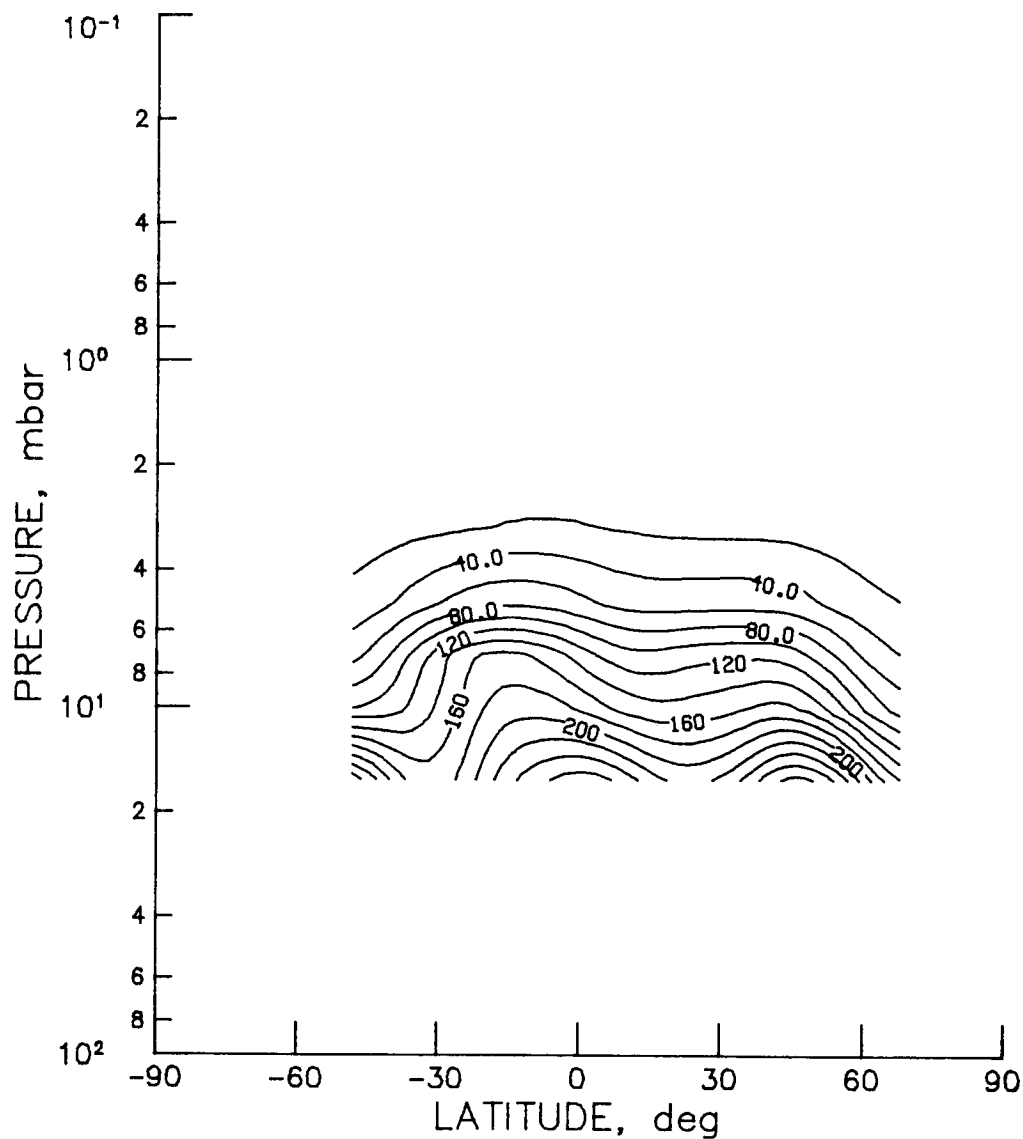


Figure CHN-24 - SAMS monthly zonal mean N_2O cross section for December 1979
(contour interval is 20.0 ppbv).

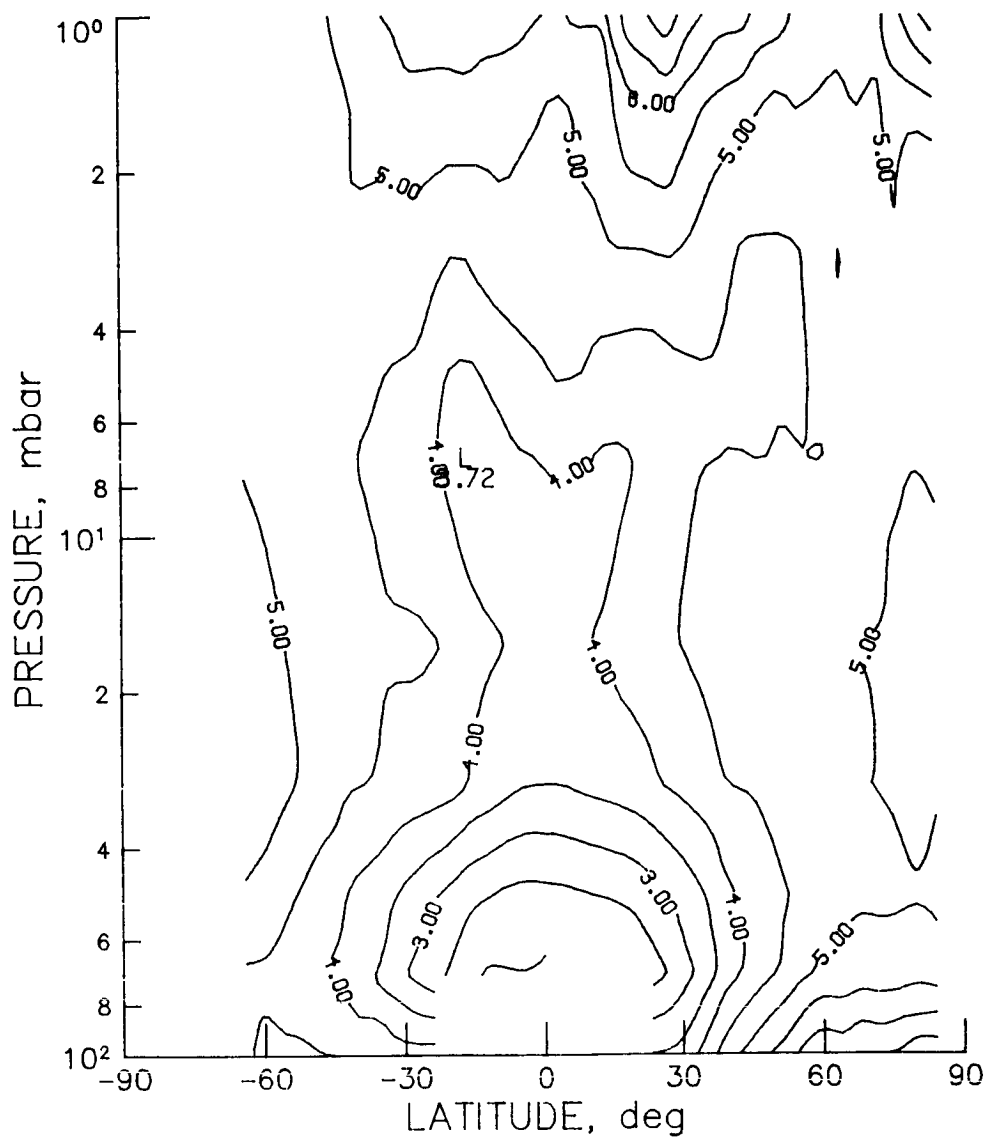


Figure CHN-25 - LIMS monthly zonal mean H₂O cross section for November 1978
(contour interval is 0.5 ppmv).

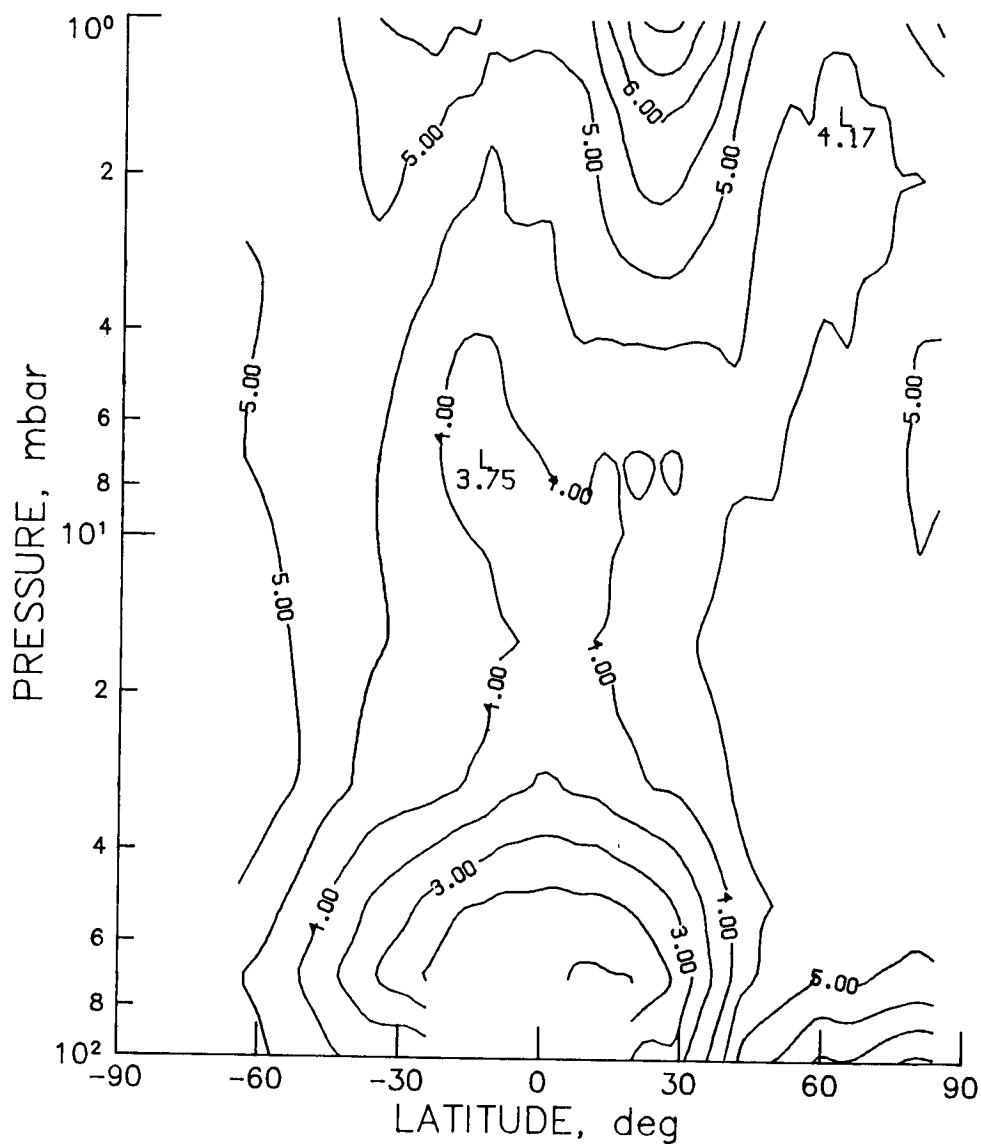


Figure CHN-26 - LIMS monthly zonal mean H₂O cross section for December 1978 (contour interval is 0.5 ppmv).

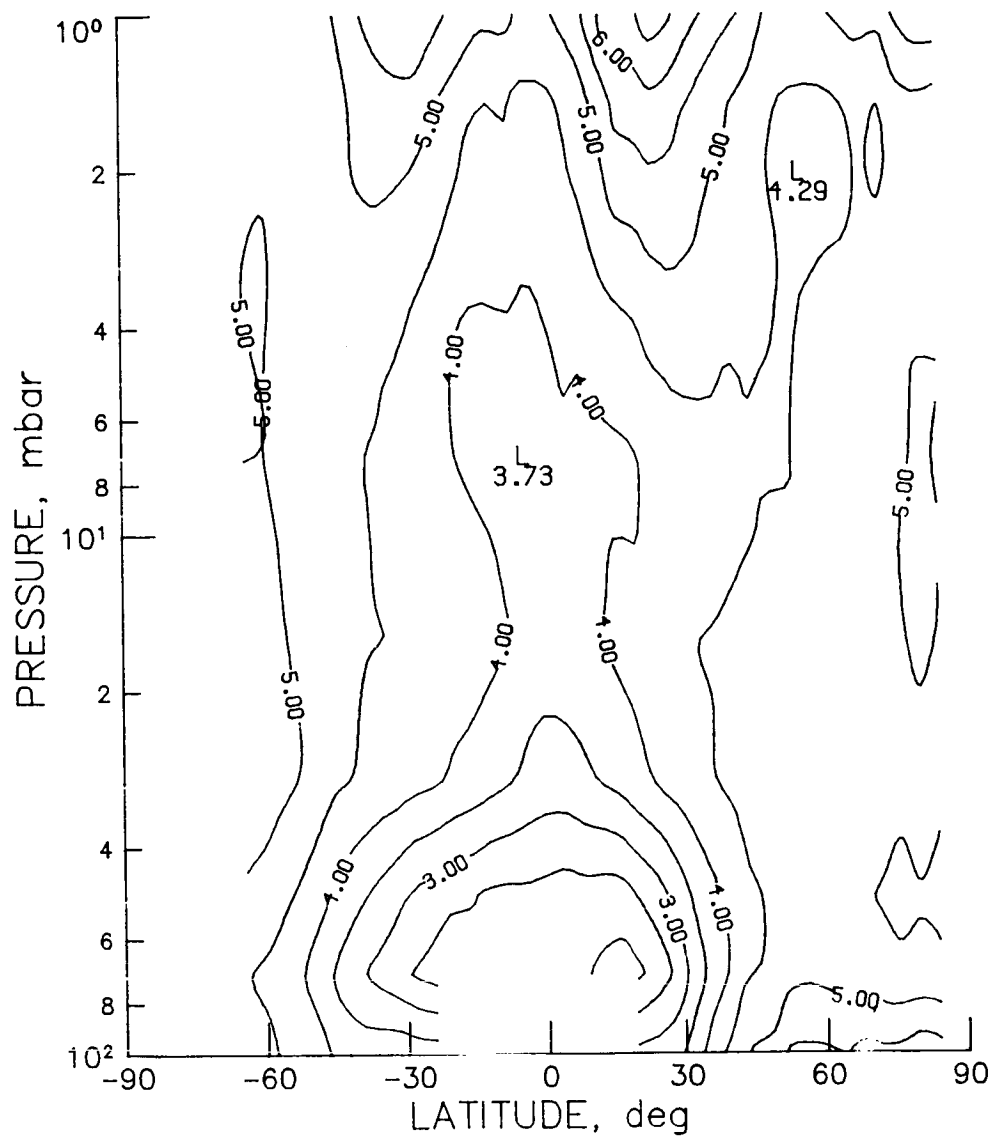


Figure CHN-27 - LIMS monthly zonal mean H_2O cross section for January 1979
(contour interval is 0.5 ppmv).

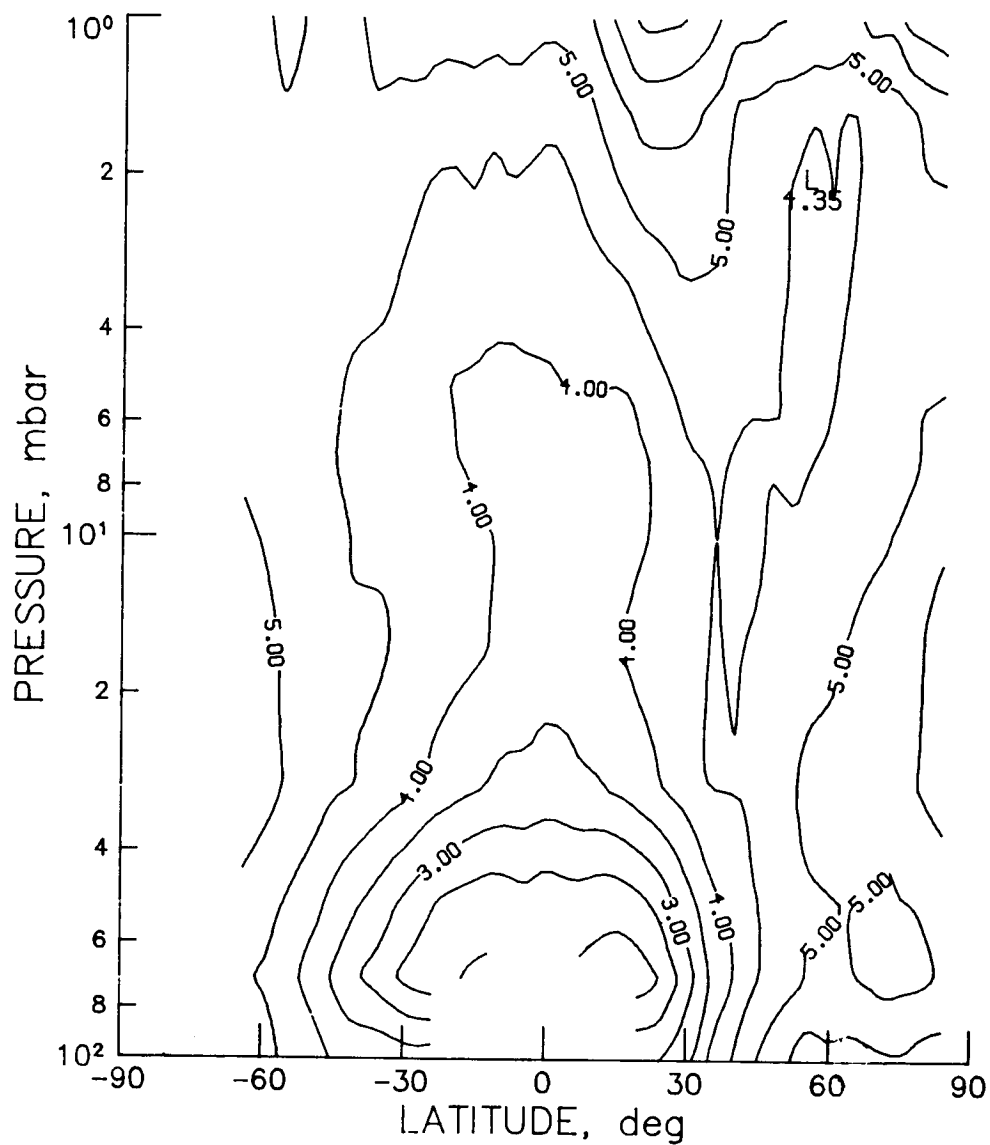


Figure CHN-28 - LIMS monthly zonal mean H_2O cross section for February 1979
(contour interval is 0.5 ppmv).

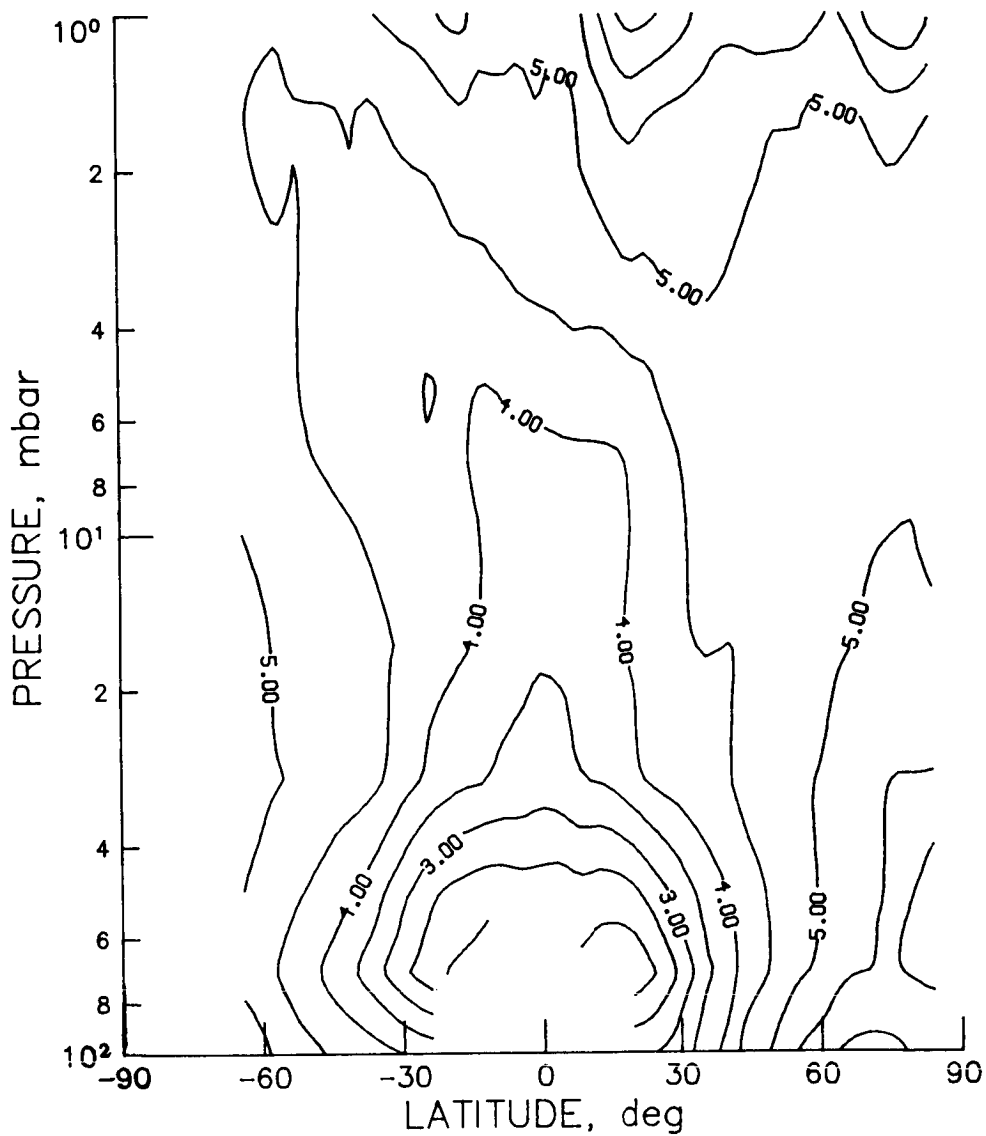


Figure CHN-29 - LIMS monthly zonal mean H_2O cross section for March 1979
(contour interval is 0.5 ppmv).

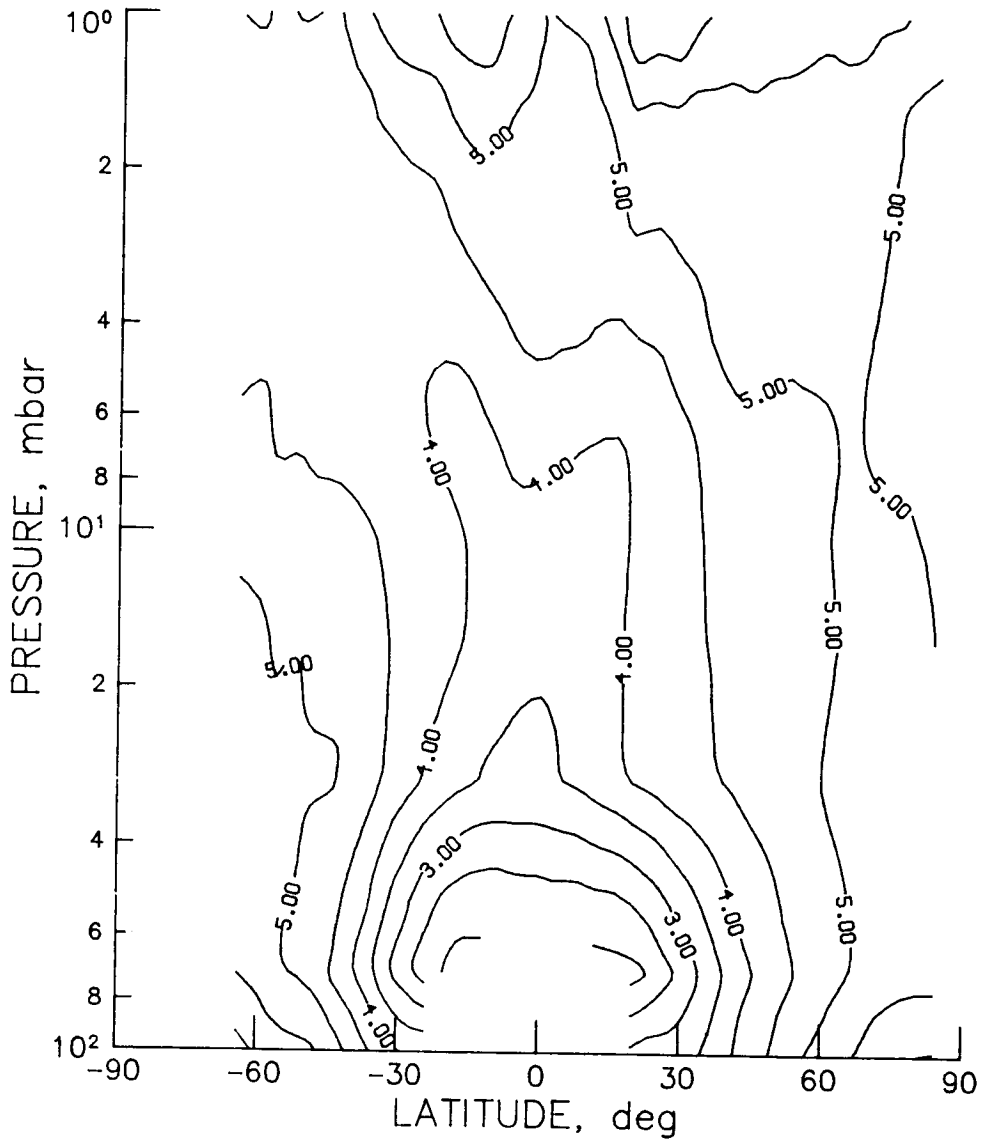


Figure CHN-30 - LIMS monthly zonal mean H_2O cross section for April 1979
(contour interval is 0.5 ppmv).

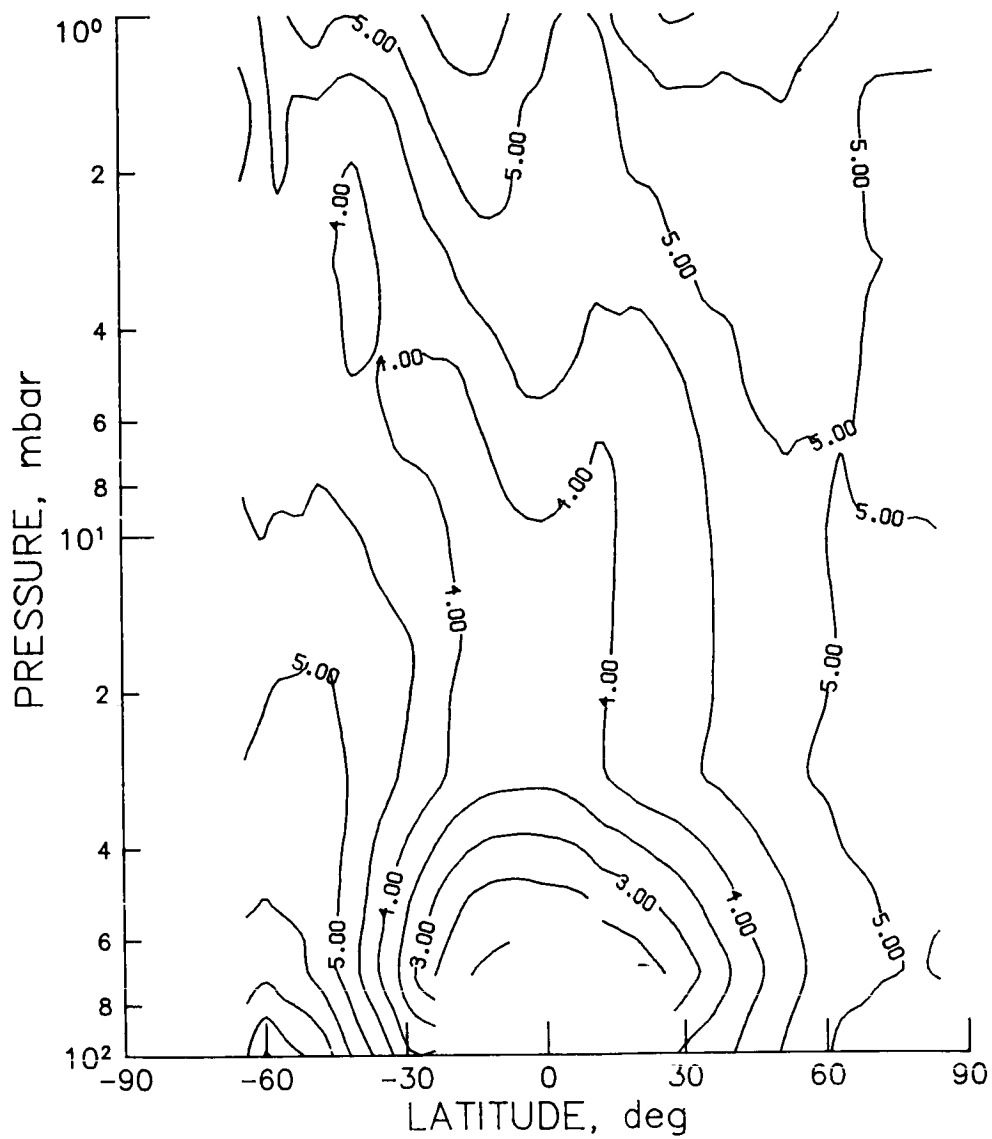
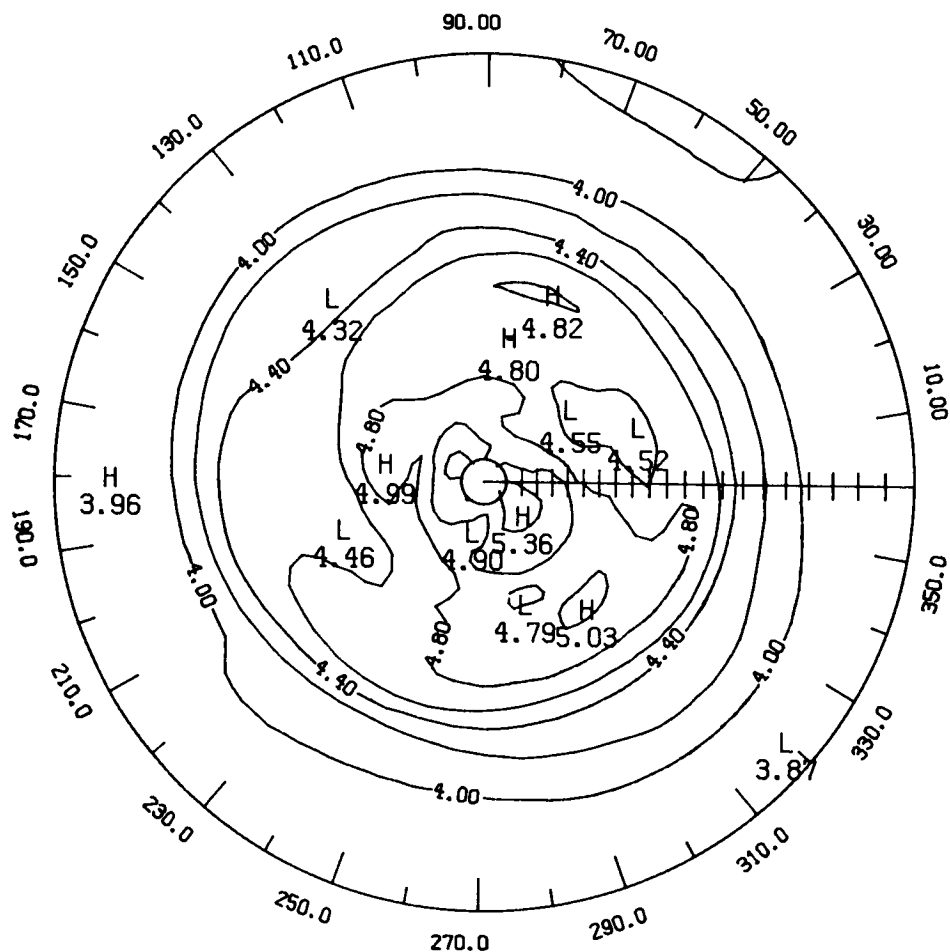
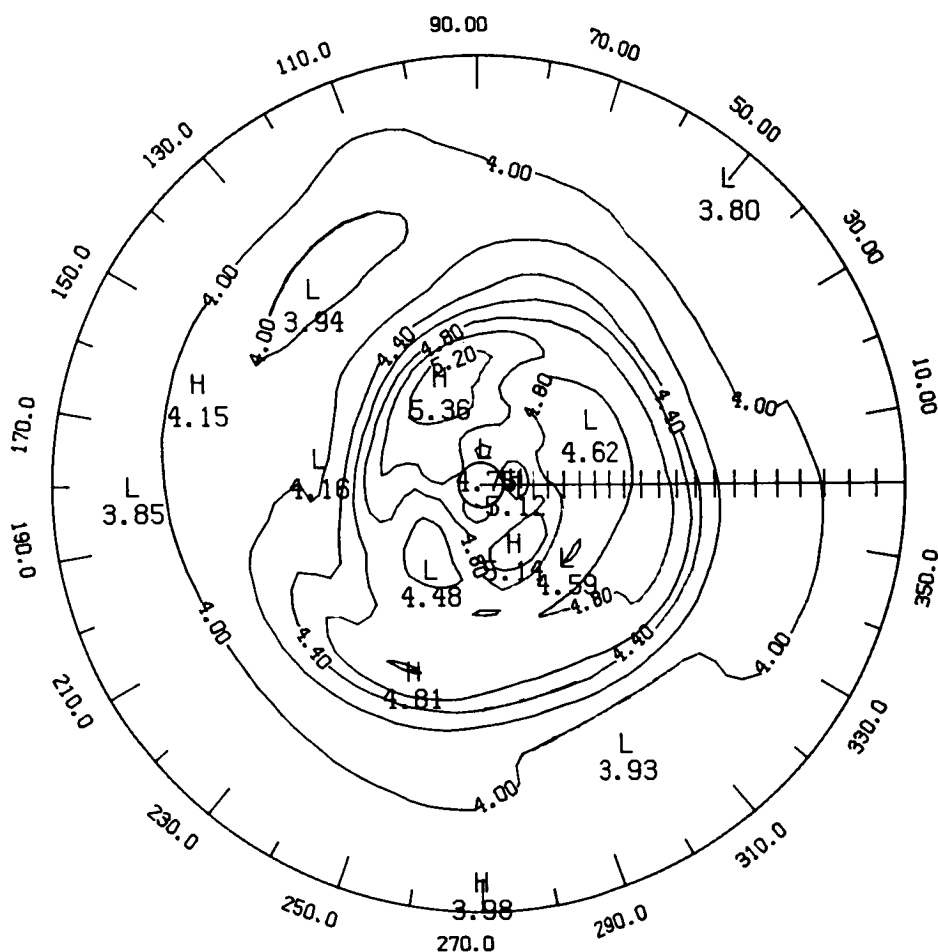


Figure CHN-31 - LIMS monthly zonal mean H_2O cross section for May 1979
(contour interval is 0.5 ppmv).



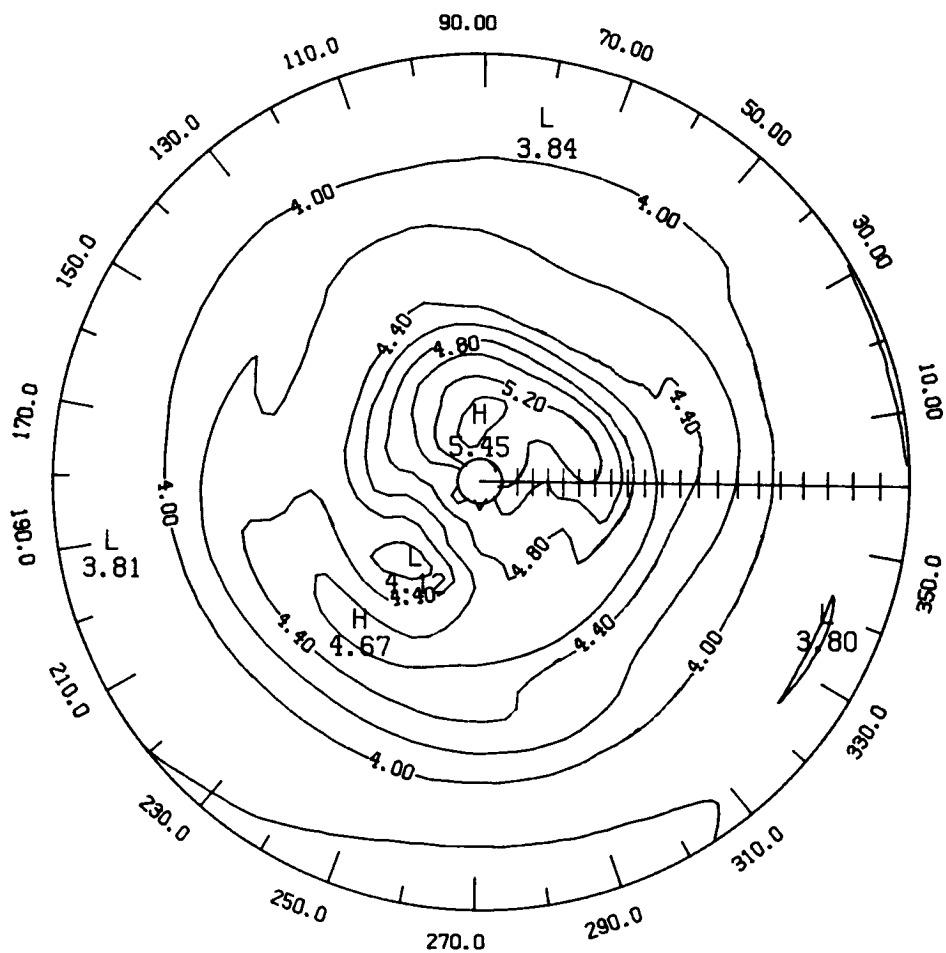
LATITUDE 0. TO 84.
1 2 1 LAT SMOOTHING

Figure CHN-32 - LIMS monthly mean 10 mb H₂O polar stereographic plot for November 1978 (contour interval is 0.2 ppmv).



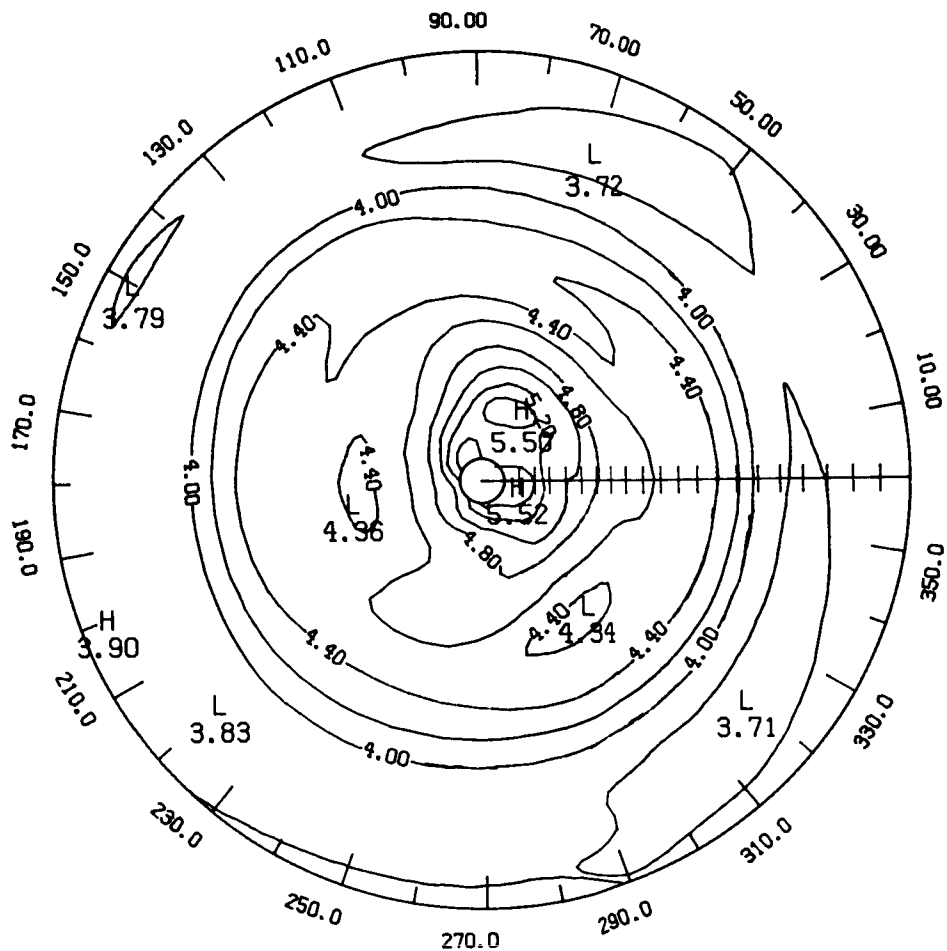
LATITUDE 0. TO 84.
1 2 1 LAT SMOOTHING

Figure CHN-33 - LIMS monthly mean 10 mb H_2O polar stereographic plot for December 1978 (contour interval is 0.2 ppmv).



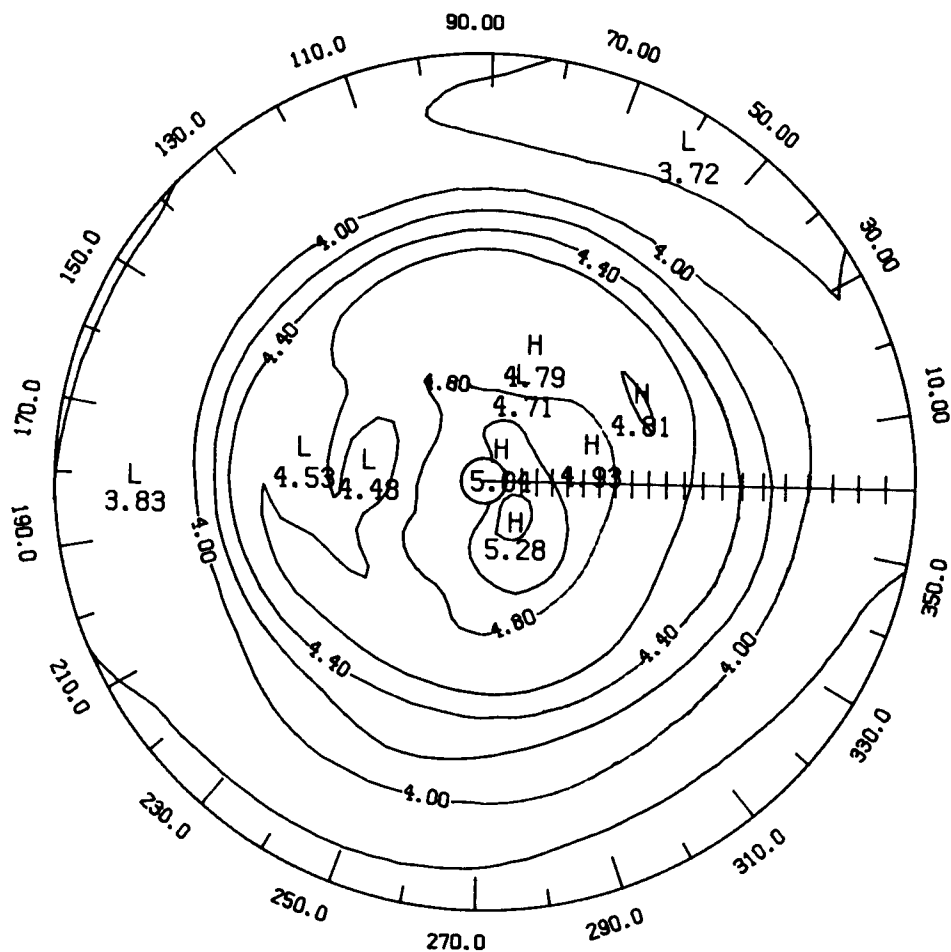
LATITUDE 0. TO 84.
1 2 1 LAT SMOOTHING

Figure CHN-34 - LIMS monthly mean 10 mb H₂O polar stereographic plot for January 1979 (contour interval is 0.2 ppmv).



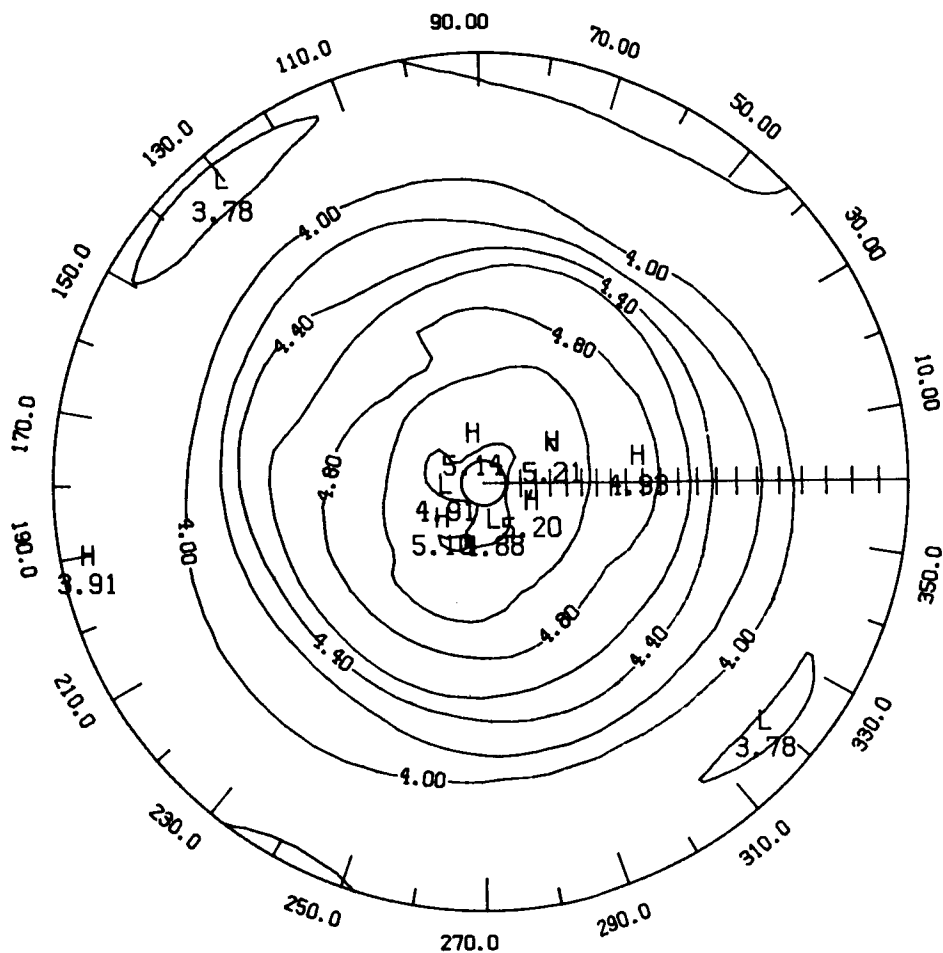
LATITUDE 0. TO 84.
1 2 1 LAT SMOOTHING

Figure CHN-35 - LIMS monthly mean 10 mb H₂O polar stereographic plot for February 1979 (contour interval is 0.2 ppmv).



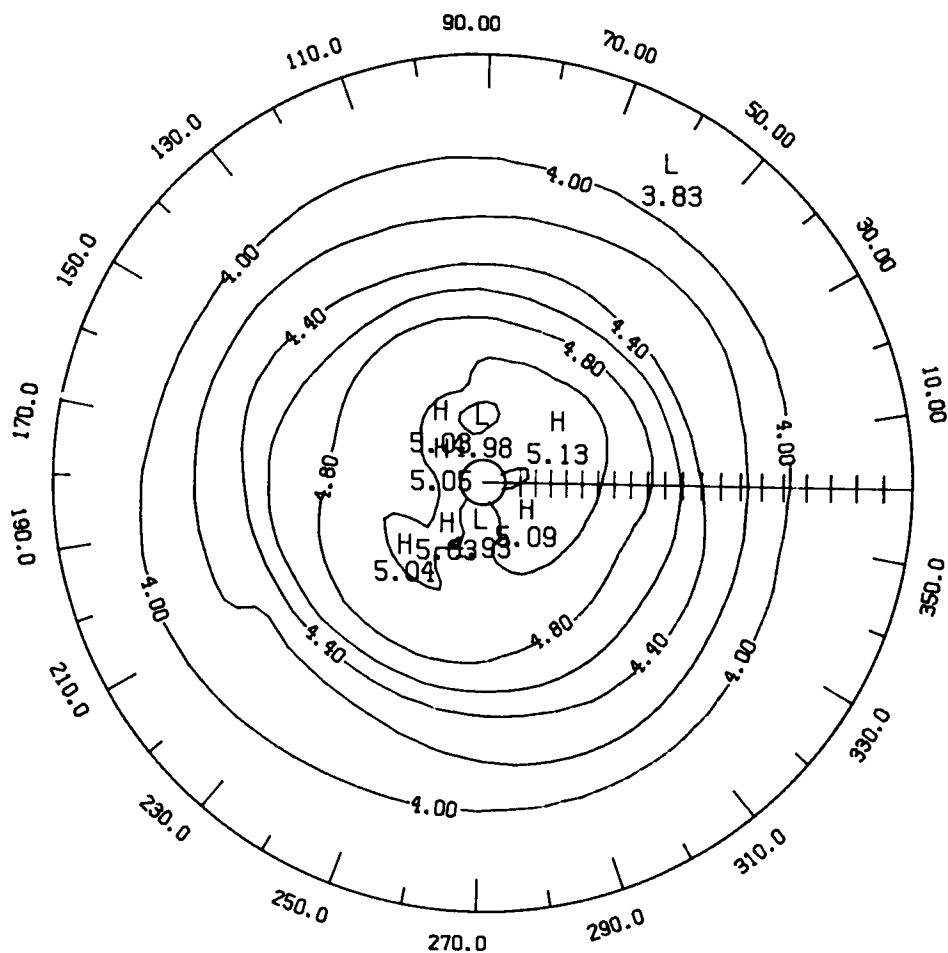
LATITUDE 0. TO 84.
1 2 1 LAT SMOOTHING

Figure CHN-36 - LIMS monthly mean 10 mb H₂O polar stereographic plot for March 1979 (contour interval is 0.2 ppmv).



LATITUDE 0. TO 84.
1 2 1 LAT SMOOTHING

Figure CHN-37 - LIMS monthly mean 10 mb H₂O polar stereographic plot for April 1979 (contour interval is 0.2 ppmv).



LATITUDE 0. TO 84.
1 2 1 LAT SMOOTHING

Figure CHN-38 - LIMS monthly mean 10 mb H₂O polar stereographic plot for May 1979 (contour interval is 0.2 ppmv).

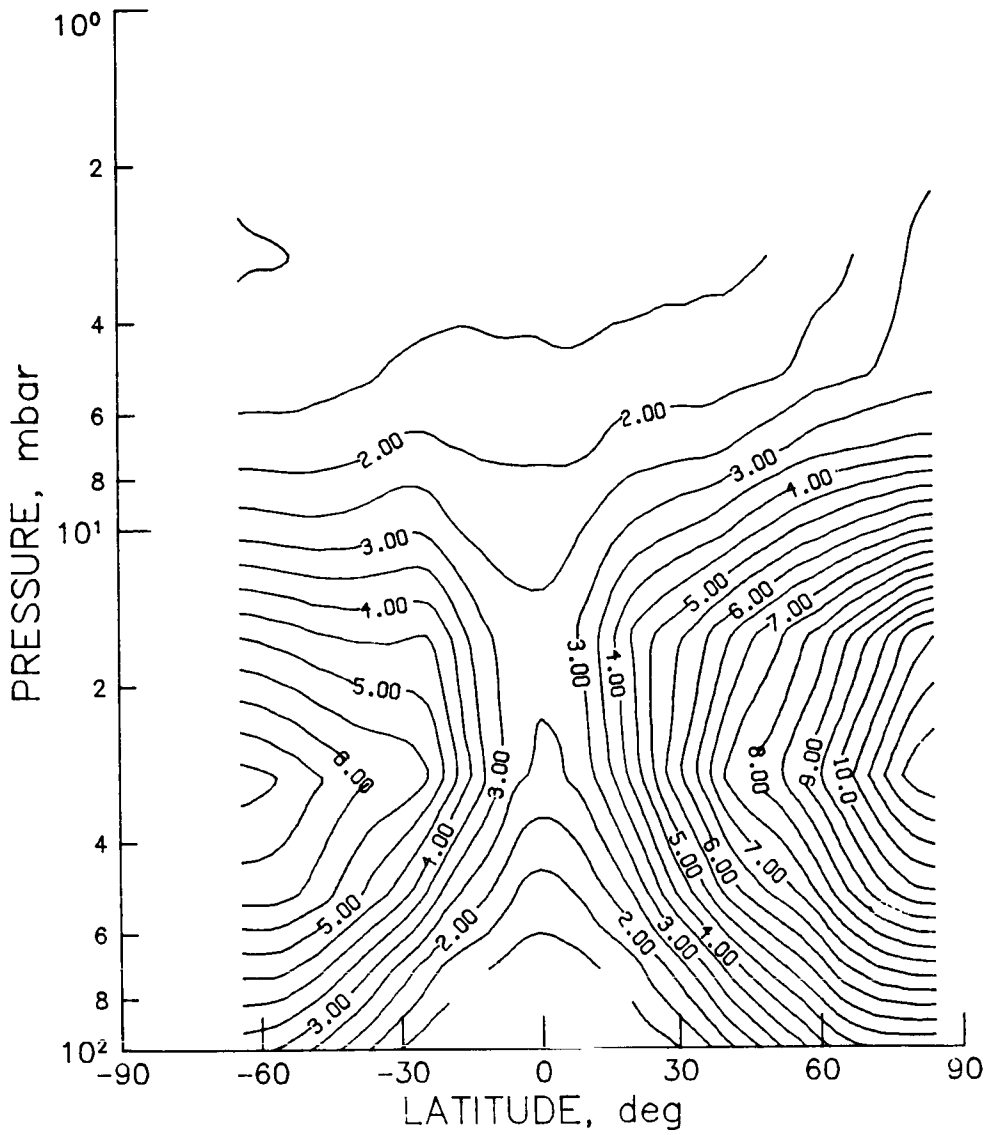


Figure H-1 - LIMS monthly zonal mean HNO_3 cross section for November 1978
(contour interval is 0.5 ppbv).

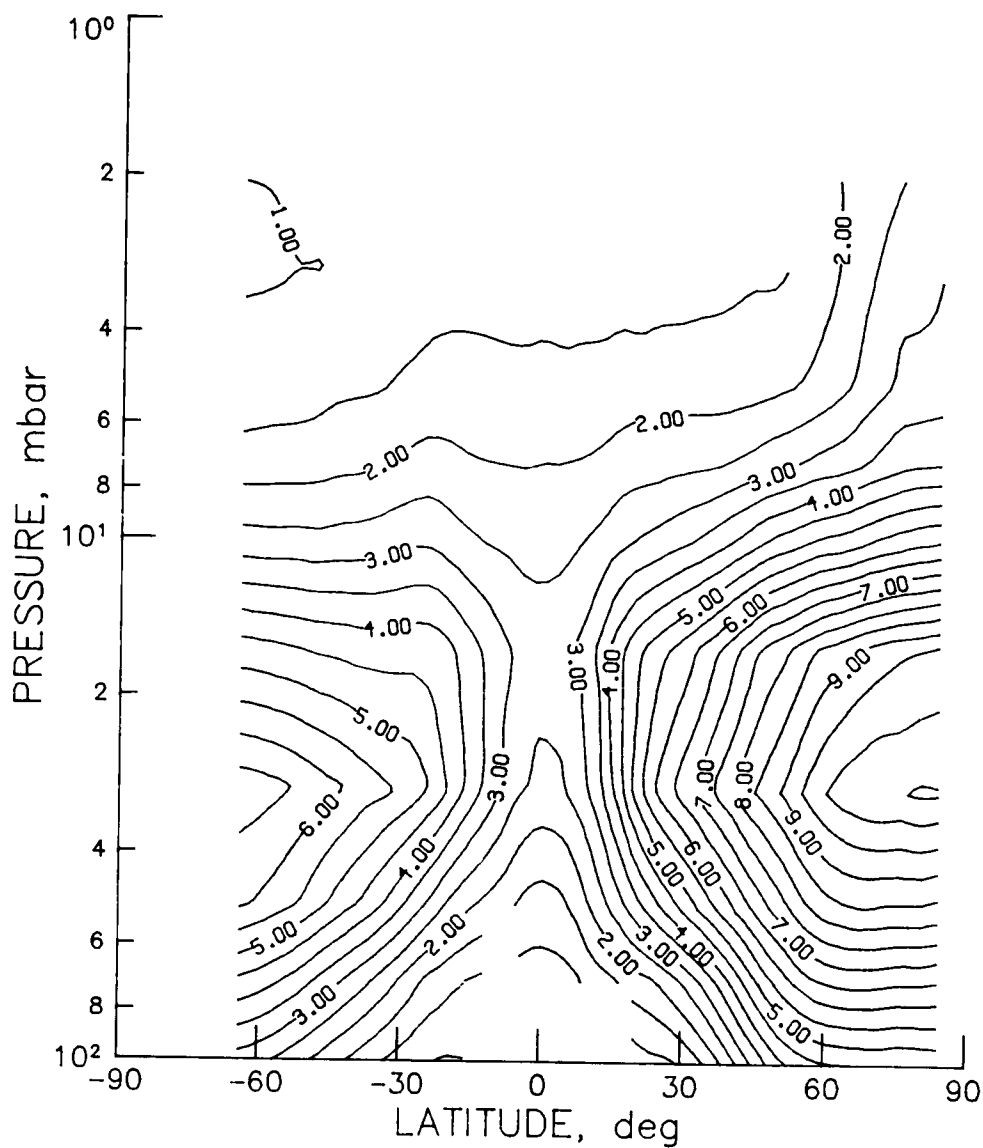


Figure H-2 - LIMS monthly zonal mean HNO_3 cross section for December 1978 (contour interval is 0.5 ppbv).

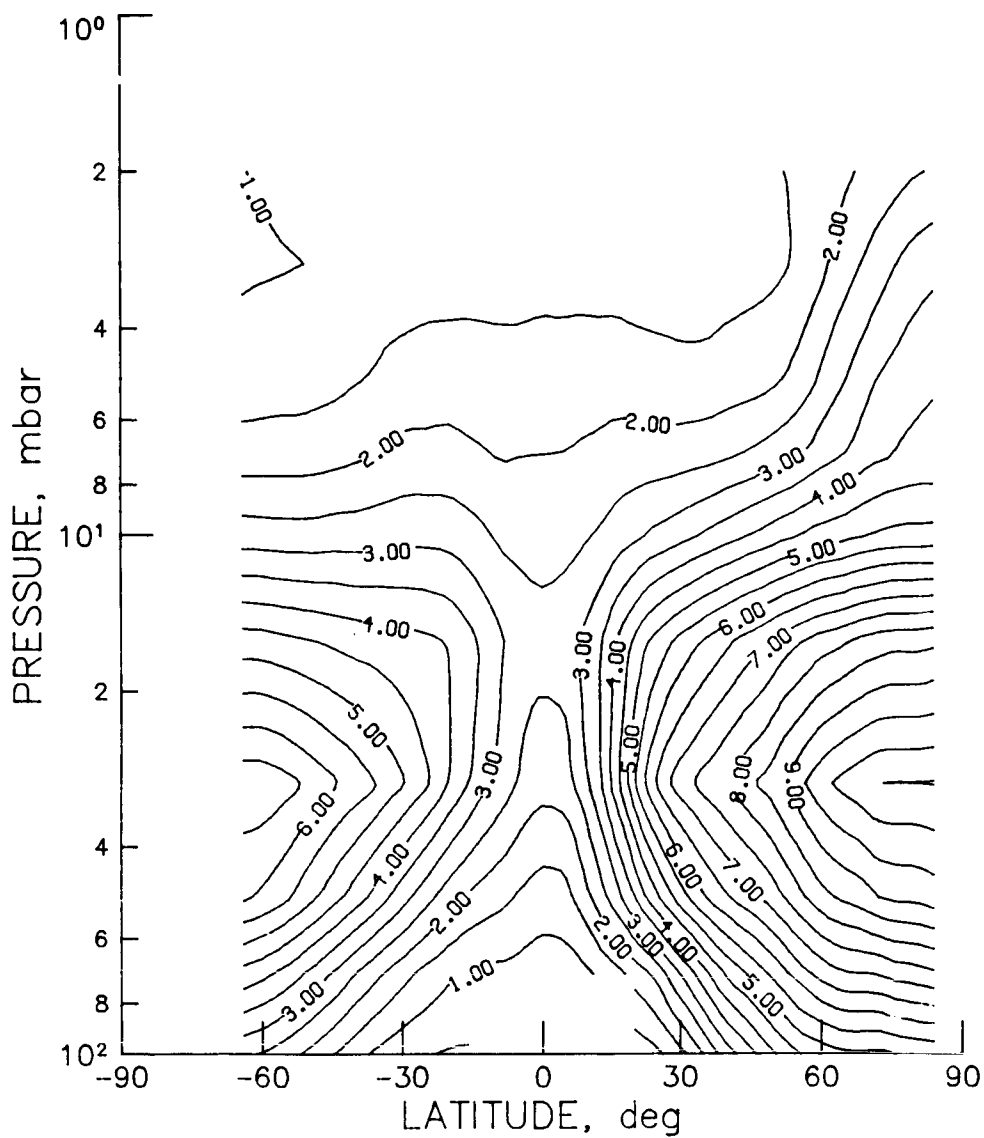


Figure H-3 - LIMS monthly zonal mean HNO_3 cross section for January 1979
(contour interval is 0.5 ppbv).

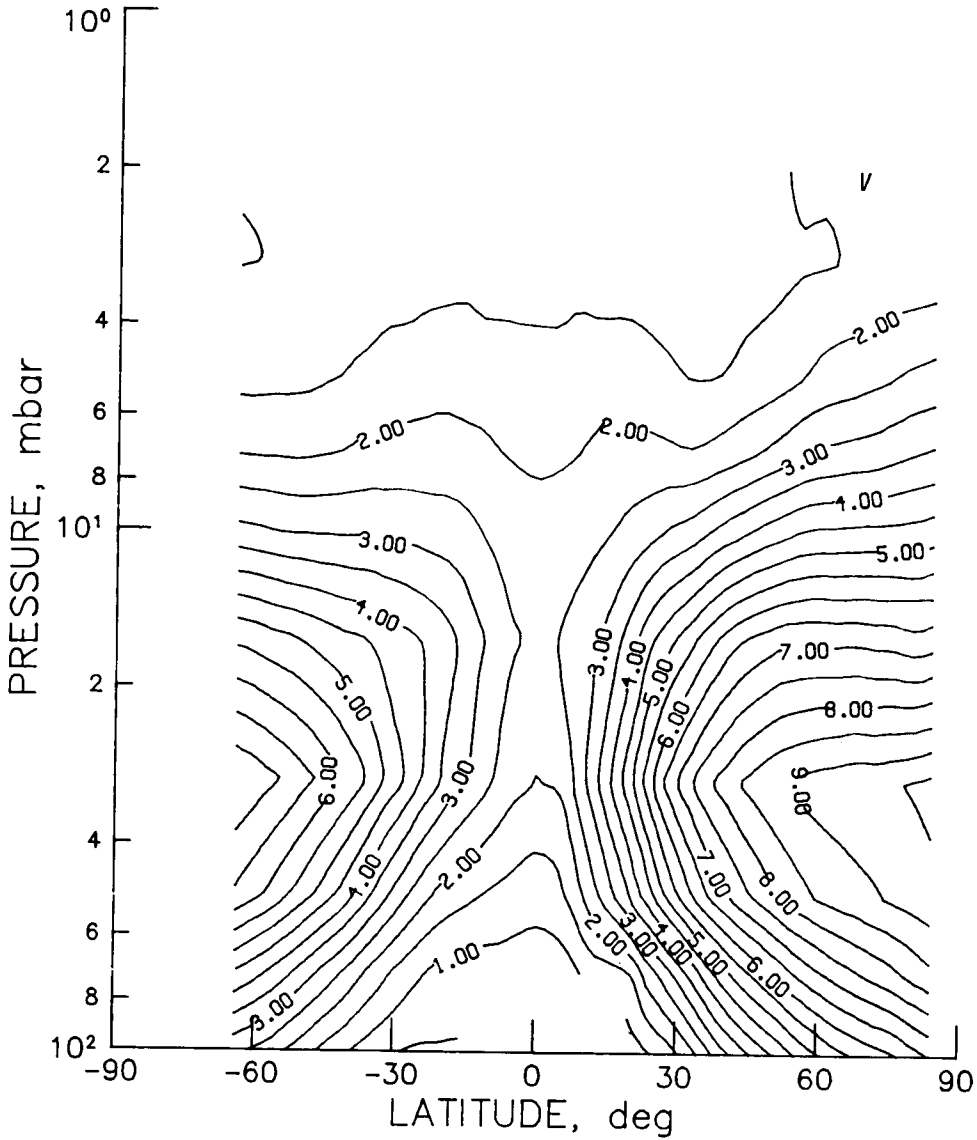


Figure H-4 - LIMS monthly zonal mean HNO_3 cross section for February 1979 (contour interval is 0.5 ppbv).

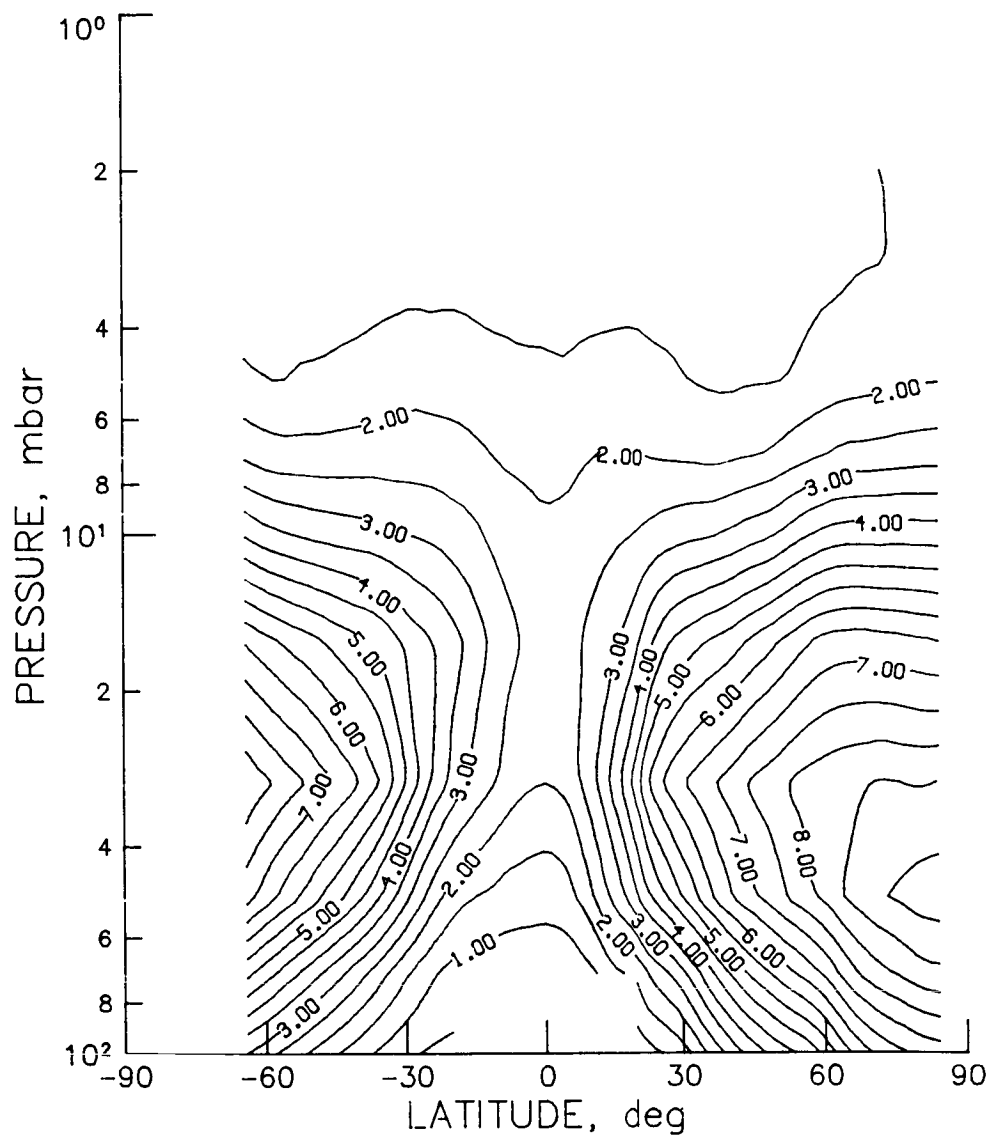


Figure H-5 - LIMS monthly zonal mean HNO_3 cross section for March 1979 (contour interval is 0.5 ppbv).

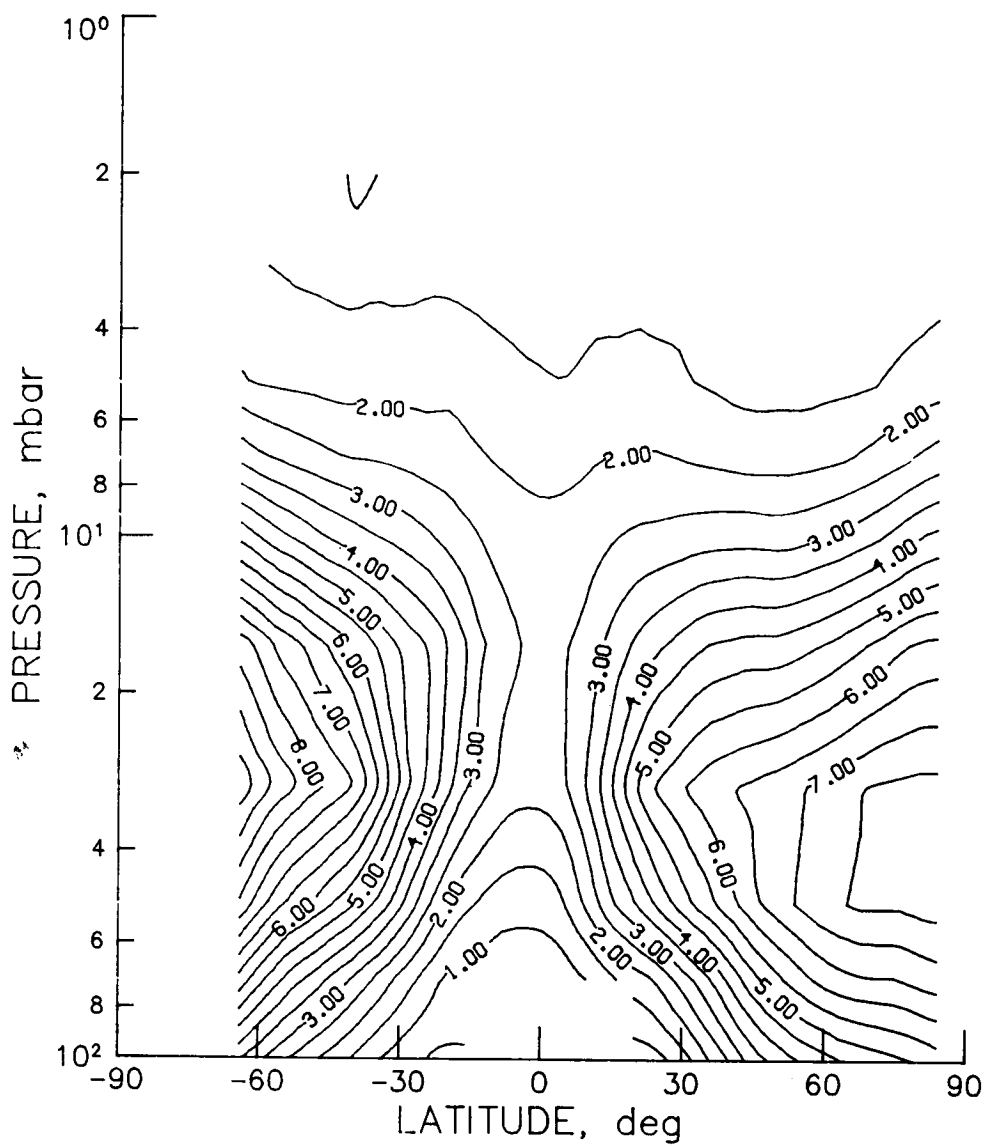


Figure H-6 - LIMS monthly zonal mean HNO_3 cross section for April 1979 (contour interval is 0.5 ppbv).

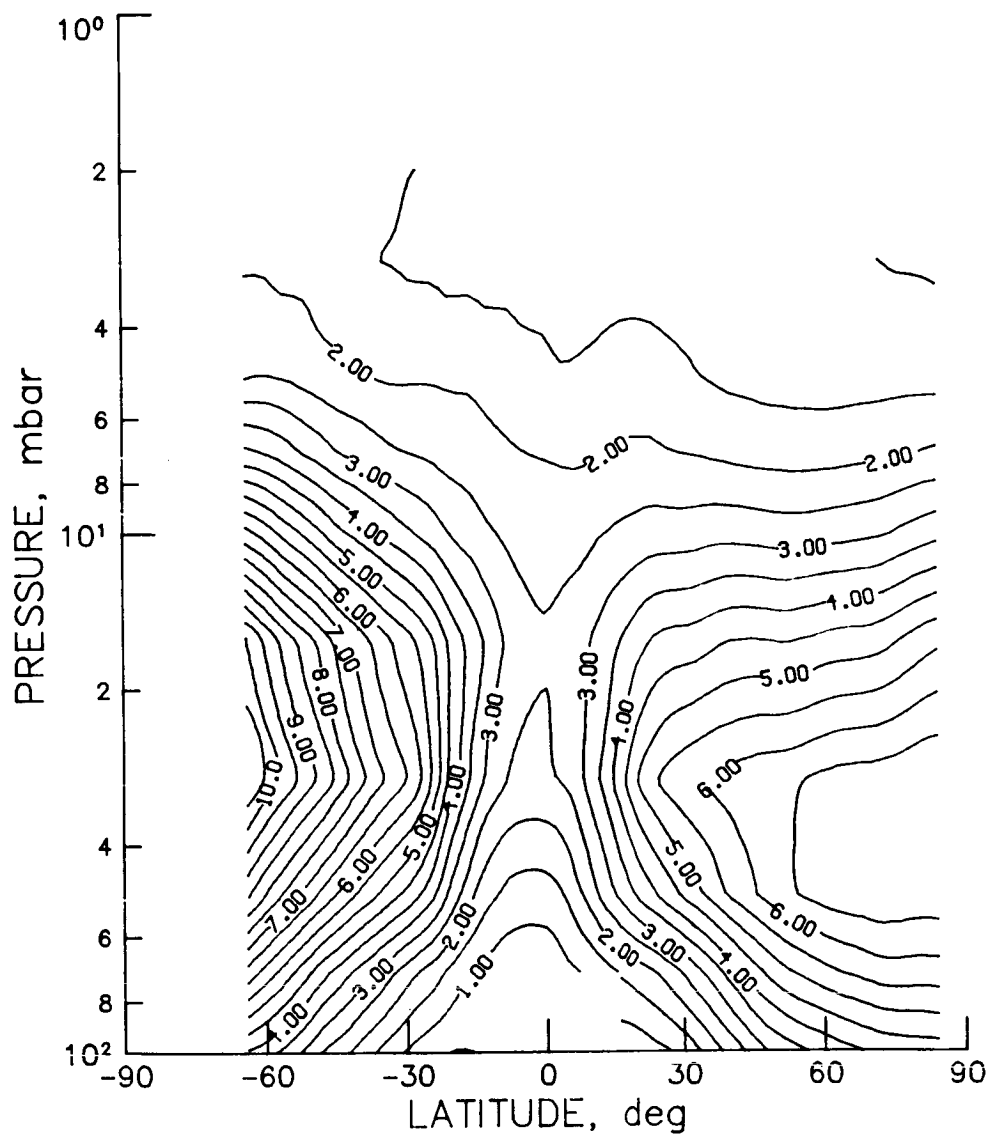
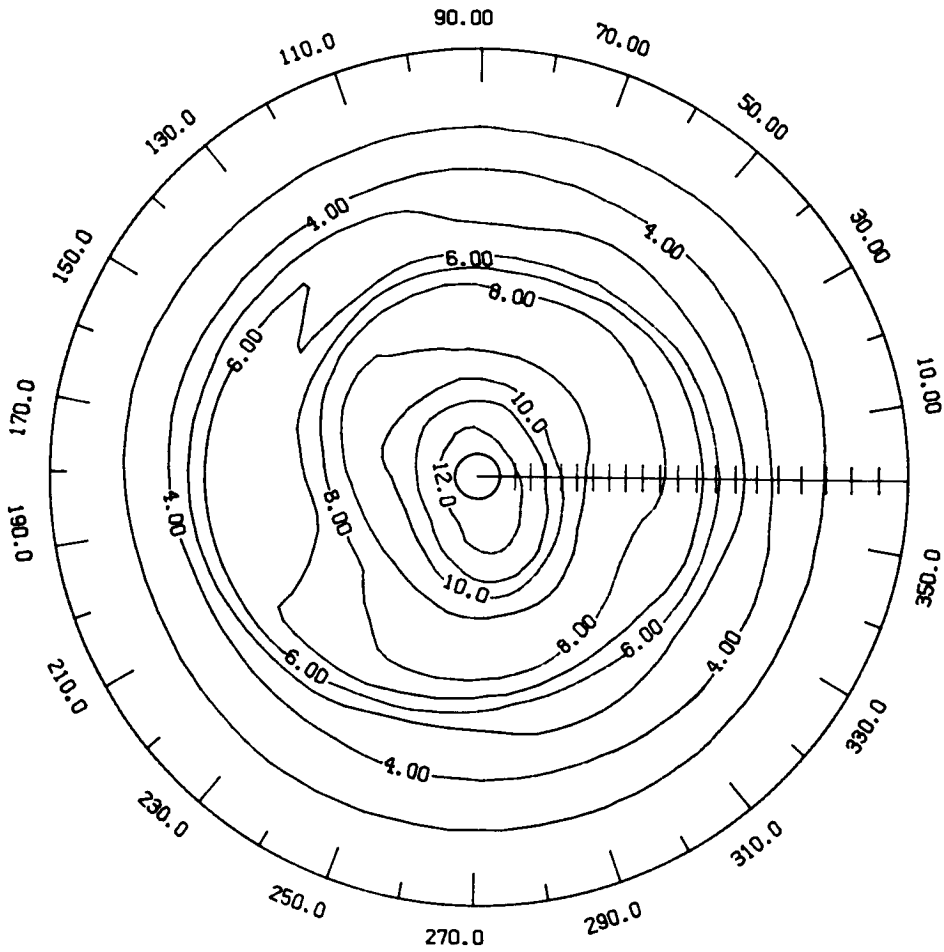
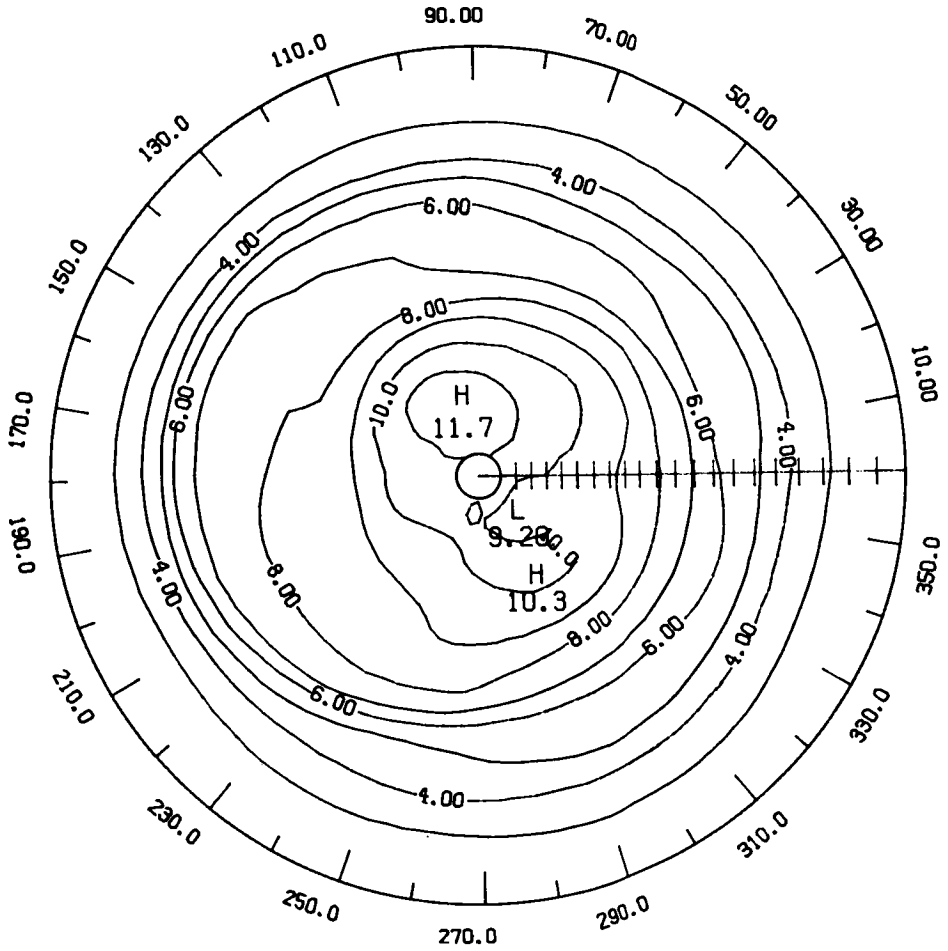


Figure H-7 - LIMS monthly zonal mean HNO₃ cross section for May 1979
(contour interval is 0.5 ppbv).



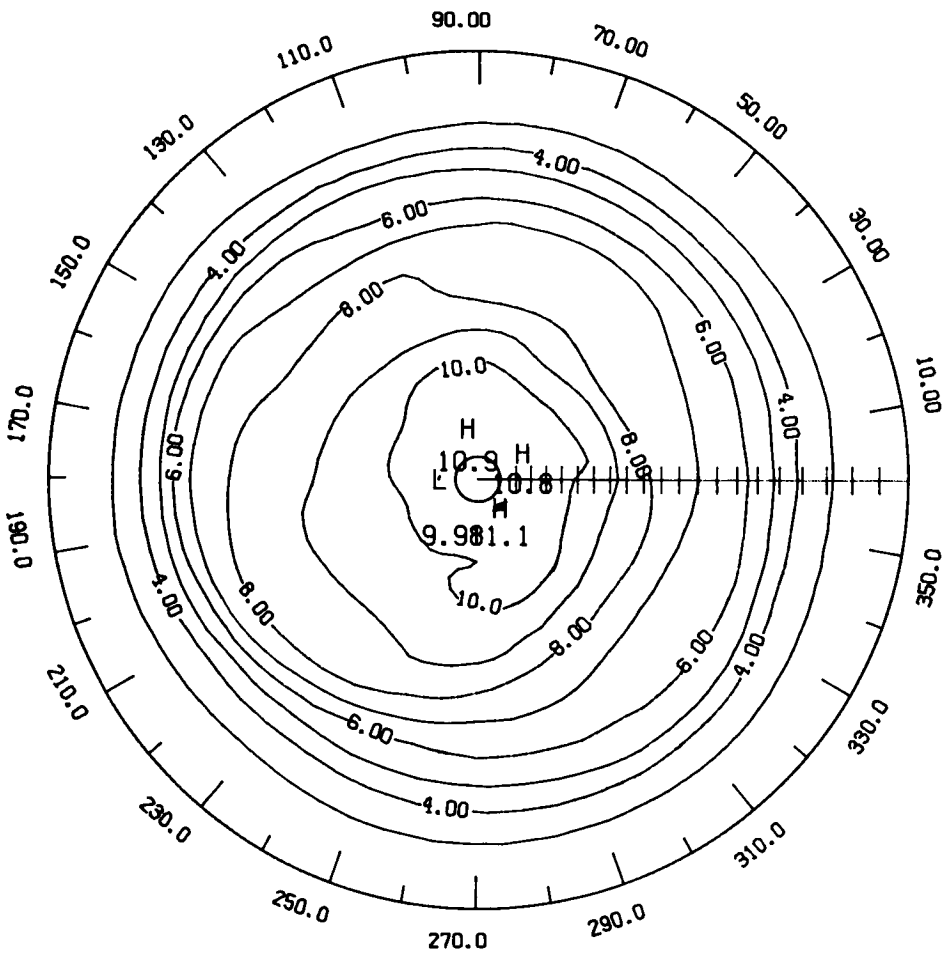
LATITUDE 0. TO 84.

Figure H-8 - LIMS monthly mean HNO₃ 30 mb polar stereographic plot for November 1978 (contour interval is 1.0 ppbv).



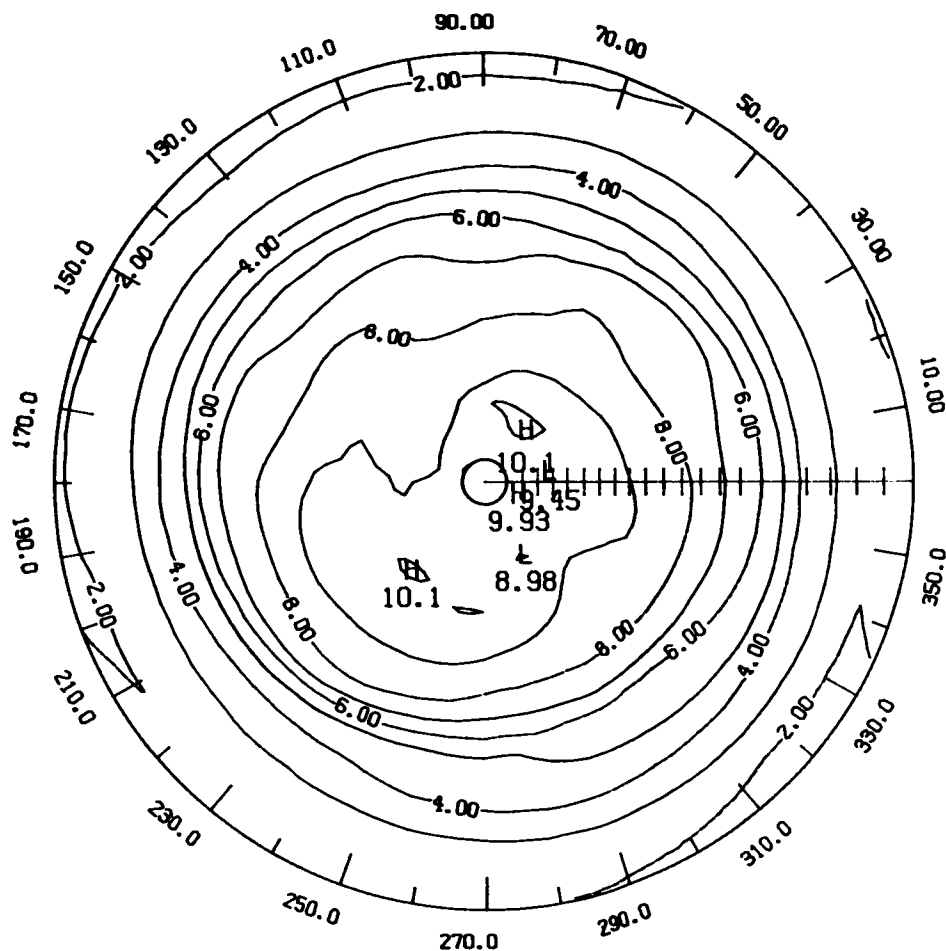
LATITUDE 0. TO 84.

Figure H-9 - LIMS monthly mean HNO₃ 30 mb polar stereographic plot for December 1978 (contour interval is 1.0 ppbv).



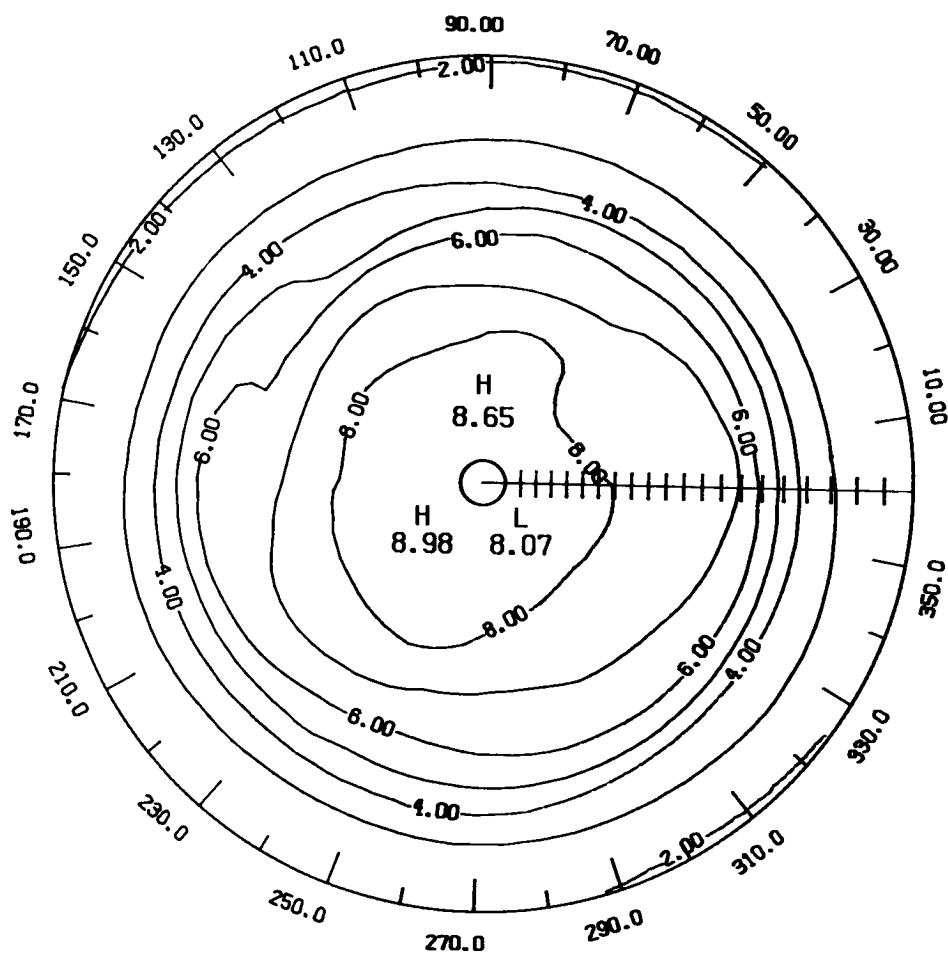
LATITUDE 0. TO 84.

Figure H-10 - LIMS monthly mean HNO₃ 30 mb polar stereographic plot for January 1979 (contour interval is 1.0 ppbv).



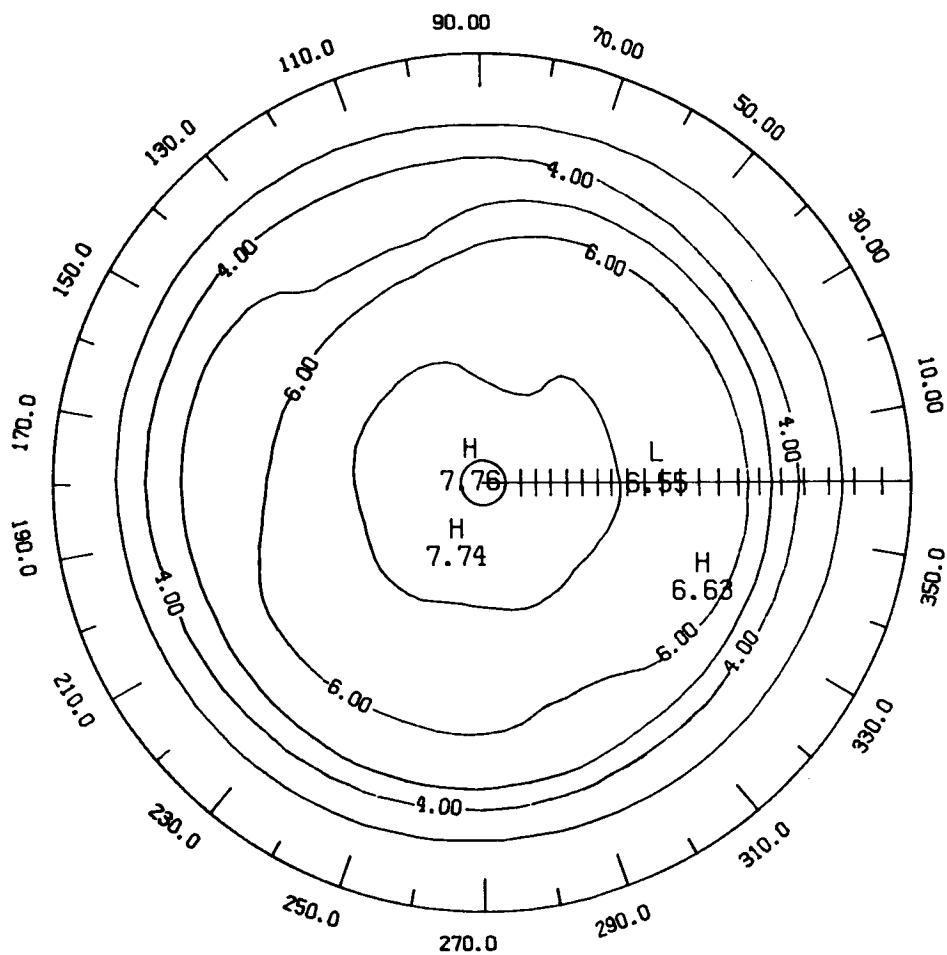
LATITUDE 0. TO 84.

Figure H-11 - LIMS monthly mean HNO_3 30 mb polar stereographic plot for February 1979 (contour interval is 1.0 ppbv).



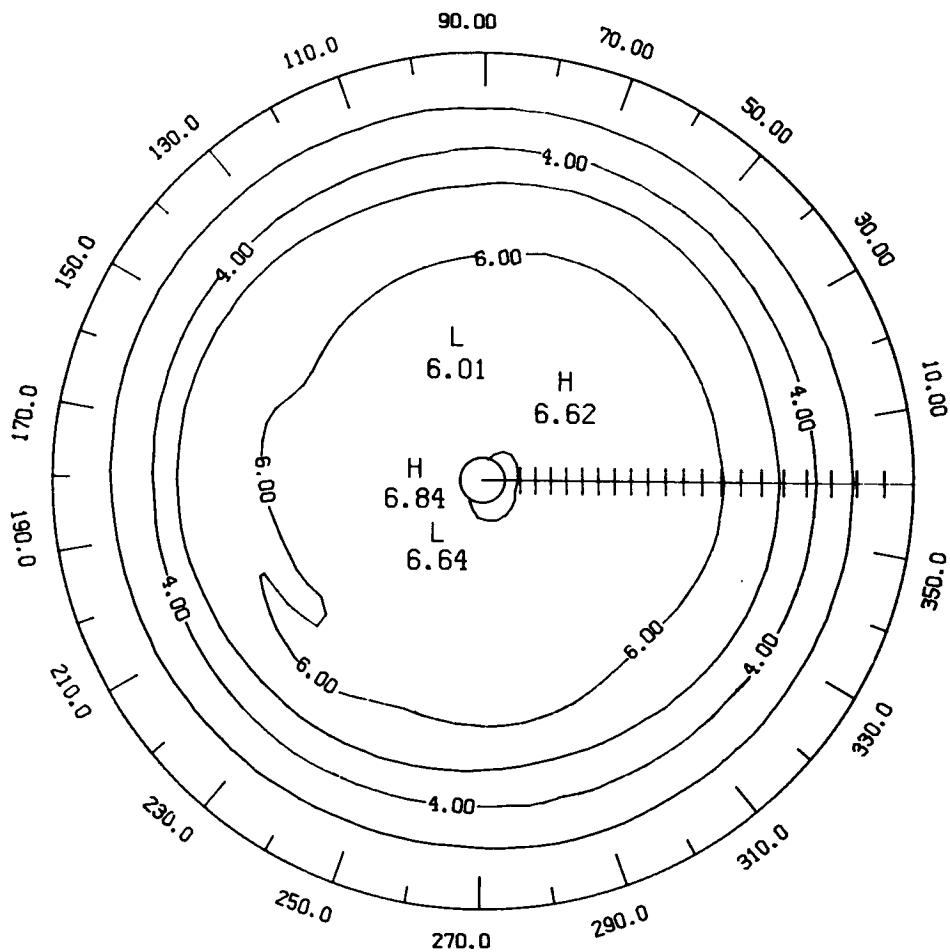
LATITUDE 0. TO 84.

Figure H-12 - LIMS monthly mean HNO₃ 30 mb polar stereographic plot for March 1979 (contour interval is 1.0 ppbv).



LATITUDE 0. TO 84.

Figure H-13 - LIMS monthly mean HNO_3 30 mb polar stereographic plot for April 1979 (contour interval is 1.0 ppbv).



LATITUDE 0. TO 84.

Figure H-14 - LIMS monthly mean HNO_3 30 mb polar stereographic plot for May 1979 (contour interval is 1.0 ppbv).

C-4

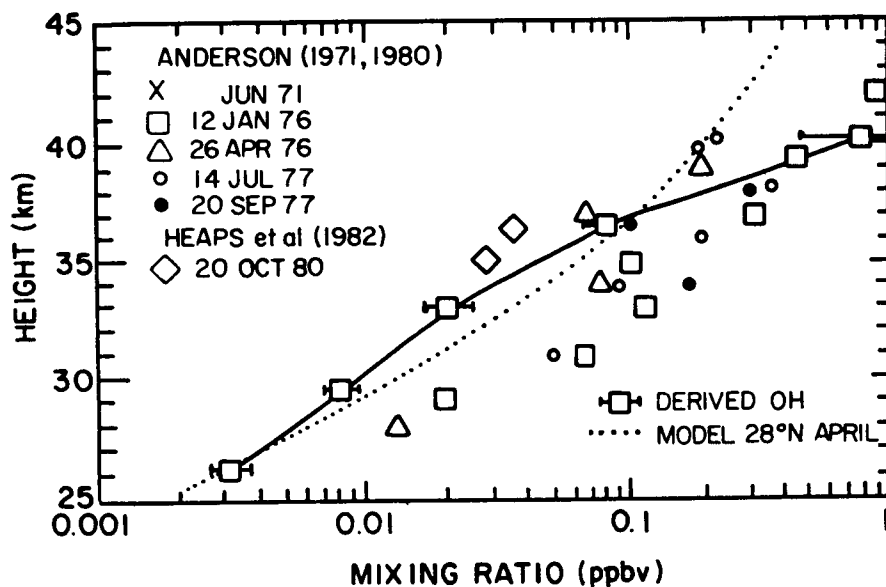


Figure H-15 - Derived OH (ppbv) at 32°N for 27 March - 1 April from LIMS data compared with in situ observations and a model calculation (From Pyle et al., 1983)

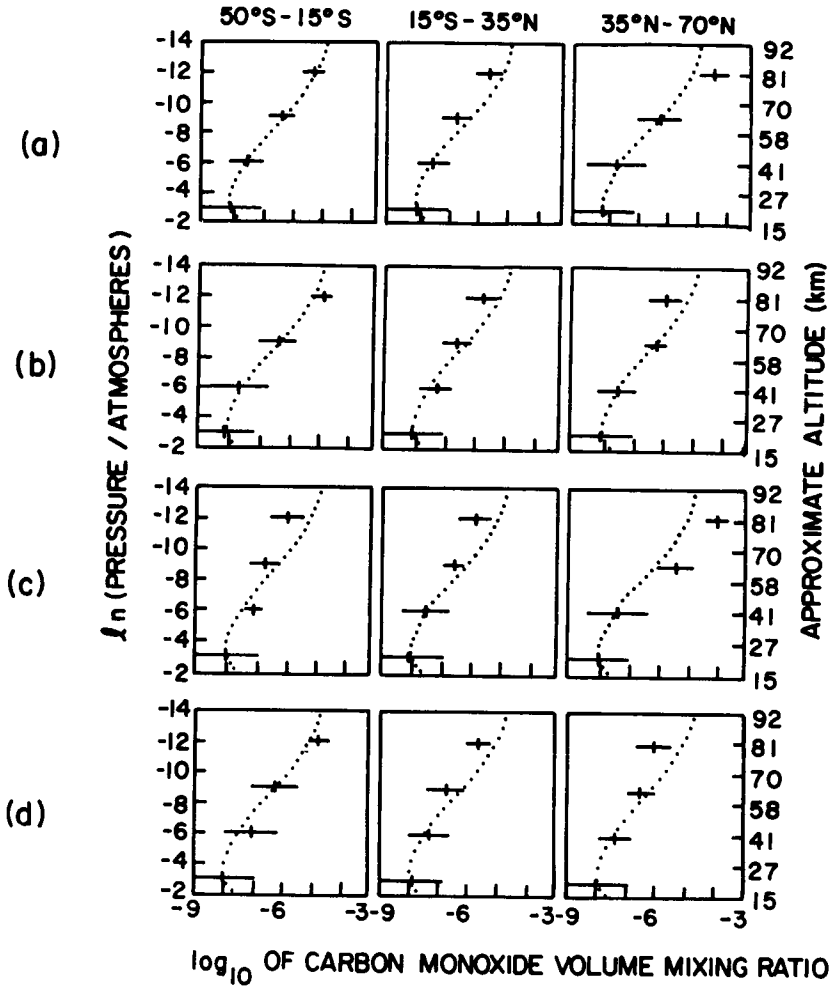


Figure CO-1 - SAMS carbon monoxide volume mixing ratio profiles averaged over latitude and time for the period from December, 1978 to November, 1980 (a) is for the period December 24, 1978 to November 31, 1979, (b) April 1, 1979 to October 1, 1979, (c) October 2, 1979 to March 1, 1980, and (d) April 1, 1980 to October 1, 1980. (from MURPHY, 1985)

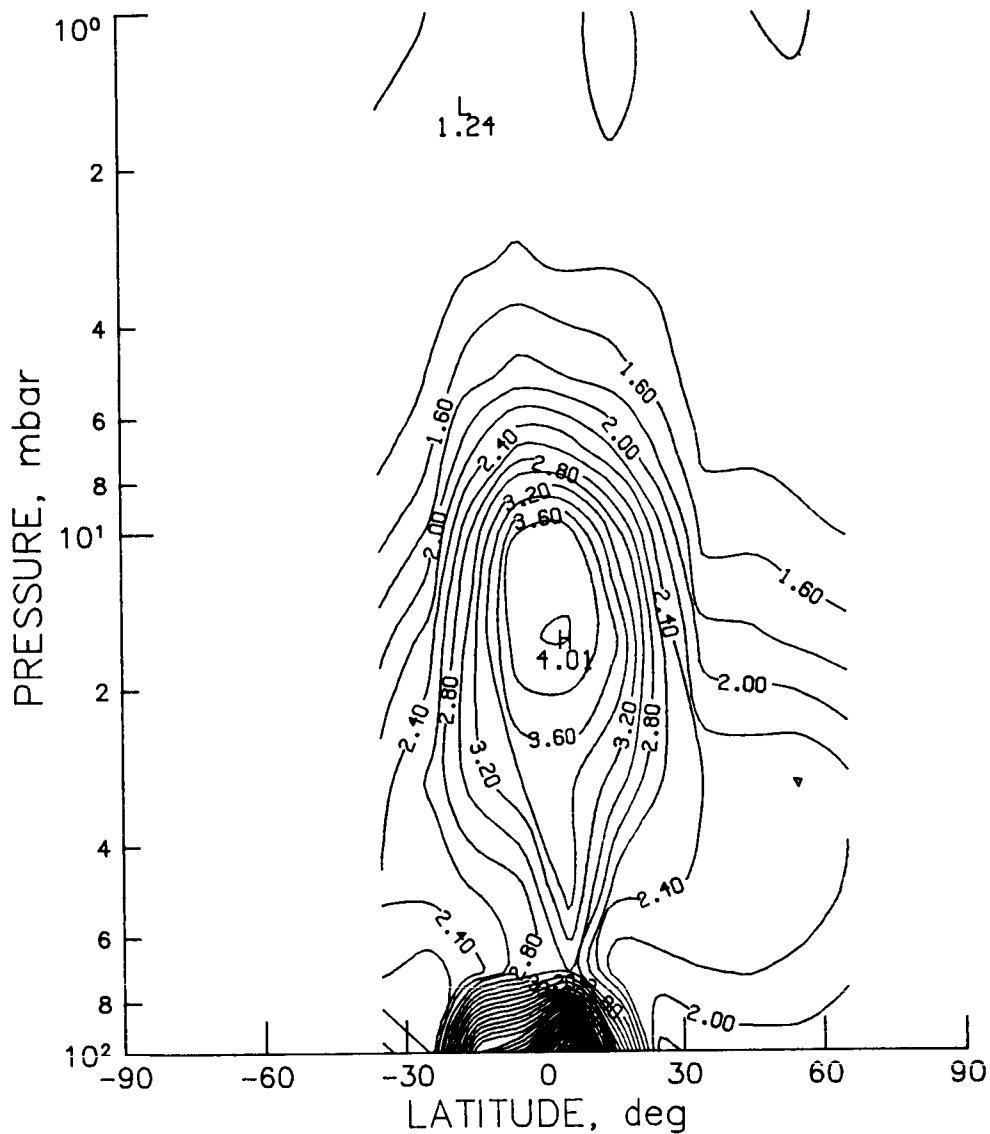


Figure A-1 - SAGE sunset monthly zonal mean aerosol extinction ratio for March 1979 (contour interval is 0.2).

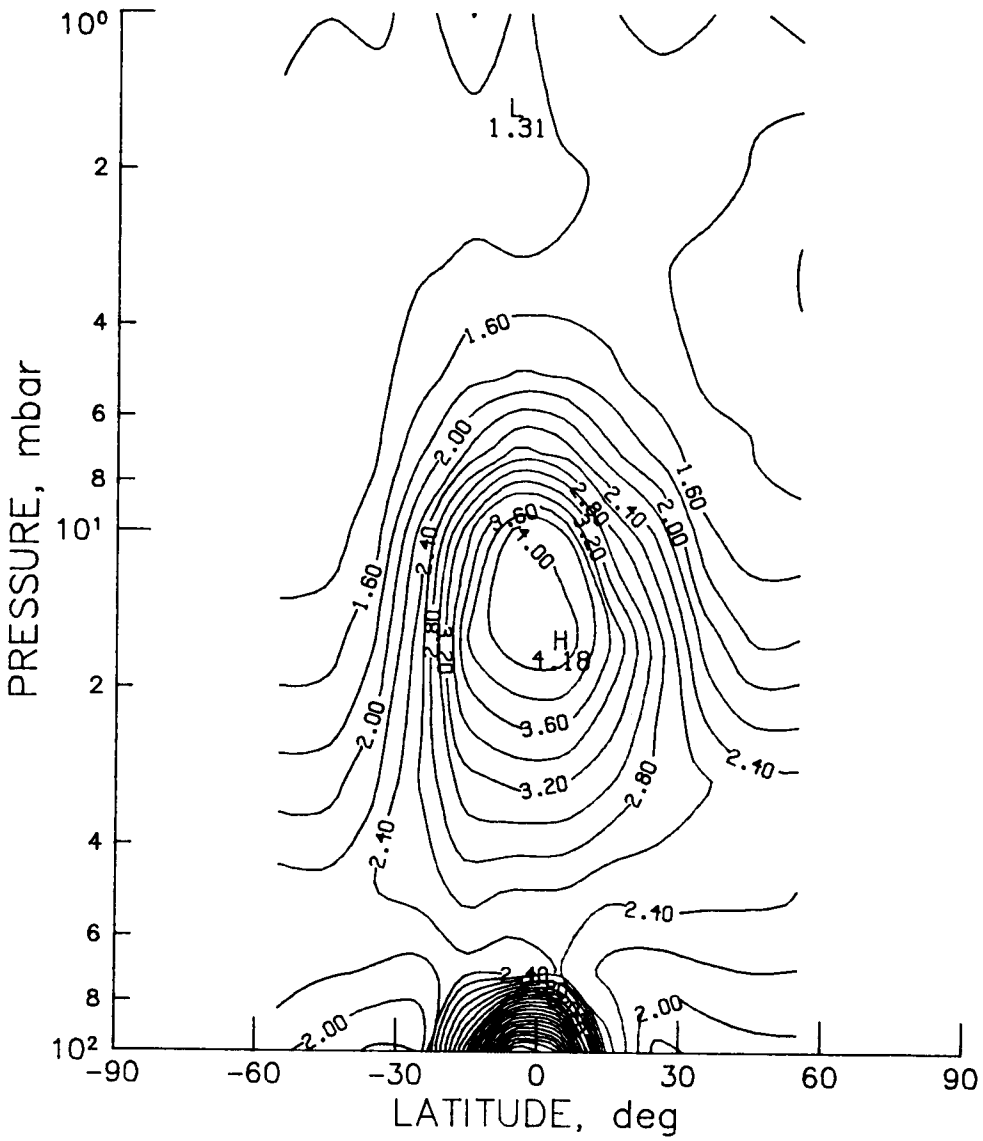


Figure A-2 - SAGE sunset monthly zonal mean aerosol extinction ratio for April 1979 (contour interval is 0.2).

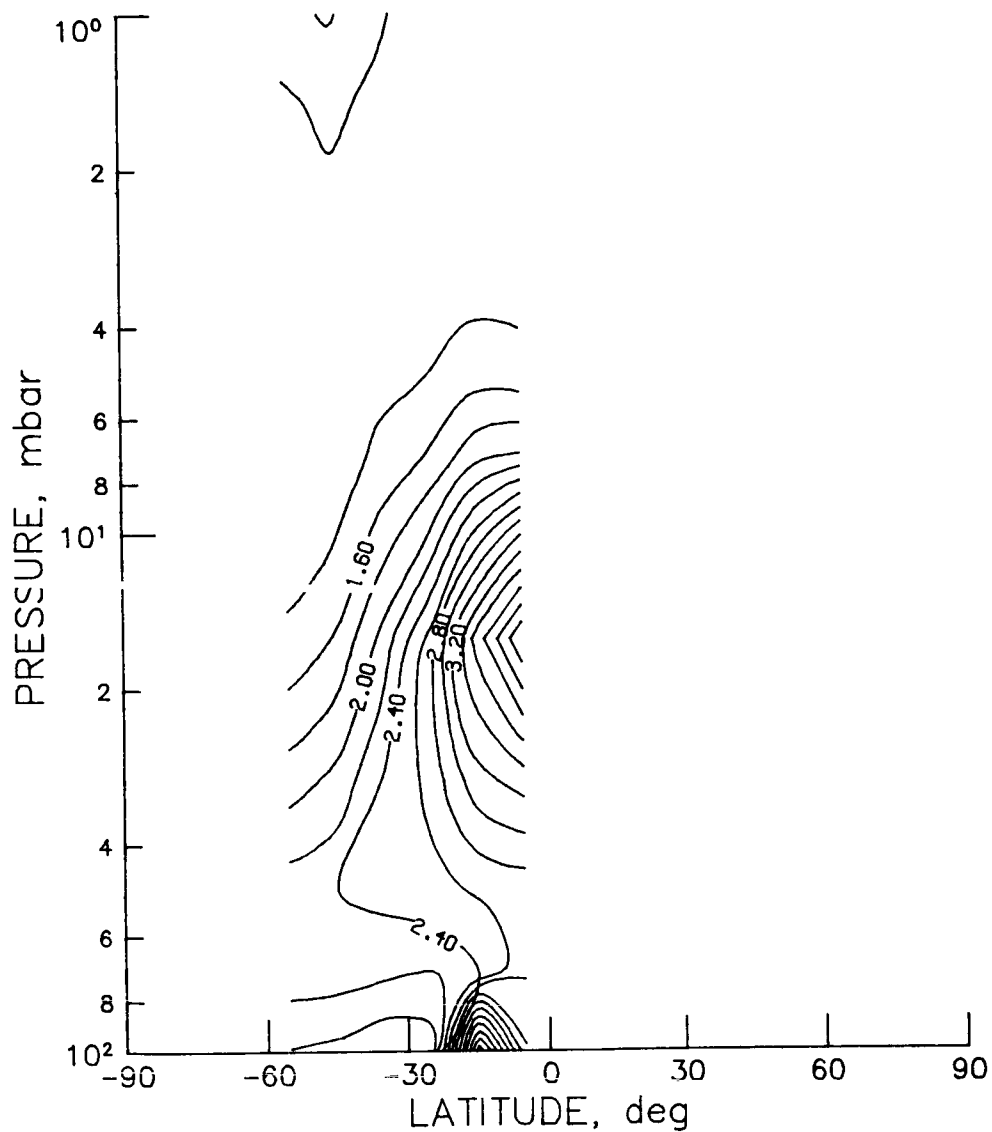


Figure A-3 - SAGE sunset monthly zonal mean aerosol extinction ratio for May 1979 (contour interval is 0.2).

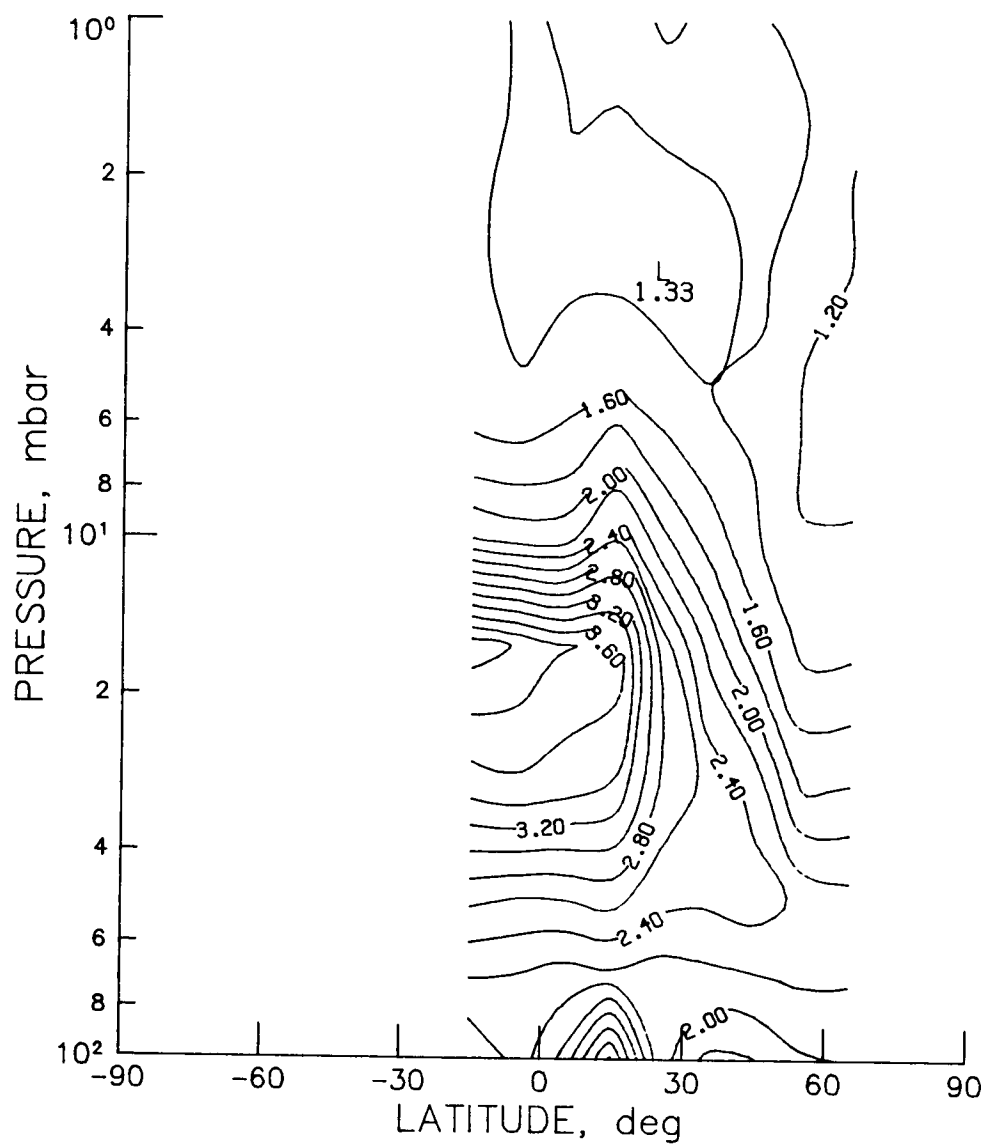


Figure A-4 - SAGE sunset monthly zonal mean aerosol extinction ratio for August 1979 (contour interval is 0.2).

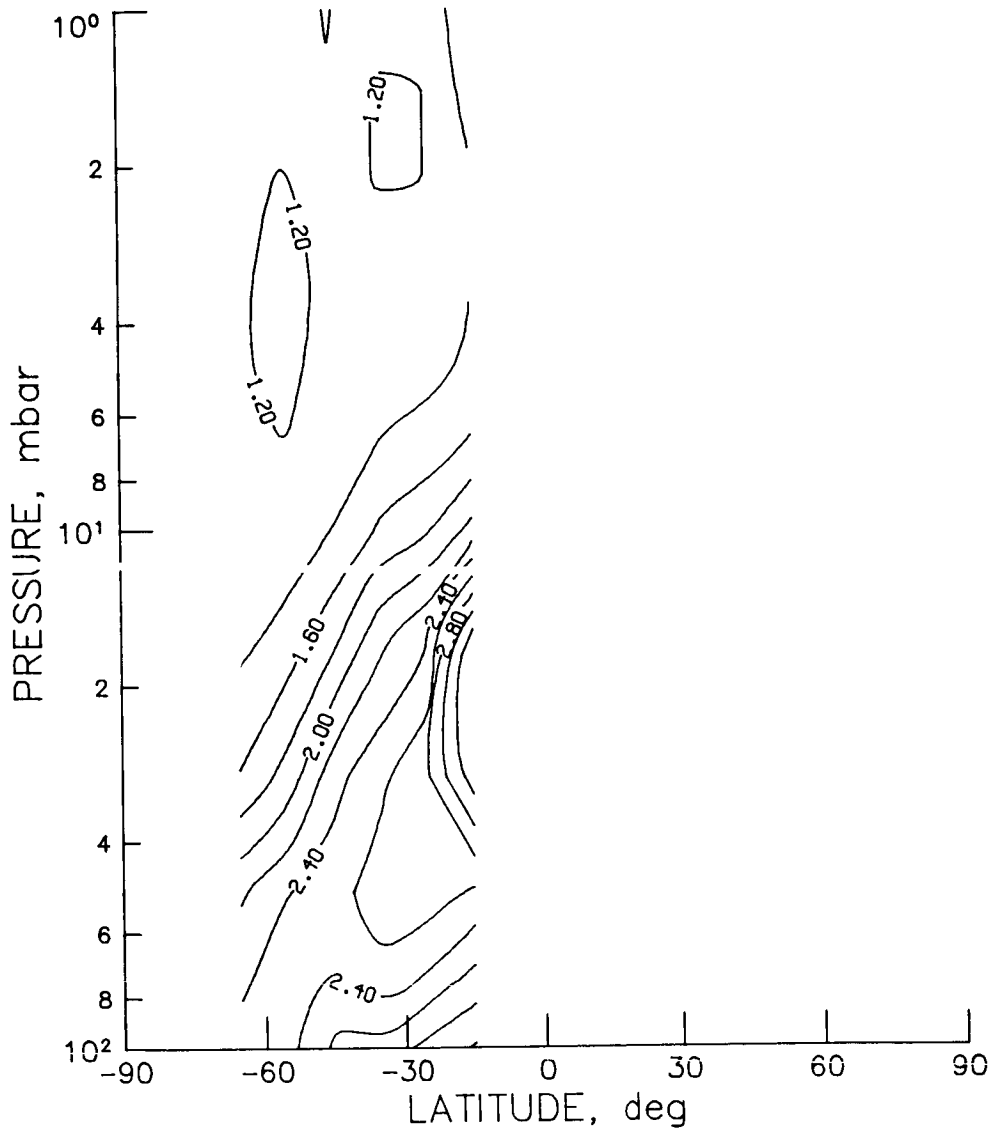


Figure A-5 - SAGE sunset monthly zonal mean aerosol extinction ratio for September 1979 (contour interval is 0.2).

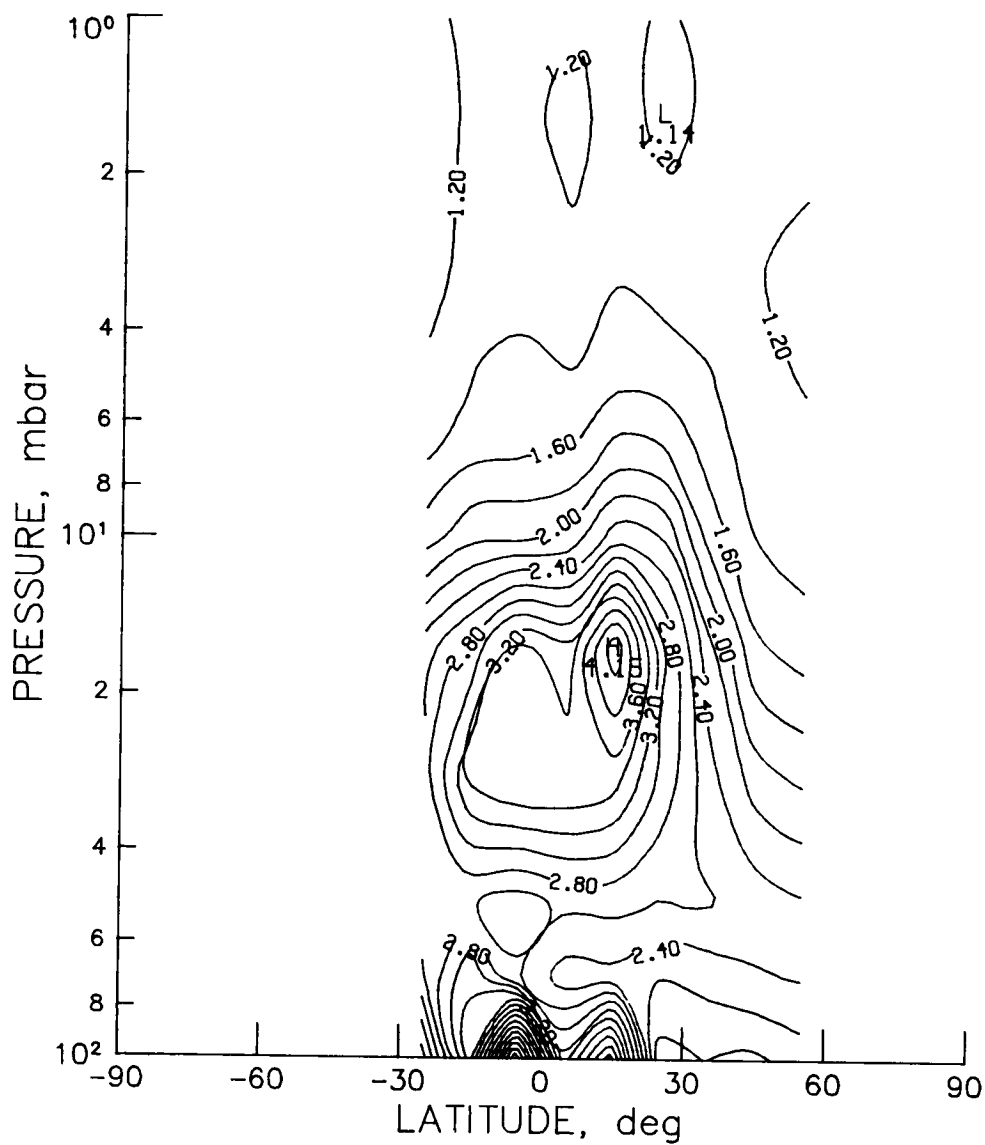


Figure A-6 - SAGE sunset monthly zonal mean aerosol extinction ratio for October 1979 (contour interval is 0.2).

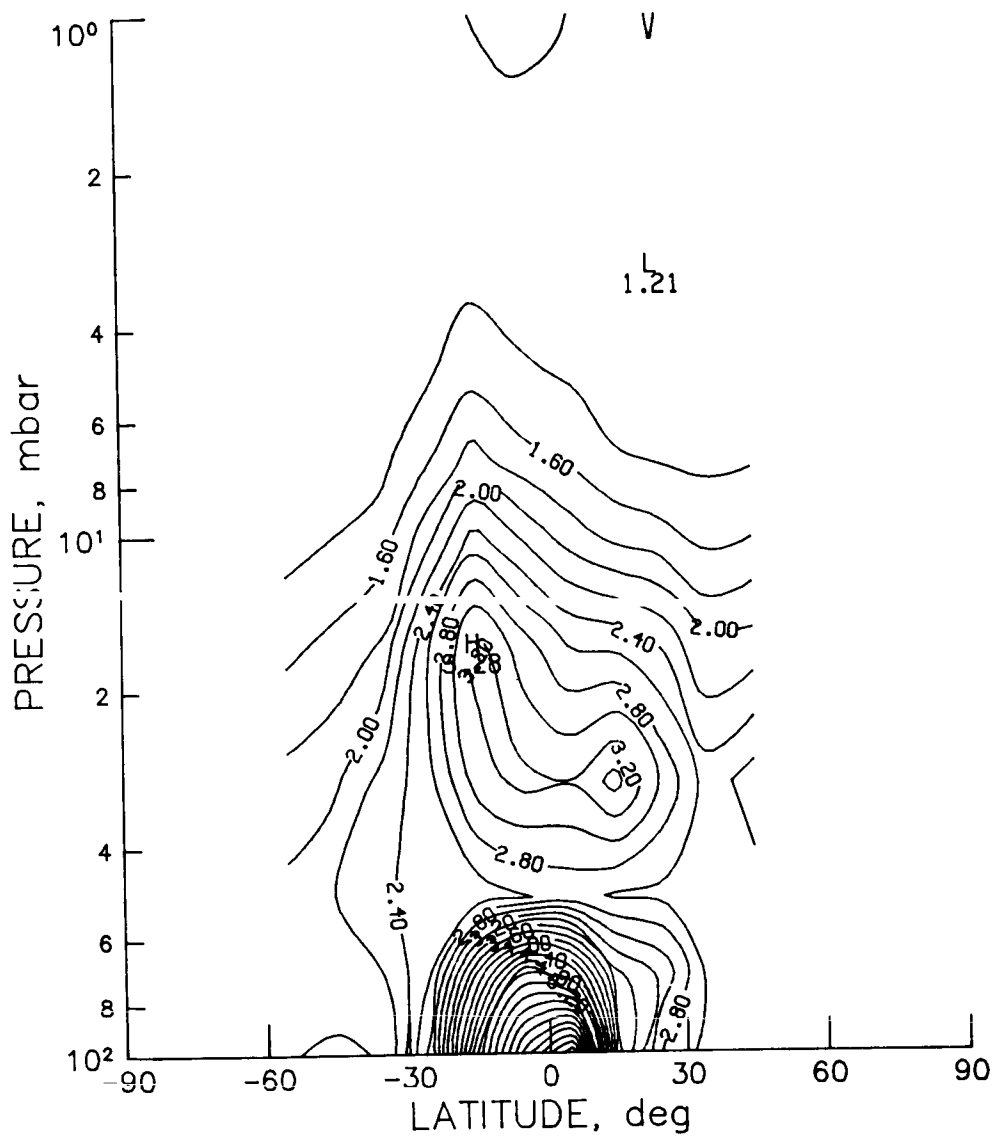


Figure A-7 - SAGE sunset monthly zonal mean aerosol extinction ratio for December 1979 (contour interval is 0.2).

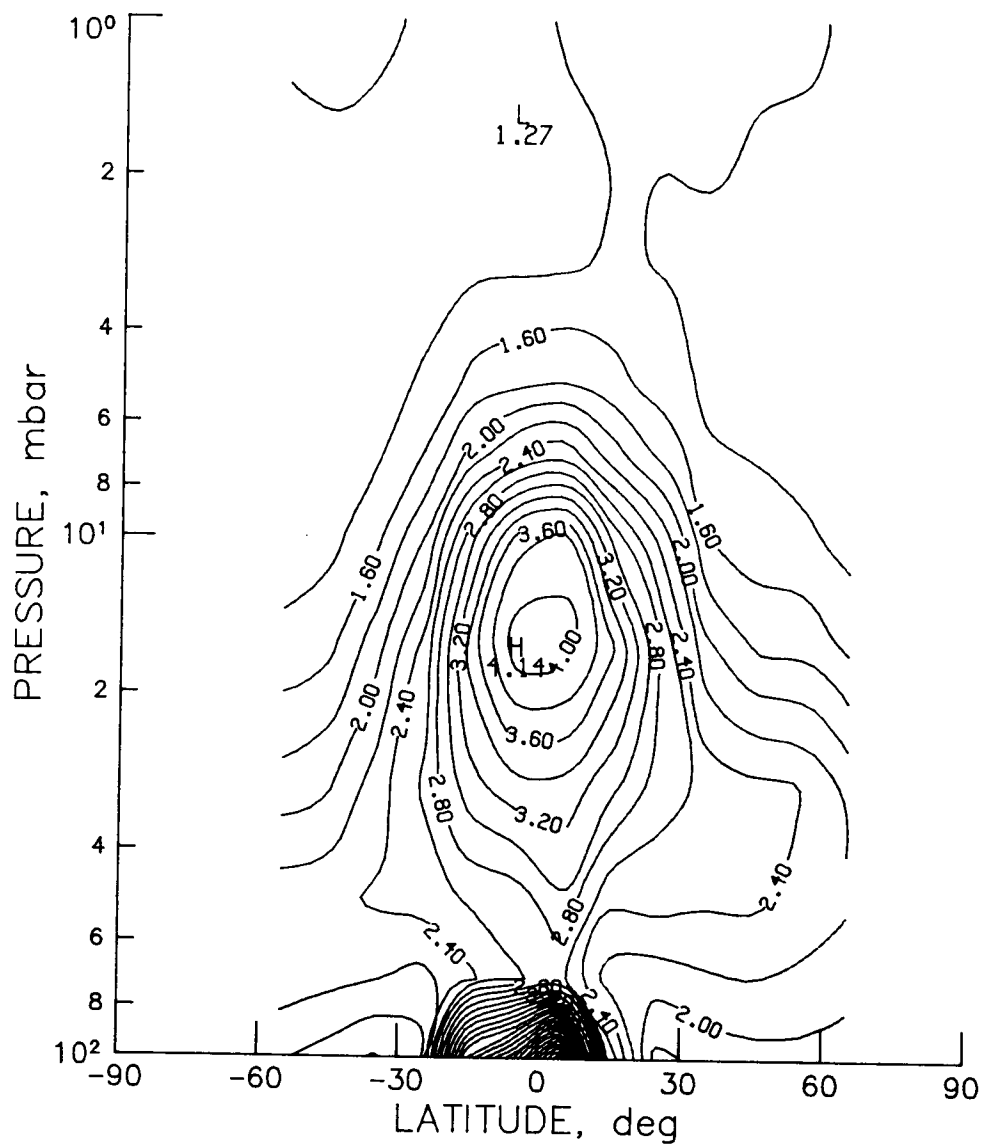


Figure A-8 - SAGE sunset seasonal zonal mean aerosol cross section for March, April, and May 1979 (contour interval is 0.2).

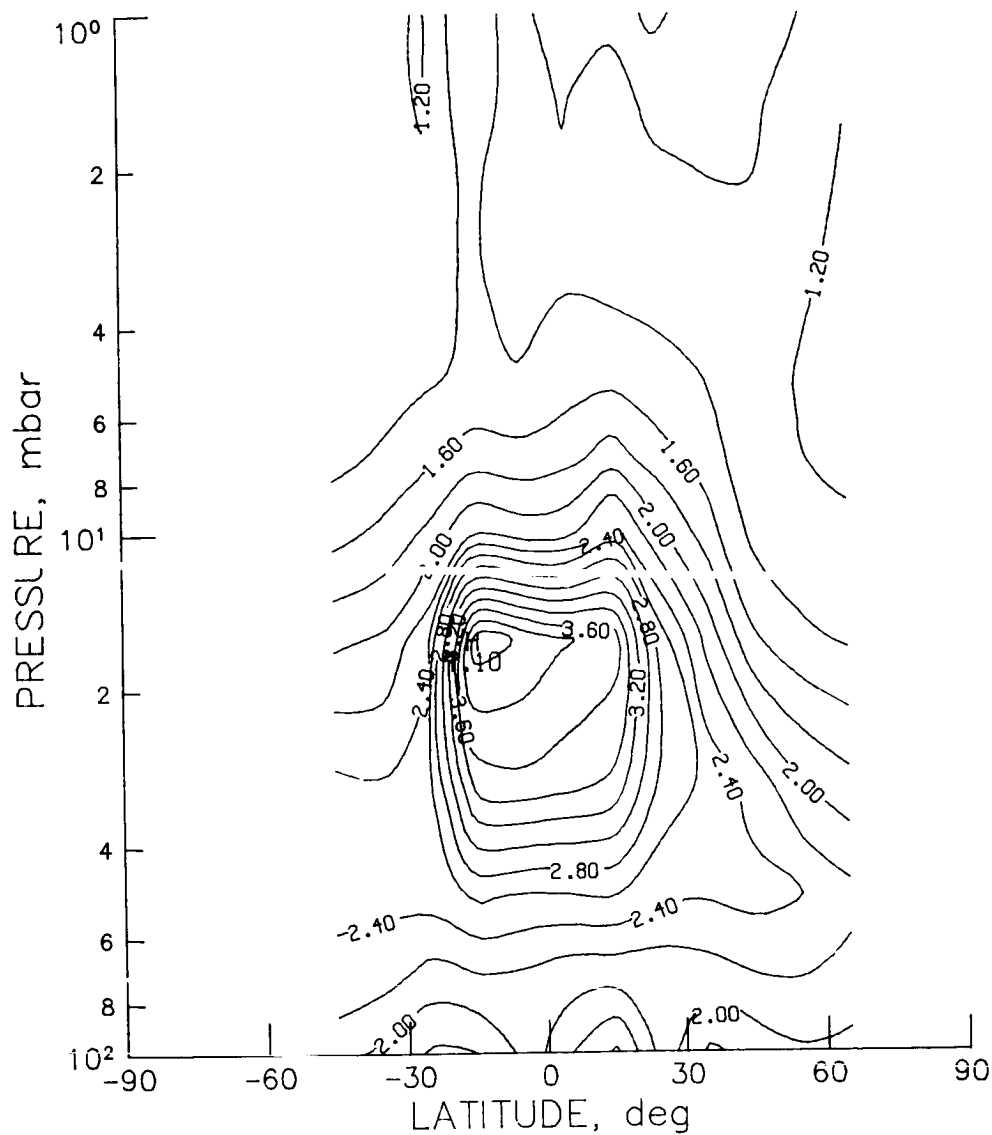


Figure A-9 - SAGE sunset seasonal zonal mean aerosol cross section for June, July, and August 1979 (contour interval is 0.2).

Figure A-10 - SAGE sunset seasonal zonal mean aerosol cross section for September, October, and November 1979 (contour interval is 0.2).

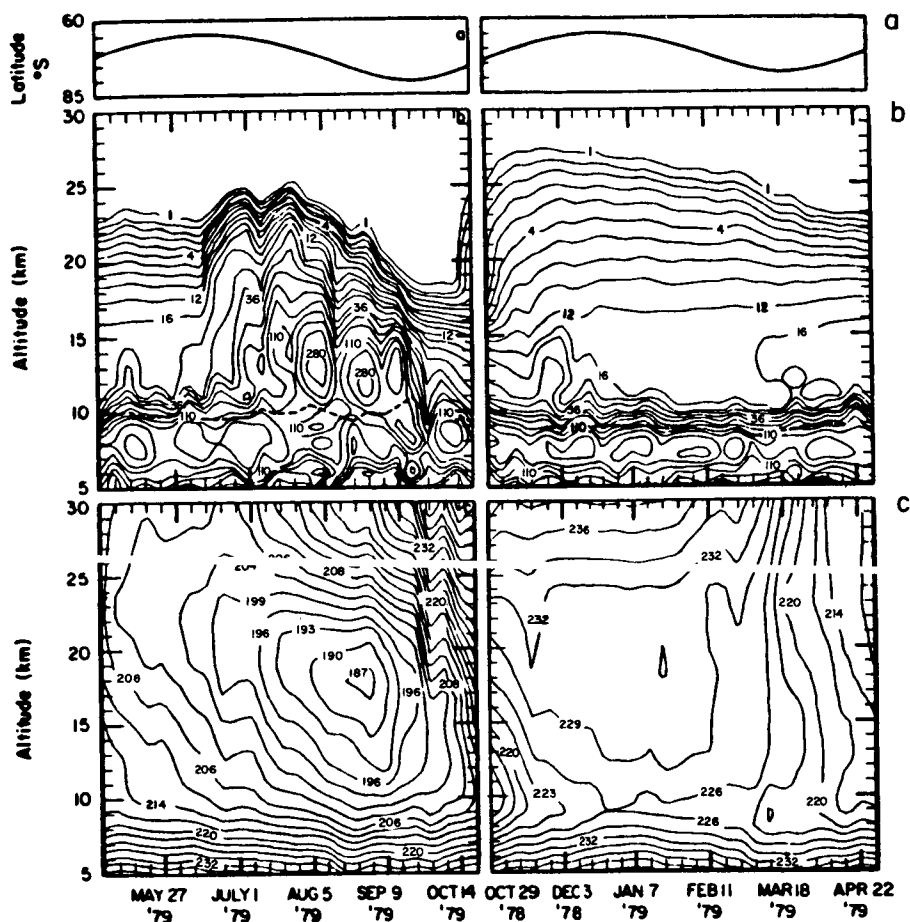


Figure A-11 - SAM II measurements in the Northern Hemisphere. Data show isopleths of weekly averaged aerosol extinction at $1.0 \mu\text{m}$, where the date marked on the horizontal axis is the first day of the week to which the average value corresponds. (a) Latitude of SAM II measurements; (b) Aerosol extinction isopleths in units of 10^{-5} km^{-1} . Dashed line shows averaged tropopause heights; (c) Corresponding temperature field at the location of aerosol measurements.

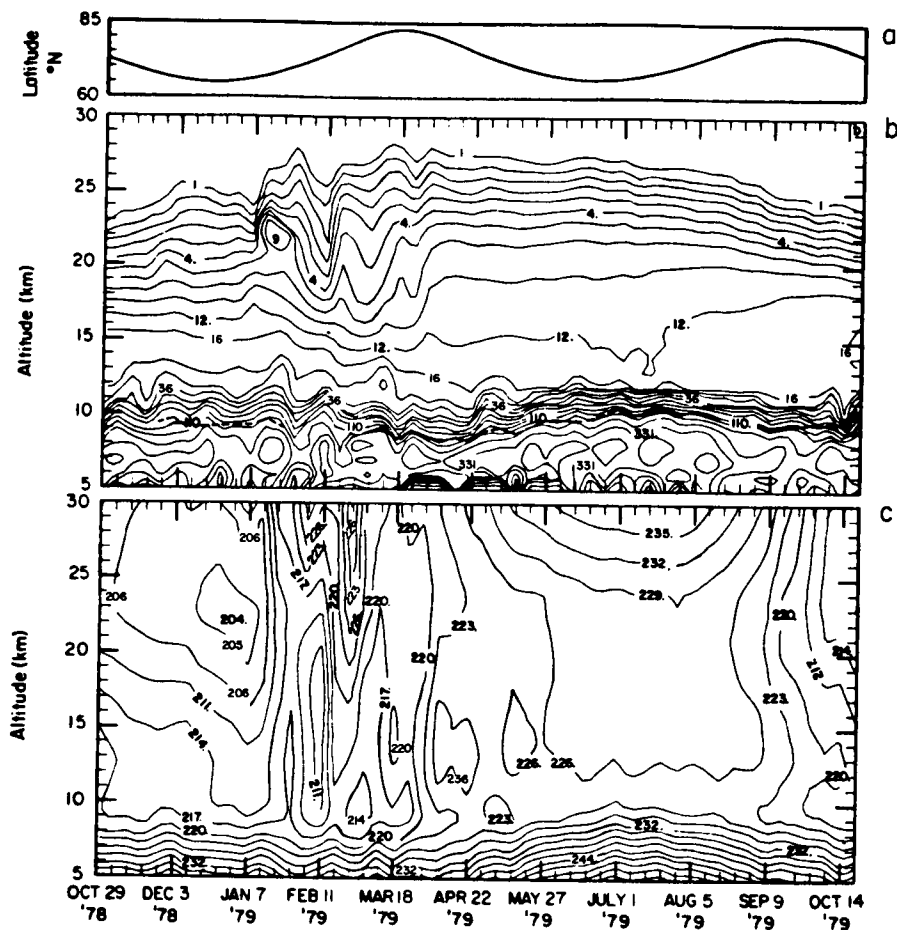


Figure A-12 - SAM II measurements in the Southern Hemisphere. Data show isopleths of weekly averaged aerosol extinction at $1.0 \mu\text{m}$, where the date marked on the horizontal axis is the first day of the week to which the average value corresponds. (a) Latitude of SAM II measurements; (b) Aerosol extinction isopleths in the units of 10^{-5} km^{-1} . Dashed line shows averaged tropopause height; (c) Corresponding temperature field at the location of the aerosol measurements. Figure A-11 covers the same time interval as Figure A-12, but the latter was divided into two halves which were interchanged so that similar seasons in the two figures are aligned.

CUMULATIVE LISTING FOR THE MAP HANDBOOK

Volume	Contents	Date of Publication
1	National Plans, PMP-1 Report, PMP-2 Report, PMP-3 Report, Approved MAP Projects	June 1981
2	Symposium on Middle Atmosphere Dynamics and Transport (Extended Abstracts)	June 1981
3	PMP-5 Report, MSG-1 Report, MSG-2 Report, MSG-3 Report, Antarctic Middle Atmosphere Project (AMA), EXOS-C Scientific Observations, WMO Report No. 5, Updated Chapter 2 of MAP Planning Document, Condensed Minutes of MAPSC Meetings	November 1981
4	Proceedings of MAP Assembly held in Edinburgh, 14-15 August 1981, Condensed Minutes of MAP Steering Committee Meetings held in Edinburgh, Proceedings of MAP Open Meeting held in Hamburg, 19 August 1981	April 1982
5	A Catalogue of Dynamic Parameters Describing the Variability of the Middle Stratosphere during the Northern Winters	May 1982
6	MAP Directory	November 1982
7	Acronyms, Condensed Minutes of MAP Steering Committee Meetings, Ottawa, May 1982, MAP Project Reports, National Reports, Committee Reports, PMP and MSG Reports, Workshop Reports, Announcements and Corrigendum	December 1982
8	MAP Project Reports: DYNAMICS, GLOBUS, and SSIM, MSG-7 Report, National Reports: Czechoslovakia, USA	July 1983
9	Papers presented at the URSI/SCOSTEP Workshop on Technical Aspects of MST Radar, May 23-27, 1983, Urbana	December 1983
10	Papers presented at the International Symposium on Ground-Based Studies of the Middle Atmosphere, May 9-13, 1983, Schwerin, German Democratic Republic	May 1984
11	Condensed Minutes of the MAP Steering Committee Meetings held in Hamburg 13-14 August 1983, Research Recommendations for Increased US Participation in the Middle Atmosphere Program, GRATMAP Project Report, MAP Study Group MSG-7 Report	June 1984
12	Coordinated Study of the Behavior of the Middle Atmosphere in Winter (PMP-1) Workshops	July 1984
13	Ground-Based Techniques	November 1984
14	Papers presented at the URSI/SCOSTEP Workshop on Technical Aspects of MST Radar, May 22-25, 1984, Urbana	December 1984
15	Balloon Techniques	June 1985
16	Atmospheric Structure and its Variation in the Region 20 to 120 km: Draft of a New Reference Middle Atmosphere	July 1985
17	Condensed Minutes of MAP Steering Committee Meeting, Condensed Minutes of MAP Assembly, MAP Projects and Study Group Reports, National Reports	August 1985
18	Papers presented at MAP Symposium, November 26-30, 1984, Kyoto (Extended Abstracts)	December 1985
19	Rocket Techniques	March 1986
20	Papers presented at the URSI/SCOSTEP Workshop on Technical and Scientific Aspects of MST Radar, October 21-25, 1985, Aguadilla, Puerto Rico	June 1986
21	MAPSC Minutes, ATMAP Workshop, Atmospheric Tides Workshop, MAP/WINE Experimenters Meetings, National Reports: Coordinated Study of the Behavior of the Middle Atmosphere in Winter	July 1986
22	Middle Atmosphere Composition Revealed by Satellite Observations	September 1986

MIDDLE ATMOSPHERE COMPOSITION REVEALED BY SATELLITE OBSERVATIONS

CONTENTS

Introduction	1
Experiment Descriptions.	4
Satellite Data Descriptions.	18
Summary.	32
References	32

FIGURES

Temperature.	39
Ozone.	77
Nitrogen	197
Methane, Nitrous Oxide, and Water Vapor.	237
Nitric Oxide	275
Carbon Monoxide.	290
Aerosols	291